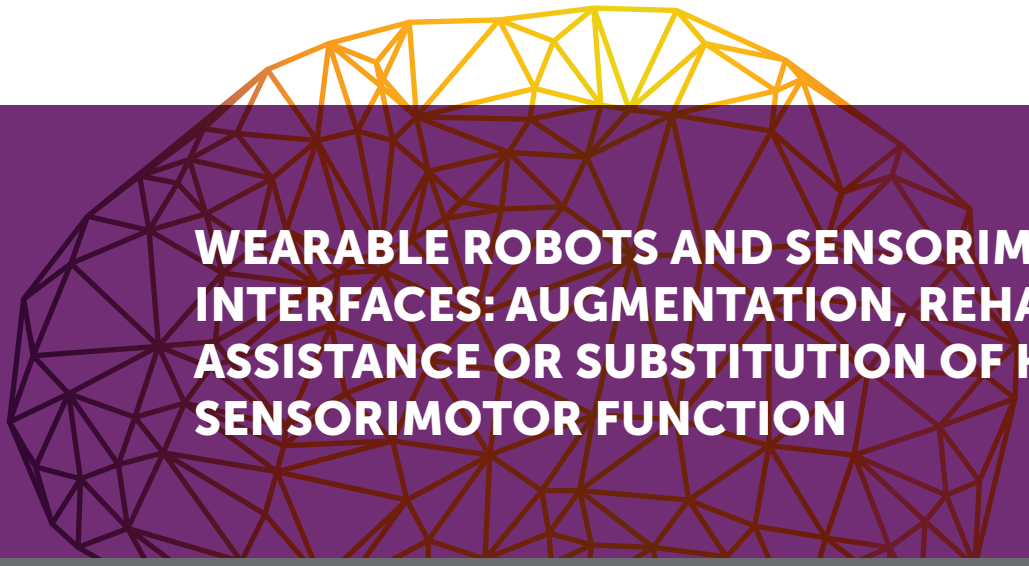

WEARABLE ROBOTS AND SENSORIMOTOR INTERFACES: AUGMENTATION, REHABILITATION, ASSISTANCE OR SUBSTITUTION OF HUMAN SENSORIMOTOR FUNCTION

EDITED BY: Irfan Hussain, Dongming Gan, Domenico Prattichizzo, Chad Gregory Rose and Yasar Ayaz

PUBLISHED IN: Frontiers in Neurorobotics

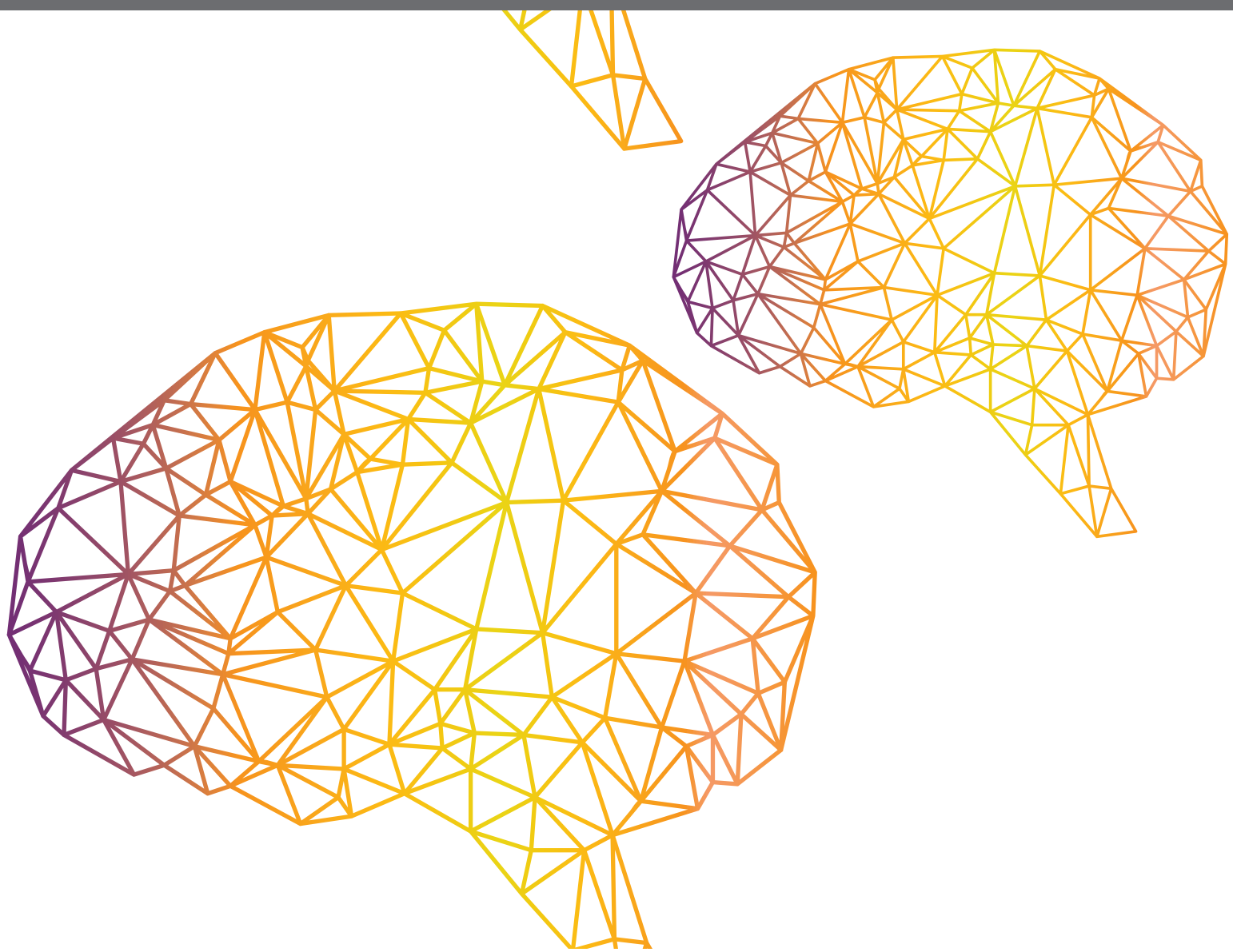

frontiers Research Topics

frontiers

ISSN 1664-8714
ISBN 978-2-88976-588-1
DOI 10.3389/978-2-88976-588-1

About Frontiers

Frontiers is more than just an open-access publisher of scholarly articles: it is a pioneering approach to the world of academia, radically improving the way scholarly research is managed. The grand vision of Frontiers is a world where all people have an equal opportunity to seek, share and generate knowledge. Frontiers provides immediate and permanent online open access to all its publications, but this alone is not enough to realize our grand goals.

Frontiers Journal Series

The Frontiers Journal Series is a multi-tier and interdisciplinary set of open-access, online journals, promising a paradigm shift from the current review, selection and dissemination processes in academic publishing. All Frontiers journals are driven by researchers for researchers; therefore, they constitute a service to the scholarly community. At the same time, the Frontiers Journal Series operates on a revolutionary invention, the tiered publishing system, initially addressing specific communities of scholars, and gradually climbing up to broader public understanding, thus serving the interests of the lay society, too.

Dedication to Quality

Each Frontiers article is a landmark of the highest quality, thanks to genuinely collaborative interactions between authors and review editors, who include some of the world's best academicians. Research must be certified by peers before entering a stream of knowledge that may eventually reach the public - and shape society; therefore, Frontiers only applies the most rigorous and unbiased reviews.
Frontiers revolutionizes research publishing by freely delivering the most outstanding research, evaluated with no bias from both the academic and social point of view. By applying the most advanced information technologies, Frontiers is catapulting scholarly publishing into a new generation.

What are Frontiers Research Topics?

Frontiers Research Topics are very popular trademarks of the Frontiers Journals Series: they are collections of at least ten articles, all centered on a particular subject. With their unique mix of varied contributions from Original Research to Review Articles, Frontiers Research Topics unify the most influential researchers, the latest key findings and historical advances in a hot research area! Find out more on how to host your own Frontiers Research Topic or contribute to one as an author by contacting the Frontiers Editorial Office: frontiersin.org/about/contact

WEARABLE ROBOTS AND SENSORIMOTOR INTERFACES: AUGMENTATION, REHABILITATION, ASSISTANCE OR SUBSTITUTION OF HUMAN SENSORIMOTOR FUNCTION

Topic Editors:
Irfan Hussain, Khalifa University, United Arab Emirates
Dongming Gan, Purdue University, United States
Domenico Prattichizzo, University of Siena, Italy
Chad Gregory Rose, Auburn University, United States
Yasar Ayaz, National University of Sciences and Technology (NUST), Pakistan

Citation: Hussain, I., Gan, D., Prattichizzo, D., Rose, C. G., Ayaz, Y., eds. (2022). Wearable Robots and Sensorimotor Interfaces: Augmentation, Rehabilitation, Assistance or Substitution of Human Sensorimotor Function.
Lausanne: Frontiers Media SA. doi: 10.3389/978-2-88976-588-1

Table of Contents

frontiers | Frontiers in Neurorobotics

EDITORIAL
published: 23 June 2022
doi: 10.3389/fnbot.2022.954865

Editorial: Wearable Robots and Sensorimotor Interfaces: Augmentation, Rehabilitation, Assistance or Substitution of Human Sensorimotor Function

Chad G. Rose[1]*, *Dongming Gan*[2] and *Irfan Hussain*[3]

[1] Department of Mechanical Engineering, Auburn University, Auburn, AL, United States, [2] Polytechnic Institute, Purdue University, West Lafayette, IN, United States, [3] Department of Mechanical Engineering, Center of Autonomous Robotics Systems, Khalifa University, Abu Dhabi, United Arab Emirates

Keywords: wearable robotics, prosthetics, control, electroencephalography, electromyography, neurorehabilitation, user-centered design

Editorial on the Research Topic

Wearable Robots and Sensorimotor Interfaces: Augmentation, Rehabilitation, Assistance or substitution of Human Sensorimotor Function

Research in wearables for rehabilitation, assistance, and augmentation have generally focused solely on motor or sensory (in particular haptic) aspects. Considering the combined sensorimotor aspects of such wearables can create new research directions, and stands to improve the function seen in state of the art devices. In this topic, authors contributed works along three broad themes: design, control, and assessment.

With the design theme of the topic, a major motivation and emphasis was placed by Varghese et al. and Alvarado-Rivera et al. on the importance of managing the pressures at the interface between the wearer and the robot, or the combined wearer-robot system and the environment in order to achieve high performance goals. The other papers in this group focused on the challenging design requirements in prosthetic hands, proposing designs to incorporate human-like capabilities or distribute the control strategies into passive or mechanically-intelligent structures. Gao et al. presented a differential mechanism to accommodate the high degrees of freedom of the hands with a reduced set of actuators. Hocaoglu and Patoglu focused on recreating the variable stiffness capabilities of human hands with a novel mechanism. Lastly, Weiner et al. developed a prosthetic hand capable of semi-autonomous grasping, relying on a multi-modal sensor network combined with adaptive underactuated mechanisms.

Several papers within the topic coalesced around a theme of control and intent detection to support wearable robotic implementations. Gantenbein et al. presented a review of intent detection strategies for upper limb orthoses. Hocaoglu and Patoglu presented an sEMG-based control strategy to leverage the performance of the variable stiffness actuator introduced in a previous paper in the topic. Instead of seeking to recreate the human impedances, Kumar et al. proposed an admittance controller to enable human-like gait on arbitrary slopes. Also aiming to improve the control of lower limb prosthetics, Hong et al. presented the connections between torso kinematics and gait phase estimation. Lastly, with a focus on rehabiliation instead of augmentation or prosthetics, Topini et al. proposed an admittance controller for use in VR training environments, and examined its performance in a single subject pilot.

Edited and reviewed by:
Florian Röhrbein, Technische Universität Chemnitz, Germany

***Correspondence:**
Chad G. Rose
chadgrose@auburn.edu

Received: *27 May 2022*
Accepted: *07 June 2022*
Published: *23 June 2022*

Citation:
Rose CG, Gan DM and Hussain I (2022) Editorial: Wearable Robots and Sensorimotor Interfaces: Augmentation, Rehabilitation, Assistance or Substitution of Human Sensorimotor Function. Front. Neurorobot. 16:954865. doi: 10.3389/fnbot.2022.954865

Several manuscripts focused on a third theme, that of assessment of the combined human-robot system. Dissanayake et al. investigated the fatigue in upper limb motions via changes detectable via EEG. Lastly, Patrick, Kumar, and Hur and Patrick, Kumar, Hong, and Hur examined the biomechanical implications of the orthotic and prosthetic kinematic structure, respectively, on the kinematics and kinetics of gait.

Taken together, the works in this Research Topic underscore the far ranging applications of considering sensorimotor aspects in wearable robotics, ranging from the design of human-robot interfaces to EEG assessments. These new designs and results are another step toward achieving the potential of wearables, but there are still many open questions and unknowns in this highly interdisciplinary field, which will require further investigation and collaboration.

A fundamental limitation in the current research model is the difficulty at achieving long duration studies with large population sizes. In some areas, this may be overcome via commercialization, but in others, the field may need to rely on large studies on standardized equipment, such as open-source designs, such as the Open Source Leg (Azocar et al., 2020), which can be a starting point toward accumulating the "big data" which drives much innovation in robotics and machine learning.

To make the next generation of devices, controllers, and interfaces, assessment and inclusion of end users in the initial design and validation process, such as the usability and evaluation from authors such as Gantenbien et al. are the first steps in this direction. Next steps may look like the creation of standardized performance metrics and methods, such as those proposed for prosthetics (Light et al., 2002) for orthoses, or open-source designs for wearer surrogates such as mannikins to complement standard object sets (Calli et al., 2015). Additional efforts aimed at enabling end users to be not only the assessors, but the designers, can further democratize and accelerate the design process.

While kinematic and kinetic assessments have been well established, with advances presented in this topic, the field can also benefit from additional investigation into the connections between sensory and motor function, such as Lowrey et al. (2020). Future work could further tease out the interconnections between motor and sensory function, identifying new design guidelines, control strategies, and assessment methods for all the wearable devices including the one newly proposed and known as supernumerary robotics limbs (Hussain and Prattichizzo, 2020).

Lastly, and at the risk of understatement, the future work is dependent on continued advancement in the miniaturization, proliferation, and optimization of the requisite mechatronic subsystems. As these fields advance, wearable robotics need to be prepared to take advantage of the opportunities the latest, lightest, most efficient, and lowest-cost batteries, sensors, and actuators, and computational resources affords us.

AUTHOR CONTRIBUTIONS

All authors listed have made a substantial, direct, and intellectual contribution to the work and approved it for publication.

FUNDING

This work was partially supported by the Khalifa University of Science and Technology under Award No. RC1-2018-KUCARS and FSU-2021-019.

ACKNOWLEDGMENTS

The authors are grateful to the co-editors of the topic Domenico Prattichizzo and Yasar Ayaz for their contributions to the conception and management of the topic.

REFERENCES

Azocar, A. F., Mooney, L. M., Duval, J.-F., Simon, A. M., Hargrove, L. J., and Rouse, E. J. (2020). Design and clinical implementation of an open-source bionic leg. *Nat. Biomed. Eng.* 4, 941–953. doi: 10.1038/s41551-020-00619-3

Calli, B., Walsman, A., Singh, A., Srinivasa, S., Abbeel, P., and Dollar, A. M. (2015). Benchmarking in manipulation research: the ycb object and model set and benchmarking protocols. *arXiv[Preprint].arXiv:1502.03143*. doi: 10.1109/MRA.2015.2448951

Hussain, I., and Prattichizzo, D. (2020). *Augmenting Human Manipulation Abilities with Supernumerary Robotic Limbs*. Cham: Springer.

Light, C. M., Chappell, P. H., and Kyberd, P. J. (2002). Establishing a standardized clinical assessment tool of pathologic and prosthetic hand function: normative data, reliability, and validity. *Arch. Phys. Med. Rehabil.* 83, 776–783. doi: 10.1053/apmr.2002.32737

Lowrey, C. R., Blazevski, B., Marnet, J.-L., Bretzke, H., Dukelow, S. P., and Scott, S. H. (2020). Robotic tests for position sense and movement discrimination in the upper limb reveal that they each are highly reproducible but not correlated in healthy individuals. *J. Neuroeng. Rehabil.* 17, 1–13. doi: 10.1186/s12984-020-00721-2

Conflict of Interest: The authors declare that the research was conducted in the absence of any commercial or financial relationships that could be construed as a potential conflict of interest.

Publisher's Note: All claims expressed in this article are solely those of the authors and do not necessarily represent those of their affiliated organizations, or those of the publisher, the editors and the reviewers. Any product that may be evaluated in this article, or claim that may be made by its manufacturer, is not guaranteed or endorsed by the publisher.

frontiers in Neurorobotics

ORIGINAL RESEARCH
published: 18 October 2021
doi: 10.3389/fnbot.2021.702031

On Differential Mechanisms for Underactuated, Lightweight, Adaptive Prosthetic Hands

Geng Gao[1†], *Mojtaba Shahmohammadi*[1†], *Lucas Gerez*[1], *George Kontoudis*[2] *and Minas Liarokapis*[1*]

[1] New Dexterity Research Group, Department of Mechanical Engineering, University of Auckland, Auckland, New Zealand,
[2] The Bradley Department of Electrical and Computer Engineering, Virginia Tech, Blacksburg, VA, United States

Over the last decade underactuated, adaptive robot grippers and hands have received an increased interest from the robotics research community. This class of robotic end-effectors can be used in many different fields and scenarios with a very promising application being the development of prosthetic devices. Their suitability for the development of such devices is attributed to the utilization of underactuation that provides increased functionality and dexterity with reduced weight, cost, and control complexity. The most critical components of underactuated, adaptive hands that allow them to perform a broad set of grasp poses are appropriate differential mechanisms that facilitate the actuation of multiple degrees of freedom using a single motor. In this work, we focus on the design, analysis, and experimental validation of a four output geared differential, a series elastic differential, and a whiffletree differential that can incorporate a series of manual and automated locking mechanisms. The locking mechanisms have been developed so as to enhance the control of the differential outputs, allowing for efficient grasp selection with a minimal set of actuators. The differential mechanisms are applied to prosthetic hands, comparing them and describing the benefits and the disadvantages of each.

Keywords: upper-limb prosthesis, differential mechanisms, robot hands, grasping, underactuated mechanisms

Edited by:
Irfan Hussain,
Khalifa University,
United Arab Emirates

Reviewed by:
Dong Hyun Kim,
Korea Advanced Institute of Science and Technology, South Korea
Wenbin Chen,
Huazhong University of Science and Technology, China

***Correspondence:**
Minas Liarokapis
minas.liarokapis@auckland.ac.nz

*These authors share first authorship

Received: *28 April 2021*
Accepted: *12 July 2021*
Published: *18 October 2021*

Citation:
Gao G, Shahmohammadi M, Gerez L, Kontoudis G and Liarokapis M (2021) On Differential Mechanisms for Underactuated, Lightweight, Adaptive Prosthetic Hands. Front. Neurorobot. 15:702031. doi: 10.3389/fnbot.2021.702031

1. INTRODUCTION

The human hand is a powerful tool enabling humans to perform a wide range of tasks that range from interacting with objects used in daily living to executing gestures in social activities. According to Ziegler-Graham et al. (2008), approximately 540,000 amputees have suffered from upper limb loss in the US, with the expected projections to be doubled by 2050. In Italy and the UK, approximately 3,500 and 5,200 upper limb amputations occur every year (Cordella et al., 2016). Amputations can have a detrimental effect on an amputee's quality of life, preventing them from executing critical grasps needed in activities of daily living (ADL).

The latest technological advancements have helped improve prosthetic hand development toward becoming increasingly dexterous devices. Despite this, design tradeoffs between the dexterity of the prosthesis and weight, form factor, and cost of the device still exist (Bicchi, 2000). Although there are highly dexterous robot hands capable of emulating the dexterity of the human hand (Kochan, 2005; Grebenstein et al., 2010; Cerulo et al., 2017), the number of independent degrees of freedom (DOF) and the actuators utilized make it challenging to control

such devices without compromising the weight, form factor, and affordability needed by amputees so as to adopt these hands for ADL.

In order to develop affordable, lightweight, and compact prostheses, researchers have employed synergistic methods (Xiong et al., 2016; Della Santina et al., 2018) and adaptive systems through the use of differential mechanisms that reduce the number of actuators needed to control multiple fingers simultaneously. Differential mechanisms in adaptive robotic and prosthetic hands distribute a single input torque to numerous fingers, resulting in stable and efficient grasps (Birglen et al., 2007). Such mechanisms allow the fingers to passively adapt to object shapes during the grasp, maximizing the number of contact points. The maximization of the contact areas during grasping also leads to the maximization of the grasping stability (Liarokapis et al., 2015). An even force/torque transmission in prosthetic and robotic devices can be achieved by different types of mechanisms, such as geared differentials, ball differentials, combination of pulleys, whiffletree mechanisms, and fluidic differentials. The geared differential is the most popular mechanism for force/torque transmission, and it is applied in different fields. This system can be implemented with different gears, such as planetary gears, spur gears, and bevel gears. The geared differential's main advantages is the ability to handle large torques and constant torque output regardless of the configuration. However, the added complexity of gears can make the implementations large and heavy (Martin et al., 2004; Birglen et al., 2007). Different from the geared differentials, ball differentials can be easily miniaturized by replacing a set of gears with several miniature ball bearings rotating between two plates (Keller et al., 2015). On the other hand, ball differentials require constant maintenance and can handle less torque than the traditional gear differentials.

Another type of differentials, the pulley differentials, use multiple moving pulleys to convert a single input into multiple outputs. Selection of pulley diameters and arrangements can be made to offer a mechanical advantage to the system so as to improve the force exertion capabilities (Ma et al., 2013). However, the main disadvantage of the floating pulley systems is that they need to maintain tension in the cables as loose cables can cause them to escape from the pulleys compromising the tendon routing. Similar to the pulley differential, in the whiffletree differential, a series of cables/tendons are used to suspend a floating mechanism/bar, which distributes a force equally across the outputs. Instead of pulleys, the whiffletree differential uses levers/bars. The tendons are attached to the end of the levers. Although the design is compact, the levers can limit the range of motion that is achievable by the differential.

Finally, an unusual type of differential mechanism applied to robotic devices is the fluidic t-pipe differential. This differential utilizes fluids such as air, water, or oil to transmit force from an input to multiple outputs through t-pipes (Birglen and Gosselin, 2006). Unlike traditional differentials, the ability of the fluid used to compress can provide actuation compliance to the system. Although such a differential mechanism allows for the absorption of shocks depending on the selected type of fluid, leaking phenomena typically affect the performance and robustness of the mechanism making it hard to repair and maintain and leaks may damage neighboring components.

Many authors have employed differential mechanisms in prosthetic hands. In Kontoudis et al. (2015) and Leddy and Dollar (2018), the authors introduce robotic hands that use whiffletree differential mechanisms to control the robot fingers using a single motor. The whiffletree differentials evenly transmit the forces among the fingers. However, they require additional space to operate, and a precise tendon tension calibration is needed. In Gosselin et al. (2008) and Belter and Dollar (2013), the authors describe the design of robot hands that uses pulley differentials and one actuator to actuate five fingers simultaneously. Multiple objects can be grasped with these lightweight designs. Similarly, the pulley mechanisms take a considerable amount of space in the robotic hands. Additionally, the friction between the tendons and the pulleys reduces the efficiency of the system.

In Xu et al. (2015), the authors proposed a continuum differential mechanism applied to a prosthetic hand. The particular robotic device employs one actuator and combines a rack-pinion-based system and the traditional whiffletree mechanism to drive five fingers. In Cheon et al. (2014), the authors proposed a robotic hand using a differential gear mechanism to distribute one input from the actuator to the finger joints. In Cipriani et al. (2011), Mitsui et al. (2013), and Chen et al. (2015), the authors used elastic elements connected in-between the driveshaft and the actuated fingers to achieve an adaptive transmission, which allows the robot hand to conform to the grasped object. Although the transmission facilitates adaptive grasping, the system requires additional force to be applied to deform the elastic element and produce adaptive behaviors at the outputs, consuming more energy compared to other differential systems. One of the advantages of the aforementioned robotic grippers is that they can grasp a wide range of objects without requiring complex control algorithms or force sensors at the finger pads. Additionally, the use of a minimal number of actuators, such a design advantage makes this category of robot hands intuitive to operate and highly affordable.

In order to expand the capabilities of underactuated devices, appropriate locking mechanisms have been employed by researchers to facilitate the execution of various grasp poses and gestures in prosthetic hands. In Belter and Dollar (2013), the authors proposed the use of a bistable ratchet locking mechanism to enable control over the opposition of the thumb allowing for four independent grasping postures to be achieved with a single actuator. In Baril et al. (2013), the authors designed mechanical selectors, which are capable of obstructing the motion of a whiffletree differential allowing for three grasping modes to be executed with a single actuator by adjusting a slider-selector with the intact hand. However, this design is limited to a maximum of three grasping postures requiring the user to switch between different slider-selectors to achieve alternative grasping postures. In Chu et al. (2008) on the other hand, the authors used a cam ball clutch lock the robotic fingers in various configurations to conserve motor power. However, when wedging the balls into the cam to prevent further motion, a high wear rate from the friction is experienced in the mechanism. This wearing effect limits the

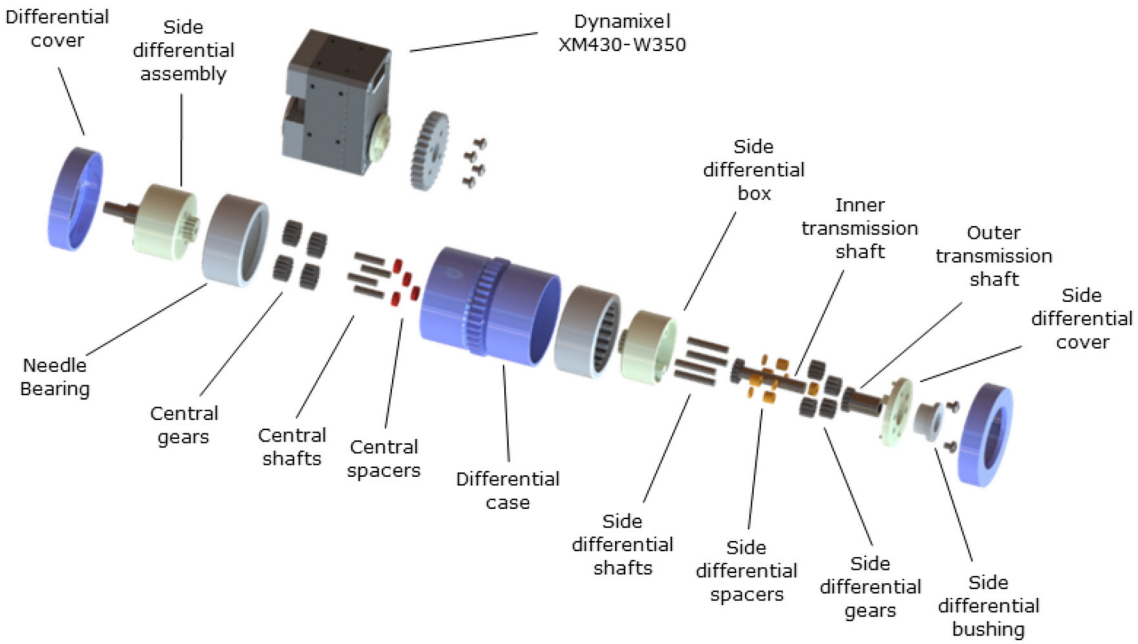

FIGURE 1 | The four-output gear differential consists of three main structures: a central barrel and two lateral assemblies. The central barrel is composed of the differential case, two needle bearings, and four central gears, shafts, and spacers. The integrated gear on the differential case allows input torque from the Dynamixel XM430-W350-R motor to provide power to the mechanism. Each lateral assembly is comprised of an inner and outer transmission shaft, where the outer shaft is hollow to facilitate the inner shaft. Bushings and bearings in the system allow the system to rotate with minimal friction and in an efficient manner.

materials that can be used in prosthetic hands compromising their durability, which is of critical importance.

In this paper, we present two different types of differential mechanisms and various manual and automated selectively lockable differential mechanisms that can be applied to underactuated, lightweight, adaptive prosthetic hands. The proposed designs are experimentally evaluated, and we also compare them, discussing the benefits, applicability, and disadvantages of each of them. The rest of the paper is organized as follows: section Design presents the designs of the four types of differential mechanisms, section Experiments and Results details the experimental setup used for the tests and presents the experimental results, section Discussion discusses the advantages and disadvantages of the differentials developed, while section conclusion concludes the paper.

2. DESIGN

In this section, we present the designs of the proposed differential mechanisms as well as the designs of the manual and automated lockable mechanisms that have been implemented and integrated into the developed differentials to provide control over the outputs.

2.1. Four-Output Gear Differential

The four-output gear differential mechanism is composed of three main parts, a central barrel, and two different lateral assemblies, as shown in **Figure 1**. The central barrel is composed of a plastic cylinder, two needle bearings, and a combination of four spur gears that operate as a spur gear differential (Biermann et al., 2013). The outside geared ring is used to provide the torque input. Each lateral assembly is composed of six gears, two steel shafts, and a plastic case with a geared tip connected to the central barrel. A spur gear is connected to the end of the inner and outer shaft. Each lateral assembly has two shafts directed to the same side, an inner and an outer shaft. The outer shaft has a hollowed center where the inner shaft is placed, allowing both shafts to rotate with minimal friction. The bearings in the central barrel allow for the free rotation of the lateral assemblies. Such a design choice guarantees that all four shafts are placed on the same axis that facilitates a four-output gear differential operation. **Figure 2** shows the position of the differential when incorporated into a prosthetic hand. The operation of the four-output gear differential is depicted in **Figure 3**.

In order to determine the most suitable motor and the gear ratio required between the motor and the differential mechanism, the maximum applicable forces of each output were calculated by applying (Equations 1–5). More precisely, τ_d is defined as the torque applied to the differential that is divided into four outputs, τ_1, τ_2, τ_3, and τ_4 (Equation 1). The torque is equally distributed among the outputs, as shown in Equation (2).

$$\tau_d = \tau_1 + \tau_2 + \tau_3 + \tau_4 \tag{1}$$

$$\tau_1 = \tau_2 = \tau_3 = \tau_4 = \frac{\tau_d}{4} \tag{2}$$

The output torque can be written in terms of the tendon tension (tangential force) and the radius of the pulley (Equation 3). The radius of all pulleys are the same, so the tension of all tendons will also be the same.

$$\tau_i = F_i r_i \tag{3}$$

The torque of the differential is proportional to the torque applied by the motor, τ_m, being multiplied by the gear ratio, i_g, between the motor gear and the differential, as follows:

$$\tau_d = i_g \tau_m \tag{4}$$

The force transmitted to each tendon can be written as shown in Equation (5).

In the differential proposed, the motor can apply a torque up to 3 N.m, the pulley channel has a diameter of 14 mm, and the gear ratio is 1.26. Thus, a maximum force of about 135 N can be achieved by each tendon, as follows:

$$F_i = \frac{i_g \tau_m}{4 r_i}. \tag{5}$$

FIGURE 2 | The four-output gear differential can be integrated into a prosthetic hand with the four outputs connected to the index, middle, ring, and pinky fingers. A single motor is used to distribute the load of the actuator to the four fingers through the outer gear module of the differential case.

2.2. Series Elastic Differential

The series elastic differential extends the work presented in Shahmohammadi and Liarokapis (2021) and is composed of a rod-shaped main bar with four round slots in it. Elastic elements (made out of urethane rubber Smooth-On PMC-780) are placed inside each slot and then a rotating attachment is inserted inside the slots behind the elastic elements. Finally, the slots are blocked by a plastic piece to make sure that the elastic elements cannot rotate freely. **Figure 4** shows an exploded view of this differential. This differential distributes the torque from the single motor (τ_m) to the four series-elastic outputs (see **Figure 5**). Depending on the compression of the elastic element and the element properties, the output forces of the differential mechanism can vary significantly. The developed differential consists of four outputs that can be connected to the index, middle, ring, and pinky fingers of an anthropomorphic hand with the thumb being controlled separately.

This differential can work in two different modes: "Compliance Mode" and "Power Mode." The Compliance

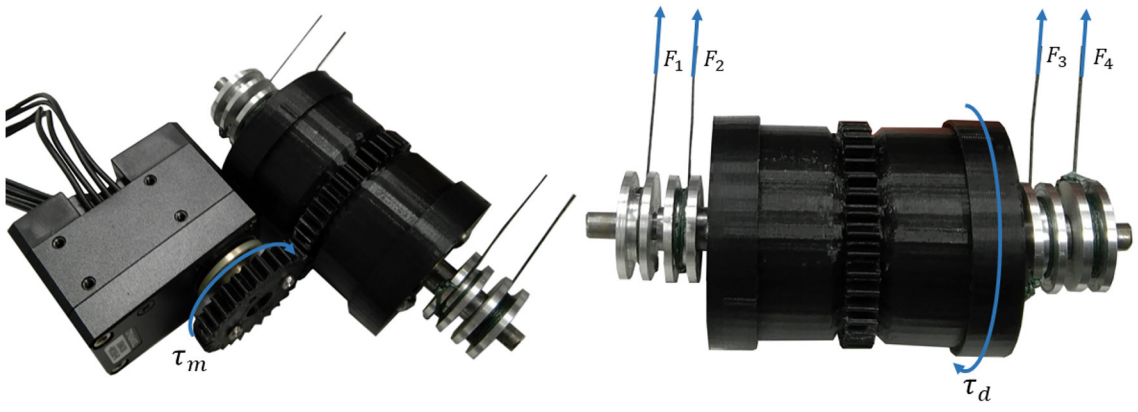

FIGURE 3 | The four-output geared differential is driven by an input torque provided by the motor (τ_m), which drives the differential generating a torque τ_d. The torque τ_d is then evenly distributed across the four outputs of the differential: F_1, F_2, F_3, and F_4.

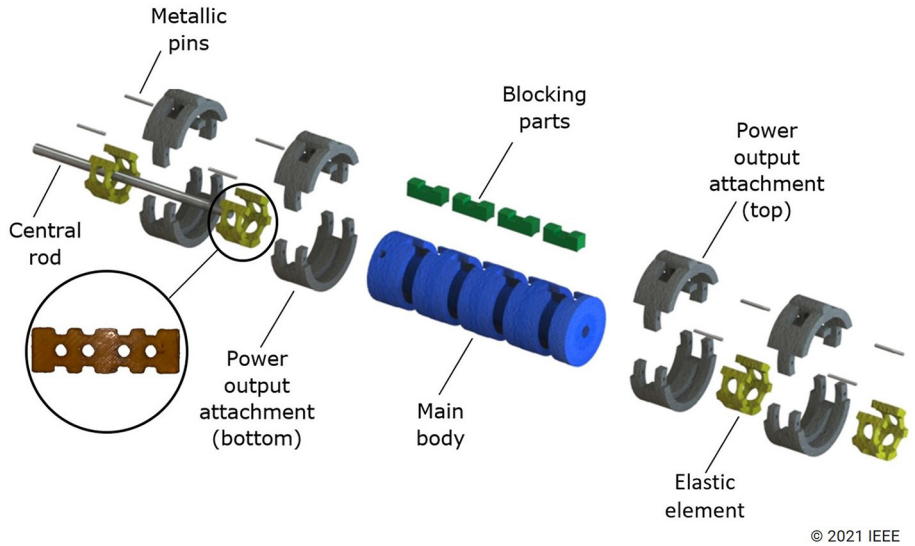

FIGURE 4 | Exploded view of the proposed differential mechanism and robotic gripper. Elastic elements (yellow parts) inserted in slots of the main body. Then, power output attachments are inserted in the same slots over the elastic elements. Finally, plastic pieces (green parts) are inserted in the same slot to block the rotation of the elastic elements. The metallic rod at the center of the main body is used to prevent bending under heavy loads.

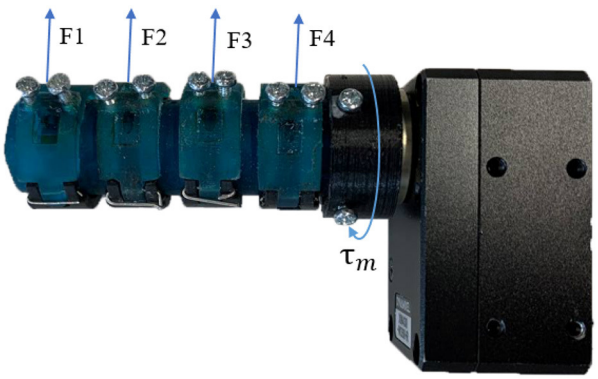

FIGURE 5 | The four-output series elastic differential is driven by an input torque provided by the motor (τ_m). This torque is evenly distributed across the four series-elastic elements that allow the gripper to conform to the object shape by getting proportionally compressed.

Mode transitions through three stages during grasping. Initially, the force at the output is lower than the required force to compress the elastic element (fingers move in sync with each other). The second stage starts upon contact with the object's surface. At this stage, the acting forces on the elastic element become higher, and eventually, they start compressing it, offering the required grasping adaptability between the fingers. During this compression stage, the output attachment does not move since the required force for compressing the elastic element is lower than the acting force on the finger. This allows the remaining non-contacting outputs to continue moving. The elastic material keeps compressing until the required force is again higher than the force acting on the finger. When all fingers have made contact with the object's surface, forcing all elastic elements to reach their maximum compression, the outputs will start to move at the same speed again. In Power Mode, the main body rotates away from the elastic element (counterclockwise) and directly establishes contact with the hard stop end of the output attachment. By doing this, there are no energy losses due to contact with the elastic element, and the exerted forces are higher at the output. This mode is suitable for situations when compliance is not necessary.

To evaluate the elastic elements' behavior during loading, finite element modeling (FEM) was used to simulate the compression behavior. For the FEM analysis, the Abaqus simulation software was used with Mooney-Rivlin equations for hyperelasticity. This simulation allowed the calculation of how much force is required for initiating the compression of the elastic elements. More precisely, for an elastic element with 1.8 mm thickness, the compression starts at 3 N of force, which is small enough for a delicate grasp yet large enough to facilitate the successful execution of various grasps. Then we experimentally validated the accuracy of this number by performing a uniaxial compression test. The needed force can be easily adjusted by changing the thickness of the elastic element. **Figure 6** presents both the simulation and the experiment conducted for comparison purposes.

2.3. Selectively Lockable Differentials

The design of the selectively lockable differential is motivated by the multiple grasping strategies that the human can choose for a given task. For that reason, we have proposed a mechanism based on the well-known whiffletree differential and the two new differentials that we have proposed. The use of a locking mechanism allows the user to select a grasp strategy from a wide range of possible combinations (Kontoudis et al., 2015).

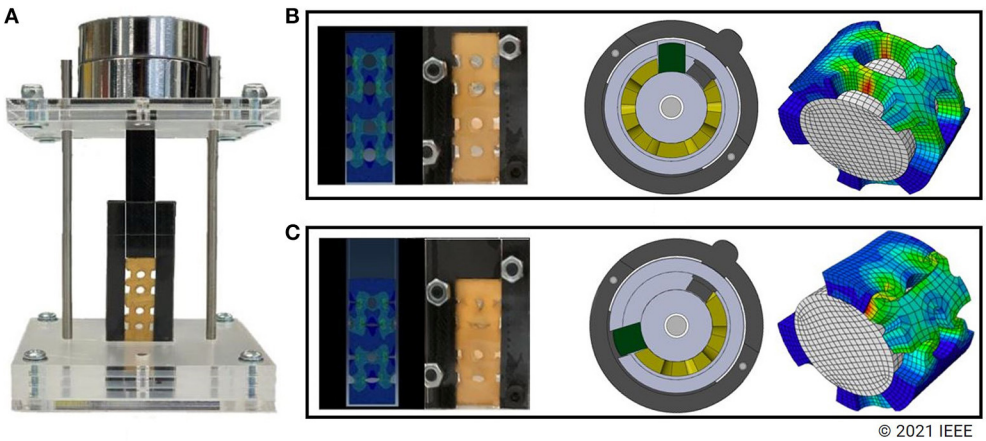

FIGURE 6 | A uniaxial compression test was used to compare the simulated and the real compression of the elastic elements. **(A)** Presents the experimental setup, while **(B,C)** present the elastic element before and after compression respectively (both in simulation and reality).

2.3.1. Manual Selectively Lockable Differentials

The manual selectively lockable differential mechanisms can block the motion of each finger, using a simple locking mechanism that works like a button, allowing the user to select in an intuitive manner the desired finger combinations and implement different grasping postures or gestures. When the buttons are pressed they elongate and obstruct the motion of the differentials.

The whiffletree used with the locking mechanism consists of three bars: one bar connects the index and middle fingers (bar 1), one bar connects the ring and pinky fingers (bar 2), and the main bar (bar 3) connects bar 1 and bar 2, as depicted in **Figures 7A,B**. In this mechanism, the adapted whiffletree upon contact of one finger with the environment or the object surface, the whiffletree facilitates the motion of the rest unconstrained fingers. The whiffletree allows one motor to control multiple fingers in a coordinated fashion, so a small linear displacement of the tendon causes appropriate proportional angular displacements at all robot joints. The whiffletree has been appropriately designed with protruding pins on the top two bars of the whiffletree that interact with the elongated buttons. When pressed, the button restricts the motion of the whiffletree by blocking the pins from moving. Similar to the whiffletree locking mechanism, the buttons were employed to block the rotational motion at the outputs of the four-output gear differential and the series elastic differential. Utilizing a similar principle to the whiffletree, the four-output gear differential and the series elastic differential can both be fitted with protruding pins. The pins allow the button locking mechanism to obstruct the differential outputs, facilitating the execution of multiple grasping postures and gestures. This locking mechanism was expanded and integrated into the four output gear differential and the series elastic differential, providing an improved means of controlling the differentials outputs.

A total of 16 different finger combinations can be implemented using the selectively lockable differential mechanism. A single motor, which is combined with the six discrete positions of the thumb, can produce a total of 96 different grasping postures and gestures.

2.3.2. Automated Selectively Lockable Differential

Similarly to the manually selectively lockable differential, the automated selectively lockable differential utilizes an alternative mechanism capable of facilitating the execution of multiple selectable grasping strategies. Unlike the manually selectively lockable differential, the automated lockable differential uses a small, low torque micro-servo (DFRobot DF 9 g micro-servo) to select the desired differential outputs, rather than manually locking and unlocking buttons in place. The active locking allows the implementation of controllable whiffletrees to be fully automatic in prosthetic hands. This enables amputees to perform bimanual tasks with increased efficiency, as the opposite hand is not required to adjust the grasp pose of the prosthetic hand before the task, since the pose can be selected autonomously during the task. To showcase automated locking, the selectively lockable whiffletree differential was used to select various finger combinations that can facilitate the execution of efficient grasps with underactuated prosthetic hands.

The locking mechanism is composed of four pulleys, a belt, a single actuator, two potentiometers, and a whiffletree differential as seen in **Figure 8**. The whiffletree differential output is connected to four fingers (index, middle, ring, and pinky), while the input of the differential is connected to a single Dynamixel XM430-W350-R smart motor. Each pulley contains a different cam profile, which rotates in sync while interacting with the whiffletree differential's protrusions, providing obstructed and unobstructed tendon motion at the whiffletree outputs. This can be seen in **Figure 9**. In order to organize these combinations effectively, such that the cam profile is strong and less prone to error during output selections, a gray code format is used over a binary code format. Two potentiometers are connected out of phase from each other on two cams to detect the lockable mechanism's current combination over a complete revolution.

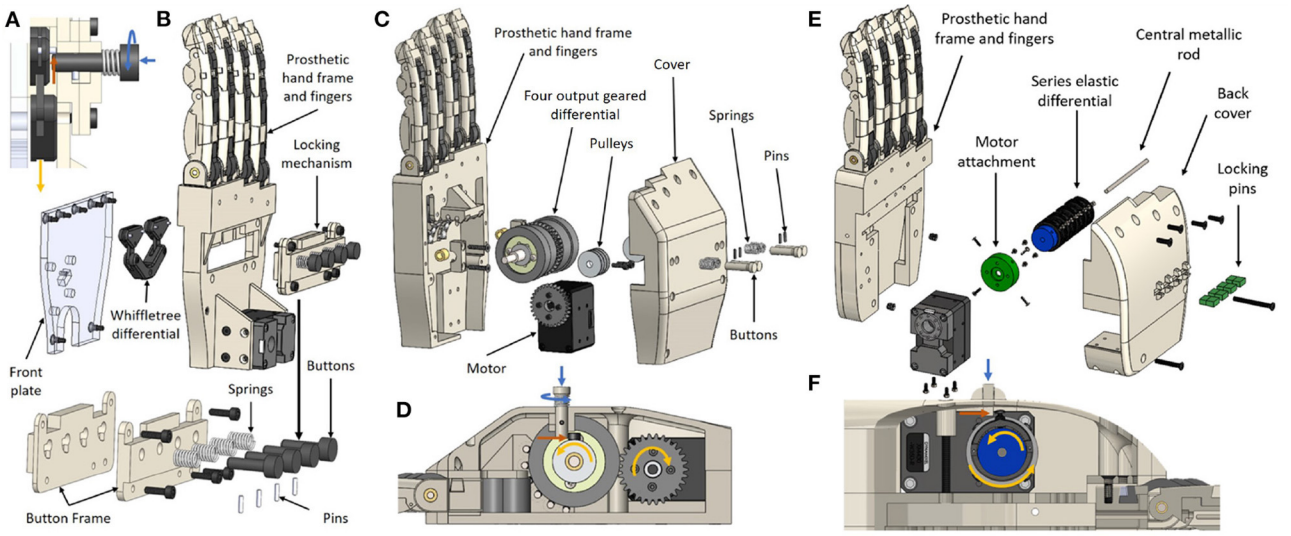

FIGURE 7 | The manual selectively lockable mechanism has been integrated into three differentials: the whiffletree differential **(A,B)**, the four output geared differential **(C,D)**, and the series elastic differential **(E,F)**. **(A)** Illustrates how the locking mechanism blocks a selected output on the whiffletree differential. Button locking is executed through a pushing and twisting action, which engages the button for locking (this is shown with the blue arrows). When the whiffletree is actuated (represented by the yellow arrow), the button provides a blocking force (orange arrow) holding the selected output in place. **(B)** presents how the manual locking mechanism and the whiffletree differential are integrated into the prosthetic hand. Similarly, **(C)** presents the structure of the prosthetic hand when the lockable four output geared differential is used. The locking mechanism utilizes a similar button mechanism to block the motion of a pulley in the four output geared differential, as depicted in **(D)**. The exploded view of the series elastic differential is presented in **(E)**, showcasing the assembly of the locking system when integrated in the series elastic differential. Locking the series elastic differential involves pushing the locking pins down to block the output attachments from rotating. This is illustrated in **(F)**.

A total of 16 finger combinations can be achieved with the four fingers (index, middle, ring, and pinky). Although this system is implemented for a whiffletree differential, the locking mechanism can be adapted to accommodate other differential mechanisms.

3. EXPERIMENTS AND RESULTS

Different experiments were conducted to assess the performance of the proposed differential mechanisms. The first experiment evaluated how much the fingertip force exertion capabilities were affected when the fingers where selectively locked. The second experiment focused on assessing the selectively lockable differential mechanisms capability in providing various hand gesture combinations with the different differentials. The third experiment assessed the grasping capabilities of the differentials when they are integrated into prosthetic hands. The fourth and fifth experiments focused on evaluating the maximum tendon tension and maximum tendon displacement that can be achieved at the outputs of the differentials.

The force exertion experiments were conducted on the selectively lockable differential to investigate the effect on force exertion when the differential mechanism experiences locking/blocking. The relationship between displacement at the input and force exertion at the outputs, is presented in **Figure 10** with different finger combinations being compared. When blocking the fingers we are able to maximize the force applied by the free fingers at there fingertips (e.g., precision grasps). If needed the user can utilize this behavior to maximize the force transmitted from the servo motor to the fewer active fingertips.

3.1. Gesture Execution Experiments

The second experiment assessed the proposed selectively lockable differentials capabilities in executing various grasp poses and hand gestures. To evaluate the abilities of the selectively lockable mechanisms to enhance the performance of all the proposed differentials, the mechanisms were incorporated into a prosthetic hand with a single actuator so as to demonstrate the different achievable hand poses. To showcase the different grasp postures, the buttons of the selectively lockable differentials were locked into different combinations. The three differentials were capable of achieving the full 16 different combinations. This is depicted in **Figure 11**. The importance of controlling the differential's outputs is critical for selecting grasping strategies and allows: i) different hand gestures to be signed, ii) reaching an object in a narrow space, or iii) executing non-prehensile manipulation tasks (e.g., pressing buttons or moving sliders).

3.2. Grasping Performance Experiments

The third experiment was conducted to evaluate the ability of the differentials to improve the grasping performance of prosthetic hands in executing activities of daily living. To do so, the YCB object set designed by Calli et al. (2017), was used to evaluate the grasping efficiency of the prosthetic hands with the proposed differentials integrated. Twelve objects from the object set were selected: a credit card, a washer, a dice, a marble, a tuna fish

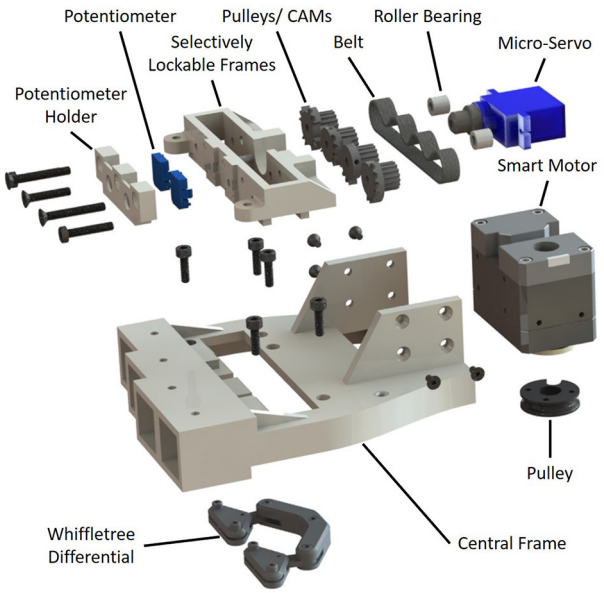

FIGURE 8 | The automated selectively lockable differential consists of two main mechanisms: a selector mechanism that rotates so as to select the differential output behavior and a whiffletree differential for distributing the input load evenly across four outputs. The selector is composed of four pulley/cams, two roller bearings, two potentiometers, a belt, an input pulley, a micro-servo, and a selector frame.

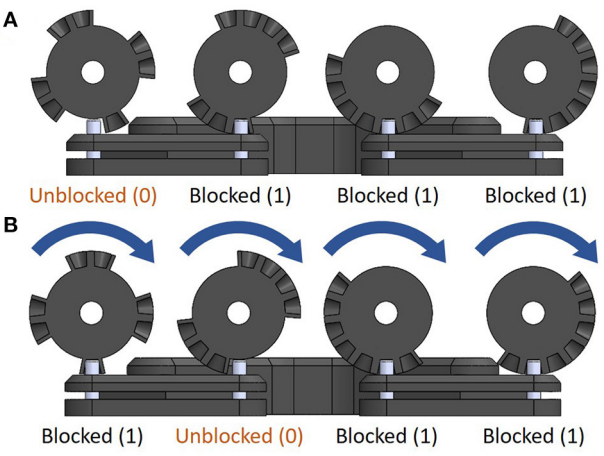

FIGURE 9 | The automated selectively lockable differential performs controllable locking by blocking and unblocking the motion of the whiffletree. This is depicted in **(A)**. In **(B)** the cams are rotated in sync with the micro-servo so as to provide the desired differential output.

can, a golf ball, a pear, a Lego Dublo block, a mustard bottle, a box of sugar, a drill, and a baseball. All hands were capable of grasping all twelve objects. This can be seen in **Figure 12**, where the selectively lockable differential mechanism allows the hand to execute different grasping postures, achieving optimal grasping performance for the encountered objects.

3.3. Tendon Tension Experiments

The fourth experiment focused on testing the mechanical limits of the designed differentials. The experiment consisted of measuring the tendon's tension until either the tendon, the differential, or the motor failed. Hanging weights of increasing masses were attached to the output ends of the differentials until it was unable to lift the weight. To perform the experiment, equal weights of 100 g were incrementally added at the end of the tendon in all four outputs while the differential was running until the system could not withstand the load. The results of the total exerted forces of all four outputs of each differential are provided in **Table 1**. The whiffletree differential used in the developed prosthetic hands in section 3.1, was capable of holding up to 42.8 N of tendon tension per output before failure. The four-output geared differential obtained a maximum tendon tension of 39 N per output during the experiments. Although the maximum theoretical tendon tension calculated in section 2.1 can be more than 100 N per output, the calculation does not consider efficiency loss due to friction between components, the operating conditions of the motor, or the mechanical resistance of the components used in the differential. When using the series elastic differential it is capable of switching between a rigid and a compliant mode allowing the differential to select when the elastic elements should be used. The maximum tendon tension force of 53.8 N per output was achieved when in the rigid mode, while a maximum force of 45.8 N per output was obtained for the compliant mode. Note that the stiffness of the elastic element of the series elastic differential mechanism can be selected according to the requirements of the application.

3.4. Tendon Displacement Experiment

The last experiment focused on measuring the amount of achievable displacement in each output of the three differential mechanisms. This displacement is important as it offers the required adaptability needed for grasping a wide range of objects, conforming to the object shape, and maximizing the contact patches between the fingers and the object surface, increasing also grasping quality. The three differentials were actuated in an unblocked state to achieve the maximum obtainable displacement at the differentials outputs. Additionally, the three differentials were also tested with three of the four outputs being blocked, allowing for the minimum achievable tendon displacement to be measured. When unblocked the whiffletree was capable of 21 mm of tendon displacement, but was only limited by the available translation length, which is limited by the length of the palm of the prosthetic hand. In the second test scenario where three of the four outputs are blocked, the whiffletree differential was able to obtain a displacement of 10 mm, which was limited by the length of the upper whiffletree bars. The four-output geared differential was able to perform continuous rotations at the outputs in both locked and unlocked scenarios providing continuous displacement. The maximum tendon displacement of this design is only limited by the amount of tendon the pulleys at the output shafts can hold. The series elastic differential when unblocked is capable of continuous rotation similarly to the four-output geared differential, but this continuous rotation only applies to cases when all four

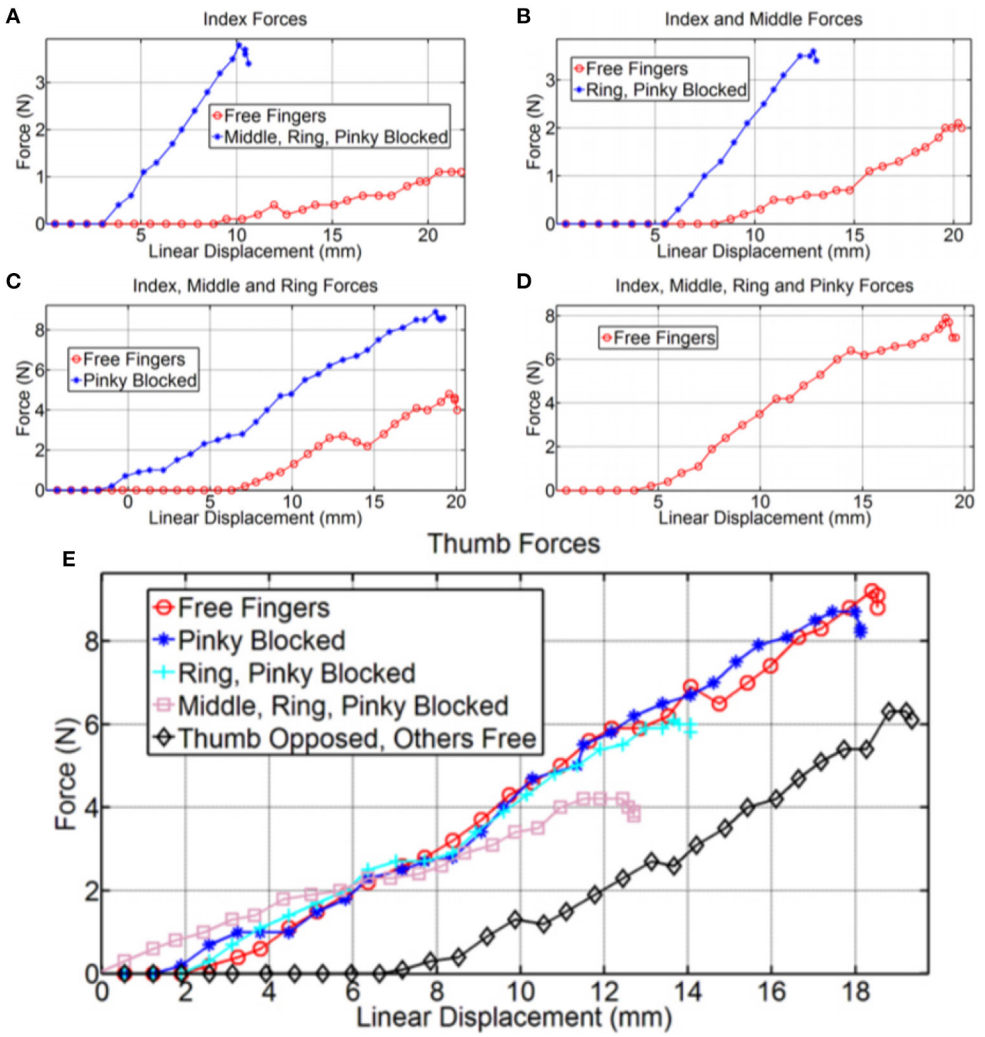

FIGURE 10 | The relationship between tendon displacement and finger forces for different grasp poses are compared with blocked and unblocked fingers. **(A)** Shows the force output when only the index is unblocked. **(B)** Depicts the force exerted when only the middle finger is unblocked. Similarly, **(C)** Presents the forces but with only the pinky finger experiencing blocking. The force output when all fingers are unblocked can be seen in **(D)**. A comparison of all forces is illustrated in **(E)**.

outputs are allowed to move continuously. When one or more outputs is blocked, the series elastic differential can only provide displacements up to 43 mm.

4. DISCUSSION

Two differential mechanisms and four different locking mechanisms have been proposed, each capable of improving the grasping capabilities of prosthetic hands in different circumstances. The selectively lockable differentials offer increased controllability of the differential outputs facilitating the execution of all 16 finger flexion/extension combinations (e.g., controlled flexion across the index, middle, ring, and pinky fingers on a prosthetic hand). For grasps, which do not need the involvement of all four fingers (index, middle, ring, and pinky) to oppose the thumb to complete the grasp, the subsidiary fingers can be blocked to maximize the force transmitted to the active fingers by the motor. The developed selectively lockable differentials have been designed to accommodate different user requirements. The manual selectively lockable differential utilizes manually lockable buttons meaning the design does not require additional electronics and actuators to use the mechanism. Hence, utilizing a body-powered approach enables the mechanism to significantly reduce the cost of implementation in a prosthetic device where the price is an essential element. Although the automated selectively lockable differential requires an additional actuator to operate, unlike the manually lockable whiffletree differential, this actuator does not need a high torque rating as the high loads exerted by the differential are parallel to the axis of the actuator. This allows the chosen actuator to be small and compact, reducing the size, and cost of the total system significantly. The increased autonomy offered by the system's active approach allows the use of selectively lockable differential mechanisms to increase efficiency in bi-manual tasks for amputees and reduce intervention and effort needed

to switch the gesture or grasp pose of the hand. The automated selectively lockable differential can also be adopted in robotic systems, where full autonomy is required.

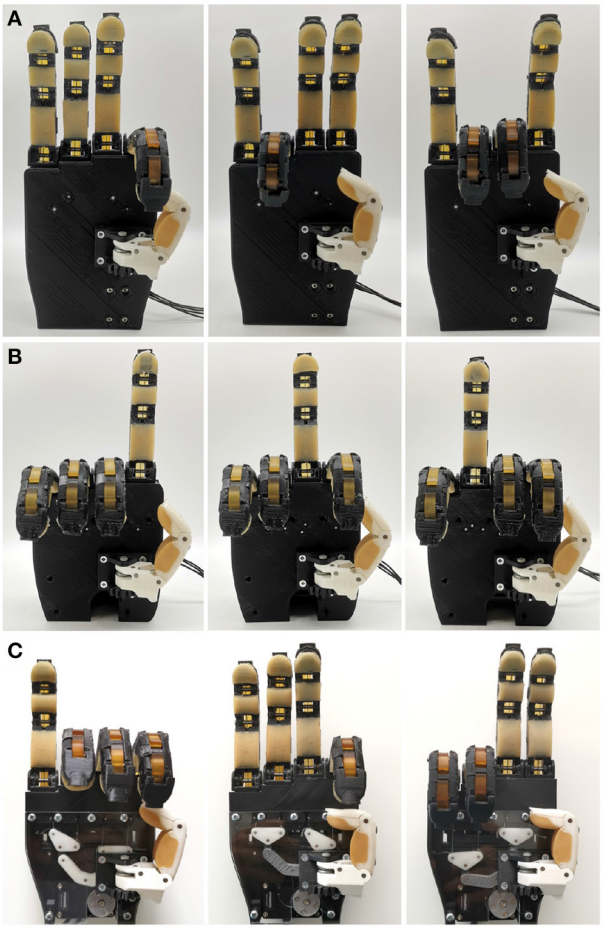

FIGURE 11 | Hand gesture combinations executed by a prosthetic hand equipped with a selectively lockable differential mechanism. The Locking mechanism was implemented on the four output geared differential **(A)**, the series elastic differential **(B)**, and the whiffletree **(C)** on similar prosthetic hands, altering the index, middle, ring, and pinky fingers flexion combination patterns.

Other than the whiffletree differentials, which have a limited range of motion, rotary mechanisms like the four-output gear differential grant continuous rotation at the outputs. The benefit of using a rotary mechanism is its ability to operate within a fixed volume size. In contrast, traditional pulley and whiffletree differential mechanisms require additional space to accommodate the mechanism's translational motion. This is generally not an issue in anthropomorphic prosthetic hand designs (Laliberté et al., 2002; Weiner et al., 2018), where a large plane usually is available to accommodate the movements of the pulley and whiffletree differentials. However, for prosthetic devices that require large

FIGURE 12 | Grasping experiments conducted with the three prosthetic hands equipped with the proposed differential mechanisms whiffletree **(A)**, four output gear differential **(B)**, and series elastic **(C)**. The three differentials can be seen allowing a prosthetic hand to execute a variety of grasping strategies (pinch, tripod, and power grasps).

TABLE 1 | Comparison of the proposed differentials.

Differentials	Whiffletree differential	Four-output differential	Series elastic differential
Inputs	1	1	1
Outputs	4	4	4
Total displacement	Limited[a]	Continuous[b]	Continuous[b]
Displacement between outputs	Limited[c]	Continuous[b]	Limited[d]
Size[e] (mm)	23 x (54 + T) × 81	41 × 100 × 41	57 × 23 × 23
Weight (g)	46	169.8	22.5
Max force output[f] (N)	171	156	215 (rigid mode)

[a] *The total displacement of the whiffletree is limited by the translation length available.*
[b] *The rotary motion of the mechanism allows for continuous winding at the outputs.*
[c] *The adaptability of the differential is limited by the length of the whiffletree bars.*
[d] *The adaptability is limited by the max compression displacement of the elastic elements.*
[e] *T is the travel distance needed for the mechanism to adapt.*
[f] *The max force output is the total force of all outputs.*

displacements at the differential outputs to reach their maximum range of motion, pulley and whiffletree differentials are not sufficiently compact.

Finally, the series elastic differential offers a simpler and smaller solution than the four-output differential via the implementation and utilization of passive elastic elements. This results in a mechanism with fewer components and reduced weight. However, passive elastic elements in series with the actuator output can produce a parasitic force reducing the maximum achievable force output. This is because the actuator must use some energy to compress the elastic element before achieving the desired differential displacement. To overcome this, the series elastic differential has been developed such that the differential is capable of switching between a compliant and adaptive mode and a rigid mode based on the rotating direction of the connected actuator. The ability to switch between compliant and rigid modes led to a force output difference of up to 17.4%. Similar to the whiffletree differential, where the maximum displacement between outputs is limited by the bar length, for the series elastic differential, this is constrained by the circumference of the main body and the maximum compressible length of the elastic elements. Thus, this design choice limits the differential's maximum adaptability. However, the total displacement of the series elastic differential is continuous if all outputs wind together. In contrast the whiffletree differential also has a limited total displacement, which is constrained by the operating volume allocated for the differential to translate in. The four-output gear differential, is capable of independently rotating each output continuously until all four outputs experience an equal load, where it will then wind the outputs together providing a continuous total displacement. A comparison of the proposed differential systems is presented in **Table 1**.

5. CONCLUSION

In this paper, we presented a set of lightweight and compact differential mechanisms for prosthetic hands where low weight, small size, and affordability are key requirements for a successful design. Locking mechanisms for improving the controllability of the three examined differentials (a four-output geared differential, a series elastic differential, and a whiffletree differential) were developed. Two different locking approaches were implemented with one being manual and the other using a small low torque actuator to allow for active control. The locking mechanisms facilitated all 16 different finger flexion and extension combinations (across the index, middle, ring, and pinky fingers). The four-output geared differential was developed in a compact manner allowing for the development of lightweight prosthetic hands. The proposed device is capable of exerting 39 N of tendon tension per output. The final differential type developed is a series elastic differential that is capable of switching between a compliance mode for adaptive behavior and a power mode for a non-adaptive behavior which is capable of exerting up to 17.5% more force. The tendon tension per output of the differential was 45.75 N in its compliance mode and 53.75 N in its power mode. All differentials are experimentally tested and compared.

Regarding future directions, we plan to integrate the automated locking into more differentials such as the four-output gear differential and the series elastic differential. Our future work will also focus on equipping the fingers with appropriate tactile and force torque sensors as well as on further evaluating how underactuation affects grasping quality and grasp stability through a forces-oriented quantitative analysis. Such an analysis will require redesigning all the utilized prostheses to accommodate the sensing elements and a series of new experiments and comparisons. Finally, we also intend to integrate the proposed differential mechanisms in devices other than prosthetic hands in order to showcase all feasible use cases.

DATA AVAILABILITY STATEMENT

Publicly available datasets were analyzed in this study. This data can be found here: https://github.com/newdexterity/Differentials.

AUTHOR CONTRIBUTIONS

GG contributed to the design of the selectively lockable differential mechanisms. MS developed the series elastic differential. LG developed four-output geared differential. GK contributed to the development of the manually selectively lockable whiffletree differential. ML contributed on the ideas and supervised. GG, MS, LG, and GK in the implementation of the different differentials. The manuscript were prepared by the authors collectively. All authors contributed to the article and approved the submitted version.

REFERENCES

Baril, M., Laliberte, T., Gosselin, C., and Routhier, F. (2013). On the design of a mechanically programmable underactuated anthropomorphic prosthetic gripper. *J. Mech. Des.* 135, 121008. doi: 10.1115/1.4025493

Belter, J. T., and Dollar, A. M. (2013). "Novel differential mechanism enabling two dof from a single actuator: application to a prosthetic hand," in *2013 IEEE 13th International Conference on Rehabilitation Robotics (ICORR)* (Seattle, WA: IEEE), 1–6.

Bicchi, A. (2000). Hands for dexterous manipulation and robust grasping: A difficult road toward simplicity. *IEEE Trans. Rob. Autom.* 16, 652–662. doi: 10.1109/70.897777

Biermann, T., Hohn, B.-R., and Kurth, F. (2013). *Spur Gear Differential*. US Patent 8,480,532.

Birglen, L., and Gosselin, C. M. (2006). Force analysis of connected differential mechanisms: application to grasping. *Int. J. Rob. Res.* 25, 1033–1046. doi: 10.1177/0278364906068942

Birglen, L., Laliberté, T., and Gosselin, C. M. (2007). *Underactuated Robotic Hands, Vol. 40*. Berlin; Heidelberg: Springer-Verlag.

Calli, B., Singh, A., Bruce, J., Walsman, A., Konolige, K., Srinivasa, S., et al. (2017). Yale-cmu-berkeley dataset for robotic manipulation research. *Int. J. Rob. Res.* 36, 261–268. doi: 10.1177/0278364917700714

Cerulo, I., Ficuciello, F., Lippiello, V., and Siciliano, B. (2017). Teleoperation of the schunk s5fh under-actuated anthropomorphic hand using human hand motion tracking. *Rob. Auton. Syst.* 89, 75–84. doi: 10.1016/j.robot.2016.12.004

Chen, W., Xiong, C., and Yue, S. (2015). Mechanical implementation of kinematic synergy for continual grasping generation of anthropomorphic hand. *IEEE/ASME Trans. Mechatr.* 20, 1249–1263. doi: 10.1109/TMECH.2014.2329006

Cheon, S., Choi, W., Oh, S.-R., and Oh, Y. (2014). "Development of an underactuated robotic hand using differential gear mechanism," in *2014 11th International Conference on Ubiquitous Robots and Ambient Intelligence (URAI)* (Kuala Lumpur: IEEE), 328–334.

Chu, J.-U., Jung, D.-H., and Lee, Y.-J. (2008). "Design and control of a multifunction myoelectric hand with new adaptive grasping and self-locking mechanisms," in *2008 IEEE International Conference on Robotics and Automation* (Pasadena, CA: IEEE), 743–748.

Cipriani, C., Controzzi, M., and Carrozza, M. C. (2011). The smarthand transradial prosthesis. *J. Neuroeng. Rehabil.* 8, 1–14. doi: 10.1186/1743-0003-8-29

Cordella, F., Ciancio, A. L., Sacchetti, R., Davalli, A., Cutti, A. G., Guglielmelli, E., et al. (2016). Literature review on needs of upper limb prosthesis users. *Front. Neurosci.* 10:209. doi: 10.3389/fnins.2016.00209

Della Santina, C., Piazza, C., Grioli, G., Catalano, M. G., and Bicchi, A. (2018). Toward dexterous manipulation with augmented adaptive synergies: The Pisa/IIT SoftHand 2. *IEEE Trans. Robot.* 34, 1141–1156. doi: 10.1109/TRO.2018.2830407

Gosselin, C., Pelletier, F., and Laliberte, T. (2008). "An anthropomorphic underactuated robotic hand with 15 dofs and a single actuator," in *2008 IEEE International Conference on Robotics and Automation* (Pasadena, CA: IEEE), 749–754.

Grebenstein, M., Chalon, M., Hirzinger, G., and Siegwart, R. (2010). "A method for hand kinematics designers 7 billion perfect hands," in *Proceedings of 1st International Conference on Applied Bionics and Biomechanics* (Venice).

Keller, A., Shelepov, A., and Istomin, D. (2015). Study on screw-ball differential gear operating process. *Procedia Eng.* 129, 535–541. doi: 10.1016/j.proeng.2015.12.054

Kochan, A. (2005). Shadow delivers first hand. *Indust. Rob.* 32, 15–16. doi: 10.1108/01439910510573237

Kontoudis, G. P., Liarokapis, M. V., Zisimatos, A. G., Mavrogiannis, C. I., and Kyriakopoulos, K. J. (2015). "Open-source, anthropomorphic, underactuated robot hands with a selectively lockable differential mechanism: towards affordable prostheses," *in IEEE/RSJ International Conference on Intelligent Robots and Systems* (Hamburg: IEEE), 5857–5862.

Laliberté, T., Birglen, L., and Gosselin, C. (2002). Underactuation in robotic grasping hands. *Mach. Intell. Rob. Control* 4, 1–11. Available online at: https://www.semanticscholar.org/paper/Underactuation-in-robotic-grasping-hands-Birglen-Gosselin/58c29c7563d61235bd6015cc30e46bd742ad7a88#citing-papers

Leddy, M. T., and Dollar, A. M. (2018). "Preliminary design and evaluation of a single-actuator anthropomorphic prosthetic hand with multiple distinct grasp types," in *2018 7th IEEE International Conference on Biomedical Robotics and Biomechatronics (Biorob)* (Enschede: IEEE), 1062–1069.

Liarokapis, M. V., Dollar, A. M., and Kyriakopoulos, K. J. (2015). "Humanlike, task-specific reaching and grasping with redundant arms and low-complexity hands," in *International Conference on Advanced Robotics (ICAR)* (Istanbul: IEEE), 490–497.

Ma, R. R., Odhner, L. U., and Dollar, A. M. (2013). "A modular, open-source 3d printed underactuated hand," in *2013 IEEE International Conference on Robotics and Automation* (Karlsruhe: IEEE), 2737–2743.

Martin, E., Desbiens, A. L., Laliberté, T., and Gosselin, C. (2004). "Sarah hand used for space operation on stvf robot," in *Proceedings of the International Conference on Intelligent Manipulation and Grasping* (Genova), 279–284.

Mitsui, K., Ozawa, R., and Kou, T. (2013). "An under-actuated robotic hand for multiple grasps," in *2013 IEEE/RSJ International Conference on Intelligent Robots and Systems* (Tokyo: IEEE), 5475–5480.

Shahmohammadi, M., and Liarokapis, M. (2021). "A series elastic, compact differential mechanism: On the development of adaptive, lightweight robotic grippers and hands," in *IEEE/RSJ International Conference on Intelligent Robots and Systems (IROS)* (Prague).

Weiner, P., Starke, J., Hundhausen, F., Beil, J., and Asfour, T. (2018). "The kit prosthetic hand: design and control," in *2018 IEEE/RSJ International Conference on Intelligent Robots and Systems (IROS)* (Madrid: IEEE), 3328–3334.

Xiong, C.-H., Chen, W.-R., Sun, B.-Y., Liu, M.-J., Yue, S.-G., and Chen, W.-B. (2016). Design and implementation of an anthropomorphic hand for replicating human grasping functions. *IEEE Trans. Rob.* 32, 652–671. doi: 10.1109/TRO.2016.2558193

Xu, K., Liu, H., Liu, Z., Du, Y., and Zhu, X. (2015). "A single-actuator prosthetic hand using a continuum differential mechanism," in *2015 IEEE International Conference on Robotics and Automation (ICRA)* (Seattle, WA: IEEE), 6457–6462.

Ziegler-Graham, K., MacKenzie, E. J., Ephraim, P. L., Travison, T. G., and Brookmeyer, R. (2008). Estimating the prevalence of limb loss in the united states: 2005 to 2050. *Arch. Phys. Med. Rehabil.* 89, 422–429. doi: 10.1016/j.apmr.2007.11.005

Conflict of Interest: The authors declare that the research was conducted in the absence of any commercial or financial relationships that could be construed as a potential conflict of interest.

Publisher's Note: All claims expressed in this article are solely those of the authors and do not necessarily represent those of their affiliated organizations, or those of the publisher, the editors and the reviewers. Any product that may be evaluated in this article, or claim that may be made by its manufacturer, is not guaranteed or endorsed by the publisher.

frontiers in Neurorobotics

ORIGINAL RESEARCH
published: 11 January 2022
doi: 10.3389/fnbot.2021.790060

Control Framework for Sloped Walking With a Powered Transfemoral Prosthesis

Namita Anil Kumar[1], *Shawanee Patrick*[1], *Woolim Hong*[1] *and Pilwon Hur*[2]*

[1] Department of Mechanical Engineering, Texas A&M University, College Station, TX, United States, [2] Department of Mechanical Engineering, Gwangju Institute of Science and Technology, Gwangju, South Korea

User customization of a lower-limb powered Prosthesis controller remains a challenge to this date. Controllers adopting impedance control strategies mandate tedious tuning for every joint, terrain condition, and user. Moreover, no relationship is known to exist between the joint control parameters and the slope condition. We present a control framework composed of impedance control and trajectory tracking, with the transitioning between the two strategies facilitated by Bezier curves. The impedance (stiffness and damping) functions vary as polynomials during the stance phase for both the knee and ankle. These functions were derived through least squares optimization with healthy human sloped walking data. The functions derived for each slope condition were simplified using principal component analysis. The weights of the resulting basis functions were found to obey monotonic trends within upslope and downslope walking, proving the existence of a relationship between the joint parameter functions and the slope angle. Using these trends, one can now design a controller for any given slope angle. Amputee and able-bodied walking trials with a powered transfemoral prosthesis revealed the controller to generate a healthy human gait. The observed kinematic and kinetic trends with the slope angle were similar to those found in healthy walking.

Keywords: transfemoral prosthesis control, impedance control, rehabilitation, sloped walking, biomedical

OPEN ACCESS

Edited by:
Dongming Gan,
Purdue University, United States

Reviewed by:
Jiahao Chen,
Institute of Automation, Chinese Academy of Sciences (CAS), China
Deepak Joshi,
Indian Institutes of Technology (IIT), India
Xikai Tu,
North Carolina State University, United States

***Correspondence:**
Pilwon Hur
pilwonhur@gist.ac.kr

Received: *06 October 2021*
Accepted: *06 December 2021*
Published: *11 January 2022*

Citation:
Anil Kumar N, Patrick S, Hong W and Hur P (2022) Control Framework for Sloped Walking With a Powered Transfemoral Prosthesis. Front. Neurorobot. 15:790060. doi: 10.3389/fnbot.2021.790060

1. INTRODUCTION

Despite decades of research in the field of human rehabilitation, energetically passive devices are the only commercially available solutions to a population of 1.3 million lower-limb amputees (Ziegler-Graham et al., 2008). An energetically passive device is one that stores and dissipates energy without providing net positive work to the gait cycle. The lacking positive work is compensated for by the user's residual limb, which overexerts the hip and pelvic muscles, eventually leading to severe gait asymmetries (Kaufman et al., 2012). Powered prostheses, on the other hand, provide a net positive work and consequently lower a user's metabolic cost (Herr and Grabowski, 2012; Goldfarb, 2013). The Ossur Power knee is the only powered prosthesis currently on the market, however it tends to not fair well with middle aged and older users (Hafner and Askew, 2015). It also performs poorly while walking on sloped terrain (Wolf et al., 2012; Morgenroth et al., 2018). Other Powered prosthesis knees remain viable only in academic settings due to numerous challenges. Setting aside the more obvious challenges like battery limitations and the bulkiness of motors, a less tackled obstacle is the difficulty in customizing the powered prosthesis to the user.

User customization of a prosthesis involves changes to the mechanical and control system. Mechanical customization is actively studied and some solutions include customized sockets, adjustable height and foot stiffness (Colombo et al., 2010; Fey et al., 2013; Comotti et al., 2015; Beck et al., 2017; Lecomte et al., 2021). Customization of control systems, on the contrary, has seen minor contributions with the most significant being the implementation of machine learning for auto-tuning level walking control parameters (Wen et al., 2020). The lack of contributions on this topic is primarily due to the problem's sheer magnitude. Since each mode of operation (e.g., standing, walking, stair ascent or descent) has its own control law, user customization of the control system involves tuning an unmanageable large number of tuning parameters. At this point, any solution that simplifies this behemoth of a task is appreciated. In this paper, we will focus on walking controllers for transfemoral prostheses on sloped terrain. We will study the complexities of walking on slopes and then propose a framework with far fewer tuning parameters than the state-of-the-art, thus simplifying user-customization of prosthesis control.

1.1. Background on Sloped Walking Control

There are two well-known approaches to prosthesis walking control: impedance control and variants of feedback linearization. The known implementations of the latter are limited to level and upslope walking (Paredes et al., 2016). The former has been extensively used for level and sloped walking (both upslope and downslope). Almost all implementations of impedance control involves sectioning a gait cycle into 4–6 phases. These phases form the states in a finite state machine. A gait cycle is defined to begin and end with a heel-strike on the same limb. We will refer to the progress in a gait cycle using t which is 0 at gait cycle initiation and 1 (equivalent to 100%) at completion. Important kinematic moments in the gait cycle like heel-off and maximum knee flexion during swing phase are chosen as switching points between states. **Figure 1** presents the gait cycle with important kinematic instances. The control input at any instant t is given by

$$\tau(t) = K(\theta(t) - \theta_{ref}) + D\dot{\theta}(t) \tag{1}$$

where K and D represent the joint stiffness and viscous damping, respectively. The term θ_{ref} is the reference or equilibrium angle of the joint, while $\theta(\cdot)$ and $\dot{\theta}(\cdot)$ signify the joint's position and velocity.

Within each state of the finite state machine, the joint parameters (i.e., K, D, and θ_{ref}) can be assigned constant values or vary as a function of some gait characteristic. In Sup et al. (2008), the joint parameters were constant within each state in the finite state machine. Estimates for the parameters were determined through a least squares optimization that minimized the difference between the torque from Equation (1) and the joint torque from healthy human walking data. While this approach has been proven to emulate healthy walking kinematics and kinetics, it involves careful tuning of the initially estimated joint parameters (numbering at 12–18 per joint). In Sup et al. (2011), the authors recognized similarities between gait kinematics and kinetics on different slope angles, and suggested using the same impedance control strategy as in Sup et al. (2008) but with different joint parameters. Despite its success, this process involved re-tuning the joint parameters for every slope angle. Wen et al. (2020) attempted solving this issue through machine learning, but their attempts are limited to level walking. Additionally, the manner in which we produce a labeled data-set is debatable since we are yet to quantify crucial parameters like user comfort.

Varying the parameters as a function of gait characteristics has the benefit of fewer states in the finite state machine and hence fewer tuning parameters. Fey et al. (2014) and Bhakta et al. (2019) varied K and θ_{ref} as functions of the joint angle and the vertical ground reaction force during mid and terminal stance phases. The parameters were held constant during all other states in the finite state machine. While amputee trials proved the controller's success, the results in Fey et al. (2014) were limited to level and upslope walking and Bhakta et al. (2019) did not discuss gait kinetics. Furthermore, the controller's reliance on a load cell increases the ultimate cost and weight of the prosthesis. In Anil Kumar et al. (2020), the joint parameters varied as a function of t during stance phase, thus no longer requiring a load cell. However, the proposed control scheme was limited to the ankle joint and level walking. While the above approaches lessened the number of states during the stance phase, Lawson et al. (2014) and Hong et al. (2019) lessened the number of states during the swing phase by tracking healthy human walking trajectories. In fact, Hong et al. (2019) exploited the similarities between the sloped walking knee swing trajectories by tracking the level walking trajectory regardless of the slope angle. The smooth transitioning between stance and swing phases was facilitated by Bezier curves and a low gain PD controller toward the end of the gait cycle helped with terrain adaptation. Despite having fewer tuning parameters, the application of the above approaches to sloped walking still requires re-tuning several parameters for every slope angle.

1.2. Objectives

The problem of re-tuning the joint parameters for every slope angle is worsened by the absent relationship between the joint parameters and the slope angle. Our primary objective is to fill this gap in knowledge. The methods used in Anil Kumar et al. (2020) and Hong et al. (2019) form the foundation of our work. We first study the kinematics and kinetics of sloped walking, based on which we determine the objectives of our control framework for sloped walking (refer to section 2). In section 3, we present the control framework with our estimates of the joint control parameters across all slope angles. The estimation is an extension of the one presented in Anil Kumar et al. (2020) wherein K and D are polynomials of t. Upon estimating the joint control parameters for all slope angles, we extract basis functions spanning the entire set and propose a mapping between the joint parameters and the slope angle. Said mapping and the basis functions form the two contributions of this paper. In section 4, we discuss the implementation of our control framework on a powered transfemoral prosthesis. We

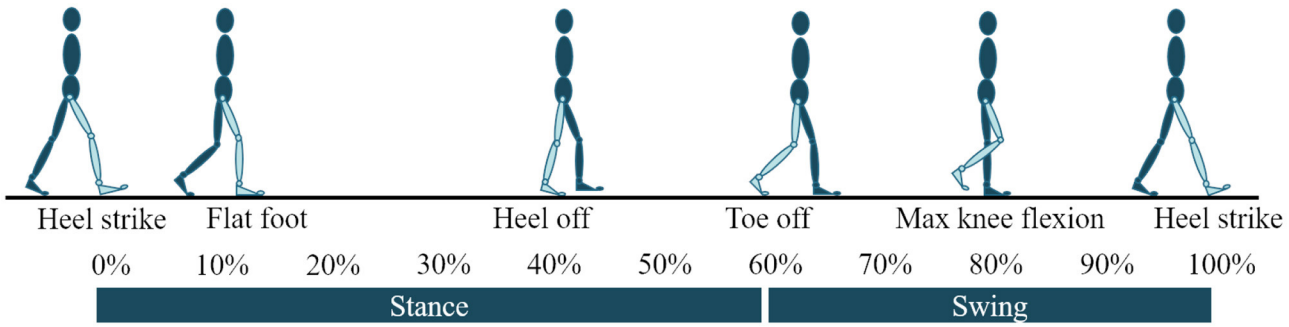

FIGURE 1 | Gait cycle with important kinematic moments used as switching conditions in a finite state machine.

also present a thorough tuning regime for our control strategy. The experimental results with an amputee and an able-bodied subject are then reported and discussed in section 5. Section 6 will have our concluding remarks.

2. A BRIEF ANALYSIS OF SLOPED WALKING

General practice in the field of walking assistive devices deems a device successful if it can emulate healthy gait kinetics and kinematics. In accordance to this norm, we determined control objectives by studying sloped walking kinematics and kinetics. Useful resources include: a $n = 20$ study by Montgomery and Grabowski (2018), a $n = 10$ study by Embry et al. (2018b) which also has a publicly available data-set (Embry et al., 2018a). The study (Montgomery and Grabowski, 2018) presents data for 7 slope angles (-9° to $+9^\circ$ at 3° increments), while the study (Embry et al., 2018a) presents results for 9 slope angles (-10° to $+10^\circ$ at 2.5° increments). We discuss the kinematics and kinetics of sloped walking in the following sections. Since our goal is to design a controller for a transfemoral prosthesis, we limit our discussion to the knee and ankle joint. The highlighted points will form the means by which we evaluate the performance of our controller.

2.1. Kinematics

Some important kinematic aspects of sloped walking are as follows. (i) The switching conditions of a finite state machine (shown in **Figure 1**) change with the slope and walking speed. The instants of flat-foot (ϕ_{FF}) and heel-off (ϕ_{HO}) occur earlier as the slope angle varies from steep downslope to steep upslope. On the other hand, toe-off (ϕ_{TO}) is delayed as the slope varies. (ii) The amount of ankle plantar-flexion at toe-off increases as the slope varies from steep downslope to steep upslope. (iii) The ankle angle at the beginning of the gait cycle changes with the slope angle to facilitate terrain adaptation (i.e., the ankle is more dorsiflexed on upslopes). (iv) The amount of knee-flexion during initial stance phase increases with the steepness of the slope be it upslope or downslope.

2.2. Kinetics

The most important trends in sloped walking kinetics are: (i) the increase in push-off peak ankle torque and power as the slope varies from steep downslope to upslope; (ii) more knee flexion torque during initial stance phase on steeper slopes; (iii) more knee extension torque during terminal stance phase on upslopes. These trends are more strictly obeyed in Montgomery and Grabowski (2018), while the data pertaining to -5°, -2.5° in Embry et al. (2018a) deviate from the trends. In fact, the entire downslope walking torque data from Embry et al. (2018a) is higher than that found in Montgomery and Grabowski (2018) by a factor of 1.3–1.5. We believe (Montgomery and Grabowski, 2018) to be more accurate owing to the larger sample size. On the other hand, the data in Embry et al. (2018a) spans more slope conditions which helps greatly while determining the relationship between control parameters and the slope angle. So, we continue to use the data from Embry et al. (2018a), keeping in mind some anomalies are to be expected during downslope walking. We will account for these anomalies during implementation and accordingly adjust our final proposed control scheme.

3. PROPOSED CONTROL FRAMEWORK

As stated in Lawson et al. (2014), it is beneficial to use impedance control during stance phase since the limb is in contact with the terrain. During swing phase, it suffices to merely track healthy human trajectories. We thus propose a finite state machine with 4 states for the ankle and 5 for the knee. Both joints have three states during stance phase with the switches at ϕ_{FF}, ϕ_{HO}, and ϕ_{TO}. In other words, State 1 begins at heel-strike and ends with ϕ_{FF}, followed by State 2 which concludes at ϕ_{HO}. State 3, the last state in the stance phase, ends at ϕ_{TO}. During these three states, we adopted the same strategy as in Anil Kumar et al. (2020). That is, K and D vary as polynomial functions of t, while θ_{ref} assumes constant values during each state.

During swing phase, ankle angle does not vary much regardless of the slope angle–a motion achievable using constant K, D, and θ_{ref} values. The knee, on the contrary, is more animated, requiring a more motion rich trajectory. To achieve the desired motion while having few tuning parameters, we

adopted the strategy proposed in Hong et al. (2019) to control the knee joint. That is, a single level-walking trajectory is tracked using a PD controller regardless of the slope angle. The level walking trajectory in Embry et al. (2018a) was used as the desired trajectory. A Bezier curve was generated in real-time to smoothly transition from the instantaneous position and velocity at ϕ_{TO} to a predefined point in the level-walking desired swing trajectory. Refer to **Supplementary Figure 1** for a pictorial representation of the control framework.

3.1. Estimation of Joint Parameter Functions

To emulate healthy human gait kinetics using the impedance control strategy, we select joints parameters such that the torque produced is similar to that of healthy human walking, say τ_{data}. This study used the sloped walking data reported in Embry et al. (2018a) for τ_{data}, θ, and $\dot{\theta}$. The latter two are replaced by real-time angle and velocity feedback during implementation. We formulate an optimization that minimizes the norm of the difference between τ in (Equation 1) and τ_{data}. Since the knee is controlled via impedance control only during stance phase, the knee's impedance estimation (and thereby cost function) was limited to the stance phase.

Supposing m and n represent the order of the K and D polynomials, respectively, the impedance parameters at instant $t \in [0, 1]$ can be computed as follows,

$$K(t) = \begin{cases} \sum_{i=0}^{m} k_i t^i & \text{for } 0 \leq t < \phi_{TO} \\ k_0 & \text{for } \phi_{TO} \leq t \leq 1 \end{cases} \quad (2)$$

$$D(t) = \begin{cases} \sum_{i=0}^{n} d_i t^i & \text{for } 0 \leq t < \phi_{TO} \\ d_0 & \text{for } \phi_{TO} \leq t \leq 1 \end{cases} \quad (3)$$

The coefficients of the stiffness and damping polynomials are given by k_i and d_i, respectively. The stiffness and damping parameters are assigned the values k_0 and d_0 during the swing phase. Doing so enforces continuity of the impedance parameters at heel-strike [i.e., $K(0) = K(1)$ and $D(0) = D(1)$]. Presented below is the optimization problem:

$$\min_{\theta_{ref}, k_i, d_i} \quad \|\tau_{data} - \tau\|_2 \quad (4)$$

$$\text{Subject to:} \quad K(t) \geq 0 \qquad D(t) \geq 0 \quad (5)$$

$$\text{Continuity of } K \text{ and } D \text{ at } t = \phi_{TO} \quad (6)$$

$$|\theta_{ref}| \leq c_1 \quad (7)$$

$$|\Delta\tau / \Delta t| \leq c_2 \quad (8)$$

The decision variables are $\{\theta_{ref}, k_i, d_i\}$, where θ_{ref} is a set of reference angles, one for each state of the finite state machine. The constraints listed in Equation (5) force K and D to be positive. The constraint Equation (8) assures continuity of the joint parameter functions at toe-off. The scalar, c_1, is a bound on the reference angles. $c_1 = 16^\circ$ for the ankle and $c_1 = 36^\circ$ for the knee. Further, the constraint Equation (8) forces the resulting τ to be Lipschitz continuous with constant c_2. Additional bounds were added, as needed, to restrict the value of the damping parameters.

TABLE 1 | Ankle and knee reference angles that resulted from solving the optimization problem and post tuning.

	From optimization				Post tuning			
	Ankle reference angles (deg)							
Slope	**State 1**	**State 2**	**State 3**	**State 4**	**State 1**	**State 2**	**State 3**	**State 4**
−10.0°	−0.03	−3.94	−5.56	3.58	0.00	2.50	−5.00	0.00
−5.0°	−2.45	−5.30	−14.59	2.75	0.00	0.50	−7.50	0.00
0°	5.60	−11.06	−16.00	0.84	0.00	−2.00	−10.00	2.00
+5°	4.82	−14.78	−16.00	0.75	4.00	−2.00	−10.00	4.00
+10.0°	7.19	−15.0	−16.00	6.37	8.00	−2.00	−10.00	8.00
	Knee reference angles (deg)							
Slope	**State 1**	**State 2**	**State 3**		**State 1**	**State 2**	**State 3**	
−10.0°	8.90	10.36	30.00		11.97	10.26	16.33	
−5.0°	13.32	14.21	26.00		11.12	8.04	13.86	
0°	10.26	5.83	13.86		10.26	8.00	13.86	
+5.0°	23.52	15.80	20.17		11.12	8.04	13.85	
+10.0°	36.00	24.61	20.00		11.97	10.26	13.85	

Values for the slope angles not included can be found through linear interpolation.

The optimization problem was solved using Scipy's minimization function. Owing to the non-convex nature of the problem, a unique solution does not exist. Results from perturbation studies (Lee et al., 2016) and past studies using least squares approaches (Sup et al., 2011) helped judge the feasibility of the estimated joint parameter functions. Future efforts will involve solving the optimization problem using heuristics to decouple the stiffness and reference angles, and guarantee convergence.

3.2. Joint Control Parameter Functions

For both the ankle and the knee, $m = n = 4$ achieved the best results. The resulting ankle control parameter functions obeyed some monotonic trends across slope angles: (A1) Ankle stiffness during State 1-2 (ϕ_{HS} to ϕ_{HO}) was higher on steeper downslope and upslope terrain. The higher stiffness aids in stability during load transference from the trailing limb to the leading limb. (A2) During State 3, ankle stiffness increased as downslope angle grew less steep and the upslopes angle grew more steep. Here, the higher stiffness helps store more potential energy, resulting in higher push-off work. (A3) Ankle damping was found to be higher in downslope walking during State 1–2. The higher damping helps counter the higher heel-strike impact. (A4) The ankle reference angle during State 1 and State 4 was close to 0° during level and downslope walking, while it was dorsiflexed to match the slope angle during upslope walking. (A5) In State 2-3, the ankle reference angle greatly influences the generated push-off work. The angle is mildly plantarflexed during State 2, followed by a higher plantarflexed angle in State 3. The steepness of the reference angles increased with the steepness of the slope angle. The values of the angles have been reported in **Table 1**.

The following points are some of the key trends observed in the knee joint parameter functions. (K1) The knee stiffness

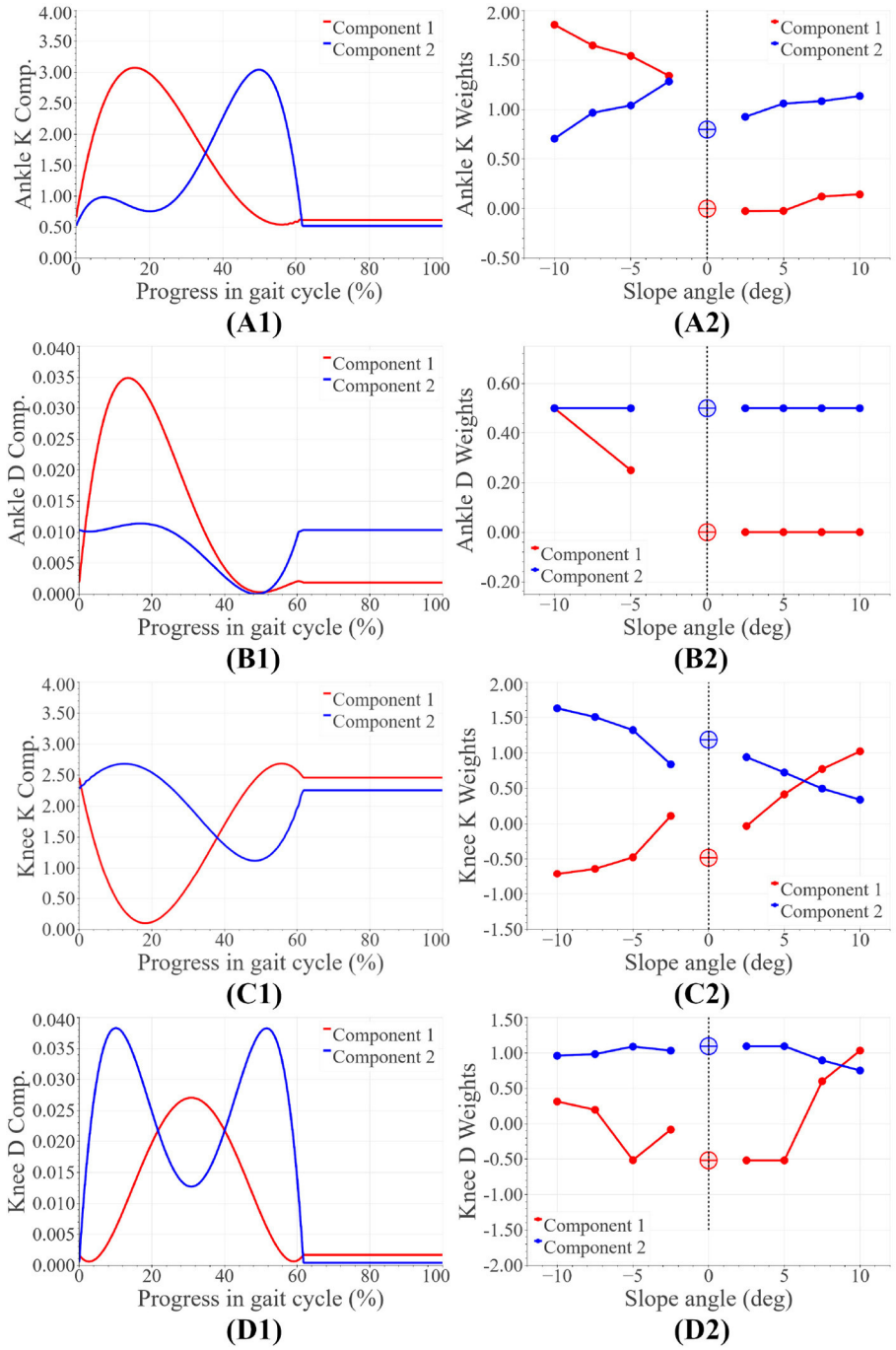

FIGURE 2 | Basis joint parameter functions: panels **(A1,B1)** represent the ankle stiffness (Nm/rad/kg) and damping (Nm/rad/kg) basis functions, while panels **(A2,B2)** are the corresponding weights. Panels **(C1,D1)** represent the knee stiffness (Nm/rad/kg) and damping (Nms/rad/kg) basis functions, while panels **(C2,D2)** are the corresponding weights.

during State 1–2 was higher at steeper downslope angles, aiding again in countering heel-strike impact and load-transference. (K2) On upslope terrain, the knee stiffness obeyed an opposite trend during State 1–2. The decrease in knee stiffness with the steepness in the upslope angle is believed to enable the required higher knee flexion for terrain adaptation. (K3) During State 3, the knee stiffness is higher on steeper upslope angles allowing for more propulsive knee extension while climbing up. (K4) Knee damping was found to be high during State 2 at steeper slopes (upslope or downslope), while remaining relatively the same

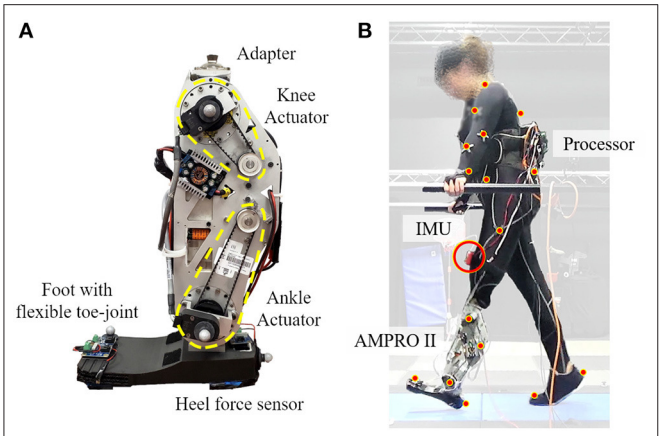

FIGURE 3 | Experimental set up: panel **(A)** is the powered transfemoral prosthesis, AMPRO II, panel **(B)** shows the amputee walking with AMPRO II in a motion capture environment.

during less steep slopes. (K4) The knee reference angles were more flexed on steeper slopes (downslope and Supslope).

Basis functions spanning all stiffness and damping functions for each joint were extracted using Principal Component Analysis. The functions and their weights have been shown in **Figure 2**. The entire set of stiffness and damping functions can be found in **Supplementary Figure 2**. The weights of the basis functions were found to vary monotonically within downslope and upslope walking. Some aberrations were observed, namely: (i) the ankle stiffness weights were higher than anticipated during downslope walking, leading to a discontinuity in weights from downslope to level walking. (ii) the ankle damping weights during downslope walking did not portray strong monotonicity. (ii) the weights corresponding to the knee's functions at -2.5° did not abide by the monotonic trends. We attribute these observations to the anomalies in the data set (discussed in section 2.2). We account for these peculiarities during controller implementation and tuning. The corrective measures are reported in the sections that follow.

4. IMPLEMENTATION

The proposed controller was tested on a powered transfemoral prosthesis, AMPRO II (shown in **Figure 3A**). The following subsections present details on the hardware, controller implementation, and the experiment with an amputee and an able-bodied subject.

4.1. Hardware

AMPRO II is operated by an embedded system (BeagleBone Black, element14, Leeds, United Kingdom) that controls an actuated ankle and knee joint. The prosthesis is equipped with a 3D printed foot with a toe joint. A force sensor (FlexiForce A502, Tekscan, South Boston, MA) placed under the heel helps detect heel-strike, while an Inertial Measurement Unit (MPU 9150, SparkFun Electronics, Niwot, CO) affixed to the user's thigh measures the thigh angle. These two parameters help determine the state in the finite state machine and the progress within each state.

4.2. State Estimation

The progress in the gait cycle (t) is identified using a phase variable that monotonically increases from 0 to 1 as the gait progresses from 0 to 100%. The variable is initialized upon heel-strike detection. A phase portrait of the thigh angle against its integral over the course of gait cycle presents an ellipse. The arc-tangent of the two plotted parameters is among the most successful and popular candidates for a phase variable (Villarreal and Gregg, 2016). Normalizing factors determined in real-time from prior gait cycles, help manipulate the usual elliptical phase portrait into a more circular one. Doing so results in a more linearly varying phase variable and consistent state estimation (Hong et al., 2021).

4.3. Controller Tuning

Given the slope's angle, an initial guess for joint stiffness and damping can be found using the impedance basis functions and their weights. The resulting stiffness and damping functions can be tuned further to generate the desired gait kinematics and kinetics. Prior to tuning, both joint parameter functions should be multiplied by the subject's body mass. This study proposes tuning the joint parameter functions as follows.

$$K_{tuned}(t) = \alpha K(t) + \gamma \tag{9}$$

$$D_{tuned}(t) = \beta D(t) \tag{10}$$

where α and β are scaling factors, and γ is an offset. Each joint has its own scaling and offset terms. Enumerated below is the tuning procedure. This study recommends tuning the controller for level, -10°, and $+10^{\circ}$ slope, followed by linearly interpolating parameters for other slope angles.

1. The factor α affects the amount of resistance provided by the system to ankle dorsiflexion and knee flexion. With the ankle, lowering α reduces push-off assistance, while with the knee, lowering α challenges the stability of a flexed knee. Perform the following in iterations.
   (a) Decrease α until the desired ankle dorsiflexion and knee flexion is observed in State 2. This study targeted 5° of ankle dorsiflexion and 10° of knee flexion.
   (b) According to the participant's preference, increase or decrease push-off assistance by, respectively, increasing or decreasing the ankle's plantarflexed reference angle during State 3.
2. Tune β to reach a compromise between the amount of damping preferred by the participant at heel-strike and smooth terrain adaptation post heel-strike.
3. Increase the offset γ to counter gravity and maintain ankle dorsiflexion during swing phase and knee flexion during terminal stance phase.
4. For downslope walking:
   (a) Set the ankle's swing reference angle to 0°.

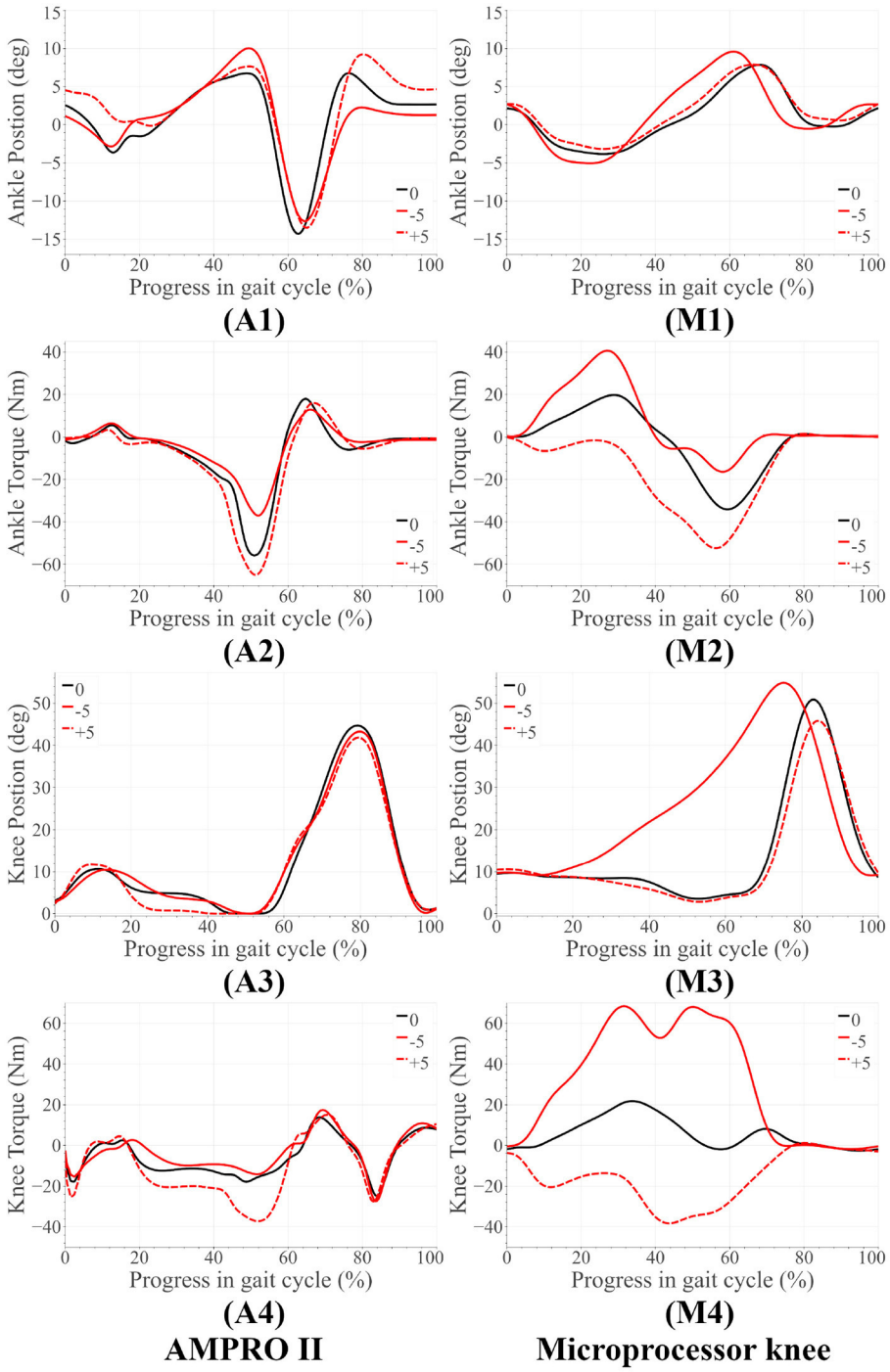

FIGURE 4 | Amputee results for upslope walking and downslope walking. The subfigures labeled **(A)** correspond to the AMPRO II ankle joint, **(M)** are for the Microprocessor knee prosthesis.

(b) Reduce the knee's reference angles to within the acceleration limits of the actuators while maintaining more flexion than level walking. The reference angle during State 2 ensures smooth transition from State 1 to State 3.

5. For upslope walking:

(a) Increase ankle dorsiflexion and knee flexion in State 1 to facilitate terrain adaptation while respecting the actuators' acceleration limits.

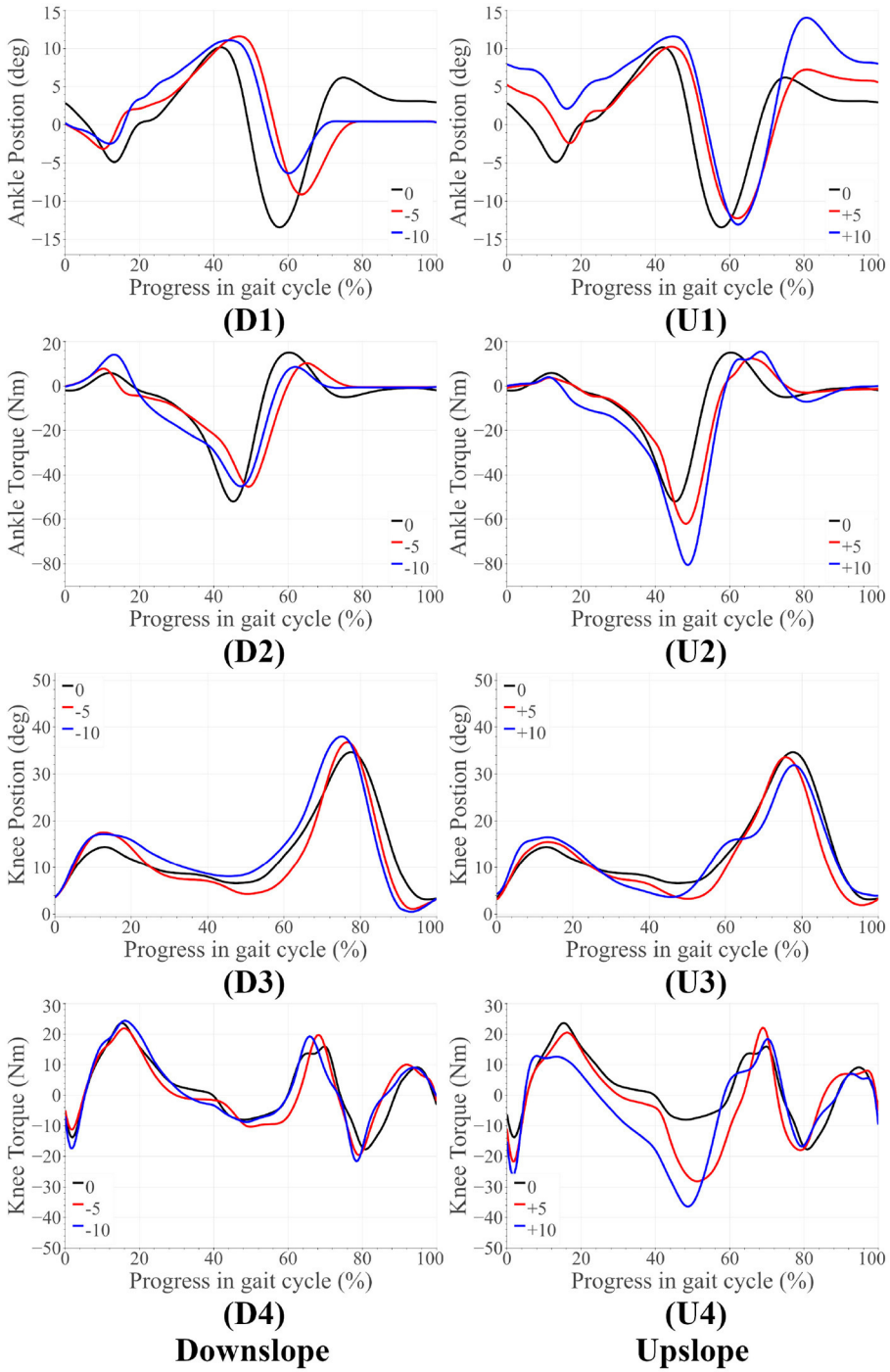

FIGURE 5 | Able-bodied subject results for upslope walking and downslope walking. The subfigures labeled **(U)** correspond to the upslope walking, while those labeled **(D)** are for downslope walking.

(b) Set the ankle's swing reference angle to be equal to that in State 1.
(c) Reduce the knee's reference angle during State 2 to be lower than that in State 1. Accordingly reduce State 3 reference angle to obey the actuators' acceleration limits.
6. Tune the ankle's State 2 reference angle to allow easy transitioning from State 1 to State 3.

4.4. Experiment

An indoor experiment was conducted with a transfemoral amputee (female, 164 cm, 66 kg w/o prosthesis). She utilizes

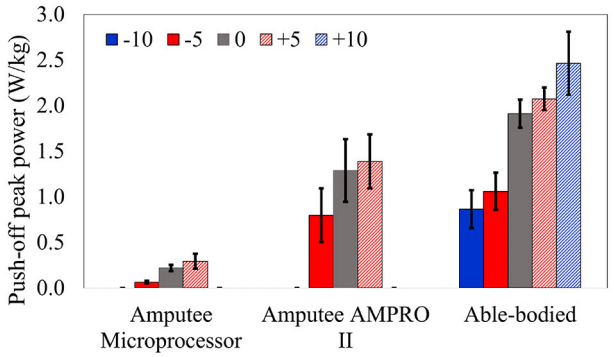

FIGURE 6 | Peak ankle push-off power experienced by the amputee with the microprocessor knee and AMPRO II. Also shown is the peak push-off power experienced by the able-bodied subject with AMPRO II.

a microprocessor knee, X3 Knee (Ottobock), with a Freedom Runaway Foot (Ottobock). **Figure 3** depicts the amputee walking with Ampro II. The amputee found walking on slopes uncomfortable even with the accustomed microprocessor prosthesis. Thus the amputee was only asked to walk on slopes angles $-5°$, $+5°$ with both AMPRO II and her microprocessor knee. The amputee underwent 8 training sessions with AMPRO II before data collection. To demonstrate feasibility of the controller on steeper slopes, a healthy young subject (female, 164 cm, 50 kg) was asked to walk with the prosthesis used a L-shape simulator. The healthy subject walked at $-10°$, $-5°$, $0°$, $+5°$, and $+10°$. All trials were conducted on an AMTI force-sensing tandem treadmill in a motion capture facility with Vicon Vantage motion capture cameras. The amputee chose to walk at 0.54 m/s on slopes, while the able-bodied subject walked at 0.62 m/s. A low speed was selected to avoid fatigue and assure safety. The chosen walking speed was fixed across all slope conditions. The controller was also tested with the amputee at 0.72 m/s on level ground to demonstrate the feasibility of the proposed controller at different walking speeds. The safety of the participant was assured with handrails located on either side of the treadmill. More images of the experiment can be found in **Supplementary Figures 3**, **4**. The experiment protocol has been approved by the Institutional Review Board (IRB) at Texas A&M University (IRB2015-0607F).

To assess the amputee's gait dynamics with the microprocessor knee markers were places on the lower body bony landmarks. Vicon Nexus was used to capture, filter, and interpolate marker data. Visual 3D software was then used to create a model specific to the user and calculate angles and torques.

5. RESULTS AND DISCUSSION

For both amputee and able-bodied subject, the ankle's and knee's tuning parameters were as follows. $\alpha = 1$, $\beta = 1$, and $\gamma = 50$ for level and upslope walking. During downslope walking, $\alpha = 0.67$. This value is consistent with our observation in section 2.1, i.e., the downslope walking kinematic data in Embry et al. (2018a) is higher than the expected value by a factor of $1.5 = 1/\alpha$. The tuned reference angles can be found in **Table 1**. The final proposed scheme in section 6 accounts for this corrective factor. The results for the amputee have been presented in **Figures 4**, **7**, while those for the able-bodied subject can be found in **Figure 5**. The gathered kinematics and kinetics were filtered using a Butterworth filter with a cut-off frequency of 20 Hz. The results correspond to the average of 10 gait cycles. **Figure 6** reports the peak ankle push-off for both subjects.

5.1. Amputee Trials

Figure 7 presents the amputee's walking data with AMPRO II at two speeds. As the walking speed increased, we noted an increase in ankle dorsiflexion during terminal stance phase and ankle plantarflexion during toe-off. The amputee's gait with both AMPRO II and the microprocessor knee on slopes (**Figure 4**) portrayed some trends similar to those found in healthy walking (see section 2). The ankle push-off moment, amount of knee extension moment between 40 and 60% of the gait cycle, and peak ankle push-off power increased as the slope varied from downslope to upslope. Also observed was higher ankle dorsiflexion at the beginning and end of the gait cycle during upslope walking. During downslope walking, the amputee's microprocessor knee was heavily flexed during stance phase, resulting in high knee flexion moment.

The amputee was able to walk with AMPRO II at various walking speeds. The push-off assistance and the kinematic differences noted earlier have been well-documented in able-bodied walking studies (Embry et al., 2018a; Montgomery and Grabowski, 2018). This proves the feasibility of the control scheme at different walking speeds. While using AMPRO II, the amputee's sloped walking kinematics and kinetics obeyed the monotonic trends found in healthy walking. With more gait training, these results are expected to improve. While using the microprocessor knee on downslopes, knee flexion gradually increased from heel-strike to approximately 70% of the gait cycle (**Figure 4M3**). This gradual yielding is due to the passive nature of the device, i.e., the device offers no active resistance to knee flexion. Studies such as Alexander et al. (2017) have made similar observations with other microprocessor knees. Additionally, the higher ankle dorsiflexion at the beginning and end of the gait cycle while walking upslope implies terrain adaptation. These results prove the feasibility of the control scheme for amputees.

5.2. Able-Bodied Trials

Some notable trends observed in ankle kinematics include: (i) higher dorsiflexed ankle at the beginning and end of the gait cycle on upslopes with the dorsiflexion increasing as the steepness of the slope increased, (ii) lesser toe-off plantarflexion on downslopes, (iii) higher knee flexion during initial stance phase on sloped terrain than level ground. In terms of kinetics, we observed: (i) that the ankle peak torque and power (**Figure 7**) varied monotonically with the angle as it varied from $-10°$ to $+10°$, (ii) higher knee extension torque on upslopes.

The variation in ankle angle at the beginning and end of the gait cycle facilitates terrain adaptation. The higher plantarflexion

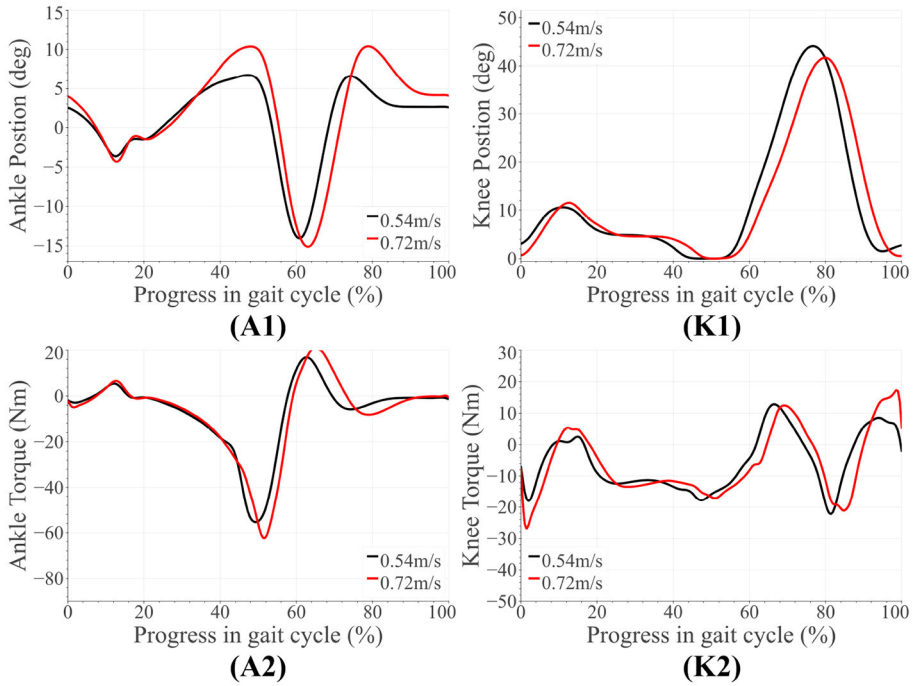

FIGURE 7 | Amputee results for level walking with AMPRO II at different speeds. The subfigures labeled **(A1,A2)** correspond to the ankle, while those labeled **(K1,K2)** are for the knee.

at toe-off during upslope walking is correlated to the higher push-off torque and power. Higher push-off assistance is required as the slope varies -10° to $+10^\circ$. The higher extension torque, ankle push-off torque and power on upsloped terrain are all correlated with this need for higher push-off assistance. All of these trends are observed in healthy walking (detailed in section 2), proving the feasibility of the control scheme on steeper slopes.

5.3. Comparison Against the State-of-the-Art

As mentioned in section 1.1, other attempts at sloped walking with impedance control strategies include (Sup et al., 2011; Fey et al., 2014; Bhakta et al., 2019). In this section, we will compare our results against the cited works using three metrics: number of tuning parameters per joint, capability of terrain adaptation, and variation in push-off assistance with the slope angle. Sup et al. (2011) had 15 tuning parameters per joint, of which 8–12 parameters were manually tuned for each tested slope condition (0°, $+5^\circ$, $+10^\circ$). The results indicated terrain adaptation and increase in push-off power as the slope angle increased. Both Fey et al. (2014) and Bhakta et al. (2019) implemented control strategies wherein the parameters varied as linear functions of the instantaneous joint angle or shank force. Overall, there were at least 12 tuning parameters per joint. Fey et al. (2014) tested the strategy at 0° and $+10^\circ$. The results showed no sign of terrain adaptation, however the push-off torque increased from level to inclined walking. Bhakta et al. (2019), on the other hand, tested the control strategy on various up and downslope walking conditions: $0^\circ, \pm 7.8^\circ, \pm 11.0^\circ, \pm 12.4^\circ, \pm 14.0^\circ$). The kinematic results showed some signs of terrain adaptation from level to sloped walking, but there was no identifiable difference from one slope angle to another within downslope or upslope walking results. Moreover, Bhakta et al. (2019) does not present kinetic results, limiting our ability to gauge the controller's performance.

Of all prior listed works, Sup et al. (2011) is the only study that successfully accomplished terrain adaptation and slope-based power assistance scaling during upslope walking. Our controller accomplishes the same with far fewer tuning

TABLE 2 | The coefficients of the implemented stiffness and damping polynomials.

Comp.	k_4	k_3	k_2	k_1	k_0
Ankle stiffness (Nm/rad/kg)					
Comp. 1	−108.61	234.61	−160.63	35.23	0.66
Comp. 2	−476.16	493.56	−146.91	14.63	0.52
Knee stiffness (Nm/rad/kg)					
Comp. 1	−13.291	−74.669	96.030	−27.672	2.525
Comp. 2	77.418	−41.999	−8.480	2.949	2.317
Comp.	d_4	d_3	d_2	d_1	d_0
Ankle damping (Nms/rad/kg)					
Comp. 1	−3.41	5.75	−3.18	0.58	0.00
Comp. 2	1.75	−1.60	0.36	−0.02	0.01
Knee damping (Nms/rad/kg)					
Comp. 1	3.905	−4.844	1.622	−0.074	0.001
Comp. 2	−13.022	16.146	−6.402	0.866	0.000

The word Component has been abbreviated to Comp.

TABLE 3 | Weight functions for the ankle and knee joint control parameter basis functions.

	Ankle	Knee
$w_{K1}(\psi)$	$-0.137\psi - 0.060$ for $\psi < 0$, 0 otherwise	$0.005\psi^2 + 0.090\psi - 0.270$
$w_{K2}(\psi)$	$0.032\psi + 0.84$	$-0.001\psi^2 - 0.065\psi + 1.106$
$w_{D1}(\psi)$	-0.05ψ for $\psi < 0$, 0 otherwise	$0.001\psi^3 + 0.014\psi^2 - 0.002\psi - 0.621$
$w_{D2}(\psi)$	0.5	$-0.003\psi^2 - 0.007\psi + 1.118$

parameters per joint (7–8 parameters per joint) than all three listed works. Unlike (Sup et al., 2011; Fey et al., 2014), our controller was tested on both up and downslope walking conditions, further strengthening our controller's performance. Further, unlike (Bhakta et al., 2019) which is limited to kinematic analysis, our controller can reproduce both kinematic and kinetic trends of healthy human sloped walking. Said trend reproduction is observable not only from downslope to upslope walking, but also from one slope angle to another within both downslope and upslope walking. Thus, our controller is a significant improvement on existing sloped walking impedance control strategies.

6. CONCLUSION

We propose a sloped walking control framework with fewer tuning parameters than the state-of-the-art controllers. The framework includes impedance control during stance phase and trajectory tracking during swing phase. The smooth transition between the two is facilitated by Bezier curves. The joint control parameters were determined through a data-driven optimization. Basis functions spanning the entire set of joint parameter functions were found through Principle Component Analysis. Given any slope angle, the stiffness and damping control parameters can be found as follows:

$$K_{tuned}(t) = \alpha(w_{K1}(\psi)K_{Comp1}(t) + w_{K2}(\psi)K_{Comp2}(t)) + \gamma \quad (11)$$

$$D_{tuned}(t) = \beta(w_{D1}(\psi)D_{Comp1}(t) + w_{D2}(\psi)D_{Comp2}(t)) \quad (12)$$

where K_{Comp1}, K_{Comp2} represent stiffness basis functions, while D_{Comp1}, D_{Comp2} are the damping basis functions. The associated polynomial coefficients can be found in **Table 2**. The weights for these basis polynomials vary as functions of the slope angle and are represented by $w_{K1}(\psi), w_{K2}(\psi), w_{D1}(\psi)$ and $w_{D2}(\psi)$. The coefficients of the weights have been tabulated in **Table 3**. A thorough tuning routine has also been prescribed in this paper. The tuning process can be automated using rule-based fuzzy logic. Testing with an amputee and able-bodied subject proved the feasibility of the proposed scheme at varying slope angles. Monotonic trends consistent with healthy human walking data were observed in both kinematics and kinetics. To name a few: push-off assistance (from both ankle and knee joint) increased as the slope angle increased from downslope angles to upslope angles, and the ankle angle at the beginning and end of the gait cycle varied according to the slope angle–enabling terrain adaptation.

Future work involves improving the phase variable based estimation scheme for sloped walking. Currently, phase variable schemes do not account the relationship between toe-off timing and slope angle (i.e., toe-off timing is delayed as the slope varies from steep downslope to steep upslope terrain). Improving the scheme would greatly reduce the standard deviations of peak push-off power seen in **Figure 6**. A possible approach is to mount a force sensor at the toe and update the toe-off timing–in the finite state machine–from one gait cycle to another. Another improvement to the existing control scheme involves employing a continuously varying reference angle. Doing so would improve the stability of the system under uncertainties in state estimation (Mohammadi and Gregg, 2019). Additionally, a continuously varying reference angle could further reduce the number of states in the finite state machine, further easing user customization of the proposed control scheme.

DATA AVAILABILITY STATEMENT

The raw data supporting the conclusions of this article will be made available by the authors, without undue reservation.

ETHICS STATEMENT

The studies involving human participants were reviewed and approved by Institutional Review Board at Texas A&M University. The patients/participants provided their written informed consent to participate in this study.

AUTHOR CONTRIBUTIONS

NA was the primary contributor for the proposed control scheme, data collection and processing. SP contributed to data collection and analysis. WH assisted with implementation of the control scheme. PH served as the principal investigator. All authors contributed to writing and reviewing this paper.

SUPPLEMENTARY MATERIAL

The Supplementary Material for this article can be found online at: https://www.frontiersin.org/articles/10.3389/fnbot.2021.790060/full#supplementary-material

REFERENCES

Alexander, N., Strutzenberger, G., and Schwameder, H. (2017). The use of the gradual yielding mechanism during downhill walking in transfemoral amputee gait-a case study. *ISBS Proc. Arch*. 35:249. doi: 10.1097/JPO.0000000000000293

Anil Kumar, N., Hong, W., and Hur, P. (2020). "Impedance control of a transfemoral prosthesis using continuously varying ankle impedances and multiple equilibria," in *2020 IEEE International Conference on Robotics and Automation* (Paris: ICRA), 1755–1761. doi: 10.1109/ICRA40945.2020.9197565

Beck, O. N., Taboga, P., and Grabowski, A. M. (2017). Prosthetic model, but not stiffness or height, affects the metabolic cost of running for athletes with unilateral transtibial amputations. *J. Appl. Physiol*. 123, 38–48. doi: 10.1152/japplphysiol.00896.2016

Bhakta, K., Camargo, J., Kunapuli, P., Childers, L., and Young, A. (2019). Impedance control strategies for enhancing sloped and level walking capabilities for individuals with transfemoral amputation using a powered multi-joint prosthesis. *Military Med*. 185, 490–499. doi: 10.1093/milmed/usz229

Colombo, G., Filippi, S., Rizzi, C., and Rotini, F. (2010). A new design paradigm for the development of custom-fit soft sockets for lower limb prostheses. *Comput. Indus*. 61, 513–523. doi: 10.1016/j.compind.2010.03.008

Comotti, C., Regazzoni, D., Rizzi, C., and Vitali, A. (2015). "Multi-material design and 3D printing method of lower limb prosthetic sockets," in *ACM International Conference Proceeding Series* (Lisbon), 42–45. doi: 10.1145/2838944.2838955

Embry, K., Villarreal, D., Macaluso, R., and Gregg, R. (2018a). The effect of walking incline and speed on human leg kinematics, kinetics, and EMG. *IEEE Dataport*. doi: 10.21227/gk32-e868

Embry, K. R., Villarreal, D. J., Macaluso, R. L., and Gregg, R. D. (2018b). Modeling the kinematics of human locomotion over continuously varying speeds and inclines. *IEEE Trans. Neural Syst. Rehabil. Eng*. 26, 2342–2350. doi: 10.1109/TNSRE.2018.2879570

Fey, N. P., Klute, G. K., and Neptune, R. R. (2013). Altering prosthetic foot stiffness influences foot and muscle function during below-knee amputee walking: a modeling and simulation analysis. *J. Biomech*. 46, 637–644. doi: 10.1016/j.jbiomech.2012.11.051

Fey, N. P., Simon, A. M., Young, A. J., and Hargrove, L. J. (2014). Controlling knee swing initiation and ankle plantarflexion with an active prosthesis on level and inclined surfaces at variable walking speeds. *IEEE J. Transl. Eng. Health Med*. 2, 1–12. doi: 10.1109/JTEHM.2014.2343228

Goldfarb, M. (2013). Consideration of powered prosthetic components as they relate to microprocessor knee systems. *J. Prosthet. Orthot*. 25, P65–P75. doi: 10.1097/JPO.0b013e3182a8953e

Hafner, B. J., and Askew, R. L. (2015). Physical performance and self-report outcomes associated with use of passive, adaptive, and active prosthetic knees in persons with unilateral, transfemoral amputation: Randomized crossover trial. *J. Rehabil. Res. Dev*. 52, 677–700. doi: 10.1682/JRRD.2014.09.0210

Herr, H. M., and Grabowski, A. M. (2012). Bionic ankle-foot prosthesis normalizes walking gait for persons with leg amputation. *Proc. R. Soc. B Biol. Sci*. 279, 457–464. doi: 10.1098/rspb.2011.1194

Hong, W., Kumar, N. A., and Hur, P. (2021). A phase-shifting based human gait phase estimation for powered transfemoral prostheses. *IEEE Robot. Automat. Lett*. 6, 5113–5120. doi: 10.1109/LRA.2021.3068907

Hong, W., Paredes, V., Chao, K., Patrick, S., and Hur, P. (2019). "Consolidated control framework to control a powered transfemoral prosthesis over inclined terrain conditions," in *2019 International Conference on Robotics and Automation (ICRA)*, 2838–2844. doi: 10.1109/ICRA.2019.8794140

Kaufman, K. R., Frittoli, S., and Frigo, C. A. (2012). Gait asymmetry of transfemoral amputees using mechanical and microprocessor-controlled prosthetic knees. *Clin. Biomech*. 27, 460–465. doi: 10.1016/j.clinbiomech.2011.11.011

Lawson, B. E., Mitchell, J., Truex, D., Shultz, A., Ledoux, E., and Goldfarb, M. (2014). A robotic leg prosthesis: design, control, and implementation. *IEEE Robot. Automat. Mag*. 21, 70–81. doi: 10.1109/MRA.2014.2360303

Lecomte, C., Ármannsdóttir, A. L., Starker, F., Tryggvason, H., Briem, K., and Brynjolfsson, S. (2021). Variable stiffness foot design and validation. *J. Biomech*. 122:110440. doi: 10.1016/j.jbiomech.2021.110440

Lee, H., Rouse, E. J., and Krebs, H. I. (2016). Summary of human ankle mechanical impedance during walking. *IEEE J. Transl. Eng. Health Med*. 4, 1–7. doi: 10.1109/JTEHM.2016.2601613

Mohammadi, A., and Gregg, R. D. (2019). Variable impedance control of powered knee prostheses using human-inspired algebraic curves. *J. Comput. Nonlinear Dyn*. 14, 1–10. doi: 10.1115/1.4043002

Montgomery, J. R., and Grabowski, A. M. (2018). The contributions of ankle, knee and hip joint work to individual leg work change during uphill and downhill walking over a range of speeds. *R. Soc. Open Sci*. 5:180550. doi: 10.1098/rsos.180550

Morgenroth, D. C., Roland, M., Pruziner, A. L., and Czerniecki, J. M. (2018). Transfemoral amputee intact limb loading and compensatory gait mechanics during down slope ambulation and the effect of prosthetic knee mechanisms. *Clin. Biomech*. 55, 65–72. doi: 10.1016/j.clinbiomech.2018.04.007

Paredes, V., Hong, W., Patrick, S., and Hur, P. (2016). "Upslope walking with transfemoral prosthesis using optimization based spline generation," in *2016 IEEE/RSJ International Conference on Intelligent Robots and Systems (IROS)* (Daejeon), 3204–3211. doi: 10.1109/IROS.2016.7759495

Sup, F., Bohara, A., and Goldfarb, M. (2008). Design and control of a powered transfemoral prosthesis. *Int. J. Robot. Res*. 27, 263–273. doi: 10.1177/0278364907084588

Sup, F., Varol, H. A., and Goldfarb, M. (2011). Upslope walking with a powered knee and ankle prosthesis: initial results with an amputee subject. *IEEE Trans. Neural Syst. Rehabil. Eng*. 19, 71–78. doi: 10.1109/TNSRE.2010.2087360

Villarreal, D. J., and Gregg, R. D. (2016). "Unified phase variables of relative degree two for human locomotion," in *2016 IEEE 38th Annual International Conference of the Engineering in Medicine and Biology Society (EMBC)* (Orlando: IEEE), 6262–6267. doi: 10.1109/EMBC.2016.7592160

Wen, Y., Si, J., Brandt, A., Gao, X., and Huang, H. H. (2020). Online reinforcement learning control for the personalization of a robotic knee prosthesis. *IEEE Trans. Cybernet*. 50, 2346–2356. doi: 10.1109/TCYB.2019.2890974

Wolf, E. J., Everding, V. Q., Linberg, A. L., Schnall, B. L., Czerniecki, J. M., and Gambel, J. M. (2012). Assessment of transfemoral amputees using C-leg and power knee for ascending and descending inclines and steps. *J. Rehabil. Res. Dev*. 49, 831–842. doi: 10.1682/JRRD.2010.12.0234

Ziegler-Graham, K., MacKenzie, E. J., Ephraim, P. L., Travison, T. G., and Brookmeyer, R. (2008). Estimating the prevalence of limb loss in the United States: 2005 to 2050. *Arch. Phys. Med. Rehabil*. 89, 422–429. doi: 10.1016/j.apmr.2007.11.005

Conflict of Interest: The authors declare that the research was conducted in the absence of any commercial or financial relationships that could be construed as a potential conflict of interest.

frontiers in Neurorobotics

ORIGINAL RESEARCH
published: 12 January 2022
doi: 10.3389/fnbot.2021.789743

Variable Admittance Control of a Hand Exoskeleton for Virtual Reality-Based Rehabilitation Tasks

*Alberto Topini†, William Sansom†, Nicola Secciani†, Lorenzo Bartalucci†, Alessandro Ridolfi and Benedetto Allotta**

Department of Industrial Engineering, University of Florence, Florence, Italy

Robot-based rehabilitation is consolidated as a viable and efficient practice to speed up and improve the recovery of lost functions. Several studies highlight that patients are encouraged to undergo their therapies and feel more involved in the process when collaborating with a user-friendly robotic environment. Object manipulation is a crucial element of hand rehabilitation treatments; however, as a standalone process may result in being repetitive and unstimulating in the long run. In this view, robotic devices, like hand exoskeletons, do arise as an excellent tool to boost both therapy's outcome and patient participation, especially when paired with the advantages offered by interacting with virtual reality (VR). Indeed, virtual environments can simulate real-life manipulation tasks and real-time assign a score to the patient's performance, thus providing challenging exercises while promoting training with a reward-based system. Besides, they can be easily reconfigured to match the patient's needs by manipulating exercise intensity, e.g., Assistance-As-Needed (AAN) and the required tasks. Modern VR can also render interaction forces when paired to wearable devices to give the user some sort of proprioceptive force or tactile feedback. Motivated by these considerations, a Hand Exoskeleton System (HES) has been designed to be interfaced with a variable admittance control to achieve VR-based rehabilitation tasks. The exoskeleton assists the patient's movements according to force feedback and following a reference value calculated inside the VR. Whenever the patient grasps a virtual object, the HES provides the user with a force feedback sensation. In this paper, the virtual environment, developed within the Webots framework and rendering a HES digital-twin mapping and mimicking the actual HES motion, will be described in detail. Furthermore, the admittance control strategy, which continuously varies the control parameters to best render the force sensation and adapt to the user's motion intentions, will be investigated. The proposed approach has been tested on a single subject in the framework of a pilot study.

Keywords: wearable robots, rehabilitation robotics, hand exoskeletons, variable admittance control, virtual reality

OPEN ACCESS

Edited by:
Chad Gregory Rose,
Auburn University, United States

Reviewed by:
Richard A. Foulds,
New Jersey Institute of Technology, United States
Monica Malvezzi,
University of Siena, Italy

***Correspondence:**
Benedetto Allotta
benedetto.allotta@unifi.it

†These authors have contributed equally to this work

Received: *05 October 2021*
Accepted: *15 December 2021*
Published: *12 January 2022*

Citation:
Topini A, Sansom W, Secciani N, Bartalucci L, Ridolfi A and Allotta B (2022) Variable Admittance Control of a Hand Exoskeleton for Virtual Reality-Based Rehabilitation Tasks. Front. Neurorobot. 15:789743. doi: 10.3389/fnbot.2021.789743

1. INTRODUCTION

Exoskeletons are a promising technology with a vast range of applications from the military to the industrial fields, from healthcare to injury prevention in physically stressful jobs. Besides, such devices are not only used to support the human body but can be exploited to drive an external robot in a primary-replicas fashion (Huang et al., 2018; Petrenko et al., 2019) or in imitation learning

applications (Huang et al., 2019; Hua et al., 2021). In the last decades, an increasing number of exoskeletons have been designed for patients affected by motor dysfunctions or disabilities and applied in rehabilitation therapies, guided training, or assistance in everyday actions (Molteni et al., 2018; Shi et al., 2019; du Plessis et al., 2021). Robot-based therapy has in fact been proved to be effective and beneficial for both patients, reducing recovery time while increasing results, and therapists, who can exploit real-time monitoring to assess progress and tune the exercises accordingly (Lum et al., 2002; Staubli et al., 2009).

The excellent mobility, characterized by 27 Degrees of Freedom (DOFs), the small size, and the intensive use make the hand one of the most challenging body parts to support with an exoskeleton. Nevertheless, Hand Exoskeletons Systems (HESs) are widely investigated as the hand's primary and crucial role in human's quality of life, making them extremely valuable (du Plessis et al., 2021). Key components in developing HESs are the mechanical design and the implementation of a proper control system. The former concerns the process that shall guarantee a coherent motion with the wearer's body; the latter regards instead the management of the exoskeleton motion that shall match the user's intentions. In this paper, the attention will focus on the control strategy.

Commonly, control techniques involve a combination of a low-level controller, usually a PID or a model-based inverse dynamics controller, and a high-level one, e.g., adaptive control, sliding mode, impedance/admittance model, and AI-based strategies (Anam and Al-Jumaily, 2012). Impedance/admittance control is largely used in applications that involve Human-Robot Interaction (HRI) since it allows to shape the perceived robot's dynamic properties (i.e., inertia, damping, and stiffness) while interacting with the surrounding environment (Song et al., 2019). Indeed, it has been observed that, in order to perform complex actions, like walking or grasping an object, the human body not only exerts a force through the muscles but also changes the limbs' impedance to adapt to the interaction with the various kinds of objects. This very same idea has been successfully applied in many robotic applications to perform a fluid and safe HRI. A field of particular interest arose to be Robotics for Medicine and Healthcare where impedance/admittance control strategies have been widely investigated in robotic rehabilitation for upper and lower limbs (Keemink et al., 2018) or, more recently, for post-stroke hand (Sandison et al., 2020) and arm (Qian et al., 2021) therapy. Another relevant feature of this strategy is the possibility of controlling simultaneously both position and contact forces in all the robot's workspace, thus keeping the interactions smooth and safe for the people, environment, and robot. This latter capability also sets apart admittance control from other hybrid position/force control strategies that divide the workspace into sub-regions.

Hand-in-hand with Robotics, another fast-growing technology is virtual reality (VR) with applications that span from education (Kavanagh et al., 2017; Radianti et al., 2020) and tourism (Yung and Khoo-Lattimore, 2019) to engineering design (Wang et al., 2018; Wolfartsberger, 2019) and surgical training (Pfandler et al., 2017; Bielsa, 2021). VR is low cost, has high flexibility, and great adaptability; these characteristics make it a noteworthy tool for rehabilitation allowing the design of personalized and safe sets of exercises and, at the same time, providing real-time feedback both for patients and therapists (Rose et al., 2018). Repetitive and boring sessions may become more stimulating, making the patient feel actively involved. Indeed, it has been demonstrated that VR training is an effective rehabilitation tool providing both short and long term improvement on motor functions and better psychological effects on patients over other traditional methods (de Araújo et al., 2019; Lei et al., 2019). Modern computers supply enough computational power that, combined with advanced developing tools and solvers, allow for the simulation of complex environments providing a very immersive experience.

Combining together exoskeletons with virtual environments, enhancing their inherent properties could lead to devices with an extraordinary capability to customize exercises and therapies. Additionally, given their flexibility, many applications can also be developed in different fields (e.g., pilot training).

1.1. Contribution and Paper Structure

This work's main contributions can be summarized in the following points:

- Development and validation of a VR environment for a HES comparing three different simulators: Gazebo[1] Pybullet[2] and Webots[3].
- Study, implementation, and testing of two different admittance control strategies with parameter tuning on a custom-developed digital twin and refinement over a real exoskeleton.
- Link, through a robot operating system (ROS)[4] architecture, the real exoskeleton to the virtual environment, thus enabling a user to physically perceive virtual objects on his hand through force feedback.
- Testing the whole system to assess its performance by means of a pilot study involving a single subject.

In this section, an outline of the motivation for the proposed work has been given, along with a first overview of the technical and theoretical tools employed. The remainder of the paper will be organized as follows: (i) Section 2 provides background information about the hand exoskeleton at the core of this work, the involved HRI framework, and the theoretical basis of the admittance control technique; (ii) Section 3 explores in detail about the whole design process, from the building and validation of the virtual environment to the description of the two admittance control strategies, through the explanation of each of the main design choices; (iii) Section 3 describes the design process from the beginning to the control strategy implementation; (iv) Section 4 outlines the achieved results at the end of a two-stage experimental test setup; (v) Section 5 concludes the paper exposing some final considerations.

[1]http://gazebosim.org (last accessed: 28th September 2021).
[2]https://pybullet.org (last accessed: 28th September 2021).
[3]https://cyberbotics.com (last accessed: 28th September 2021).
[4]https://www.ros.org (last accessed: 28th September 2021).

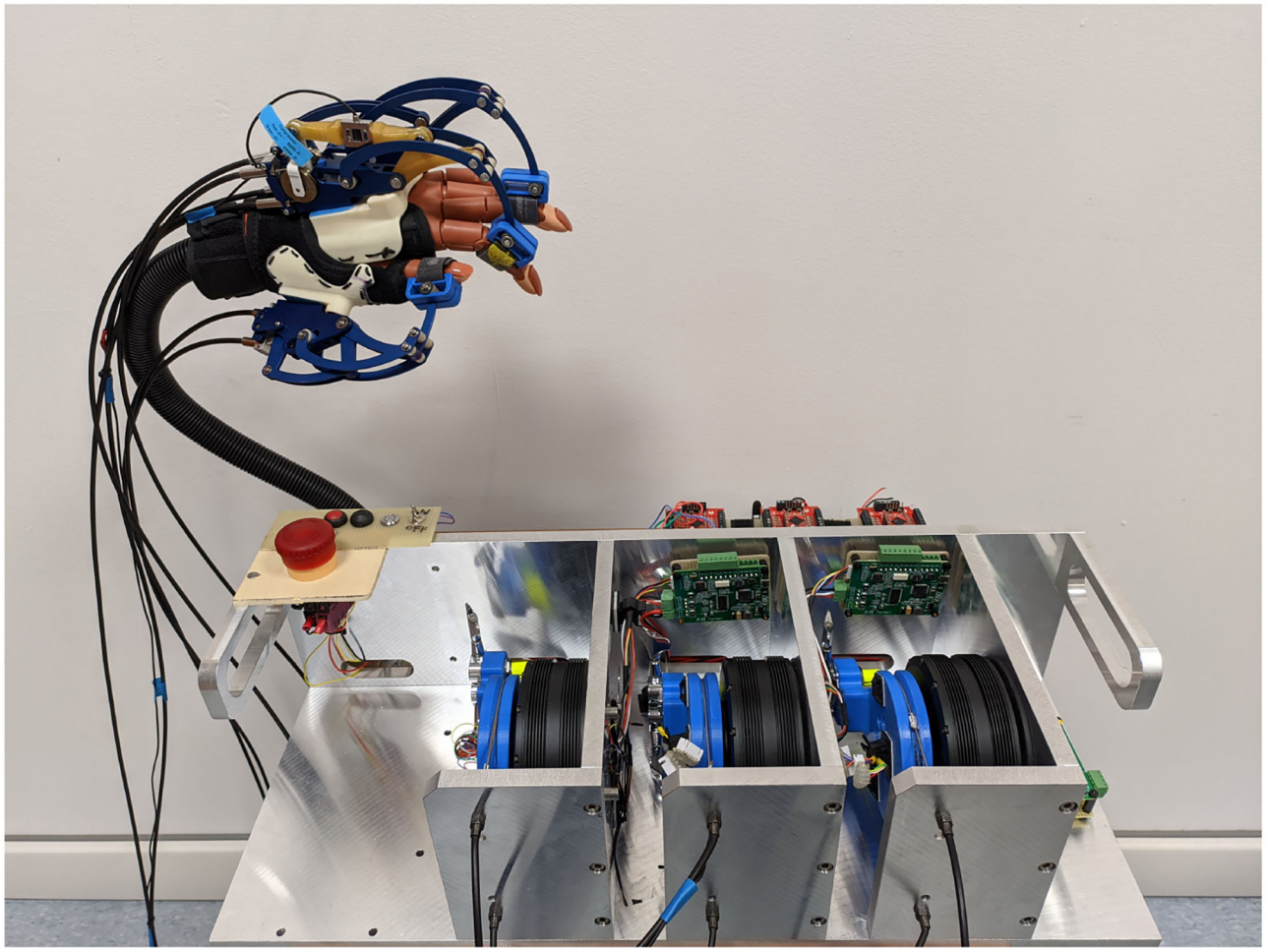

FIGURE 1 | The hand exoskeleton system (HES) developed, designed and realized by the Department of Industrial Engineering of the University of Florence (UNIFI DIEF) within the Brain machine interface in space manned missions: amplifying FOCUSed attention for error counterbalancing research project. The figure shows the wearable part mounted on a mannequin hand and the remote actuation system in foreground.

2. BACKGROUND

This section will present an overview of the hand exoskeleton exploited in this work, then the general framework for the HRI involved in this study, and, last, some background theory for admittance control. These topics reported here are useful background concepts for a comprehensive understanding of the subsequent sections.

2.1. The BMIFOCUS HES

The BMIFOCUS hand exoskeleton has been designed by a research team from the Mechatronics and Dynamic Modeling Laboratory (MDM Lab) at the Department of Industrial Engineering of the University of Florence (UNIFI DIEF) and MOV'IT S.r.l. (Pisa, Italy) as an innovative HES for Assistance-As-Needed (AAN) rehabilitation for tasks, such as grasping and pinching (Bartalucci et al., 2020). The previous exoskeleton already addressed the issue of mechanically reproducing complex finger kinematics with great accuracy exploiting a single-DOF rigid kinematism (Conti et al., 2017). This innovative device has been realized in the framework of the BMIFOCUS research project (funded by the Tuscany Region, Italy) on the basis of a previously developed prototype (Bartalucci et al., 2020). The HES has been redesigned to satisfy the new project requirements:

- the independent motion of, at least, three fingers (i.e., thumb, index, and middle finger);
- maximum load on each finger mechanism end-effector[5]: 20 N;
- reversibility for patients' safety in case of involuntary muscle contractions;
- the total mass of the wearable part below 0.5 kg;
- adaptability to different hand sizes.

The BMIFOCUS HES is comprised of two distinct parts: the Remote Actuation System (RAS) and the wearable exoskeleton, shown in **Figure 1**, respectively, on the left and on the right. The wearable part is composed of a base platform housing from one to four different finger mechanisms made of aluminum alloy

[5]According to the HES architecture presented in Bartalucci et al. (2020), the finger mechanism end-effector acts on the corresponding finger middle phalanx.

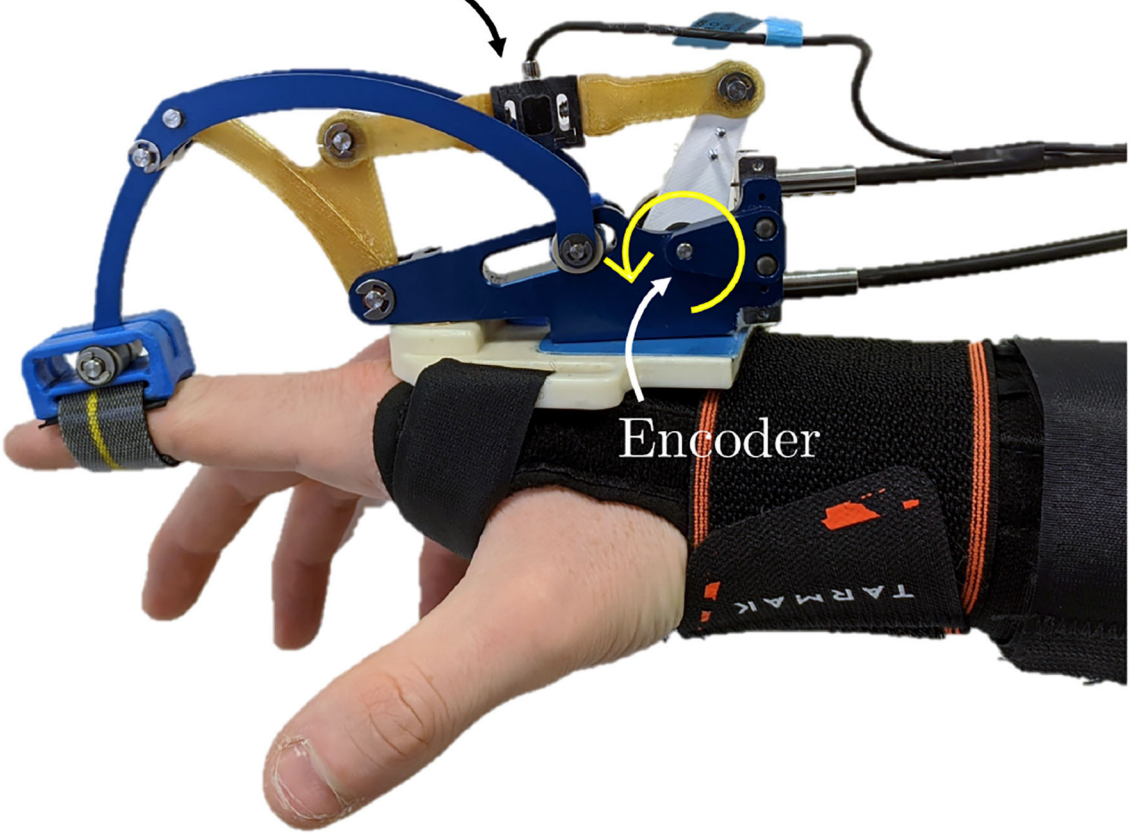

FIGURE 2 | Overview of the sensors mounted on each finger mechanism. The yellow arrow identifies the only Degrees of Freedom (DOF) of the particular kinematic structure.

that exploit a four-bar linkage to actuate the finger. Encoders and load cells (one per each finger mechanism) provide feedback measurements of angular position, speed, and exerted force (as shown in **Figure 2**). The RAS has a modular structure to make each finger independent from one another. It is based on a Bowden-cable transmission system connected to each of the finger mechanisms by means of a custom pulley. Thanks to this structure, the system minimizes the number of components on the user's limb and allows for remote placement of the actuation system without limiting the user's movements. The actuation is performed by means of brush-less DC motors (one per each finger involved) speed-controlled by an independent PID controller specifically tuned for the corresponding finger. By design choice, the motors have no extra gears and the pulleys on the finger mechanisms have diameter four times smaller than the one of the motor pulleys: this guarantees that the user is always able to overcome the motor torque to avoid injuries during, for example, an involuntary muscle spasm.

2.2. Physical Human-Robot Interaction (pHRI)

A valuable framework for understanding pHRI is described in Losey et al. (2018), which provides guidance in designing such systems and setting proper requirements. The study identifies three crucial points in applications with shared control between humans and robots: intent detection, arbitration, and feedback.

Intent detection is defined as "*the need for the robot to have knowledge of some aspect of the human's planned action in order for the robot to appropriately assist toward achieving that action*." This means that the control system needs to acquire some kind of signal and from this data infer the user's intention in order to properly drive the robot. Many possible approaches can be adopted. Complex data like ElectroEncephaloGraphy (EEG) or ElectroMyoGraphy (EMG) can be exploited to collect signals and then interpret them through machine learning algorithms, e.g., Support Vector Machines (SVMs), Hidden Markov Models (HMMs), or Artificial Neural Networks (ANNs). Conversely, intents can be deduced from simpler signals, like force or torque measurements, exploiting Kalman filters or other heuristics methods.

In this project, force measurements are acquired from load cells directly attached to the exoskeleton finger mechanisms. These measurements, as detailed in Section 3.2, have been either directly passed as a reference for the control system for the classical admittance control, or compared with the finger angular speed direction for the variable admittance control. In the latter

case, the finger angular speeds, acquired from the magnetic encoders mounted on each finger mechanism, become part of the data necessary for intent detection.

Arbitration is intended as *"the division of control among agents when attempting to accomplish some tasks"* where the word *agents* refer to both human operator(s) and robot(s). Four types of arbitration can be distinguished: (i) *co-activity* where each agent performs his/its own sub-tasks; (ii) *primary-replica* where one agent (usually the robot) follows the other's intention (commonly the human operator); (iii) *teacher-student*, often referred to as AAN in rehabilitation, consists of *"attempting to train humans using robotic platforms"*; (iv) *collaboration* where human and robot work together to reach a desired goal.

The admittance control strategy adopted in our system performs a combination of the primary-replica and teacher-student kind of arbitration.

Feedback to the human operator can be provided through visual, aural, or force signals. It is easy to provide visual and aural information through monitors and speakers. Force feedback instead is more challenging and, at the same time, of great interest in HRI because of its similarity with sensors embedded in our muscles and skin. The most common wearable force feedback devices are based on vibration, skin stretch, or pressure while other technologies rely on direct nerve stimulation.

Losey et al. (2018) identify several benefits in combining visual and force feedback. In the proposed work, both have been used. Visual feedback is provided by means of VR environment representation on a computer screen, while force feedback is obtained from the exoskeleton's finger mechanisms acting on the user's fingers thus providing a way for the user to feel reaction forces computed in the VR when interacting with virtual objects.

Focusing on the proposed research activity, the overall pHRI architecture is reported in **Figure 3**. Intention detection is first performed exploiting the force sensors on the exoskeleton; specifically, the intention detection algorithms investigates if the user wants to accelerate or decelerate the motion of each finger independently. At the same time, the position sensors mounted on each of the finger mechanisms drive the motion of the virtual replica of the exoskeleton. While VR gives visual feedback to the user, the virtual reality controller calculates the possible interaction forces with virtual objects. This information is fed to the admittance control algorithm (high-level control) that provides the speed reference for each of the motors. PID-based motor drivers (low-level control) then track such references, allowing the exoskeleton to produce the desired motion.

In other words, the exoskeleton assists the patient's movements according to the detected intention and following a reference force value calculated inside the VR (which renders the digital-twin mapping and mimicking the real exoskeleton motion). Whenever the patient grasps a virtual object, the VR changes the reference force value and the HES provides the user with force feedback as he/she was physically interacting with it.

2.3. Impedance/Admittance Control

As already reported, impedance/admittance control is one of the most used strategies in exoskeletons ad rehabilitation robots (Anam and Al-Jumaily, 2012; Song et al., 2019). Its core idea is applying some corrections to the robot's trajectory in order to achieve a desired dynamic interaction between robot and environment. This is performed through two nested control loops: the high-level one that computes the desired dynamical behavior generating references for the low-level one that usually controls either the robot's position, force, or torque.

The *impedance control* technique, also known as force/torque-based control, exploits an impedance model that, starting from the error between the desired end-effector's position (x_d) and the measured one (x), computes the desired contact force (Fc) between the robot and the environment (in this case, the human operator). An inner loop applies this torque reference (τ) to the robot actuators once mapped according to its transposed Jacobian (J^T). The actual force (F) exerted by the robot on the environment then produce the actual end-effector's position (x), from which the further iteration starts. This control strategy scheme is shown in **Figure 4**.

The *admittance control* method, known instead as position-based control, adopts the opposite approach. First, the contact force (F) is measured and input into the admittance model that calculates a relative displacement (Δx), intended as the estimated difference between where the robot is (x) and where it should be. Last, the error between the desired trajectory (x_d) and the relative displacement guides the robot through a position control loop. This second implementation is shown in **Figure 5**.

Impedance and admittance control strategies are two sides of the same coin, both methods have their advantages and disadvantages, choosing one over the other depends on the kind of sensors present on the manipulator, whether the environment is stiff or soft, if it is more important to control precisely position or contact force in the given application, and other factors. Some guidelines are provided in Song et al. (2019) and Schumacher et al. (2019).

In the proposed study, the admittance control method has been preferred over the impedance control technique. The reason for this choice lays in the architecture of the system: according to **Figure 3**, the control strategy takes as input one or more force signals and calculates a reference speed value for the motors. The general control scheme, therefore, becomes of the position-based type, as the one shown in **Figure 5**.

2.3.1. Mathematical Formulation

Mechanical impedance represents the relationship between motion and applied force (admittance is instead defined as the inverse of impedance), in Laplace domain, it is defined as:

$$Z(s) = \frac{F(s)}{\dot{X}_r(s)} \tag{1}$$

where $X_r(s)$ is the relative displacement between actual and equilibrium position, i.e. $X_r(s) = X(s) - X_d(s)$, $F(s)$ is the applied force, and $Z(s)$ is the impedance model, usually assumed in the following linear form Song et al. (2019):

$$Z(s) = Ms + B + \frac{K}{s} \tag{2}$$

M, B, and K represent, respectively, the inertia, damping, and stiffness matrices and represent the model's parameters to be

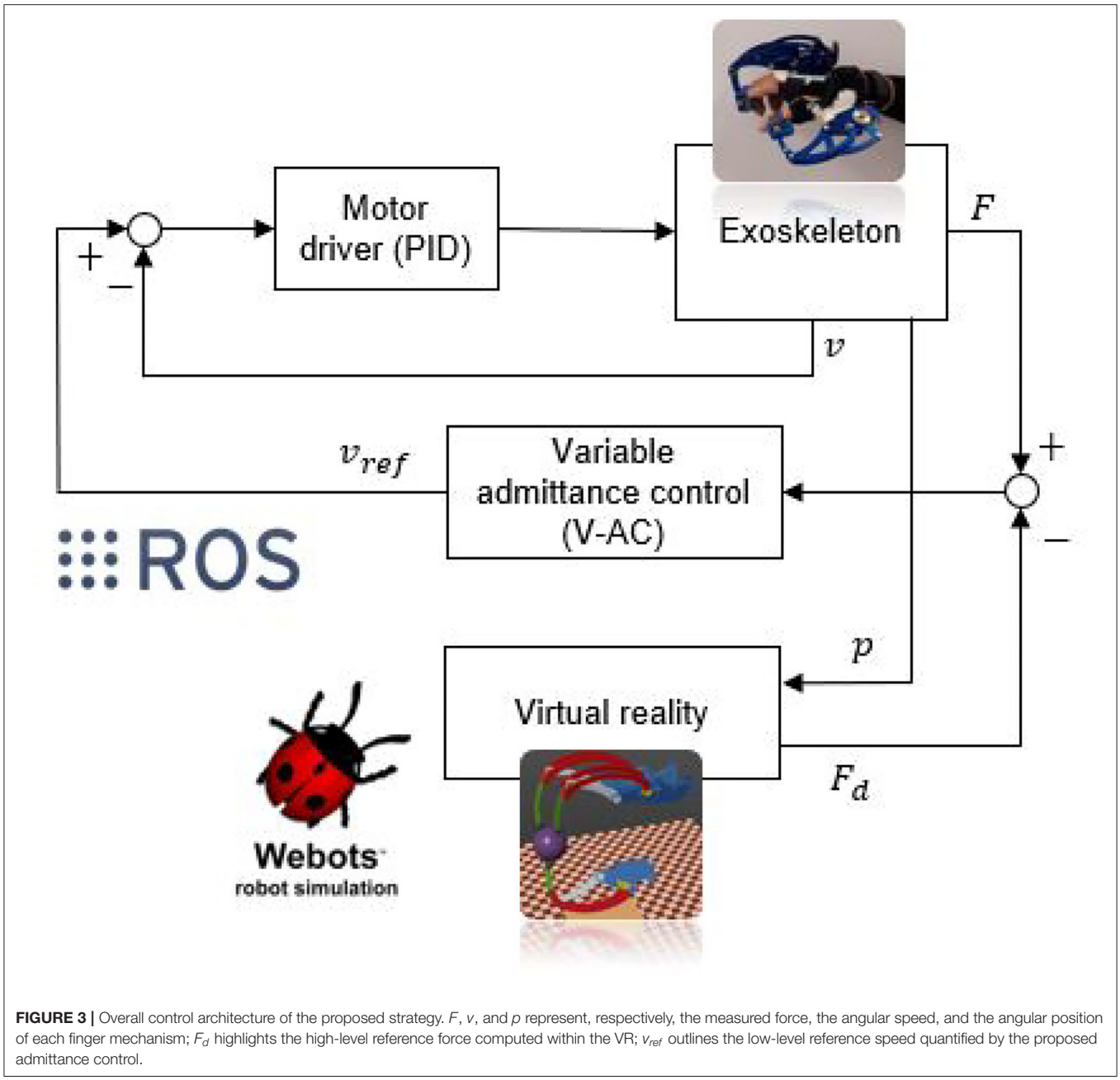

FIGURE 3 | Overall control architecture of the proposed strategy. F, v, and p represent, respectively, the measured force, the angular speed, and the angular position of each finger mechanism; F_d highlights the high-level reference force computed within the VR; v_{ref} outlines the low-level reference speed quantified by the proposed admittance control.

defined. By merging Equation 1 and 2, and translating the result into the time domain, the following is obtained:

$$M(\ddot{x} - \ddot{x}_d) + B(\dot{x} - \dot{x}_d) + K(x - x_d) = F(t) \quad (3)$$

where $F(t)$ represents the contact force, $x(t)$ and $x_d(t)$ represent the actual and desired end-effector's position, respectively.

As a means to overcome some practical challenges in impedance control, like unknown environment's characteristics, a modified version of Equation 3 has been proposed in Seraji and Colbaugh (1997), Jung et al. (2004), and Roveda et al. (2015):

$$M(\ddot{x} - \ddot{x}_d) + B(\dot{x} - \dot{x}_d) + K(x - x_d) = F(t) - F_d(t) \quad (4)$$

where $F_d(t)$ is the desired contact force. This strategy is named *force-tracking admittance control* and is represented in **Figure 6**.

Its advantage lies in the capability of following simultaneously a force and position reference while enforcing the motion characteristics (K, B, M) defined in the model. This property has been exploited in this project to provide force feedback computed within a virtual environment to a patient's hand wearing the exoskeleton (see section 4). Besides, the same feature could be used for AAN treatments if a proper fitting reference F_d is generated.

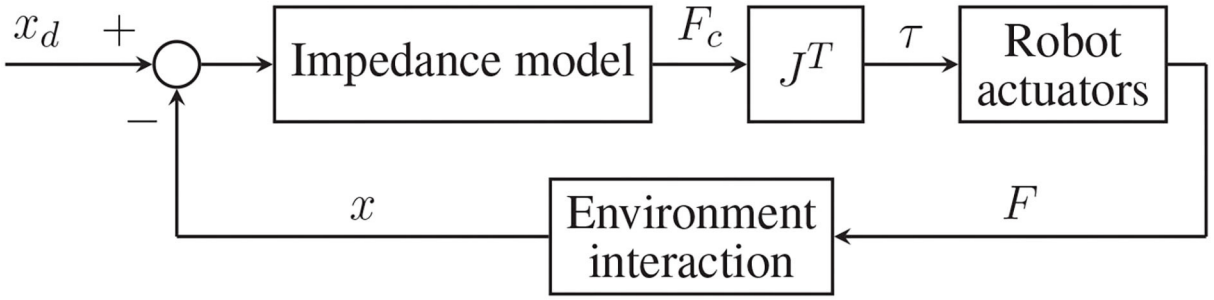

FIGURE 4 | General scheme of an impedance (torque-based) control.

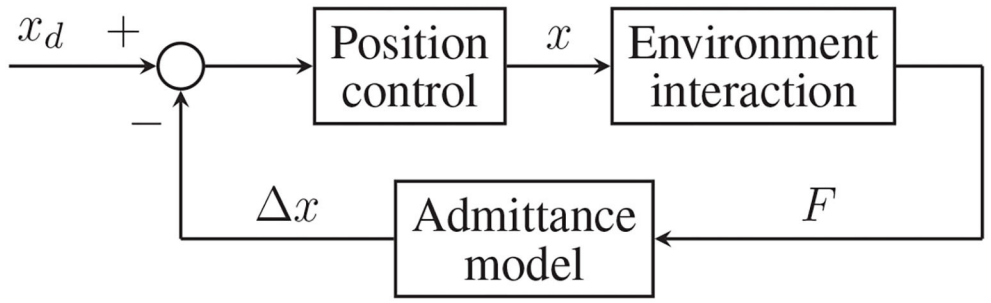

FIGURE 5 | General scheme of the admittance (position-based) control.

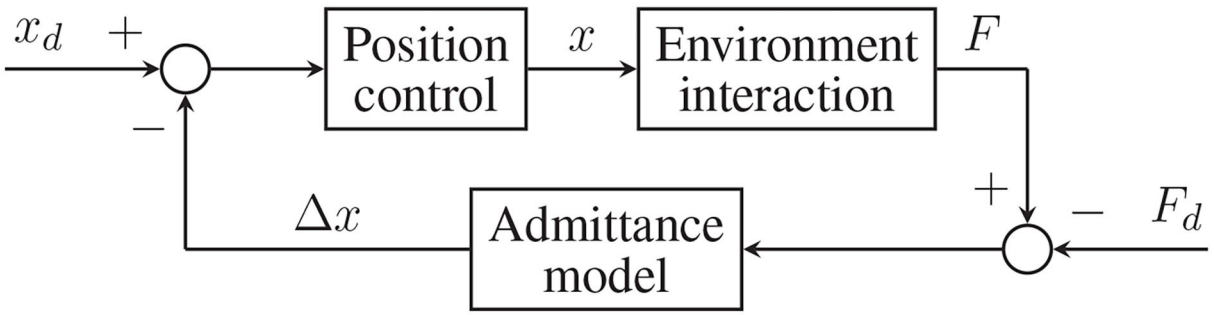

FIGURE 6 | Force-tracking admittance control general scheme.

2.3.2. Stability

Investigating the so-called *coupled stability* is considered one of the most efficient ways to study the stability of admittance control strategies (Song et al., 2019). This property consists in the stability for the robot-environment coupled system and it is crucial in our analysis because of the complex interactions that may occur. Additionally, two different operating modes are usually necessary, namely, the constrained and free motion, that is when the manipulator and environment are or are not in direct contact. In the free motion phase, the controller characteristics alone are enough to determine the system's stability, while during the constrained phase performance is influenced by the environment's properties.

A passivity criterion has been proposed for passive environments (Colgate and Hogan, 1988; Hogan and Buerger, 2018) to analyze coupled stability. However, in HRI, the "environment" is typically a limb that can hardly be modeled as passive since it can move through muscles activation. Therefore, the Passivity criterion should not be directly applied to such applications. Nonetheless, as reported in Kim et al. (2018), it has been proved that stability is preserved when the environment's stiffness is not too high, as in the case of human limbs.

In the proposed work, the trial and error process suggested in Lecours et al. (2012) has been used to identify the stability limit values for inertia and damping of the coupled system. The rigid component of the system K has been neglected by considering, as a first approximation, the limb interaction fully compliant

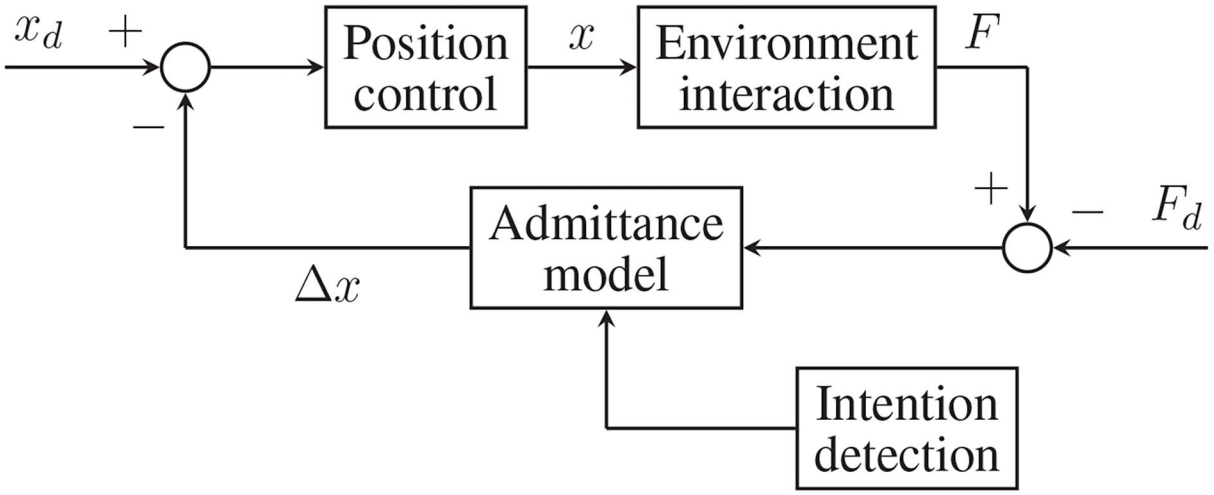

FIGURE 7 | Variable admittance control scheme with force-tracking capabilities.

with the exoskeleton motion. Such boundaries have been set by incrementally varying the parameter values until instability (shown as critical fluctuating vibrations) arose for minimum inertia of 0.005 kgm^2 ($M \geq 0.005$) and maximum damping of 0.25 Ns/m ($B \leq 0.25$). The stiffness component of the system K has been neglected by considering, as a first approximation, the limb interaction fully compliant with the exoskeleton motion.

2.4. Advanced Implementations

Several new approaches derived from the classical admittance control described above have been proposed in the scientific literature (Ikeura et al., 2002; Sado et al., 2014; Li et al., 2017; Souzanchi-K et al., 2017; Song et al., 2019). Some of them are based on robust and adaptive methods, machine learning techniques, and variable impedance/admittance.

Robust impedance control has the purpose of maintaining desired mechanical dynamics in presence of model parametric uncertainties, unknown environments, and other common sources of disturbances. Solutions based on the sliding mode control technique have been proposed (Lu and Goldenberg, 1995). Other methods use neural networks to model uncertainty compensation (Jung and Hsia, 1998) or direct and indirect adaptive algorithms for online parameter modulation (Hogan, 1984; Tsumugiwa et al., 2002).

Learning techniques have been successfully employed to determine optimal impedance values and trajectories. Frequently used models are neural networks combined with reinforcement learning methods, these strategies are called "inverse dynamic model learning" or "nonlinear regulator learning" (Gomi and Kawato, 1993; Li et al., 2017; Song et al., 2019).

Variable admittance strategies (see **Figure 7**) are the ones that aim at imitating human's approach to motion: specifically, humans change their bodies, dynamic properties while performing complex movements like walking or interacting with different objects (Hogan, 1984). This same idea has been explored in the human-robot interaction field resulting in many different strategies (Ikeura et al., 1994; Tsumugiwa et al., 2002; Duchaine and Gosselin, 2007; Abu-Dakka and Saveriano, 2020). The user's intention is detected during a preliminary phase through sensors and inference algorithms, then input into the admittance model and proper parameters values (K, B, and M) are computed with some heuristics technique (Lee and Buss, 2008; Song et al., 2019). One of these methods has been implemented and tested in this project and will be described more in detail in section 3.2.

3. METHODOLOGY

In this section, the implementation details of the proposed overall architecture will be deeply highlighted. First, the several design guidelines upon which the virtual environment has been built and validated will be illustrated. Subsequently, the implemented admittance control strategies will be described by considering both the theoretical aspects as well as the experimental outcomes.

3.1. VR Environment Selection and Development

In order to design a suitable VR environment, several required features have been taken into accounts. Primarily, the physics simulator framework or library needs to provide the possibility to build custom robots and/or robot-like objects so as to straightforwardly implement a faithful digital replica of the BMIFOCUS exoskeleton device. In the second place, the virtual twin should be capable of being motion controlled while supplying realistic sensory feedback signals. Additionally, the digital exoskeleton requires to be embeddable in software architecture (e.g., the ROS framework) enabling an effortless, peer-to-peer interaction with the real BMIFOCUS device as far as both the exchanged force signals and a comprehensive visual representation are concerned. Motivated by these considerations, three distinct physics simulators have been identified as

appropriate to fit the above-mentioned requirements: Gazebo, Pybullet, and Webots. A brief overview of each framework along with the respective features and drawbacks will be introduced to argue the final selection for this research activity.

Gazebo represents the default ROS physics simulator and, therefore, has been extensively employed for robotics simulations in a wide range of application fields. Based on the Bullet Physics library, the robots properties can be easily defined in the Universal Robot Description Format (URDF) format[6], and the robot links can be driven by means of dedicated ROS packages. Despite being specifically integrated for a ROS-based software architecture, this solution has been discarded after several excessively unstable simulation tests caused by numerical approximations of the complex exoskeleton kinematics.

Pybullet is the python binding of the Bullet Physics library and is strongly recommended for robotics and VR applications. Its multi-thread internal structure allows for straightforward incorporation with ROS: a robot structure can be loaded from a URDF file whereas the simulation itself is handled by the library API. However, even in this case, the simulation of the BMIFOCUS exoskeleton closed chain kinematics has outlined not negligible undesired behaviors leading to an overall instability of the simulated scene.

Finally, **Webots: robot simulator** has been checked as well. Based on the Open Dynamics Engine (ODE) project, contrary to Gazebo and Pybullet, it does not make use of the URDF standard for the robot definition. Conversely, the VRML97 description language is exploited. A specific ROS package, *webots_ros*[7], is provided so as to smoothly integrate the Webots API controllers into ROS nodes. Arising more stable than the others, Webots has been picked as the ideal solution to handle the VR requirements explained in the first paragraph of this section.

Once identified Webots as the proper virtual simulator, the BMIFOCUS exoskeleton digital-twin has been developed in order to provide visual guidance to a user during rehabilitation exercises as well as sensory feedback from the VR environment (as shown in **Figure 8**). The kinematics of the real device has been replicated by means of virtual components (i.e., links and joints) that physically mimic the mechanical characteristics of the real parts. Each virtual exoskeleton's finger mechanism is driven with a virtual motor positioned in correspondence with their only DOF so as to actuate them the same way the real ones are. These virtual actuators are position controlled with a PID following the real exoskeleton's position as a reference and regulated through a custom ROS node. Force feedback signals are measured from virtual force sensors placed on each virtual finger mechanism end-effector (the gray spheres in **Figure 8**). This solution enables a good matching of the virtual and real exoskeletons behavior (as shown in **Figure 9**) providing the perfect test bench to preliminarily try the proposed control strategy.

3.2. Proposed Admittance Control

As previously illustrated in section 2.3, an admittance control architecture comprises of two nested feedback loops: the outer regulates the desired dynamics and the inner correctly drives the actuation system. In this case, since the BMIFOCUS exoskeleton actuators are handled by a PID-based speed-controller, the admittance filter is designed so as to provide speed references for the exoskeleton device. More specifically, the proposed admittance control is decentralized over the three HES finger mechanism; therefore, despite being presented hereafter for a single finger approach, the implemented architecture has been extended to the whole set of mechanisms. Aiming not to impair the patient's movements and simulate a free motion when not handling virtual objects or, conversely, providing the patient with the correct force feedback when instead is interacting with them, the following admittance model has been adopted:

$$M\ddot{x} + B\dot{x} = F(t) - F_d(t) \tag{5}$$

where $F_d(t)$ is supplied by the virtual force sensors. A block diagram representation is reported in **Figure 10**.

By further discretizing Equation 5 with sampling time T_s, the speed reference at the discrete time step k for the PID control of the HES inner loop can be expressed as:

$$v(k) = v(k-1) + \frac{F(k) - F_d(k) - Bv(k-1)}{M} T_s \tag{6}$$

Starting from this mathematical representation, two distinct admittance control strategies have been specifically designed, implemented, and tested:

- *Classical Admittance Control* (C-AC): the canonical controller with force-tracking ability reported in Equation 6;
- *Variable Admittance Control* (V-AC): the former C-AC controller was modified so as the inertia (M) and damping (B) terms are online adapted to the user's motion intention. As previously mentioned, such a procedure has been inspired by Lecours et al. (2012); however, the application field is clearly distinct from the original one. Furthermore, in Lecours et al. (2012), neither a desired reference force nor a VR system, source of such force reference value, were introduced.

Both the mentioned methodologies will be hereafter detailed along with a comparative analysis of the achieved results.

3.2.1. Classical Admittance Control

As outlined in Equation 5, this technique requires the inertia as well as the damping term to be heuristically tuned. From a qualitative point of view, in order to have a fast dynamic response, very low inertia is desired; on the other hand, an excessively low value may cause system instability. Consequently, after a precise parameter-tuning stage, a final value $M = 0.008\ kgm^2$ has been selected, slightly larger than the estimated stability threshold of $M = 0.005\ kgm^2$ (refer to section 2.3.2). Turning to the damping tuning procedure, several different values have been tested. Tests highlighted that a large damping value provides a fast filter response characterized by a reactive reference modification following the trend of the force measurements from the HES. However, as reported in section 2.3.2, high damping values may

[6]http://wiki.ros.org/urdf
[7]http://wiki.ros.org/webots_ros

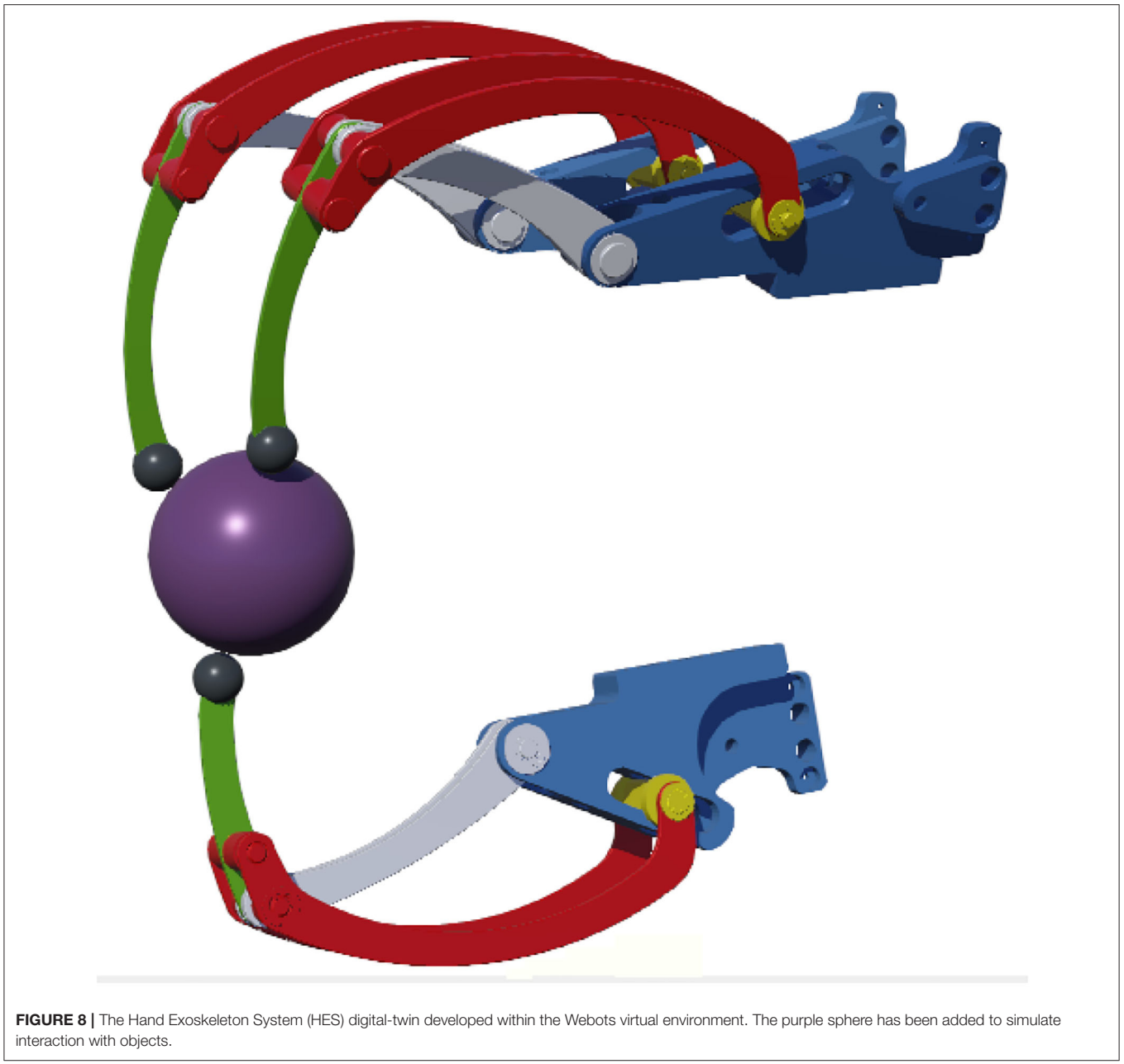

FIGURE 8 | The Hand Exoskeleton System (HES) digital-twin developed within the Webots virtual environment. The purple sphere has been added to simulate interaction with objects.

also cause system instability. As a result, the value of $B = 0.145\ Ns/m$ has been set as the optimal damping value for the proposed system.

3.2.2. Variable Admittance Control (V-AC)

As previously mentioned, this approach has been implemented relying on the key idea to real-time vary the admittance model parameters so as to actively assist the patient's desired motion and enhance the BMIFOCUS device transparency. Indeed, the inertia and damping coefficient of Equation 5 are adjusted online according to the user's intention. A primary heuristic criterion has been employed to achieve the user's motion detection; if the actual finger mechanism angular acceleration and velocity show the same direction (i.e., have the same sign), the intention to keep moving further is detected; otherwise, the desire to stop or invert the motion is inferred.

Once the user's intention is detected, the approach proposed in Lecours et al. (2012) is implemented to achieve the variable-admittance behavior. In the first case, in order to promote acceleration and thus the device responsivity, the desired damping B is decreased by exploiting a correction factor proportional to the desired acceleration;

$$B_{acc} = B_f - \alpha|\ddot{x}_d| \tag{7}$$

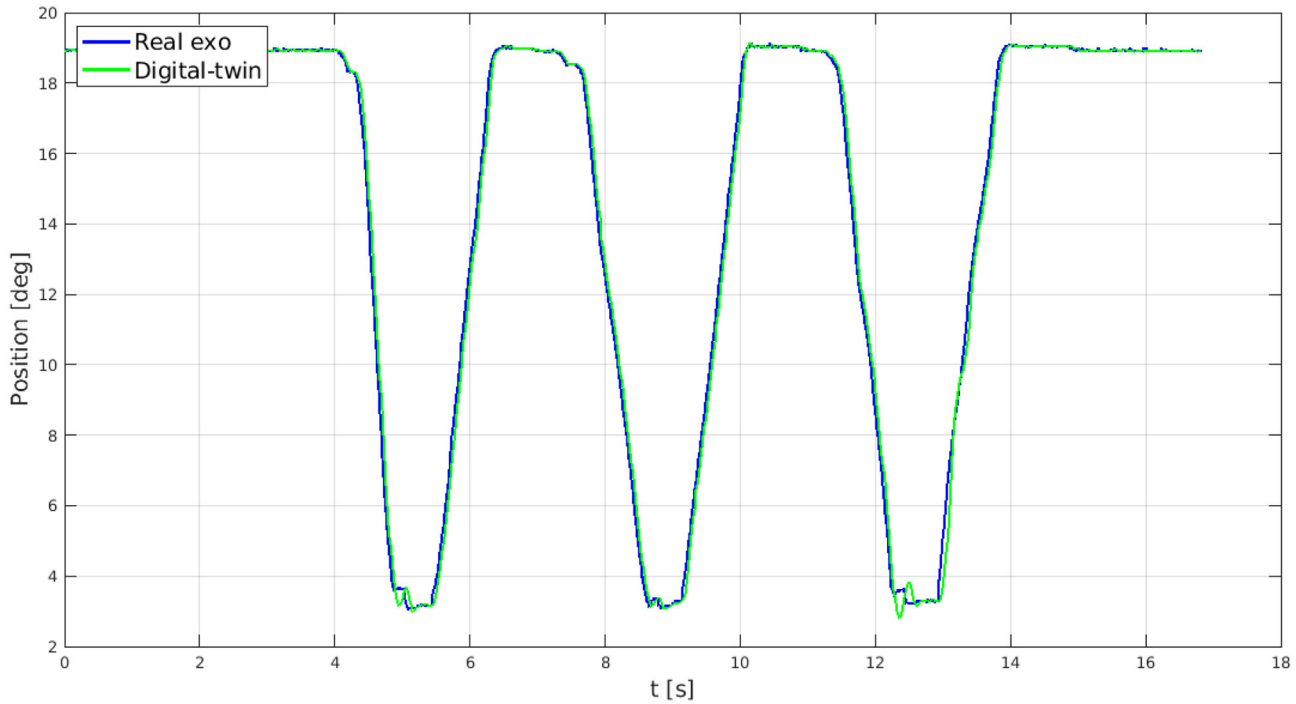

FIGURE 9 | Comparison between the angular position of a real finger mechanism (in blue) and the one from the virtual replica (in green).

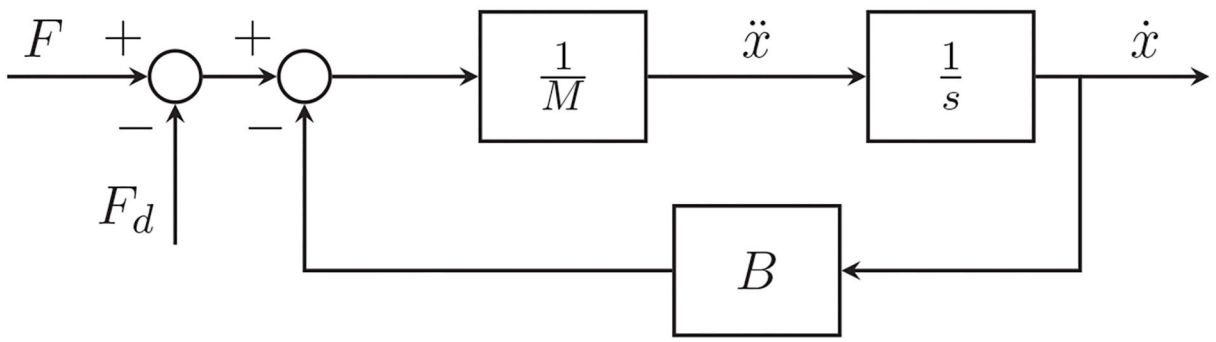

FIGURE 10 | Block diagram of the admittance control strategy implemented.

where B_f is the apriori defined damping default value $B_f = 0.145\ Ns/m$.

In the second case, by pursuing a coherent approach, the damping values are increased whenever the user requires a deceleration phase:

$$B_{dec} = B_f + \alpha|\ddot{x}_d| \tag{8}$$

Two different equations can be exploited to modify the inertia value according to the modified damping coefficient:

$$M_{acc} = M_f \frac{B_{acc}}{B_f} \tag{9}$$

$$M_{dec} = M_f \frac{B_{dec}}{B_f}(1 - \beta(1 - e^{-\gamma(B_{dec}-B)})) \tag{10}$$

where M_f is the previously tuned inertia default value $M_f = 0.008\ kgm^2$, and α, β, and γ are correction factors heuristically tuned to finely adjust the exoskeleton behavior. While accelerating is safely handled with the proportional action of Equation 9, decelerating needs to be tackled more carefully to avoid possible discontinuities due to the inversion of motion. The exponential function reported in Equation 10 is exploited to handle such possibilities.

However, during some preliminary tests for the system under investigation, the variation of the M parameter was found to be low and directed toward the instability margin

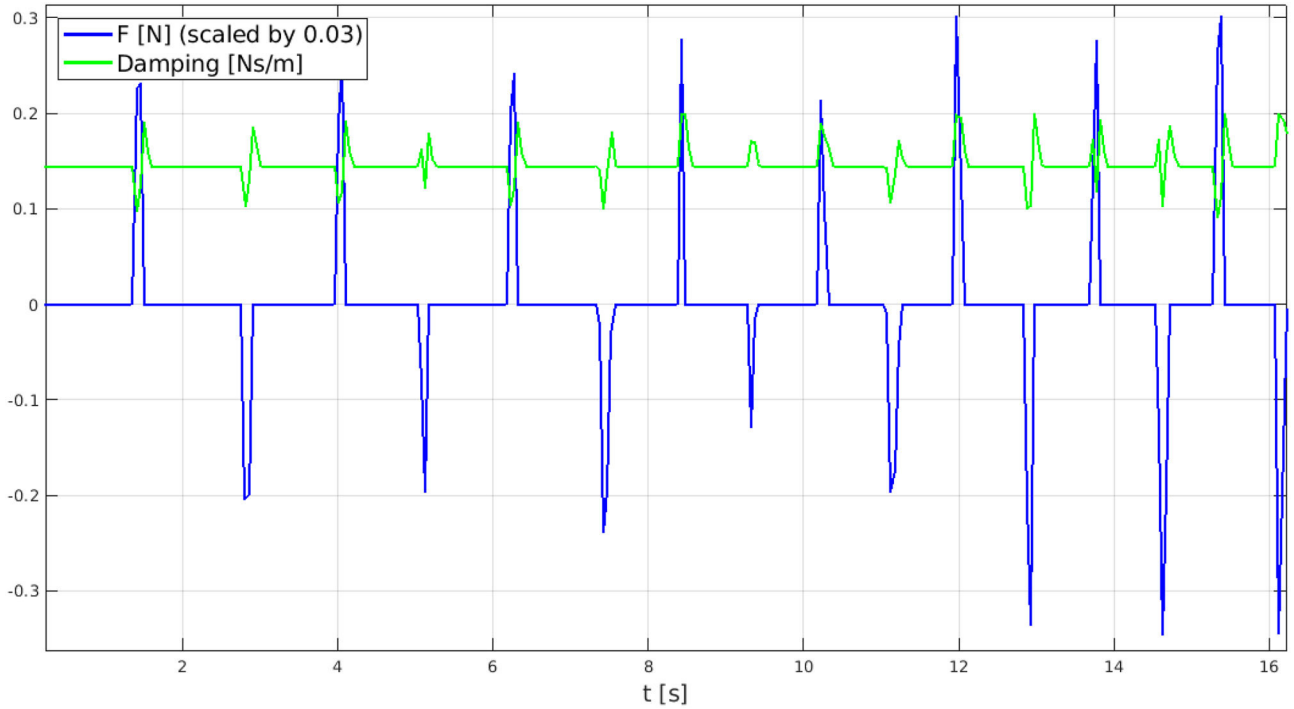

FIGURE 11 | Real time damping variation (in green) according to force sensor measurements (in blue) with $\alpha = 0.0005$ chosen after some tests. As reported within the legend, force measures are scaled with a 0.03 factor for plot readability.

($M = 0.005\ kgm^2$). For this reason, the choice to leave the value of the inertia term to its default value $M = 0.008\ kgm^2$ seemed the most reasonable.

It is primary to outline that as the inertia is kept constant while varying the damping value, the controller bandwidth, inferiorly limited by the damping to inertia ratio (B/M), would change as well. This effect may slow the system response during the acceleration phase and might cross the stability border when decelerating. In light of these observations, the damping value is constrained between 0.004 Ns/m and 0.2 Ns/m to preserve the system stability ($B \leq 0.25\ Ns/m$) and a minimum bandwidth of 0.5 Hz[8] ($B/M \geq 0.5\ kgm^2$). As a consequence of these design guidelines, the damping term does arise as the only independent parameter to be tuned for the V-AC approach and, for sake of brevity, just its variation along the detected user's intention will be reported. The variation of the damping coefficient following the user's interaction with the exoskeleton (namely, the user's intention) is reported in **Figure 11**.

As shown from the graph, the intention detection system performs as expected. The user exerts a force (either positive or negative) to accelerate, the damping parameter decreases to reduce its dissipating action; conversely, when the measured force drops back to zero, thus identifying a deceleration intention, the damping value increases to quickly stop the motion. As can be further expected from the V-AC mathematical formulation, for large α values, the damping increase is sharper. After some tests, a suitable value of $\alpha = 0.0005$ has been identified.

4. TESTS AND RESULTS

This section illustrates the overall interaction between the admittance controlled HES and the developed Webots-based VR environment. In order to evaluate the functionality of the whole system a pilot study composed of two distinct experiments has been setup: (i) in the first proposed scenario, the *free motion* mode has been considered; (ii) second, a trial with a graspable virtual object (namely, the sphere visible in **Figure 8**) has been arranged. The choice of these two experimental setups has been delineated to clearly outline both the transparency of the device and the capability to render force feedback. As already reported, both these characteristics are crucial when it comes to rehabilitative robot systems as the basis for the implementation of safe, customizable, engaging, and stimulating VR-based exercises for patients. The tests have been conducted involving a single healthy subject (male, 27 years old, trained to interact with the HES and the VR) as the exoskeleton geometry is optimized to fit a specific target hand (as reported in Bartalucci et al., 2020). Since the admittance control strategy is decentralized and replicated over each finger with a shared Webots VR, for the sake of simplicity, just the results of a single finger are reported.

[8]Such bandwidth of 0.5 Hz is intended as the lowest frequency the system has to operate and it has been identified (with the help of clinical staff) considering a worst-case scenario where the finger mechanisms are asked to fully open or close the corresponding finger at least every 2 seconds.

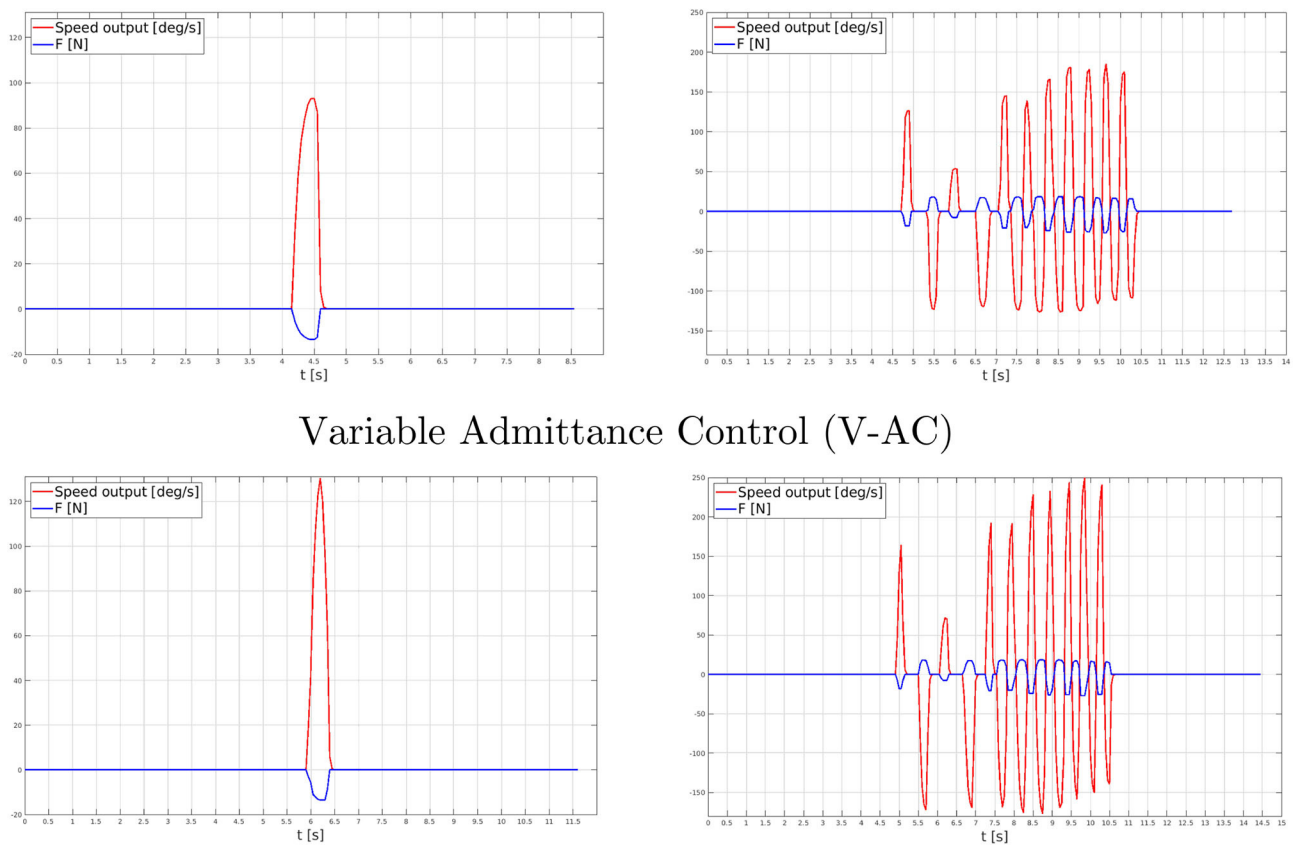

FIGURE 12 | Performance comparison between the C-AC (top graph) and V-AC (bottom graph) during the preliminary assessment tests. On the left, the control response to a single force impulse; on the right, the control response to a variable-frequency impulse train.

4.1. Preliminary Assessment

In order to provide a preliminary objective analysis of the proposed AC methodologies, the system responses to custom, pre-recorded force signals have been studied. The need for such a study arises for both inspecting, in a uniform way, the strategy outputs for equivalent inputs as well as for a pragmatical necessity, since repeatedly providing an identical force signal multiple times does result as impossible even for an expert user. In particular, with the aim of achieving force signals as realistic as possible, instead of exploiting simulated, scripted, force signals, the subject has been asked to apply two distinct forces on the load cell: a single impulse as well as a variable-frequency impulse sequence.

Figure 12 shows the C-AC and V-AC methodology outcomes as long as both the two different force signals have been applied. In particular, a graphical investigation outlines the correct functionality of both the strategies (i.e., the reference speed values coherently react to the input force signals). Nevertheless, the promptness capability evidently differs between the two approaches: V-AC increases and decays the velocity output more rapidly, with larger amplitude variations, than C-AC by achieving a HES device more reactive to follow the user's intentions.

4.2. Free Motion Mode

The V-AC strategy arose to be the most reactive during the preliminary assessment. However, before claiming which of the two approaches was best suited for rehabilitation application, the actual results of such reactivity had to be tested in a real-use scenario, in which the actual interaction between the HES and the user had to be analyzed.

In order to compare the performance of the two proposed control strategies, data has been acquired while performing some repetitive motion of the index finger. More specifically, the index finger mechanism has been worn on a healthy subject and, then, the wearer has been asked to repeatedly tap the finger with variable frequency. The HES was switched on and the control was set on *free motion* mode to assess how the exoskeleton would follow the user's intentions: since no virtual objects are introduced in the Webots VR, the desired reference forces, provided by the virtual force

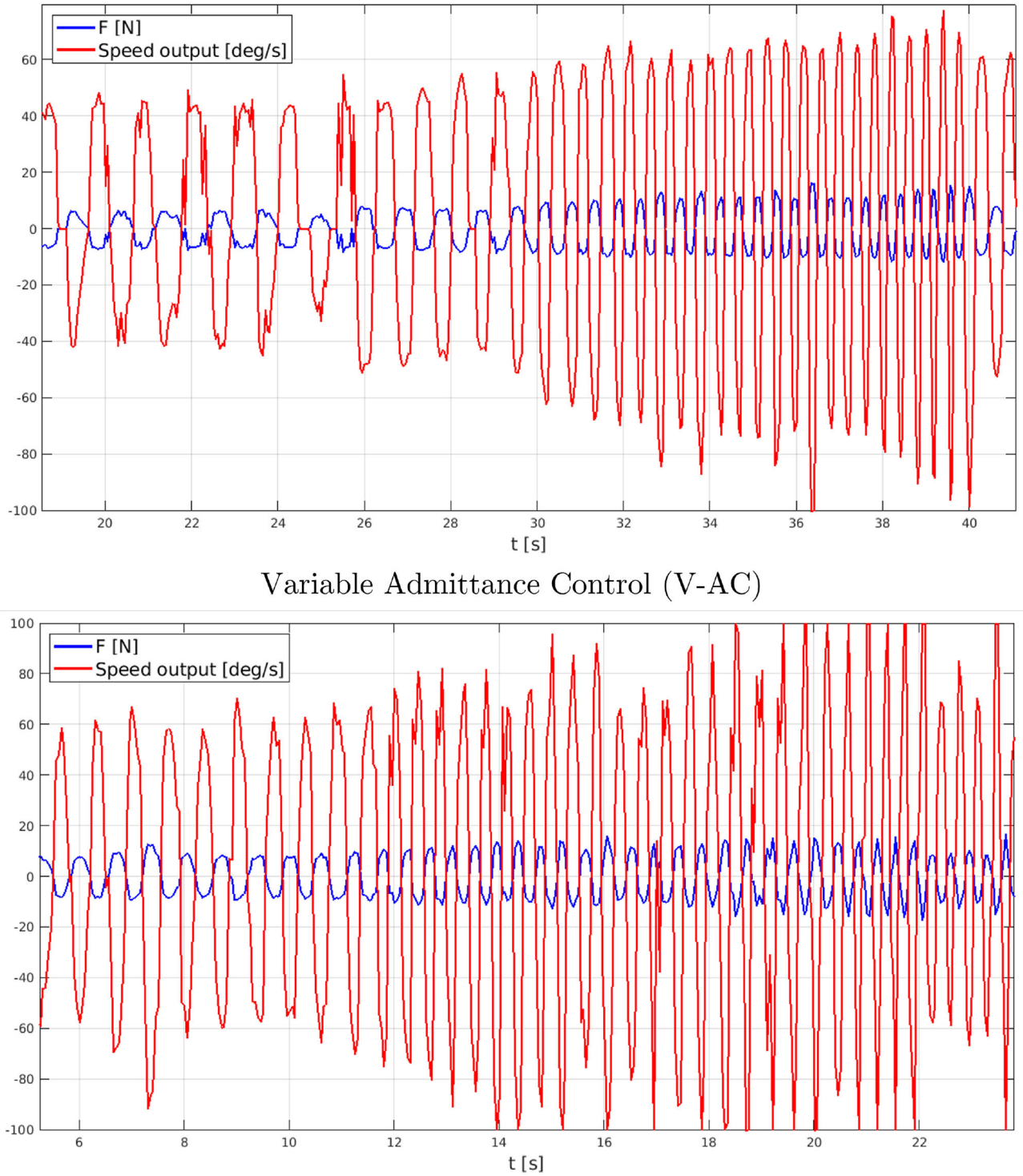

FIGURE 13 | Performance comparison between the C-AC (top graph) and V-AC (bottom graph) during the free motion mode tests.

sensors, was set to zero. Force measurements have been collected from the load cell and compared with the speed reference output from the admittance model, as reported in **Figure 13**. During the test, the subject could also rely on visual feedback coming from the VR following the exoskeleton motion.

The first designed experiment not only aimed to assess the BMIFOCUS HES transparency but also to identify the most suitable admittance control strategy for rehabilitation applications. These results have highlighted that both the C-AC and V-AC approaches show the ability to precisely follow the user's intentions, overall proving remarkable transparency of the BMIFOCUS exoskeleton. However, as clearly visible, the pHRI resulting from C-AC and V-AC was different when varying the tapping frequency. Before going into the details of the performance comparison, it is important to state that the results shown in **Figure 13** represent the actual interaction between the user and the device: this implies that the interaction force (in blue) and the admittance model output (in red) mutually influence each other. In light of this premise, the graphs show that the pHRI produced by the C-AC method results in being overall noisy, while the V-AC one is smoother at low frequencies, while it appears noisier at high frequencies. In the first analysis, this behavior might derive from the higher reactivity of the V-AC strategy making this approach itself more prone to undesired patterns due to disturbances when the dynamics of the system increases. The evident noise reduction while performing pHRI with V-AC at low frequencies makes the interaction with the exoskeleton more natural and transparent. This feature, contextualized in a rehabilitation scenario results crucial, as the operating frequencies that characterize therapy sessions are usually low to guarantee patients' safety and comfort. In conclusion, although a quantitative evaluation comparison between the two implemented approaches outlines just minor differences, the V-AC technique has been selected as the control strategy that is most suitable for the application under investigation and has been hence exploited during the further tests about the interaction with virtual objects.

4.3. Interaction With Virtual Objects

The second trial focused instead on the interaction with virtual objects to be used to enhance the immersivity of rehabilitation exercises. This key property is achieved thanks to the force-tracking ability of the developed admittance control strategy; such a valuable resource is carried out upon the following hierarchical, but still concurrent, stages:

- while the user moves his hand when wearing the exoskeleton the digital-twin mirrors such motion;
- as long as the virtual model does not encounter any obstacle, the system persists in the free motion mode and the reference force tracked by the admittance control system has zero value;
- once the virtual HES comes into contact with a virtual object, the Webots physics simulator engine generates a reaction force provided by a measured force from a virtual force sensor;
- the virtual force values are used as reference signals and, combined with the force feedback from the real exoskeleton, input into the implemented admittance control strategy;
- the admittance control supplies the velocity references for the HES internal PID controllers that, by tracking them, allow the finger mechanism to exert a reaction force on the user's finger;
- at this phase, if the patient is able to perform an identical but opposite force on the finger mechanism an equilibrium

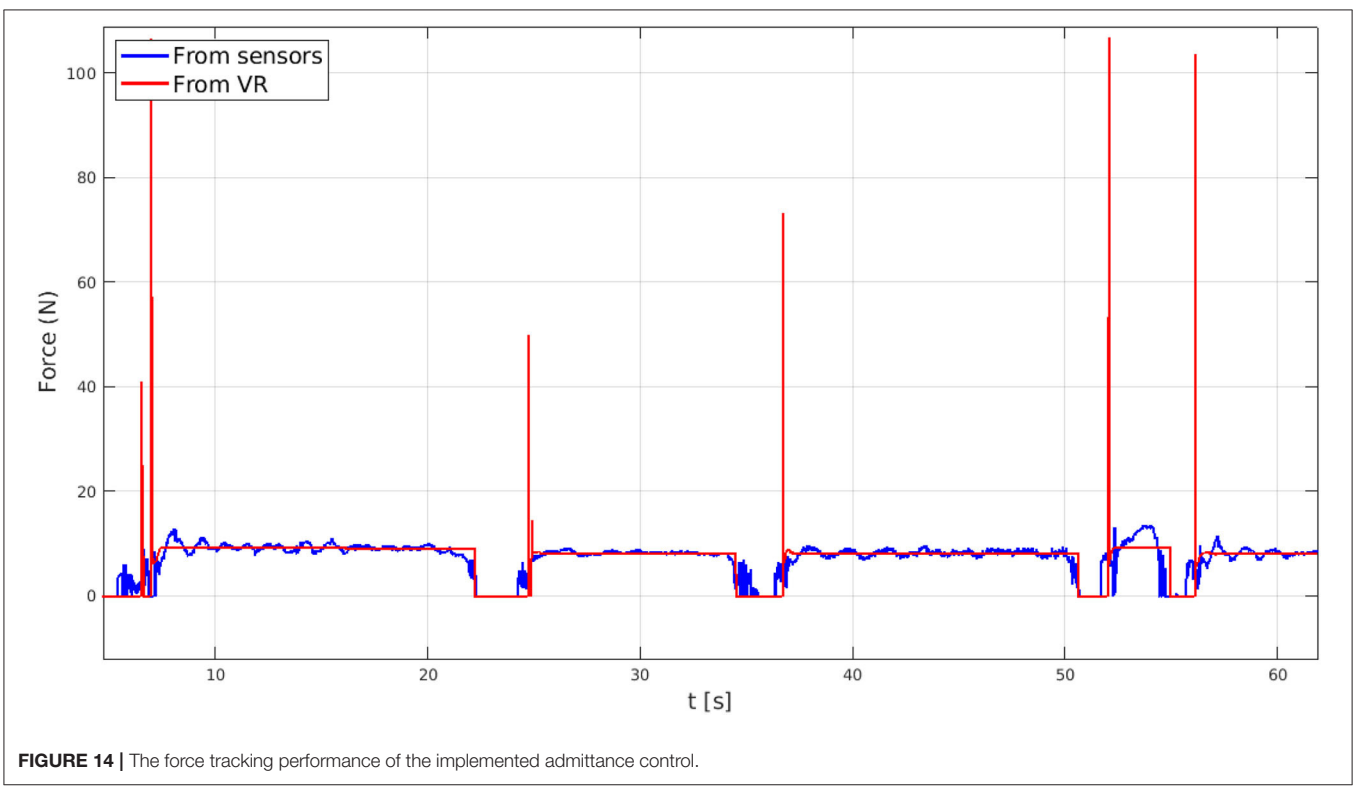

FIGURE 14 | The force tracking performance of the implemented admittance control.

position will be reached: the digital-twin holding (or pushing) a virtual object while the user feels the reaction forces as if the object were in his/her hand.

The results of the test with a virtual spherical object are reported hereafter. In **Figure 14**, the comparison between the force applied by the user on the exoskeleton and the one computed in VR is displayed. As the HES digital replica touches the virtual sphere in a grasping action, the simulated force sensor supplies a step-comparable force reference, which the admittance control architecture handles by accomplishing the force tracking feature. Instead, while the BMIFOCUS exoskeleton digital-twin is not in contact with the VR object, the desired reference force is set to zero and *free motion* mode is suitably fulfilled. For sake of completeness, it is worth noting that several steep peaks are present among the virtual reaction forces. This pattern, arising as impulsive forces due to the HES contact with a rigid object in the Webots framework, is, however, filtered by the mechanics of the system and does not cause excessive undesired motion and, therefore, is not perceived by the user.

5. CONCLUSION

The presented work describes the design process of a rehabilitation tool bringing together the benefits of robotic exoskeletons and VR. This research activity tackles a rehabilitation scenario in which a patient, suffering from hand reduced mobility, is requested to perform manipulation tasks. A pre-existing hand exoskeleton, designed and developed by the researchers at UNIFI DIEF in the framework of the regional research project BMIFOCUS, has been the basis of the presented research activity since it already exhaustively fulfilled the mechanical requirements for a safe, flexible, and comfortable robot-based rehabilitation. Due to the very nature of the device involved in this research activity, the treatment under consideration must necessarily take place in a clinic under the supervision of a therapist. The patient is asked to interact with virtual objects while wearing the exoskeleton. From this point of view, the integrated system (intended as a set of the exoskeleton and VR) has a 3-fold purpose: on the one hand, it provides help to the patient according to the guidelines of the AAN approach; on the other hand, it is a valuable tool for monitoring the progress of the patient in real-time by measuring both the kinematics of the hand and the forces exerted; finally, thanks to the interaction with VR, it can easily propose different exercises, adapted to the specific needs of the patient and designed in order to increase the patient's involvement in the exercises.

After a minute selection of a suitable physics simulator, a HES digital-twin has been realized in the *Webots: robot simulator* framework as well as thoroughly tested to check consistency with the real exoskeleton. Such a simulated device does represent a strategical tool in providing a patient with VR-based visual feedback over the therapy activity. Besides, it is proved that interactive VR environments integrated with physical devices arise as noteworthy tools to boost the patient's engagement during rehabilitation exercises by simulating the user immersively interacting with virtual scenes and objects. In particular, the proposed system simulates object grasping sensations, providing the patients with both force and visual feedback.

The scientific literature identifies admittance control as a satisfactory methodology to achieve the aforementioned purpose. Indeed, this procedure, along with its force-tracking ability, manifests the ability to simultaneously handle the end-effector position and contact force control. Besides, admittance control paves the way toward the shaping of the complex pHRI by allowing, with a proper tuning process of the inertia and damping terms, for a more transparent interaction between the user and the exoskeleton device. By exploiting this control technique, users can move their hands with a minimally invasive HES presence during free motion, while feeling opposing forces every time, a virtual grasping action is performed.

Two distinct architectures have been implemented and tested **involving a healthy subject**: classical (C-AC) and variable (V-AC) admittance control. C-AC reflects the original formulation with fixed inertia and damping values. V-AC varies the model parameters according to the patient's intention in order to better assist his desired movements. In this view, default damping values have been tuned by employing a trial and error process, while the user's motion detector, based on a heuristic criterion based on desired speed and acceleration, has been proven effective.

Finally, the interaction between the user, the HES, and the VR environment has been analyzed. Both the C-AC and V-AC control strategies have highlighted promising performance while following the user's free motion, proving HES remarkably transparent for the user. However, when it comes to rehabilitation applications, the V-AC resulted best suited thanks to the smoother behavior at low operating frequencies. Besides, in terms of force feedback rendering, the chosen strategy showed the potential to provide a noteworthy physical human-robot interaction.

In conclusion, the control strategy described in this pilot study presents an excellent starting point for the development of a complete rehabilitation system as described above. The further steps in the development of this device will certainly involve extending the sample of subjects involved in the tests, possibly including real patients and characterizing the actual forces of interaction with objects that the exoskeleton is capable of rendering.

DATA AVAILABILITY STATEMENT

The original contributions presented in the study are included in the article/supplementary material, further inquiries can be directed to the corresponding author.

ETHICS STATEMENT

Ethical review and approval was not required for the study on human participants in accordance with the local legislation and institutional requirements. The patients/participants

provided their written informed consent to participate in this study.

AUTHOR CONTRIBUTIONS

BA and AR have supervised the research activity. All authors contributed to the article and approved the submitted version.

FUNDING

This work has been supported by the Don Carlo Gnocchi Foundation and by two Italian projects: the HERMES project, funded by the Ente Cassa di Risparmio di Firenze, and the BMIFOCUS, funded by the Tuscany Region (POR FESR 2014–2020).

REFERENCES

Abu-Dakka, F. J., and Saveriano, M. (2020). Variable impedance control and learning-a review. *arXiv preprint* arXiv:2010.06246. doi: 10.3389/frobt.2020.590681

Anam, K., and Al-Jumaily, A. A. (2012). Active exoskeleton control systems: State of the art. *Procedia Eng*. 41:988–994. doi: 10.1016/j.proeng.2012.07.273

Bartalucci, L., Secciani, N., Gelli, J., Della Valle, A., Ridolfi, A., and Allotta, B. (2020). "Rehabilitative hand exoskeleton system: a new modular mechanical design for a remote actuated device," in *The International Conference of IFToMM ITALY* (Naples: Springer), 128–136.

Bielsa, V. F. (2021). Virtual reality simulation in plastic surgery training. literature review. *J. Plastic Reconstr. Aesthet. Surg*. 74, 2372–2378. doi: 10.1016/j.bjps.2021.03.066

Colgate, J. E., and Hogan, N. (1988). Robust control of dynamically interacting systems. *Int. J. Control*. 48, 65–88. doi: 10.1080/00207178808906161

Conti, R., Meli, E., Ridolfi, A., Bianchi, M., Governi, L., Volpe, Y., et al. (2017). Kinematic synthesis and testing of a new portable hand exoskeleton. *Meccanica* 52, 2873–2897. doi: 10.1007/s11012-016-0602-0

de Araújo, A. V. L., Neiva, J. F., d,. O., Monteiro, C. B. d. M., and Magalh aes, F. H. (2019). Efficacy of virtual reality rehabilitation after spinal cord injury: a systematic review. *Biomed. Res. Int*. 2019:7106951. doi: 10.1155/2019/7106951

du Plessis, T., Djouani, K., and Oosthuizen, C. (2021). A review of active hand exoskeletons for rehabilitation and assistance. *Robotics* 10, 40. doi: 10.3390/robotics10010040

Duchaine, V., and Gosselin, C. M. (2007). "General model of human-robot cooperation using a novel velocity based variable impedance control," in *Second Joint EuroHaptics Conference and Symposium on Haptic Interfaces for Virtual Environment and Teleoperator Systems (WHC'07)* (Tsukuba: IEEE), 446–451.

Gomi, H., and Kawato, M. (1993). Neural network control for a closed-loop system using feedback-error-learning. *Neural Netw*. 6, 933–946. doi: 10.1016/S0893-6080(09)80004-X

Hogan, N. (1984). Adaptive control of mechanical impedance by coactivation of antagonist muscles. *IEEE Trans. Automat. Contr*. 29, 681–690. doi: 10.1109/TAC.1984.1103644

Hogan, N., and Buerger, S. P. (2018). "Impedance and interaction control," in *Robotics and Automation Handbook* (Boca Raton, FL: CRC Press), 375–398.

Hua, J., Zeng, L., Li, G., and Ju, Z. (2021). Learning for a robot: Deep reinforcement learning, imitation learning, transfer learning. *Sensors* 21, 1278. doi: 10.3390/s21041278

Huang, G., Zhang, W., Meng, F., Yu, Z., Chen, X., Ceccarelli, M., et al. (2018). Master-slave control of an intention-actuated exoskeletal robot for locomotion and lower extremity rehabilitation. *Int. J. Precision Eng. Manufact*. 19, 983–991. doi: 10.1007/s12541-018-0116-x

Huang, R., Cheng, H., Qiu, J., and Zhang, J. (2019). Learning physical human-robot interaction with coupled cooperative primitives for a lower exoskeleton. *IEEE Trans. Autom. Sci. Eng*. 16, 1566–1574. doi: 10.1109/TASE.2018.2886376

Ikeura, R., Monden, H., and Inooka, H. (1994). "Cooperative motion control of a robot and a human," in *Proceedings of 1994 3rd IEEE International Workshop on Robot and Human Communication* (Nagoya: IEEE), 112–117.

Ikeura, R., Moriguchi, T., and Mizutani, K. (2002). "Optimal variable impedance control for a robot and its application to lifting an object with a human," in *Proceedings. 11th IEEE International Workshop on Robot and Human Interactive Communication* (Berlin: IEEE), 500–505.

Jung, S., and Hsia, T. (1998). Neural network impedance force control of robot manipulator. *IEEE Trans. Ind. Electr*. 45, 451–461. doi: 10.1109/41.679003

Jung, S., Hsia, T. C., and Bonitz, R. G. (2004). Force tracking impedance control of robot manipulators under unknown environment. *IEEE Trans. Control Syst. Technol*. 12, 474–483. doi: 10.1109/TCST.2004.824320

Kavanagh, S., Luxton-Reilly, A., Wuensche, B., and Plimmer, B. (2017). A systematic review of virtual reality in education. *Themes Sci. Technol. Educ*. 10, 85–119.

Keemink, A. Q., van der Kooij, H., and Stienen, A. H. (2018). Admittance control for physical human-robot interaction. *Int. J. Rob. Res*. 37, 1421–1444. doi: 10.1177/0278364918768950

Kim, H., Kwon, J., Oh, Y., You, B. J., and Yang, W. (2018). "Weighted hybrid admittance-impedance control with human intention based stiffness estimation for human-robot interaction," in *2018 IEEE/RSJ International Conference on Intelligent Robots and Systems (IROS)* (Madrid: IEEE), 1–6.

Lecours, A., Mayer-St-Onge, B., and Gosselin, C. (2012). "Variable admittance control of a four-degree-of-freedom intelligent assist device," in *2012 IEEE International Conference on Robotics and Automation* (Saint Paul, MN: IEEE), 3903–3908.

Lee, K., and Buss, M. (2008). Force tracking impedance control with variable target stiffness. *IFAC Proc*. 41, 6751–6756. doi: 10.3182/20080706-5-KR-1001.01144

Lei, C., Sunzi, K., Dai, F., Liu, X., Wang, Y., Zhang, B., et al. (2019). Effects of virtual reality rehabilitation training on gait and balance in patients with parkinson's disease: A systematic review. *PLoS ONE* 14:e0224819. doi: 10.1371/journal.pone.0224819

Li, Z., Liu, J., Huang, Z., Peng, Y., Pu, H., and Ding, L. (2017). Adaptive impedance control of human-robot cooperation using reinforcement learning. *IEEE Trans. Ind. Electron*. 64, 8013–8022. doi: 10.1109/TIE.2017.2694391

Losey, D. P., McDonald, C. G., Battaglia, E., and O'Malley, M. K. (2018). A review of intent detection, arbitration, and communication aspects of shared control for physical human-robot interaction. *Appl. Mech. Rev*. 70, 010804. doi: 10.1115/1.4039145

Lu, Z., and Goldenberg, A. A. (1995). Robust impedance control and force regulation: Theory and experiments. *Int. J. Rob. Res*. 14, 225–254. doi: 10.1177/027836499501400303

Lum, P. S., Burgar, C. G., Shor, P. C., Majmundar, M., and Van der Loos, M. (2002). Robot-assisted movement training compared with conventional therapy techniques for the rehabilitation of upper-limb motor function after stroke. *Arch. Phys. Med. Rehabil*. 83, 952–959. doi: 10.1053/apmr.2001.33101

Molteni, F., Gasperini, G., Cannaviello, G., and Guanziroli, E. (2018). Exoskeleton and end-effector robots for upper and lower limbs rehabilitation: narrative review. *PM R* 10, S174–S188. doi: 10.1016/j.pmrj.2018.06.005

Petrenko, V., Tebueva, F., Gurchinsky, M., Ryabtsev, S., and Trofimuk, O. (2019). "Exoskeleton for operator's motion capture with master-slave control," in *7th Scientific Conference on Information Technologies for Intelligent Decision Making Support (ITIDS 2019)* (Ufa: Atlantis Press), 152–158.

Pfandler, M., Lazarovici, M., Stefan, P., Wucherer, P., and Weigl, M. (2017). Virtual reality-based simulators for spine surgery: a systematic review. *Spine J*. 17, 1352–1363. doi: 10.1016/j.spinee.2017.05.016

Qian, C., Li, W., Jia, T., Li, C., Lin, P.-J., Yang, Y., et al. (2021). Quantitative assessment of motor function by an end-effector upper limb rehabilitation robot based on admittance control. *Appl. Sci*. 11, 6854. doi: 10.3390/app11156854

Radianti, J., Majchrzak, T. A., Fromm, J., and Wohlgenannt, I. (2020). A systematic review of immersive virtual reality applications for higher education: design elements, lessons learned, and research agenda. *Comput. Educ*. 147:103778. doi: 10.1016/j.compedu.2019.103778

Rose, T., Nam, C. S., and Chen, K. B. (2018). Immersion of virtual reality for rehabilitation-review. *Appl. Ergon*. 69, 153–161. doi: 10.1016/j.apergo.2018.01.009

Roveda, L., Iannacci, N., Vicentini, F., Pedrocchi, N., Braghin, F., and Tosatti, L. M. (2015). Optimal impedance force-tracking control design with impact formulation for interaction tasks. *IEEE Rob. Autom. Lett*. 1, 130–136. doi: 10.1109/LRA.2015.2508061

Sado, F., Sidek, S. N., and Yusof, H. M. (2014). "Adaptive hybrid impedance control for a 3dof upper limb rehabilitation robot using hybrid automata,". in *2014 IEEE Conference on Biomedical Engineering and Sciences (IECBES)* (Kuala Lumpur: IEEE), 596–601.

Sandison, M., Phan, K., Casas, R., Nguyen, L., Lum, M., Pergami-Peries, M., et al. (2020). "HandMATE: wearable robotic hand exoskeleton and integrated android app for at home stroke rehabilitation," in *2020 42nd Annual International Conference of the IEEE Engineering in Medicine Biology Society (EMBC)* (Montreal, QC: IEEE), 4867–4872.

Schumacher, M., Wojtusch, J., Beckerle, P., and von Stryk, O. (2019). An introductory review of active compliant control. *Rob. Auton. Syst*. 119, 185–200. doi: 10.1016/j.robot.2019.06.009

Seraji, H., and Colbaugh, R. (1997). Force tracking in impedance control. *Int. J. Rob. Res*. 16, 97–117. doi: 10.1177/027836499701600107

Shi, D., Zhang, W., Zhang, W., and Ding, X. (2019). A review on lower limb rehabilitation exoskeleton robots. *Chin. J. Mech. Eng*. 32, 1–11. doi: 10.1186/s10033-019-0389-8

Song, P., Yu, Y., and Zhang, X. (2019). A tutorial survey and comparison of impedance control on robotic manipulation. *Robotica* 37, 801–836. doi: 10.1017/S0263574718001339

Souzanchi-K. M., Arab, A., Akbarzadeh-T. M.-R., and Fateh, M. M (2017). Robust impedance control of uncertain mobile manipulators using time-delay compensation. *IEEE Trans. Control Syst. Technol*. 26, 1942–1953. doi: 10.1109/TCST.2017.2739109

Staubli, P., Nef, T., Klamroth-Marganska, V., and Riener, R. (2009). Effects of intensive arm training with the rehabilitation robot armin ii in chronic stroke patients: four single-cases. *J. Neuroeng. Rehabil*. 6, 1–10. doi: 10.1186/1743-0003-6-46

Tsumugiwa, T., Yokogawa, R., and Hara, K. (2002). "Variable impedance control based on estimation of human arm stiffness for human-robot cooperative calligraphic task," in *Proceedings 2002 IEEE International Conference on Robotics and Automation (Cat. No. 02CH37292)*, *Vol. 1* (Washington, DC: IEEE), 644–650.

Wang, P., Wu, P., Wang, J., Chi, H.-L., and Wang, X. (2018). A critical review of the use of virtual reality in construction engineering education and training. *Int. J. Environ. Res. Public Health* 15, 1204. doi: 10.3390/ijerph15061204

Wolfartsberger, J. (2019). Analyzing the potential of virtual reality for engineering design review. *Autom. Construct*. 104, 27–37. doi: 10.1016/j.autcon.2019.03.018

Yung, R., and Khoo-Lattimore, C. (2019). New realities: a systematic literature review on virtual reality and augmented reality in tourism research. *Curr. Issues Tourism* 22, 2056–2081. doi: 10.1080/13683500.2017.1417359

Conflict of Interest: The authors declare that the research was conducted in the absence of any commercial or financial relationships that could be construed as a potential conflict of interest.

Publisher's Note: All claims expressed in this article are solely those of the authors and do not necessarily represent those of their affiliated organizations, or those of the publisher, the editors and the reviewers. Any product that may be evaluated in this article, or claim that may be made by its manufacturer, is not guaranteed or endorsed by the publisher.

frontiers in Neurorobotics

ORIGINAL RESEARCH
published: 20 January 2022
doi: 10.3389/fnbot.2021.788494

EEG Spectral Feature Modulations Associated With Fatigue in Robot-Mediated Upper Limb Gross and Fine Motor Interactions

Udeshika C. Dissanayake, Volker Steuber and Farshid Amirabdollahian*

School of Physics, Engineering and Computer Science, University of Hertfordshire, Hatfield, United Kingdom

This paper investigates the EEG spectral feature modulations associated with fatigue induced by robot-mediated upper limb gross and fine motor interactions. Twenty healthy participants were randomly assigned to perform a gross motor interaction with HapticMASTER or a fine motor interaction with SCRIPT passive orthosis for 20 min or until volitional fatigue. Relative and ratio band power measures were estimated from the EEG data recorded before and after the robot-mediated interactions. Paired-samples *t*-tests found a significant increase in the relative alpha band power and a significant decrease in the relative delta band power due to the fatigue induced by the robot-mediated gross and fine motor interactions. The gross motor task also significantly increased the $(\theta + \alpha)/\beta$ and α/β ratio band power measures, whereas the fine motor task increased the relative theta band power. Furthermore, the robot-mediated gross movements mostly changed the EEG activity around the central and parietal brain regions, whereas the fine movements mostly changed the EEG activity around the frontopolar and central brain regions. The subjective ratings suggest that the gross motor task may have induced physical fatigue, whereas the fine motor task may have induced mental fatigue. Therefore, findings affirm that changes to localised brain activity patterns indicate fatigue developed from the robot-mediated interactions. It can also be concluded that the regional differences in the prominent EEG spectral features are most likely due to the differences in the nature of the task (fine/gross motor and distal/proximal upper limb) that may have differently altered an individual's physical and mental fatigue level. The findings could potentially be used in future to detect and moderate fatigue during robot-mediated post-stroke therapies.

Keywords: electroencephalogram, fatigue in upper limb robot-mediated interactions, HapticMASTER, SCRIPT passive orthosis, relative band power, band power ratios, independent component analysis, statistical analysis

OPEN ACCESS

Edited by:
Chad Gregory Rose,
Auburn University, United States

Reviewed by:
Nikunj Arunkumar Bhagat,
University of Houston, United States
Eduardo Ros,
University of Granada, Spain

****Correspondence:***
Udeshika C. Dissanayake
udeshikad@outlook.com

Received: *02 October 2021*
Accepted: *20 December 2021*
Published: *20 January 2022*

Citation:
Dissanayake UC, Steuber V and Amirabdollahian F (2022) EEG Spectral Feature Modulations Associated With Fatigue in Robot-Mediated Upper Limb Gross and Fine Motor Interactions. Front. Neurorobot. 15:788494. doi: 10.3389/fnbot.2021.788494

1. INTRODUCTION

Fatigue experienced during post-stroke upper limb rehabilitation and its implications for the therapy outcome are often overlooked in existing therapy sessions. Many stroke survivors (about 30 to 70%) have reported persistence of fatigue as a debilitating symptom (Staub and Bogousslavsky, 2001; Lerdal et al., 2009). It is more likely that the increased motor/cognitive processing demands required during motor retraining exercises may exacerbate stroke patients' fatigue levels. The

elevated fatigue levels may impair motivation and compliance to effectively perform the therapeutic interactions and the long-term commitment toward rehabilitation. Furthermore, some studies have reported that high-intensity fatiguing tasks are detrimental to both motor performance and learning (Godwin and Schmidt, 1971; Carron, 1972; Thomas et al., 1975; Williams and Singer, 1975; Branscheidt et al., 2019), whereas some investigations have only found performance impairments (Alderman, 1965; Carron, 1969; Cotten et al., 1972). Sterr and Furlan (2015) hypothesised that the relationship between training intensity and motor performance of constraint-induced therapy in chronic hemiparetic stroke patients is modulated by fatigue in addition to the residual motor ability. Foong et al. (2019) also suggested that the poor performance in the nBETTER (Neurostyle Brain Exercise Therapy Towards Enhanced Recovery) system could be due to the mental fatigue that progressed during the therapy. In Prasad's et al. (2010) study where chronic hemiplegic stroke patients performed both physical practice and motor imagery, a trend of more considerable variability in the brain-computer interface (BCI) performance was observed with the rise in individual fatigue levels. Therefore, it is highly questionable whether continuing a stroke therapy while or beyond fatigued conditions would impede motor performance and motor skill relearning during therapeutic interactions.

Despite its clinical importance, there exists no unambiguous and universally agreed definition for the term fatigue. In general, fatigue is a sensation of tiredness, weariness or lack of energy that is experienced following or during prolonged physical or mental activity. Fatigue can be broadly categorised into two types: physical (or muscular) fatigue and mental fatigue. Physical fatigue is defined as a failure to maintain force (or power output) during sustained muscle contractions (Gibson and Edwards, 1985). In contrast, mental fatigue is a subjective feeling of tiredness experienced during or after prolonged periods of demanding cognitive activity (Lorist et al., 2005). Recent studies have also shown that mental fatigue impairs physical performance, especially in sports-related activities (Marcora et al., 2009; Mehta and Parasuraman, 2014; Van Cutsem et al., 2017). Electroencephalogram (EEG) has shown to be the most predictive and promising biomarker of fatigue (Lal and Craig, 2001; Tran et al., 2020). To date, many studies have investigated EEG feature modulations associated with fatigue, including fatigue induced by driving tasks (Lal and Craig, 2002; Eoh et al., 2005; Tran et al., 2008; Jap et al., 2009; Craig et al., 2012; Zhao et al., 2012; Borghini et al., 2014), voluntary motor tasks (Yao et al., 2009; Wang et al., 2017), cognitive tasks (Massar et al., 2010; Tanaka et al., 2012; Trejo et al., 2015), brain-computer interfaces (Käthner et al., 2014), exercises and sports-related activities (Bailey et al., 2008; Barwick et al., 2012; Baumeister et al., 2012; Xu et al., 2018), visual display terminal tasks (Cheng and Hsu, 2011; Fan et al., 2015). However, the alterations in EEG activity caused by fatigue accumulated following robot-mediated interactions have not yet been comprehensively explored to the author's knowledge. EEG-based fatigue indices could be used to mitigate fatigue accumulated during human-robot interactions, thereby enhancing the efficacy of rehabilitation and reducing fatigue-related risks in human-robot collaboration tasks.

EEG consists of a wide frequency spectrum, and spectral features (band power and band power ratios) are frequently used as indicators of fatigue. **Table 1** summarises the findings of 16 studies over the last two decades identified by a systematic review on EEG spectral feature modulations caused by fatigue. It was evident that in most studies, θ and α band power increased and β band power decreased significantly as a result of fatigue (Lal and Craig, 2002; Eoh et al., 2005; Barwick et al., 2012; Craig et al., 2012; Zhao et al., 2012; Käthner et al., 2014; Fan et al., 2015; Trejo et al., 2015; Zou et al., 2015; Wang et al., 2017; Xu et al., 2018). Some studies investigated the variations in delta band power as well; however, not many studies were able to identify significant variations with fatigue (Caldwell et al., 2002; Lal and Craig, 2002; Jap et al., 2009; Craig et al., 2012; Tanaka et al., 2012; Zhao et al., 2012; Chen et al., 2013; Fan et al., 2015). In these studies, EEG band power is given as absolute band power or relative band power. The relative band power is defined as a ratio between the absolute band power of each frequency band and the total power of all frequency bands in consideration. EEG band power ratios: $(\theta + \alpha)/\beta$, α/β, $(\theta + \alpha)/(\alpha + \beta)$, and θ/β were also used in some studies since the basic band powers can be insufficient to observe the shift of brain activity from fast waves to slow waves (Eoh et al., 2005; Jap et al., 2009; Fan et al., 2015). EEG band power ratios showed a significant increase with fatigue build-up. Eoh et al. (2005) stated that the index $(\theta+\alpha)/\beta$ was a more reliable fatigue indicator during a simulated driving task due to the mutual addition of α and θ activity during the repetitive phase transition between wakefulness and microsleep. Jap et al. (2009) also reported a greater increase in the index $(\theta + \alpha)/\beta$, in comparison to the other power ratios, when a person experienced a fatigued state at the end of a monotonous simulated driving task. Most studies have also found a widespread topographical distribution in the changes in EEG spectral features with fatigue. However, some studies are equivocal and need further exploration (Jap et al., 2009; Cheng and Hsu, 2011; Baumeister et al., 2012; Tanaka et al., 2012; Chen et al., 2013). Variations in methodological approaches, including low sample size, differences in the fatiguing study protocol, the number of electrodes used, the electrode placement and the feature definition, could be a possible explanation for the discrepancies across the studies.

The type of fatigue experienced during robot-mediated exercises may depend on the exercise mode, intensity and condition of the patient. For instance, the upper limb joints and muscles involved in an interaction may vary from one therapy to another depending on the severity of the impairment of fine or gross motor skills. Gross motor skill retraining exercises such as arm reach/return exercises are primarily involved in the movement and coordination of proximal joints and muscles of the upper limb (shoulder and arm). In contrast, fine motor skill retraining exercises involve coordination of the distal joints and muscles of the upper limb (hand, wrist, and fingers). Cowley and Gates (2017) found that proximal fatigue in a repetitive,

Abbreviations: α_{relative}, relative alpha band power; β_{relative}, relative beta band power; δ_{relative}, relative delta band power; θ_{relative}, relative theta band power.

TABLE 1 | Literature summary on modulations in the EEG spectral features with fatigue.

Reference	Description	No of participants	No of electrodes	δ	θ	α	β	$\frac{(\theta+\alpha)}{\beta}$	$\frac{\alpha}{\beta}$	$\frac{(\theta+\alpha)}{(\alpha+\beta)}$	$\frac{\theta}{\beta}$	Electrode locations or brain regions modulated by fatigue
Barwick et al. (2012)	Fatigue during administration of a neuropsychological test battery	14	42	-	$\uparrow^{R}$	$\uparrow^{R}$	$\downarrow^{R}$	-	-	-	-	F, C, P, O
Baumeister et al. (2012)	Effects of fatigue induced by a cycling exercise on knee joint reproduction task	12	22	-	$\downarrow$	$\downarrow^{L,U}$	-	-	-	-	-	F3, Fz, F4, FC3, FCz, FC4, P4, O1, Oz, O2, T5
Chen et al. (2013)	Fatigue induced by watching 3DTV	10	16	$\uparrow^{R}$	NS	$\downarrow^{R}$	$\downarrow^{R}$	$\uparrow$	$\uparrow$	$\uparrow$	$\uparrow$	FP1, FP2, F3, C3, C4, F7, F8, T5
Cheng and Hsu (2011)	Mental fatigue induced by visual display terminal tasks	20	7	-	$\uparrow^{R}$	$\downarrow^{R}$	NS	$\downarrow$	NS[a]	-	-	F3, Fz, F4, Cz, Pz, O1, O2
Craig et al. (2012)	Fatigue induced by monotonous simulated driving task	48	32	NS	$\uparrow$	$\uparrow^{L,U}$	$\uparrow$	-	-	-	-	FL, FM, FR, CL, CM, CR, POL, POM, POR
Eoh et al. (2005)	Fatigue during a simulated driving task	8	8	-	NS	$\uparrow^{R}$	$\downarrow^{R}$	$\uparrow$	$\uparrow^{a}$	-	-	
Fan et al. (2015)	Mental fatigue in visual search task	10	64	NS	NS	$\uparrow^{R}$	$\downarrow^{R}$	$\uparrow$	$\uparrow$	$\uparrow$	$\uparrow$	FP, IF, F, C, P, O, T, PT
Jap et al. (2009)	Fatigue induced during a monotonous driving session	52	30	*	*	$\downarrow$	$\downarrow$	$\uparrow$	$\uparrow$	$\uparrow$	$\uparrow$	F, C, P, T, EB
Käthner et al. (2014)	Mental fatigue during P300 brain computer interface	12	31	-	$\uparrow$	$\uparrow$	-	-	-	-	-	F3, Fz, F4, FC5, FC3, FCz, FC4, FC6, C5, C3, Cz, C4, C6, CP5, CP3, CPz, CP4, CP6, P3, P1, Pz, P2, P4,PO7, PO3, POz, PO4, PO8, O1, O2
Lal and Craig (2002)	Fatigue during simulated driving task	35	19	$\uparrow$	$\uparrow$	$\uparrow$	$\uparrow$	-	-	-	-	EB
Tanaka et al. (2012)	Mental fatigue induced by $0^{(NS)}$ or 2-back test	18	11	NS	$\uparrow$	$\downarrow$	$\downarrow$	-	-	-	$\uparrow$	Fz, P3, Pz, O1, O2
Trejo et al. (2015)	Mental fatigue induced by a sustained low-workload mental arithmetic task	16	2	-	$\uparrow$	$\uparrow$	-	-	-	-	-	Fz, Pz
Wang et al. (2017)	Muscle fatigue during right arm side lateral raise task with loads	18	2	-	-	$\uparrow$	NS	-	-	-	-	C3, C4
Xu et al. (2018)	Fatigue in mental$^{(NS)}$ and physical-mental task	14	16	-	-	-	$\downarrow^{R}$	-	$\uparrow$	-	-	C3, P3, Pz, Oz, T3, T4, T5
Zhao et al. (2012)	Mental fatigue in simulated driving task	13	32	NS	$\uparrow^{R}$	$\uparrow^{R}$	$\downarrow^{R}$	-	-	-	-	F, C, P, O, T
Zou et al. (2015)	Stereoscopic 3D visual fatigue caused by vergence-accommodation conflict	11	30	-	NS	$\uparrow^{R}$	$\downarrow^{R}$	*	*	NS	NS	F, C, P, EB

*$\uparrow$ = significant increase; $\downarrow$ = significant decrease; * = significant, but the direction of change is not specified; NS = no significant change; - = not reported; R = relative band power measures were considered; L, U = lower and upper bands were considered; a = β/α was reported; The brain regions denoted by FP, IF, F, FL, FM, FR, FC, C, CL, CM, CR, P, PO, O, T, PT, POL, POM, POR, and EB corresponds to frontopolar (or pre-frontal), inferior frontal, frontal, left frontal, midline frontal, right frontal, fronto-central, central, central left, midline central, central right, parietal, parieto-occipital, occipital, temporal, posterior temporal, posterior left, midline posterior, posterior right and entire brain average.*

timed movement task significantly changes the movement in trunk shoulder and elbow kinematics, whereas the changes were mainly in wrist and hand movement due to distal muscle fatigue. Therefore, in general, repetitive gross motor skill retraining exercises may induce more physical fatigue than fine motor skill retraining exercises. In addition, most therapeutic fine motor activities require considerable attention and decision-making skills combined with hand, wrist and finger movements; therefore, they may induce more mental fatigue than most gross motor exercises. As the type of prominent fatigue developed during a robot-mediated interaction may vary depending on the physical and mental workload associated with the task, cortical

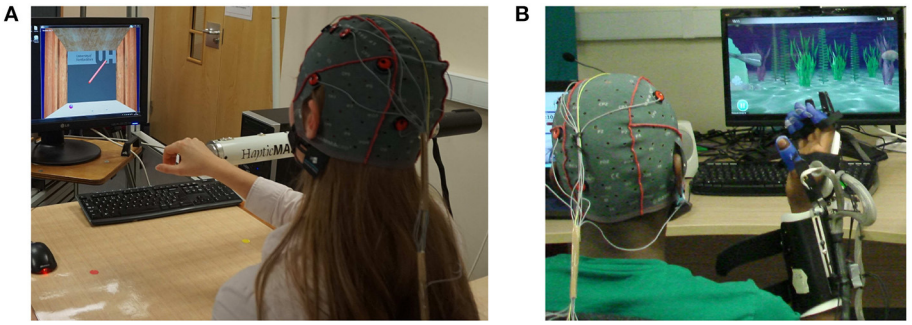

FIGURE 1 | Fatigue inducing robot-mediated interactions. **(A)** Robot-mediated gross motor interaction (arm reach/return task) using HapticMASTER, and **(B)** robot-mediated fine motor interaction (hand open/close task) using SCRIPT passive orthosis.

sites that show significant variations in EEG spectral features following fatigue may differ between interactions. However, these differences between gross and fine motor robot-mediated interactions are not systematically investigated.

In this preliminary experiment, we hypothesised that the EEG correlates of fatigue induced by robot-mediated interactions are specific to the physical or cognitive nature of the task and the differences in the usage of the proximal or distal upper limb. The gross movements (arm reach/return) were performed using the HapticMASTER (Motekforce Link, The Netherland) (Amirabdollahian et al., 2007; Chemuturi et al., 2013), and the fine movements (hand open/close) were performed using the SCRIPT passive orthosis (Amirabdollahian et al., 2014). Given the differences in the two tasks, it could be expected that the gross motor task may induce more physical fatigue than the fine motor task, in which more mental fatigue may be visible. Therefore, it was anticipated that the resulting statistically significant differences in EEG spectral features might show varying topographical distributions between the two robot-mediated interactions. Furthermore, significant changes to the EEG spectral features localised around the motor cortex were expected following the robot-mediated gross movements since fatigue may affect motor coordination skills. In the fine motor robot-mediated interaction that requires more attention and decision making, significant changes to the frontopolar brain activities were expected in addition to the attenuation in the activities around the motor cortex.

2. MATERIALS AND METHODS

2.1. Ethical Approval

The experiment was approved by the Science and Technology Ethics Committee with Delegated Authority of the University of Hertfordshire (Protocol numbers: COM/PG/UH/00100 and aCOM/PG/UH/00100).

2.2. Participants

Twenty healthy right-handed volunteers, who were at least 20 years of age (average age of the sample was 32 ± 10 years; mean ± SD) and with no history of severe injury to the head, brain, or right hand participated in this experiment. Right-handedness was considered since both robotic interfaces were constrained to be used only by the right upper limb due to their hardware configurations and setup. All participants had normal vision or corrected to normal vision. All participants signed informed consent forms before participation.

2.3. Fatigue Inducing Robot-Mediated Interactions

Given the consent to take part in the experiment, participants were randomly assigned into two groups: A and B, with 10 participants in each group. Participants in group A performed visually guided arm reach/return movements with HapticMASTER (gross motor task, **Figure 1A**), whereas participants in group B performed hand open/close movements with SCRIPT passive orthosis (fine motor task, **Figure 1B**). Both robot-mediated interactions were performed for 20-min or until volitional fatigue. The virtual reality environment of the GENTLE/A rehabilitation system (Chemuturi et al., 2013) was used for the gross motor task. Target point locations were modified so that the trajectory covered by the movement of the HapticMASTER robot arm was mapped into a straight line connecting only two virtual target points. In addition, the HapticMASTER was set to active mode so that the participants should initiate the movement and reach the target points by themselves. The virtual reality game "sea shell," developed for the SCRIPT system, was used as the fine motor task (Amirabdollahian et al., 2014). Participants performed hand open/close gestures to open/close a seashell underwater to catch a fish near the seashell. Both robot-mediated interactions were performed using only the right hand, and participants were asked to keep their left hand in a relaxed position throughout the task. The distance between the computer monitor and the participant's eye was set to around 120 cm for both groups.

2.4. EEG Data Acquisition

Continuous EEG signals were recorded before, during and after the robotic interactions using an eight-channel EEG data acquisition system, g.MOBIlab+ (g.tec medical engineering GmbH, Austria) with active electrodes. According to the International 10-10 system of electrode placement (American, 2006), FP1, F3, FC3, C3, C4, P3, O1, and T7 electrode

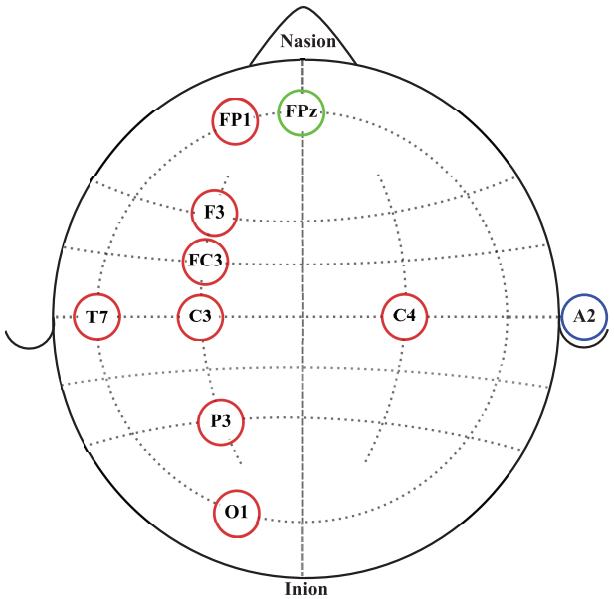

FIGURE 2 | EEG electrode placement according to the International 10-10 system of electrode placement. Red circles represent the eight active electrodes selected for the data acquisition. The blue circle represents the reference electrode location. The green circle represents the ground electrode location.

locations were selected as shown in **Figure 2**. All electrodes were referenced to the right earlobe (A2), and FPz was used as the ground electrode. Signals acquired by the active electrodes are pre-amplified directly at the electrode (Pinegger et al., 2016). Also, the active electrode system reduces or avoids artifacts caused by high impedance between the electrode(s) and the skin (e.g., 50/60 Hz coupling, electrode or cable movement artifacts, background noise) (g.tec medical engineering GmbH, 2014b). The sampling rate, lower and upper cut-off frequencies of the bandpass filter of the amplifier are fixed at 256, 0.5, and 100 Hz, respectively, by the manufacturer. Therefore, signals acquired from this device were sampled at 256 Hz and had a fixed EEG bandwidth of 0.5 to 100 Hz.

2.5. Experimental Procedure

On arrival at the laboratory, participants were informed about the experiment protocol, given time to familiarise themselves with the assigned robotic interaction and were prepared for the EEG data collection according to the guidelines given in g.tec medical engineering GmbH (2014a). The flow diagram of the proposed experiment is given in **Figure 3**. Following the standardised EEG recording protocol, EEG data were recorded before, during and after the robot-mediated interactions. Participants were instructed to close and open their eyes for 180 s each when EEG data were recorded before and after the gross and fine motor tasks. In order to reduce artifacts in the EEG data recorded with eyes opened/closed, participants were instructed to sit still while minimising eye blinks, eye movements, swallowing, jaw clenching, or any other severe body movements.

In this paper, only the EEG data recorded with eyes opened are further analysed. Participant's feedback on their physical and mental fatigue level before and after the tasks were obtained using two statements with a 5-point Likert rating scale (i.e., 1 = "Not at all fatigued," 2 = "somewhat fatigued," 3 = "moderately fatigued," 4 = "very fatigued," and 5 = "extremely fatigued"). Also, the participant's feedback on the task-associated physical and mental workload was obtained using two statements with a 5-point Likert rating scale (i.e., 1 = "Not at all demanding," 2 = "somewhat demanding," 3 = "moderately demanding," 4 = "very demanding," and 5 = "extremely demanding") (Dissanayake, 2021). Moreover, all participants performed the assigned task for 20 min.

2.6. EEG Data Analysis

This paper reports the modulation of EEG spectral features during eyes opened states before and after the fatiguing robot-mediated interactions. EEG features extracted from the data recorded before the task is referred to as baseline, and the data recorded after the task is referred to as recovery, respectively, throughout this paper. These states can be considered to reflect the restfulness of the participant before and after the robotic interactions; thereby, any changes in these states could be a reflection of fatigue. Previous studies have also compared EEG data recorded before and after a task to identify EEG feature modulations associated with fatigue induced by physical and mental tasks (Ng and Raveendran, 2007; Cheng and Hsu, 2011; Tanaka et al., 2012; Chen et al., 2013). The EEG data processing pipeline followed for each participant during baseline and recovery states is illustrated in **Figure 4**. EEG preprocessing and feature extraction was performed offline using custom MATLAB scripts.

Preprocessing

Firstly, the DC offset of each recording was removed by subtracting the channel-wise mean from each data point. Then, a Type II Chebyshev low-pass filter with a stopband frequency of 45 Hz and an order of 20 was applied to eliminate the power line noise (50 Hz) distortions.

The EEG research community widely uses independent component analysis (ICA) to separate and remove artifacts in EEG signals (Makeig et al., 1996; Jung et al., 1998; Delorme et al., 2007; Debener et al., 2010). ICA is a linear decomposition technique used to recover a set of n unobserved independent source signals given only $m \geq n$ observed instantaneous mixtures of these source signals. If we denote the n independent source signals at time t by a $n \times 1$ vector $\mathbf{s}(t)$ and the observed signals by a $m \times 1$ vector $\mathbf{x}(t)$, the mixing model can be written as,

$$\mathbf{x}(t) = \mathbf{A}\mathbf{s}(t), \tag{1}$$

where the $m \times n$ matrix $\mathbf{A}$ represents the unknown "mixing matrix". The elements in each row of $\mathbf{A}$ corresponds to the contributions from each source signal to each observation (i.e., $x_i(t) = \sum_{j=1}^{n} a_{ij}s_j(t)$ for all $i = 1$ to m). The objective of ICA is to find a separating matrix, i.e., a $n \times m$ matrix $\mathbf{W}$ such that

$$\mathbf{u}(t) = \mathbf{W}\mathbf{x}(t) \tag{2}$$

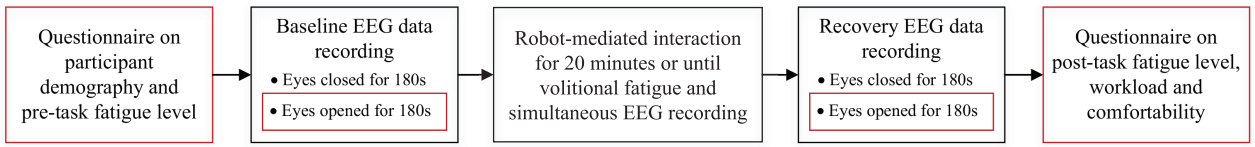

FIGURE 3 | Flow diagram of the proposed experiment.

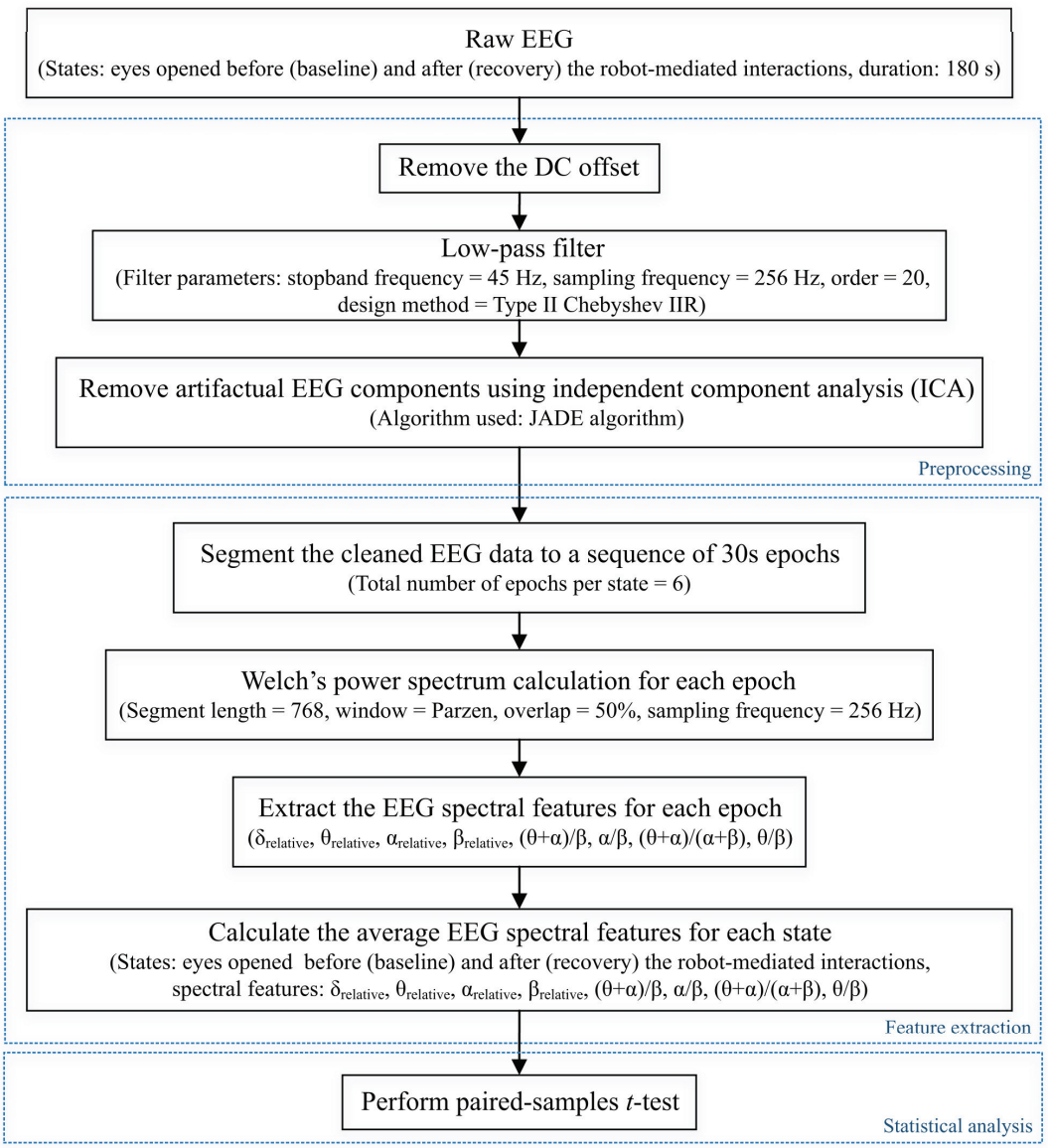

FIGURE 4 | EEG data processing pipeline followed to preprocess raw EEG data and extract EEG spectral features of each state for each participant to perform the statistical analysis. Dotted boxes represent the three main steps involved in the pipeline: data preprocessing, feature extraction, and statistical analysis. δ_{relative}, θ_{relative}, α_{relative}, and β_{relative} indicate the relative δ, θ, α and β band powers, respectively, and $(\theta+\alpha)/\beta$, α/β, $(\theta+\alpha)/(\alpha+\beta)$, and θ/β indicate the power ratios.

is an estimate of the original source signals. The elements in the $n \times 1$ vector $\mathbf{u}(t)$ (i.e., independent components) are identical to the original source signals up to permutations and changes of scales and signs (Cardoso, 1998).

The joint approximate diagonalisation of eigenmatrices (JADE) algorithm (Cardoso and Souloumiac, 1993) was used in this experiment to separate and remove in-band artifacts, including eye blinking, eye movement, swallowing, jaw clenching, and cardiac activity from the independent components. **Figure 5** illustrates the artifact removal process using ICA for a single subject. When applying ICA to separate EEG artifacts from brain activity patterns, it was assumed that the signals emitted by the unobserved sources are independent, and the number of independent sources is the same as the number of electrodes used in the experiment (i.e., $m = n = 8$). The relative projection strengths of each independent component onto the scalp electrodes were given by the columns of the inverse separation matrix $\mathbf{W}^{-1}$, which is an estimate of the mixing matrix $\mathbf{A}$ in Equation 1. The "corrected" EEG signal was then derived as, $\hat{\mathbf{x}}(t) = W^{-1}\hat{\mathbf{u}}(t)$, where $\hat{\mathbf{u}}(t)$ was derived from the matrix of activation waveforms $\mathbf{u}(t)$, by setting the rows representing the artifactual components identified by visual inspection to zero (Jung et al., 2000).

Feature Extraction

The corrected EEG signals at the two states: baseline and recovery for each participant were segmented into epochs of 30 s length (i.e., 7680 samples per epoch and 6 epochs in total per state). The power spectral density for all epochs was estimated using Welch's averaged modified periodogram method (Welch, 1967) with a 3 s segment length (i.e., 768 samples), 50% overlap, and a Parzen window. Subsequently, the relative band power of δ (1-<4 Hz), θ (4-<8 Hz), α (8–13 Hz), and β (<13–30 Hz) (denoted by δ_{relative}, θ_{relative}, α_{relative}, and β_{relative}, respectively, in this paper) for each epoch were calculated as a ratio between the average band power of each frequency band and the total band power (i.e., the summation of average δ, θ, α, and β band powers). The four ratio band power measures: $(\theta + \alpha)/\beta$, α/β, $(\theta + \alpha)/(\alpha + \beta)$, and θ/β for each epoch were also calculated. Finally, the average of each EEG spectral feature within the 180 s duration (i.e., six epochs) of each state was calculated to represent the corresponding spectral EEG feature index of the baseline and recovery states, respectively (Dissanayake, 2021).

Statistical Analysis

Statistical analysis was carried out using the *IBM SPSS Statistics 25* software. A p-value<0.05 was considered statistically significant, denoting a 95% confidence interval. It was of interest to investigate whether the significant differences in EEG spectral features caused by fatigue are localised to different electrode locations due to the differences in the nature of the task (fine/gross motor and distal/proximal upper limb). Normality of the differences between EEG spectral features extracted from baseline and recovery states were assessed using the Kolmogorov-Smirnov test. Upon confirmation of normal distribution, two-tailed paired-samples t-tests were performed separately on the eight electrode locations to identify the significant differences between the baseline and recovery states of each EEG spectral feature for each robot-mediated interaction. The effect sizes were expressed by the Pearsons' correlation coefficient, $r = \sqrt{\frac{t^2}{(t^2+df^2)}}$. Multiple paired-samples t-tests were also used in previous fatigue studies to evaluate the changes in EEG features at different brain regions (Tanaka et al., 2012; Zhao et al., 2012; Chen et al., 2013; Fan et al., 2015).

3. RESULTS

3.1. Modulations in EEG Spectral Features Following the Robot-Mediated Gross Motor Interaction With HapticMASTER

Table 2 summarises the paired-samples t-test results of the statistically significant EEG spectral feature modulations following the gross motor interaction with HapticMASTER. **Figure 6** shows the sample mean and standard deviation of the substantive EEG spectral features during baseline and recovery states. Comparison of the sub-figures shows that α_{relative} changed the most due to fatigue induced by the gross motor interaction with HapticMASTER. In **Figure 6B**, there is a clear increase in the sample mean of α_{relative} across all electrodes, with statistically significant differences visible on the three electrodes placed over the contralateral motor cortex: FC3 ($t(9)$ = -2.378, p = 0.041, r = 0.621), C3 ($t(9)$ = -3.148, p = 0.012, r = 0.724) and P3 ($t(9)$ = -2.646, p = 0.027, r = 0.661). As well as being statistically significant, the effect of the variation in α_{relative} on FC3, C3, and P3 electrodes is large. These electrodes correspond to motor activities using the right hand; thereby, the significant increase in α_{relative} reflects a decreased cortical activation, which is an indication of fatigue. Similarly, **Figures 6C,D** show that fatigue induced by the gross motor task significantly increased both $(\theta + \alpha)/\beta$ ($t(9)$ = -2.787, p = 0.021, r = 0.681) and α/β ($t(9)$ = -2.403, p = 0.040, r = 0.625) on the C3 electrode. A larger effect size was also visible on the C3 electrode for both $(\theta + \alpha)/\beta$ and α/β. These findings show that fatigue induced by gross movements increased the low-frequency power and decreased the fast wave activities on the C3 electrode, resulting in a significant difference when combined. In contrast, **Figure 6A** indicates that there has been a drop in δ_{relative} following the gross movements (except on T7). Also, a significant variation with larger effect was found on the C3 electrode ($t(9)$ = 2.593, p = 0.029, r = 0.654). This result is somewhat counter-intuitive because previous studies have shown a significant increase or no change in delta activity as fatigue progressed; however, it is reasonable to assume that this inconsistency may be related to the differences in experimental protocols.There were no significant differences visible in θ_{relative}, β_{relative}, $(\theta + \alpha)/(\alpha + \beta)$, and θ/β due to fatigue induced by the gross motor task. Overall, these results show a reduced activation around the sensorimotor cortex due to fatigue induced by robot-mediated gross movements. **Figure 7** shows the brain topographies of the difference between recovery and baseline states (i.e., difference = recovery - baseline) of δ_{relative}, α_{relative}, $(\theta + \alpha)/\beta$ and α/β for one participant who reported a greater increase in physical fatigue than mental fatigue following the gross motor task. Topographical distributions also show that the

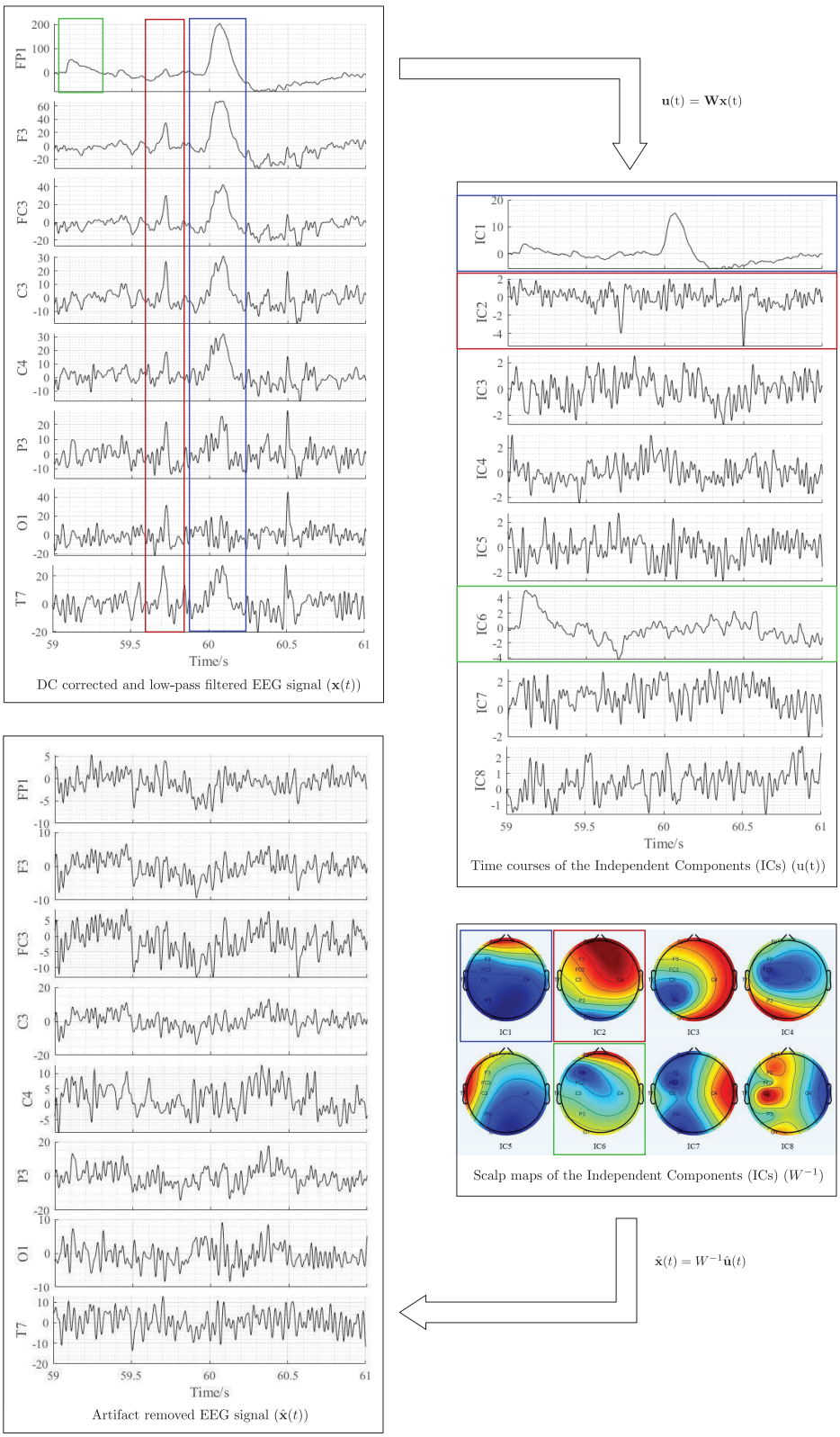

FIGURE 5 | Illustration of EEG artifactual components identification using ICA for one participant. The red, blue, and green rectangles correspond to cardiac activity, eye blink, and eye movement artifacts, respectively. All data were referenced to the right earlobe (A2).

TABLE 2 | Significant EEG spectral feature modulations and the corresponding electrode locations following the gross motor interaction with HapticMASTER.

Spectral feature	Electrode location	Sample mean ± std		Paired samples *t*-test				Direction of change
		Baseline	Recovery	*t*	*df*	*p*-value	*r*	
δ_{relative}	C3	0.542 ± 0.109	0.476 ± 0.067	2.593	9	0.029	0.654	↓
	FC3	0.180 ± 0.068	0.225 ± 0.069	-2.378	9	0.041	0.621	↑
α_{relative}	C3	0.198 ± 0.070	0.259 ± 0.095	-3.148	9	0.012	0.724	↑
	P3	0.271 ± 0.094	0.330 ± 0.154	-2.646	9	0.027	0.661	↑
$\frac{(\theta+\alpha)}{\beta}$	C3	8.151 ± 4.349	8.923 ± 4.167	-2.787	9	0.021	0.681	↑
$\frac{\alpha}{\beta}$	C3	4.213 ± 2.612	4.997 ± 2.812	-2.403	9	0.040	0.625	↑

↑ = *significant increase.* ↓ = *significant decrease.*

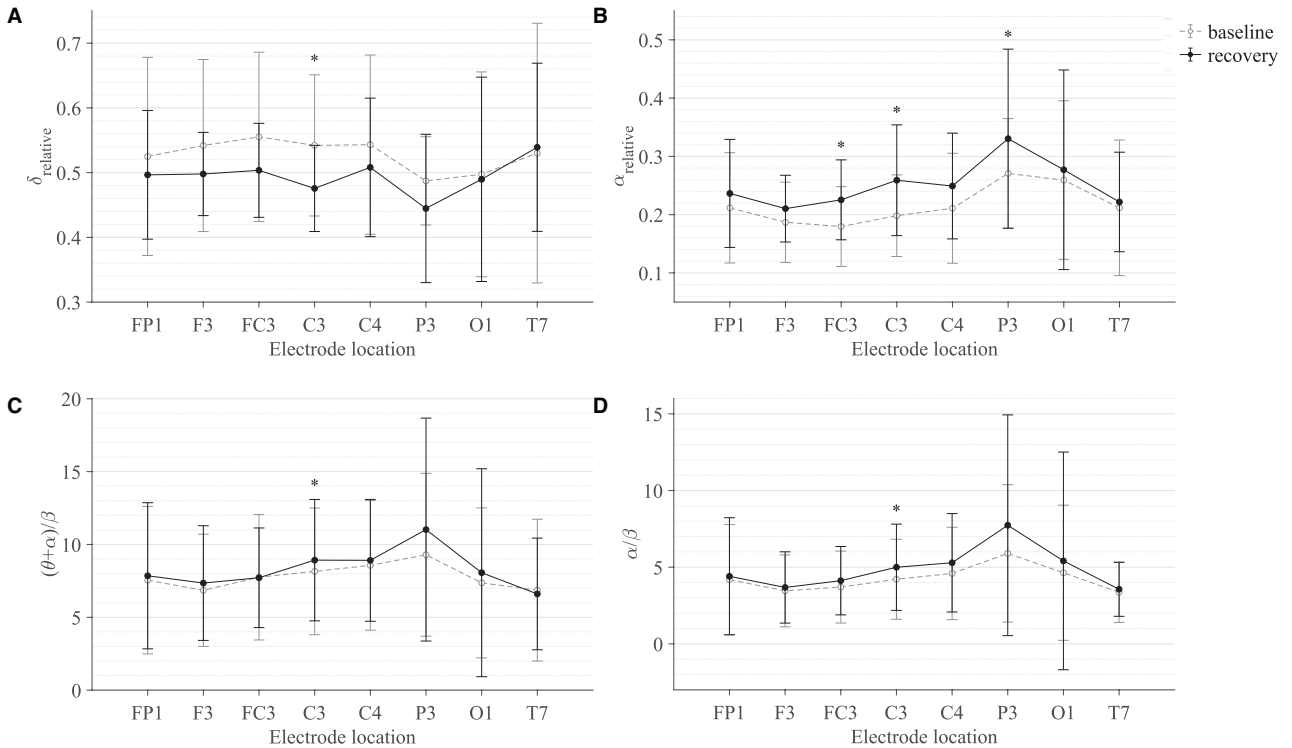

FIGURE 6 | Comparison of the sample mean and standard deviation of **(A)** δ_{relative}, **(B)** α_{relative}, **(C)** $(\theta+\alpha)/\beta$, and **(D)** α/β of all participants between baseline and recovery states for the gross motor interaction with HapticMASTER. The statistical significance is represented by an asterisk: i.e., *p < 0.05.

fatigue induced by the gross movements may have altered the EEG activity around the left central and left parietal regions.

3.2. Modulations in EEG Spectral Features Following the Robot-Mediated Fine Motor Interaction With SCRIPT Passive Orthosis

Table 3 summarises the paired-samples *t*-test results of the statistically significant EEG spectral feature modulations following the fine motor interaction with SCRIPT passive orthosis. **Figure 8** shows the sample mean and standard deviation of the substantive EEG spectral features during baseline and recovery states. An increase of θ_{relative} and α_{relative} is visible in both **Figures 8B,C** on all electrodes. A significant increase in α_{relative} is visible on FP1 (t = -2.871, p = 0.018, r = 0.691) and C3 (t = -2.555, p = 0.031, r = 0.648) electrodes, whereas the significant difference in θ_{relative} is on the C4 electrode (t = -3.507, p = 0.007, r = 0.760). The effect of these significant variations in α_{relative} and θ_{relative} are also of larger magnitude, thereby suggesting that these variations are substantive findings. In contrast, a general decrease in δ_{relative} on all electrodes and a significant decrease on the FP1 electrode with a larger effect size (t = 3.066, p = 0.013, r = 0.715) can be found in **Figure 8A**. No significant differences were visible in β_{relative} and ratio band power measures. In general, these results show that the fatigue induced by fine motor interactions alters not only the activities

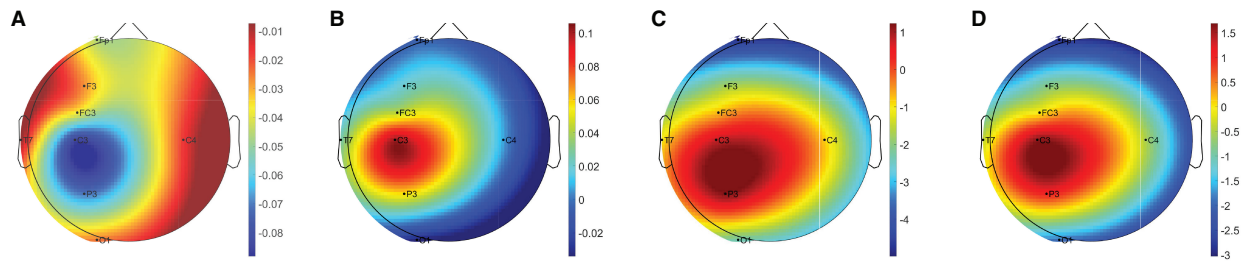

FIGURE 7 | Brain topographies for the difference between recovery and baseline states (i.e., difference = recovery - baseline) of **(A)** δ_{relative}, **(B)** α_{relative}, **(C)** $(\theta + \alpha)/\beta$, and **(D)** α/β for one participant following the gross motor interaction with HapticMASTER. In each brain map, the nose is represented by the triangle on the top, and the right hemisphere is on the right. For α_{relative}, $(\theta + \alpha)/\beta$, and α/β, the red-shaded areas indicate a larger increase whereas the blue-shaded areas indicate a decrease. For δ_{relative}, the blue-shaded areas indicate a larger decrease whereas the red-shaded areas indicate a smaller decrease.

around the sensorimotor cortex but also the frontopolar cortex. **Figure 9** shows the brain topographies of the difference between recovery and baseline states (i.e., difference = recovery - baseline) of the substantive EEG features for one participant who reported a greater increase in mental fatigue than physical fatigue following the fine motor task. Topographical distributions also show that the variations in the EEG features around frontopolar and central brain regions may have been caused by the fatigue that resulted from the robot-mediated fine motor interaction.

3.3. Subjective Measures of Fatigue Level and Workload

Most participants who performed the robot-mediated gross motor interaction with HapticMASTER reported increased physical fatigue following the task. Six participants showed a greater change in physical fatigue scores than in mental fatigue scores, and two participants showed an equal rise in both physical and mental fatigue scores. Therefore, the subjective ratings suggest that the gross motor interaction may have induced physical fatigue. In contrast, most participants who performed the fine motor task reported that their mental fatigue was increased following the robotic interaction. Four participants showed a greater change in mental fatigue scores than physical fatigue scores, and two participants showed an equal rise in both physical and mental fatigue scores. Therefore, the subjective ratings suggest that the fine motor interaction, on the other hand, may have induced mental fatigue. Furthermore, most participants reported that the gross motor task was more physically demanding than mentally demanding. In contrast, most participants revealed that the fine motor task required greater mental demand or equally physical and mental demand. A comparison of the subjective measures of physical and mental fatigue levels before and after the robot-mediated gross and fine motor interactions and the physical and mental workload of the two tasks is shown in **Figure 10**.

Figure 11 shows the association between the variations in fatigue levels and the rated workload following the robot-mediated gross and fine motor interactions. All participants who experienced a greater increase in physical fatigue than the change in mental fatigue following the gross motor task also rated that the underlying physical workload of the gross motor task was greater than the mental workload. All participants who experienced a greater increase in mental fatigue than physical fatigue following the fine motor task rated that the fine motor task required a greater mental demand than the physical demand. The gross motor task involves the movement and coordination of proximal joints and muscles of the upper limb (shoulder and arm) to control the robot arm between target points. The fine motor task requires considerable attention and decision-making skills combined with hand and finger movements to catch the fish when it reaches the seashell. Therefore, the subjective responses imply that the gross motor task performed with HapticMASTER may have greatly contributed to the development of physical fatigue due to the increased physical demand. In contrast, the fine motor task performed with SCRIPT passive orthosis may have mainly induced mental fatigue due to the increased mental demand required during the task.

3.4. Association of Changes in Fatigue Level With the Substantive EEG Feature Modulations

Most participants who reported an increase in physical fatigue following the robot-mediated gross motor interaction also showed a greater increase in α_{relative} on FC3, C3, and P3 electrodes, $(\theta+\alpha)/\beta$ and α/β on the C3 electrode in comparison to the participants who reported no change or reduction in physical fatigue. Similarly, a greater decrease in δ_{relative} on the C3 electrode was also found in most participants who experienced increased physical fatigue. Therefore, the above findings show that the significant changes in δ_{relative}, α_{relative}, $(\theta + \alpha)/\beta$ and α/β around the motor cortex are likely related to the physical fatigue accumulated following the gross motor task. All six participants who reported increased mental fatigue following the robot-mediated fine motor interaction showed a decrease in δ_{relative} on the FP1 electrode. Five participants also showed an increase in α_{relative} on FP1 and C3 electrodes, and four

TABLE 3 | Significant EEG spectral feature modulations and the corresponding electrode locations following the fine motor interaction with SCRIPT passive orthosis.

Spectral feature	Electrode location	Sample mean ± std		Paired samples *t*-test				Direction of change
		Baseline	Recovery	*t*	*df*	*p*-value	*r*	
$\delta_{relative}$	FP1	0.550 ± 0.096	0.504 ± 0.106	3.066	9	0.013	0.715	↓
$\theta_{relative}$	C4	0.193 ± 0.033	0.226 ± 0.039	-3.507	9	0.007	0.760	↑
$\alpha_{relative}$	FP1	0.179 ± 0.075	0.211 ± 0.104	-2.871	9	0.018	0.691	↑
	C3	0.202 ± 0.127	0.227 ± 0.117	-2.555	9	0.031	0.648	↑

↑ = *significant increase.* ↓ = *significant decrease.*

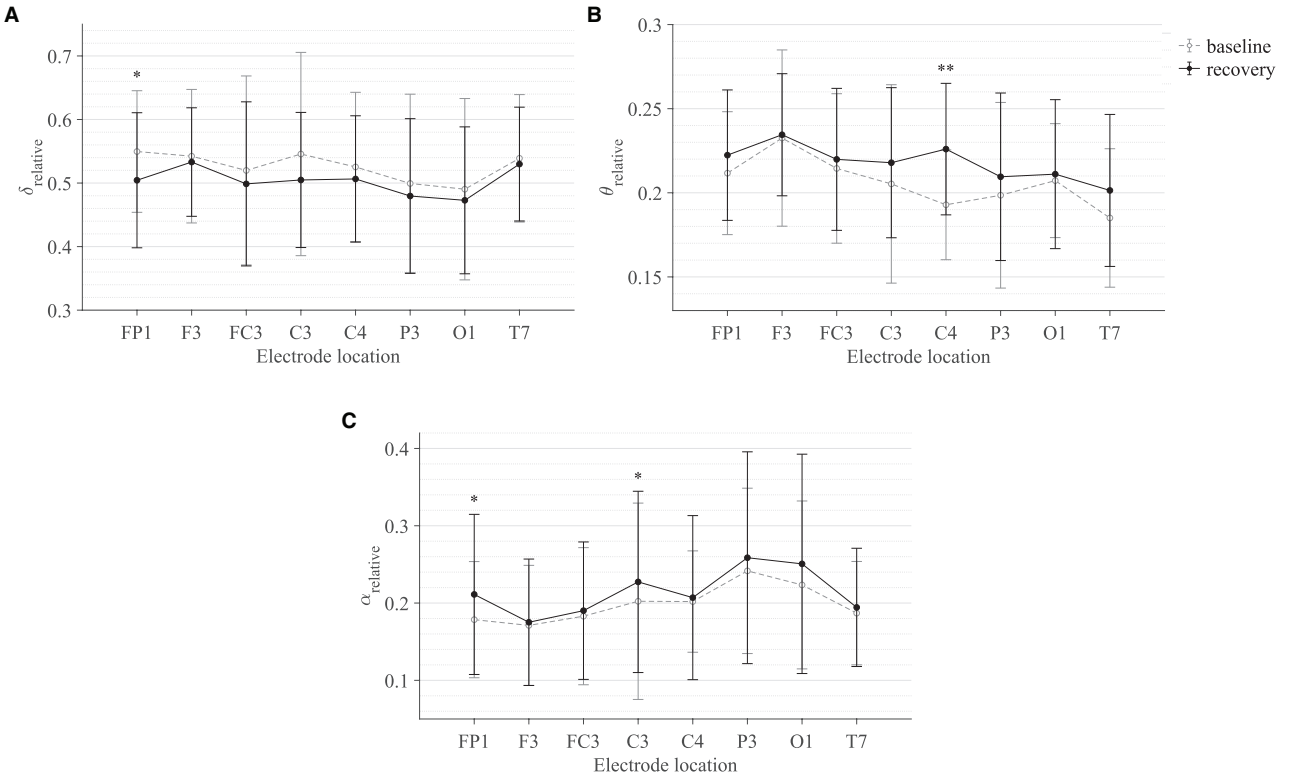

FIGURE 8 | Comparison of the sample mean and standard deviation of **(A)** $\delta_{relative}$, **(B)** $\theta_{relative}$, and **(C)** $\alpha_{relative}$ of all participants between baseline and recovery states for the fine motor interaction with SCRIPT passive orthosis. The statistical significance is represented by an asterisk: i.e., *p < 0.05 and **p < 0.01.

participants showed an increase in $\theta_{relative}$ on C4. Therefore, the modulations in EEG spectral features around the prefrontal cortex presumably reflect increased mental fatigue following the robot-mediated fine movements. **Figure 12** shows the association between the modulations in $\delta_{relative}$ and $\alpha_{relative}$ and the variations in subjective measures of physical and mental fatigue levels following the robot-mediated gross and fine motor tasks.

4. DISCUSSION

This preliminary experiment investigated cortical-related changes associated with fatigue in upper limb robot-mediated gross and fine motor interactions. The findings of this experiment indicate that it is possible to monitor fatigue induced by robot-mediated interactions using EEG spectral features, which can have further utility for robot-mediated post-stroke therapy.

The most prominent finding was a significant increase in the $\alpha_{relative}$ following both the robot-mediated gross and fine motor interactions. It is known that α activity is most commonly visible during relaxed conditions and decreased attention levels. Also, in drowsy but wakeful states when increased efforts are taken to maintain the level of attention and alertness, increased α activity is visible (Klimesch, 1999). In contrast, when an individual is in an alert state, suppression of α activity is visible. Task-related desynchronisation, which leads to a decrease in α activity, can be interpreted as an electrophysiological correlate of increased activation of the cortical areas (excited neural structures) that produce motor behaviour or process sensory or cognitive information (Pfurtscheller et al., 1996; Pfurtscheller, 1997). Therefore, the increased $\alpha_{relative}$ following the robot-mediated interactions may reflect decreased cortical activity and a reduced capacity for information processing in the underlying

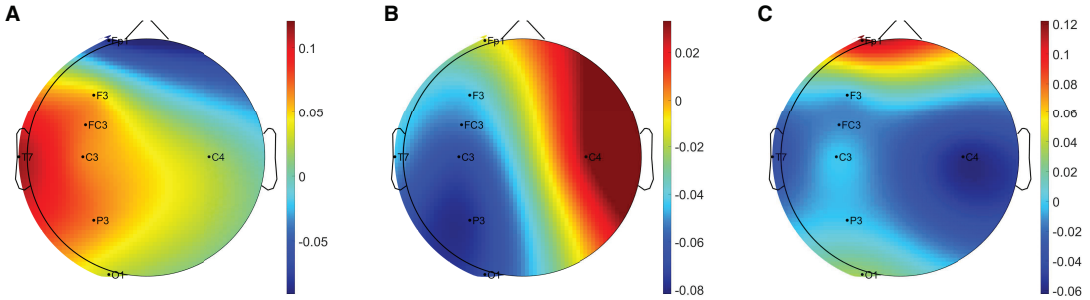

FIGURE 9 | Brain topographies for the difference between recovery and baseline states (i.e., difference = recovery - baseline) of **(A)** $\delta_{relative}$, **(B)** $\theta_{relative}$, and **(C)** $\alpha_{relative}$ for one participant following the fine motor interaction with SCRIPT passive orthosis. In each brain map, the nose is represented by the triangle on the top, and the right hemisphere is on the right. The red-shaded areas indicate a larger increase whereas the blue-shaded areas indicate a larger decrease.

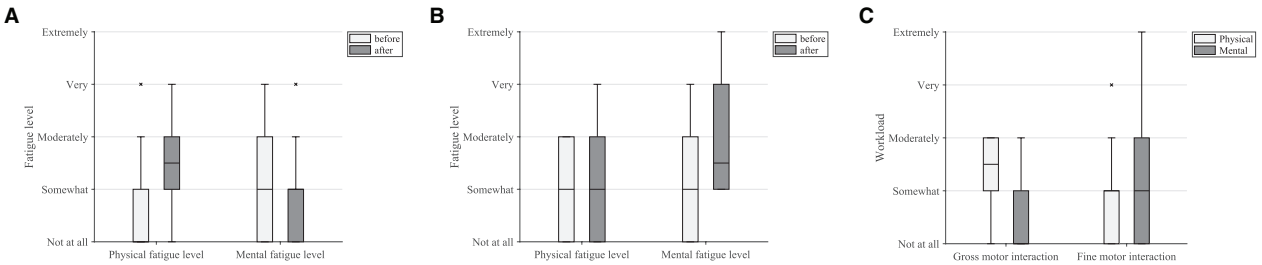

FIGURE 10 | Subjective measures of fatigue level and workload. **(A)** Comparison of the subjective measures of fatigue level before and after the gross motor interaction with HapticMATER. **(B)** Comparison of the subjective measures of fatigue level before and after the fine motor interaction with SCRIPT passive orthosis. **(C)** Comparison of the subjective measures of physical and mental workload following the gross and fine motor interactions.

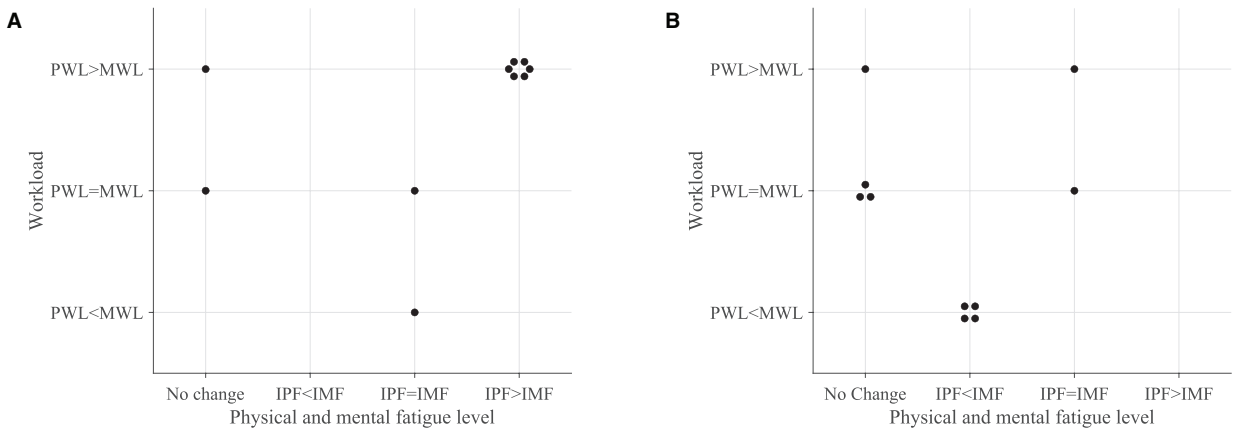

FIGURE 11 | Association between the variations in fatigue levels and the rated workload following the **(A)** robot-mediated gross motor interaction with HapticMASTER and **(B)** robot-mediated fine motor interaction with SCRIPT passive orthosis. The "IPF" and "IMF" refers to the increase in physical and mental fatigue scores following the robot-mediated interactions, respectively. No change refers to no increase or a decrease in both fatigue levels. The "PWL" and "MWL" refers to the rated physical and mental workload, respectively.

cortical regions due to fatigue. This finding is in agreement with the findings of previous fatigue studies (Eoh et al., 2005; Barwick et al., 2012; Zhao et al., 2012; Fan et al., 2015; Zou et al., 2015). Thus, we suggest that the observed modulations in $\alpha_{relative}$ presumably reflect the changes in an individual's fatigue level following upper limb robot-mediated interactions. Furthermore,

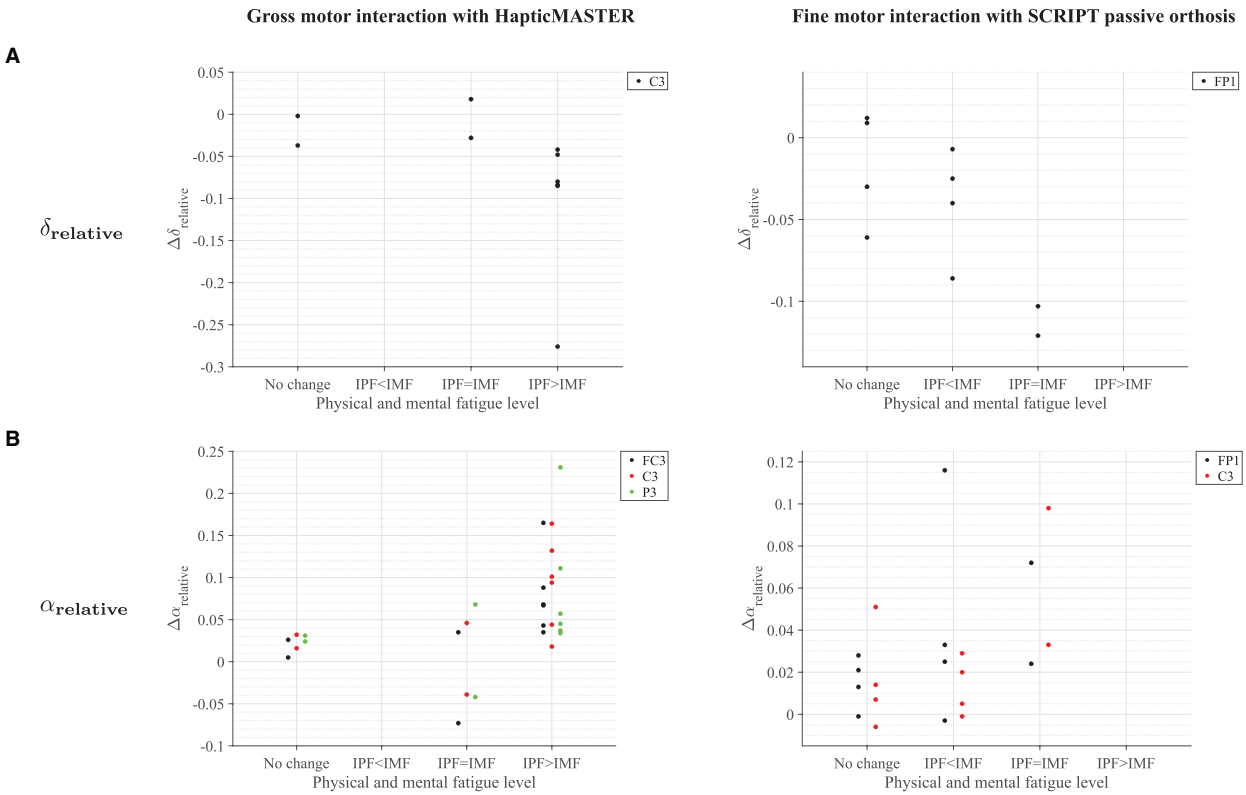

FIGURE 12 | Comparison of the modulations in $\delta_{relative}$ and $\alpha_{relative}$ with the variations in fatigue levels following the **(A)** robot-mediated gross motor interaction with HapticMASTER and **(B)** robot-mediated fine motor interaction with SCRIPT passive orthosis. The Δ represents the difference in each EEG feature following the robot-mediated interactions (i.e., recovery - baseline). The "IPF" and "IMF" refers to the increase in physical and mental fatigue scores following the robot-mediated interactions, respectively. No change refers to no increase or a decrease in both fatigue levels.

the above inference was also supported by the participants' feedback on the changes in their physical and mental fatigue levels after the assigned task; thereby suggesting that $\alpha_{relative}$ is a reliable EEG-based fatigue index that can be used to monitor fatigue accumulated during human-robot interactions.

Topographical differences found in the prominent EEG spectral features indicate that the brain regions most affected by fatigue may depend on the physical and mental workload associated with the task and the differences in the usage of the proximal and distal upper arm. In the gross motor interaction, participants were instructed to move the HapticMASTER robot arm in a linear trajectory to reach the two target points visible in the virtual reality environment. In a visually guided reaching task, the sensory system extracts spatial information about the target, and a movement plan is created and executed by the motor cortex (Sabes, 2000; Gevins and Smith, 2007). The premotor cortex, primary somatosensory cortex, and posterior parietal cortex integrate motor and sensory information for planning and coordinating complex movements. Also, HapticMASTER is an end-effector based robot, and the proximal upper limbs (arm and shoulder) are predominantly used when moving the robot arm between target points during the gross motor task. Therefore, the significant rise in $\alpha_{relative}$ found at FC3, C3, and P3 electrode locations presumably reflects the inhibition of premotor cortex, primary somatosensory cortex, and posterior parietal cortex due to physical fatigue accumulated during the arm reach/return task. A previous study has also shown that the upper limb reaching tasks performed using the HapticMASTER induced muscle fatigue (Thacham Poyil et al., 2020a,b). Conversely, in the fine motor task, participants were expected to perform hand open/close gestures only when a fish was near the seashell in the virtual environment. Therefore, the fine motor task required more sustained attention and decision-making than the gross motor task. Laureiro-Martínez et al. (2014) also found that a stronger activation in the frontopolar cortex is associated with higher decision-making efficiency. In addition, active movements consisting of repetitive opening and closing of the hand are shown to activate the contralateral primary sensorimotor cortex (Guzzetta et al., 2007). Therefore, the increased $\alpha_{relative}$ over FP1 and C3 electrodes following the repetitive fine movements appear to reflect an altered decision-making efficiency of an individual, in addition to the deactivation in the motor cortex associated with fatigue. The topographical variations in $\alpha_{relative}$ were also supported by the participants' feedback on their fatigue level after each interaction. The greater changes in $\alpha_{relative}$ following the gross motor task were also associated with a greater increase

in physical fatigue. In contrast, the greater changes in α_{relative} following the fine motor task were associated with a greater increase in mental fatigue or an equal increase in both physical and mental fatigue levels.

It has been established in the literature that EEG activity shifts from high frequencies toward slower waves with the progression of fatigue; thus, the ratio between low-frequency and high-frequency power can also be considered as a reliable measure of fatigue (Eoh et al., 2005; Jap et al., 2009). This experiment found significant differences only in $(\theta + \alpha)/\beta$ and α/β on the C3 electrode following the physically fatiguing gross motor task. These findings were also supported by the participants' feedback on their fatigue level. Furthermore, there were no significant differences in the power ratios due to the fine motor task. Although the significant changes on the C3 electrode were only visible for α_{relative}, a slight increase in θ_{relative} and a decrease in β_{relative} were also found after the gross motor task. Therefore, the findings suggest that gross motor interaction increased the low-frequency activities while suppressing the high-frequency activities on the C3 electrode, which may have caused the significant increase of $(\theta + \alpha)/\beta$ and α/β. Eoh et al. (2005), Jap et al. (2009), Chen et al. (2013), Fan et al. (2015) also reported a significant rise in both $(\theta + \alpha)/\beta$ and α/β with fatigue.

The suppression in δ_{relative} following the robot-mediated interactions is contrary to some previous studies that have suggested a statistically significant increase or no significant difference in δ activities due to fatigue (Lal and Craig, 2002; Craig et al., 2012; Zhao et al., 2012). However, a non-significant reduction in δ_{relative} around all brain regions after a simulated driving task was reported in Zhao et al. (2012). In this experiment, a significant decrease in δ_{relative} was found on the C3 electrode following the gross motor task and on the FP1 electrode following the fine motor task. Most participants who reported an increase in their physical fatigue level after the robot-mediated gross motor task also have experienced a decrease in δ_{relative} on the C3 electrode. Similarly, all participants who reported an increase in their mental fatigue level following the robot-mediated fine motor task also showed a decrease in δ_{relative}. Therefore, the subjective measures of fatigue level support the suppression in δ_{relative} due to fatigue build-up and the topographical variations found in the two tasks. The methodological differences of the previous studies could explain these discrepancies as these studies were based on vehicle driving tasks, whereas our experiment was focused on gross and fine motor tasks in a human-robot interaction scenario. Harmony et al. (1996) proposed that increased attention to internal processing (i.e., "internal concentration") during mental tasks might cause an increase in the delta activity. In order to accurately perform the two tasks in this experiment, higher concentration and attention levels are essential. Therefore, the reduction in δ_{relative} associated with the robotic interactions may suggest deficient inhibitory control and information-processing mechanisms. This finding, while preliminary, suggests that fatigue may have negatively affected an individual's attention and internal concentration levels. Therefore, δ_{relative} could also be used as an EEG-based measure of fatigue in robot-mediated interactions.

The ipsilateral primary somatosensory cortex is also shown to increase its level of activation during prolonged sustained and intermittent sub-maximal muscle contractions to compensate for fatigue (Liu et al., 2003). In this experiment, a significant change in the C4 electrode was visible only for θ_{relative} following the fine motor task. Theta oscillations in EEG have shown to be prominent during cognitive processing that requires higher mental effort and is positively related to task difficulty (Gevins et al., 1997). Barwick et al. (2012), Cheng and Hsu (2011), and Zhao et al. (2012) also reported an increase in θ_{relative} due to fatigue build-up. Therefore, the rise in θ_{relative} on C4 may reflect the fatigue-related changes in the ipsilateral brain activation caused by the fine motor task.

The spatial precision of the EEG recordings taken in this experiment was limited since the EEG data acquisition system could only support eight electrode locations. Furthermore, only a limited number of participants were tested, and each participant interacted with only one robotic interface. Therefore, future research should examine more electrode locations and consider a cross-over study design with a higher sample size where each participant is exposed to both fatiguing robotic interactions.

5. CONCLUSION

This paper investigates the modulations in EEG spectral features associated with fatigue induced by robot-mediated upper limb gross and fine motor interactions. It was found that the fatigue induced by the gross movements mostly altered the EEG activity around the central and parietal brain regions, whereas the fine movements mostly altered the EEG activity around the frontopolar and central brain regions. These regional differences in significant EEG spectral features are most likely due to the differences in the nature of the task (fine/gross motor and distal/proximal upper limb) that may have differently altered the physical and mental fatigue level of an individual. We have shown that EEG correlates of fatigue progressed during robot-mediated interactions are specific to the physical or cognitive nature of the task performed using the proximal or distal upper limb. Further studies will explore whether the specificity is due to the difference in the motor skills considered (fine/gross motor) or the usage of upper limbs (distal/proximal upper limb). Given that fatigue during robot-mediated therapy can be estimated via EEG spectral features, we believe that the findings could potentially be used to moderate the level of fatigue during post-stroke rehabilitation, acknowledging that stroke patients are more likely to be fatigued than healthy individuals. Moreover, it would be possible to derive more personalised robot-mediated post-stroke rehabilitation regimes that would utilise the individual fatigue levels as a tool to increase the efficacy of upper limb robot-mediated rehabilitation.

DATA AVAILABILITY STATEMENT

The datasets presented in this article are not readily available because ethical consent to share the data publicly alongside publications was not sought at data collection, and therefore

it is not possible to share the data. Requests to access the datasets should be directed to Farshid Amirabdollahian, f.amirabdollahian2@herts.ac.uk.

ETHICS STATEMENT

The studies involving human participants were reviewed and approved by Science and Technology Ethics Committee with Delegated Authority of the University of Hertfordshire. The patients/participants provided their written informed consent to participate in this study.

AUTHOR CONTRIBUTIONS

UD carried out the data collection, analysis, and wrote the first draft of the manuscript. FA and VS obtained the research funding and supervised the research. All authors contributed to the conception and design of the experiment, manuscript revision, and approved the submitted version.

FUNDING

This work was supported by the Ph.D studentship awarded to UD from the University of Hertfordshire, United Kingdom.

ACKNOWLEDGMENTS

This experiment was conducted as part of the Ph.D programme pursued by UD at the University of Hertfordshire, United Kingdom. The authors would like to thank all the participants who contributed their time and effort to this experiment. A preprint of this paper is available on bioRxiv (Dissanayake et al., 2021).

REFERENCES

Alderman, R. B. (1965). Influence of local fatigue on speed and accuracy in motor learning. *Res. Quart. Amer. Assoc. Health Phys. Educ. Recreat.* 36, 131–140. doi: 10.1080/10671188.1965.10614670

American Clinical Neurophysiology Society. (2006). Guideline 5: guidelines for standard electrode position nomenclature. *J. Clin. Neurophysiol.* 23, 107–110. doi: 10.1097/00004691-200604000-00006

Amirabdollahian, F., Ates, S., Basteris, A., Cesario, A., Buurke, J., Hermens, H., et al. (2014). Design, development and deployment of a hand/wrist exoskeleton for home-based rehabilitation after stroke - SCRIPT project. *Robotica* 32, 1331–1346. doi: 10.1017/S0263574714002288

Amirabdollahian, F., Loureiro, R., Gradwell, E., Collin, C., Harwin, W., and Johnson, G. (2007). Multivariate analysis of the Fugl-Meyer outcome measures assessing the effectiveness of GENTLE/S robot-mediated stroke therapy. *J. NeuroEng. Rehabil.* 4, 4. doi: 10.1186/1743-0003-4-4

Bailey, S. P., Hall, E. E., Folger, S. E., and Miller, P. C. (2008). Changes in EEG during graded exercise on a recumbent cycle ergometer. *J. Sports Sci. Med.* 7, 505–11.

Barwick, F., Arnett, P., and Slobounov, S. (2012). EEG correlates of fatigue during administration of a neuropsychological test battery. *Clin. Neurophysiol.* 123, 278–284. doi: 10.1016/j.clinph.2011.06.027

Baumeister, J., Reinecke, K., Schubert, M., Schade, J., and Weiss, M. (2012). Effects of induced fatigue on brain activity during sensorimotor control. *Eur. J. Appl. Physiol.* 112, 2475–2482. doi: 10.1007/s00421-011-2215-6

Borghini, G., Astolfi, L., Vecchiato, G., Mattia, D., and Babiloni, F. (2014). Measuring neurophysiological signals in aircraft pilots and car drivers for the assessment of mental workload, fatigue and drowsiness. *Neurosci. Biobehav. Rev.* 44, 58–75. doi: 10.1016/j.neubiorev.2012.10.003

Branscheidt, M., Kassavetis, P., Anaya, M., Rogers, D., Huang, H. D., Lindquist, M. A., et al. (2019). Fatigue induces long-lasting detrimental changes in motor-skill learning. *eLife* 8, e40578. doi: 10.7554/eLife.40578

Caldwell, J. A., Hall, K. K., and Erickson, B. S. (2002). EEG data collected from helicopter pilots in flight are sufficiently sensitive to detect increased fatigue from sleep deprivation. *Int. J. Aviation Psychol.* 12, 19–32. doi: 10.1207/S15327108IJAP1201_3

Cardoso, J. F. (1998). Blind signal separation: statistical principles. *Proc. IEEE* 86, 2009–2025. doi: 10.1109/5.720250

Cardoso, J. F., and Souloumiac, A. (1993). "Blind beamforming for non-gaussian signals," in *IEE Proceedings F (Radar and Signal Processing)*, Vol. 140 (IET), 362–370.

Carron, A. (1972). Motor performance and learning under physical fatigue. *Med. Sci. Sports* 4, 101–106.

Carron, A. V. (1969). Physical fatigue and motor learning. *Res. Quart. Amer. Assoc. Health Phys. Educ. Recreat.* 40, 682–686. doi: 10.1080/10671188.1969.10614902

Chemuturi, R., Amirabdollahian, F., and Dautenhahn, K. (2013). Adaptive training algorithm for robot-assisted upper-arm rehabilitation, applicable to individualised and therapeutic human-robot interaction. *J. Neuroeng. Rehabil.* 10, 102. doi: 10.1186/1743-0003-10-102

Chen, C., Li, K., Wu, Q., Wang, H., Qian, Z., and Sudlow, G. (2013). EEG-based detection and evaluation of fatigue caused by watching 3DTV. *Displays* 34, 81–88. doi: 10.1016/j.displa.2013.01.002

Cheng, S. Y., and Hsu, H. T. (2011). "Mental fatigue measurement using EEG," in *Risk Management Trends*, ed G. Nota (IntechOpen). doi: 10.5772/16376

Cotten, D. J., Thomas, J. R., Spieth, W. R., and Biasiotto, J. (1972). Temporary fatigue effects in a gross motor skill. *J. Motor Behav.* 4, 217–222.

Cowley, J. C., and Gates, D. H. (2017). Proximal and distal muscle fatigue differentially affect movement coordination. *PLoS ONE* 12, e0172835. doi: 10.1371/journal.pone.0172835

Craig, A., Tran, Y., Wijesuriya, N., and Nguyen, H. (2012). Regional brain wave activity changes associated with fatigue. *Psychophysiology* 49, 574–582. doi: 10.1111/j.1469-8986.2011.01329.x

Debener, S., Thorne, J., Schneider, T. R., and Viola, F. C. (2010). "Using ICA for the analysis of multi-channel EEG data," in *Simultaneous EEG and fMRI: Recording, Analysis, and Application*, eds M. Ullsperger, and D. Stefan (New York, NY: Oxford University Press), 121–133. doi: 10.1093/acprof:oso/9780195372731.003.0008

Delorme, A., Sejnowski, T., and Makeig, S. (2007). Enhanced detection of artifacts in EEG data using higher-order statistics and independent component analysis. *Neuroimage* 34, 1443–1449. doi: 10.1016/j.neuroimage.2006.11.004

Dissanayake, U. C. (2021). *Assessment of Fatigue in Robot-Mediated Upper Limb Interactions Using EEG*. (Hatfield: University of Hertfordshire).

Dissanayake, U. C., Steuber, V., and Amirabdollahian, F. (2021). EEG spectral feature modulations associated with fatigue in robot-mediated upper limb gross motor and fine motor interactions. *bioRxiv*. doi: 10.1101/2021.04.22.440968

Eoh, H. J., Chung, M. K., and Kim, S. H. (2005). Electroencephalographic study of drowsiness in simulated driving with sleep deprivation. *Int. J. Ind. Ergon.* 35, 307–320. doi: 10.1016/j.ergon.2004.09.006

Fan, X., Zhou, Q., Liu, Z., and Xie, F. (2015). Electroencephalogram assessment of mental fatigue in visual search. *Bio Med. Mater. Eng.* 26, S1455–S1463. doi: 10.3233/BME-151444

Foong, R., Ang, K. K., Quek, C., Guan, C., Phua, K. S., Kuah, C. W. K., et al. (2019). Assessment of the efficacy of EEG-based MI-BCI with visual feedback and EEG correlates of mental fatigue for upper-limb stroke rehabilitation. *IEEE Trans. Biomed. Eng.* 67, 786–795. doi: 10.1109/TBME.2019.2921198

g.tec medical engineering GmbH (2014a). *g.GAMMACap2 EEG sensor cap: Instructions for use V2.14.00*. Austria: g.tec medical engineering GmbH.

g.tec medical engineering GmbH (2014b). *g.GAMMAsys Active Electrode System: Instructions for use V2.14.01*. Austria: g.tec medical engineering GmbH.

Gevins, A., and Smith, M. E. (2007). "Electroencephalography (EEG) in neuroergonomics," in *Neuroergonomics: The brain at Work*, eds R. Parasuraman and M. Rizzo (New York, NY: Oxford University Press), 15–31.

Gevins, A., Smith, M. E., McEvoy, L., and Yu, D. (1997). High-resolution EEG mapping of cortical activation related to working memory: effects of task difficulty, type of processing, and practice. *Cereb. Cortex* 7, 374–385. doi: 10.1093/cercor/7.4.374

Gibson, H., and Edwards, R. (1985). Muscular exercise and fatigue. *Sports Med.* 2, 120–132. doi: 10.2165/00007256-198502020-00004

Godwin, M. A., and Schmidt, R. A. (1971). Muscular fatigue and learning a discrete motor skill. *Res. Quart. Amer. Assoc. Health Phys. Educ. Recreat.* 42, 374–382. doi: 10.1080/10671188.1971.10615084

Guzzetta, A., Staudt, M., Petacchi, E., Ehlers, J., Erb, M., Wilke, M., et al. (2007). Brain representation of active and passive hand movements in children. *Pediatric Res.* 61, 485–490. doi: 10.1203/pdr.0b013e3180332c2e

Harmony, T., Fernández, T., Silva, J., Bernal, J., Díaz-Comas, L., Reyes, A., et al. (1996). EEG delta activity: an indicator of attention to internal processing during performance of mental tasks. *Int. J. Psychophysiol.* 24, 161–171. doi: 10.1016/S0167-8760(96)00053-0

Jap, B. T., Lal, S., Fischer, P., and Bekiaris, E. (2009). Using EEG spectral components to assess algorithms for detecting fatigue. *Exp. Syst. Appl.* 36, 2352–2359. doi: 10.1016/j.eswa.2007.12.043

Jung, T.P., Makeig, S., Humphries, C., Lee, T.W., Mckeown, M. J., Iragui, V., et al. (2000). Removing electroencephalographic artifacts by blind source separation. *Psychophysiology* 37, 163–178. doi: 10.1111/1469-8986.3720163

Jung, T. P., Humphries, C., Lee, T. W., Makeig, S., McKeown, M. J., Iragui, V., et al. (1998). "Extended ICA removes artifacts from electroencephalographic recordings," in *Advances in Neural Information Processing Systems* (Cambridge, MA: MIT Press), 894–900.

Käthner, I., Wriessnegger, S. C., Müller-Putz, G. R., Kübler, A., and Halder, S. (2014). Effects of mental workload and fatigue on the P300, alpha and theta band power during operation of an ERP (P300) brain-computer interface. *Biol. Psychol.* 102, 118–129. doi: 10.1016/j.biopsycho.2014.07.014

Klimesch, W. (1999). EEG alpha and theta oscillations reflect cognitive and memory performance: a review and analysis. *Brain Res. Rev.* 29, 169–195. doi: 10.1016/S0165-0173(98)00056-3

Lal, S. K., and Craig, A. (2002). Driver fatigue: electroencephalography and psychological assessment. *Psychophysiology* 39, 313–321. doi: 10.1017/S0048577201393095

Lal, S. K. L., and Craig, A. (2001). A critical review of the psychophysiology of driver fatigue. *Biol. Psychol.* 55, 173–194. doi: 10.1016/S0301-0511(00)00085-5

Laureiro-Martínez, D., Canessa, N., Brusoni, S., Zollo, M., Hare, T., Alemanno, F., et al. (2014). Frontopolar cortex and decision-making efficiency: comparing brain activity of experts with different professional background during an exploration-exploitation task. *Front. Human Neurosci.* 7:927. doi: 10.3389/fnhum.2013.00927

Lerdal, A., Bakken, L. N., Kouwenhoven, S. E., Pedersen, G., Kirkevold, M., Finset, A., et al. (2009). Poststroke fatigue - a review. *J. Pain Symptom Manage.* 38, 928–949. doi: 10.1016/j.jpainsymman.2009.04.028

Liu, J. Z., Shan, Z. Y., Zhang, L. D., Sahgal, V., Brown, R. W., and Yue, G. H. (2003). Human brain activation during sustained and intermittent submaximal fatigue muscle contractions: an fMRI study. *J. Neurophysiol.* 90, 300–312. doi: 10.1152/jn.00821.2002

Lorist, M. M., Boksem, M. A., and Ridderinkhof, K. R. (2005). Impaired cognitive control and reduced cingulate activity during mental fatigue. *Cogn. Brain Res.* 24, 199–205. doi: 10.1016/j.cogbrainres.2005.01.018

Makeig, S., Bell, A. J., Jung, T. P., and Sejnowski, T. J. (1996). "Independent component analysis of electroencephalographic data," in *Advances in Neural Information Processing Systems* (Cambridge, MA: MIT Press), 145–151.

Marcora, S. M., Staiano, W., and Manning, V. (2009). Mental fatigue impairs physical performance in humans. *J. Appl. Physiol.* 106, 857–864. doi: 10.1152/japplphysiol.91324.2008

Massar, S. A., Wester, A. E., Volkerts, E. R., and Kenemans, J. L. (2010). Manipulation specific effects of mental fatigue: evidence from novelty processing and simulated driving. *Psychophysiology* 47, 1119–1126. doi: 10.1111/j.1469-8986.2010.01028.x

Mehta, R. K., and Parasuraman, R. (2014). Effects of mental fatigue on the development of physical fatigue: a neuroergonomic approach. *Hum. Factors* 56, 645–656. doi: 10.1177/0018720813507279

Ng, S. C., and Raveendran, P. (2007). "EEG peak alpha frequency as an indicator for physical fatigue," in *11th Mediterranean Conference on Medical and Biomedical Engineering and Computing 2007*, (Berlin: Springer), 517–520.

Pfurtscheller, G. (1997). EEG event-related desynchronization (ERD) and synchronization (ERS). *Electroencephalograph. Clin. Neurophysiol.* 1, 26.

Pfurtscheller, G., Stancak, A. Jr., and Neuper, C. (1996). Event-related synchronization (ERS) in the alpha band - an electrophysiological correlate of cortical idling: a review. *Int. J. Psychophysiol.* 24, 39–46. doi: 10.1016/S0167-8760(96)00066-9

Pinegger, A., Wriessnegger, S. C., Faller, J., and Müller-Putz, G. R. (2016). Evaluation of different EEG acquisition systems concerning their suitability for building a brain-computer interface: case studies. *Front. Neurosci.* 10:441. doi: 10.3389/fnins.2016.00441

Prasad, G., Herman, P., Coyle, D., McDonough, S., and Crosbie, J. (2010). Applying a brain-computer interface to support motor imagery practice in people with stroke for upper limb recovery: a feasibility study. *J. Neuroeng. Rehabil.* 7, 60. doi: 10.1186/1743-0003-7-60

Sabes, P. N. (2000). The planning and control of reaching movements. *Curr. Opin. Neurobiol.* 10, 740–746. doi: 10.1016/S0959-4388(00)00149-5

Staub, F., and Bogousslavsky, J. (2001). Fatigue after stroke: a major but neglected issue. *Cerebrovascul. Dis.* 12, 75–81. doi: 10.1159/000047685

Sterr, A., and Furlan, L. (2015). A case to be made: theoretical and empirical arguments for the need to consider fatigue in post-stroke motor rehabilitation. *Neural Regener. Res.* 10, 1195–1197. doi: 10.4103/1673-5374.162689

Tanaka, M., Shigihara, Y., Ishii, A., Funakura, M., Kanai, E., and Watanabe, Y. (2012). Effect of mental fatigue on the central nervous system: an electroencephalography study. *Behav. Brain Funct.* 8, 48. doi: 10.1186/1744-9081-8-48

Thacham Poyil, A., Steuber, V., and Amirabdollahian, F. (2020a). Adaptive robot mediated upper limb training using electromyogram-based muscle fatigue indicators. *PLoS ONE* 15, e0233545. doi: 10.1371/journal.pone.0233545

Thacham Poyil, A. T., Steuber, V., and Amirabdollahian, F. (2020b). Influence of muscle fatigue on electromyogram - kinematic correlation during robot-assisted upper limb training. *J. Rehabil. Assist. Technol. Eng.* 7, 2055668320903014. doi: 10.1177/2055668320903014

Thomas, J. R., Cotten, D. J., Spieth, W. R., and Abraham, N. L. (1975). Effects of fatigue on stabilometer performance and learning of males and females. *Med. Sci. Sports* 7, 203–206. doi: 10.1249/00005768-197500730-00018

Tran, Y., Craig, A., Craig, R., Chai, R., and Nguyen, H. (2020). The influence of mental fatigue on brain activity: evidence from a systematic review with meta-analyses. *Psychophysiology* 57, e13554. doi: 10.1111/psyp.13554

Tran, Y., Wijesuryia, N., Thuraisingham, R. A., Craig, A., and Nguyen, H. T. (2008). "Increase in regularity and decrease in variability seen in electroencephalography (EEG) signals from alert to fatigue during a driving simulated task," in *2008 30th Annu. Int. Conf. IEEE Eng. Med. Biol. Soc.* (IEEE) (Vancouver), 1096–1099.

Trejo, L. J., Kubitz, K., Rosipal, R., Kochavi, R. L., and Montgomery, L. D. (2015). EEG-based estimation and classification of mental fatigue. *Psychology* 6, 572. doi: 10.4236/psych.2015.65055

Van Cutsem, J., Marcora, S., De Pauw, K., Bailey, S., Meeusen, R., and Roelands, B. (2017). The effects of mental fatigue on physical performance: a systematic review. *Sports Med.* 47, 1569–1588. doi: 10.1007/s40279-016-0672-0

Wang, Y., Cao, L., Hao, D., Rong, Y., Yang, L., Zhang, S., et al. (2017). Effects of force load, muscle fatigue and extremely low frequency magnetic stimulation on EEG signals during side arm lateral raise task. *Physiol. Meas.* 38, 745. doi: 10.1088/1361-6579/aa6b4b

Welch, P. (1967). The use of fast fourier transform for the estimation of power spectra: a method based on time averaging over short, modified periodograms. *IEEE Trans. Audio Electroacoust.* 15, 70–73. doi: 10.1109/TAU.1967.1161901

Williams, J., and Singer, R. N. (1975). Muscular fatigue and the learning and performance of a motor control task. *J. Motor Behav.* 7, 265–269. doi: 10.1080/00222895.1975.10735044

Xu, R., Zhang, C., He, F., Zhao, X., Qi, H., Zhou, P., et al. (2018). How physical activities affect mental fatigue based on EEG energy, connectivity, and complexity. *Front. Neurol.* 9:915. doi: 10.3389/fneur.2018.00915

Yao, B., Liu, J. Z., Brown, R. W., Sahgal, V., and Yue, G. H. (2009). Nonlinear features of surface EEG showing systematic brain signal adaptations with muscle force and fatigue. *Brain Res.* 1272, 89–98. doi: 10.1016/j.brainres.2009.03.042

Zhao, C., Zhao, M., Liu, J., and Zheng, C. (2012). Electroencephalogram and electrocardiograph assessment of mental fatigue in a driving simulator. *Accident Anal. Prevent.* 45, 83–90. doi: 10.1016/j.aap.2011.11.019

Zou, B., Liu, Y., Guo, M., and Wang, Y. (2015). EEG-based assessment of stereoscopic 3D visual fatigue caused by vergence-accommodation conflict. *J. Display Technol.* 11, 1076–1083. doi: 10.1109/JDT.2015.2451087

Conflict of Interest: The authors declare that the research was conducted in the absence of any commercial or financial relationships that could be construed as a potential conflict of interest.

Publisher's Note: All claims expressed in this article are solely those of the authors and do not necessarily represent those of their affiliated organizations, or those of the publisher, the editors and the reviewers. Any product that may be evaluated in this article, or claim that may be made by its manufacturer, is not guaranteed or endorsed by the publisher.

frontiers in Neurorobotics

ORIGINAL RESEARCH
published: 18 February 2022
doi: 10.3389/fnbot.2021.727534

Designing Physical Human-Robot Interaction Interfaces: A Scalable Method for Simulation Based Design

Rohit John Varghese[1,2*†], *Gaurav Mukherjee*[3†] *and Ashish Deshpande*[1]

[1] Department of Mechanical Engineering, University of Texas at Austin, Austin, TX, United States, [2] Harmonic Bionics Inc., Austin, TX, United States, [3] Department Mechanical Engineering, University of Washington, Seattle, WA, United States

Designing the physical coupling between the human body and the wearable robot is a challenging endeavor. The typical approach of tightening the wearable robot against the body, and softening the interface materials does not work well. It makes the task of simultaneously improving comfort, and anchoring the robot to the body at the physical human robot interaction interface (PHRII), difficult. Characterizing this behavior experimentally with sensors at the interface is challenging due to the soft-soft interactions between the PHRII materials and the human tissue. Therefore, modeling the interaction between the wearable robot and the hand is a necessary step to improve design. In this paper, we introduce a methodology to systematically improve the design of the PHRII by combining experimentally measured characteristics of the biological tissue with a novel dynamic modeling tool. Using a novel and scalable simulation framework, HuRoSim, we quantified the interaction between the human hand and an exoskeleton. In the first of our experiments, we use HuRoSim to predict complex interactions between the hand and the coupled exoskeleton. In our second experiment, we then demonstrate how HuRoSim can be coupled with experimental measurements of the stiffness of the dorsal surface of the hand to optimize the design of the PHRII. This approach of data-driven modeling of the interaction between the body and a wearable robot, such as a hand exoskeleton, can be generalized to other forms of wearable devices as well, demonstrating a scalable and systematic method for improving the design of the PHRII for future devices coupled to the body.

Keywords: simulation, wearable, robot, haptics, comfort, hand, design methodology, soft tissue artefact

OPEN ACCESS

Edited by:
Dongming Gan,
Purdue University, United States

Reviewed by:
Dong Hyun Kim,
Korea Advanced Institute of Science and Technology, South Korea
Muhammad Zubair Iqbal,
University of Siena, Italy

***Correspondence:**
Rohit John Varghese
rohitjohnv@utexas.edu

†These authors have contributed equally to this work

Received: *18 June 2021*
Accepted: *15 December 2021*
Published: *18 February 2022*

Citation:
John Varghese R, Mukherjee G and Deshpande A (2022) Designing Physical Human-Robot Interaction Interfaces: A Scalable Method for Simulation Based Design. Front. Neurorobot. 15:727534. doi: 10.3389/fnbot.2021.727534

1. INTRODUCTION

Robots coupled to the human body assist in the rehabilitation of impaired mobility (Gupta and O'Malley, 2006; Kim and Deshpande, 2017; Yun et al., 2017), provide assistance to humans in performing tasks (Bogue, 2009; Walsh et al., 2016), and augment physical interactions in virtual and augmented reality (Choi et al., 2016; Pezent et al., 2019; Young and Kuchenbecker, 2019). These robotic systems function by transmitting forces across the physical interface between the robot and the human. Often referred to as the Physical Human Robot Interaction Interface (PHRII) **Figure 1**, these attachment locations are complex sub-systems that involve multiple layers of tissue (skin, fascia, sub-cutaneous tissue, muscle, etc.) along with compliant padding and attachment straps of the device.

When forces are applied across the stack of PHRII and tissues, complex static and dynamic interactions occur, resulting in phenomenon, such as slip (Akiyama et al., 2016), localized pressure (Krouskop et al., 1985), and lift-off of the robot from the skin. These complex interactions cause significant uncertainty in estimating the relative position and force distribution between the robot and the human. These uncertainties adversely impact the control framework of the robot, as well as the ergonomics and safety considerations for the human. For example, minor relative displacements, or slip, can cause misalignment between the joint axes of the human and robot (Schiele and Van Der Helm, 2006) resulting in high undesired forces on the human joints (Colombo et al., 2000). These relative displacements also cause errors in the control model of the coupled human-robot system which can lead to instability, especially when using model-sensitive strategies such as adaptive control (Dubowsky and Desforges, 2015). Currently, the behavior of the PHRII is not well understood, which limits our ability to design and control the interaction between the human and the wearable robot. Therefore, to optimize the PHRII, we must first characterize the behavior at this interface. To achieve this goal, we present a novel data-driven approach of characterizing the tissue properties locally to model and optimize the global design of the PHRII.

While an overall model for the PHRII doesn't exist in the literature, prior studies have addressed some issues related to PHRII design and robot control: (Schiele and Van Der Helm, 2006) looked at ensuring concentricity of the joint axes of the coupled human-robot system by using extra degrees of freedom in the exoskeleton for passive realignment. Agarwal et al. (2015) showed that the use of redundant measurements on joint angles followed by optimization techniques could be used as estimators of the unknown positions of the human in control. Petron (2016) proposed that the most effective method of force transfer across prosthetic leg socket while minimizing discomfort and tissue damage was to tune the stiffness map of the socket to ensure equalized pressure distribution at all points of contact. However, this approach has not been tested for the upper limb. Quinlivan et al. (2015) experimentally showed the benefit of inverting the stiffness profile of he human hip to design the attachment, which is in contact with superficial skeletal structures than surfaces resting against softer tissue. Most studies in this area are recent, and the design of the PHRII is most commonly performed through an iterative, prototype-based process (Bouzit et al., 2002; Kim and Deshpande, 2009). Designers iterate through options for parameters such as compliance of the PHRII for their specific device (Silver et al., 2001), and use features such as the positional errors between the human and robot (Cempini et al., 2014) to measure the effectiveness of the PHRII. This approach is time consuming, expensive, and is difficult to standardize.

To standardize the approach of designing the PHRII, we must first characterize the interaction between the human and the coupled wearable robot. To do this, we developed a novel simulation-based model of the PHRII in MATLAB (Mathworks Inc., MA). This model, called HuRoSim, includes the viscoelastic properties of the human skin and soft tissue, along with an interface material, and attachment straps of the device. HuRoSim focuses on relative movement between the human and the robot, and forces generated at the PHRII as a result of applying loads across it. This approach can be used to compute optimal values of the design parameters, such as geometry, compliance, strap stiffness, pre-tension, etc., quickly by systematically varying them in simulation. It also enables the analysis of robot configurations and the effects of variations in human size and tissue properties.

In the sections that follow, we first introduce our novel simulational framework, HuRoSim followed by two experiments to outline our novel method of optimizing the PHRII (**Figure 2**). In our first experiment, we design an isometric loading condition for the simulation environment and predict

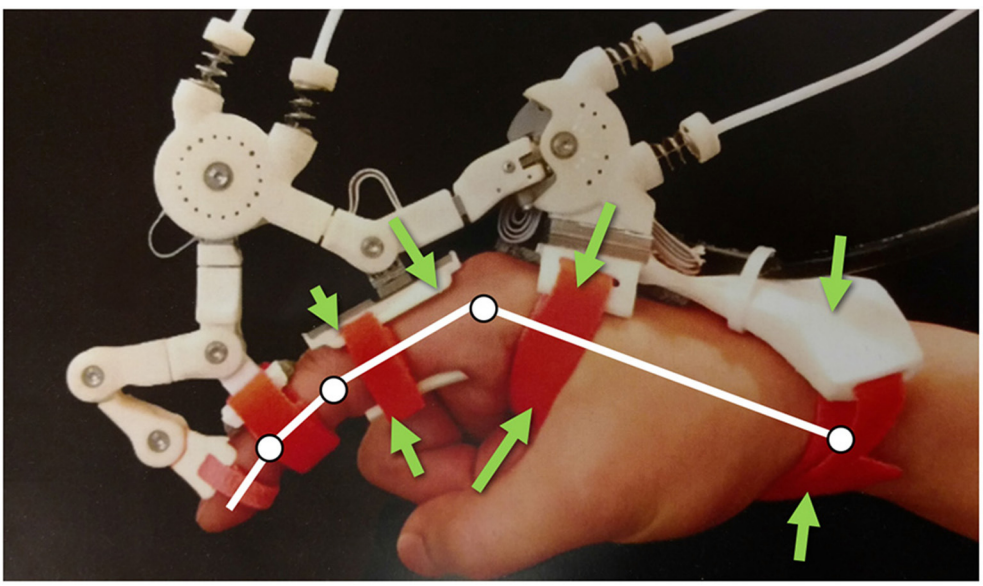

FIGURE 1 | Maestro Hand Exoskeleton from Agarwal et al. (2015), with force arrows indicating various locations of PHRII in this system.

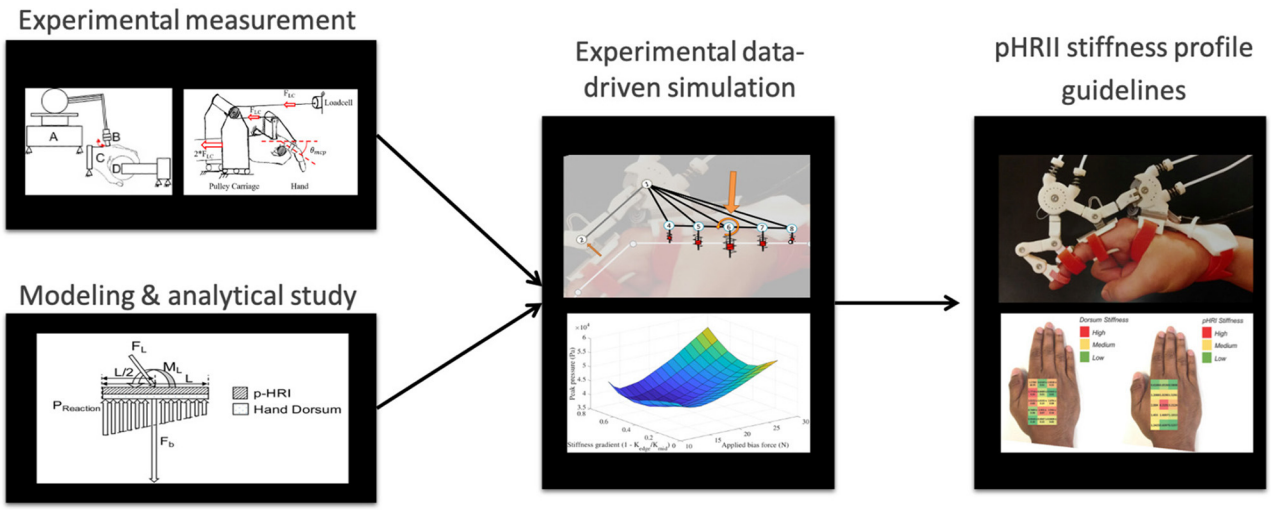

FIGURE 2 | A schematic of our methodology for optimizing the PHRII for the hand dorsum using a data-driven simulation approach.

the kinematic behavior of an exoskeleton attached to the hand, under an externally applied load. We then test the predictions from HuRoSim with an experimental set-up. In the second experiment, we demonstrate how the measurement of parameters of the biological tissue, such as dorsum stiffness of the hand, can be used to design a PHRII to optimize comfort.

2. MATERIALS AND METHODS

2.1. HuRoSim: The PHRII Simulation Environment

HuRoSim is a dynamic simulation framework built in Matlab 2016 (Mathworks, MA), to characterize the interaction behavior at the PHRII between the hand exoskeleton and the hand. HuRoSim is built as a lumped parameter system, arranged as a network of nodes in 3D space. These nodes are connected by constraints, each with its own set of parameters and properties. This modularity allows the user of HuRoSim the ability to reconfigure the nodes, and simulate a variety of PHRII systems. The user is also able to choose the complexity of the simulational representation of the PHRII, thus trading between computational load and accuracy.

Our simulation model of the PHRII includes a number of features that can affect the interaction between the rigid reference structure of the robot and the human reference (skeletal) structure. This includes: viscoelastic properties of the human tissue (skin, fascia, and subcutaneous tissue) PHRII dimensions and geometry, mechanical properties of the padding used at the interface, slip along the interface, and the mechanical properties including the initial force between the device and tissues or pre-tension of attachment straps.

2.1.1. Viscoelastic Properties in HuRoSim

Figure 3 (Left) shows a schematic cross section view of a typical PHRII. The human reference structure (the skeletal bone) is shown in the middle, completely encased by soft tissue both above and below it. The bone in this figure is the proximal phalanx of the index finger, and it's dorsal surface (above the bone in this figure) can be approximated to a straight line. Over the bone is a layer of soft tissue and skin represented by arrows showing its mechanical compliance in compression and sliding. Above the finger is the rigid plate of the robot attachment represented by a solid line, and its compliant padding in contact with the skin on the dorsal surface is similarly represented by arrows showing its mechanical compliance.

The PHRII region is defined by this contact surface described above, and it extends from the rigid reference geometry of the human to the rigid component of the robot. Also visible in **Figure 3 (Left)** is the antagonistic strap that is in contact with the skin on the palmar surface of the hand (below the bone in this figure). Identical to the considerations on the dorsal surface discussed previously, in this PHRII, we also have the two mechanically compliant regions of human soft tissue and device padding between the bone and the inelastic fibers of the strap which we consider as its reference geometry.

The **Figure 3 (Left)** also shows individual sources of movement as colored arrows. The strain distribution in the human soft tissue and the device padding are shown in purple and blue, respectively. Shear strain in the padding is also accounted for in our model, but not explicitly highlighted here. The human skin can also glide over the underlying layers of fascia, as shown in red. The reaction forces to this movement come from two main sources: stretching of the skin itself, which is dominated by the viscoelastic properties of the dermis, and the connective tissue linking the dermis to the underlying structures in the hypodermis and fascia. Lastly, we also have surface effects of slip and lift-off at the actual interface surface, as shown in green.

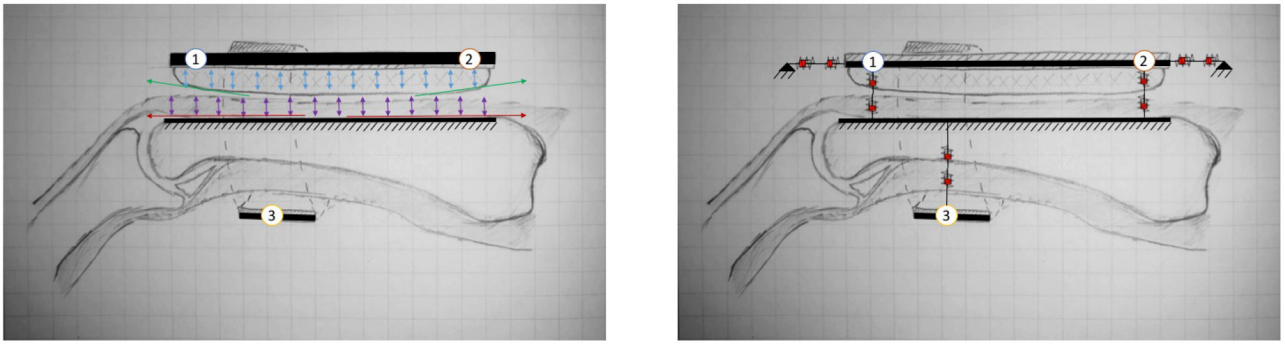

FIGURE 3 | (Left) A cross section view of a typical PHRII showing the human reference structure as the ground (the proximal phalanx of the index finger in this case) and the rigid reference structures of the robot above and below it. The numbered circles represent the PHRII units that this structure will be simplified to later in the analysis. **(Right)** A typical PHRII with a schematic representation of the viscoelastic elements. Each simulated point is considered as two elements coupled in series, representing the human soft tissue and the device's compliant padding, respectively.

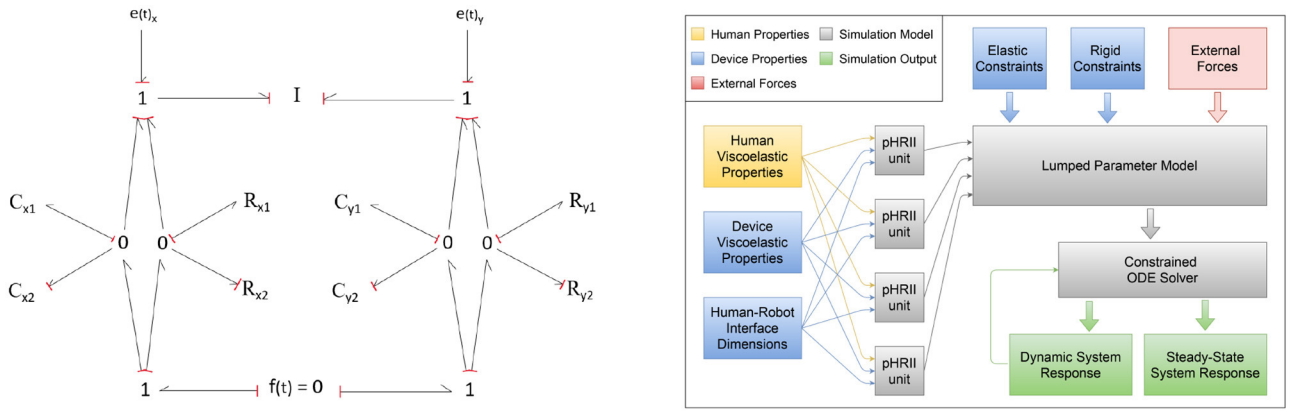

FIGURE 4 | (Left) Bond graph of a single PHRII unit. The left half represents features in the tangential or *x*-direction while the right represents normal or the *y*-direction. **(Right)** Block diagram showing information flow across the different elements of the simulation environment.

2.1.2. The Individual PHRII Unit

All components in the PHRII unit are modeled as viscoelastic elements. We use lumped parameter models to represent the robot and strap structures as linked point masses, and the human bone as the reference ground. With this approach, we represent the soft structures in the PHRII as viscoelastic elements connected in series as shown in **Figure 3 (Right)**. This system can be viewed as being composed of three PHRII units, represented by the numbered circles. Each PHRII unit is connected to the human reference ground through series viscoelastic elements, and to each other either with compliant, or with inelastic constraints.

Figure 4 shows a bond graph representation of a single PHRII unit. The left half represents features in the tangential or *x*-direction while the right represents normal or the *y*-direction. Therefore, C_{1y} & C_{2y} represent the compressive elastic properties of the soft tissue and padding, while C_{1x} & C_{2x} represent the stretching/sliding of skin over layers of fascia and the padding shear strain. R_{1x}, R_{1y}, R_{2x}, and R_{2y} represent the viscous properties of each of these elements. The normal and the tangential strains are orthogonal and considered independently. However, they are still connected to the same inertia and reference ground. This individual unit is replicated at every PHRII and is used as the building block for the simulation environment. As seen in **Figure 4 (Right)**, these units are coupled by both elastic and inelastic constraints, as well as external forces and this is the input to the primary lumped parameter model. The lumped parameter model is solved using a constrained ODE solved detailed in the next sub-section. The steady state and dynamic responses of the solver are the outputs which we use for further analysis.

In our example system, the dorsum of the hand has two such PHRII units connected by an inelastic constraint (simulating a rigid body) The palmar surface has a single one which is connected to the dorsal link via another viscoelastic element (simulating the strap). We will be discussing the construction of more complex systems with this building block as we go forward. Note that we have made the assumption of coupling the elastic elements in series separately from the viscous ones. Condition checks were included in the simulation of the system to ensure

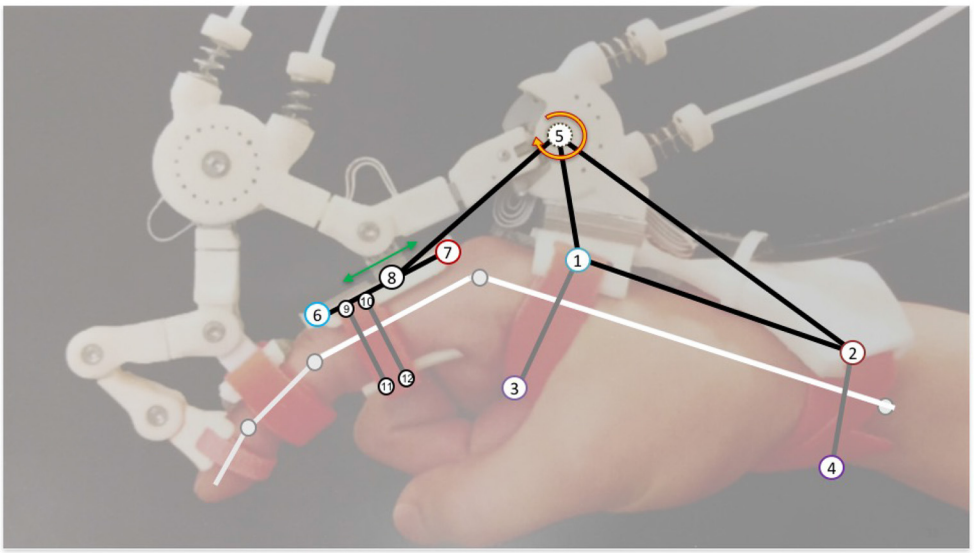

FIGURE 5 | Annotated Maestro system showing the symbolic human reference geometry (white), and the different pieces of the lumped parameter structure used to model and simulate the behavior of this system. Each numbered circle represents a PHRII (Though points 5 and 8 have their viscoelastic values set to zero as described in this section). The black lines represent inelastic constraints while the gray ones represent viscoelastic ones.

that this does not create unrealistic behavior in exception cases. These include negative normal forces at the interface on rapid withdrawal of loading.

We use experimentally obtained values for human tissue parameters where available in the literature. These include tensile viscoelastic properties of the skin (Silver et al., 2001; van Kuilenburg et al., 2012; Dabrowska et al., 2016), and compressive viscoelastic properties of the skin and the sub-cutaneous tissue (Wu et al., 2007). The thickness and size of all these regions across population samples are obtained from anthropometric data. The geometry and mechanical properties of the padding and straps can either be selected from a list of commonly used configurations or else optimized by the simulation to be returned as a design input.

2.1.3. Combining Individual PHRII Units to Create a Simulation System

Using the PHRII units defined above as our building block, we create larger systems for simulation. **Figure 5** shows the system of the Maestro hand exoskeleton with our simulation model superposed over it. We first draw attention to the numbered point masses shown connected by inelastic constraints. Ternary links or sets of three connected masses (such as 1-2-5 and 6-8-7) move together essentially as a rigid body. The gray connections are elastic constraints to simulate compliance of the straps or in the exoskeleton linkage. Note that the human reference structure (shown as white linkages) will not be explicitly visualized in this system going forward, since it is considered as the reference ground. The proximal phalanx is considered as a moving reference ground based on transformations on the human MCP joint. Lastly, not all of the numbered points are in actual contact with the human (for example, points 5 & 8). The PHRII viscoelastic properties for these are set to zero while those for all others are set based on the human and padding viscoelastic properties discussed above.

These lumped parameter models are used in our dynamic simulations, allowing a system approximation that can be tuned to give reasonably accurate results while still being light enough to run in a real-time control loop. Since many of the experimentally determined properties of skin in literature have been approximated to piece-wise linear models (Silver, et al. Wu, et al.), our simulation also uses smoothed piece-wise linear models for tissue viscoelastic properties wherever possible based upon the desired complexity.

2.1.4. Solving the Constrained Multi-Body System Through Time

Dynamic simulations of the resulting multi-body system are formulated with ODE (Ordinary Differential Equation) solvers, and constraints are implemented with the option of simulating in both 2D and 3D using Lagrangian mechanics by Udwadia and Kalaba's method (Udwadia and Kalaba, 2002) as shown in Equation 1 (Here q's are the coordinates of each point, M is the overall inertia matrix, Q is the array of non-constraint forces for all points, and A & b are coefficients of the constraint equations after differentiating twice and grouping in the form of Equation 2). This method was chosen over penalty methods and simultaneous solutions for numerical stability and computational simplicity (Bayo and Ledesma, 1996; Witkin and Witkin, 2001).

$$M\ddot{q} = Q + M^{1/2}(AM^{-1/2})^{\dagger}(b - AM^{-1}Q) \tag{1}$$

$$A(\dot{q}, q, t)\ddot{q} = b(\dot{q}, q, t) \tag{2}$$

To simulate dynamics through time, the ODE's can be solved both by implicit, as well as explicit methods. Standard ODE solvers are available for both kinds, with each having their respective advantages. Explicit adaptive step Range Kutta solvers such as Matlab's ODE45 are the most common type employed for differential equations. However, with numerically stiff systems, they tend to decrease step size drastically resulting in long computation times. Implicit solvers on the other hand are more resistant to this phenomenon and are capable of computing the dynamics of the system with far fewer temporal steps. However, care must be taken while using them as they are much more prone to numerical instability depending on the system parameters. The simulation environment makes use of both types of solvers to allow for explicit solvers for computational in general cases and for the use of implicit solvers in numerically stiff regions of the system.

The entire simulation was custom built in the Matlab environment (Mathworks Inc.) and provides both steady state and transient responses. However, due to the slow and almost quasi-static movement speed that is used in rehabilitation, assistance, and assessment, our results focused largely on the steady state response.

2.2. Experiment 1: Predicting Physical Interaction Using HuRoSim

In this experiment, we study the case of a hand exoskeleton attached to the dorsal aspect of the hand. Using HuRoSim, we apply an extension moment load about the MCP joint to the virtual finger which is fixed at an angle. From this simulation study, we predict the kinematic movement of the coupled hand-exoskeleton system. We then replicate this set-up with the Maestro hand exoskeleton attached to a human hand to measure the actual kinematic effect of applying an isometric load across the MCP joint.

2.2.1. Simulation Experiment

We configured HuRoSim to study the effects of applying an isometric extension load across the MCP joint. The input load to the simulation is in the form of an applied moment from the exoskeleton (to a maximum of 0.5 Nm), and the studied outputs are the final displacements and forces present in the system on reaching a steady state.

The human and exoskeleton interface material parameters were gathered from literature sources, most notably (Silver et al., 2001) which establishes the piece-wise linear approximation of stiffness properties of human skin caused by the behavior of different fibers (elastin and collagen) within the dermis of the skin. In the tangential direction, the values from this source start with an initial elastic stiffness of 0.1 MPa upto a strain of 0.4, followed by a sharp increase trending up to 18.8 MPa. Wu et al. (2007) similarly establishes values of compressive stress-strain curves for both skin and sub-cutaneous tissue that were used in the simulation. It should be noted that detailed *in-vivo* measurements of the tissue properties of the surfaces of the human hand have not been widely studied, leading to a lack of available literature to obtain measurements from. This scarcity contributed to the motivation for indentation experiments in section 2.3.3 that gather *in-vivo* stiffness data of the hand dorsum for use by HuRoSim.

The device parameters were measured directly on the maestro hand exoskeleton, having a dorsal rigid surface of 50 mm length for the metacarpal region and 30 mm for the proximal phalanx of the index finger, with strap widths of 10 mm.

From the applied moment loads to the isometric finger and the tissue properties chosen, we are able to simulate the dynamic loads that develop. These load patterns generate kinematic behavior that we then tested with an experimental set-up with the Maestro hand exoskeleton and the hand.

2.2.2. Experimental Measurement

We test the predicted kinematic behavior from the simulation with an experimental test bed. We instrument the maestro hand exoskeleton **Figure 6** to enable easier measurement of the effects of applying an isometric load across the MCP joint. The index finger was locked about the MCP, PIP, and DIP joints, and an external moment identical to that applied in the simulation was developed over the hand.

Only the index finger of Maestro was attached to the human test subject, and loads were applied via Maestro's MCP joint. The subject's arm is immobilized at the forearm and wrist, in addition to the palmar surfaces of the hand, fingers, and thumb. Phase space X2E motion capture markers were attached to multiple points on key linkages of the maestro exoskeleton. Markers were also placed on the metacarpal, MCP and PIP joints of the index finger and the base of the thumb to track the position of the palm and the index finger. This enables a fair comparison to the simulated system by confirming that the movement of the human hand is minimal.

The required moment load was applied using the Maestro exoskeleton's torque sensing series elastic actuators. To achieve a known level of strap tension, pre-tensioning was carried out using a calibrated Omega DFG55 load cell, rated for 25N. Strap pre-tensioning was performed prior to placing the hand in the brace of the experimental setup by affixing the Maestro grounding link to a rigid fixture through a dovetail joint and aligning the hand within it. The straps were then pulled to the target tension with the load cell attached in series. To ensure minimal effects of friction between the strap and the palm during this step, both ends of all straps were pre-tensioned individually in a consistent order of: distal-lateral, proximal-lateral, distal-medial, proximal-medial. A maximum displayed error of 0.1N was allowed in the experiment protocol during the fastening process.

2.3. Experiment 2: Optimizing the Design of the Hand Dorsum PHRII

In addition to characterizing reduced order interactions between lumped parameter representations of interaction, HuRoSim has the ability to provide trends across surfaces of lumped parameter representations to understand the effects of variations in parameters describing neighboring regions. To evaluate this feature of the simulation approach and to demonstrate the value of a simulation tool in the design of the PHRII, we designed an

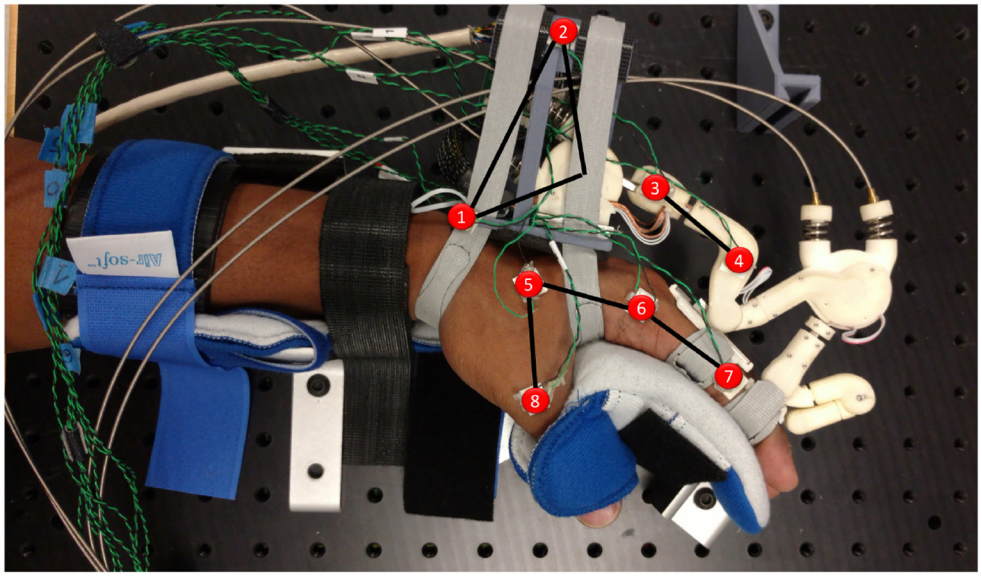

FIGURE 6 | Experimental setup for comparison to the simulated system. The human hand is held in a commercial brace reinforced and bolted down with aluminum channels (seen between the fingers and the thumb on the palmar surface of the hand). The Maestro hand exoskeleton is affixed with a modified base (link 1–2) that allows calibrated pre-tensioning of both straps. The Motion capture sensors are highlighted in red.

experiment to optimize the design of the PHRII for comfort, and evaluate the new design for performance.

To optimize the PHRII between the hand dorsum and the hand worn exoskeleton for user comfort, we developed a workflow in the HuRoSim simulation framework by defining the spatial relationship between individual lumped mass representations of the points on the hand dorsum and adding in experimentally quantified biological tissue properties (Silver et al., 2001; Wu et al., 2007). At each of the points, the pressure distribution across the PHRII is tracked by HuRoSim as a measure of discomfort. This approach was taken to ensure that an overall picture of the distribution of pressures could be derived to inform an optimization framework.

We chose pressure as a measure of discomfort based on the concept of the pain-pressure threshold (Belda-Lois et al., 2008), a pressure level that causes pain even on short duration of application. The exact value of this threshold varies significantly across body sections and population groups, and can cause pain at significantly lower pressures when applied for longer durations [reported as much as 50% lower by (Belda-Lois et al., 2008)].

We model the PHRII (**Figure 7 Left**) as a discrete array of springs representing the hand dorsum (k_{dorsum}) and the PHRII (k_{pHRI}), respectively. These two arrays of springs are in series with each other (**Figure 7 Right**). This system is loaded with a constant bias force normal to the surface representing a generalized net force from one or more straps. External loading is resolved into the generalized net force and moment vectors, explained in more detail in section 2.3.1. Through analysis of the simplified system under external load, we deduce the shape of the desired effective stiffness (k_{eff}) of this series spring model that allows us to minimize the peak pressures at the contact surface (Section 2.3.1). Using a numerical simulation environment, we compute the optimal effective stiffness gradient which satisfies the deduced shape profile from the analysis, and that also minimizes peak pressure (Section 2.3.2). Next, we quantify the stiffness profile of the experimenter's hand (k_{dorsum}) through an indentation experiment with a robot (Section 2.3.3). The k_{eff} computed from the numerical simulation and k_{dorsum}, obtained experimentally, are then used to compute the k_{pHRI}, the optimal stiffness of the PHRII (Section 2.3.4).

2.3.1. Analytical Determination of Optimal Stiffness Profile for the PHRII

To design an optimal PHRII for the hand dorsum, we simplify the complex interaction at the interface as two plates of length L and uniform width sandwiched between the rigid reference plate of the Maestro robot, and the rigid human bone. The robot reference plate is held to the dorsum by a bias force mimicking a strap (F_b), applied normally and at L/2 as seen in **Figure 8 (Left)**. We then load the PHRII with an external force mimicking the reaction forces from the Maestro actuators. Using the principle of transmissibility, we express the applied external force to the attachment plate as a combination of an equivalent force and moment applied at the center of the plate, placed coaxially with the bias force. The resulting reaction pressure ($P_{reaction}$) distribution balances the net force (F_b plus the normal component of F_L) and the external moment (M_L) [**Figure 8 (Right)**].

Our objective is to balance the applied force and moment while minimizing peak reaction pressure (C_i) along the contact

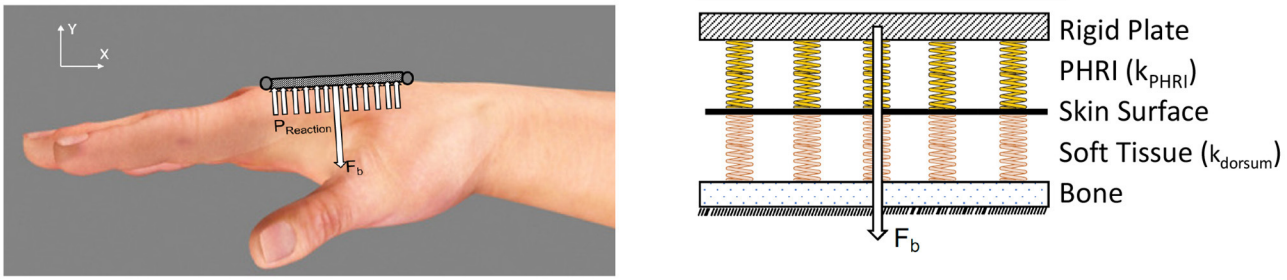

FIGURE 7 | (Left) Hand dorsum and simplified PHRII with uniform stiffness, bias force (F_b), applied using straps and approximated as a point load at the center, and reaction pressure ($P_{reaction}$). **(Right)** Modeling all compliant elements between the human reference structure (our skeleton) and the rigid links of the robot. The stiffness of the hand dorsum (k_{dorsum} indicating the orange springs) and the PHRII (k_{pHRI} indicating the yellow springs) behave as a set of viscoelastic springs in series.

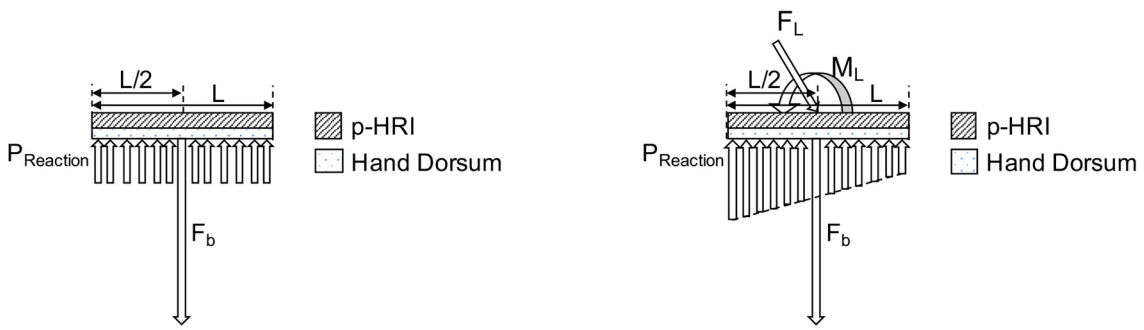

FIGURE 8 | Model of hand dorsum and PHRII with uniform stiffness, bias force (F_b), and uniform reaction pressure ($P_{reaction}$) distribution.

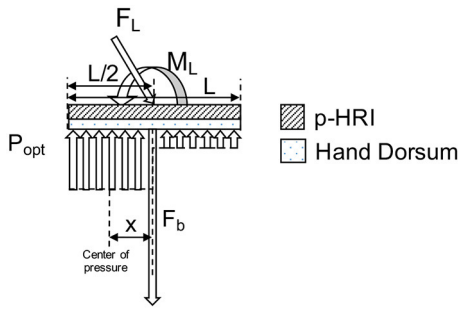

FIGURE 9 | Model of hand dorsum and PHRII with minimized pressure distribution, bias force (F_b), externally applied force (F_L), moment load (M_L) and resulting two regions of optimal reaction pressure (P_{opt}) distribution.

surface between the two plates.

$$C_i = max(P_{reaction}) \tag{1}$$

Under the counter-clockwise external moment, M_L, applied on the system, minimizing the cost function, C_i gives us a pressure distribution with two regions of optimized uniform reaction pressure (P_{opt}) below the plate (**Figure 9**).

Since we assume that the sum of pressure is equal to the applied load, minimizing the peak pressure would distribute it over a larger area giving us a region of uniform pressure. However, uniform pressure across the entire plate cannot balance the counter-clockwise applied moment, which explains the existence of two sections of different uniform pressure. The direction of this reaction pressure distribution (seen in **Figure 9**) depends on the direction of the external loading and reverses itself when the external loading is in the clockwise direction.

The boundaries of the regions of uniform pressure shift depending on the ratio of external applied moment (M_L) to the external applied force (F_L). The position of "x," the center of the highest pressure region in the optimal distribution (P_{opt}), and "P_{peak}," the magnitude of the highest pressure between the two uniform distributions, are computed in Equations (2) and (3).

$$x = \frac{M_L}{F_L + F_b} \tag{2}$$

$$P_{peak} = \frac{F_L + F_b}{L - 2x} \tag{3}$$

The optimal value of bias force, F_b of the attachment against the dorsum, to minimize C_i for the given force and moment loading configuration, is calculated to be the lowest value that gives us a non-negative pressure region (4):

$$F_b = \frac{4M_L}{L} - F_L \tag{4}$$

By analyzing the possible solutions to achieve this optimal pressure, (P_{opt}), a hyperbolic distribution with high stiffness in the center of the plate which tapers off toward the edge in the direction of the applied moment, M_L, is a solution to the equation, though its exact parameters are yet to be computed. We approximate this hyperbolic representation to a linear stiffness profile for our experiment, decreasing from the highest stiffness at the middle of the attachment (k_{mid}), and symmetrically tapering off to a minimum at each edge (k_{edge}). The symmetry allows the resulting profile to hold true for external moment loads in either direction. To obtain k_{pHRI}, we need to obtain k_{dorsum} in addition to knowing k_{eff}.

2.3.2. Numerical Computation of the Desired Stiffness Profile

We used the HuRoSim environment to compute the effective spatial stiffness gradient that minimizes peak pressure. The environment was also used to characterize the relationship between the bias force, the gradient of stiffness, relative displacement between the robot and the human, and the peak pressure over the hand dorsum.

For this experiment, the dorsum surface was discretized into 15 total points, with the PHRII interacting with the underlying human metacarpal through the stiffnesses k_{pHRI} and k_{dorsum} in series at each point. Piece-wise linear values for both stiffness were used, with k_{dorsum} taken from our experimental results. The system was simulated for varying applied force (F_L) and moment loads (M_L) with varying k_{pHRI} profiles to examine the resulting pressure distribution. The relative displacement of the PHRII with respect to the underlying bone, due to F_L, was also captured for each stiffness profile, and these results are presented in the next section.

2.3.3. Quantifying Tissue Response to Indentation

Tissue stiffness on the human body is quantified by applying force over a range of displacement.

To measure k_{dorsum}, we designed an indentation system comprised of a Phantom Premium 1.5 high force haptic renderer, which has a high positional accuracy of the end effector ($7 * 10^{-6}$m). This was used along with an ATI Nano 17 force torque transducer (having a high force torque sensing accuracy of 0.001N) attached at the end of the linkage as an indenter to probe the hand dorsum (**Figure 10**). We selected five points along a line between the metacarpophalangeal joint and the radial styloid process along the 2^{nd} metacarpal bone, the 3^{rd} metacarpal bone, and along a line between the two metacarpal bones, in the inter-metacarpal region. This region was selected to correspond to the area of the attachment plate on the Maestro exoskeleton. **Figure 10 (Middle)** shows the regions selected for indentation.

The wrist and arm were supported in braces, and a consistent grasp object was used across trials to minimize its influence on stiffness distributions due to the changes in bone locations and muscle recruitment strategy, as seen in **Figure 10 (Left)**. The wrist and arm supports were positioned to level the hand dorsum in the transverse anatomical plane. The phantom probe is then manually led once to each point marked on the dorsum for indentation. The probe uses these points as input into an interpolator to compute a spatial trajectory to follow. The phantom is driven in an open-loop position controlled configuration.

$$k_{dorsum} = \frac{k_{measured} * k_{indenter}}{k_{indenter} - k_{measured}} \tag{5}$$

Quantifying the stiffness of the indentation system in the direction normal to the hand dorsum demonstrated the need to account for this value in estimating the stiffness of the hand dorsum. The stiffness of the indentation system ($k_{indenter}$) was found to be 2.67 N/mm along the workspace. We account for this stiffness in the measurement of the hand dorsum stiffness (k_{dorsum}) by modeling the interaction between the indentation system and the hand dorsum as two springs in series. The measured stiffness of the hand dorsum, $k_{measured}$, (**Figure 10 Right**) is used along with $k_{indenter}$ to calculate the k_{dorsum} Equation (5).

We made five sequential repeated measures to estimate the variance in the measured stiffness at each point. The observed variance was attributed to movement in the hand. The hand dorsum stiffness data is collected from one pilot subject only, and with a probe having a square base with $4mm$ edges and $1.5mm$ filets on each edge to minimize discomfort during indentation. The indenter profile and size were chosen iteratively based on the relative distribution of the hard and soft tissue structures in the hand. Increasing the resolution of the grid beyond the current levels introduced errors due to partial overlap of soft and hard tissue at the points of measurement.

2.3.4. Calculating the Optimized Padding Stiffness

In our model, k_{eff} between the human bone and the Maestro robot's reference plate is comprised of k_{dorsum} and k_{pHRI} in series. Therefore, once we have numerically computed k_{eff}, and measured k_{dorsum} through the indentation experiment, the required k_{pHRI} can be calculated at every point on the attachment surface Equation (6). This gives us a PHRII stiffness profile that should generate the minimum peak pressure, or the optimal pressure profile (P_{opt}) on the hand dorsum for the given F_L and M_L.

$$k_{pHRI} = \frac{k_{eff} * k_{dorsum}}{k_{dorsum} - k_{eff}} \tag{6}$$

3. RESULTS

3.1. Experiment 1: Predicting Physical Interaction Using HuRoSim

HuRoSim offered many insights into the interaction between the exoskeleton and the hand at the PHRII. Specifically, the simulation environment was able to predict the directions and magnitude of displacements and forces that one would expect on the PHRII. The following sections describe some of the observations predicted by HuRoSim that were also confirmed by empirical experiments with the Maestro hand exoskeleton under identical conditions.

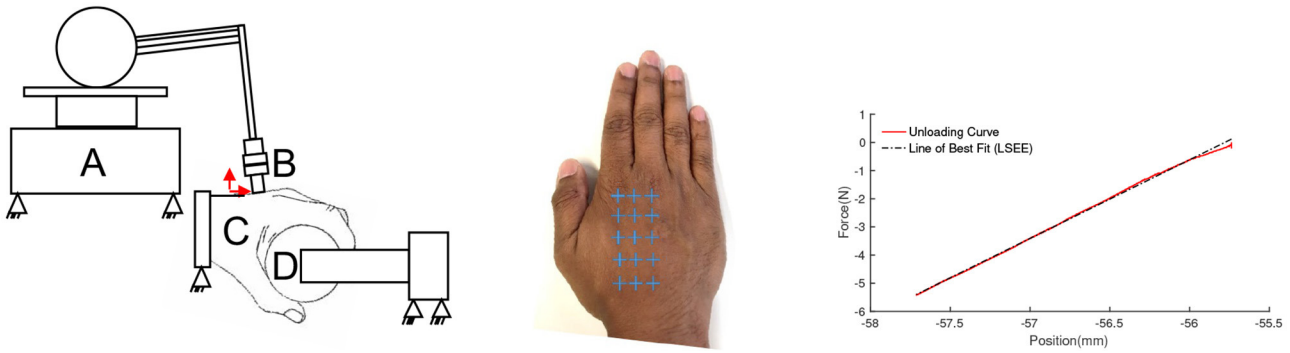

FIGURE 10 | (Left) Phantom premium 1.5 high force haptic renderer **(A)**, instrumented with an ATI nano 17 6-axis force torque transducer **(B)**, probing the hand dorsum **(C)** over a spatial grid while the subject grasps a spherical object instrumented with an ATI Nano 17 **(D)**. **(Middle)** Locations of measured stiffness measured over the 2nd & 3rd metacarpal, and 2nd-3rd intermetacarpal region. The blue "+" symbols represent the sites of indentation on the hand dorsum. **(Right)** Fitting a line to the force deflection curve from indentation experiments. The slope of the fitted line corresponds to the measured stiffness.

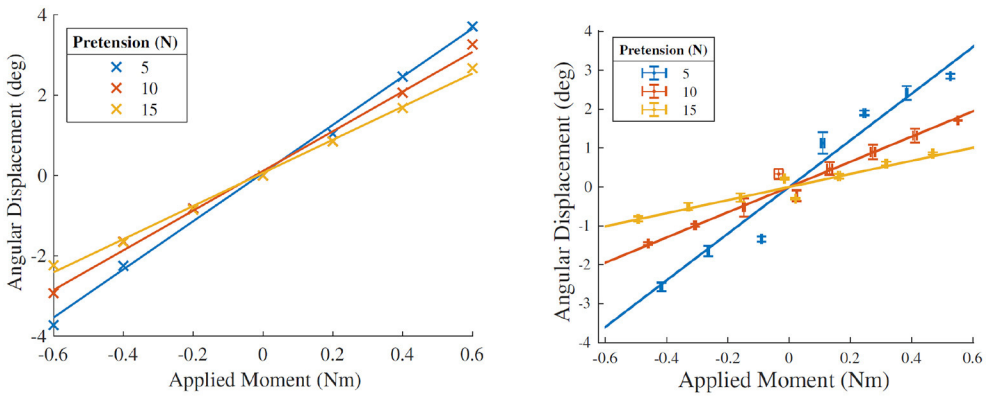

FIGURE 11 | (Left) Simulated angular displacement of the rigid surface of the dorsum attachment on application of moment loading under different conditions of strap stiffness. **(Right)** Angular displacement observed under identical conditions in the physical experiment. The HuRoSim model is able to predict the trends in effect of both the varied parameters of strap pretension and moment loading. However, under higher pretension, where the non-linear behavior of human soft tissue becomes more pronounced, there is expected divergence between the predicted and experimental values.

3.1.1. The Effects of Strap Pretension and Applied Moment Load

The effect of varying the applied moment loading and the strap pretension were studied in both the HuRoSim environment, as well as in the physical experiment. **Figure 11 (Left)** shows the angular displacement of the exoskeleton dorsum attachment on application of moment load by the exoskeleton about the MCP joint. HuRoSim predicted an angular displacement that increased approximately proportional to the applied moment load, and that was reduced on increased strap pretension. Physical experiments under the same conditions confirmed both trends as seen in **Figure 11 (Right)**. The experimental values of angular displacement under low strap pretension matched the predicted values quite closely. However, under higher pretension, where the non-linear behavior of human soft tissue becomes more pronounced, there is expected divergence between the predicted and experimental values.

In addition, when the exoskeleton applies an extension torque about the MCP joint, HuRoSim also predicted an increase in pressure at the location on the PHRII on the hand dorsum closer to the joint while the location further away from the MCP joint experiences a reduction in pressure. The inverse is true when the actuator applies a flexion torque about the MCP joint. HuRoSim indicated that the magnitude of these increases with respect to the applied moment was found to be dependent on the length of the exoskeleton attachment and on the geometry of the PHRII at the contact locations on the hand dorsum.

3.1.2. Liftoff From the Finger Surface

As a consequence of the distribution of pressures described above, HuRoSim predicted that the end of the PHRII closest to the MCP joint would lift off and lose contact with the skin surface on the application of extension torques by the exoskeleton. When we replicated the simulation empirically with the Maestro hand

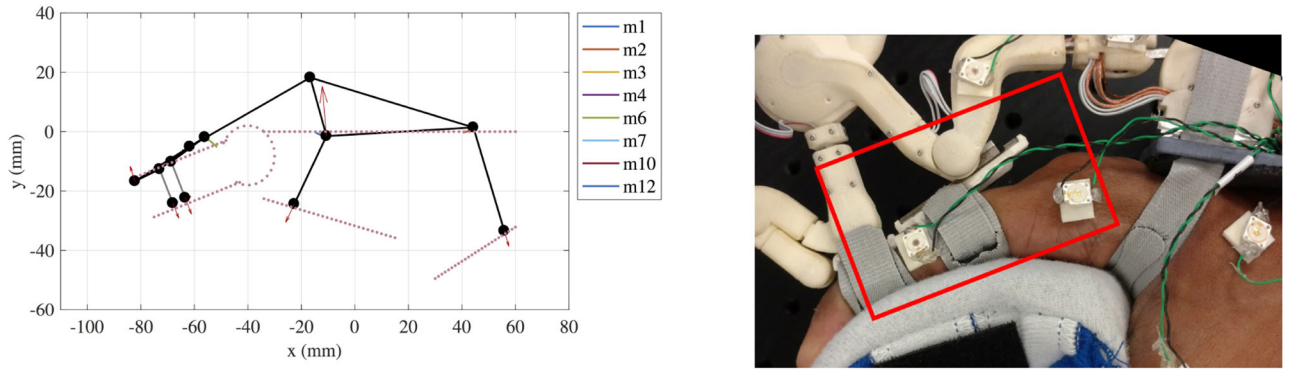

FIGURE 12 | (Left) An example of simulated prediction of liftoff at the proximal phalanx attachment. **(Right)** The physical manifestation of the same during experimental characterization.

exoskeleton, we observed the lift off phenomenon predicted by HuRoSim (**Figure 12**).

3.1.3. Effect of Varying Strap Stiffness

The effect of varying strap stiffness was studied using the simulation environment to identify the optimal strap stiffness to minimize both output metrics (relative displacement and forces across the interface). HuRoSim's initial results indicated that the best performance on both metrics occurred with effectively inelastic straps, or straps with extremely high stiffness.

This result was unexpected since pilot user feedback with the maestro exoskeleton reported that mild elasticity was the most comfortable. Exploring different variables in the system, it was observed that in the actual human hand, co-contraction of muscles in response to the applied load leads to an increase in the thickness of the muscle body as it is flexed, and resulting changes in the cross sectional thickness of the hand. These also vary depending on the musculature of the individual subject and the magnitude of voluntary contraction. When the simulation was tested with approximate values of the cross section variation, a slightly reduced strap stiffness was found to produce lower pressure distributions with minimal trade-off in the relative displacement values.

The values of this optimal reduced stiffness, however, are dependent on the magnitude of cross section increase due to co-contraction. Future work can perform the simulation using magnitudes of cross sectional variation sourced from literature or experiment to inform design values of this optimal stiffness.

3.2. Experiment 2: Optimizing the Design of the Hand Dorsum PHRII

The stiffness of the hand dorsum was measured and characterized with five repetitions over each of the 15 chosen points, distributed equally over the 2nd metacarpal, 3rd metacarpal and the inter-metacarpal gap between these bones on a single subject's hand (**Figure 13**). On average, k_{dorsum} was measured to be 1.0876 ± 0.40 N/mm over a range of from 0.54 to 1.59 N/mm. The region of the dorsum above the metacarpal bones was found to be stiffer (1.1285 ± 0.43 N/mm) than the region between the bones (1.0060 ± 0.36 N/mm) that accommodate soft tissue. Increasing force of grasp led to an increase in measured dorsum stiffness (**Figure 13**), however, the PHRII stiffness computed here is for a grasp force of 0 N.

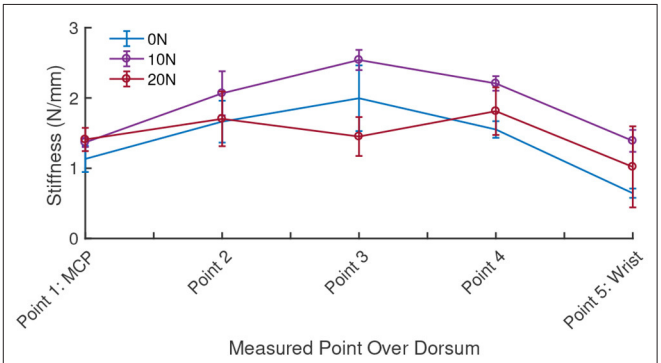

FIGURE 13 | Measured stiffness of the hand dorsum for five equally spaced points along the second metacarpal at three levels of grasp force applied by the subject.

For our optimization experiment, the key metrics of performance considered were the peak pressure over the dorsum, and the relative displacement of the exoskeleton with respect to the hand. The system was simulated across a range of applied moment, bias force and stiffness gradient to characterize the effects of these variables on our performance metrics. **Figure 14** shows a surface of the combined effect on peak pressure at the dorsum interface due to changes in bias force and stiffness profiles, while holding the applied moment constant. It shows that the minimum peak pressure is achieved at the bias load as calculated in Equation (4) for all stiffness profiles. When viewing the effect of varying stiffness profile gradients, we again observe a local minimum in the peak pressure at the dorsum, which is explained in more detail below.

Looking at stiffness profile, the highest values of peak pressure are observed at the highest applied moment load for all effective stiffness profiles. However, for any given fixed applied moment,

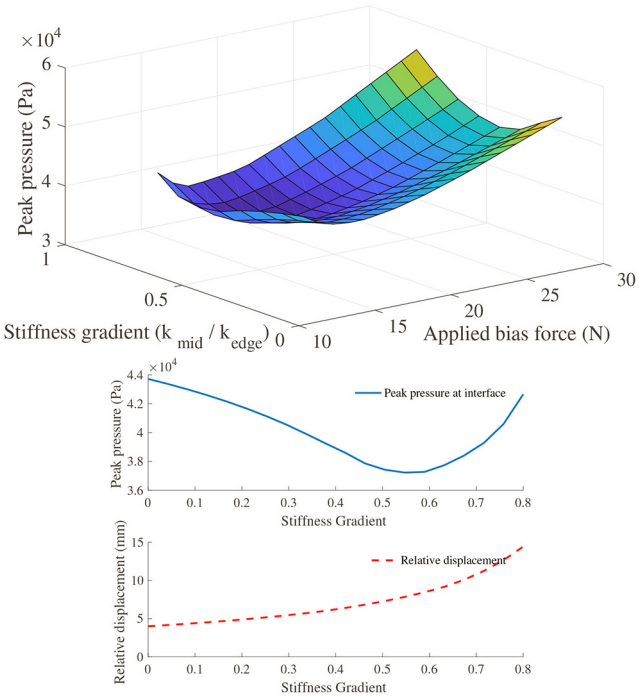

FIGURE 14 | (Top) Surface plot showing the effect of varying bias force and stiffness profiles on the peak pressure (as a measure of user comfort) across the PHRII on the hand dorsum. **(Bottom)** Trade-off between peak pressure (as a measure of user comfort) and relative displacement on varying the stiffness profile gradient.

we observe an improvement in peak pressure at the dorsum when the effective stiffness between the human bone and the robot is varied in a gradient from the center to the edge of the interface, as seen in **Figure 15 (Left)**. The percentage improvement increases with increasing applied moment for the same value of bias force. Additionally, the optimal value of stiffness profile gradient is seen to increase with the applied moment. This corroborates well with our analytical prediction of the a load dependent optimal value of stiffness gradient.

When considering the effect of these same variables on the relative displacement, it becomes evident that we have a trade-off between our performance metrics of comfort and relative displacement. **Figure 15 (Right)** shows the effect on relative displacement due to a change in stiffness profiles with the applied force and moment loading held constant for each of the plotted lines. Contrary to the effect on peak pressure shown earlier, the relative displacement increases with the stiffness profile gradient.

This is more clearly illustrated in **Figure 14**, where the two output metrics are plotted against a common x-axis of the stiffness profile gradient. It shows that increasing the stiffness profile gradient to improve the peak pressure across the interface has an adverse effect on the relative displacement. Thus, a practical design would be one in which we choose a trade-off between the two desired outcomes and pick our stiffness gradient based on an optimal weighting between the two.

4. DISCUSSION

4.1. Simulation Insights

We presented a novel method to optimize the design of the PHRII between a wearable exoskeleton and the human hand. By characterizing the mechanical properties of tissues at a few locations on the hand dorsum, we demonstrated how limited experimental data can be used to optimize the design of the PHRII through the use of a custom simulation environment, HuRoSim.

For this simulation, input parameters of interest were strap pre-tension and the applied moment load. Important simulation output parameters were the relative displacement between the exoskeleton and the human hand, and human comfort (measured as peak pressure across the dorsum surface).

Relative displacement was found to increase non-linearly with increasing applied moment. Relative displacement was similarly found to decrease with increasing strap pre-tension. This relation is expected since almost all of the stiffness in the human system, as well as the padding and straps are non-linear and increase with increasing strain. It is important to note that the magnitudes and directions of the above effects are configuration dependent and can change drastically with different link lengths of the robot exoskeleton, MCP joint angle, and other joints in the system as well. These dependencies, however, are very easily accepted as inputs to the numerical simulation model if we wish to study them independently.

These results are the first of its kind for the hand. The trends observed here for this PHRII study agree with results observed by other experiments conducted on the lower limbs (Quinlivan et al., 2015).

4.2. Experiment 1: Predicting Physical Interaction Using HuRoSim

Experimental characterization of the identical system as simulated was carried out to confirm the behavior of the simulated system in a physical setting. This experimental setup is a highly instrumented version of an actual human-robot system specifically to study the effects of force across the PHRII interface. The results gained from this experimentation show the level of experimental characterization required to achieve similar insights that a simulation approach makes possible. This simulation approach could be advantageous in both cost and time for the iterative stages of design refinement during a coupled human-robot system's design lifecycle.

Future work of simulation models could be to develop bounds on a range of slip along the skin surface, since this movement is an important part of the PHRII sstem.

By producing outcomes that align with the experimental results, this experiment demonstrates that HuRoSim is capable of predicting phyisiologically observed behavior with only estimated information of the individual components of the system. Further study will definitely benefit from more detailed experimental characterization, accounting for anthropometric variations. This could further improve simulation accuracy.

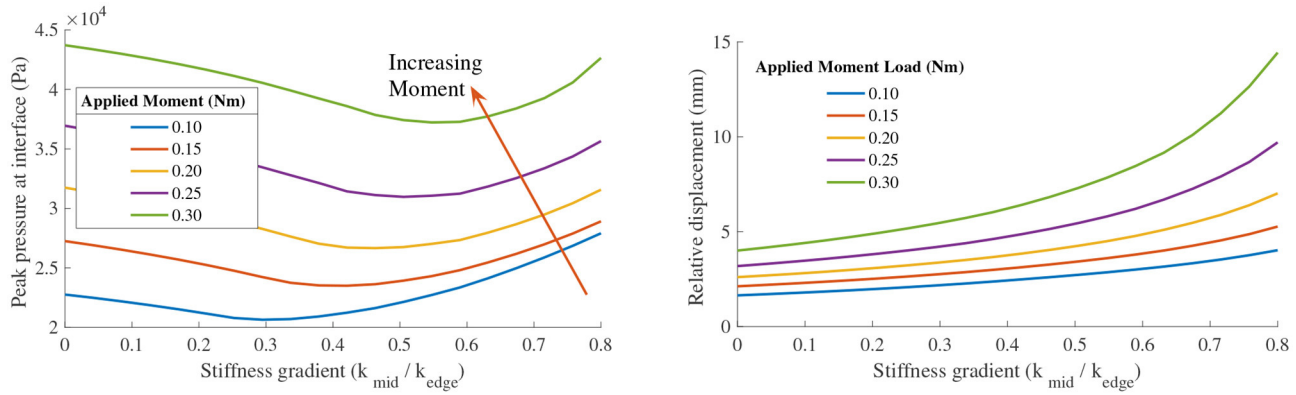

FIGURE 15 | (Left) Plot of peak pressure at the PHRII interface (as a measure of user comfort) vs the stiffness profile gradient for different applied moment loads at constant bias force. **(Right)** Plot of the effect on relative displacement between the human skeleton and the attachment base on changing the stiffness profile gradient of the PHRII.

4.3. Experiment 2: Optimizing the Design of the Hand Dorsum PHRII

We used a simulation based approach to assess the pressure distribution that would be generated across a single PHRII due to the application of force and moment loading. Our simulation of a simple PHRII system involving just a single interaction surface shows that it is possible to identify optimal values of parameters such as the strap bias load, and the padding stiffness profile. This is an important result that can be used in the design of more ergonomic and effective PHRIIs for coupled human robot systems.

Validation of the existence of these optimal PHRI parameters was carried out using analytical calculations of the test cases. While experimental characterization should be done as well in our future work, these analytical calculations of our system provided us with a theoretical explanation of the optimal values that were numerically identified by simulation. In the case of the optimal bias force for a given applied moment, we were also able to obtain a predicted optimal value from the analytical calculation, and this matched well with the simulation results.

We also identified the tradeoff between the peak pressure at the interface as a measure of user comfort, and the relative displacement across the interface which is a measure of position error in the system. Parameters that produce such tradeoffs in optimal pressure distributions include the stiffness profile gradient and the bias force of the PHRII. Knowledge of this tradeoff from simulation outputs allows us to make informed design choices when choosing the parameters of our PHRIIs.

We would recommend simulating a PHRII during its design phase in order to better choose its properties at the onset rather than having to go through theoretical iterations. While a lot of the optimal parameters do depend on the applied loads and geometry of the system, our analysis does bring out one general recommendation as well. Any PHRI that is to be subjected to high moment loading should ideally be designed with stiffer regions near its center, and regions of low stiffness close to its edges.

The design of such custom designed properties across a PHRII surface has already been successfully shown by Petron et al. (2016) in their design of the variable impedance socket for transtibial amputees. The work presented in this paper expands on the idea by using a more generalized setting of a single PHRII rather than a closed socket, and also focuses on cases that involve a high application of moment loads. We propose that by the use of our simulation based approach, effects of different parameters of the PHRII and the applied loads can be effectively characterized and used to drive design choices.

HuRoSim's simulation engine was custom built on Matlab (Mathworks Inc., MA) to have a greater control over the design of the dynamic solver. Future versions of this environment can be implemented on commercial multi-body physics platforms to build a real-time system capable of solving continuous dynamics of the system. The experimental characterization of the tissue properties was quasi-static and can be extended to quantify dynamic response of the tissue to loading. Modeling the tissue response in greater detail can enable the design of PHRII optimized for dynamic loads applied during task performance.

HuRoSim's modular construction enables it to not be limited to applications of just the hand, but to any human-robot coupling where both comfort and positional accuracy are of importance. Other upper extremety examples such as supernumary fingers (Hussain et al., 2017; Salvietti et al., 2017) and lower extremity examples such as ankle-foot orthoses (Kim et al., 2020). Simulation based design could potentially be of significant use for such applications.

5. CONCLUSION

In this paper, we presented a novel systematic approach to quantifying the complex interactions at the Physical Human

Robot Interaction Interface (PHRII) for wearable robots coupled to the body. We demonstrated how a novel simulation environment (HuRoSim) can be utilized with experimental data to improve the design of the PHRII for optimal comfort and performance. By utilizing this approach, design loops can leverage the power of limited experimental measurements that inform fast and inexpensive simulation tools to generate design recommendations.

Our approach fills an important gap in the literature between difficult and error-prone experimental characterization of the behavior of the pHRII, and expensive iterative physical prototyping for the design of the interface between the human body and the device.

We demonstrate that reduced order models informed by limited experimental measurements of human tissue provide sufficient information to optimize PHRII design. This work represents the beginning of a step change in the design of PHRII for robots attached to the body. It demonstrates how complex physical interactions between man and machine can be simplified using first principles to generate actionable recommendations for reduced design time and complexity.

DATA AVAILABILITY STATEMENT

The raw data supporting the conclusions of this article will be made available by the authors, without undue reservation.

ETHICS STATEMENT

The studies involving human participants were reviewed and approved by Institutional Review Board, University of Texas at Austin. Study number: 2013-05-0126. The patients/participants provided their written informed consent to participate in this study.

AUTHOR CONTRIBUTIONS

RJ contributed to the development of the simulation engine of the platform under the guidance of AD. GM contributed to experimental acquisition of the hand dorsum properties. RJ and GM contributed to analysis of the data from simulation and physical experiments. All authors contributed to writing, reviewing, and proofreading the manuscript.

ACKNOWLEDGMENTS

The authors would like to thank Dr. Raymond King for his advice and guidance while designing the HuRoSim platform, Kevin Shimasaki and Dr. Andrew Doxon for sharing their expertise in manufacturing and controls. We would also like to thank Dr. Chad Rose, Kevin Warburton, Kaci Madden, Paria Esmatloo, and all other members of the ReNeu Robotics lab at the University of Texas at Austin for their assistance with experiments, feedback on the HuRoSim platform, and for reviewing this manuscript.

REFERENCES

Agarwal, P., Fox, J., Yun, Y., OMalley, M. K., and Deshpande, A. D. (2015). An index finger exoskeleton with series elastic actuation for rehabilitation: design, control and performance characterization. *Int. J. Robot. Res.* 34, 1747–1772. doi: 10.1177/0278364915598388

Akiyama, Y., Okamoto, S., Yamada, Y., and Ishiguro, K. (2016). Measurement of contact behavior including slippage of cuff when using wearable physical assistant robot. *IEEE Trans. Neural Syst. Rehabil. Eng.* 24, 784–793. doi: 10.1109/TNSRE.2015.2464719

Bayo, E., and Ledesma, R. (1996). Augmented lagrangian and mass-orthogonal projection methods for constrained multibody dynamics. *Nonlin. Dyn.* 9, 113–130. doi: 10.1007/BF01833296

Belda-Lois, J.M., Poveda, R., and Vivas, M. (2008). *Analysis of Pressure Distribution and Tolerance Areas for Wearable Robots*. 154–156.

Bogue, R. (2009). Exoskeletons and robotic prosthetics: a review of recent developments. *Ind. Robot Int. J.* 36, 421–427. doi: 10.1108/01439910910980141

Bouzit, M., Burdea, G., Popescu, G., and Boian, R. (2002). The rutgers master II - new design force-feedback glove. *IEEE/ASME Trans. Mech.* 7, 256–263. doi: 10.1109/TMECH.2002.1011262

Cempini, M., Marzegan, A., Rabuffetti, M., Cortese, M., and Vitiello, N. (2014). Analysis of relative displacement between the HX wearable robotic exoskeleton and the user's hand. *J. Neuroeng. Rehabil.* 18, 147. doi: 10.1186/1743-0003-11-147

Choi, I., Hawkes, E. W., Christensen, D. L., Ploch, C. J., and Follmer, S. (2016). "Wolverine: a wearable haptic interface for grasping in virtual reality," in *2016 IEEE/RSJ International Conference on Intelligent Robots and Systems (IROS)* (Daejeon: IEEE), 986–993.

Colombo, G., Jorg, M., and Dietz, V. (2000). "Driven gait orthosis to do locomotor training of paraplegic patients," in *Annual International Conference of the IEEE Engineering in Medicine and Biology - Proceedings* (Chicago, IL), 3159–3163.

Dabrowska, A., Rotaru, G. M., Spano, F., Affolter, C., Fortunato, G., Lehmann, S., et al. (2016). A water-responsive, gelatine-based human skin model. *Tribol. Int.* 113, 316–322. 10.1016/j.triboint.2017.01.027

Dubowsky, S., and Desforges, D. T. (2015). The application of model-referenced adaptive control to robotic manipulators. *J. Dyn. Sys. Meas. Control* 101, 193–200. doi: 10.1115/1.3426424

Gupta, A., and O'Malley, M. K. (2006). Design of a haptic arm exoskeleton for training and rehabilitation. *IEEE/ASME Trans. Mechatron.* 11, 280–289. doi: 10.1109/TMECH.2006.875558

Hussain, I., Spagnoletti, G., Salvietti, G., and Prattichizzo, D. (2017). Toward wearable supernumerary robotic fingers to compensate missing grasping abilities in hemiparetic upper limb. *Int. J. Robot. Res.* 36, 1414–1436. doi: 10.1177/0278364917712433

Kim, B., and Deshpande, A. D. (2009). An upper-body rehabilitation exoskeleton with an anatomical shoulder mechanism: design, modeling, control, and performance evaluation. *Int. J. Robot Res.* 36, 414–435.

Kim, B., and Deshpande, A. D. (2017). An upper-body rehabilitation exoskeleton harmony with an anatomical shoulder mechanism: design, modeling, control, and performance evaluation. *Int. J. Robot. Res.* 36, 414–435. doi: 10.1177/0278364917706743

Kim, S. J., Park, J., Shin, W., Lee, D. Y., and Kim, J. (2020). "Proof-of-concept of a pneumatic ankle foot orthosis powered by a custom compressor for drop foot correction," in *2020 IEEE International Conference on Robotics and Automation (ICRA)* Paris: IEEE).

Krouskop, T. A., Williams, R., Krebs, M., Herszkowicz, I., and Garber, S. (1985). Effectiveness of mattress overlays in reducing interface pressures during recumbency. *J. Rehabil. Res. Develop.* 22, 7–10. doi: 10.1682/jrrd.1985.07.0007

Petron, A., Duval, J.-F., and Herr, H. (2016). Multi-indenter device for in vivo biomechanical tissue measurement. *IEEE Trans. Neural Syst. Rehabil. Eng.* 25, 1. doi: 10.1109/TNSRE.2016.2572168

Petron, A. J. (2016). Prosthetic socket design: from a multi-indenter device for in vivo biomechanical tissue measurement to a quasi-passive transtibial socket interface. 197. Available online at: https://dspace.mit.edu/handle/1721.1/106068

Pezent, E., Israr, A., Samad, M., Robinson, S., Agarwal, P., Benko, H., and Colonnese, N. (2019). "Tasbi: multisensory squeeze and vibrotactile wrist haptics for augmented and virtual reality," in *2019 IEEE World Haptics Conference (WHC)* (Tokyo: IEEE), 1–6.

Quinlivan, B., Asbeck, A., Wagner, D., Ranzani, T., Russo, S., and Walsh, C. J. (2015). Force transfer characterization of a soft exosuit for gait assistance. *Volume 5A: 39th Mechanisms and Robotics Conference* (Bostan, MA), V05AT08A049.

Salvietti, G., Hussain, I., Cioncoloni, D., Taddei, S., Rossi, S., and Prattichizzo, D. (2017). Compensating hand function in chronic stroke patients through the robotic sixth finger. *IEEE Trans. Neural Syst. Rehabil. Eng.* 25, 142–150. doi: 10.1109/TNSRE.2016.2529684

Schiele, A., and Van Der Helm, F. C. T. (2006). Kinematic design to improve ergonomics in human machine interaction. *IEEE Trans. Neural Syst. Rehabil. Eng.* 14, 456–469. doi: 10.1109/TNSRE.2006.881565

Silver, F. H., Freeman, J. W., and DeVore, D. (2001). Viscoelastic properties of human skin and processed dermis. *Skin Res. Technol.* 7, 18–23. doi: 10.1034/j.1600-0846.2001.007001018.x

Udwadia, F., and Kalaba, R. E. (2002). What is the general form of the explicit equations of motion for constrained mechanical systems? *J. Appl. Mech.* 69, 335. doi: 10.1115/1.1459071

van Kuilenburg, J., Masen, M. a., and van der Heide, E. (2012). Contact modelling of human skin: What value to use for the modulus of elasticity? *Proc. Inst. Mech. Eng. Part J J. Eng. Tribol.* 227, 349–361. doi: 10.1177/1350650112463307

Walsh, C., Asbeck, A. T., Bujanda, I. G., Ding, Y., Dyer, R. J., Larusson, A. F., et al. (2016). *Soft Exosuit for Assistance With Human Motion.* U.S. Patent 9,351,900.

Witkin, A., and Witkin, A. (2001). *Physically based modeling constrained dynamics constrained dynamics*. Pixar Animation Studios.

Wu, J. Z., Cutlip, R. G., Andrew, M. E., and Dong, R. G. (2007). Simultaneous determination of the nonlinear-elastic properties of skin and subcutaneous tissue in unconfined compression tests. *Skin Res. Technol.* 13, 34–42. doi: 10.1111/j.1600-0846.2007.00182.x

Young, E. M., and Kuchenbecker, K. J. (2019). Implementation of a 6-dof parallel continuum manipulator for delivering fingertip tactile cues. *IEEE Trans. Hapt.* 12, 295–306. doi: 10.1109/TOH.2019.2920928

Yun, Y., Dancausse, S., Esmatloo, P., Serrato, A., Merring, C. A., Agarwal, P., et al. (2017). "Maestro: an emg-driven assistive hand exoskeleton for spinal cord injury patients," in *Robotics and Automation (ICRA), 2017 IEEE International Conference on* (Singapore: IEEE), 2904–2910.

Conflict of Interest: RJ was employed by the company Harmonic Bionics Inc.

The remaining authors declare that the research was conducted in the absence of any commercial or financial relationships that could be construed as a potential conflict of interest.

Publisher's Note: All claims expressed in this article are solely those of the authors and do not necessarily represent those of their affiliated organizations, or those of the publisher, the editors and the reviewers. Any product that may be evaluated in this article, or claim that may be made by its manufacturer, is not guaranteed or endorsed by the publisher.

frontiers in Neurorobotics

REVIEW
published: 21 February 2022
doi: 10.3389/fnbot.2022.815693

Intention Detection Strategies for Robotic Upper-Limb Orthoses: A Scoping Review Considering Usability, Daily Life Application, and User Evaluation

Jessica Gantenbein[1]*, *Jan Dittli*[1], *Jan Thomas Meyer*[1], *Roger Gassert*[1,2] and *Olivier Lambercy*[1,2]

[1] *Rehabilitation Engineering Laboratory, Department of Health Sciences and Technology, ETH Zurich, Zurich, Switzerland,* [2] *Future Health Technologies, Singapore-ETH Centre, Campus for Research Excellence and Technological Enterprise (CREATE), Singapore, Singapore*

Wearable robotic upper limb orthoses (ULO) are promising tools to assist or enhance the upper-limb function of their users. While the functionality of these devices has continuously increased, the robust and reliable detection of the user's intention to control the available degrees of freedom remains a major challenge and a barrier for acceptance. As the information interface between device and user, the intention detection strategy (IDS) has a crucial impact on the usability of the overall device. Yet, this aspect and the impact it has on the device usability is only rarely evaluated with respect to the context of use of ULO. A scoping literature review was conducted to identify non-invasive IDS applied to ULO that have been evaluated with human participants, with a specific focus on evaluation methods and findings related to functionality and usability and their appropriateness for specific contexts of use in daily life. A total of 93 studies were identified, describing 29 different IDS that are summarized and classified according to a four-level classification scheme. The predominant user input signal associated with the described IDS was electromyography (35.6%), followed by manual triggers such as buttons, touchscreens or joysticks (16.7%), as well as isometric force generated by residual movement in upper-limb segments (15.1%). We identify and discuss the strengths and weaknesses of IDS with respect to specific contexts of use and highlight a trade-off between performance and complexity in selecting an optimal IDS. Investigating evaluation practices to study the usability of IDS, the included studies revealed that, primarily, objective and quantitative usability attributes related to effectiveness or efficiency were assessed. Further, it underlined the lack of a systematic way to determine whether the usability of an IDS is sufficiently high to be appropriate for use in daily life applications. This work highlights the importance of a user- and application-specific selection and evaluation of non-invasive IDS for ULO. For technology developers in the field, it further provides recommendations on the selection process of IDS as well as to the design of corresponding evaluation protocols.

Keywords: intention detection, wearable robotics, upper limb orthosis, user studies, human robot interaction, usability evaluation

OPEN ACCESS

Edited by:
Irfan Hussain, Khalifa University, United Arab Emirates

Reviewed by:
Emilia Biffi, Eugenio Medea (IRCCS), Italy
Christine Azevedo Coste, Research Centre Inria Sophia Antipolis Méditerranée, France

***Correspondence:**
Jessica Gantenbein
relab.publications@hest.ethz.ch

Received: *15 November 2021*
Accepted: *24 January 2022*
Published: *21 February 2022*

Citation:
Gantenbein J, Dittli J, Meyer JT, Gassert R and Lambercy O (2022) Intention Detection Strategies for Robotic Upper-Limb Orthoses: A Scoping Review Considering Usability, Daily Life Application, and User Evaluation. Front. Neurorobot. 16:815693. doi: 10.3389/fnbot.2022.815693

1. INTRODUCTION

Our upper limbs are essential for numerous tasks in our daily lives, allowing us to interact physically and socially with our environment. Functional limitations of the upper limbs, e.g., due to impairment from neurological injury or disease, may have a substantive impact on independence, health, and wellbeing of the people affected, not only on physical but also on emotional, cognitive, and behavioral levels (Poltawski et al., 2016). In recent years, robotic wearable orthoses for the upper limbs, i.e., for the shoulder, elbow, wrist, hand or fingers, emerged as tools to compensate for functional impairments and therefore aim to improve quality of life of their users. Orthoses assist movements by being worn around and operated in parallel to the user's impaired limb (Tucker et al., 2015). The potential of wearable upper-limb orthoses (ULO), in this context often called "exoskeletons," has further been exploited not only for people with impairments but also to complement or augment upper limb function of non-impaired users, e.g., by enhancing their strength or endurance in specific tasks in their work environment (Bergamasco and Herr, 2016; Thalman and Artemiadis, 2020).

However, wearable robotic orthoses are not yet easily available and widely accepted by end-users. Previous studies have shown that insufficient usability can lead to low user acceptance of assistive technologies such as ULO, and consequently to high device abandonment rates (Biddiss and Chau, 2007; Ravneberg, 2012; Sugawara et al., 2018). The usability of a device describes how well it can be used by a specific user and context of use (ISO 9241-11, 2018). A critical factor in the use of an ULO is the way the user can trigger the desired robot motion. Thus, we hypothesize that the intention detection strategy (IDS) as the interface between users and their ULO plays an essential role in the usability of the overall device perceived by the user. Therefore, ensuring a high usability of an IDS is crucial to promote the adoption of an ULO to its targeted context of use. The question of whether a person is able and willing to use a specific IDS also highly depends on the person's residual sensorimotor capabilities and the tasks for which the device is intended. As such, the appropriateness of an IDS for an ULO depends not only on its technical advantages and limitations but also on the target user and the intended usage scenario. However, research papers describing the development or application of IDS for ULO rarely cover all these decisive factors.

Previous reviews have provided exhaustive overviews of IDS for movement assistive devices. Lobo-Prat et al. (2014) reviewed non-invasive IDS for active movement assistive devices in general, not specifically focusing on ULO. Other reviews were published focusing on specific strategies based on electromyography (EMG) (Parajuli et al., 2019; Hameed et al., 2020; Rodríguez-Tapia et al., 2020) or brain-computer-interfaces (BCI) (Millán et al., 2010; Khan et al., 2020; Rashid et al., 2020). However, the scopes of these reviews only cover a specific section of the broad range of available IDS. Chu and Patterson (2018) and du Plessis et al. (2021) published narrative reviews discussing robotic devices for hand rehabilitation and assistance, in which also IDS were briefly discussed. However, all these existing reviews primarily focus on the concepts and technical design of IDS. As such, a review systematically analyzing various IDS with respect to their daily life applicability and usability is yet missing.

Through this work, we aim to provide technology developers with an evidence-based overview of the key aspects to consider for the selection of appropriate non-invasive IDS for ULO applications. We further present recommendations for the choice of usability attributes to promote a more comprehensive and standardized evaluation of IDS for ULO from a user-centered point of view. This work is important, as it provides a novel analysis of how different IDS are applied and in which context, paving the way for more informed selection of IDS in wearable robotics, which could ultimately improve the acceptance of such technologies.

Abbreviations: ADL, activities of daily living; DOF, degrees of freedom; EEG, electroencephalography; EMG, electromyography; EOG, electrooculography; ERP, event-related potential; FMG, force myography; fMRI, functional magnetic resonance imaging; fNIRS, functional near-infrared spectroscopy; IDS, intention detection strategy; IMU, intertial measurement unit; MEG, magnetoencephalography; MMG, mechanomyography; NASA-TLX, national aeronautics and space administration task load index; QUEST, Quebec user evaluation of satisfaction with assistive technology; SD, standard deviation; SSVEP, steady state visually evoked potential; SUS, system usability scale; ULO, upper-limb orthosis; ULS, upper-limb segment(s); USE, usefulness, satisfaction, ease-of-use.

2. METHODS

This scoping review was conducted in compliance with the Preferred Reporting Items for Systematic Reviews and Meta-Analyses requirements extension for scoping reviews (PRISMA-ScR) (Tricco et al., 2018).

2.1. Literature Search

A literature search was conducted in August 2021 on five electronic databases (Web of Science, Scopus, PubMed, Embase, and IEEE Xplore). An example of the search string used for Web of Science is shown in **Figure 1A**. Search strings for the other databases were built analogously but adapted to the databases' specific requirements wherever needed.

2.2. Study Selection

In order to select eligible studies from the obtained manuscripts, a set of criteria were predefined.

Inclusion criteria were: (I1) manuscripts describing the evaluation of a human intent-controlled wearable or portable ULO or non-invasive IDS used in combination with an ULO; (I2) full-text manuscripts in English language.

Exclusion criteria were: (E1) manuscripts not providing information on which IDS was used; (E2) IDS requiring invasive interventions; (E3) evaluation not involving human participants wearing the ULO during data collection; (E4) non-real-time control of the ULO; (E5) third person, autonomous, purely gravity-compensating, or master-slave controlled ULO (i.e., not based on intent from the user); (E6) studies only considering rehabilitative effects of the ULO over multiple sessions as outcome; (E7) same IDS and ULO already assessed in a newer included study by same authors.

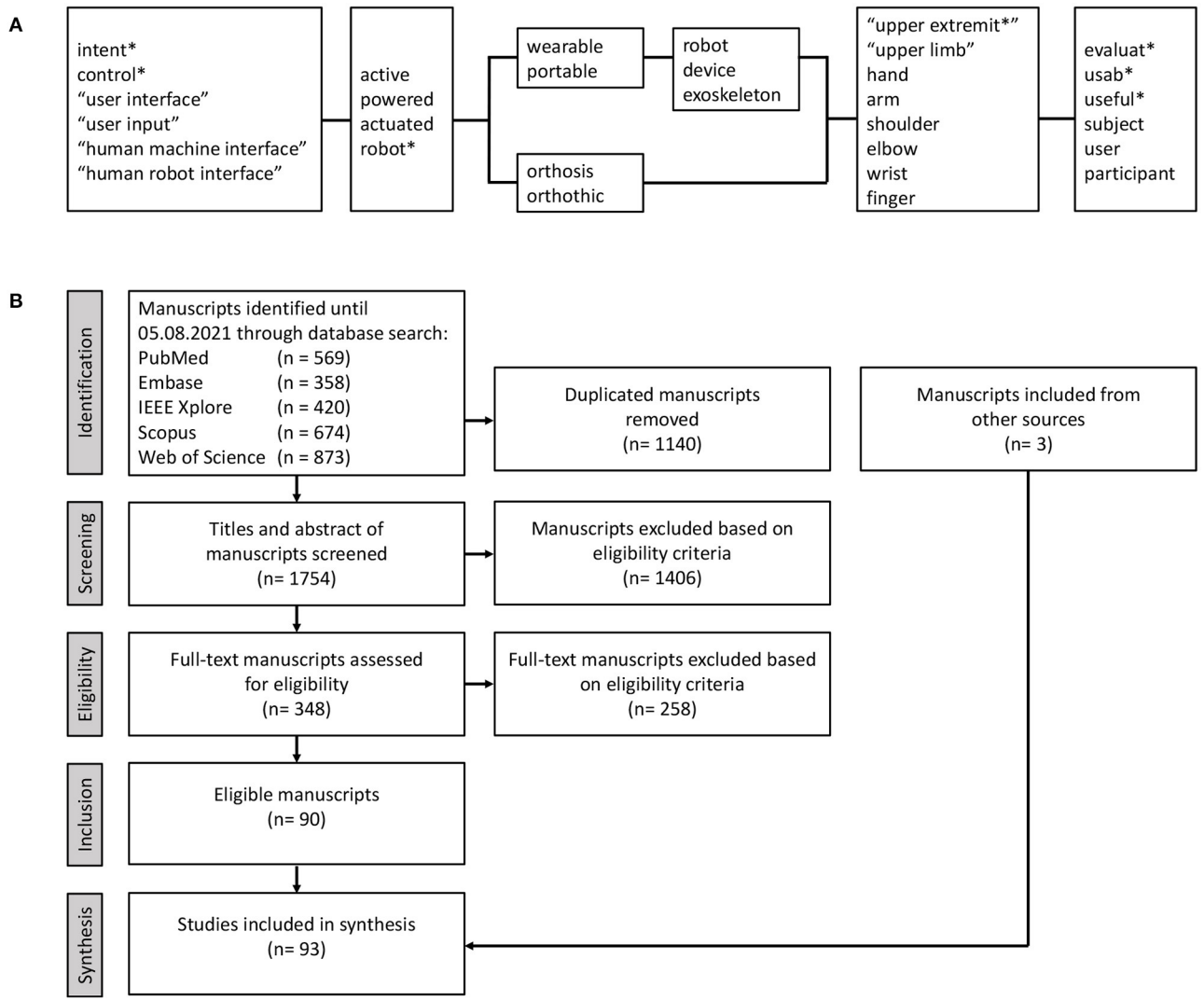

FIGURE 1 | Methods of manuscript search and study selection. **(A)** Exemplary search string used for Web of Science. Parallel blocks denote OR-operator, serial blocks denote AND-operator, asterisk (*) denotes truncation-operator. **(B)** PRISMA-ScR flowchart for the conducted literature search. Flowchart adapted from Moher et al. (2009).

The reasons for choosing these exclusion criteria were either because the focus of the considered manuscript was not within the review targeting user evaluation of IDS (E1, E2, E5, E6), because the methods of the study did not sufficiently reflect the actual intended use of the ULO in daily life, i.e., the validity of the user evaluation results for application in daily life was not given (E3, E4), or because the core information of the study was duplicated, e.g., pilot study and subsequent full study (E7). In case a manuscript discussed an evaluation protocol consisting of multiple methods, of which not all comply with the exclusion criteria (e.g., offline and online assessment of reliability within the same manuscript), the manuscript was included, but only the methods complying with the defined criteria were considered for the data extraction. In case a manuscript did not provide sufficient information to determine its compliance with a specific exclusion criterion, the manuscript was included, provided that it complied with all the other criteria. Since this scoping review aims to provide an overview of all the studies evaluating ULO controlled by an IDS, no critical appraisal was conducted and thus no studies were excluded based on their methodological quality.

Screening of the manuscripts based on these eligibility criteria was conducted by three unblinded reviewers (JG, JD, JTM) using the online systematic review management tool Covidence (Veritas Health Innovation Ltd., Australia). For title and abstract screening, the first half of the manuscripts was screened by two reviewers independently, and a third reviewer was consulted in case of disagreements. Single screening of the second half of manuscripts and subsequent full texts screening was split

between the three reviewers, and a second reviewer was consulted in case of uncertainty.

2.3. Data Extraction

A data extraction form was developed in a spreadsheet software (Microsoft Excel, Microsoft Corporation, USA) and piloted by two reviewers (JG, JD). Subsequent data extraction was conducted in Excel by the leading reviewer (JG) to ensure consistency.

The core part of the data extraction consisted of usability evaluation findings reported in the studies, which were structured according to a list of 12 usability attributes. The international standard ISO 9241-11 defines usability as *"the extent to which a system, product, or service can be used by specified users to achieve specified goals with effectiveness, efficiency, and satisfaction in a specified context of use"* (ISO 9241-11, 2018), whereas in this work, we considered IDS as the *"system, product, or service"* of interest. The 12 usability attributes presumed to be relevant for IDS were selected based on the findings of a recent survey on common practices in usability evaluation of wearable robots (Meyer et al., 2021). For the purpose of grouping information within this review, each usability attribute was also assigned to one of three usability dimensions: "effectiveness" defined as *"the accuracy and completeness with which users achieve specified goals"*, "efficiency" as *"the resources set in relation to the results achieved,"* and "satisfaction" as *"the extent to which the user's physical, cognitive, and emotional responses that result from the use of a system, product, or service meet the user's needs and expectations"* (ISO 9241-11, 2018). The list of usability attributes and the corresponding usability dimensions is shown in **Table 1**. General usability assessments which could not be assigned to a specific attribute were not included in the data extraction since they do not provide sufficiently detailed information to be synthesized.

Besides the usability attributes, the data extraction form included technical information to provide an overview of existing IDS and information about the context of use, i.e., the ULO for which the IDS was used, the target user, and the intended application. Lastly, information about the user evaluation methods used in the studies was extracted, including information about the used test protocol and the number and kind of participants.

TABLE 1 | Predefined list of usability attributes and their definitions applied in regards to IDS.

Group	Attribute	Definition applied
Effectiveness	Reliability	Does the IDS perform its requested functions under stated conditions?
	Robustness	Does the IDS continue to function in the presence of invalid inputs or stressful or changing environmental conditions?
Efficiency	Mental workload	How mentally demanding is the generation of a command?
	Physical workload	How physically demanding is the generation of a command?
	Temporal workload	How much time does the generation of a command take (incl. computational time, excl. practice and classifier training)?
	Learnability	What influence does practice have on the ability to generate a command?
	Ease-of-use	How easy does the user find the generation of a command?
	Cost	What are acquisition and/or maintenance costs (financial or time)?
Satisfaction	Naturalness	How natural does the generation of a command feel to the user compared to unimpaired movement?
	Comfort	How physically comfortable and ergonomic does the user perceive the IDS during use?
	Simplicity of setup	How simple is the setup of the IDS (e.g., to calibrate, or to don & doff)?
	Enjoyability	How much did the user enjoy using the IDS (e.g., in terms of mood, motivation, frustration)?

2.4. Data Synthesis

2.4.1. Synthesis of Assessed Usability Attributes

Depending on the aim of a study, only a subset of usability attributes might be considered relevant by technology developers and was thus included in the study protocol. In order to investigate which usability attributes were assessed the most, the number of studies in which a particular usability attribute was evaluated was determined. An attribute was counted as "assessed," if it was evaluated or discussed quantitatively or qualitatively in a study. Depending on whether a study assessed the usability attribute directly based on the defined user evaluation protocol or indirectly based on the observation or interpretation of the study authors, the collected data was categorized as "data-driven finding" or "indirect finding," respectively. The methods with which each attribute was assessed were summarized and will be described in Section 3.2.

2.4.2. Synthesis of Types of IDS

To classify the IDS, the four-level classification scheme for IDS proposed by Lobo-Prat et al. (2014) was adapted. Following the user-centered scope of this review, we considered the user's body part that generates the command, i.e., the local source of the input signal, as level 1. This source directly relates to the user's residual functional capabilities and thus their ability to use a specific IDS. On level 1, the IDS were assigned to three groups. "IDS sourcing from targeted upper-limb segment(s)" were defined as those related to the physiological execution of the desired movement, e.g., actuation of the finger joints of the ULO initiated by residual movement of the fingers or activation of the finger muscles in the ipsilateral forearm. On the contrary, "IDS sourcing from non-targeted upper-limb segments" were defined as those not relating to the physiological execution of the desired movement but still

sourcing from the upper limb. It should be noted that the "non-targeted upper-limb segment(s)" does not necessarily imply that the source is contralateral to the upper limb targeted by the ULO. For example, actuation of the finger joints of the ULO could be initiated by muscle activation from the ipsilateral upper-arm or from the forearm muscles contralateral to the ULO. "IDS sourcing from other body parts" were defined as all remaining IDS, e.g., sourcing from the brain or the tongue. Levels 2–4 of the classification scheme were defined similarly to Lobo-Prat et al. (2014) as: the corresponding physiological phenomena related to the IDS used (level 2), the corresponding measured signals (level 3), and the used sensors to measure these signals (level 4).

When analyzing the findings from the usability evaluations (Section 3.3), the IDS are discussed on level 2, since the most distinct differences in perceived usability were expected on that level. In the following, each IDS from level 2 are described in three parts: first, by a general introduction of the principle and overall strengths and benefits, second by reviewing studies which used the described IDS, and third, by synthesizing results with respect to usability attribute data extracted from the included studies. For the IDS where no usability attribute data was reported in the studies, this is stated accordingly. Due to the heterogeneity and partially qualitative nature of this data, the results of the synthesis will be described narratively, and IDS are compared to each other only on a qualitative level where possible.

3. REVIEW

3.1. Characteristics of Included Studies

After the full-text screening of 348 manuscripts, 93 eligible studies were identified and included in the data extraction. The flowchart of study inclusion is given in **Figure 1B**. Included studies were published between 2000 and 2021, whereas 50.5% were published since 2018. A condensed version of the data extraction tables, including references to all included studies, can be found in **Supplementary Material 1**. The complete, detailed data extraction table can be obtained from the authors upon request.

An overview of the distribution of the intended scenarios of use of the ULO, as well as the actuated upper-limb segments by these ULO, is given in **Figures 2A,B**, respectively. 83.9% of the ULO were intended to be used as assistive and/or rehabilitative device, whereas the occurrences of these two groups were relatively well balanced. The actuated joints or movements of these ULOs were finger joint(s) (70.9%), elbow joint (24.7%), shoulder joint (16.1%), wrist joint (11.8%), and forearm pronation/supination (1.1%). **Figure 2C** summarizes which scenarios of use were intended for which IDS sourcing from specific body parts (i.e., classification level 1). Assistive applications were targeted in 56.9% of ULO with IDS sourcing from targeted upper-limb segments and in 70.7% of ULO with IDS sourcing from non-targeted upper-limb segments. Rehabilitative applications were targeted in 43.1 and 41.5%, respectively of the same groups. For IDS sourcing from other body parts, those from brain signals were more often targeting rehabilitative applications (58.8%) while those sourcing from eyes, jaw, tongue, and vocal cords were more often targeting assistive applications (62.5%). Most industrial applications were targeted for ULO with IDS sourcing from targeted upper-limb segments (75%).

A distinctive eligibility criterion of this scoping review was the exclusion of studies that did not involve any human participants in the evaluation of the ULO controlled by the specific IDS. On average, 5.044.41 (SD 4.41) participants were involved in the studies, of which 2.07 (SD 3.42) participants belonged to the stated target population. Overall, at least one target user was involved in 40.9% of studies, whereas 46.2% involved only participants not belonging to the target population, and 12.9% did not provide sufficient information to determine whether the participants belonged to the target population.

A total of 28 different IDS were disclosed in the included studies and were organized in **Table 2** according to the proposed four-level classification scheme. Of the 93 included studies, 69 used IDS with sources from the targeted upper-limb segments, 40 used IDS with sources from non-targeted upper-limb segments, and 26 used IDS with sources from other body parts. The total number of 133 exceeds the number of included studies ($n = 93$) as some studies reported more than one and up to four IDS. A total of 14 studies assessed ULOs with multimodal IDS, i.e., multiple different IDS used simultaneously, whereas 20 studies assessed ULOs, which allowed to choose between different IDS and compare performance.

3.2. Usability Attributes and Methods of Evaluation

Out of the twelve usability attributes defined in **Table 1**, the studies assessed on average 1.47 (SD 1.50) different attributes related to the IDS, whereas 31 studies did not assess a single attribute specifically related to the IDS. From all reported assessments of usability attributes, 75.5% were direct data-driven findings. The three attributes related to the IDS which were assessed the most were "reliability" (36.6%), "temporal workload" (29.0%), and "ease of use" (22.6%). "Cost," "naturalness," and "comfort" were the least assessed attributes being reported in only two studies each. Usability attributes assigned to the usability dimensions "effectiveness" and "efficiency" appeared to be more frequently assessed, compared to attributes assigned to "satisfaction." The frequency of assessment of usability attributes along with the distribution of direct data-driven findings and indirect statements is shown in **Figure 3**. The methods of assessing individual usability attributes are further discussed below, in order of decreasing frequency of occurrence in the included studies.

3.2.1. Reliability

Reliability was the most frequently assessed attribute, with all data-driven findings being reported in 35 studies. In the context of IDS, reliability is alternatively also often called accuracy and describes how good an IDS performs its requested functions under stated, non-varying conditions. However, in real-time control, the stated, non-varying conditions are often difficult to adhere to, making a clear differentiation between reliability and robustness difficult.

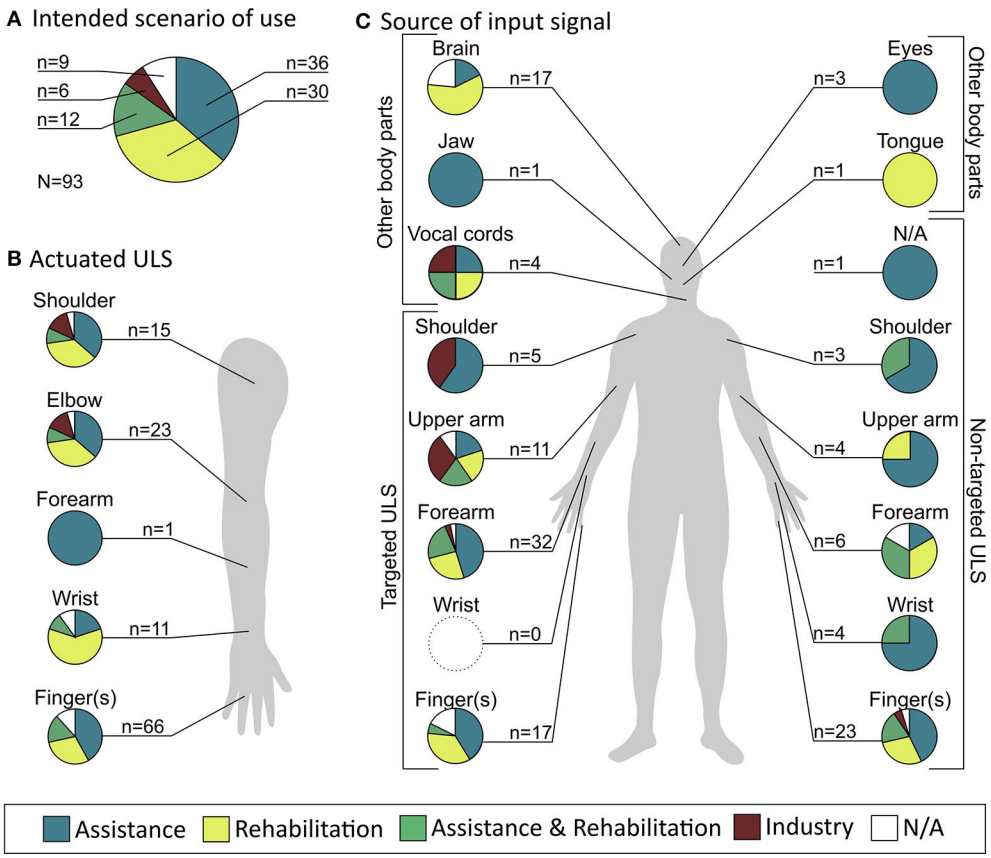

FIGURE 2 | Overview of characteristics of upper limb orthoses (ULO) assessed and sources of input signals. **(A)** Distribution of contexts of use of ULO over all included studies. **(B)** Distribution of contexts of use in relation to the upper limb segment (ULS) actuated by the ULO. **(C)** Distribution of contexts of use of ULO in relation to the source of input signal.

Some studies did report reliability qualitatively based on user feedback (e.g., Song and Chai, 2013). However, most of the included studies did express it as the number or percentage of successes or errors (e.g., Park et al., 2019) or classification accuracy of the IDS (e.g., Lu et al., 2019). Some subdivided these classes further according to the type of success or error (e.g., Zhou et al., 2019), i.e., true/false positives or true/false negatives. Many studies compared their achieved success or error rates to those of other studies to rate their IDS. However, no studies reported a generally accepted target value a good IDS should achieve in terms of reliability.

3.2.2. Temporal Workload

The temporal workload was assessed in 28 studies of which all presented data-driven findings. We defined the temporal workload of an IDS as the time delay between actual user intent and its detection, including the time required for the user to give the input and computational time. Most studies measured temporal workload by task duration (e.g., Zhang et al., 2019) or task speed by means of blocks per minute in the standardized Box and Block Test (e.g., Yurkewich et al., 2020b), therefore not only measuring the actual temporal workload of the IDS, but also including the inherent mechanical delay of the ULO and the time required for conducting the task. This is therefore only a valid option to rate temporal workload if these two parameters are approximately constant, i.e., when used to compare two different IDS used in combination with the same ULO and for the same task. Other studies have only measured the delay as the computational time between signal acquisition and classification or movement onset of the ULO (e.g., Delijorge et al., 2020), or the minimum possible time between two consecutive movements (e.g., Ortner et al., 2011). Some studies rated the temporal workload in term of the participant's subjective perception through non-standardized feedback (e.g., Ngeo et al., 2013), or through the NASA-TLX questionnaire by Hart and Staveland (1988) (e.g., Badesa et al., 2020).

3.2.3. Ease-of-Use

The ease of use was assessed in 21 studies, of which nine were based on indirect findings. Since there is no formal definition of the ease-of-use, for this review, it was loosely defined as how easy the user found controlling the device using the IDS, i.e., it sums up whether they managed to use it with few explanations and low mental or physical workload. In literature, the term "intuitiveness" is sometimes used interchangeably with "self-explanatory" (Mohs et al., 2006), "familiar" or "using readily

TABLE 2 | Classification of intention detection strategies.

			Level 1: Source of input signal																		
			Targeted ULS					Non-targeted ULS						Other body parts							
Level 2: Physiological phenomenon	**Level 3: Signal**	**Level 4: Sensor**	**Finger**	**Wrist**	**Forearm**	**Upper arm**	**Shoulder**	**Not defined**	**Finger**	**Wrist**	**Forearm**	**Upper arm**	**Shoulder**	**Jaw**	**Tongue**	**Vocal cords**	**Eyes**	**Brain**	**Total level 4**	**Total level 3**	**Total level 2**
Muscle activation	EMG	Electrodes	0	0	22	8	5	1	0	0	5	4	2	0	x	x	x	x	47	47	47
Muscle contraction	FMG	Force sensors	0	0	3	1	0	0	0	0	1	0	0	1	x	x	x	x	6	6	6
Isometric force	Exerted force/torque	Force/torque sensors	13	0	6	0	0	0	1	0	0	0	0	0	x	x	x	x	20	20	20
UL movement	Kinematics	IMUs	0	0	1	2	0	0	0	1	0	0	0	x	x	x	x	x	4	5	12
		Load cells	0	0	0	0	0	0	0	0	0	0	1	x	x	x	x	x	1		
	Joint rotation	Bending sensors	4	0	x	x	0	0	0	3	x	x	0	x	x	x	x	x	7	7	
Tongue movement	Magnetic field	Magnet sensor	x	x	x	x	x	x	x	x	x	x	x	x	1	x	x	x	1	1	1
Eye movement	EOG	Electrodes	x	x	x	x	x	x	x	x	x	x	x	x	x	x	2	x	2	2	3
	Corneal reflection	Cameras	x	x	x	x	x	x	x	x	x	x	x	x	x	x	1	x	1	1	
Brain activity	EEG	Electrodes	x	x	x	x	x	x	x	x	x	x	x	x	x	x	x	16	16	16	17
	fNIRS	Optodes	x	x	x	x	x	x	x	x	x	x	x	x	x	x	x	1	1	1	
Speech	Sound	Microphones	x	x	x	x	x	x	x	x	x	x	x	x	x	4	x	x	4	4	4
N/A	Manual trigger	Buttons/switches	x	x	x	x	x	x	15	x	x	x	x	x	x	x	x	x	15	22	22
		Joysticks	x	x	x	x	x	x	4	x	x	x	x	x	x	x	x	x	4		
		Touchscreens	x	x	x	x	x	x	3	x	x	x	x	x	x	x	x	x	3		
Total level 1			17	0	32	11	5	1	23	4	6	4	3	1	1	4	3	17	**132**		
			65					41						26							

The four-level classification scheme was adapted from Lobo-Prat et al. (2014). Columns show the first level (source of input signal), rows show second to fourth levels (physiological phenomenon, signal, sensor). The numbers indicate the number of included studies, which used the corresponding IDS, (x) indicates technically impossible IDS. Total number of included studies per IDS for each level is indicated. ULS, upper limb segment; EMG, electromyography; FMG, force myography; EOG, electrooculography; EEG, electroencephalography; N/A, not applicable. Shades of grey from dark to bright represent four classification levels from 1 to 4.

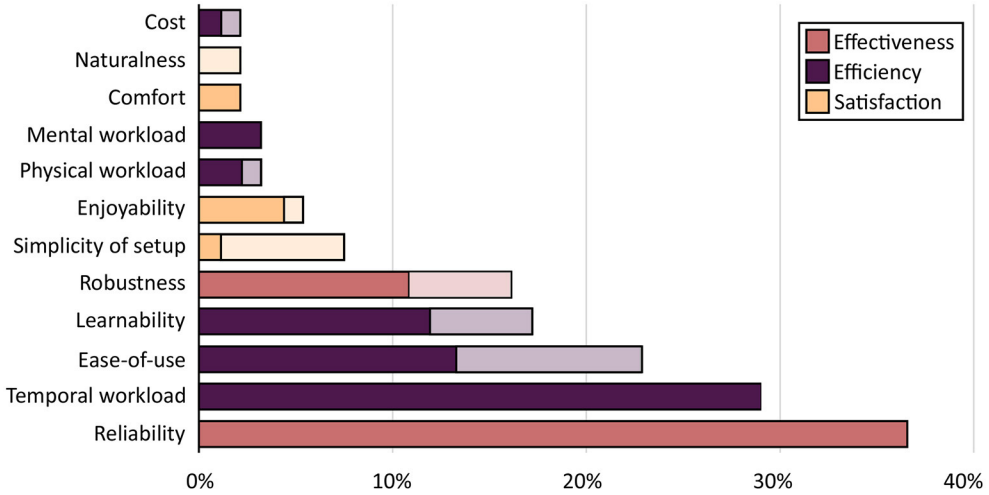

FIGURE 3 | Frequency of assessment of usability attributes. List of usability attributes ranked by the percentage of studies, in which they were assessed. Colors indicate the assigned usability grouping. Dark bar sections indicate "data-driven findings," bright bar sections indicate "indirect findings."

transferred, existing skills" (Raskin, 1994) and thus, in the broader sense, also relating to "easy to use." However, a uniform definition of the term has not been established yet (Naumann et al., 2007). Therefore, for studies reporting "intuitiveness," we interpreted from the given context whether the information was related to ease-of-use.

The indirect findings related to ease of use were mostly based on observations whether the users managed to use the IDS without problems (e.g., Ambrosini et al., 2014a) or without further instructions (e.g., Park et al., 2019). Data-driven findings were based on direct qualitative user feedback (e.g., Xing et al., 2008) or reported quantitatively with different scales and questionnaires including a custom numbered rating scale (e.g., Bermúdez i Badia et al., 2014), Usefulness, Satisfaction, Ease-of-use (USE) questionnaire by Lund (2001), the Quebec User Evaluation of Satisfaction with Assistive Technolgy (QUEST 2.0) questionnaire by Demers et al. (2002) (e.g., Yurkewich et al., 2020a) or the System Usability Scale (SUS) by Brooke (1996) (e.g., Shafti and Faisal, 2021).

3.2.4. Learnability

A total of 16 studies assessed learnability, five reporting indirect statements. The learnability describes how much practice is required to be able to use the IDS appropriately or what influence prolonged use of an IDS has on the achieved performance. The included studies have described the learnability by three different metrics. Most of the studies did report how much practice participants needed until they were able to control the device according to their intent with acceptable performance. For indirect statements, this was done by observation (e.g., Hennig et al., 2020), data-driven findings were supported by measuring the required practice time (e.g., Yurkewich et al., 2020b) or by the participant's subjective perception on the ease of learning on a customized Likert-scale (e.g., Yap et al., 2017b) or as a subcategory on the SUS (e.g., Shafti and Faisal, 2021). Others reported the learning effect, e.g., the improvement of performance, which was observed for the same users after repeated use of the IDS (e.g., Webb et al., 2012). A small number of studies have also investigated learnability by comparing the performance of experienced and inexperienced users (e.g., King et al., 2014).

3.2.5. Robustness

In contrast to the reliability, the robustness describes how an IDS performs under varying conditions, e.g., invalid user inputs, or stressful or changing environments. Some studies did assess the robustness analogously to the reliability by measuring success or error rates under varying conditions, e.g., with changing arm positions (Park et al., 2020), when distracting the participant (Ortner et al., 2011), or when the ULO is used with or without arm support (Park et al., 2019). Others provided a qualitative indication of the robustness of the IDS by identifying factors that do or do not influence its performance (e.g., Siu et al., 2018).

3.2.6. Simplicity of Setup

Simplicity of IDS setup was discussed in seven studies. Six studies reported indirect, qualitative statements related to donning and doffing (Dwivedi et al., 2019), sensor placement (Meeker et al., 2017), or ease of calibration (Pedrocchi et al., 2013). One study assessed the donning and doffing process of the overall system systematically, but not of the IDS specifically (Lambelet et al., 2020).

3.2.7. Enjoyability

Enjoyability was reported in five studies. The enjoyability sums up the user's mood, motivation, or frustration while using the IDS. One study reported enjoyability from indirect statements based on observation of the participants (Delijorge et al., 2020). The other studies reported enjoyability in terms of general qualitative direct user feedback (Ortner et al., 2011), numbered rating scales reporting "perceived fun" (Bermúdez i Badia et al.,

2014), a visual-analog scale rating "mood" and "motivation" (Chowdhury et al., 2018) or frustration as subsection of the NASA-TLX (Badesa et al., 2020).

3.2.8. Physical Workload

The physical workload was assessed in three studies. The reported physical workload provides an indication of how physically demanding the generation of a command is to the user. One study assessed physical demand using the NASA-TLX (Badesa et al., 2020) and one reported qualitative user feedback about the effort of use (Ambrosini et al., 2014a). The third study made an indirect statement about the appropriateness of the IDS in terms of the user's tendency to fatigue easily (Park et al., 2019).

3.2.9. Mental Workload

Three studies assessed mental workload of the IDS. The mental workload describes how much mental/cognitive effort the user perceives or needs to exert while using the IDS. One of the included studies assessed mental demand using the NASA-TLX (Badesa et al., 2020), and two studies assessed the mental fatigue or exhaustion either by subjective comparison to other IDS (Soekadar et al., 2015) or on a visual-analog scale (Chowdhury et al., 2018).

3.2.10. Naturalness

Two studies, both based on indirect statements, assessed naturalness. The naturalness describes how "natural" controlling the ULO by the specific IDS feels, compared to the normal, physiological initiation of the assisted or augmented movements. In contrast to what was described in the "ease-of-use"-section, the term "intuitive" is sometimes also used interchangeably with "natural" or "subconscious" (Lobo-Prat et al., 2014). Therefore, for studies that reported intuitiveness, we interpreted from the given context whether the information was related to naturalness. Both studies described their IDS qualitatively as "intuitive" (Kooren et al., 2016) or "more intuitive" compared to another IDS (Park et al., 2020).

3.2.11. Comfort

Comfort were assessed in two studies, defined as the physical comfort or ergonomics perceived by the users during use. Both studies reported comfort based on qualitative user feedback, either in general (Delijorge et al., 2020), or related to specific aspects related to ergonomics, such as weight or obstruction of movement (Hennig et al., 2020).

3.2.12. Cost

With only two assessments, cost (together with naturalness and comfort) was the least assessed attribute. Costs were defined as the financial effort to acquire or maintain usage of an IDS. However, both included studies discussed only acquisition, either as absolute price of the overall system (Webb et al., 2012) or relative to the performance of the IDS, i.e., cost-effectiveness (Araujo et al., 2021).

3.3. Types of Intention Detection Strategies

3.3.1. Muscle Activation

Using electromyography (EMG), i.e., electric signals generated during muscle activation, was the most commonly used IDS, being used in 40.2% of the studies. Measuring the EMG signal as IDS has clear benefits for applications in daily life. The signal acquisition is relatively easy and feasible with standard commercially available hardware and the emerging use of dry, wireless electrodes allows their integration into wearable armbands such as the Myo armband (Thalmic Labs, Kitchener, Ontario, Canada; Meeker et al., 2017; Mohammadi et al., 2018; Park et al., 2019, 2020; Lambelet et al., 2020; Yurkewich et al., 2020a) or sleeves (Dwivedi et al., 2019), enabling very simple donning and doffing. However, EMG signals also have some inherent limitations. They are not robust against changing electrode placement, the electrical impedance of the skin, sweat, or muscular fatigue (Hameed et al., 2020). Further, for some users, EMG activation patterns might not be sufficiently strong or reproducible for effective intention decoding (Riley and Bilodeau, 2002; Park et al., 2020).

Purely binary or proportional controllers were used to control hand orthoses (DiCicco et al., 2004; Fujita et al., 2016; Dunaway et al., 2017; Lince et al., 2017; Yap et al., 2017a; Fardipour et al., 2018; Wang et al., 2018; Gerez et al., 2019, 2020; Yoo et al., 2019; Bos et al., 2020; Nam et al., 2020; Yurkewich et al., 2020a), and wrist (Yoo et al., 2019; Lambelet et al., 2020; Nam et al., 2020), elbow (Ambrosini et al., 2014a; Bermúdez i Badia et al., 2014; Fujita et al., 2016; Dunaway et al., 2017; Koh et al., 2017; Nam et al., 2020), or shoulder orthoses (Ambrosini et al., 2014a; Fujita et al., 2016; Scheuner et al., 2016; Zhou et al., 2021). Three studies did not provide unambiguous information about the used control method (Pedrocchi et al., 2013; Mohammadi et al., 2018; Rose and O'Malley, 2019). A total of 15 studies used pattern recognition-EMG techniques to control hand orthoses (Ngeo et al., 2013; Kawase et al., 2017; Meeker et al., 2017; Siu et al., 2018; Burns et al., 2019; Dwivedi et al., 2019; Farinha et al., 2019; Lu et al., 2019; Park et al., 2019, 2020; Secciani et al., 2019; Zhang et al., 2019), and wrist, elbow, or shoulder orthoses (Kiguchi, 2007; Kawase et al., 2017; Kilic, 2017; Lotti et al., 2020). To do so, up to 12 EMG channels were used (Kiguchi, 2007), controlling up to a maximum of six different states (Dwivedi et al., 2019; Lu et al., 2019; Zhang et al., 2019). Various studies reported conventional, i.e., binary or proportional, EMG control as being easy to understand or use (Gerez et al., 2019; Yoo et al., 2019; Yurkewich et al., 2020a). Yurkewich et al. (2020a) further reported an average reliability of 84.7% (n = 9, stroke) to control three states of a 1-DOF hand orthosis using the Myo armband with eight electrodes. Bos et al. (2020) found a strong training effect in a force tracking task using a proportionally controlled 1-DOF hand orthosis (n = 1, duchenne muscular dystrophy). For pattern recognition-EMG techniques, primarily, reliability, robustness, and temporal workload were reported. Siu et al. (2018) determined how much faster the ULO can be controlled by EMG compared to exerted forces. They found average anticipation times, i.e., the time that EMG detects intent earlier than the increase of pressure measured at the thumb,

between 190 and 290 ms. Lotti et al. (2020) achieved a delay below 53.8 ms in 95% of trials, also suggesting that this IDS might be faster than other approaches based on interaction forces. The reported reliability varied largely between and within studies from 40% (six states, $n = 1$, stroke; Lu et al., 2019) up to 96.4% (six states, $n = 6$, neurologically intact; Zhang et al., 2019). The achieved reliability has been shown to depend on a number of factors, e.g., chosen classifier (Dwivedi et al., 2019), impairment of the subject (Lu et al., 2019), or co-activation of surrounding muscles (Park et al., 2019). Although some studies have shown very high reliability, this large variability and dependence on many factors indicate that pattern recognition techniques might not yet be robust enough for applications in daily living. For the other studies, no relevant usability attributes related to this IDS were reported.

3.3.2. Muscle Contraction

Various approaches have been explored to measure mechanical muscle contraction: either by means of low-frequency vibrations of the muscle fibers, i.e., mechanomyography (MMG) (Courteville et al., 1998; Ibitoye et al., 2014), or by measuring a change in muscular stiffness patterns, i.e., force myography (FMG), also referred to as kinetic imaging, muscle pressure mapping, pressure distribution mapping, or tactile myography (Xiao and Menon, 2019). The operating principle and target application of FMG is very similar to EMG. Therefore, these IDS share some benefits, i.e., physiological operating principle and the possibility to integrate the sensors into wearables (Kudo et al., 2014; Dwivedi et al., 2019), but also related inherent limitations, i.e., sensor placement or muscular fatigue. Sensors mechanically measuring the muscle contraction are robust to moisture and not susceptible to electromagnetic noise (Fajardo et al., 2019; Xiao and Menon, 2019).

No studies were found using MMG, but six studies used FMG as IDS for ULO. Dwivedi et al. (2019) integrated five resusable FMG sensors and three EMG sensors into a textile sleeve to differentiate between six grasp types of a soft robotic glove. Yap et al. (2016) integrated three FMG sensors into a textile band worn on the contralateral forearm to differentiate between finger flexion and extension. Moromugi et al. (2013) and Kim et al. (2012) used pressure sensors on the fore- or the upper arm to control one DOF of a hand or elbow orthosis, respectively. Fajardo et al. (2019) presented a system using two optical fiber sensors which measure the muscle deformation by the displacement of the fibers. A special application of FMG as IDS was presented by Kudo et al. (2014), where they used FMG signals from the temporalis muscle. They integrated soft force sensors into a headphone-like interface to trigger the grasp of a 1-DOF hand orthosis.

Dwivedi et al. (2019) achieved classification accuracies above 87% for six grasp types, requiring $<0.12s$ processing time ($n = 2$, impairment not reported). Yap et al. (2016) compared the temporal workload in terms of task time between using a button and FMG, where they found a 2% higher task time for FMG ($n = 1$, neurologically intact). For the remaining studies, no data about the usability of their IDS was reported.

3.3.3. Upper Limb Movement

Intention can be interfered from joint rotation or kinematics of upper limb segments, allowing natural and easy operation. However, this IDS depends on sufficient residual upper-limb function, thus being primarily applicable for devices targeting augmentation of neurologically-intact users, or orthoses to support people with limited, but residual upper limb functionality. For people with more severe impairments or full paralyses, these IDS are not a feasible alternative.

Seven studies used bending sensors to detect finger (Ab Patar et al., 2014; Popov et al., 2017; Xiloyannis et al., 2018; Park et al., 2019) or wrist motion (Kaneishi et al., 2019; Rose and O'Malley, 2019) to control hand orthoses, or wrist motion to control a shoulder-elbow-orthosis (Koo et al., 2009). Four studies detected residual upper limb movement by using inertial measurement units (IMUs) attached to a segment of the upper limb. Song et al. (2012) and Wang et al. (2020) attached IMUs to the forearm and the upper arm to control elbow and shoulder orthoses, respectively. In both cases, the initiated movement measured by the IMU was directly converted to the actuated movement of the ULO. Yurkewich et al. (2020b) attached a single IMU to the dorsal side of the hand and triggered opening and closing of a 1-DOF hand orthosis when the rotational velocity of the hand exceeded a predefined threshold. Zhou et al. (2021) used kinematics measured by IMUs at the upper arm and the trunk to control a 1-DOF industrial shoulder exoskeleton. Park et al. (2020) measured shoulder movement (i.e., a shrug) using a shoulder harness with integrated load cell. Although perceived as less natural than EMG, they presented this IDS as an alternative for users who can't modulate sufficient EMG signals.

Ab Patar et al. (2014) and Koo et al. (2009) both qualitatively reported ease of use of the IDS. Yurkewich et al. (2020b) compared their IMU-based strategy to a conventional button, where they found lower temporal workload, but also longer practice needed and lower reliability than for the button ($n = 11$, stroke). Five participants reported that they would prefer the IMU- over the button mode, if the former would work more reliably. Zhou et al. (2021) compared their IMU-based strategy to control by threshold-based EMG. They found the former to be more reliable and robust, but slightly slower than the EMG based method ($n = 8$, neurologically intact). The remaining studies did not present any relevant usability attributes related to this IDS.

3.3.4. Isometric Force Generation

Similar to joint rotation or UL kinematics, the intent can be detected by measuring isometric forces when initiating a movement of the upper limbs. Since the initiation of the desired motion is (partly) restricted by the mechanical structure of the ULO, isometric forces or torques will be measurable between upper limb and ULO or between ULO and the physical environment. However, same as for IDS based on upper limb movements, this IDS depends on sufficient residual upper-limb function.

In the case of hand orthoses, force, or torque sensors were attached to the tips of the actuated fingers to control grasping proportionally or by a threshold-based trigger (Xing et al., 2008;

Song and Chai, 2013; Heo and Kim, 2014; Ma et al., 2016; Prange-Lasonder et al., 2017; Chowdhury et al., 2018; Siu et al., 2018; Triolo et al., 2018; Xiloyannis et al., 2018; Park et al., 2019; Zhou et al., 2019; Hennig et al., 2020; Sandison et al., 2020). Hong et al. (2019) have triggered hand orthosis opening and closing by a strain gauge attached to the non-actuated ipsilateral thumb. For wrist, elbow or shoulder orthoses, the sensors were placed between the respective upper arm segment and mechanical structure of the ULO (Sasaki et al., 2005; Kiguchi, 2007; Lee et al., 2008; Yonezawa et al., 2013; Kooren et al., 2016; Kapsalyamov et al., 2019).

Using a strategy where the hand orthosis closed when the pressure between finger tips and objects to be grasped exceeded a predefined threshold, Zhou et al. (2019) and Hennig et al. (2020) found false positive rates of 9.9% (n = 3, spinal cord injury) and 6.9% (n = 3, neurologically intact), respectively. Other studies reported qualitatively that the IDS was intuitively controlled (n = 1, neurologically intact; Kooren et al., 2016), easy to use (n = 3, neurologically intact; Xing et al., 2008), and that the sensors directly embedded in the ULO allow for quick and easy setup (Sandison et al., 2020). Park et al. (2019) compared multimodal control (pattern recognition-EMG, pressure sensor on thumb, bending sensors on each finger) to pure EMG control of a 1-DOF hand orthosis and found higher reliability but higher temporal workload for the multimodal control when used without passive arm support (n = 4, stroke). For the other studies, no relevant usability attributes related to this IDS were reported.

3.3.5. Brain Activity

Brain-computer interface (BCI) research has been a focus of interest for the past decades, maturing the technology from simple communication devices in controlled laboratory environments to more practical application for rehabilitation (Mane et al., 2020) or assistive technologies in daily life (Millán et al., 2010; Kübler, 2020). For example, at the CYBATHLON 2016, pilots used four commands (i.e., three active commands and one "rest" command) to maneuver a BCI-controlled avatar through a virtual racetrack (Riener, 2016; Novak et al., 2018). Undeniably, the most significant advantage of BCIs is that they do not rely on any residual motor control. In the most severe case of paralysis, for people with total locked-in syndrome, a neurological disorder that results in a complete inability for any muscular movement, BCIs represent the sole viable approach for communication and interaction with their surrounding (Kübler, 2020). Still, it has been shown that BCIs fail to correctly detect the desired state for an estimate of 20% of people, presumably due to the complete inability of the users to modulate respective brain signals, so-called BCI illiteracy (Allison et al., 2010; Blankertz et al., 2010). This apparently inevitable limitation effectively excludes a large subset of potential users of BCI. In terms of daily life applicability, the rather complicated setup and hardware required might not yet be sufficiently easy to use for users without extensive technical knowledge (e.g., calibration or donning and doffing).

The most common non-invasive technique to measure brain activity is electroencephalography (EEG), i.e., using electrodes placed on the scalp to measure the electrical activity of groups of nerve cells from the cerebral cortex. For multichannel measurements, arrays of electrodes, e.g., incorporated in wearable caps, are used to ease donning and doffing and ensure the precision of placement (Teplan, 2002). On the highest level, BCIs can be grouped into endogenous and exogenous techniques. In endogenous techniques, the subject can actively operate the BCI at free will by performing (motor execution) or imagining to perform (motor imagery) a specific task. A meta-analysis by Hétu et al. (2013) has shown that motor imagery activates fronto-parietal, subcortical and cerebellar regions of the brain. However, although there are some regions which are involved in motor execution as well as motor imagery, the latter does not consistently activate the primary motor cortex (Hétu et al., 2013). Therefore, a clear distinction between these two strategies is required. In contrast, in exogenous techniques, the brain activity elicited by external stimuli is used to operate the BCI (Nicolas-Alonso and Gomez-Gil, 2012). These technique use event-related potentials (ERP) based on changes in the EEG signal evoked in response to external sensory, motor, or cognitive events (Sur and Sinha, 2009), e.g., focusing on flickering icons on a screen (Pedrocchi et al., 2013), or steady-state visually evoked potentials (SSVEP), based on EEG response evoked by visual stimuli at specific frequencies (Guger et al., 2012), e.g. focusing on two light-emitting diodes flickering at different frequencies (Ortner et al., 2011).

From all included studies, 16 used EEG-based systems based on motor imagery (Pfurtscheller et al., 2000; Webb et al., 2012; Xiao et al., 2014; Soekadar et al., 2015; Bi et al., 2017; Cantillo-Negrete et al., 2018; Kapsalyamov et al., 2019; Zhang et al., 2019; Badesa et al., 2020; Araujo et al., 2021), motor execution (Fok et al., 2011; King et al., 2014; Lee et al., 2017; Chowdhury et al., 2018), SSVEP (Ortner et al., 2011), or ERP (Pedrocchi et al., 2013; Delijorge et al., 2020) to control the ULO. One included study by Lee et al. (2017) exploited brain activation not directly by EEG, but indirectly by measuring hemodynamic responses, using functional near-infrared spectroscopy (fNIRS), i.e., the varying concentration of oxygen in the blood in activated nerve cells in the cerebral cortex (Naseer and Hong, 2015). They used an fNIRS-setup in a motor-execution study to trigger the opening and closing of a 1-DOF hand orthosis. All BCI studies differentiated only between two states, e.g., "open/close" or "confirm/reject."

From the 17 studies, 15 assessed reliability, achieving classification accuracies in a controlled laboratory environment between 70% (n = 8, neurologically intact; Cantillo-Negrete et al., 2018) and 91.5% (n = 1, neurologically intact; Araujo et al., 2021). However, the variance in performance could not be traced back to an individual factor, but may be influenced by many. The included studies varied largely in terms of, e.g., the number and type of electrodes used [from one (Ortner et al., 2011) up to 40 (Zhang et al., 2019)], the type of signal modulation (motor imagery, , motor execution , SSVEP , or ERP), unrejected motion artifacts, or the chosen classification approach. However, BCI performance also largely depends on the user's ability to modulate brain signals of sufficient quality (Allison et al., 2010). Practice and experience of the user are widely considered as influential aspects to promote BCI performance (Millán et al.,

2010), as underlined by Webb et al. (2012), and King et al. (2014) in their motor imagery-based study who both showed higher accuracies in the second session (n = 4, neurologically intact) or for BCI-experienced compared to BCI-naive users (n = 6, neurologically intact), respectively. On the contrary, Ortner et al. (2011) did not find differences in reliability between experienced and naive participants and between sessions in an exogenous application (n = 6, neurologically intact). Ten studies further assessed the temporal workload of EEG-based BCIs in the order of 2–10 s (Ortner et al., 2011; Webb et al., 2012; King et al., 2014; Xiao et al., 2014; Bi et al., 2017; Zhang et al., 2019). The fNIRS-motor execution study by Lee et al. (2017) reported 78% classification accuracy and measured time from signal acquisition to movement onset as 5.84 ms (n = 6; neurologically intact).

3.3.6. Tongue Movement

Movement of the tongue has been used to control computers or assistive devices for people with severe motor disabilities (Struijk, 2006). In general, since there is no evident natural relation between tongue- and upper-limb movement, users need to learn which inputs result in the desired actions, requiring high initial mental effort. Many conditions leading to upper-limb impairment do not affect tongue movement, making the approach feasible for a broad group of target users with impaired upper-limb function. However, the need for a distinctive tongue movement makes using the device and talking simultaneously impossible, potentially restricting the use for some applications in daily life.

Tongue movement was used in only a single study. Kim et al. (2013) used a headset that positions four magnetic sensors near the user's cheek to trace the movement of a small magnetic tracer temporarily glued to the tip of the user's tongue. The position of the tracer in the oral cavity was then mapped to the angle of an actuated 1-DOF wrist orthosis for rehabilitation. The study compared three control methods (tongue movement binary up/neutral/down, proportional left/right, or proportional anterior/posterior) in a trajectory tracking task, where participants achieved highest tracking accuracies with the proportional left/right control (n = 3, neurologically intact).

3.3.7. Eye Movement

Eye movement plays a crucial role in human motion planning by gathering information about the object or the environment to be manipulated before initiating the movement (Land, 2006). Visual input, e.g., from tracking the user's eye motion or gaze point, can thus be used to guide the movement of the upper limb supported by the ULO for reaching or grasping tasks (Cognolato et al., 2018). Since most neurological deficits resulting in limited upper limb functionality do not affect eye movement, eye-tracking is a feasible IDS for a broad target population. Different eye-tracking techniques exist, two prominent examples being video-oculography, measuring the position of the eye by the corneal reflection with video cameras or electrooculography (EOG), i.e., measuring the difference in the electrical potential between the retina and cornea through electrodes placed in the area around the eye (Barea et al., 2002). The natural relationship between eye movement and movement intention and comparably simple calibration methods (Pedrocchi et al., 2013) makes eye movement-based IDS easy to learn and to use to control ULO. However, an inherent challenge of this IDS is to differentiate between non-specific visual scanning and actual movement intent. Thus, eye-tracking is often used in combination with other IDS.

Three of the included studies used IDS based on eye movement. Soekadar et al. (2015) proposed an EOG-EEG-based system, where the users could look to the left or to the right to approve or reject the EEG-based movement decisions. Zhang et al. (2019) used EOG to detect eye movements to the left or right and double blinks to select between two grasp types or switch between different multimodal IDS (EOG, EMG, or EEG). The third included study, Shafti and Faisal (2021) used an IDS involving corneal reflection measurements using eye-tracking glasses and object recognition. They triggered the movement of the ULO when the user fixated a specific area of the object to be grasped.

When using EOG in combination with EEG, Soekadar et al. (2015) found a significant improvement in reliability and participants reported lower mental workload and higher ease-of-use, compared to only using EEG (n = 5, neurologically intact, n = 1 brachial plexus injury). Zhang et al. (2019) found that, after a training phase of under 2 min, participants were able to use the EOG-based IDS with an accuracy of 94.2% and an average temporal workload of 1.2 s per action (n = 6, neurologically intact). For the object recognition technique used by Shafti and Faisal (2021), they achieved a 96.6% success rate at first attempt and all participants rated learnability and ease-of-use between 3 and 5 out of five points on the SUS (n = 5, neurologically intact).

3.3.8. Speech

Nowadays, using voice control is predominantly known for controlling consumer electronics such as smartphones or home automation systems. However, it has also been used in medical technologies such as wheelchairs (Simpson and Levine, 2002), surgical robots (Zinchenko et al., 2017), or ULO. Similar to eye movement, voice control is feasible for a broad target population with a wide range of impairments, as long as speech is not drastically affected. The number of distinguishable states is theoretically infinite, practically limited only by the computational power, the used software, and the potential need for internet connectivity for recognition. However, in a noisy environment with interfering sources of sound or voices, the performance accuracy may be affected. For other specific scenarios, e.g., in an otherwise quiet environment such as the theater or during spoken conversations with other people, some users may find the need to pronounce distinct words disturbing.

Voice control was used in four studies to trigger the movement of the ULO, where the user needed to pronounce a specific word to actuate three (Ochoa et al., 2009; Kim et al., 2018), six (Dalla Gasperina et al., 2019), respectively seven (Wang et al., 2018) states of the ULO. Each word was assigned to a specific action of the ULO, e.g., corresponding to opening and closing of a hand orthosis (Ochoa et al., 2009) or controlling the position end-effector of a shoulder-elbow-wrist exoskeleton by words

corresponding to the six main directions in the cartesian space (Dalla Gasperina et al., 2019). Wang et al. (2018) is the only study assessing usability aspects of voice control. They found correct recognition rates above 94% with recognition times between 47 and 50 ms (n = 2, impairment not reported).

3.3.9. Manual Triggers

Manual triggers, i.e., buttons, joysticks, or touchscreens, are often the first IDS of choice for ULO. Most users are accustomed to the use and look of these interfaces since these are commonly known from other conventional devices in daily life. Although the relationship between the operation principle of these IDS and their initiated action is not natural, they are mostly self-explanatory and require minimal to no training or calibration. They are generally easy to use and provide high reliability and robustness since they are not dependent on any physiological signal or complex processing. The number of states or actions of the ULO can be increased arbitrarily, e.g., by increasing the number of buttons, however only at the expense of increased cognitive workload for the user. Manual triggers are commercially available in many variants, and can be placed anywhere, e.g., directly on the ULO, on a body part of the user, or on the table, enabling easy adaptability to the users' capabilities. However, using touchscreens, joysticks, and—depending on their size and placement—buttons usually requires some residual function and movement accuracy in the upper limbs from the users. Further, using an upper limb segment—in most cases the fingers or the hands—to control the trigger restricts their use for bimanual or simultaneous tasks, which considerably limits the applicability in daily life tasks.

In 21 studies, conventional manual triggers such as buttons/switches (Ochoa et al., 2009; Pedrocchi et al., 2013; Ambrosini et al., 2014a; Yap et al., 2016, 2017a; Meeker et al., 2017; Fardipour et al., 2018; Otten et al., 2018; Butzer et al., 2019, 2021; Farinha et al., 2019; Correia et al., 2020; Gerez et al., 2020; Muehlbauer et al., 2021), joysticks (Hasegawa and Oura, 2011; Dalla Gasperina et al., 2019; Ismail et al., 2019; Tiseni et al., 2019), or touchscreens (Yap et al., 2017b; Mohammadi et al., 2018; Sandison et al., 2020) have been used.

Presumably due to the simplicity of these manual triggers and the previous familiarity of most users with them, none of these studies assessed usability attributes specifically only related to these IDS. Instead, many of the included studies used these inputs as baseline to compare to alternative IDS, such as EMG or IMU-based systems (Ambrosini et al., 2014a; Yap et al., 2016; Meeker et al., 2017; Yurkewich et al., 2020b). Other studies used them in combination with other IDS to control only a subset of actions, e.g., to select grasp type before using a different IDS as trigger (Gerez et al., 2020).

4. DISCUSSION

This scoping review provides a comprehensive overview of studies evaluating non-invasive IDS in combination with ULO for applications in daily life. Further, it describes methods of usability evaluation used in these studies. By including only studies that involved human participants in the evaluation, a focus was set on the appropriateness of the IDS from a user point of view. The basic operation principles, as well as the usability of the proposed IDS, were reviewed and discussed. In addition, evidence of their appropriateness for different target users, type of devices, and usage scenarios were gathered, considering predominant usability attributes. This work extends existing reviews in the field (Lobo-Prat et al., 2014; Chu and Patterson, 2018; du Plessis et al., 2021) by refreshing the current state of the art in IDS (as reflected by more than half of the included studies being published within the last 3 years), as well as by analysing these under a different angle, giving less priority to the technical aspects, but focusing on the usability evaluation of IDS with real users.

4.1. Considerations When Selecting an Appropriate IDS

4.1.1. IDS Presented in This Scoping Review

The included studies revealed the breath of IDS that were used to control ULOs in the literature. On the level of the physiological phenomenon (level 2), IDS were presented based on muscle activation, muscle contraction, force exertion, residual upper limb movement, brain activity, tongue and eye movement, speech, and manual triggers. A previous review conducted by Lobo-Prat et al. (2014) investigated IDS for all active movement assistive devices such as prostheses and orthoses for the upper and lower limbs or powered wheelchairs. They presented some IDS which were not found in the included studies of this review: based on brain activity [magnetoencephalography (MEG), functional magnet resonance imaging (fMRI)], muscle contraction [MMG, sonomyography (SMG)], and head movement. Some of these IDS are not suitable for ULO since they are either not wearable (fMRI, MEG) or too cumbersome to use (SMG) (Lobo-Prat et al., 2014). MMG however, although it has been used only rarely and primarily in upper limb prosthetic control so far (Silva et al., 2005; Woodward et al., 2015), might be a viable option for ULO as well. It was already used by Antonelli et al. (2009) to control lower limb orthoses, allows wearability, and has similarities in signal acquisition and processing to EMG and FMG. IDS based on head movement are primarily used for powered wheelchair control (Kupetz et al., 2010; Solea et al., 2019). However, this IDS is primarily used for people for whom head movement is one of the sole possible movements. Thus, although generally possible, this might not be the most desirable option to control ULOs.

Further, there are other studies presenting IDS which were neither presented in Lobo-Prat et al. (2014) nor in this review. Kojima et al. (2017) and Cunningham et al. (2018) presented a supernumerary robotic arm and thumb, respectively, which were controlled through toe or ankle motion. To control flexion and extension of a wearable supernumerary finger, Hussain et al. (2017) embedded EMG sensors in a baseball cap to detect EMG signals from the frontalis muscles, which are contracted by moving the eyebrows upwards. Similarly, Kocejko (2017) used binary one-channel EMG to detect contractions of the temporal is muscle while tightening the jaw to select from three gestures of an arm prosthesis. Commercially available

sip-and-puff systems were used for wheelchair control (Grewal et al., 2018) or communication devices (Jones et al., 2010) only. Although all these IDS are relatively rarely used due to their limited applicability to broader contexts of use, these could be additional options for specific ULO beyond the ones presented in this work.

4.1.2. Avoiding the Restriction of Other Body Functions

This review has identified the strengths and weaknesses of IDS used in combination with ULO in specific contexts of use. As depicted by the vast majority of studies using IDS sourcing from the targeted upper-limb segments, the use of signals related to the physiological movement execution, whenever possible, is preferred by most users and researchers. The rationale behind linking the actual intention to its physiological motor consequence is two-fold: the IDS does not restrict other body functions, and neuroplasticity, i.e., the reorganization of the central nervous system in response to intrinsic or extrinsic stimuli (Cramer et al., 2011), may be enhanced. Therefore, for contexts of use where recovery is considered realistic and the primary target, using physiological signals as IDS may promote a rehabilitative effect. Based on this, we expected that other IDS based on non-physiological movement, e.g., manual triggers or IDS sourcing from other body parts than the targeted upper-limb segments or the brain, were primarily considered when the physiological signals are either not sufficiently strong, or if the ULO targets assistive rather than therapeutic applications. The found distribution of the intended scenario showed tendencies which strengthen this assumption, however they were not sufficiently strong to make an unambiguous conclusion.

By far, the IDS exploited the most is EMG. However, EMG showed some challenges and inherent limitations, currently restricting its transfer to real-life applications. These limitations encouraged researchers to explore alternative IDS, such as mechanically measuring muscle contraction or residual movement. However, evidence demonstrating an absolute superiority of these IDS over EMG is still scarce. For users who do not have sufficient residual muscle activity and motor function in their upper limbs, IDS sourcing from other body parts are an alternative. The wide variety in terms of the source of the signal offers adaptability to the user's individual capabilities and preferences. However, except for inputs from the brain, these IDS do not resemble the physiological movement generation. Thus, IDS sourcing from other body parts than the ULO are not perceived as natural and require the users to learn which input—usually a specific motion or activation of a muscle—results in the desired movement. Further, their biggest drawback is that they can only be used at the expense of restricting other body functions during use. Therefore, for these IDS, it is crucial to individually weigh the impact such a restriction might have against the potential benefit the ULO would provide in the intended usage scenario. Unquestionably, in theory, BCIs offer a vast potential as the most natural and most broadly applicable IDS. However, the current state of non-invasive BCI research for ULO has not yet managed to overcome the usability hurdle (i.e., in terms of robustness, temporal workload, and simplicity of setup) to be used in real applications outside the controlled laboratory environment.

4.1.3. Balancing Performance and Complexity

In many studies, the rationale behind the usability attributes assessed is not always explicitly or sufficiently stated. While some requirements are unambiguously given by the application (i.e., number of states to be controlled or functional capabilities by the targeted user), others might call for a more in-depth focus on the user and the intended usage scenario. Unfortunately, in most studies, information on the latter is provided on a very high level or lacks completely. A central decision when selecting an appropriate IDS is the trade-off between high performance (i.e., high reliability and robustness) and low complexity (i.e., high ease of use and learnability and low workload for the user). As a guiding principle, the IDS achieving the highest usability are those which are as simple as possible but as complex as needed to achieve the required performance. In commercial devices, mostly incorporating a relatively low number of states, presumably simpler IDS (e.g., push-buttons or conventional EMG control methods) are currently used. The same reliance on simpler solutions can also be observed for assistive technologies provided to persons with sensorimotor disabilities for use in daily life. However, in-depth evaluations of the usability of simple IDS might not have been considered worth investigating by scientific researchers. This potential bias toward more complex IDS leads to the speculation that simpler IDS are underrepresented in the field (and in this review) in comparison to their apparent high usability for commercial devices. However, especially for applications requiring multiple states to be controlled simultaneously, the trade-off between complexity and performance is often harder to find. The required performance seems to be very challenging to achieve with the choice of a single IDS, which is usually simple but only applicable to a low number of states or very complex itself, i.e., pattern recognition techniques in EMG or BCI research. Thus, many studies combined multiple different IDS for a single application. Such multimodal approaches have been successfully implemented to improve the overall functionality of the IDS. Some studies used multiple IDS to increase the reliability of controlling a single state (e.g., opening/closing of a 1-DOF hand orthosis using EEG and EOG; Soekadar et al., 2015), while others used multiple IDS to simultaneously control one state each (e.g., selection of movement type by buttons and movement trigger by EMG signals; Gerez et al., 2020). However, although each implemented IDS separately might be comparably simple to use, simultaneously providing inputs sourcing from different body parts may become cognitively challenging. Although not included in the scope of this review, promising approaches to tackle this issue are shared-control methods (Losey et al., 2018). These methods combine high-level control by the user with autonomous low-level control by the robots, e.g., through camera-based object recognition (Markovic et al., 2015; Fajardo et al., 2018) to relieve the physical and mental burden from the users, while still leaving them in control.

4.2. Considerations When Evaluating an IDS

4.2.1. Tendency to Prefer Objective Over Subjective Attributes

By determining the frequency of assessment of the predefined usability attributes, we found that the majority of evaluations focused on attributes which could be evaluated objectively and quantitatively, e.g., reliability or temporal workload. Although specifically only including studies with human participants in this review, subjective or qualitative aspects, often acquired from user feedback or observation, were reported less frequently or not in a data-driven format. Overall, attributes assigned to the groups "effectiveness" or "efficiency" tended to be assessed more frequently than those assigned to the group "satisfaction." Although this finding has to be treated with caution due to the unbalance in the total number of attributes per group, this might lead to the assumption that most evaluations highlighted rather technical than strongly user-focused aspects of the IDS. This coincides well with the initial observation of the technical focus of many existing literature reviews and our recent survey on wearable robotics usability evaluation (Meyer et al., 2021). While the technical performance is unarguably an essential prerequisite for meaningful use of an IDS, the impact of usability attributes with a stronger focus on the user such as satisfaction or perceived physical or mental workload should not be neglected. As an example, a systematic review investigating user needs for assistive technologies for the upper limbs after stroke by Ommeren et al. (2018) listed—among other attributes—comfort, donning/doffing, and setup (i.e., "simplicity" according to this review's definition) as relevant themes to achieve higher levels of user satisfaction and device acceptance. Yet, comfort and simplicity were only assessed in 3 and 7%, respectively, of the studies included in this work. The lower frequency of reporting qualitative attributes than quantitative ones could result from a publishing bias. Quantitative outcomes are often objectively verifiable, comparable and allow statistical analysis, allowing "high quality" evidence. However, in subjective user evaluations, only few attributes are *per se* quantitatively measurable. Therefore, many studies quantify the qualitative findings by assigning to them a ranked numeric value, allowing statistical analysis and comparability to other studies. However, the problem of subjectivity remains and thus potentially lowers the research interest in these findings. In summary, all these observations point to an important realization: the frequency of reporting of a usability attribute might not necessarily correlate with its importance for the users and the application of the IDS in daily life.

4.2.2. Determining Appropriateness of an IDS

A recurring challenge when selecting an appropriate IDS is the fact that most studies compare their results to other studies to demonstrate superiority, but lack a clear benchmark to specify whether their results are actually good (and thus the IDS appropriate) or not. An illustrating example is the classification accuracy in EMG. While unarguably an accuracy of e.g., 90% is better than 86%, if achieved under comparable conditions, it is not clear whether 90% is sufficient. Thus, to properly be able to rate the acceptability of the reported accuracy values and of the IDS, an appropriate benchmark for acceptance should be defined. For brain-computer communication such as cursor control, Kübler et al. (2006) assumed a minimally required threshold of 70% accuracy. However, in ULO, erroneous actions can lead to serious safety issues, assumingly increasing the required threshold. This question was also discussed in the "hot coffee problem" (Ajiboye and Weir, 2005), a thought experiment describing a system with 99% accuracy. In a task-oriented manner, this would mean that users would spill hot coffee over themselves in 1 out of 100 trials—a safety risk that seems unacceptably high. Following that logic, an acceptably reliable and thus safe IDS would need to achieve performance accuracies similar to the non-impaired limb (Ajiboye and Weir, 2005), a value that has not yet been experimentally determined. Unfortunately, such benchmarks for usability attributes are impossible to define in a generalized manner since they largely depend on the context of use of the IDS. Instead, they would need to be customized to one specific context of use, e.g., by consulting target users. In addition to the common approach to compare the results to other studies or IDS, such benchmarks would allow for a standalone and objective rating of the appropriateness of an IDS for the targeted context of use.

4.3. Limitations of This Work

One limitation of this work is also one of the biggest hurdles in the field of usability evaluation of wearable robots in general: there's a lack of a common understanding or standardized definitions of usability attributes. Thus, the selection of attributes as well as their definitions were done based on the subjective experience and interpretations of the authors of this work. For some cases, these definitions might not match the one from the authors of the included studies, potentially leading to different subjective interpretations of the collected data. It should also be noted that studies which evaluated the IDS without human participants or without the ULO being actually worn by the participants were excluded. Although this was intended in the review protocol to focus on a more realistic real-life scenario, this might have excluded many potentially interesting IDS. Specifically, many IDS currently under development might not yet be at a sufficient level of technology maturity to be safe and robust enough for testing with human participants, despite having the potential to become highly usable and broadly applicable. The technology maturity of the IDS does presumably also have an impact on the assessed usability in the included studies. Thus, some of these IDS might have the potential to achieve higher usability in a future development stage. However, since the maturity of the presented technologies was often not reported or not reported systematically, this aspect could not be taken into account for the synthesis. Further, many studies assessed the overall device consisting of ULO and IDS as a single unit instead of two interacting but separate systems. Despite efforts to only include specific usability attributes only concerning IDS and exclusion of findings which were clearly influenced by the ULO, the possibility that some of the reported findings may be biased by the usability of the ULO itself, can't

be ruled out. Lastly, the partially qualitative nature and the heterogeneity of the collected data did not allow an objective and systematic rating of the individual IDS, nor a statistical or meta-analysis. A more quantitative comparison between IDS would be more beneficial for an objective selection of IDS. However, the available data did not allow such an analysis.

4.4. Implications and Recommendations for Future Research

This review provides a comprehensive understanding of the evaluation practices and results for IDS used in combination with ULO. The collected data on specific usability attributes for a wide range of IDS and their respective applications to various contexts of use can serve as a catalog of solutions for technology developers needing to select an appropriate IDS for their application. Although this work's scope is focused on ULO, its conclusions may also apply for other devices sharing similar challenges, such as neuroprosthetics (Taylor et al., 2002; Ambrosini et al., 2014b; Fonseca et al., 2019), supernumerary limbs (Hussain et al., 2017; Cunningham et al., 2018), or prosthetics (Micera et al., 2010; Parajuli et al., 2019). The importance of a user- and application-specific selection of IDS for such devices is underlined by the finding that no IDS can be rated as being generally superior to another without specifying the detailed context of use, i.e., the type of device for which the IDS is intended, the target user's capabilities and preferences, as well as the targeted usage environment and the tasks for which the device should be used.

Based on the insights from this review, we propose four recommendations to technology developers in the field, related to the selection of IDS, as well as to the design of corresponding evaluation protocols:

1. When designing or selecting an IDS, researchers should carefully consider the detailed context of use in which the ULO is intended to be used. Accordingly, these considerations should be described in the respective publications to allow for an informed evaluation of the IDS with respect to the intended context of use.
2. To reach a broader target population, ULO should offer their users a selection of different IDS to choose from or to combine to accommodate for the user's individual capabilities, preferences, and usage scenarios. For example, while specific users might prefer voice control at home they might want to switch to a button to be able to control their ULO more quietly in a restaurant or at the cinema.
3. Based on the user requirements, appropriate protocols to evaluate the usability of an IDS should be set up. These protocols should combine different scales and methodologies and cover not only technical aspects related to the efficiency or effectiveness of the IDS but also critically take user satisfaction, e.g., obtrusiveness, simplicity for donning/doffing, or comfort, into consideration. Such a comprehensive user evaluation protocol would allow for better interpretation of the usability evaluation results, help to set benchmarks and set the findings from the evaluation in relation to potential implications for the overall device acceptance by the target users.
4. When evaluating specific usability attributes, IDS, and ULO should, whenever possible, be assessed as two separate entities, interacting with each other and with the user, instead of as a single unit. Such an independent evaluation would allow discovering the source of potentially arising design- or usability issues related to the IDS or the ULO more easily and earlier.

5. CONCLUSION

Choosing an optimal IDS for a given application remains a recurring challenge since it is highly dependent on many factors, such as the intended usage scenario and target user's capabilities, limitations and preferences. By providing a comprehensive overview and recommendations for future development, this work encourages technology developers in the field to administer a user- and application-specific selection of appropriate IDS for ULO. Such a selection would positively affect the usability of the overall device and thus the device acceptance by the target users, ultimately promoting the leap of such technologies out of research laboratories into the target user's homes to positively impact the quality of life of end-users.

AUTHOR CONTRIBUTIONS

JG, OL, and RG designed the aim and scope of the review. JG conducted the database search, performed the data extraction and the quality assessment, analyzed the review findings, and wrote the manuscript. JG, JD, and JM conducted the study selection. JG and JD piloted the data extraction table. All authors provided critical feedback on the manuscript. All authors reviewed and approved the final manuscript.

FUNDING

This work was supported by the Swiss National Science Foundation SNSF through the National Centre of Competence in Research on Robotics, the Vontobel Foundation, the Gemeinnützige Stiftung ACCENTUS, the ETH Zurich Foundation in collaboration with Hocoma AG, and the National Research Foundation, Prime Minister's Office, Singapore under its Campus for Research Excellence and Technological Enterprise (CREATE) program.

SUPPLEMENTARY MATERIAL

The Supplementary Material for this article can be found online at: https://www.frontiersin.org/articles/10.3389/fnbot.2022.815693/full#supplementary-material

REFERENCES

Ab Patar, M. N. A., Komeda, T., Low, C. Y., and Mahmud, J. (2014). System integration and control of finger orthosis for post stroke rehabilitation. *Proc. Technol.* 15, 755–764. doi: 10.1016/j.protcy.2014.09.048

Ajiboye, A. B., and Weir, R. F. (2005). A heuristic fuzzy logic approach to EMG pattern recognition for multifunctional prosthesis control. *IEEE Trans. Neural Syst. Rehabil. Eng.* 13, 280–291. doi: 10.1109/TNSRE.2005.847357

Allison, B. Z., Neuper, C., Allison, B. Z., Neuper, C., Tan, D. S., and Nijholt, A. (2010). *Could Anyone Use a BCI*? London: Human-Computer Interaction Series, 35–54. doi: 10.1007/978-1-84996-272-8_3

Ambrosini, E., Ferrante, S., Rossini, M., Molteni, F., Gföhler, M., Reichenfelser, W., et al. (2014a). Functional and usability assessment of a robotic exoskeleton arm to support activities of daily life. *Robotica* 32, 1213–1224. doi: 10.1017/S0263574714001891

Ambrosini, E., Ferrante, S., Schauer, T., Klauer, C., Gaffuri, M., Ferrigno, G., et al. (2014b). A myocontrolled neuroprosthesis integrated with a passive exoskeleton to support upper limb activities. *J. Electromyogr. Kinesiol.* 24, 307–317. doi: 10.1016/j.jelekin.2014.01.006

Antonelli, M. G., Zobel, P. B., and Giacomin, J. (2009). Use of MMG signals for the control of powered orthotic devices: Development of a rectus femoris measurement protocol. *Assist. Technol.* 21, 1–12. doi: 10.1080/10400430902945678

Araujo, R. S., Silva, C. R., Netto, S. P. N., Morya, E., and Brasil, F. L. (2021). Development of a low-cost EEG-controlled hand exoskeleton 3D printed on textiles. *Front. Neurosci.* 15:661569. doi: 10.3389/fnins.2021.661569

Badesa, F. J., Diez, J. A., Barios, J. A., Catalan, J. M., and Garcia-Aracil, N. (2020). "Evaluation of performance and heart rate variability during intensive usage of a BCI-controlled hand exoskeleton," in *2020 8th IEEE RAS/EMBS International Conference for Biomedical Robotics and Biomechatronics (BioRob)* (New York, NY), 164–169. doi: 10.1109/BioRob49111.2020.9224322

Barea, R., Boquete, L., Mazo, M., and López, E. (2002). System for assisted mobility using eye movements based on electrooculography. *IEEE Trans. Neural Syst. Rehabil. Eng.* 10, 209–218. doi: 10.1109/TNSRE.2002.806829

Bergamasco, M., and Herr, H. (2016). "Human-robot augmentation," in *Springer Handbook of Robotics*, eds B. Siciliano and O. Khatib (Berlin; Heidelberg: Springer Nature), 1875–1906. doi: 10.1007/978-3-319-32552-1_70

Bermúdez i Badia, S., Lewis, E., and Bleakley, S. (2014). Combining virtual reality and a myoelectric limb orthosis to restore active movement after stroke: a pilot study. *Int. J. Disabil. Hum. Dev.* 13, 393–399. doi: 10.1515/ijdhd-2014-0333

Bi, Q., Yang, C., Yang, W., Fan, J., and Wang, H. (2017). "Hand exoskeleton control for cerebrum plasticity training based on brain-computer interface," in *Wearable Sensors and Robots*, eds P. W. Jordan, B. Thomas, B. A. Weerdmeester, and I. L. McClelland (London: Springer), 395–410. doi: 10.1007/978-981-10-2404-7_31

Biddiss, E., and Chau, T. (2007). Upper limb prosthesis use and abandonment: a survey of the last 25 years. *Prosthet. Orthot. Int.* 31, 236–257. doi: 10.1080/03093640600994581

Blankertz, B., Sannelli, C., Halder, S., Hammer, E. M., Kübler, A., Müller, K. R., et al. (2010). Neurophysiological predictor of SMR-based bci performance. *NeuroImage* 51, 1303–1309. doi: 10.1016/j.neuroimage.2010.03.022

Bos, R. A., Nizamis, K., Koopman, B. F. J. M., Herder, J. L., Sartori, M., and Plettenburg, D. H. (2020). A case study with symbihand: an SEMG-controlled electrohydraulic hand orthosis for individuals with duchenne muscular dystrophy. *IEEE Trans. Neural Syst. Rehabil. Eng.* 28, 258–266. doi: 10.1109/TNSRE.2019.2952470

Brooke, J. (1996). "SUS: a 'quick and dirty' usability scale," in *Usability Evaluation in Industry*, eds C. Yang, H. Yang, and G. S. Virk (Singapore: CRC Press), 207–212. doi: 10.1201/9781498710411-35

Burns, M. K., Pei, D., and Vinjamuri, R. (2019). Myoelectric control of a soft hand exoskeleton using kinematic synergies. *IEEE Trans. Biomed. Circuits Syst.* 13, 1351–1361. doi: 10.1109/TBCAS.2019.2950145

Butzer, T., Dittli, J., Lieber, J., Hedel, H. J. V., Meyer-Heim, A., Lambercy, O., et al. (2019). Pexo - a pediatric whole hand exoskeleton for grasping assistance in task-oriented training. *IEEE Int. Conf. Rehabil. Robot.* 2019:8779489. doi: 10.1109/ICORR.2019.8779489

Butzer, T., Lambercy, O., Arata, J., Gassert, R., Bützer, T., Lambercy, O., et al. (2021). Fully wearable actuated soft exoskeleton for grasping assistance in everyday activities. *Soft Robot.* 8, 128–143. doi: 10.1089/soro.2019.0135

Cantillo-Negrete, J., Carino-Escobar, R. I., Carrillo-Mora, P., Elias-Vinas, D., and Gutierrez-Martinez, J. (2018). Motor imagery-based brain-computer interface coupled to a robotic hand orthosis aimed for neurorehabilitation of stroke patients. *J. Healthc. Eng.* 2018:1624637. doi: 10.1155/2018/1624637

Chowdhury, A., Meena, Y. K., Raza, H., Bhushan, B., Uttam, A. K., Pandey, N., et al. (2018). Active physical practice followed by mental practice using BCI-driven hand exoskeleton: a pilot trial for clinical effectiveness and usability. *IEEE J. Biomed. Health Inform.* 22, 1786–1795. doi: 10.1109/JBHI.2018.2863212

Chu, C. Y., and Patterson, R. M. (2018). Soft robotic devices for hand rehabilitation and assistance: a narrative review. *J. Neuroeng. Rehabil.* 15, 1–14. doi: 10.1186/s12984-018-0350-6

Cognolato, M., Atzori, M., and Müller, H. (2018). Head-mounted eye gaze tracking devices: an overview of modern devices and recent advances. *J. Rehabil. Assist. Technol. Eng.* 5:2055668318773991. doi: 10.1177/2055668318773991

Correia, C., Nuckols, K., Wagner, D., Zhou, Y. M., Clarke, M., Orzel, D., et al. (2020). Improving grasp function after spinal cord injury with a soft robotic glove. *IEEE Trans. Neural Syst. Rehabil. Eng.* 28, 1407–1415. doi: 10.1109/TNSRE.2020.2988260

Courteville, A., Gharbi, T., and Cornu, J.-Y. (1998). MMG measurement: a high-sensitivity microphone-based sensor for clinical use. *IEEE Trans. Biomed. Eng.* 45, 145–150. doi: 10.1109/10.661262

Cramer, S. C., Sur, M., Dobkin, B. H., O'Brien, C., Sanger, T. D., Trojanowski, J. Q., et al. (2011). Harnessing neuroplasticity for clinical applications. *Brain* 134, 1591–1609. doi: 10.1093/brain/awr039

Cunningham, J., Hapsari, A., Guilleminot, P., Shafti, A., and Faisal, A. A. (2018). "The supernumerary robotic 3rd thumb for skilled music tasks," in *Proceedings of the IEEE RAS and EMBS International Conference on Biomedical Robotics and Biomechatronics* (Enschede), 665–670. doi: 10.1109/BIOROB.2018.8487609

Dalla Gasperina, S., Gandolla, M., Manti, A., Aquilante, L., Longatelli, V., D'Angelo, M., et al. (2019). "Upper-limb actuated exoskeleton for muscular dystrophy patients: preliminary results," in *2019 41st Annual International Conference of the IEEE Engineering in Medicine and Biology Society (EMBC)* (Berlin), 4431–4435. doi: 10.1109/EMBC.2019.8857725

Delijorge, J., Mendoza-Montoya, O., Gordillo, J. L., Caraza, R., Martinez, H. R., and Antelis, J. M. (2020). Evaluation of a p300-based brain-machine interface for a robotic hand-orthosis control. *Front. Neurosci.* 14:589659. doi: 10.3389/fnins.2020.589659

Demers, L., Weiss-Lambrou, R., and Ska, B. (2002). The quebec user evaluation of satisfaction with assistive technology (QUEST 2.0): an overview and recent progress. *Technol. Disabil.* 14, 101–105. doi: 10.3233/TAD-2002-14304

DiCicco, M., Lucas, L., and Matsuoka, Y. (2004). Comparison of control strategies for an EMG controlled orthotic exoskeleton for the hand. *IEEE Int. Conf. Robot. Autom.* 2004, 1622–1627. doi: 10.1109/ROBOT.2004.1308056

du Plessis, T., Djouani, K., and Oosthuizen, C. (2021). A review of active hand exoskeletons for rehabilitation and assistance. *Robotics* 10:40. doi: 10.3390/robotics10010040

Dunaway, S., Dezsi, D. B., Perkins, J., Tran, D., and Naft, J. (2017). Case report on the use of a custom myoelectric elbow-wrist-hand orthosis for the remediation of upper extremity paresis and loss of function in chronic stroke. *Milit. Med.* 182, e1963–e1968. doi: 10.7205/MILMED-D-16-00399

Dwivedi, A., Gerez, L., Hasan, W., Yang, C.-H., and Liarokapis, M. (2019). A soft exoglove equipped with a wearable muscle-machine interface based on forcemyography and electromyography. *IEEE Robot. Autom. Lett.* 4, 3240–3246. doi: 10.1109/LRA.2019.2925302

Fajardo, J., Ferman, V., Munoz, A., Andrade, D., Neto, A. R., and Rohmer, E. (2018). "User-prosthesis interface for upper limb prosthesis based on object classification," in *Proceedings - 15th Latin American Robotics Symposium, 6th Brazilian Robotics Symposium and 9th Workshop on Robotics in Education, LARS/SBR/WRE 2018* (Pessoa), 396–401. doi: 10.1109/LARS/SBR/WRE.2018.00076

Fajardo, J., Neto, A. R., Silva, W., Gomes, M., Fujiwara, E., and Rohmer, E. (2019). "A wearable robotic glove based on optical FMG driven controller," in *2019 4th IEEE International Conference on Advanced Robotics and Mechatronics, ICARM 2019* (Toyonaka), 81–86. doi: 10.1109/ICARM.2019.8834067

Fardipour, S., Bahramizadeh, M., Arazpour, M., Jafarpisheh, A. S., and Azimian, M. (2018). First prototype of EMG-controlled power

hand orthosis for restoring hand extension in stroke patients. *Proc. Inst. Mech. Eng. Part H* 232, 1176–1181. doi: 10.1177/0954411918808322

Farinha, D., Dias, J., Neves, P., Pereira, K., Ferreira, C., and Pires, G. (2019). "Assistive robotic hand orthosis (ARHO) controlled with EMG: evaluation of a preliminary prototype*," in *IEEE 6th Portuguese Meeting on Bioengineering (ENBENG)* (Lisbon). doi: 10.29007/lqsv

Fok, S., Schwartz, R., Wronkiewicz, M., Holmes, C., Zhang, J., Somers, T., et al. (2011). "An EEG-based brain computer interface for rehabilitation and restoration of hand control following stroke using ipsilateral cortical physiology," in *Proceedings of the Annual International Conference of the IEEE Engineering in Medicine and Biology Society, EMBS* (Boston, MA), 6277–6280. doi: 10.1109/IEMBS.2011.6091549

Fonseca, L., Tigra, W., Navarro, B., Guiraud, D., Fattal, C., Bó, A., et al. (2019). Assisted grasping in individuals with tetraplegia: improving control through residual muscle contraction and movement. *Sensors* 19:4532. doi: 10.3390/s19204532

Fujita, T., Kawamoto, H., and Sankai, Y. (2016). "Voluntary motion support by an upper limb support system based on bioelectrical signals for heavy overhead tasks," in *2016 IEEE International Conference on Robotics and Biomimetics, ROBIO 2016* (Qingdao), 1075–1080. doi: 10.1109/ROBIO.2016.7866468

Gerez, L., Chen, J., and Liarokapis, M. (2019). On the development of adaptive, tendon-driven, wearable exo-gloves for grasping capabilities enhancement. *IEEE Robot. Autom. Lett.* 4, 422–429. doi: 10.1109/LRA.2019.2890853

Gerez, L., Dwivedi, A., and Liarokapis, M. (2020). "A hybrid, soft exoskeleton glove equipped with a telescopic extra thumb and abduction capabilities," in *2020 IEEE International Conference on Robotics and Automation (ICRA)* (Paris), 9100–9106. doi: 10.1109/ICRA40945.2020.9197473

Grewal, H. S., Matthews, A., Tea, R., Contractor, V., and George, K. (2018). "Sip-and-puff autonomous wheelchair for individuals with severe disabilities," in *2018 9th IEEE Annual Ubiquitous Computing, Electronics and Mobile Communication Conference, UEMCON 2018* (New York, NY), 705–710. doi: 10.1109/UEMCON.2018.8796679

Guger, C., Allison, B. Z., Großwindhager, B., Prückl, R., Hintermüller, C., Kapeller, C., et al. (2012). How many people could use an SSVEP BCI? *Front. Neurosci.* 6:169. doi: 10.3389/fnins.2012.00169

Hameed, H. K., Hassan, W. Z. W., Shafie, S., Ahmad, S. A., and Jaafar, H. (2020). A review on surface electromyography-controlled hand robotic devices used for rehabilitation and assistance in activities of daily living. *J. Prosthet. Orthot.* 32, 3–13. doi: 10.1097/JPO.0000000000000277

Hart, S. G., and Staveland, L. E. (1988). Development of NASA-TLX (task load index): results of empirical and theoretical research. *Adv. Psychol.* 52, 139–183. doi: 10.1016/S0166-4115(08)62386-9

Hasegawa, Y., and Oura, S. (2011). "Exoskeletal meal assistance system (EMAS II) for progressive muscle dystrophy patient," in *IEEE International Conference on Rehabilitation Robotics* (Zurich). doi: 10.1109/ICORR.2011.5975444

Hennig, R., Gantenbein, J., Dittli, J., Chen, H., Lacour, S. P., Lambercy, O., et al. (2020). "Development and evaluation of a sensor glove to detect grasp intention for a wearable robotic hand exoskeleton," in *2020 8th IEEE RAS/EMBS International Conference for Biomedical Robotics and Biomechatronics (BioRob)* (New York, NY) 19–24. doi: 10.1109/BioRob49111.2020.9224463

Heo, P., and Kim, J. (2014). Power-assistive finger exoskeleton with a palmar opening at the fingerpad. *IEEE Trans. Biomed. Eng.* 61, 2688–2697. doi: 10.1109/TBME.2014.2325948

Hétu, S., Grégoire, M., Saimpont, A., Coll, M. P., Eugène, F., Michon, P. E., et al. (2013). The neural network of motor imagery: an ale meta-analysis. *Neurosci. Biobehav. Rev.* 37, 930–949. doi: 10.1016/j.neubiorev.2013.03.017

Hong, M. B., Kim, S. J., Ihn, Y. S., Jeong, G. C., and Kim, K. (2019). Kulex-hand: an underactuated wearable hand for grasping power assistance. *IEEE Trans. Robot.* 35, 420–432. doi: 10.1109/TRO.2018.2880121

Hussain, I., Spagnoletti, G., Salvietti, G., and Prattichizzo, D. (2017). Toward wearable supernumerary robotic fingers to compensate missing grasping abilities in hemiparetic upper limb. *Int. J. Robot. Res.* 36, 1414–1436. doi: 10.1177/0278364917712433

Ibitoye, M. O., Hamzaid, N. A., Zuniga, J. M., and Wahab, A. K. A. (2014). Mechanomyography and muscle function assessment: a review of current state and prospects. *Clin. Biomech.* 29, 691–704. doi: 10.1016/j.clinbiomech.2014.04.003

Ismail, R., Ariyanto, M., Hidayat, T., and Setiawan, J. D. (2019). "Design of fabric-based soft robotic glove for hand function assistance," in *2019 6th International Conference on Information Technology, Computer and Electrical Engineering (ICITACEE)* (Semarang), 1–5. doi: 10.1109/ICITACEE47699.2019.8972668

ISO 9241-11 (2018). *Ergonomics of Human-System Interaction - Part 11: Usability: Definitions and Concepts*. Geneva: Standard, International Organization for Standardization.

Jones, M., Grogg, K., Anschutz, J., and Fierman, R. (2010). A sip-and-puff wireless remote control for the apple IPOD. *Assist. Technol.* 20, 107–110. doi: 10.1080/10400435.2008.10131937

Kaneishi, D., Leu, J. E., O'Donnell, J., Affleck, C., Matthew, R. P., McPherson, A., et al. (2019). "Design and assessment of a single-size semi-soft assistive mitten for people with cervical spinal cord injuries," in *2019 IEEE-RAS 19th International Conference on Humanoid Robots (Humanoids)* (Toronto, ON), 614–621. doi: 10.1109/Humanoids43949.2019.9035027

Kapsalyamov, A., Hussain, S., Sharipov, A., and Jamwal, P. (2019). Brain-computer interface and assist-as-needed model for upper limb robotic arm. *Adv. Mech. Eng.* 11:168781401987553. doi: 10.1177/1687814019875537

Kawase, T., Sakurada, T., Koike, Y., and Kansaku, K. (2017). A hybrid BMI-based exoskeleton for paresis: EMG control for assisting arm movements. *J. Neural Eng.* 14:16015. doi: 10.1088/1741-2552/aa525f

Khan, M. A., Das, R., Iversen, H. K., and Puthusserypady, S. (2020). Review on motor imagery based BCI systems for upper limb post-stroke neurorehabilitation: from designing to application. *Comput. Biol. Med.* 123:103843. doi: 10.1016/j.compbiomed.2020.103843

Kiguchi, K. (2007). Active exoskeletons for upper-limb motion assist. *Int. J. Hum. Robot.* 4, 607–624. doi: 10.1142/S0219843607001175

Kilic, E. (2017). EMG based neural network and admittance control of an active wrist orthosis. *J. Mech. Sci. Technol.* 31, 6093–6106. doi: 10.1007/s12206-017-1154-5

Kim, J., Bulach, C., Richards, K. M., Wu, D., Butler, A. J., and Ghovanloo, M. (2013). "An apparatus for improving upper limb function by engaging synchronous tongue motion," in *6th International IEEE/EMBS Conference on Neural Engineering (NER)* (San Diego, CA), 1574–1577. doi: 10.1109/NER.2013.6696248

Kim, K., Hong, K. J., Kim, N. G., and Kwon, T. K. (2012). Assistance of the elbow flexion motion on the active elbow orthosis using muscular stiffness force feedback. *J. Mech. Sci. Technol.* 25, 3195–3203. doi: 10.1007/s12206-011-0923-9

Kim, Y. G., Xiloyannis, M., Accoto, D., and Masia, L. (2018). "Development of a soft exosuit for industriale applications," in *Proceedings of the IEEE RAS and EMBS International Conference on Biomedical Robotics and Biomechatronics* (Enschede), 324–329. doi: 10.1109/BIOROB.2018.8487907

King, C. E., Dave, K. R., Wang, P. T., Mizuta, M., Reinkensmeyer, D. J., Do, A. H., et al. (2014). Performance assessment of a brain-computer interface driven hand orthosis. *Ann. Biomed. Eng.* 42, 2095–2105. doi: 10.1007/s10439-014-1066-9

Kocejko, T. (2017). "Gaze controlled prosthetic arm with EMG and EEG input interface," in *21st European Microelectronics and Packaging Conference (EMPC) & Exhibition* (Warsaw), 1–9. doi: 10.23919/EMPC.2017.8346906

Koh, T. H., Cheng, N., Yap, H. K., and Yeow, C. H. (2017). Design of a soft robotic elbow sleeve with passive and intent-controlled actuation. *Front. Neurosci.* 11:597. doi: 10.3389/fnins.2017.00597

Kojima, A., Yamazoe, H., and Lee, J. H. (2017). "User friendly podalic interface for light weighted wearable robot arm," in *2017 14th International Conference on Ubiquitous Robots and Ambient Intelligence, URAI 2017* (Jeju), 181–184. doi: 10.1109/URAI.2017.7992706

Koo, B., Montes, J., Gamarnik, V., Yeager, K., Marra, J., Dunaway, S., et al. (2009). "Design and evaluation of a hybrid passive and active gravity neutral orthosis (GNO)," in *Annual International Conference of the IEEE Engineering in Medicine and Biology Society* (Minneapolis, MN), 1573–1576. doi: 10.1109/IEMBS.2009.5332578

Kooren, P. N., Lobo-Prat, J., Keemink, A. Q., Janssen, M. M., Stienen, A. H., Groot, I. J. D., et al. (2016). "Design and control of the active a-gear: a wearable 5 DOF arm exoskeleton for adults with duchenne muscular dystrophy," in *Proceedings of the IEEE RAS and EMBS International Conference on Biomedical Robotics and Biomechatronics* (Singapore), 637–642. doi: 10.1109/BIOROB.2016.7523697

Kübler, A. (2020). The history of BCI: from a vision for the future to real support for personhood in people with locked-in syndrome. *Neuroethics* 13, 163–180. doi: 10.1007/s12152-019-09409-4

Kübler, A., Neumann, N., Wilhelm, B., Hinterberger, T., and Birbaumer, N. (2006). Predictability of brain-computer communication. *J. Psychophysiol*. 18, 121–129. doi: 10.1027/0269-8803.18.23.121

Kudo, S., Oshima, K., Arizono, M., Hayashi, Y., and Moromugi, S. (2014). "Electric-powered glove for CCI patients to extend their upper-extremity function," in *2014 IEEE/SICE International Symposium on System Integration* (Tokyo), 638–643. doi: 10.1109/SII.2014.7028113

Kupetz, D. J., Wentzell, S. A., and BuSha, B. F. (2010). "Head motion controlled power wheelchair," in *Proceedings of the 2010 IEEE 36th Annual Northeast Bioengineering Conference, NEBEC 2010* (New York, NY). doi: 10.1109/NEBC.2010.5458224

Lambelet, C., Temiraliuly, D., Siegenthaler, M., Wirth, M., Woolley, D. G., Lambercy, O., et al. (2020). Characterization and wearability evaluation of a fully portable wrist exoskeleton for unsupervised training after stroke. *J. Neuroeng. Rehabil*. 17:132. doi: 10.1186/s12984-020-00749-4

Land, M. F. (2006). Eye movements and the control of actions in everyday life. *Prog. Retin. Eye Res*. 25, 296–324. doi: 10.1016/j.preteyeres.2006.01.002

Lee, H., Yu, S., Lee, S., Han, J., and Han, C. (2008). "Development of human-robot interfacing method for assistive wearable robot of the human upper extremities," in *2008 SICE Annual Conference* (Tokyo), 1755–1760.

Lee, J., Mukae, N., Arata, J., Iwata, H., Iramina, K., Iihara, K., et al. (2017). A multichannel-near-infrared-spectroscopy-triggered robotic hand rehabilitation system for stroke patients. *IEEE Int. Conf. Rehabil. Robot*. 2017, 158–163. doi: 10.1109/ICORR.2017.8009239

Lince, A., Celadon, N., Battezzato, A., Favetto, A., Appendino, S., Ariano, P., et al. (2017). "Design and testing of an under-actuated surface EMG-driven hand exoskeleton," in *International Conference on Rehabilitation Robotics (ICORR)* (London), 670–675. doi: 10.1109/ICORR.2017.8009325

Lobo-Prat, J., Kooren, P. N., Stienen, A. H., Herder, J. L., Koopman, B. F., and Veltink, P. H. (2014). Non-invasive control interfaces for intention detection in active movement-assistive devices. *J. NeuroEng. Rehabil*. 11, 1–22. doi: 10.1186/1743-0003-11-168

Losey, D. P., McDonald, C. G., Battaglia, E., and O'Malley, M. K. (2018). A review of intent detection, arbitration, and communication aspects of shared control for physical human-robot interaction. *Appl. Mech. Rev*. 70:010804. doi: 10.1115/1.4039145

Lotti, N., Xiloyannis, M., Durandau, G., Galofaro, E., Sanguineti, V., Masia, L., et al. (2020). Adaptive model-based myoelectric control for a soft wearable arm exosuit: a new generation of wearable robot control. *IEEE Robot. Autom. Mag*. 27, 43–53. doi: 10.1109/MRA.2019.2955669

Lu, Z., Tong, K. Y., Zhang, X., Li, S., and Zhou, P. (2019). Myoelectric pattern recognition for controlling a robotic hand: a feasibility study in stroke. *IEEE Trans. Biomed. Eng*. 66, 365–372. doi: 10.1109/TBME.2018.2840848

Lund, A. (2001). Measuring usability with the use questionnaire. *Usabil. Interface*. 8, 3–6.

Ma, Z., Ben-Tzvi, P., and Danoff, J. (2016). Hand rehabilitation learning system with an exoskeleton robotic glove. *IEEE Trans. Neural Syst. Rehabil. Eng*. 24, 1323–1332. doi: 10.1109/TNSRE.2015.2501748

Mane, R., Chouhan, T., and Guan, C. (2020). BCI for stroke rehabilitation: motor and beyond. *J. Neural Eng*. 17:041001. doi: 10.1088/1741-2552/aba162

Markovic, M., Dosen, S., Popovic, D., Graimann, B., and Farina, D. (2015). Sensor fusion and computer vision for context-aware control of a multi degree-of-freedom prosthesis. *J. Neural Eng*. 12:066022. doi: 10.1088/1741-2560/12/6/066022

Meeker, C., Park, S., Bishop, L., Stein, J., and Ciocarlie, M. (2017). EMG pattern classification to control a hand orthosis for functional grasp assistance after stroke. *IEEE Int. Conf. Rehabil. Robot*. 2017, 1203–1210. doi: 10.1109/ICORR.2017.8009413

Meyer, J. T., Gassert, R., and Lambercy, O. (2021). An analysis of usability evaluation practices and contexts of use in wearable robotics. *J. NeuroEng. Rehabil*. 18, 1–15. doi: 10.1186/s12984-021-00963-8

Micera, S., Carpaneto, J., and Raspopovic, S. (2010). Control of hand prostheses using peripheral information. *IEEE Rev. Biomed. Eng*. 3, 48–68. doi: 10.1109/RBME.2010.2085429

Millán, J. D., Rupp, R., Müller-Putz, G. R., Murray-Smith, R., Giugliemma, C., Tangermann, M., et al. (2010). Combining brain-computer interfaces and assistive technologies: state-of-the-art and challenges. *Front. Neurosci*. 4:161. doi: 10.3389/fnins.2010.00161

Mohammadi, A., Lavranos, J., Choong, P., and Oetomo, D. (2018). "Flexo-glove: a 3D printed soft exoskeleton robotic glove for impaired hand rehabilitation and assistance," in *Annual International Conference of the IEEE Engineering in Medicine and Biology Society* (Honolulu, HI), 2120–2123. doi: 10.1109/EMBC.2018.8512617

Moher, D., Liberati, A., Tetzlaff, J., and Altman, D. G. (2009). Preferred reporting items for systematic reviews and meta-analyses: the prisma statement. *BMJ* 339, 332–336. doi: 10.1136/bmj.b2535

Mohs, C., Hurtienne, J., Scholz, D., and Rotting, M. (2006). Intuitivitt: definierbar, beeinflussbar, überprüfbar. *VDI Berich*. 1946:215.

Moromugi, S., Tanaka, T., Higashi, T., Feng, M. Q., and Ishimatsu, T. (2013). Pneumatically driven prehension orthosis with force control function. *J. Robot. Mechatron*. 25, 973–982. doi: 10.20965/jrm.2013.p0973

Muehlbauer, P., Schimbera, M., Stewart, K., and Pott, P. P. (2021). "Twisted string actuation for an active modular hand orthosis," in *ACTUATOR; International Conference and Exhibition on New Actuator Systems and Applications 2021*, 1–4.

Nam, C., Rong, W., Li, W., Cheung, C., Ngai, W., Cheung, T., et al. (2020). An exoneuromusculoskeleton for self-help upper limb rehabilitation after stroke. *Soft Robot*. doi: 10.1089/soro.2020.0090. [Epub ahead of print].

Naseer, N., and Hong, K. S. (2015). fNIRS-based brain-computer interfaces: a review. *Front. Hum. Neurosci*. 9:3. doi: 10.3389/fnhum.2015.00003

Naumann, A., Hurtienne, J., Israel, J. H., Mohs, C., Kindsmüller, M. C., Meyer, H. A., et al. (2007). "Intuitive use of user interfaces: defining a vague concept, in *International Conference on Engineering Psychology and Cognitive Ergonomics* (Beijing). Lecture Notes in Computer Science, 128–136. doi: 10.1007/978-3-540-73331-7_14

Ngeo, J., Tamei, T., Shibata, T., Orlando, M. F., Behera, L., Saxena, A., et al. (2013). "Control of an optimal finger exoskeleton based on continuous joint angle estimation from EMG signals," in *Annual International Conference of the IEEE Engineering in Medicine and Biology Society* (Osaka), 338–341. doi: 10.1109/EMBC.2013.6609506

Nicolas-Alonso, L. F., and Gomez-Gil, J. (2012). Brain computer interfaces, a review. *Sensors* 12, 1211–1279. doi: 10.3390/s120201211

Novak, D., Sigrist, R., Gerig, N. J., Wyss, D., Bauer, R., Götz, U., et al. (2018). Benchmarking brain-computer interfaces outside the laboratory: the cybathlon 2016. *Front. Neurosci*. 11:756. doi: 10.3389/fnins.2017.00756

Ochoa, J. M., Jia, Y., Dev, N., and Kamper, D. G. (2009). "Development of a portable actuated orthotic glove to facilitate gross extension of the digits for therapeutic training after stroke," in *Annual International Conference of the IEEE Engineering in Medicine and Biology Society* (Minneapolis, MN), 6918–6921. doi: 10.1109/IEMBS.2009.5333630

Ommeren, A. L. V., Smulders, L. C., Prange-Lasonder, G. B., Buurke, J. H., Veltink, P. H., and Rietman, J. S. (2018). Assistive technology for the upper extremities after stroke: systematic review of users' needs. *JMIR Rehabil. Assist. Technol*. 5:e10510. doi: 10.2196/10510

Ortner, R., Allison, B. Z., Korisek, G., Gaggl, H., and Pfurtscheller, G. (2011). An SSVEP BCI to control a hand orthosis for persons with tetraplegia. *IEEE Trans. Neural Syst. Rehabil. Eng*. 19, 1–5. doi: 10.1109/TNSRE.2010.2076364

Otten, B. M., Weidner, R., and Argubi-Wollesen, A. (2018). Evaluation of a novel active exoskeleton for tasks at or above head level. *IEEE Robot. Autom. Lett*. 3, 2408–2415. doi: 10.1109/LRA.2018.2812905

Parajuli, N., Sreenivasan, N., Bifulco, P., Cesarelli, M., Savino, S., Niola, V., et al. (2019). Real-time EMG based pattern recognition control for hand prostheses: a review on existing methods, challenges and future implementation. *Sensors* 19:4596. doi: 10.3390/s19204596

Park, S., Fraser, M., Weber, L. M., Meeker, C., Bishop, L., Geller, D., et al. (2020). User-driven functional movement training with a wearable hand robot after stroke. *IEEE Trans. Neural Syst. Rehabil. Eng*. 28:2265. doi: 10.1109/TNSRE.2020.3021691

Park, S., Meeker, C., Weber, L. M., Bishop, L., Stein, J., and Ciocarlie, M. (2019). Multimodal sensing and interaction for a robotic hand orthosis. *IEEE Robot. Autom. Lett*. 4, 315–322. doi: 10.1109/LRA.2018.2890199

Pedrocchi, A., Ferrante, S., Ambrosini, E., Gandolla, M., Casellato, C., Schauer, T., et al. (2013). Mundus project: multimodal neuroprosthesis for daily

upper limb support. *J. NeuroEng. Rehabil.* 10, 1–20. doi: 10.1186/1743-000 3-10-66

Pfurtscheller, G., Guger, C., Müller, G., Krausz, G., and Neuper, C. (2000). Brain oscillations control hand orthosis in a tetraplegic. *Neurosci. Lett*. 292, 211–214. doi: 10.1016/S0304-3940(00)01471-3

Poltawski, L., Allison, R., Briscoe, S., Freeman, J., Kilbride, C., Neal, D., et al. (2016). Assessing the impact of upper limb disability following stroke: a qualitative enquiry using internet-based personal accounts of stroke survivors. *Disabil. Rehabil*. 38, 945–951. doi: 10.3109/09638288.2015.1068383

Popov, D., Gaponov, I., and Ryu, J. H. (2017). Portable exoskeleton glove with soft structure for hand assistance in activities of daily living. *IEEE/ASME Trans. Mechatron*. 22, 865–875. doi: 10.1109/TMECH.2016.2641932

Prange-Lasonder, G. B., Radder, B., Kottink, A. I., Melendez-Calderon, A., Buurke, J. H., and Rietman, J. S. (2017). Applying a soft-robotic glove as assistive device and training tool with games to support hand function after stroke: Preliminary results on feasibility and potential clinical impact. *IEEE Int. Conf. Rehabil. Robot*. 2017, 1401–1406. doi: 10.1109/ICORR.2017.8009444

Rashid, M., Sulaiman, N., Majeed, A. P. P. A., Musa, R. M., Ahmad, A. F., Bari, B. S., et al. (2020). Current status, challenges, and possible solutions of EEG-based brain-computer interface: a comprehensive review. *Front. Neurorobot*. 14:25. doi: 10.3389/fnbot.2020.00025

Raskin, J. (1994). Intuitive equals familiar. *Commun. ACM* 37, 17–19. doi: 10.1145/175247.175261

Ravneberg, B. (2012). Usability and abandonment of assistive technology. *J. Assist. Technol*. 6, 259–269. doi: 10.1108/17549451211285753

Riener, R. (2016). The cybathlon promotes the development of assistive technology for people with physical disabilities. *J. NeuroEng. Rehabil*. 13, 1–4. doi: 10.1186/s12984-016-0157-2

Riley, N. A., and Bilodeau, M. (2002). Changes in upper limb joint torque patterns and EMG signals with fatigue following a stroke. *Disabil. Rehabil*. 24, 961–969. doi: 10.1080/0963828021000007932

Rodríguez-Tapia, B., Soto, I., Marínez, D. M., and Arballo, N. C. (2020). Myoelectric interfaces and related applications: current state of EMG signal processing-a systematic review. *IEEE Access* 8, 7792–7805. doi: 10.1109/ACCESS.2019.2963881

Rose, C. G., and O'Malley, M. K. (2019). Hybrid rigid-soft hand exoskeleton to assist functional dexterity. *IEEE Robot. Autom. Lett*. 4, 73–80. doi: 10.1109/LRA.2018.2878931

Sandison, M., Phan, K., Casas, R., Nguyen, L., Lum, M., Pergami-Peries, M., et al. (2020). "Handmate: wearable robotic hand exoskeleton and integrated android app for at home stroke rehabilitation," in *Annual International Conference of the IEEE Engineering in Medicine and Biology Society* (Montreal, QC), 4867–4872. doi: 10.1109/EMBC44109.2020.9175332

Sasaki, D., Noritsugu, T., and Takaiwa, M. (2005). Development of pneumatic power assist splint "assist" operated by human intention. *J. Robot. Mechatron*. 17, 568–574. doi: 10.20965/jrm.2005.p0568

Scheuner, E., Fabech, J., Textor, D., Kuster, R., and Heinlein, B. (2016). Patient assistive system for the shoulder joint. *Curr. Direct. Biomed. Eng*. 2, 731–734. doi: 10.1515/cdbme-2016-0159

Secciani, N., Bianchi, M., Meli, E., Volpe, Y., and Ridolfi, A. (2019). A novel application of a surface electromyography-based control strategy for a hand exoskeleton system: a single-case study. *Int. J. Adv. Robot. Syst*. 16:1–13. doi: 10.1177/1729881419828197

Shafti, A., and Faisal, A. A. (2021). "Non-invasive cognitive-level human interfacing for the robotic restoration of reaching & grasping," in *2021 10th International IEEE/EMBS Conference on Neural Engineering (NER)*, 872–875. doi: 10.1109/NER49283.2021.9441453

Silva, J., Heim, W., and Chau, T. (2005). A self-contained, mechanomyography-driven externally powered prosthesis. *Arch. Phys. Med. Rehabil*. 86, 2066–2070. doi: 10.1016/j.apmr.2005.03.034

Simpson, R. C., and Levine, S. P. (2002). Voice control of a powered wheelchair. *IEEE Trans. Neural Syst. Rehabil. Eng* 10, 122–125. doi: 10.1109/TNSRE.2002.1031981

Siu, H. C., Arenas, A. M., Sun, T., and Stirling, L. A. (2018). Implementation of a surface electromyography-based upper extremity exoskeleton controller using learning from demonstration. *Sensors* 18:467. doi: 10.3390/s18020467

Soekadar, S. R., Witkowski, M., Vitiello, N., and Birbaumer, N. (2015). An EEG/EOG-based hybrid brain-neural computer interaction (BNCI) system to control an exoskeleton for the paralyzed hand. *Biomed. Eng*. 60, 199–205. doi: 10.1515/bmt-2014-0126

Solea, R., Margarit, A., Cernega, D., and Serbencu, A. (2019). "Head movement control of powered wheelchair," in *2019 23rd International Conference on System Theory, Control and Computing, ICSTCC 2019 - Proceedings* (Sinaia), 632–637. doi: 10.1109/ICSTCC.2019.8885844

Song, K. T., and Chai, Y. Y. (2013). "Compliance control of wearable robotic fingers for rehabilitation applications," in *CACS International Automatic Control Conference (CACS)* (Nantou), 306–311. doi: 10.1109/CACS.2013.6734151

Song, Z., Guo, S., Xiao, N., Gao, B., and Shi, L. (2012). Implementation of human-machine synchronization control for active rehabilitation using an inertia sensor. *Sensors* 12, 16046–16059. doi: 10.3390/s121216046

Struijk, L. N. A. (2006). An inductive tongue computer interface for control of computers and assistive devices. *IEEE Trans. Biomed. Eng*. 53, 2594–2597. doi: 10.1109/TBME.2006.880871

Sugawara, A. T., Ramos, V. D., Alfieri, F. M., Battistella, L. R., Sugawara, A. T., cius Ramos, V. D., et al. (2018). Abandonment of assistive products: assessing abandonment levels and factors that impact on it. *Disabil. Rehabil*. 13, 716–723. doi: 10.1080/17483107.2018.1425748

Sur, S., and Sinha, V. K. (2009). Event-related potential: an overview. *Indus. Psychiatry J*. 18:70. doi: 10.4103/0972-6748.57865

Taylor, P., Esnouf, J., and Hobby, J. (2002). The functional impact of the freehand system on tetraplegic hand function. Clinical results. *Spinal Cord* 40, 560–566. doi: 10.1038/sj.sc.3101373

Teplan, M. (2002). Fundamentals of EEG measurement. *Measure. Sci. Rev*. 2:1–11.

Thalman, C., and Artemiadis, P. (2020). *A Review of Soft Wearable Robots That Provide Active Assistance: Trends, Common Actuation Methods, Fabrication, and Applications*. Wearable Technologies. doi: 10.1017/wtc.2020.4

Tiseni, L., Xiloyannis, M., Chiaradia, D., Lotti, N., Solazzi, M., Kooij, H. V. D., et al. (2019). On the edge between soft and rigid: an assistive shoulder exoskeleton with hyper-redundant kinematics. *IEEE Int. Conf. Rehabil. Robot*. 2019:8779546. doi: 10.1109/ICORR.2019.8779546

Tricco, A. C., Lillie, E., Zarin, W., O'Brien, K. K., Colquhoun, H., Levac, D., et al. (2018). PRISMA extension for scoping reviews (PRISMA-ScR): checklist and explanation. *Ann. Intern. Med*. 169, 467–473. doi: 10.7326/M18-0850

Triolo, E. R., Stella, M. H., and Busha, B. F. (2018). "A force augmenting exoskeleton for the human hand designed for pinching and grasping," in *Annual International Conference of the IEEE Engineering in Medicine and Biology Society*, 1875–1878. doi: 10.1109/EMBC.2018.8512606

Tucker, M. R., Olivier, J., Pagel, A., Bleuler, H., Bouri, M., Lambercy, O., et al. (2015). Control strategies for active lower extremity prosthetics and orthotics: a review. *J. NeuroEng. Rehabil*. 12, 1–30. doi: 10.1186/1743-0003-12-1

Wang, D., Meng, Q., Meng, Q., Li, X., and Yu, H. (2018). Design and development of a portable exoskeleton for hand rehabilitation. *IEEE Trans. Neural Syst. Rehabil. Eng*. 26, 2376–2386. doi: 10.1109/TNSRE.2018.2878778

Wang, Z., Zhang, Y., Wu, X., Chen, C., Liu, Y., and Liu, E. (2020). "A soft wearable exosuit reduces the fatigue of biceps Brachii muscle," in *2020 IEEE International Conference on Real-Time Computing and Robotics, RCAR 2020*, 250–255. doi: 10.1109/RCAR49640.2020.9303250

Webb, J., Xiao, Z. G., Aschenbrenner, K. P., Herrnstadt, G., and Menon, C. (2012). "Towards a portable assistive arm exoskeleton for stroke patient rehabilitation controlled through a brain computer interface," in *Proceedings of the IEEE RAS and EMBS International Conference on Biomedical Robotics and Biomechatronics* (Rome), 1299–1304. doi: 10.1109/BioRob.2012.6290674

Woodward, R., Shefelbine, S., and Vaidyanathan, R. (2015). "Integrated grip switching and grasp control for prosthetic hands using fused inertial and mechanomyography measurement," in *2015 Swarm/Human Blended Intelligence Workshop, SHBI 2015* (Cleveland, OH). doi: 10.1109/SHBI.2015.7321689

Xiao, Z. G., Elnady, A. M., Webb, J., and Menon, C. (2014). "Towards a brain computer interface driven exoskeleton for upper extremity rehabilitation," in *5th IEEE RAS/EMBS International Conference on Biomedical Robotics and Biomechatronics* (Sao Paolo), 432–437. doi: 10.1109/BIOROB.2014.6913815

Xiao, Z. G., and Menon, C. (2019). A review of force myography research and development. *Sensors* 19:4557. doi: 10.3390/s19204557

Xiloyannis, M., Galli, L., Chiaradia, D., Frisoli, A., Braghin, F., and Masia, L. (2018). A soft tendon-driven robotic glove: Preliminary evaluation. *Biosyst. Biorobot*. 21, 329–333. doi: 10.1007/978-3-030-01845-0_66

Xing, K., Xu, Q., He, J., Wang, Y., Liu, Z., and Huang, X. (2008). "A wearable device for repetitive hand therapy," in *Proceedings of the 2nd Biennial IEEE/RAS-EMBS International Conference on Biomedical Robotics and Biomechatronics, BioRob 2008*, 919–923. doi: 10.1109/BIOROB.2008.4762789

Yap, H. K., Khin, P. M., Koh, T. H., Sun, Y., Liang, X., Lim, J. H., et al. (2017a). A fully fabric-based bidirectional soft robotic glove for assistance and rehabilitation of hand impaired patients. *IEEE Robot. Autom. Lett*. 2, 1383–1390. doi: 10.1109/LRA.2017.2669366

Yap, H. K., Lim, J. H., Nasrallah, F., and Yeow, C. H. (2017b). Design and preliminary feasibility study of a soft robotic glove for hand function assistance in stroke survivors. *Front. Neurosci*. 11:547. doi: 10.3389/fnins.2017.00547

Yap, H. K., Mao, A., Goh, J. C., and Yeow, C. H. (2016). "Design of a wearable FMG sensing system for user intent detection during hand rehabilitation with a soft robotic glove," in *Proceedings of the IEEE RAS and EMBS International Conference on Biomedical Robotics and Biomechatronics* (Singapore), 781–786. doi: 10.1109/BIOROB.2016.7523722

Yonezawa, K., Mizutani, N., Kato, N., Yano, K., Kobayashi, Y., Aoki, T., et al. (2013). "Extension force control considering contact with an object using a wearable robot for an upper limb," in *Proceedings - 2013 IEEE International Conference on Systems, Man, and Cybernetics, SMC 2013* (Manchester), 3555–3560. doi: 10.1109/SMC.2013.606

Yoo, H.-J., Lee, S., Kim, J., Park, C., and Lee, B. (2019). Development of 3d-printed myoelectric hand orthosis for patients with spinal cord injury. *J. NeuroEng. Rehabil*. 16:162. doi: 10.1186/s12984-019-0633-6

Yurkewich, A., Kozak, I. J., Hebert, D., Wang, R. H., and Mihailidis, A. (2020a). Hand extension robot orthosis (hero) grip glove: enabling independence amongst persons with severe hand impairments after stroke. *J. NeuroEng. Rehabil*. 17:33. doi: 10.1186/s12984-020-00659-5

Yurkewich, A., Kozak, I. J., Ivanovic, A., Rossos, D., Wang, R. H., Hebert, D., et al. (2020b). Myoelectric untethered robotic glove enhances hand function and performance on daily living tasks after stroke. *J. Rehabil. Assist. Technol. Eng*. 7:2055668320964050. doi: 10.1177/2055668320964050

Zhang, J., Wang, B., Zhang, C., Xiao, Y., and Wang, M. Y. (2019). An EEG/EMG/EOG-based multimodal human-machine interface to real-time control of a soft robot hand. *Front. Neurorobot*. 13:7. doi: 10.3389/fnbot.2019.00007

Zhou, Y. M., Hohimer, C., Proietti, T., O'Neill, C. T., and Walsh, C. J. (2021). Kinematics-based control of an inflatable soft wearable robot for assisting the shoulder of industrial workers. *IEEE Robot. Autom. Lett*. 6, 2155–2162. doi: 10.1109/LRA.2021.3061365

Zhou, Y. M., Wagner, D., Nuckols, K., Heimgartner, R., Correia, C., Clarke, M., et al. (2019). "Soft robotic glove with integrated sensing for intuitive grasping assistance post spinal cord injury," in *Proceedings - IEEE International Conference on Robotics and Automation* (Montreal, QC), 9059–9065. doi: 10.1109/ICRA.2019.8794367

Zinchenko, K., Wu, C. Y., and Song, K. T. (2017). A study on speech recognition control for a surgical robot. *IEEE Trans. Indus. Inform*. 13, 607–615. doi: 10.1109/TII.2016.2625818

Conflict of Interest: The authors declare that the research was conducted in the absence of any commercial or financial relationships that could be construed as a potential conflict of interest.

Publisher's Note: All claims expressed in this article are solely those of the authors and do not necessarily represent those of their affiliated organizations, or those of the publisher, the editors and the reviewers. Any product that may be evaluated in this article, or claim that may be made by its manufacturer, is not guaranteed or endorsed by the publisher.

frontiers in Neurorobotics

ORIGINAL RESEARCH
published: 10 March 2022
doi: 10.3389/fnbot.2022.815716

Designing Prosthetic Hands With Embodied Intelligence: The KIT Prosthetic Hands

Pascal Weiner†, Julia Starke†, Samuel Rader†, Felix Hundhausen and Tamim Asfour**

High Performance Humanoid Technologies Lab, Department of Informatics, Institute for Anthropomatics and Robotics, Karlsruhe Institute of Technology (KIT), Karlsruhe, Germany

Hand prostheses should provide functional replacements of lost hands. Yet current prosthetic hands often are not intuitive to control and easy to use by amputees. Commercially available prostheses are usually controlled based on EMG signals triggered by the user to perform grasping tasks. Such EMG-based control requires long training and depends heavily on the robustness of the EMG signals. Our goal is to develop prosthetic hands with semi-autonomous grasping abilities that lead to more intuitive control by the user. In this paper, we present the development of prosthetic hands that enable such abilities as first results toward this goal. The developed prostheses provide intelligent mechatronics including adaptive actuation, multi-modal sensing and on-board computing resources to enable autonomous and intuitive control. The hands are scalable in size and based on an underactuated mechanism which allows the adaptation of grasps to the shape of arbitrary objects. They integrate a multi-modal sensor system including a camera and in the newest version a distance sensor and IMU. A resource-aware embedded system for in-hand processing of sensory data and control is included in the palm of each hand. We describe the design of the new version of the hands, the female hand prosthesis with a weight of 377 g, a grasping force of 40.5 N and closing time of 0.73 s. We evaluate the mechatronics of the hand, its grasping abilities based on the YCB Gripper Assessment Protocol as well as a task-oriented protocol for assessing the hand performance in activities of daily living. Further, we exemplarily show the suitability of the multi-modal sensor system for sensory-based, semi-autonomous grasping in daily life activities. The evaluation demonstrates the merit of the hand concept, its sensor and in-hand computing systems.

Keywords: humanoid hands, prosthetic hand, grasping, embedded systems, underactuation, embedded sensing, sensor-based grasping

OPEN ACCESS

Edited by:
Florian Röhrbein, Technische Universität Chemnitz, Germany

Reviewed by:
Yulia Sandamirskaya, Intel, Germany
Horacio Rostro Gonzalez, University of Guanajuato, Mexico

****Correspondence:***
Pascal Weiner
pascal.weiner@kit.edu
Tamim Asfour
asfour@kit.edu

† These authors have contributed equally to this work

Received: *15 November 2021*
Accepted: *01 February 2022*
Published: *10 March 2022*

Citation:
Weiner P, Starke J, Rader S, Hundhausen F and Asfour T (2022) Designing Prosthetic Hands With Embodied Intelligence: The KIT Prosthetic Hands. Front. Neurorobot. 16:815716. doi: 10.3389/fnbot.2022.815716

1. INTRODUCTION

Hand prostheses allow amputees to regain autonomy and abilities in their daily life. Recent advances in prosthetic hand development have led to sophisticated multiarticulated devices. However, the rejection rate of myoelectric prostheses is very high with 18–23% and another 30% only use their myoelectric prosthesis as a passive device according to Biddiss and Chau (2007) and Østlie et al. (2012). One cause for this problem arises from limitations in terms of intuitiveness-of-use and a high level of user control effort to execute grasping tasks. These limitations can be relaxed

by the integration of intelligent hardware and software. Underactuated mechanisms have proven to be a very promising way to design robot hands with a small number of active degrees of freedom (DoF) as shown for example by Fukaya et al. (2000), Belter and Dollar (2013), and Catalano et al. (2014) amongst others. Such hands are able to adapt to the shape of objects to reliably execute grasps while exploiting the physical interaction with the object. In addition, intelligent control strategies significantly reduce the cognitive burden on the user by taking information about the environment and user intention into account to autonomously select suitable grasps while keeping the user in the loop. Such semi-autonomous control strategies are an emerging research topic with several recent developments e.g., by Došen et al. (2010), Markovic et al. (2015), and Ghazaei et al. (2017) amongst others. However, semi-autonomous control requires profound knowledge about the environmental situation and the user intention which must be acquired by an appropriate sensor system and sufficient computing resources to extract such knowledge from sensor data. In particular, visual perception is key for scene understanding which is needed to recognize and segment objects to be grasped.

In this paper, we present our recent work on the development of highly integrated prosthetic hands that are equipped with on-board sensors and computing power to support the realization of semi-autonomous grasping. The hands, as depicted in **Figure 1**, are driven by two DC motors, one motor for the thumb and one for the fingers, with a total of 10 DoF. Specifically, we describe the new version of our prosthetic hands, the female version, which is based on our previous work regarding the design of prosthetic hands in Weiner et al. (2018) and in-hand visual data processing for object detection by Hundhausen et al. (2019). The female prosthesis extends our previous work on the male hand in terms of sensing and visual perception capabilities, underactuated mechanism and shows the scalability of our design to different hand dimensions.

The paper is organized as follows: Section State of the Art provides an overview over the state of the art in prosthetic hand design. In Section Key Requirements the key requirements governing the development of our hand prostheses are explained. The mechanical design as well as the sensors and embedded system are detailed in Section Design and Mechatronics. Section Evaluation describes experimental results regarding main characteristics and real-world grasping studies. The paper concludes with a summary and discussion in Section Evaluation.

2. STATE OF THE ART

Throughout the last two decades the development of artificial humanoid hands has made considerable progress regarding mechatronics and control strategies of such hands. A comprehensive list with a broad overview of hand development is given by Piazza et al. (2019), including both prostheses and robotic hands. **Table 1** gives an overview of recent developments in myoelectric hand prostheses with a special focus on built-in intelligent capabilities that are needed for semi-autonomous control.

As can be seen from the degrees of freedom (DoF) and degrees of actuation (DoA), all prosthetic hands make use of underactuation to reduce the number of motors and overall control complexity. Most research prostheses address the question of how to realize adaptive hand behavior. In the SmartHand by Cipriani et al. (2011), one motor drives three fingers by an adaptive mechanism using series elastic elements to integrate compliance into the design while being not back-drivable due to a spindle drive. The Southampton Hand by Kyberd et al. (2001) actuates middle, ring and little finger with a lever-linkage mechanism allowing adaptive finger closing. The SoftHand Pro-D by Piazza et al. (2016) and the Hannes Hand by Laffranchi et al. (2020) utilize a single motor to drive all fingers via tendons.

The trade-off between size, weight and force is an important consideration for both commercial and research prostheses. **Table 1** shows that while the weight of most research prostheses is well in the range of the human hand weight, both size and grasping forces vary considerably.

Several sensors as well as an embedded system are commonly used in research prostheses. Position sensing is implemented by almost all prostheses either by means of motor relative encoders or joint angle encoders. Joint angle encoders have the advantage that the kinematic state of the prosthesis is completely known, while motor relative encoders in underactuated hands often only allow for an estimation of the state of the hand. Force sensing is either implemented by integrating tactile sensors into the fingertips, load cells inside the finger structure or in series with the tendons. Zhao et al. (2016) recently also introduced flexible tactile sensors to prosthetic hands, covering the whole finger surface. Further, several grasp force controllers have been proposed, such as in Pons et al. (2004), Carrozza et al. (2006), Huang et al. (2006), and Tavakoli et al. (2017) among others. Other sensor modalities such as cameras, distance sensors or IMUs are not yet readily available in hand prostheses, as can be seen in **Table 1**. Several prostheses integrate an embedded system based on one or more microcontrollers, which is mostly used for low-level motor control.

3. KEY REQUIREMENTS

To provide support for the user performing diverse activities of daily living (ADL), as for example food preparation, housekeeping or tool use amongst others, a prosthesis has to be reliable and versatile in terms of its grasping capabilities, i.e., it should be able to successfully perform a wide variety of ADLs (Matheus and Dollar, 2010). The user expects their prosthesis to be effortless and intuitive despite the inherent complexity of the mechatronics and control (Cordella et al., 2016). The pivotal point of our hand development is therefore to endow prosthetic hands with intelligent grasping capabilities to support intuitiveness-of-use and to reduce the cognitive burden of the user. In this work, we strive for intelligent hand mechatronics, that provide the sensor information and capabilities to render

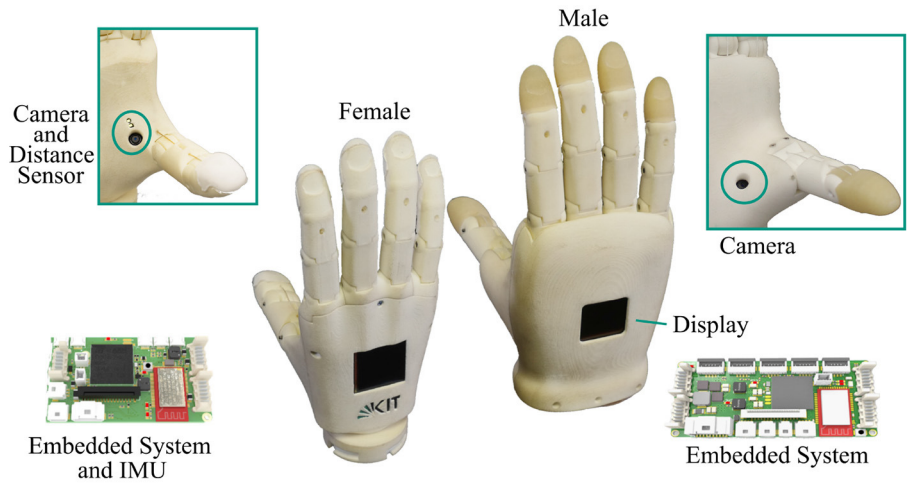

FIGURE 1 | The KIT Prosthetic Hands; female (left) and male (right) intelligent hand prostheses designed for semi-autonomous grasp control. Each hand has two DC motors actuating 10 DoF via an underactuated mechanism. Each hand is equipped with a camera in the palm, IMU and a distance sensors (female version) as well as an integrated embedded system for in-hand sensor data processing and control.

TABLE 1 | Overview of commercial and research prostheses.

Prosthesis	Actuation				Sensors					Mechanical characteristics		
	DoF	DoA	Adap. Un.[a]	Emb. Sys.[b]	Position[c]	Force	Orientation	Vision	Distance	Size[d]	Weight[e]	Force[f]
SensorHand (SensorHand, 2020)	2	1	○	●	n.a.	●	○	○	○	178–210 l	460	100 PG
iLimb pulse (Belter and Dollar, 2013)	11	5	○	●	n.a.	○	○	○	○	180–182 l x 75–80 w x 35–45 h	460–465	6.2–11.8 FF
Bebionic (Belter and Dollar, 2013)	11	5	○	●	n.a.	○	○	○	○	190–200 l x 84–92 w x 50 h	495–539	12.3–16.1 FF
Michelangelo (Belter and Dollar, 2013)	6	2	○	●	n.a.	n.a.	○	○	○	180 l	420	70 P
Vincent hand (Belter and Dollar, 2013)	11	6	○	●	n.a.	n.a.	○	○	○	145–180 l x 65–85 w	386 (XS)	4.8–8.4 FF
Taska Hand (Taska, 2020)	10	6	○	●	n.a.	n.a.	○	○	○	179–181 l x 81–88 w	556–671	6.7–22 FF
MANUS-Hand (Pons et al., 2004)	10	3	○	●	●	●	○	○	○	1.2*50th percentile male	1200[g]	60 PG
HIT/DLR Prosthetic hand (Huang et al., 2006)	13	3	S	●	●	●	○	○	○	n.a.	n.a.	n.a.
CyberHand (Carrozza et al., 2006)	16	6	○	○	●	●	○	○	○	n.a.	360	70 PG
SmartHand (Cipriani et al., 2011	16	4	S	●	●	●	○	○	○	50th percentile male	520	16–36 PG
Vanderbilt (Wiste et al., 2011)	16	4	S	○	◖	○	○	○	○	n.a.	320	10–34 FF
UT Hand I (Peerdeman et al., 2014)	15	3	W	○	●	●	○	○	○	185 l x 82 x w x 26 h	n.a.	n.a.
Vanderbilt 2 (Bennett et al., 2015)	9	4	S	●	◖	○	○	○	○	200 l x 89 w	546	15–30 FF
SoftHand Pro-D (Piazza et al., 2016)	19	1	T	●	○	○	○	○	○	235 l x 230 w x 40 h	n.a.	20 PG
SSSA-MyHand (Controzzi et al., 2017)	10	3	○	●	●	○	○	○	○	200 l x 84 w x 56 h	478	9.4–14.6 FF
Jeong et al., 2017	11	6	○	○	○	●	○	○	○	Average Male	380	15.7–48.2 FF
SCCA Hand (Wiste and Goldfarb, 2017)	11	5	S	○	◖	○	○	○	○	n.a.	437	146 PG
SoftBionic hand (Tavakoli et al., 2017)	10	2	T	●	◖	●	○	○	●	200 l x 91 w x 40 h	285	n.a.
Zhang et al. (2018)	11	6	T	●	◖	●	○	○	○	171 l x 80.2 w x 27.4 h	450	8-12 FF
PRISMA Hand II (Liu et al., 2019)	19	3	S	○	◖	●	○	○	○	210 l x 80 w	n.a.	n.a.
Galileo hand (Fajardo et al., 2020)	15	6	○	●	◖	○	●	○	○	162 l x 69.6 w x 25 h	350	50 PG
KIT Prosthetic hand male (Weiner et al., 2018)	10	2	W	●	◖	○	○	●	○	232[h] l x 87 w x 35 h	768	6.2-8.2 FF, 24.2 PG
KIT Prosthetic hand female	10	2	T	●	◖	○	●	●	●	194[h] l x 77 w x 28 h	377	9.0-12.3 FF, 40.5 PG

[a]Adaptive underactuation of multiple fingers, S for spring-based mechanism, T for tendon-based mechanism, and W for whippletree-based mechanism; [b]Embedded system integrated; [c]● in case of joint angle encoders and ◖ for motor relative encoders; [d]Dimensions in mm, l: length, w: width, h: height; [e]Measured weight in Gramm; [f]Measured force in Newton, PG: Power Grasp, FF: Finger Forces, P: Pinch; [g]Including wrist and socket; [h]Including hand adapter; ○: not included, n.a.: unknown.

intuitive, partially autonomous grasp control possible. In the following, we discuss the key requirements that should be taken into account in the context of the development of such prosthetic hands. These concern the simplicity of mechanical design, the ability to perceive and interpret the current scene, the computing system needed for sensor data processing and control as well as requirements regarding size, weight and appearance of the hand. Underactuated mechanical designs have shown how grasping behavior can be achieved by intelligent hand and finger mechanisms that are able to autonomously self-adapt the hand morphology to the object shape, see Pfeifer and Gómez (2009) and Carrozza et al. (2006). This allows the realization of basic grasping by exploiting the interaction of the hand with the object while using simple and often none precise control.

While such self-adaption of the hand reduces the control complexity for closing the hand, it does not simplify other parts of a grasping action for the prosthetic hand user. This includes the selection of a grasp type, hand preshape and hand orientation, which depend on the object to be grasped and on task-specific constraints. Thus, an intuitive-to-use prosthetic hand should be able to autonomously determine suitable grasps, hand preshapes and orientations based on the available object information and the user intention. To keep the human in the loop, the execution of the different parts of a grasping action should always be supervised by the user leading to semi-autonomous grasping behavior. Different semi-autonomous control schemes have been proposed in literature and have proven to reduce the cognitive burden for the user (Došen et al., 2010; Markovic et al., 2015; Ghazaei et al., 2017).

To achieve such semi-autonomous grasping behavior, a multi-modal sensor system is needed to perceive the scene, extract important object information as well as to capture user's state and intention. Visual perception plays a key role for scene understanding, in particular for object detection that is needed to generate suitable grasps. Thus, vision systems have been a central part of semi-autonomous grasping setups, with cameras attached to the human body or the environment to provide the necessary information. In our work, we integrate a camera, an IMU and a distance sensor in the prosthesis to provide a fully integrated system enabling semi-autonomous grasping. In addition, according to Cordella et al. (2016), providing feedback to the user about the state of their prosthetic hand is important and should be considered. For processing and interpretation of multi-modal sensory data, appropriate computing resources are needed that can be integrated in the hand while taking into account space limitations and energy consumption. In addition, resource-aware image processing and machine learning methods are needed.

Finally, the hand needs to comply with the general design requirements for prosthetic hands in terms of size, weight, grasp force, speed and appearance (Pylatiuk et al., 2007; Wijk and Carlsson, 2015; Cordella et al., 2016; Schweitzer et al., 2018). Thus, the design of the prosthetic hand should take into account the scalability in size to fit a large portion of the population. To show the feasibility of integrating the intelligent functions described above within the severe space limitations of prostheses, we design a hand with the size of a 50th percentile female hand according to the German standard specification (DIN 33402-2). According to the literature, the weight of the prosthetic hand should not exceed 400 g to match the weight of a human hand (Kaye and Konz, 1986). Further, the grasping force and closing speed of the hand should be comparable to commercial hands, as reported in Belter and Dollar (2013).

4. DESIGN AND MECHATRONICS

The KIT Prosthetic Handis an underactuated myoelectric prosthetic hand driven by two motors and controlled via muscle signals extracted by *electromyography* (EMG). In this section we present the mechanical and electrical design of the female prosthesis offering mechanical grasp support via underactuation and providing a platform for intelligent and context-aware control algorithms. The advances in design are shown in comparison to the male prosthesis described in Weiner et al. (2018).

4.1. Actuation and Adaptive Mechanism

The design of the prosthesis incorporates two DC motors (2224U012SR, Faulhaber) that are equipped with relative encoders (IEH2-512, Faulhaber) and a planetary gear (Series 20/1R, Faulhaber) with 23:1 transmission. The first motor drives the thumb flexion. All four fingers are actuated together by the second motor via an underactuated mechanism. Both versions of the mechanism in the male and female hand are depicted in **Figure 2**.

For the male hand, we presented the mechanism in **Figure 2** consisting of a rocker that is centrally pulled by a tendon on pulley ③ connected to the motor at ④. The tendons ⑥ and ⑦ connecting two fingers each are fixed on either side of the lever bar and rotate around the floating pulleys ① and ②. As long as all of the fingers can close freely, all finger tendons are pulled equally causing finger flexion. If one finger is blocked by an object, the tendon turns around its pulley, thereby further closing the second finger connected to the same tendon. If both fingers connected to a tendon cannot close any further, the lever of the mechanism rotates and allows the other two fingers to continue closing. This mechanism design provides the prosthesis with the ability to wrap around arbitrarily shaped objects without the need of complex control input.

In the female hand, the mechanism is further improved regarding the required input force, sizing and friction. The lever is replaced by two separate sliders ① and ② consisting of two connected pulleys. The sliders are free floating and move along their individual guides. The tendon coming from the motor at ④ is led around one pulley of slider ②, a fixed guiding pulley ③ and to slider ①, before it is fixed at the housing at ⑤. The tendons ⑥ and ⑦ connecting two fingers each are led around the second pulley of one slider each. By pulling the motor tendon, the force is still equally distributed to all four fingers by similarly actuating both sliders. The distribution between two fingers remains the same as in the first hand version while the lever is replaced by the two sliders distributing force between the individual pairs of fingers.

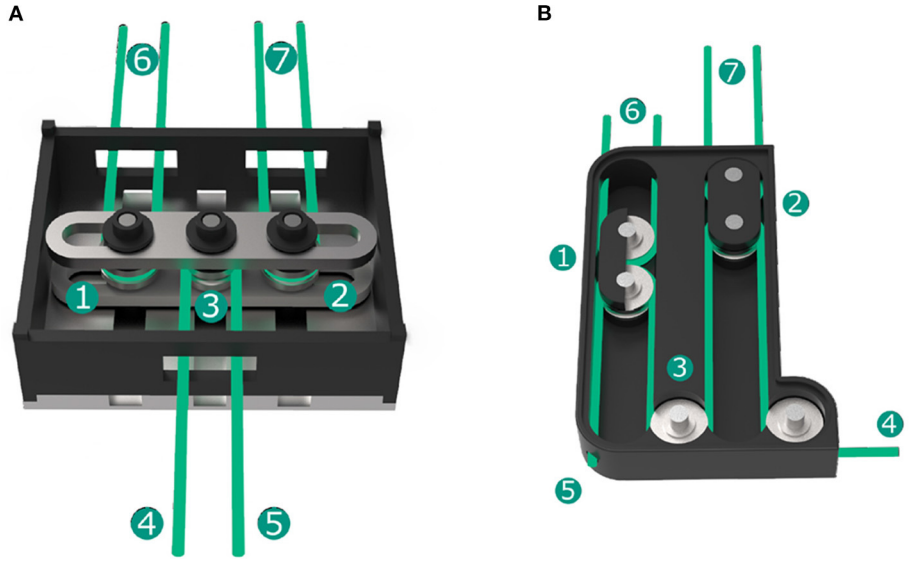

FIGURE 2 | Underactuated force distributing mechanism for the fingers; the mechanism in the male hand connects two fingers by a single tendon and the pairs of fingers by a lever **(A)**; the mechanism in the female hand actuates pairs of fingers by free floating sliders interconnected by the motor tendon **(B)**.

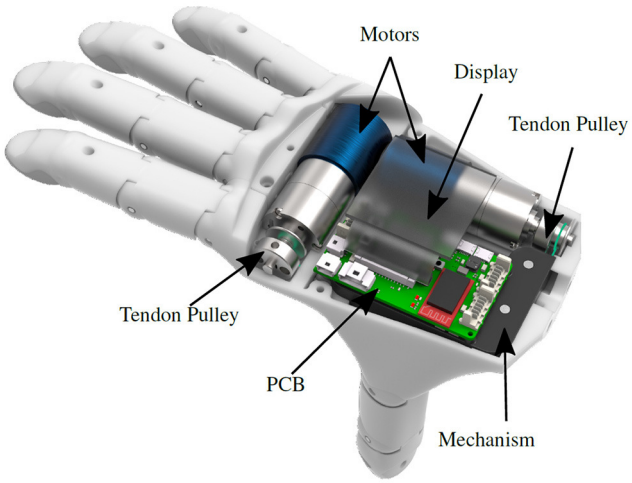

FIGURE 3 | The female prosthesis with motors, mechanism and PCB integrated into the palm. Camera and distance sensor are mounted below the mechanism. The mechanism in black is mounted below the PCB. The display is fixed on top of the PCB in the dorsal housing. The display is rendered semi-transparent to make the components underneath visible.

Apart from the reduced dimensions of the mechanism, the additional redirection of the tendon between both sliders results in a force transmission ratio of 2:1, thereby doubling the finger force compared to the tendon force on the motor pulley. Together with a decrease of the diameter of the motor pulley from 16 to 8 mm, which corresponds to an additional transmission ratio of 2:1, this allows the reduction of the transmission gear of the motor by factor four from 86:1 in the male hand to 23:1 in the female hand. Therefore, the gear needs one reduction stage less, hence making the gear shorter and lighter while also increasing transmission efficiency.

As the sliders are held in constant tension between motor and finger tendon, they are free-floating and thereby cause no friction against the mechanism walls. All pulleys are supported by ball bearings. This further reduces the friction within the mechanism, thereby increasing the resulting finger force. The design with individual sliders makes the mechanism suitable to be used with other finger designs. This has been shown in the development of the KIT Finger-Vision Soft Hand described by Hundhausen et al. (2020) in which three fingers are driven with an adapted version of this mechanism.

4.2. Mechanical Design

The mechanism and motors are placed within the palm of the hand together with the sensors and the embedded system, as shown in **Figure 3**. The male and female prostheses have the size of a 50th percentile male and female hand, respectively, according to the German standard specification (DIN 33402-2). Individual finger segment lengths are based on the human hand length study by Vergara et al. (2016). The dimensions of both prosthetic hands are listed in **Table 2**.

Despite a reduction of the integration space by 30.9 % compared to the male hand, all hardware components including the two motors, the underactuated mechanism, sensors and the embedded system are integrated into the palm of the female prosthesis. The fingers are designed based on a CAD model, which allows scaling of the hand according to the size of the user's able hand. To support a lightweight design, the housing, finger phalanges and mechanism sliders are 3D-printed using

TABLE 2 | Dimensions of the KIT prosthetic hands.

Hand part		Male (mm)	Female (mm)
Palm	Length	111	100
	Width	87	77
	Depth	30	26
Thumb	Proximal phalanx	37.0	32.7
	Distal phalanx	37.7	33.2
Index finger	Proximal phalanx	29.9	27.0
	Intermediate phalanx	28.0	26.4
	Distal phalanx	27.1	25.5
Middle finger	Proximal phalanx	33.6	30.3
	Intermediate phalanx	32.3	30.4
	Distal phalanx	28	26.3
Ring finger	Proximal phalanx	30.1	26.9
	Intermediate phalanx	31.3	29.3
	Distal phalanx	28.6	26.8
Little finger	Proximal phalanx	22.8	20.5
	Intermediate phalanx	23.9	22.6
	Distal phalanx	27.3	25.7

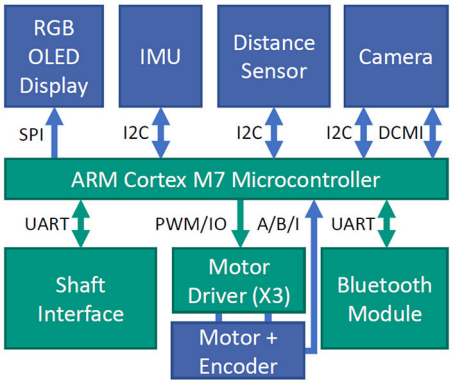

FIGURE 4 | Block diagram showing the functional units of the embedded system. Parts in green are directly placed on the central PCB, the parts in blue are separate components distributed throughout the hand.

selective laser sintering from polyamide (PA2200), a robust, yet flexible plastic.

The fingers are actuated by 0.4 mm Dyneema tendons. Each finger comprises actuated flexion in the *metacarpophalangeal joint* (MC joint) and the *proximal interphalangeal* joint (PI joint). The *distal interphalangeal joint* (DI joint) is fixed at an angle of 20°. The resulting 10 joints are equipped with ball bearings and the tendon is routed through Teflon tubes (PTFE) to minimize friction. Torsion springs are included in the finger joints and support the passive extension of the fingers. A higher pretension of the springs in the PI joints leads to a higher closing speed of the MC joints compared to the PI joints. This results in a human-like spiral fingertip closing trajectory, as shown by Kamper et al. (2003).

The fingertips are equipped with high friction finger pads to enhance the friction with the grasped object and thereby lower the required force to perform a stable grasp. The pads cover the palmar side of the medial and distal phalanges and envelop the tip as well as radial and ulnar side of the distal phalanx. They are cast from silicone and glued to the fingertip housing structure.

4.3. Embedded Sensor System

Both male and female prosthetic hands contain a multi-modal sensor system, a display and an embedded system to support intelligent sensor data processing and control without the need for external devices such as smartphones. To gain information about the proximate surroundings of the hand, the prostheses embed a camera (OV2640, OmniVision) at the base of the thumb. The camera module has a size of $8 \times 8 \times 6.3$ mm and is connected to the processor's digital camera interface (DCMI) by a 24 pin flat-flex cable. The camera is configured to provide a 176×144 pixel RGB image at 10 frames per second. In the female prosthesis, a Time of Flight (ToF) distance sensor (VL53L1X, STMicroelectronics) placed close to the camera is used to measure the distance of a target object to the hand. Relative motor encoders and, in the female version, an IMU (BNO055, Bosch Sensortec) located on the embedded system's PCB provide proprioceptive information. In addition the state of the users forearm can be estimated using the IMU.

For processing the different sensor data and camera images as well as for control, an embedded system is integrated into the hand, directly above the mechanism. An overview of the complete system inside the hand is shown in **Figure 4**. The system is based on an ARM Cortex-M7 core (STM32H7, STMicroelectronics) running at 400 MHz. The embedded system includes a shaft interface to e.g., connect to a wrist rotation unit or EMG-electrodes.

On the embedded system a resource-aware convolutional neural network is implemented to recognize a set of known objects in the camera image as described in Hundhausen et al. (2019). To this end, an RGB image obtained from the camera is resized to 72×72 pixels and is used as input for the network. The hyperparameters of the network architecture are optimized using a genetic algorithm. These hyperparameters include the number of convolution filters, kernel size, strides and pooling types. For more details on the network architecture synthesis we refer the reader to Hundhausen et al. (2019). The cost function used for optimization is rating the network's accuracy after training as well as the network's number of multiply-accumulate-operations during inference. The targeted amount of operations is set to two million operations which allows inference by the given hardware in approximately 150 ms which was identified as an acceptable delay by Farrell and Weir (2007).

The network is trained on a dataset consisting of 13 object classes with 300 images per class. The images are augmented whereby the objects are segmented in the images and the background is replaced by artificially generated noise. For inference, the network is implemented using the CMSIS:NN framework (Lai et al., 2018) that allows optimized execution on the ARM processor. Using this optimized inference, the runtime

can be reduced to 23.3 % of the not optimized implementation and inference takes 115 ms. The classification accuracy on the test set of the recorded data amounts to 96.51 %. In addition to the recognition of known objects, we also investigate object segmentation for further estimation of object orientation and for obtaining knowledge about the object shape, see Hundhausen et al. (2021). For this purpose an encoder-decoder network is designed that outputs a pixel-wise mask that segments trained objects in the images. The object class determined by the classification network in combination with inertial sensor data can be used for the selection of a suitable grasp type.

An OLED display in the back of the hand provides feedback to the user about the current status of the hand as well as the proposed grasp type and the orientation for a recognized object.

5. EVALUATION

The female prosthetic hand is evaluated and compared to the male prosthetic hand to assess the improvement of the design. The evaluation includes the hand characteristics in terms of grasping force, closing speed and hand weight. In addition, an assessment of grasping functionality using an adapted version of the YCB Assessment Protocol is performed and a task-oriented evaluation of object grasping and manipulation is conducted. The context information provided by the multi-modal sensor system is evaluated in a sensor-based grasping experiment.

5.1. Prosthesis Characteristics

The grasp force of the prosthesis in a cylindrical power grip is assessed using a sensorized wooden cylinder of 49 mm diameter that integrates a 6D force/torque sensor (Mini 40, ATI Industrial Automation). The cylinder is grasped by the prosthesis with the thumb and the fingers touching on opposite sides of the sensor and held vertically. The individual finger forces are measured by positioning the flat hand directly over the force/torque sensor. By closing the hand, one finger is pressed onto the sensor while the others close freely. This procedure is performed for every finger. Both measurements are repeated 15 times each.

The cylindrical power grasp force amounts to a mean of 24.2 N with a standard deviation of ±1.9 N for the male prosthesis and 40.5 ± 8.1 N for the female hand. The mean finger forces range between 6.2–8.2 N and 9.0–12.3 N for the male and female hands, respectively. The individual forces of the different fingers are shown in **Figure 5**. The thumb grasp force in an extended configuration amounts to 53.1 ± 1.4 N.

The hand closing time is measured in an experimental setup, in which we track the fingertip positions of index and thumb in image sequences. To determine the time, we repeated the experiments five times. The hand was placed in front of the camera lying on the back of the hand on a flat surface, exposing thumb and index finger to the camera, see **Figure 6**. This orientation of the hand represents the worst case for fast closing, as gravity in this orientation pulls the finger open and is hindering fast acceleration of the fingers, whereas rotation of the hand by 180° would result in gravity-assisted finger closing. The finger tips were marked using red tape for color-based tracking. The tracking of one corner of the red tape was performed using the video tracking software *kinovea*[1] as shown in **Figure 6**. While the male hand closes entirely in 1.32 s±0.04 s, the female hand exhibits a closing speed of 0.73 s±0.02 s. The nominal maximum motor speed is kept constant for both versions.

The female prosthesis weighs 377 g and requires material costs of 896 €, as shown in **Figure 7**. The male hand has a weight of 670 g and material costs of 1008 €. The bulk of weight

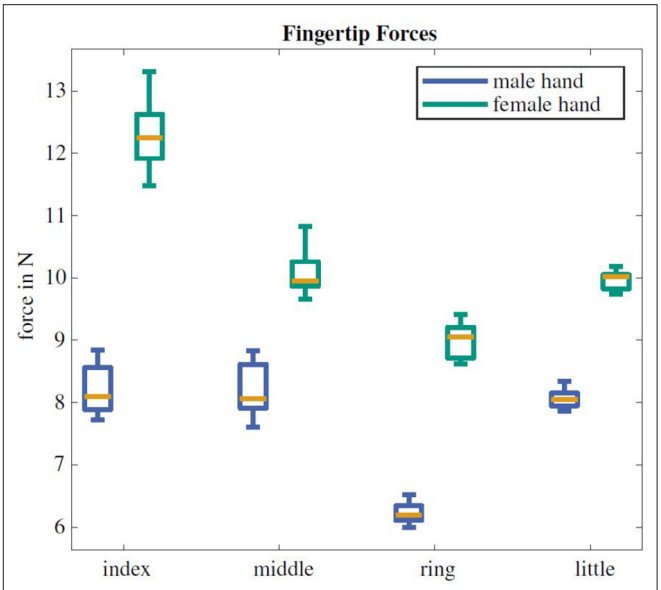

FIGURE 5 | Fingertip forces of the male and female prosthesis. The orange line marks the median force, the box boundaries denote the first and third quartile and the outer lines depict the extrema of the respective fingertip force.

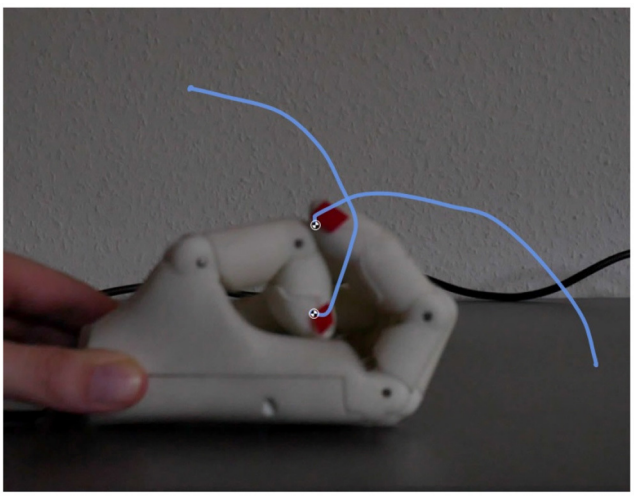

FIGURE 6 | Snapshot from the video evaluation of the female hand closing speed. Red markers on thumb and index finger are tracked in the video sequence, blue lines indicate the closing trajectories of these two fingers.

[1]https://www.kinovea.org/

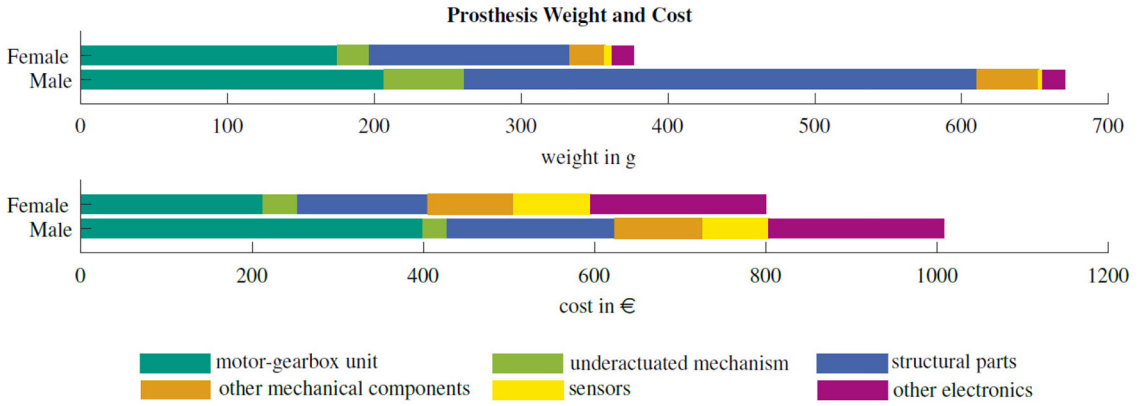

FIGURE 7 | Distribution of weight and cost among the components of the male and female KIT Prosthetic Hand.

reduction is achieved by optimizing the structural 3D-printed parts for the palm. In contrast to the mechanism in the male version, which was milled from aluminum, the mechanism in the female hand is also 3D-printed, reducing the weight by 60 %. Due to the additional transmission ratio of 2:1 in the mechanism and reduction of the diameter of the motor tendon pulley, additional weight is saved as the motor requires one reduction gear stage less.

5.2. Grasping Ability

We evaluated the grasping and manipulation abilities of the hands using 1) the *YCB Gripper Assessment Protocol* to assess grasping abilities and 2) a second *task-oriented protocol* for assessing the hand performance in activities of daily living (ADL).

YCB Gripper Assessment Protocol

The general grasping ability is assessed based on the YCB Gripper Assessment Protocol as proposed by Calli et al. (2015). In contrast to the original protocol, we include all object categories from the *YCB Object Set* except for the task items category. This category, containing e.g., a peg-in-hole board or the assembly of an airplane toy, is excluded from the evaluation as we focus on the assessment of the hand grasping abilities. Altogether, 60 objects were tested. No position offsets are applied to the objects as these are compensated by the user. The procedure consists of grasping each object from a table, holding it for 3 s and rotating it by 90°.

The procedure was applied to both the male and female prosthetic hand while being manually controlled by a human operator. One point is scored if the object is successfully lifted and held. A second point is scored if the object does not move or slide inside the hand, a third point is scored if the object remains grasped after the rotation and the fourth point is scored if the object does not move inside the hand after rotation. The maximum score that can be achieved for each object is four. For the articulated objects (table cloth, chain, rope, t-shirt) the object is grasped and lifted three times and half a point is granted for each successful attempt.

The scores were 193 and 203.5 of the possible 230 points for the male and female hand, respectively. In total 85.2 % of all objects could be grasped with the male hand and 91.8 % with the female hand. Both hands encounter difficulties in grasping thin and small objects like credit cards, nails and washers. Despite the smaller size of the female hand, there are no notable shortcomings in grasping large objects, like the wood block or the mini soccer ball from the YCB Object Set. Both hands are able to lift the heavy objects from the YCB object with a full score, for example the power drill, the table cloth and the wood block. The skillet could be lifted at the handle, but moved inside the hand during hand rotation due to the high torque on the handle.

Task-Oriented Protocol

The female hand is additionally evaluated with a task oriented protocol of common daily life activities. To this end, the prosthesis was mounted on a shaft, which can be worn below the forearm of the able hand and several activities of daily living were performed using the prosthesis. The tasks are selected based on the objects and activities proposed by Matheus and Dollar (2010). The list of the tasks is shown in **Figure 8**.

The execution of every task is repeated five times. The task execution quality is assessed with a score between 0 and 3 points. The used scoring system is designed as follows: one point is granted for achieving a stable grasp, a second point is granted for successful accomplishment of the task goal and the third point is granted when the task execution is done in a natural and comfortable manner compared to its execution with two able human hands. As an example, for the writing task, the first point is scored if the pen is stably held in the hand, the second point for writing the requested sentence on a piece of paper in a readable manner and the third point is granted only if the handwriting looks natural, the task is executed in a comfortable manner and the writing time is not disproportionally long. As defined in the Southampton Hand Assessment Procedure (SHAP) by Light et al. (2002), each task needs to be solved within eight times the time needed by an able-bodied person to be not considered disproportionally long. If the task execution requires more time, it can only be rated with two points at maximum.

The scores and execution times achieved with the female prosthesis are shown in **Figure 8**. In addition, the task failure rate over all five executions of each task is given. Over all activities, the task was not fulfilled successfully in 6.7 % of all executions. The

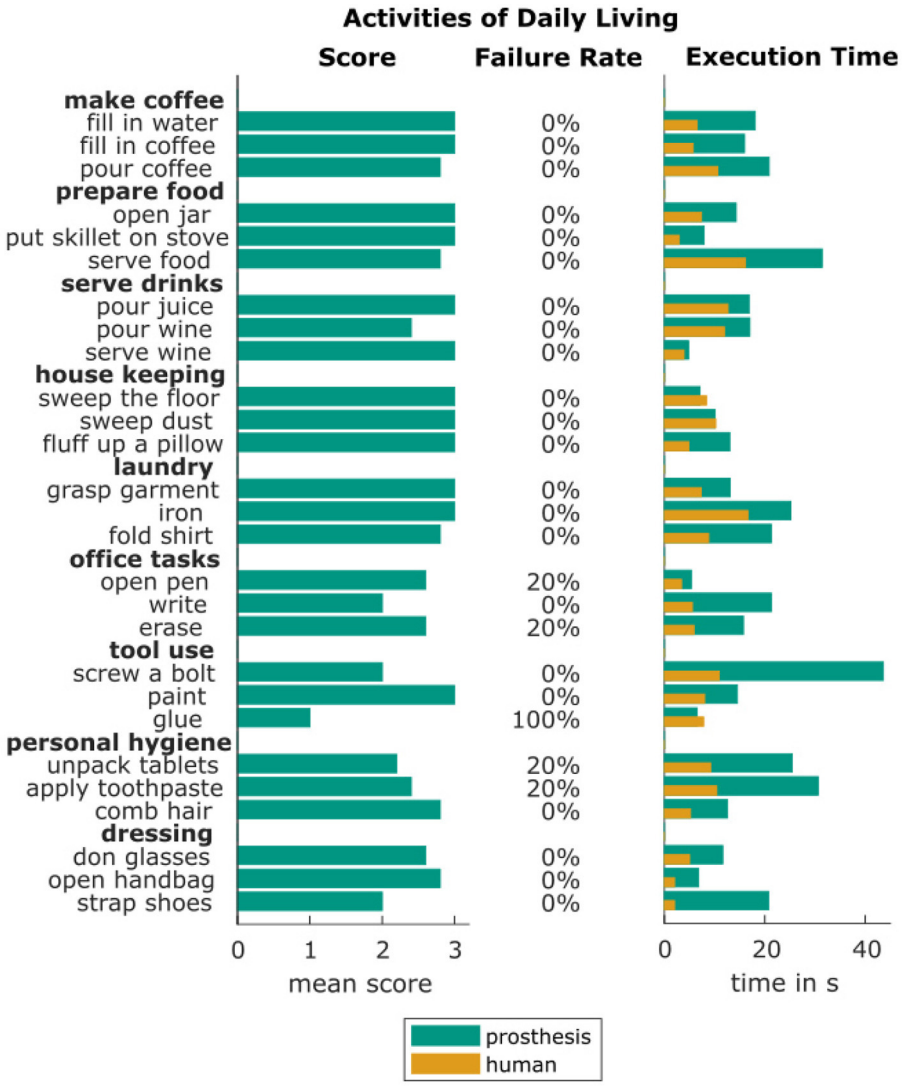

FIGURE 8 | Tasks performed in the task-oriented protocol with the mean prosthesis scores, ranging between 0 for the hand being unable to grasp the object to 3 for a comfortable task execution, the rate of failed task executions over five trials and the mean execution times with the prosthetic hand and an able human hand.

overall score of 88.6 % of achievable points indicates a satisfying functionality of the hand in performing activities of daily life.

The prosthesis was especially successful in executing everyday household activities like food preparation, house keeping and laundry. Lower task evaluation scores are mainly seen in office tasks as well as medicating and bathing tasks. This is due to the fact, that these tasks require more complex grasping and prehensile in-hand object manipulation. The only task that could not be accomplished by the prosthesis was gluing with a hot glue gun. While the gun could be grasped, the trigger could not be pressed by the index finger. The task of screwing a bolt into a nut was especially challenging, since the hand is not able to turn the screw driver within the hand, but instead the full hand needs to be rotated with the screwdriver. This results in unnatural and uncomfortable whole-body compensatory movements. No task took more than eight times the time of an execution with two able human hands. Strapping a shoe was the only task that exceeded the defined time constraint because the task took 10.4 times the time needed by a human with two able hands.

5.3. Sensor-Based Grasping

The merit of the multi-modal sensor system for grasp control is evaluated in the context of sensor-based grasping. All sensor readings are recorded and evaluated during two different grasping sequences of daily living activities. In the first sequence, a bottle of coke is grasped with the prosthesis, opened and the coke is poured into a glass. After the bottle is placed back on the table, a lemon is grasped and held firmly. A slice is cut off with a knife in the second hand and the lemon is placed on the table. The lemon slice is inserted into the glass of coke with the able hand. Before grasping, an image of the object is captured by the hand's integrated camera and the object recognition is

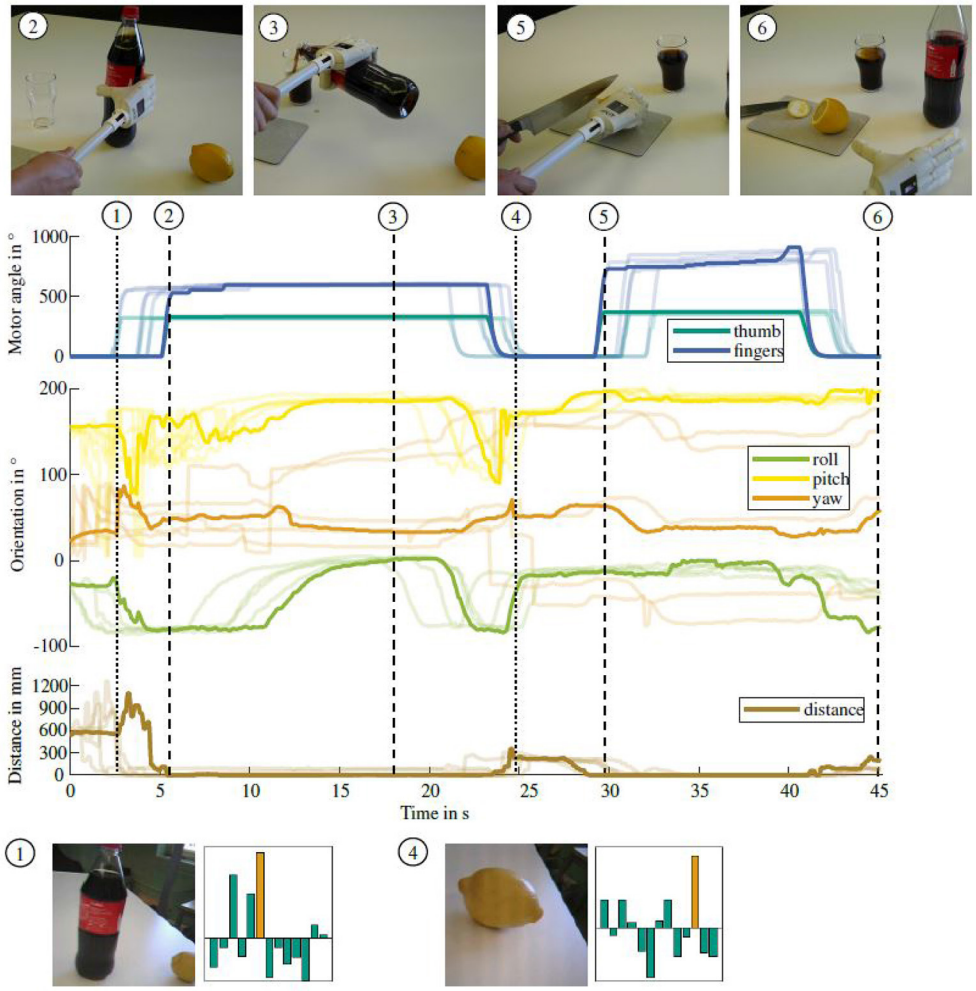

FIGURE 9 | Sensor readings while pouring coke into a glass and adding a slice cut off from a lemon. Graphs show an exemplary measurement of the motor positions, hand orientation from the IMU and object distance. Four additional experiments printed in the background underline the reliability of the sensor data. Important events of the grasping process are marked by dashed lines and corresponding images of the scene are shown above the graphs. The triggering of the object recognition is marked by dotted lines and an images captured by the hand camera together with the object recognition probabilities are shown below the graphs. The recognition probability of the coke bottle and lemon, respectively are marked in orange in the bar chart, indicating the object was recognized correctly.

run on the in-hand integrated embedded system. **Figure 9** shows the experimental procedure, the sensor readings and results of the object recognition. The camera image for object recognition is shown together with the recognition probabilities for all 13 trained objects in the bottom row. The correct object, being coke and lemon, respectively, is marked in orange in the bar chart diagrams. In both cases, the object recognition returns the highest probability for the correct object, allowing for object-specific grasp control. An in-depth evaluation and discussion of the object recognition algorithm can be found in our previous work in Hundhausen et al. (2019).

The sensor readings for five executions of the task are shown in the middle of **Figure 9**. The associated sensor readings are plotted in solid lines for an exemplary execution and in transparent lines for the remaining four executions. All sensor readings have been normalized over the execution time, to show the similarity of the acquired sensor data throughout several executions. Grasping the bottle is finished after 5.2 s, which is clearly visible in the motor position data. Similarly the bottle is placed on the table after 23.3 s, coincident with the motor position moving back to the initial state. Grasping and releasing the lemon occur at 29.9 s and 40.6 s, respectively.

Approaching the object can also be inferred from the distance sensor in the palm, which shows a decrease of the object distance from 379 mm to 15 mm between 3.6 s and 5.1 s. The grasping action can therefore be controlled based on the distance to the object which is provided by the distance sensor. As the ball of the thumb does not touch the bottle, the distance sensor does not decrease to zero throughout the grasp. The release of the object, which is also visible in the finger motor positions, is consequently followed by an increase of the object distance starting after 24.6 s.

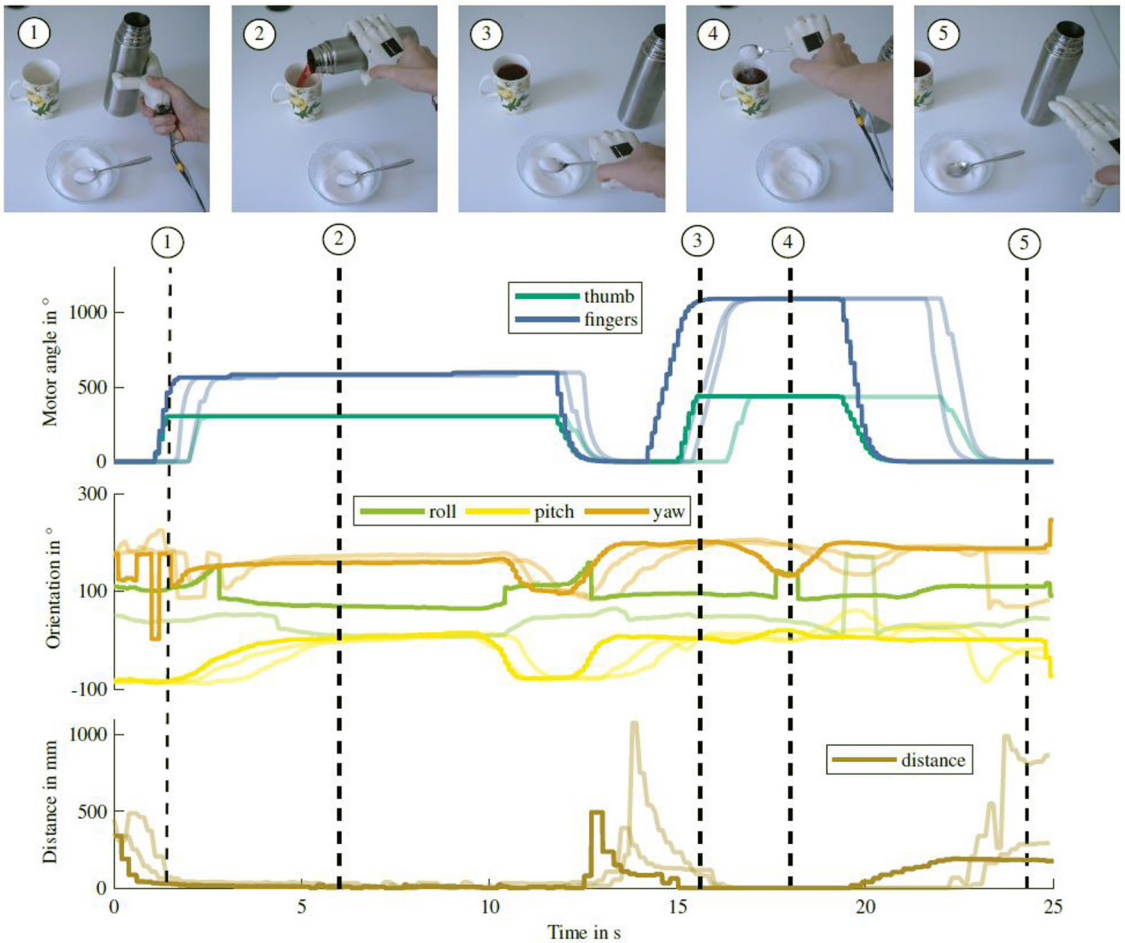

FIGURE 10 | Sensor readings while pouring tea into a cup and adding sugar with a spoon. Graph notation is similar to the lemonade preparation task shown in **Figure 9**.

The orientation data from the IMU provides additional information about the grasp. **Figure 9** shows the hand orientation in the hand coordinate system. Several rotations of the prosthesis throughout the manipulation action can be recognized. The recording starts with the hand in a horizontal position and the palm facing toward the table. After 11.1 s, when the bottle is grasped and opened, the prosthesis starts rotating with the bottle to pour coke into the glass. This is visible in the roll angle of the IMU. Once the pouring action is finished and the hand is rotated back, the placement of the bottle can be recognized based on the distance sensor data. The disturbance induced by opening the bottle and placing it back on the table can be seen in the hand's pitch angle.

To grasp the lemon, the hand is again horizontally orientated, as visible in the roll angle of the IMU. An additional example of pouring tea into a cup and adding sugar with a spoon is shown in **Figure 10**. Similar to the lemonade preparation task, different events throughout the task can be recognized based on the sensor readings. The grasps can be seen in an increase in motor position and a decrease in object distance. The tea pouring as well as tilting the spoon to add the sugar can be recognized in the IMU orientation. Both experiments show that information about the current phase of an object manipulation task can be inferred from sensor data and can be used for semi-autonomous grasp control.

6. DISCUSSION AND CONCLUSION

We present the KIT Prosthetic Hands as an example for intelligent prostheses equipped with abilities needed for the realization of semi-autonomous grasping. The hands are designed to support users in grasping objects to master daily life activities. The intelligence of the hands is achieved by combining adaptive underactuated mechanisms with a multi-modal sensor system and a resource-aware embedded system for onboard processing of sensory information and control. Thanks to the underactuated mechanism, high grasp forces can be achieved. The on-board processing of visual information relevant to the current task allows the implementation of semi-autonomous grasping behaviors.

TABLE 3 | Key characteristics of the male and female KIT prosthetic hands.

Prosthesis	Percentile	Weight	Material cost	Embedded sensors	Grasping force	Closing speed	YCB GAP score
Male	50th male	768 g	1,008€	Camera, Distance	24.2 N ± 1.9 N	1.32 s ± 0.04 s	193
Female	50th female	377 g	896€	IMU, Camera	40.5 N ± 8.1 N	0.73 s ± 0.02 s	203.5

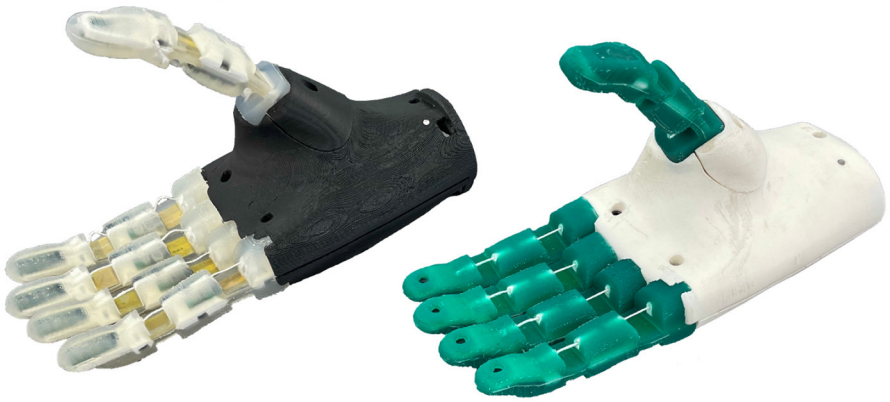

FIGURE 11 | The KIT sensorized soft hand (left) and KIT finger-vision soft hand (right) inspired by the prosthetic hand development.

The hand's size and weight comply to the requirements for a hand prosthesis. With its total weight of 377 g, the hand is lighter than any commercial myoelectric prosthetic hand as presented in **Table 1**, and is comparable to the human hand with approximately 400 g (Kaye and Konz, 1986). Compared to the male hand, the female hand shows a reduction of 44 % in weight and 30 % in cost. As shown in **Figure 7**, this is achieved by a significant improvement in lightweight design of mechanism and structural hand parts as well as the 3D-printed design of the mechanism without custom metal parts. Compared to the male hand, the closing time of the female prosthesis is decreased by 0.59 s to an absolute closing time of 0.73 s. This increase in speed is achieved by the improved mechanism design and the shorter finger dimensions requiring a smaller tendon deflection. The hand provides a cylindrical grasp force of 40.1 N and a mean fingertip force of 10.3 N within the four fingers. Compared to the male hand, the increase of the finger forces amounts on average to 35.2 %. This is within the range of commercial and research prosthetic hands as e.g., the iLimb Pulse (Belter and Dollar, 2013) or the SSSA-MyHand by Controzzi et al. (2017). With 53.4 N, the thumb is capable of providing a significantly higher force to counteract the four fingers.

The evaluation of the prosthesis based on the YCB Gripper Assessment Protocol shows a grasp functionality of 91.8 % in grasping everyday objects and the prosthesis achieves a score of 88.6 % in the execution of daily activity manipulation tasks. This shows the potential of the hand to support users throughout their daily life spanning food preparation, household and hygiene tasks, but also including their professional life, exemplary shown in office and workshop activities. The improvements of the female prosthetic hand over the male version are summarized in **Table 3**.

With these achievements, we provide important prerequisites for novel generation of prosthetic hands that integrate multi-modal sensing and resource-aware computing for the realization of semi-autonomous grasping and improving the way how users can interact with their prosthetic hands in an easy and intuitive way. We believe that the hardware design of the KIT Prosthetic Handas an intelligent and functional hand prosthesis provides a powerful platform for the development of intelligent, semi-autonomous control algorithms.

In the future we plan to design and implement a semi-autonomous control scheme that makes use of the multi-modal sensor data and the embedded system. Our goal is to endow the prosthesis with functionalities for semi-automatic preshape selection based on object recognition and IMU data as well as grasp execution based on distance information. All control algorithms and sensor data processing will be performed on the embedded system, eliminating the need for external sensor and processing resources.

Important to mention is also the fact that the underactuated mechanisms used in the KIT prosthetic hands served as the basis for the development of the hands of the humanoid robot ARMAR-6 by Asfour et al. (2019). In addition, the new version

of prosthetic hand, the female version, served as a basis for the development of several new soft humanoid robotic hands, the KIT Finger-Vision Soft Hand, see Hundhausen et al. (2020), and the KIT Sensorized Soft Hand with tactile sensing of the fingers, see Weiner et al. (2021). Both hands are shown in **Figure 11**. The hands allow an individual actuation of the thumb and the index finger. Both are driven by three motors and include an adapted version of the underactuated mechanism described in Section 4, that is designed to drive only three fingers with the same motor. The robotic hands are equipped with soft, monolithic fingers with joints and phalanx bodies made from silicone and a rigid skeleton structure in each finger phalanx. The fingers are actuated by tendons routed through the silicone. A flat band of non-stretchable material in the neutral axis of the finger provides a spring-like behavior to enhance the finger bending trajectory and protects cables routed to the sensors within the fingers. The soft robotic hands are equipped with different sensor setups in the fingers. The KIT Finger-Vision Soft Hand features one camera in the tip of each finger, as described in Hundhausen et al. (2020). The fingers of the KIT Sensorized Soft Hand are equipped with a multi-modal haptic sensor system Weiner et al. (2021). In both hands, the raw sensor information is processed in-hand on a high-performant embedded system based on the same ARM Cortex-M7 core that is also used for the prosthetic hand presented in this work. In addition, an FPGA (Artix 7, Xilinx) is integrated to enable hardware-accelerated processing of the high amount of incoming sensory data. The soft robotic hands have a length of 215 mm and a weight of about 580 g.

DATA AVAILABILITY STATEMENT

The original contributions presented in the study are included in the article/supplementary material, further inquiries can be directed to the corresponding authors.

AUTHOR CONTRIBUTIONS

SR designed the mechanics of the prosthetic hand with JS. The concept of the underactuated mechanism is based on the work of TA and was adapted by PW. PW and FH designed the sensor setup and embedded system of the prosthesis. FH, PW, and JS developed the firmware of the embedded system. The experiments were designed and conducted by JS and PW. The entire work was conceptualized and supervised by TA. The manuscript was written jointly by all authors.

FUNDING

This work has been supported by the German Federal Ministry of Education and Research (BMBF) under the project INOPRO (16SV7665) and by the Carl Zeiss Foundation through the JuBot project.

REFERENCES

Asfour, T., Wächter, M., Kaul, L., Rader, S., Weiner, P., Ottenhaus, S., et al. (2019). Armar-6: a high-performance humanoid for human-robot collaboration in real world scenarios. *IEEE Rob. Autom. Mag.* 26, 108–121. doi: 10.1109/MRA.2019.2941246

Belter, J. T., and Dollar, A. M. (2013). "Novel differential mechanism enabling two DOF from a single actuator: application to a prosthetic hand," in *IEEE International Conference on Rehabilitation Robotics (ICORR)* (Seattle, WA), 1–6.

Bennett, D. A., Dalley, S. A., Truex, D., and Goldfarb, M. (2015). A multigrasp hand prosthesis for providing precision and conformal grasps. *IEEE/ASME Trans. Mechatron.* 20, 1697–1704. doi: 10.1109/TMECH.2014.2349855

Biddiss, E. A., and Chau, T. T. (2007). Upper limb prosthesis use and abandonment: a survey of the last 25 years. *Prosthet Orthot Int.* 31, 236–257. doi: 10.1080/03093640600994581

Calli, B., Walsman, A., Singh, A., Srinivasa, S., Abbeel, P., and Dollar, A. M. (2015). Benchmarking in manipulation research: using the yale-CMU-berkeley object and model set. *IEEE Rob. Autom. Mag.* 22, 36–52. doi: 10.1109/MRA.2015.2448951

Carrozza, M. C., Cappiello, G., Micera, S., Edin, B. B., Beccai, L., and Cipriani, C. (2006). Design of a cybernetic hand for perception and action. *Biol. Cybern.* 95, 629–644. doi: 10.1007/s00422-006-0124-2

Catalano, M., Grioli, G., Farnioli, E., Serio, A., Piazza, C., and Bicchi, A. (2014). Adaptive synergies for the design and control of the Pisa/IIT SoftHand. *Int. J. Rob. Res.* 33, 768–782. doi: 10.1177/0278364913518998

Cipriani, C., Controzzi, M., and Carrozza, M. C. (2011). The SmartHand transradial prosthesis. *J. Neuroeng. Rehabil.* 8, 29. doi: 10.1186/1743-0003-8-29

Controzzi, M., Clemente, F., Barone, D., Ghionzoli, A., and Cipriani, C. (2017). The SSSA-MyHand: a dexterous lightweight myoelectric hand prosthesis. *IEEE Trans. Neural Syst. Rehabil. Eng.* 25, 459–468. doi: 10.1109/TNSRE.2016.2578980

Cordella, F., Ciancio, A. L., Sacchetti, R., Davalli, A., Cutti, A. G., Guglielmelli, E., et al. (2016). Literature review on needs of upper limb prosthesis users. *Front. Neurosci.* 10, 209. doi: 10.3389/fnins.2016.00209

Došen, S., Cipriani, C., Kostić, M., Controzzi, M., Carrozza, M., and Popović, D. (2010). Cognitive vision system for control of dexterous prosthetic hands: experimental evaluation. *J. Neuroeng. Rehabil.* 7, 42. doi: 10.1186/1743-0003-7-42

Fajardo, J., Ferman, V., Cardona, D., Maldonado, G., Lemus, A., and Rohmer, E. (2020). Galileo hand : an anthropomorphic and affordable upper-limb prosthesis. *IEEE Access* 8, 81365–81377. doi: 10.1109/ACCESS.2020.2990881

Farrell, T. R., and Weir, R. F. (2007). The optimal controller delay for myoelectric prostheses. *IEEE Trans. Neural Syst. Rehabil. Eng.* 15, 111–118. doi: 10.1109/TNSRE.2007.891391

Fukaya, N., Toyama, S., Asfour, T., and Dillmann, R. (2000). "Design of the TUAT/Karlsruhe humanoid hand," in *IEEE/RSJ International Conference on Intelligent Robots and Systems (IROS)* (Takamatsu), 1754–1759.

Ghazaei, G., Alameer, A., Degenaar, P., Morgan, G., and Nazarpour, K. (2017). Deep learning-based artificial vision for grasp classification in myoelectric hands. *J. Neural Eng.* 14, 036025. doi: 10.1088/1741-2552/aa6802

Huang, H., Jiang, L., Zhao, D. W., Zhao, J. D., Cai, H. G., Liu, H., et al. (2006). "The development on a new biomechatronic prosthetic hand based on under-actuated mechanism," in *IEEE/RSJ International Conference on Intelligent Robots and Systems (IROS)* (Beijing), 3791–3796.

Hundhausen, F., Grimm, R., Stieber, L., and Asfour, T. (2021). "Fast reactive grasping with in-finger vision and in-hand fpga-accelerated CNNs," in *IEEE/RSJ International Conference on Intelligent Robots and Systems (IROS)* (Prague), 6802–6809.

Hundhausen, F., Megerle, D., and Asfour, T. (2019). "Resource-aware object classification and segmentation for semi-autonomous grasping with prosthetic hands," in *IEEE-RAS International Conference on Humanoid Robots (Humanoids)* (Toronto, ON), 215–221.

Hundhausen, F., Starke, J., and Asfour, T. (2020). "A soft humanoid hand with in-finger visual perception," in *IEEE/RSJ International Conference on Intelligent Robots and Systems (IROS)* (Las Vegas, NV: IEEE), 8722–8728.

Jeong, S. H., Kim, K., and Kim, S. (2017). Designing anthropomorphic robot hand with active dual-mode twisted string actuation mechanism and tiny tension sensors. *IEEE Rob. Autom. Lett.* 2, 1571–1578. doi: 10.1109/LRA.2017.2647800

Kamper, D. G., Cruz, E. G., and Siegel, M. P. (2003). Stereotypical fingertip trajectories during grasp. *J. Neurophysiol.* 90, 3702–3710. doi: 10.1152/jn.00546.2003

Kaye, R., and Konz, S. (1986). Volume and surface area of the hand. *Hum. Factors Soc. Ann. Meeting* 30, 382–384. doi: 10.1177/154193128603000417

Kyberd, P. J., Light, C., Chappell, P. H., Nightingale, J. M., Whatley, D., and Evans, M. (2001). The design of anthropomorphic prosthetic hands: a study of the Southampton Hand. *Robotica* 19, 593–600. doi: 10.1017/S0263574701003538

Laffranchi, M., Boccardo, N., Traverso, S., Lombardi, L., Canepa, M., Lince, A., et al. (2020). The Hannes hand prosthesis replicates the key biological properties of the human hand. *Sci. Rob.* 5, 1–16. doi: 10.1126/scirobotics.abb0467

Lai, L., Suda, N., and Chandra, V. (2018). Cmsis-nn: Efficient neural network kernels for arm cortex-m cpus. *arXiv preprint* arXiv:1801.06601.

Light, C. M., Chappell, P. H., and Kyberd, P. J. (2002). Establishing a standardized clinical assessment tool of pathologic and prosthetic hand function: normative data, reliability, and validity. *Arch. Phys. Med. Rehabil.* 83, 776–783. doi: 10.1053/apmr.2002.32737

Liu, H., Ferrentino, P., Pirozzi, S., Siciliano, B., and Ficuciello, F. (2019). "The PRISMA Hand II: a sensorized robust hand for adaptive grasp and in-hand manipulation," in *2019 International Symposium on Robotics Research* (Hanoi), 1–16.

Markovic, M., Došen, S., Popovic, D., Graimann, B., and Farina, D. (2015). Sensor fusion and computer vision for context-aware control of a multi degree-of-freedom prosthesis. *J. Neural Eng.* 12, 066022. doi: 10.1088/1741-2560/12/6/066022

Matheus, K., and Dollar, A. M. (2010). "Benchmarking grasping and manipulation: properties of the objects of daily living," in *IEEE/RSJ International Conference on Intelligent Robots and Systems (IROS)* (Taipei: IEEE), 5020–5027.

Østlie, K., Lesj, I. M., Franklin, R. J., Garfelt, B., Skjeldal, O. H., and Magnus, P. (2012). Prosthesis rejection in acquired major upper-limb amputees: a population-based survey. *Disabil. Rehabil.* 7, 294–303. doi: 10.3109/17483107.2011.635405

Peerdeman, B., Valori, M., Brouwer, D., Hekman, E., Misra, S., and Stramigioli, S. (2014). UT hand I: a lock-based underactuated hand prosthesis. *Mech. Mach. Theory* 78, 307–323. doi: 10.1016/j.mechmachtheory.2014.03.018

Pfeifer, R., and Gómez, G. (2009). "Morphological computation-connecting brain, body, and environment," in *Creating Brain-Like Intelligence: From Basic Principles to Complex Intelligent Systems* (Berlin; Heidelberg: Springer), 66–83.

Piazza, C., Grioli, G., Catalano, M., and Bicchi, A. (2019). A century of robotic hands. *Ann. Rev. Control Rob. Auton. Syst.* 2, 1–32. doi: 10.1146/annurev-control-060117-105003

Piazza, C., Santina, C. D., Catalano, M., Grioli, G., Garabini, M., and Bicchi, A. (2016). "SoftHand Pro-D: matching dynamic content of natural user commands with hand embodiment for enhanced prosthesis control," in *IEEE International Conference on Robotics and Automation (ICRA)* (Stockholm: IEEE), 3516–3523.

Pons, J. L., Rocon, E., Ceres, R., Reynaerts, D., Saro, B., Levin, S., et al. (2004). The MANUS-HAND dextrous robotics upper limb prosthesis: mechanical and manipulation aspects. *Auton. Rob.* 16, 143–163. doi: 10.1023/B:AURO.0000016862.38337.f1

Pylatiuk, C., Schulz, S., and Döderlein, L. (2007). Results of an Internet survey of myoelectric prosthetic hand users. *Prosthet Orthot Int.* 31, 362–370. doi: 10.1080/03093640601061265

Schweitzer, W., Thali, M. J., and Egger, D. (2018). Case-study of a user-driven prosthetic arm design: Bionic hand versus customized body-powered technology in a highly demanding work environment. *J. Neuroeng. Rehabil.* 15, 1–27. doi: 10.1186/s12984-017-0340-0

SensorHand (2020). *SensorHand Speed*. Duderstadt: Otto Bock HealthCare Deutschland GmbH.

Taska (2020). *Specifications V1.1*. Christchurch: Taska TM.

Tavakoli, M., Lopes, P., Loureno, J., Rocha, R. P., Giliberto, L., de Almeida, A. T., et al. (2017). Autonomous selection of closing posture of a robotic hand through embodied soft matter capacitive sensors. *IEEE Sens. J.* 17, 5669–5677. doi: 10.1109/JSEN.2017.2726348

Vergara, M., Agost Torres, M.-J., and Gracia-Ibá nez, V. (2016). Comparison of dorsal and palmar aspect dimensions of hand anthropometry. *Hum. Factors Ergon. Manufact. Serv. Ind.* 28, 1–12. doi: 10.1002/hfm.20714

Weiner, P., Hundhausen, F., Grimm, R., and Asfour, T. (2021). "Detecting grasp phases and adaption of object-hand interaction forces of a soft humanoid hand based on tactile feedback," in *IEEE/RSJ International Conference on Intelligent Robots and Systems (IROS)* (Prague), 3956–3963.

Weiner, P., Starke, J., Hundhausen, F., Beil, J., and Asfour, T. (2018). "The kit prosthetic hand: design and control," in *IEEE/RSJ International Conference on Intelligent Robots and Systems (IROS)* (Madrid), 3328–3334.

Wijk, U., and Carlsson, I. (2015). Forearm amputees' views of prosthesis use and sensory feedback. *J. Hand Therapy* 28, 269–278. doi: 10.1016/j.jht.2015.01.013

Wiste, T., and Goldfarb, M. (2017). "Design of a simplified compliant anthropomorphic robot hand," in *2017 IEEE International Conference on Robotics and Automation (ICRA)* (Singapore: IEEE), 3433–3438.

Wiste, T. E., Dalley, S. A., Varol, H. A., and Goldfarb, M. (2011). Design of a multigrasp transradial prosthesis. *J. Med. Dev.* 5, 031009–031009-7. doi: 10.1115/1.4004653

Zhang, T., Jiang, L., and Liu, H. (2018). Design and functional evaluation of a dexterous myoelectric hand prosthesis with biomimetic tactile sensor. *IEEE Trans. Neural Syst. Rehabil. Eng.* 26, 1391–1399. doi: 10.1109/TNSRE.2018.2844807

Zhao, H., O'Brien, K., Li, S., and Shepherd, R. F. (2016). Optoelectronically innervated soft prosthetic hand via stretchable optical waveguides. *Sci. Rob.* 1, eaai7529. doi: 10.1126/scirobotics.aai7529

Conflict of Interest: The authors declare that the research was conducted in the absence of any commercial or financial relationships that could be construed as a potential conflict of interest.

frontiers in Neurorobotics

ORIGINAL RESEARCH
published: 10 March 2022
doi: 10.3389/fnbot.2022.789210

Design, Implementation, and Evaluation of a Variable Stiffness Transradial Hand Prosthesis

Elif Hocaoglu[1,2]* *and Volkan Patoglu*[1]

[1] Faculty of Engineering and Natural Sciences, Sabancı University, Istanbul, Turkey, [2] School of Engineering and Natural Sciences, Istanbul Medipol University, Istanbul, Turkey

We present the design, implementation, and experimental evaluation of a low-cost, customizable, easy-to-use transradial hand prosthesis capable of adapting its compliance. Variable stiffness actuation (VSA) of the prosthesis is based on antagonistically arranged tendons coupled to nonlinear springs driven through a Bowden cable based power transmission. Bowden cable based antagonistic VSA can, not only regulate the stiffness and the position of the prosthetic hand but also enables a light-weight and low-cost design, by the opportunistic placement of motors, batteries, and controllers on any convenient location on the human body, while nonlinear springs are conveniently integrated inside the forearm. The transradial hand prosthesis also features tendon driven underactuated compliant fingers that allow natural adaption of the hand shape to wrap around a wide variety of object geometries, while the modulation of the stiffness of their drive tendons enables the prosthesis to perform various tasks with high dexterity. The compliant fingers of the prosthesis add inherent robustness and flexibility, even under impacts. The control of the variable stiffness transradial hand prosthesis is achieved by an sEMG based natural human-machine interface.

Keywords: transradial hand prosthesis, underactuated robotic hand design, variable stiffness actuation, impedance modulation, tele-impedance control

OPEN ACCESS

Edited by:
Chad Gregory Rose,
Auburn University, United States

Reviewed by:
Alperen Acemoglu,
Italian Institute of Technology (IIT), Italy
Dong Hyun Kim,
Korea Advanced Institute of Science and Technology, South Korea

***Correspondence:**
Elif Hocaoglu
ehocaoglu@medipol.edu.tr

Received: *04 October 2021*
Accepted: *28 January 2022*
Published: *10 March 2022*

Citation:
Hocaoglu E and Patoglu V (2022) Design, Implementation, and Evaluation of a Variable Stiffness Transradial Hand Prosthesis. Front. Neurorobot. 16:789210. doi: 10.3389/fnbot.2022.789210

1. INTRODUCTION

Versatile grasping and manipulation in unstructured environments are challenging tasks, actively investigated in robotics. Multi-fingered robot hands have been developed both in academia (Dalley et al., 2009; Takaki and Omata, 2011; Chen et al., 2015) and for commercial use (Liberating Technologies Inc., 2022; Touch Bionics Inc., 2022) to achieve various tasks. Anthropomorphism (ability to emulate human-like hand shape, size, and consistency) and dexterity (successful manipulation capability even under unstructured conditions) are commonly identified as the key features to reach a satisfactory level of performance.

Anthropomorphism is an important criterion in the design of robotic end-effectors, especially for the purpose of hand prostheses (Bicchi, 2000), since the tools around the environment, such as consoles, handles, keys, are designed for the human hands. In addition, anthropomorphic designs are aesthetically and physiologically more fulfilling for amputees, as they provide natural

appearances. However, anthropomorphism alone is not sufficient; other important criteria, such as simple but robust design, ease of use, and adequate level of dexterity are also crucial factors in the design of prosthetic hands.

Dexterity is a quite evident goal for the robotic and prosthetic hands in order for them to be endowed with human-like capabilities, such as grasping objects and performing fine finger movements for precise manipulations. In order for a prosthetic hand to qualify as a dexterous design, it has to be capable of performing most of the human hand taxonomy required during the activities of daily living (ADL) (Feix et al., 2016). In the literature (Bicchi et al., 2011; Catalano et al., 2012), it has been emphasized that the majority of human grasps are power grasps, which is preferred for more than 50% of the time when the hand is used. Pinch grasp is ranked as second with a 20% preference rate (Feix et al., 2016). Hence, since power grasps and pinch grasps are the most common hand functions, providing hand prostheses with these dominant grasp types may be prioritized to execute most ADL.

Successful manipulation necessitates another significant and commonly neglected characteristic of the human hand, namely impedance modulation. Incorporating impedance modulation property in the design of a hand prosthesis makes it adaptable to interacted objects/tasks. Successful execution of many ADLs, where human physically interacts with the environment, arises from the proper modulation of the impedance level of hand based on the varying requirements of the task. For instance, some activities, such as writing and painting, necessitate highly accurate position control for which the stiffness of the fingers is increased considerably, while manipulation of soft/fragile objects, such as holding an egg or picking up an apricot, requires low stiffness of the fingers.

The impedance modulation property of human hands has inspired design and control strategies for robotic and prosthetic hands, whose goal is to improve the quality of interaction with dynamic environments, especially under unpredictable conditions. Specifically, hand prostheses become safer and more functional if the appropriate impedance level based on the physical conditions of the interacted environment can be ensured (Abul-Haj and Hogan, 1987, 1990; Mengilli et al., 2020; Tosun and Patoglu, 2020). Several studies (Blank et al., 2011, 2012, 2013; Hocaoglu, 2014; Kara and Patoglu, 2020) provide strong evidence that hand prostheses with stiffness modulation can improve the performance of an amputee when the impedance of the prosthesis is matched to the requirements of the task.

Impedance modulation approaches in robotics can be grouped into two major categories. In the first category, the compliance of the device is modulated through software, using strategies such as impedance/admittance control. In this approach, the impedance modulation is limited by the controllable bandwidth of the actuators, and for this reason, a prosthesis whose impedance is modulated with such a control strategy behaves like a rigid body for high frequency excitations, such as impacts that exceed its control bandwidth (Abul-Haj and Hogan, 1990; Mengilli et al., 2020; Tosun and Patoglu, 2020). Moreover, this approach requires continuous use of actuators and suffers from low energy efficiency.

In the second category, impedance modulation is embedded into the mechanical design of a robotic system. In this approach, the impedance of the robotic manipulator is adjusted through special mechanisms consisting of passive elastic elements, such as springs. In hardware based impedance modulation, e.g., variable stiffness actuation (VSA), the impedance change is physical and is valid for the whole frequency spectrum, including frequencies well above the controllable bandwidth of the actuators. Furthermore, this approach consumes energy only when the impedance is being modulated; hence, is energy efficient.

Achieving human level dexterity with fully actuated, high degrees of freedom prosthetic hands requires the use of complex control algorithms (Touvet et al., 2012). In the literature, there exists myoelectrically controlled hand prostheses that are capable of performing a large variety of manipulation tasks (Chu et al., 2007; Castellini et al., 2008; Li and Kuiken, 2009); however, the control of each finger joint in these systems is realized by means of sophisticated algorithms, whose complexity exposes amputees to long training periods. The burden of long training periods and complexity involved in controlling prosthetic devices are known to contribute to a high abandonment rate for these devices, reaching up to 40% (McFarland et al., 2010). A large percentage of amputees reject active prostheses since they are dissatisfied with the current level of the functionality provided by these devices, given their complexity. These amputees prefer easy to use passive prostheses, even at a cost of reduced functionality (Biddiss and Chau, 2007). To address the challenges of low adaptation and high abandonment rate of active prostheses, several research groups have focused on the simplification of mechanical design and ensuring ease of control, without losing the main functionality of prosthetic hands.

In the literature, several robotic hands employed for tasks requiring human machine interaction have been designed using VSA (Grebenstein et al., 2010; Wolf et al., 2011; Shadow Robot Company Ltd., 2022), while, to the best of authors' knowledge, no such application has been reported in the field of anthropomorphic hand prostheses. In particular, each active degree of freedom of the DLR Hand Arm System is controlled by two motors attached to antagonistically arranged nonlinear spring elements (Grebenstein et al., 2010; Wolf et al., 2011). Similarly, the impedance modulation of the anthropomorphic Shadow Hand is achieved by antagonistically arranged pneumatic artificial muscles (Shadow Robot Company Ltd., 2022). Both DLR Hand Arm System and Shadow Hand feature sophisticated mechanical designs with a large number of active degrees of freedom; hence, their size, weight, and cost make them infeasible for use as a hand prosthesis. Furthermore, grasp planning and impedance modulation of these devices necessitate complex algorithms, which renders their use quite challenging.

The employment of underactuated mechanisms for hand designs is a promising approach, as underactuated hands have been shown to provide a remarkable adaptation to various object geometries without the need for sensors or complex control algorithms. Underactuation is commonly implemented by either linkage or tendon based finger designs that are capable of performing typical human-like finger closing sequences.

Linkage based underactuated fingers (Birglen and Gosselin, 2003; Birglen et al., 2008; Kamikawa and Maeno, 2008; Prattichizzo et al., 2012; Ertas et al., 2014) are capable of shape adaptation and can endure larger forces compared to tendon based ones; however, their relatively bulky design makes them not well-suited for integration into anthropomorphic prosthetic hands. Most successfully implementations of anthropomorphic underactuated hand designs have been realized by means of tendon driven mechanisms (Massa et al., 2002; Gosselin et al., 2008; ya Nagase et al., 2011; Xu et al., 2015), since slim and lightweight fingers can be actuated with this method. For instance, in Dollar and Howe (2006), Dollar et al. (2010), and Ma et al. (2013), a compliant, underactuated, sensor integrated robotic hand with tendon driven elastic joints is introduced, and fabricated *via* support decomposition manufacturing. Moreover, in Godfrey et al. (2018), an underactuated hand with a single motor is designed to adapt to objects with different geometric shapes by means of its tendon driven elastic joints. With its underactuated finger mechanism and elastic joints, this low cost hand is capable of self-adaptation to different shaped objects under simple control methods. Similarly, a tendon driven underactuated robot hand that explores synergies of human hand motions is implemented in Catalano et al. (2014). However, neither of these underactuated hands feature impedance modulation capabilities.

In this study, we present the design, fabrication, and evaluation of a variable stiffness transradial hand prosthesis to be controlled through a natural human-machine interface. VSA of the prosthesis is based on antagonistically arranged tendons coupled to nonlinear springs driven through a Bowden cable based power transmission. Bowden cable based antagonistic VSA regulates both the impedance and the position of the hand. It also enables a light-weight hand design, by opportunistically placing the motors, batteries, and controllers to any convenient location on the human body, while nonlinear springs are conveniently integrated inside the forearm. The proposed prosthesis features tendon driven underactuated compliant fingers that enable natural adaption of the hand shape to wrap around a wide variety of object geometries and modulation of the hand's stiffness to perform various tasks with high dexterity. The compliant fingers are built from polyurethane with a low-cost manufacturing process and add inherent robustness and flexibility, even under unexpected conditions such as impacts.

The control of the variable stiffness transradial hand prosthesis is achieved by a natural human-machine interface that utilizes sEMG signals measured from the surface of the upper arm, chest, and shoulder. This natural control interface, called *tele-impedance controller*, is first presented in Hocaoglu and Patoglu (2012), while the detailed implementation of this controller and its performance evaluation are presented in Hocaoglu (2014) and Hocaoglu and Patoglu (2019).

The rest of the manuscript is organized as follows: Section 2.1 introduces the design objectives for the variable stiffness transradial hand prosthesis, while Section 2.2 reviews its sEMG-based tele-impedance control. Section 2.3 details the mechatronic design of the VSA prosthesis. Section 3 presents experimental evaluations that provide evidence of the working principle. Section 3.3 evaluates the grasping performance of the hand prosthesis with a wide variety of objects and provides a discussion of the results. Finally, Section 4 concludes the article and discusses future studies.

2. MATERIALS AND METHODS

This section presents the design objectives for the VSA hand prosthesis, overviews its sEMG-based control approach, and implementation of the proposed objectives.

2.1. Design Objectives

Following the terminology in Merlet (2006), one can categorize the performance requirements for hand prostheses into four groups: imperative, optimal, primary, and secondary requirements.

Anthropomorphism is an imperative design requirement for hand prostheses. Aesthetically pleasing natural appearance is not only necessary for the adaptation of prosthetic devices by amputees, but also anthropomorphic designs are better suited to interact with common human-oriented tools and environments. In this study, we design an anthropomorphic hand prosthesis, for which the dimensions are customizable.

Dexterity is an optimal performance requirement that needs to be maximized while designing a hand prosthesis. In particular, a hand prosthesis should be capable of grasping objects with different shapes (prismatic, spherical, cylindrical) and with various properties (soft or fragile structures, smooth or ragged surfaces) without damaging them. In this study, we ensure dexterity by designing an underactuated hand that can mimic the opening/closing sequence of human fingers to adapt to a wide variety of geometries and by enabling the stiffness of the prosthesis to be actively modulated based on the task.

The primary requirement for a hand prosthesis is ease-of-use. The control of the device should be intuitive, allowing amputees to use the device without being exposed to long training periods. Moreover, the hand prosthesis should be energy efficient and its batteries should be easily swappable for user friendliness. In this study, the use of an underactuated design simplifies the control of the device, as only the position and impedance of the drive tendon need to be controlled. The tele-impedance controller reviewed in Section II-B provides a natural sEMG interface for the control of the device, where the impedance modulation takes place automatically, allowing the amputee only to focus on the position control of the hand. Energy efficiency is ensured by hardware based impedance modulation, where no energy is wasted to maintain a desired impedance level. Finally, Bowden cable based actuation enables batteries to be opportunistically placed anywhere on the body, making them easily re-sizeable or swappable.

The secondary requirements for the device are high robustness and low cost. In this study, the compliant fingers and the VSA provide built-in physical compliance that provides inherent robustness to impacts. Besides, all parts of the prosthesis are simple to manufacture and customizable. Furthermore, since Bowden cable based actuation allows for motors, drivers, and batteries of the system to be remotely located, the cost of these

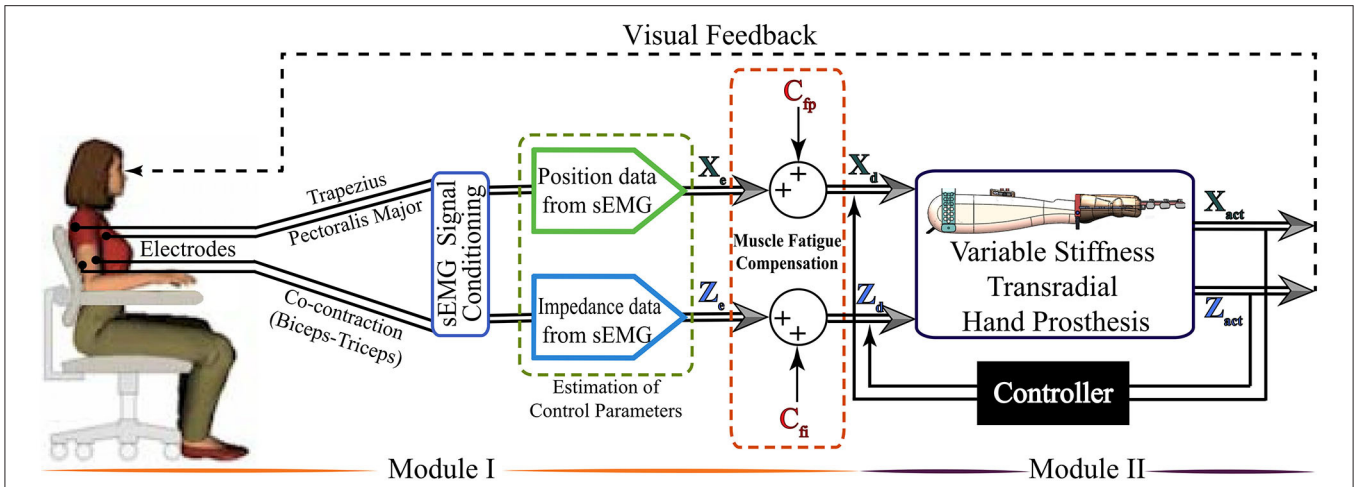

FIGURE 1 | Tele-impedance control architecture of the variable stiffness transradial hand prosthesis.

parts can be kept low, as strict size and weight constraints do not apply to these parts.

2.2. Overview of sEMG-Based Control Architecture

The tele-impedance control architecture consists of two modules, as depicted in **Figure 1**. The first module handles the measurement of sEMG signals, their conditioning, and the estimation of reference values for the hand position and stiffness. The second module implements a closed-loop controller that ensures that the position and the stiffness of the VSA prosthetic hand match the reference values. Throughout the control, visual feedback and physical coupling provide information to the amputees to adapt their sEMG signals to match the requirements of the task.

Given that transradial upper extremity amputees lack the muscle groups responsible for hand and forearm motions, sEMG signals for the position control of the hand prosthesis are measured from chest and shoulder muscles, while sEMG signals used for stiffness regulation are measured from the muscle pairs on the upper arm. The estimation of the hand position and stiffness from sEMG signals involves modeling of hand motion/stiffness based on sEMG signals, empirical determination of the parameters of these models for use in real time control, and incorporation of fatigue compensation.

Conditioned sEMG signals are discretized into several levels to map them to the physical stiffness range of the VSA and the range of motion of the fingers. A calibration procedure is performed for sEMG signals before each use, to customize the maximum voluntary contraction (MVC) levels for the user, as commonly done for commercial prosthetic hands. Since the MVC levels of the sEMG signals vary in time and are specific to users, the sEMG signals have to be normalized before each use to present accurate reference data to the controller shown in the second module in **Figure 1**. Accordingly, the required time to calibrate the sEMG signal for every initiation of the hand prosthesis is around 3 min. The first 30 s is required to gather MVC data to normalize the signal. The rest of the duration is necessary to estimate the parameters for stiffness estimation. The device sequentially records the sEMG signals of the subject while performing the specific tasks and does the implementation automatically before activating the device for the subjects. There is around a 15 s resting period between sEMG data recordings to prevent the fatigue effect in the calibration data.

The sEMG based tele-impedance control interface, together with the VSA, enables an amputee to modulate the stiffness of the prosthetic hand to properly match the requirements of the task while performing ADL under visual feedback. The regulation of stiffness is managed through the stiffness measurements of the intact upper arm, and this control takes place automatically as the amputee interacts with the environment. The position of the hand prosthesis is controlled intentionally by the amputee through the position of the shoulder, estimated using SEMG signals. This natural human-robot interface is advantageous since the impedance regulation takes place naturally without requiring amputees' attention and diminishing their functional capability. Consequently, the proposed interface does not require long training periods or interfere with the control of intact body segments and is easy to use. Details of the controller and its experimental verification are presented in Hocaoglu and Patoglu (2019).

2.3. Design of Variable Stiffness Transradial Hand Prosthesis

To satisfy the design objectives, an anthropomorphic, VSA integrated, underactuated, compliant hand prosthesis is developed as follows.

2.3.1. Bowden Cable Driven Antagonist VSA

An antagonistic VSA is utilized to control the position and the stiffness of a four-fingered, underactuated, compliant prosthetic hand. Tendon based antagonistic arrangement is preferred since it allows for the elastic elements and actuators to be conveniently

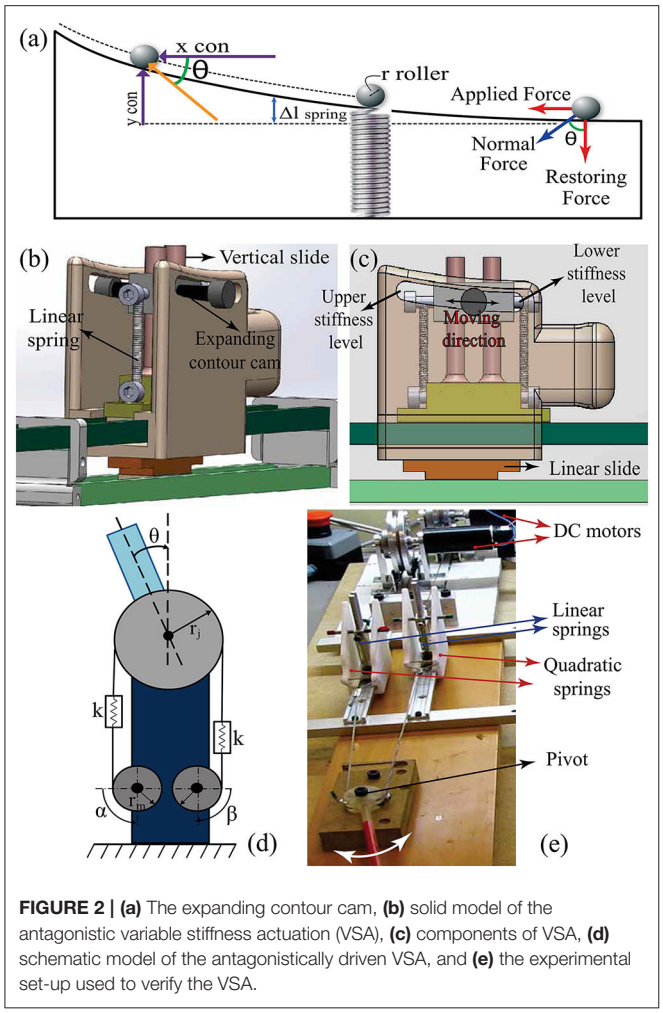

FIGURE 2 | (a) The expanding contour cam, **(b)** solid model of the antagonistic variable stiffness actuation (VSA), **(c)** components of VSA, **(d)** schematic model of the antagonistically driven VSA, and **(e)** the experimental set-up used to verify the VSA.

placed away from the fingers of the prosthesis. Furthermore, VSA is driven by a Bowden cable based transmission that enables motors, drivers, and batteries to be located at any suitable place on the body of the amputee. This not only results in a light-weight design but also enables easy customization of these parts, e.g., force output or battery capacity, for any user.

2.3.1.1. Implementation of Antagonistic VSA Using Expanding Contour Cams

It is well-established that an antagonistic VSA can mimic the independent stiffness and position control of a human limb joint under quasi-static conditions if the antagonistic spring elements of the VSA have nonlinear (typically quadratic) deflection-force characteristics (English and Russell, 1999). One way of attaining the desired nonlinear spring relationship is to utilize linear springs constrained to move on nonlinear expanding surfaces, called expanding contour cams (Migliore et al., 2007). In such an arrangement, as shown in **Figures 2a–c**, when the force is exerted on the system, linear springs extend according to the nonlinear cam surface; hence, a nonlinear relationship between the spring force and the deflection is ensured. The expanding contour cams implement the gradient of the force-deflection relationship and can be designed based on the linear spring constant and the maximum-minimum joint stiffness values.

Since the VSA aims at modulating the stiffness of prosthetic fingers, the design is implemented based on the maximum and the minimum joint stiffness values of human fingers, as given in Howe et al. (1985). These two design parameters along with the linear spring constant are sufficient to characterize the shape of the expanding contour as shown below. Different from the design in Migliore et al. (2007), our expanding contour cams are designed to be single sided, such that they are compact enough to be integrated into the forearm portion of the prosthesis. Furthermore, the springs on single sided cams are mounted on vertical slides, enabling easy connections, providing stable movements, and preventing the linear springs from bending.

To simplify the design process, the number of parameters required to determine the expanding cam profile is reduced as follows. The free lengths of the springs are selected such that the preload on the linear springs can be set to zero at the thinnest portion of the cam. Since the radius of the rollers is significantly small compared to the cam profile, their effect is neglected in the nonlinear contour equation. Consequently, the force-displacement relationship of elastic elements is chosen to satisfy the quadratic equation

$$F_{app} = ax_{con}^2 + bx_{con} + c \tag{1}$$

where F_{app} represents the applied force to the roller, x_{con} is the current position of the roller along the x-axis of the expanding contour, and a, b, and c are the coefficients of the quadratic equation. Along the y-axis, the following relationship holds for the linear springs

$$F_{restoring} = k\, y_{con} \tag{2}$$

where $F_{restoring}$ denotes the force applied by the linear spring on the cam along the y-axis, y_{con} is the current position of the roller along the y-axis of the expanding contour, and k is the spring constant of linear springs. Neglecting the frictional effects, the cam profile enforces a geometric relation between F_{app} and $F_{restoring}$ that can be expressed as

$$y_{con}^2 - \left(\frac{2a}{3k}\right)x_{con}^3 - \left(\frac{b}{k}\right)x_{con}^2 - \left(\frac{2c}{k}\right)x_{con} - m = 0 \tag{3}$$

Enforcing the following boundary conditions when the linear spring is at the initial point of the expanding contour

$$x_{con} = 0,\ y_{con} = 0 \tag{4}$$

implies that $m = 0$. In Equation (3), the parameters required to design expanding contour are a, b, c and the spring constant k of the linear springs. It can be shown that a, b, and c are directly dependent on the maximum S_{max} and the minimum S_{min} stiffness values of the VSA as follows (English and Russell, 1999):

$$F_{app} = \underbrace{\left(\frac{S_{max} - S_{min}}{4r_j^2 \Delta x_{max}}\right)}_{\mathbf{a}} x_{con}^2 + \underbrace{\left(\frac{S_{min}}{2r_j^2}\right)}_{\mathbf{b}} x_{con} - \underbrace{\left(\frac{\Delta x_{max}(S_{max}^2 - 2S_{min}^2)}{8r_j^2(S_{max} - S_{min})}\right)}_{\mathbf{c}} \quad (5)$$

where r_j denotes the radius of the pulley used to implement the VSA and Δx_{max} symbolizes the maximum deflection of the linear springs. When the linear springs are unstretched ($x_{con} = 0$), the joint stiffness level is regulated to its minimum level S_{min}. In addition to this, when the linear springs reach their maximum stretch ($x_{con} = x_{max}$), the joint stiffness is regulated at its maximum level S_{max}.

2.3.1.2. Position and Stiffness Control With Antagonist VSA

The position and the stiffness of the VSA are controlled through position control of Bowden cables driven by two geared DC motors. **Figure 2d** presents a schematic representation of the VSA. Let α and β denote the angular position of DC motors, while S and θ represent joint stiffness and angle, respectively. As a result of the physical compliant elements in its mechanical design, the VSA is advantageous as it alleviates the need for force/impedance control and allows robust motion control of actuators to be utilized to achieve high performance interaction control.

Under quasi-static conditions (English and Russell, 1999; Migliore et al., 2007), the equilibrium position θ and stiffness S of the VSA can be calculated as

$$\theta = \frac{r_m}{2r_j}(\alpha - \beta) - \frac{\tau_{load}}{2r_j^2(ar_m(\alpha + \beta) + b)} \quad (6)$$

$$S = 2ar_m r_j^2(\alpha + \beta) + 2br_j^2 \quad (7)$$

where r_m represents the radius of the pulleys attached to the geared DC motors, while the external torque applied to VSA is denoted by τ_{load}.

When control references belonging to the joint position and stiffness are provided, the desired motor positions are computed from Equations (6), (7) and the motors are motion controlled to these values.

2.3.1.3. Experimental Verification of VSA

To experimentally verify the control performance of VSA, an antagonistic VSA is implemented using expanding contour cams shown in **Figures 2b,c** and is connected to a simple pivot. The aim of this experiment is to verify the independent and simultaneous position and stiffness control of the pivot *via* VSA. Several conditions are tested using the set-up shown in **Figure 2e** to evaluate the performance of VSA under realistic conditions. In particular, the following three conditions are evaluated sequentially: i) the position of the pivot is kept stationary while its stiffness is changed, ii) the stiffness of the pivot is kept constant while its position is modulated, and iii) both the position and the stiffness are varied simultaneously. **Figures 3A–C** present sample results from these experiments.

In **Figure 3A**, the pivot stiffness is kept at a constant level, while the position is simultaneously changed to track a sinusoidal reference of $\pm\pi/2$ rad amplitude for the first 16 s and $\pm\pi/18$ rad amplitude for the rest of the experiment. The results indicate that the position tracking RMS error of the motors is less than 0.03%.

Figure 3B presents results when the pivot stiffness is changed sinusoidally between the intermediate to the high level, while the angular position of VSA is kept constant at zero. The results indicate that the position tracking RMS error of the motors is less than 0.6%.

Figure 3C presents the response of the VSA to a sinusoidally changing stiffness reference, while the position reference is gradually increased with step changes. The results verify that the position tracking RMS error of the motors is less than 0.04%.

Robust motion controllers implemented with high gains and at high control rates keep the motion tracking error of the motors low, indicating that the estimated stiffness and position of the pivot can be controlled with good performance, even under the high friction forces induced by the Bowden cables. While the estimated stiffness and position of the pivot can be controlled with high precision, there exist other sources of errors, such as unmodelled dynamics of the VSA (the control model is valid only under quasi-static conditions) and the elasticity of the cable. The experimental results indicate that the position and stiffness tracking the performance of VSA are sufficiently high for use in a prosthetic hand, given that the position and the stiffness references will be provided in an amputee-in-the-loop fashion (under visual feedback) and discrete reference levels are required as discussed in Section 2.2. In particular, precise control of these values is not crucial, as evidence in the literature suggests that even a few discrete (e.g., low, moderate, and high) levels of stiffness can significantly improve the performance of typical manipulations (Blank et al., 2011, 2012, 2013; Hocaoglu, 2014; Kara and Patoglu, 2020).

2.3.2. Underactuated Power Transmission

The proposed hand prosthesis is designed to feature underactuated power transmission, as a means of providing passive adaptation to various object geometries. Underactuation is preferred as it provides an ideal compromise between dexterous hands that provide versatile and stable grasps at high costs and computational loads, and simple grippers that excel at achieving specific tasks robustly with simple controllers at low costs but provide a relatively small set of grasps. Underactuation is the preferred alternative, since reducing the number of actuators required to control the system, not only saves weight, space, and cost but also provides energy efficiency and ease of control.

2.3.2.1. Implementation of Underactuated Power Transmission

The proposed hand prosthesis is designed to be actuated by a single VSA, such that the flexion/extension and the stiffness of fingers are controlled through antagonistic drive tendons. A pulley based power transmission, as in **Figure 4a**, distributes tendon tension to each phalanx based on the interaction forces.

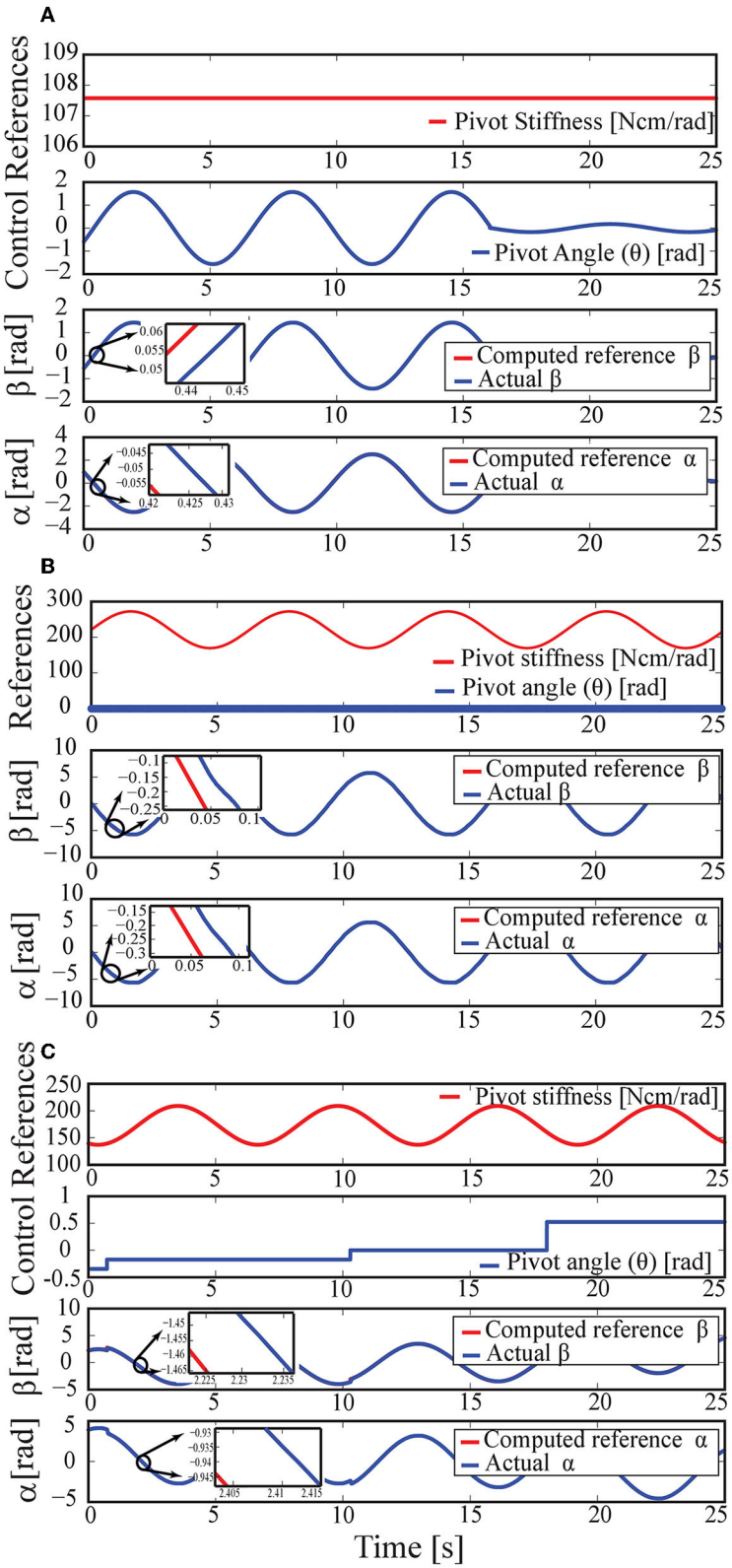

FIGURE 3 | (A) Response to a sinusoidally changing position reference when the stiffness is kept constant. **(B)** Response to a sinusoidally changing stiffness reference when the position is kept constant. **(C)** Response to a sinusoidally changing stiffness while the position reference is gradually increased.

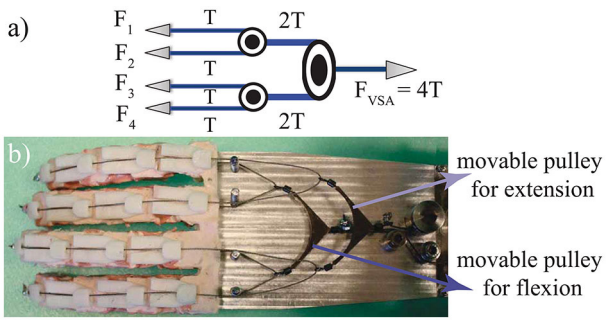

FIGURE 4 | (a) Schematic representation of the pulley based transmission that equally distributes tendon tension to each finger when no external force is acting on the fingers. **(b)** Antagonistic actuation of the hand prosthesis.

When no external force is applied, the tendon tension is transferred equally to each of the four fingers, where each finger is composed of three compliant joints. The center of the pivot of VSA can be attached directly to the tendon that flexes the fingers to achieve unidirectional functionality for the hand, where the opening of the hand is performed by passive springs. We implement an alternative, where antagonistic springs of VSA are attached to the center of a moveable pulley mechanism, as shown in **Figure 4b**. In this arrangement, one of the movable pulleys transmits forces to flex the fingers, while its companion pulley transmits forces to extend them.

2.3.2.2. Experimental Evaluation of the Underactuated Power Transmission

The natural grasping behavior of the underactuated prosthesis is tested over different shaped objects. Sample pinch and power grasps are presented in **Figure 10**.

As a result of underactuated power distribution, the compliant fingers naturally adapt to the shape of the objects to ensure that tendon tensions in each finger are equally distributed. That is, each finger seeks appropriate contact with the object (or a joint limit) to ensure proper force distribution of the tendons. As expected, the grasp type and the motion of each finger depending on the shape of the object and the relative configuration of the prosthesis.

2.3.3. Design of Compliant Fingers

The proposed hand prosthesis is designed to feature compliant underactuated fingers. Compliant construction results in physical flexibility of the fingers, increasing their adaptability to the environment and robustness toward impacts. Underactuated kinematics with three compliant joints per finger increases the dexterity of the hand, by allowing it to wrap around a wide variety of objects. Underactuation also enables size, weight, and cost reduction for each finger, since the actuators are typically the largest, heaviest, and most expensive components of the device.

The underactuated compliant fingers are designed to mimic the closing sequence of human fingers, such that a coordinated motion of the phalanges is achieved. In particular, the stiffness of each compliant joint is adjusted such that they maintain the second and third phalanges of the finger in the fully extended configuration until the first phalanx comes in contact with an obstacle or reaches its mechanical limit. When the mechanism is free of contacts and within joint limits, it behaves like a single rigid body. When the motion of a phalanx is resisted, the force generated by the tendon overcomes the spring preload, and the adjacent phalanx initiates motion. The motion continues sequentially until movements of all phalanges are resisted, due to either contacting with an object or reaching the joint limits. Hence, each compliant finger is capable of producing many of the natural finger trajectories of a human hand, and the tendon force is properly distributed over all phalanges.

2.3.3.1. Material Selection

The selection of appropriate material to cover the rigid phalanges and compliant joints is important to achieve robust fingers with a soft delicate touch. Selection of a high viscous silicon rubber results in high force requirements from the tendon and increases the energy consumption during bending, while the selection of a less viscous silicon rubber causes easy cracking of the material, decreasing the robustness of the finger. After testing many different materials, SILASTOSIL® 28-700 FG is evaluated to provide the best compromise among polyurethane materials to serve as the base material for the underactuated compliant fingers.

Implementation of proper stiffness for the compliant joints plays a crucial role in achieving the desired coordinated motion of the anthropomorphic fingers. Phalanges are fabricated with ABS plastic through rapid prototyping, while the compliant joints are fabricated using polyurethane material. Even though the polyurethane material is proper to serve as the base material to cover the compliant fingers, including the phalanges and compliant joints, it is necessary to further adjust the stiffness of each compliant joint to implement the desired coordinated motion and to anisotropically strengthen these joints against twisting and bending. Along these lines, carbon fiber strips are embedded inside each compliant joint. Lightweight carbon fiber strips not only act as leaf springs used to implement the desired level of compliance at each joint but also help support the joints by structurally reinforcing them against twisting and undesired bending forces.

2.3.3.2. Fabrication of the Compliant Fingers

Fabrication of compliant fingers consists of several stages as presented in **Figure 5**. In the first step, rigid parts, such as parts of phalanges and molds, are fabricated using additive manufacturing as shown in **Figure 5a**. Additive manufacturing enables the intricate design of phalanges and finger molds to be custom built for each amputee. Furthermore, accuracies of 100 μm are easily achievable at low manufacturing costs.

In the second step, finger molds are used for the precise arrangement of phalanges, compliant joints, and fingers. Epoxy resin infused carbon fiber sheets are incorporated into the design as in **Figure 5b**, before injecting silicone rubber in liquid form. This way, even though each joint consists of the same materials, silicone rubber molds with varying widths enable specific stiffness levels to be associated at each joint

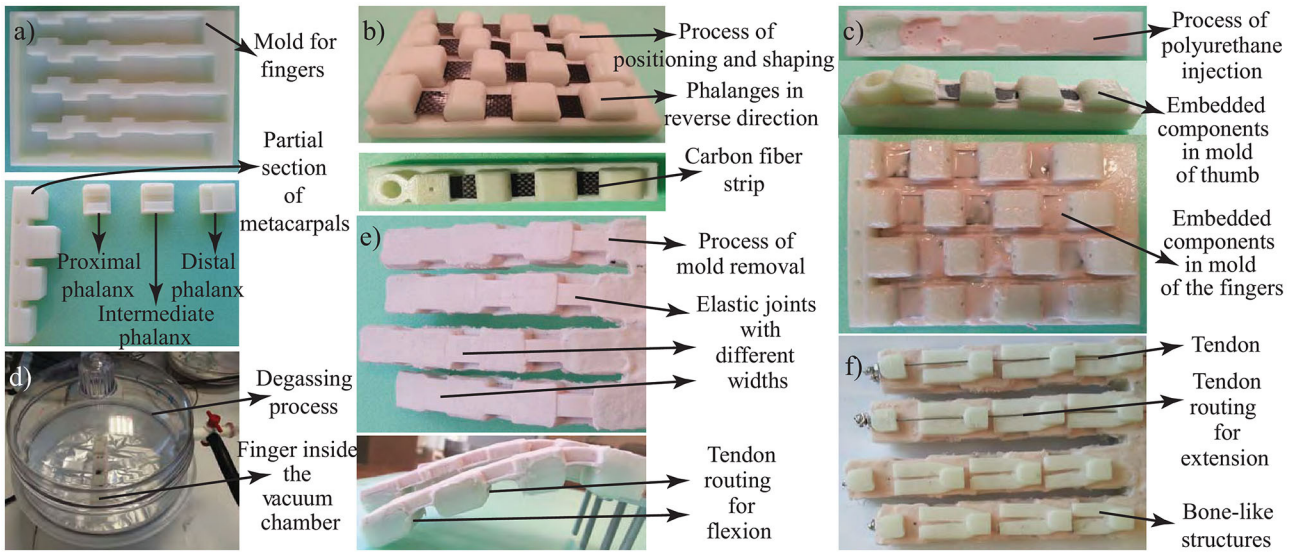

FIGURE 5 | The six step process used to fabricate the compliant fingers. **(a)** Mold. **(b)** Positioning of the fingers. **(c)** Injection of the liquid polyurethane. **(d)** Degassing process. **(e)** Mold removal process. **(f)** Assembly of the other components.

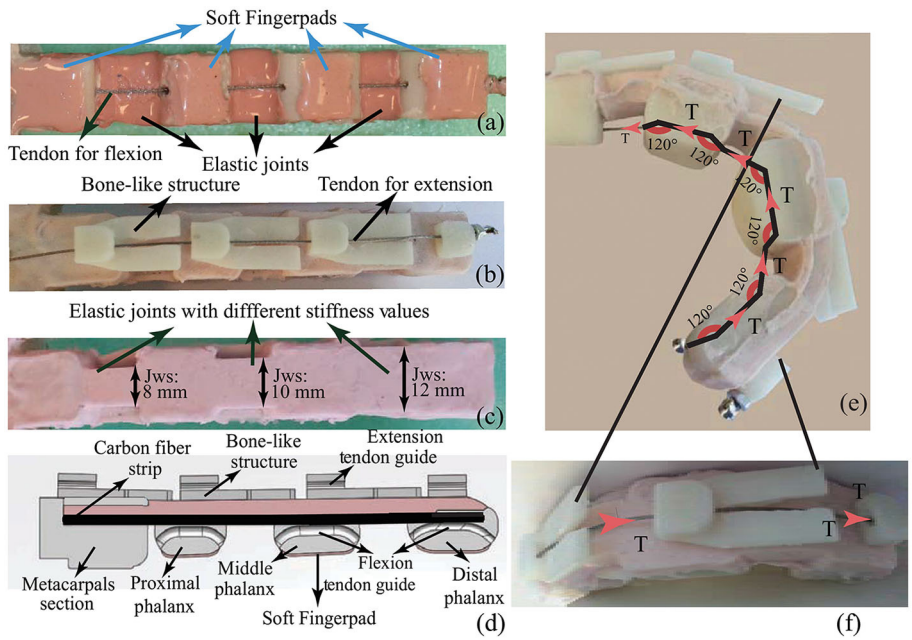

FIGURE 6 | (a) Bottom view with soft finger pads. **(b)** Top view with bone-like joint limits. **(c)** Side view with varying joint widths resulting in customized joint stiffness. **(d)** Cross-section of a solid model of the compliant finger with cable routing. **(e)** Flexion tendon routing. **(f)** Extension tendon routing.

(refer to **Figures 6c,d**). In particular, the stiffness is increased from proximal to distal joints. Consequently, the joint flexion initializes at the metacarpophalangeal joint, continues at the proximal interphalangeal joint, and finalizes at the distal interphalangeal joint.

In the third step, highly-adhesive silicone rubber is injected into the mold in its liquid form as depicted in **Figure 5c**. Before pouring the silicon resin, routing holes at phalanges are strapped in order to prevent polyurethane flow inside tendon routes. In addition, a release agent is used to avoid the bonding of cured polyurethane to mold surfaces and to facilitate the releasing of the part from the crinkled-shaped mold.

As a consequence of injecting silicon rubber into the mold, air bubbles occur inevitably, which may cause inhomogeneous material distribution, adversely affecting the stiffness of each joint; hence, the coordinated motion of the finger. In the fourth

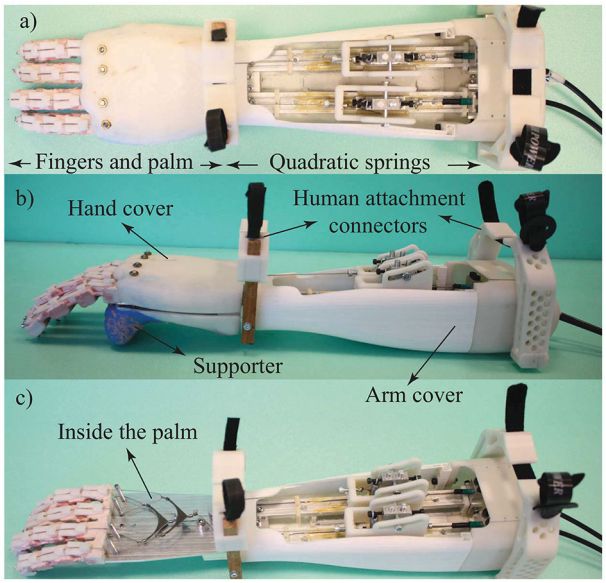

FIGURE 7 | (a) Top view, **(b)** side view, and **(c)** interior of the transradial hand prosthesis prototype.

TABLE 1 | Technical specifications.

Maximum tendon force	160 N
Minimum tendon force	20 N
Maximum tendon speed	20 mm/s
Minimum joint stiffness	135 Nmm/rad
Maximum joint stiffness	545 Nmm/rad
Weight	1.1 kg

step, degassing is implemented with −0.2 to −0.5 bar pressure to remove air bubbles from the silicone material, as presented in **Figure 5d**. The recommended cure time for the resin is about 12 h at room temperature and the complete molding process takes about 13 h.

In the fifth step, the fingers are removed from the molds and tendons responsible for force transmission are inserted into their routes, as shown in **Figure 5e**.

In the final step shown in **Figure 5f**, bone-like structures, as in **Figure 6b**, are placed on the upper surface of fingers to induce physical joint limits. These structures constrain the finger extension after it reaches its fully extended horizontal position, preventing fingers to bend in the reverse direction. High friction soft finger pads produced using the silicone material are added on the contact surfaces of phalanges to improve slip resistance of the fingers (Cutkosky et al., 1987; Shimoga and Goldenberg, 1992), as in **Figure 6a**.

2.3.3.3. Cable Routing for the Compliant Fingers

Force transmission of the compliant fingers is achieved through the flexion and the extension tendons. Due to the inherent stiffness of each compliant joint, higher forces are required while closing the fingers. To facilitate easier closing of the fingers, flexion cable channels are implemented with 120° angles, such that larger moment arms are implemented for the flexion, increasing the moments acting on the phalanges. **Figure 6d** depicts the cross-section of a solid model of a compliant finger, while **Figures 6e,f** show the flexion and extension tendon routing on a finger prototype.

2.3.4. Implementation of the Transradial Hand Prosthesis

The hand prosthesis consists of three main components: VSA, forearm, and compliant fingers. The expanding contour cams of VSA, the forearm in which the nonlinear springs of VSA are embedded on linear sliders, and device covers are fabricated through additive manufacturing, while the palm is constructed using a laser cut aluminum sheet. **Figure 7** presents an assembled prototype.

Since the actuators, motor drivers, and batteries of the Bowden cable driven VSA can be placed remotely anywhere on the body, e.g., can be kept inside a backpack, they are not integrated inside the prosthesis. This decision helps keep the device weight and cost low, as it provides extensive design flexibility while choosing/customizing these components according to the needs of the amputee. Sizing of the actuators should be decided considering the friction induced by Bowden cables. Note that, integration of this component into the forearm is also possible but induces challenging size and weight constraints for these components.

The specifications required from the drive train are characterized as follows. The maximum force required on the drive tendon such that a 1.5 kg object can be lifted at the maximum stiffness level is verified as 160 N. The force required to close the hand at the lowest stiffness level with no object in the hand is characterized as 20 N. The maximum speed required on the drive tendon is characterized as 20 mm/s, such that all fingers reach their joint limits within 2 s when the fingers are free to move.

Geared DC motors that satisfy the maximum force and speed requirements are selected to implement the drive train. With these motors, the minimum and the maximum stiffness of the drive tendon are experimentally characterized as 135 and 545 Nmm/rad, respectively. The overall weight of the device (excluding the motors, drivers, and battery) is 1.1 kg, which is lower than the natural weight of the corresponding part of the human limb (Plagenhoef et al., 1983; de Leva, 1996). Lightweight may cause less fatigue for the amputee. Note that the current research prototype is developed to verify the intended functionality and has not been optimized for size and weight. If necessary, the weight of the prosthesis can easily be adjusted to match the weight of the lost limb. The drive train specifications of the hand prosthesis are presented in **Table 1**.

To select a properly sized battery pack, the power consumption of the transradial hand prosthesis is experimentally characterized, as it is dependent on the grasp type and the friction losses in the system. Power and pinch grasps are studied as these are most commonly used. Each grasp type is repeatedly executed on a wide variety of objects, when the hand stiffness is set to high and low values, respectively. Furthermore, the average

TABLE 2 | Power consumption.

	Energy requirements [mWh]	
	Low stiffness	**High stiffness**
Power grasp	30	81
Pinch grasp	18	75
Stiffness modulation	4.9	

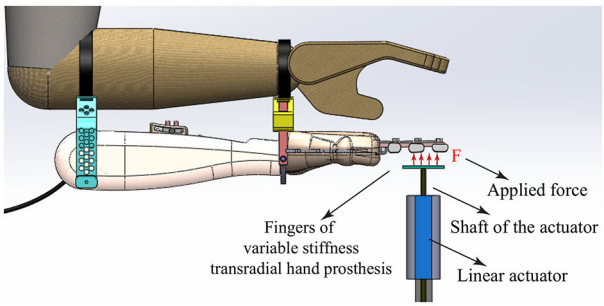

FIGURE 8 | Schematic representation of the experimental setup.

power consumed while modulating the hand stiffness from its lowest level to highest level is also characterized. The mean power consumption for each grasp type and stiffness change are presented in **Table 2**.

The highest energy consumption takes place during a power grasp when the stiffness is simultaneously modulated from low to high. The results indicate that a 50 g rechargeable LiFePo4 battery pack with 1,500 mAh enables the execution of this grasp for 120 times. Furthermore, these battery modules can be rapidly charged. The number of battery modules integrated into the system can be personalized based on the needs and preferences of the amputee.

3. RESULTS

The aim of the experimental evaluation is to reveal the feasibility of the working principle of the proposed hand prosthesis. A set of experiments is conducted in order to validate the independent position and stiffness modulation of the hand prosthesis. The experiment consists of two tasks, where the objective of the first task is to verify stiffness modulation when the position is regulated at a constant value, while the second task aims to verify that the desired position can be changed when the stiffness parameters are kept constant.

3.1. Experimental Setup and Procedure

The experimental setup consists of a direct drive linear actuator with a built-in high resolution incremental encoder, placed under the four fingers of the transradial prosthesis, as shown in **Figure 8**. During the experiments, the gravitational force acting on the actuator is compensated with a counter mass, while the actuator is force controlled. All controllers are implemented in real-time at 500 Hz with a PC workstation equipped with a DAQ card. In these experiments, the position and the stiffness levels are not controlled by the volunteers, as the goal is to perform a verification of the hand prosthesis independent of its user interface. Hence, during the experiments, the reference values for the position and the stiffness are set by the PC workstation.

The experiment is composed of two tasks with 10 repetitions for each condition of each task. During the first task, the position of the VSA is kept constant at 0°, i.e., the angular position of the metacarpophalangeal (MCP) joint is set to 0°, while the stiffness of VSA is adjusted to three distinct stiffness values that correspond to low, intermediate, and high stiffness levels for the fingers. The stiffness of the fingers is experimentally determined by applying a linearly increasing force to flex the fingers and recording their deflection.

During the second task, the stiffness of the VSA is kept constant at its intermediate level, while the position of the VSA is adjusted to three distinct position values that correspond to low, intermediate, and high flexion of the fingers. The position of the fingers is determined by recording the position of the linear actuator under zero force control, while the stiffness of the fingers is determined by applying a constant force to resist flexion of the fingers at the equilibrium position and recording the resulting deflection.

3.2. Experimental Results

Figure 9A presents the experimental results for the case when VSA is adjusted to three distinct stiffness values that correspond to low, intermediate, and high stiffness levels for the fingers, while the finger positions are kept constant. In particular, shaded regions represent all the linear fits recorded for 10 trials, while the dark line represents their mean. The slopes of these lines indicate that low, intermediate, and high stiffness for the fingers are k_l=0.091 N/mm, k_i=0.17 N/mm, and k_h=1.8 N/mm, respectively. The R values for these linear fits are evaluated to be higher than 0.98.

Figure 9B presents the experimental results for the case when VSA is adjusted to intermediate stiffness level, while the finger positions, i.e., the angle between the MCP joint of the fingers and the palm surface, are regulated to 0°, 30°, and 60°, respectively. Once again, the shaded regions represent all the linear fits recorded for 10 trials, while the dark line represents their mean. The slopes of these lines indicate that the stiffness level of the fingers are k_{0°=0.17 N/mm, k_{30°=0.17 N/mm, and k_{60°=0.18 N/mm, respectively. The R values for these linear fits are evaluated to be higher than 0.98.

Experimental results provide strong evidence that the stiffness and the position of the transradial hand prosthesis can be controlled independently, with high repeatability while executing predefined tasks. The impedance characteristics of the compliant fingers of the VSA prosthesis closely match the characteristics of human fingers as presented in Howe et al. (1985). The characterization results are also compatible with the results presented in Matsuoka and Afshar (2004), as the flexion/extension movements performed by an anatomically human-like robotic index finger necessitate a similar amount of muscle forces.

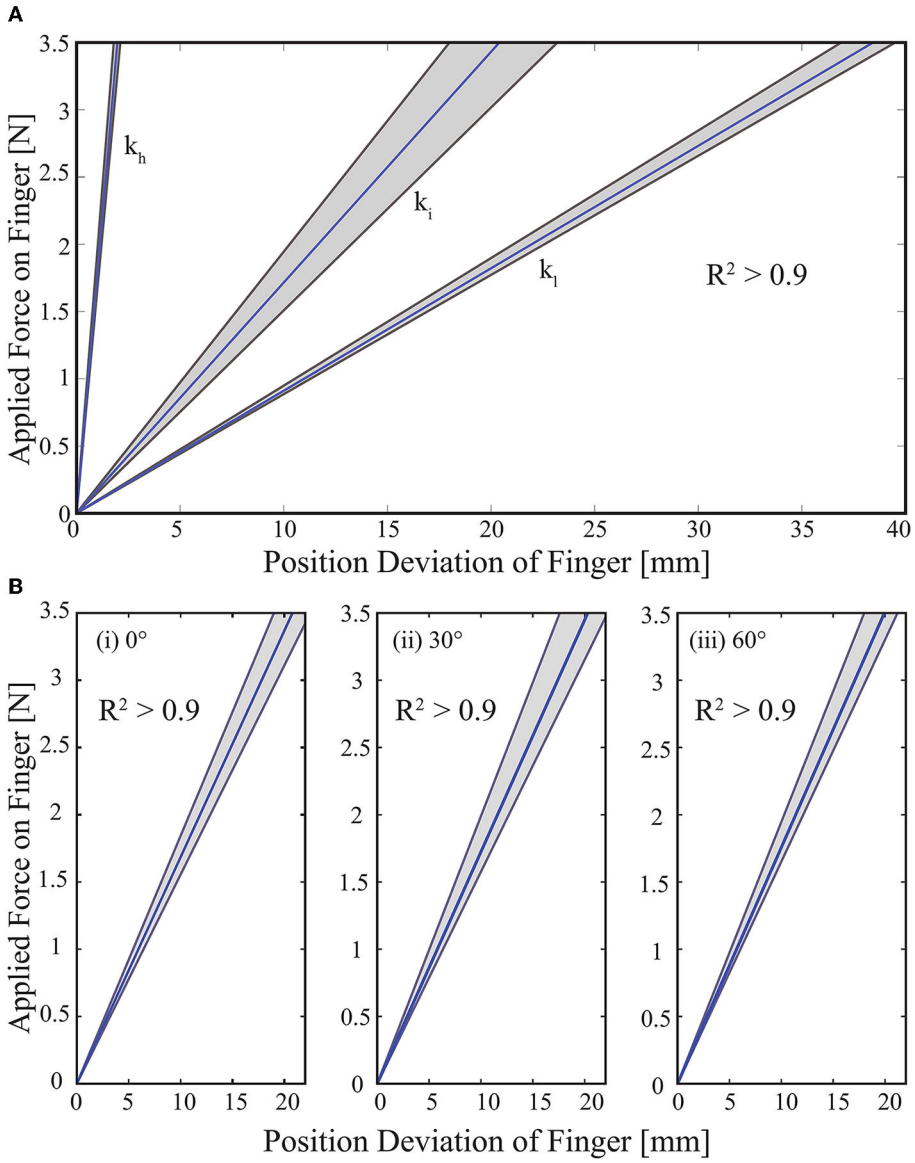

FIGURE 9 | (A) Stiffness modulation of hand prosthesis. The Gray zone presents the best linear fit of each trial and the blue line presents the average value of ten trials. **(B)** Position control of hand prosthesis. The Gray zone presents the results of each trial. The blue line presents the average value of ten trials.

3.3. Illustrative Experiments and Evaluations

Given that only the position and the stiffness of the driven tendon are directly regulated by the VSA, in general, the resulting position and stiffness of the fingers depending on the interaction. To test the usefulness of the variable stiffness transradial hand prosthesis, the device is attached to six volunteers, as shown in **Figure 8**. All volunteers signed informed consent forms approved by the IRB of Sabanci University. The volunteers were given control of the position and the stiffness of the prosthesis through the sEMG based tele-impedance controller (Hocaoglu and Patoglu, 2012, 2019).

In particular, sEMG signals measured from the surface of the upper arm, chest, and shoulder were used to automatically adjust the stiffness level of the prosthesis to that of the upper arm, while the position regulation was intentionally controlled by the volunteers by moving their shoulder muscles. With this natural control interface, the volunteers were asked to grasp 16 objects with a wide variety of shapes (e.g., rectangular, elliptic, complex) and compliance levels (e.g., rigid, elastic). Participants were asked to grasp and hold the objects for a while, then release them back onto the surface. In the same manner as in Section 3, the required stiffness level of VSA to safely grasp each object depended on the interaction. The volunteers were successful at modulating their

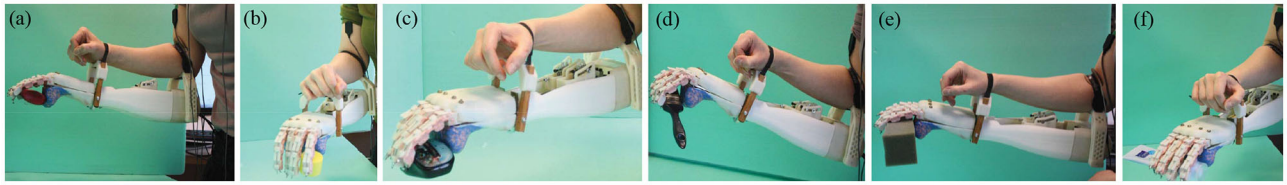

FIGURE 10 | Demonstration of variable stiffness transradial hand prosthesis performing various grasps while interacting with **(a)** a glue box, **(b)** a bottle cap, **(c)** a mouse, **(d)** a brush, **(e)** a sponge, and **(f)** a cream tube.

impedance and grasping a wide variety of objects with the sEMG interface, as shown in **Figure 10**. Videos demonstrating several illustrative grasps are available at https://hmi.sabanciuniv.edu/VSA_hand_prosthesis.mp4.

The current prototype emphasizes simplicity, ease of use, and adaptability; hence, implements a two-degree-of-freedom underactuated power transmission to allow for the position and stiffness change of the prosthetic hand. Successful employment of the prosthesis depends on the amputee making proper decisions on how to interact with the object. Our extensive experiments with volunteers indicate that humans are very skillful at learning how to interact with the environment.

On average, it took 3.2 ± 1.3 min for a volunteer to get used to the device and successfully complete the required manipulation tasks. The time elapsed for grasping and releasing the 15 objects in the video are calculated as 1.22 ± 0.56 s and 0.82 ± 0.48 s, respectively. The time required to make a fist is about 2 s. The grasping performance of the proposed prosthesis prototype is comparable to commercial ones (Touch Bionics Inc., 2022).

The robustness of the hand prosthesis is also tested during the user studies. During the user studies, volunteers repeatedly impacted the fingers to various surfaces. Compliant fingers made of silicon rubber and ABS material were robust to such impacts and did not sustain any damage.

In the current research prototype, passive support is preferred to oppose the fingers, instead of an active thumb. This decision helps keep the system and the controller simple. Our experiences with the volunteers indicate that the passive support is adequate for implementing a wide variety of functional grasps. During post trial interviews, none of our volunteers complained about the functionality of this support.

4. DISCUSSION

In this study, the design, implementation, and experimental evaluation of a low-cost, customizable, easy-to-use variable stiffness transradial hand prosthesis have been presented. User studies indicate that the device is dexterous enough to successfully interact with a wide variety of environments.

Please note that the classification of the design objectives, as presented in Section 2.1, is subjective. In general, it is up to the designer to prioritize the users' needs. Based on different prioritization of these objectives, it is possible to come up with different designs, catering to various user types. In our design, the goal has been to achieve a dexterous, anthropomorphic, adaptable, robust, low-cost mechatronic system design. Achieving such a mechatronic system design is only the half of the story toward achieving an ideal prosthesis, where the design of an easy-to-use control interface for the mechatronic system is the other half. We present such a human-machine interface, called *tele-impedance control*, in Hocaoglu and Patoglu (2019).

The goal of our design is to provide a fulfilling functionality to amputees through stiffness modulation while decreasing or even reversing the relatively high abandonment rate for current high-tech prosthetics. While some of the commercial devices provide many extra functions including active thumb and wrist movements, these devices require special training and long rehabilitation periods, which discourage the majority of amputees from continually using such devices. It is possible to add a thumb to the tendon driven power transmission of the proposed prosthesis; however, substantial effort is required for the intricate control of thumb orientation and stiffness, such that it becomes functional and enhances the grasping performance. Alternatively, to achieve an anthropomorphic look with an aesthetically pleasing appearance, a compliant unactuated thumb can be added to the system. Furthermore, prosthesis gloves can be worn over the transradial hand prosthesis to achieve the natural appearance of human skin.

Our ongoing research study includes testing the efficacy of the variable stiffness hand prosthesis and its control interface (Hocaoglu and Patoglu, 2019), and is an extension of Section 3.3. This study has a comprehensive human subject experiment design to compare variable stiffness prostheses with fixed stiffness prosthetic hands. Our preliminary results with healthy volunteers presented in Section 5 of the PhD thesis of the first author (Hocaoglu, 2014), already provide strong evidence that tasks that require stiffness regulation by sEMG signals are performed best with the variable stiffness prosthetic hand in comparison to the performance obtained by a prosthesis whose stiffness level is fixed to a constant value.

Our future study will focus on improving the anthropomorphism and functionality by the inclusion of active thumb, wrist, and auto pre-tension mechanisms to the hand prosthesis, providing a customized sizing and weight distribution of the design, evaluating the grasping performance of the hand prosthesis on the same objects by setting the stiffness of the hand to different levels, conducting comprehensive testing with larger healthy populations and also amputees to provide

evidence of the effectiveness of variable stiffness actuation, and refinement of the prosthesis based on the feedback collected from amputees.

DATA AVAILABILITY STATEMENT

The original contributions presented in the study are included in the article/supplementary material, further inquiries can be directed to the corresponding author.

ETHICS STATEMENT

The studies involving human participants were reviewed and approved by University Research Ethics Council of Sabancı University. The patients/participants provided their written informed consent to participate in this study.

AUTHOR CONTRIBUTIONS

EH was responsible for the design, fabrication, and experimental evaluation of the variable stiffness hand prosthesis. VP conceived and supervised the study. Both authors contributed to the editing and scientific presentation of the article.

FUNDING

This work has been partially supported by Tubitak Grants 219M586, 111M186, 115M698 and Marie Curie IRG Rehab-DUET.

REFERENCES

Abul-Haj, C., and Hogan, N. (1987). An emulator system for developing improved elbow-prosthesis designs. *IEEE Trans. Biomed. Eng. BME* 34, 724–737. doi: 10.1109/TBME.1987.325997

Abul-Haj, C., and Hogan, N. (1990). Functional assessment of control systems for cybernetic elbow prostheses. I. Description of the technique. *IEEE Trans. Biomed. Eng*. 37, 1025–1036. doi: 10.1109/TBME.1990.1438510

Bicchi, A. (2000). Hands for dexterous manipulation and robust grasping: a difficult road toward simplicity. *IEEE Trans. Rob. Automat*. 16, 652–662. doi: 10.1109/70.897777

Bicchi, A., Gabiccini, M., and Santello, M. (2011). Modelling natural and artificial hands with synergies. *Phil. Trans. R. Soc. Lond. B* 366, 3153–3161. doi: 10.1098/rstb.2011.0152

Biddiss, E., and Chau, T. (2007). Upper limb prosthesis use and abandonment: a survey of the last 25 years. *IEEE Rob. Automat. Mag.* 31, 236–257. doi: 10.1080/03093640600994581

Birglen, L., and Gosselin, C. (2003). On the force capability of underactuated fingers. *In IEEE Int. Conf. Rob. Automat*. 1, 1139–31145. doi: 10.1109/ROBOT.2003.1241746

Birglen, L., Laliberté, T., and Gosselin, C. (2008). *Underactuated Robotic Hand, 1st Edn*. Springer. doi: 10.1007/978-3-540-77459-4

Blank, A., Okamura, A., and Whitcomb, L. (2011). "Task-dependent impedance improves user performance with a virtual prosthetic arm," in *IEEE International Conference on Robotics and Automation* (Shanghai: IEEE), 2235–2242.

Blank, A., Okamura, A., and Whitcomb, L. (2012). "User comprehension of task performance with varying impedance in a virtual prosthetic arm: a pilot study," in *IEEE International Conference on Biomedical Robotics and Biomechatronics* (Rome: IEEE), 500–507.

Blank, A., Okamura, A., and Whitcomb, L. (2013). Task-dependent impedance and implications for upper-limb prosthesis control. *Int. J. Rob. Res*. 3, 827–846. doi: 10.1177/0278364913517728

Castellini, C., van der Smagt, P., Sandini, G., and Hirzinger, G. (2008). "Surface EMG for force control of mechanical hands," in *IEEE International Conference on Robotics and Automation* (Pasadena, CA: IEEE), 725–730.

Catalano, M., Grioli, G., Farnioli, E., Serio, A., Piazza, C., and Bicchi, A. (2014). Adaptive synergies for the design and control of the Pisa/IIT SoftHand. *Int. J. Rob. Res*. 33, 768–782. doi: 10.1177/0278364913518998

Catalano, M., Grioli, G., Serio, A., Farnioli, E., Piazza, C., and Bicchi, A. (2012). "Adaptive synergies for a humanoid robot hand," in *IEEE International Conference on Humanoid Robots* (Osaka: IEEE), 7–14.

Chen, W., Xiong, C., and Yue, S. (2015). Mechanical implementation of kinematic synergy for continual grasping generation of anthropomorphic hand. *IEEE/ASME Trans. Mech*. 20, 1249–1263. doi: 10.1109/TMECH.2014.2329006

Chu, J.-U., Moon, I., Lee, Y.-J., Kim, S.-K., and seong Mun, M. (2007). A supervised feature-projection-based real-time EMG pattern recognition for multifunction myoelectric hand control. *IEEE/ASME Trans. Mech*. 12, 282–290. doi: 10.1109/TMECH.2007.897262

Cutkosky, M., Jourdain, J., and Wright, P. (1987). Skin materials for robotic fingers. *IEEE Int. Conf. Rob. Automat*. 4, 1649–1654. doi: 10.1109/ROBOT.1987.1087913

Dalley, S. A., Wiste, T. E., Withrow, T. J., and Goldfarb, M. (2009). Design of a multifunctional anthropomorphic prosthetic hand with extrinsic actuation. *IEEE/ASME Trans. Mech*. 14, 699–706. doi: 10.1109/TMECH.2009.2033113

de Leva, P. (1996). Adjustments to Zatsiorsky-Seluyanov's segment inertia parameters. *J. Biomech*. 29, 1223–1230. doi: 10.1016/0021-9290(95)00178-6

Dollar, A., and Howe, R. (2006). A robust compliant grasper via shape deposition manufacturing. *IEEE/ASME Trans. Mech*. 11, 154–161. doi: 10.1109/TMECH.2006.871090

Dollar, A., Jentoft, L., Gao, J., and Howe, R. (2010). Contact sensing and grasping performance of compliant hands. *Auton. Robots* 28, 65–75. doi: 10.1007/s10514-009-9144-9

English, C., and Russell, D. (1999). Mechanics and stiffness limitations of a variable stiffness actuator for use in prosthetic limbs. *Mech. Mach. Theory* 34, 7–25. doi: 10.1016/S0094-114X(98)00026-3

Ertas, I. H., Hocaoglu, E., and Patoglu, V. (2014). AssistOn-Finger: an under-actuated finger exoskeleton for robot-assisted tendon therapy. *Robotica* 32, 1363–1382. doi: 10.1017/S0263574714001957

Feix, T., Romero, J., Schmiedmayer, H. B., Dollar, A. M., and Kragic, D. (2016). The grasp taxonomy of human grasp types. *IEEE Trans. Hum. Mach. Syst*. 46, 66–77. doi: 10.1109/THMS.2015.2470657

Godfrey, S. B., Zhao, K. D., Theuer, A., Catalano, M. G., Bianchi, M., Breighner, R., et al. (2018). The softhand pro: functional evaluation of a novel, flexible, and robust myoelectric prosthesis. *PLoS ONE* 13, e0205653. doi: 10.1371/journal.pone.0205653

Gosselin, C., Pelletier, F., and Laliberte, T. (2008). "An anthropomorphic underactuated robotic hand with 15 dofs and a single actuator," in *IEEE International Conference on Robotics and Automation* (Pasadena, CA: IEEE), 749–754.

Grebenstein, M., Chalon, M., Hirzinger, G., and Siegwart, R. (2010). "Antagonistically driven finger design for the anthropomorphic DLR hand arm system," in *IEEE International Conference on Humanoid Robots* (Nashville, TN: IEEE), 609–616.

Hocaoglu, E. (2014). *Design and Tele-Impedance Control of a Variable Stiffness Transradial Hand Prosthesis* (Ph.D. dissertation). Sabanci University, Istanbul, Turkey.

Hocaoglu, E., and Patoglu, V. (2012). "Tele-impedance control of a variable stiffness prosthetic hand," in *IEEE International Conference on Robotics and Biomimetics* (Guangzhou: IEEE), 1576–1582

Hocaoglu, E., and Patoglu, V. (2019). *sEMG-Based Natural Control Interface for a Variable Stiffness Transradial Hand Prosthesis*. CoRR.

Howe, A., Thompson, D., and Wright, V. (1985). Reference values for metacarpophalangeal joint stiffness in normals. *Ann. Rheum. Dis*. 44, 469–476. doi: 10.1136/ard.44.7.469

Kamikawa, Y., and Maeno, T. (2008). "Underactuated five-finger prosthetic hand inspired by grasping force distribution of humans," in *IEEE International Conference on Intelligent Robots and Systems* (Nice: IEEE), 717–722.

Kara, O. C., and Patoglu, V. (2020). VnStylus: A haptic stylus with variable tip compliance. *IEEE Trans. Haptics* 13, 777–790. doi: 10.1109/TOH.2020.2967694

Li, G., and Kuiken, T. (2009). EMG pattern recognition control of multifunctional prostheses by transradial amputees. *Annu. Int. Conf. IEEE Eng. Med. Biol. Soc*. 2009, 6914–6917. doi: 10.1109/IEMBS.2009.5333628

Liberating Technologies Inc. (2022). [Online]. Available online at: http://www.liberatingtech.com/products/elbows/LTI_Boston_Digital_Arm_Systems_for_Adults.asp

Ma, R., Odhner, L., and Dollar, A. (2013). "A modular, open-source 3D printed underactuated hand," in *2013 IEEE International Conference on Robotics and Automation* (Karlsruhe: IEEE).

Massa, B., Roccella, S., Carrozza, M., and Dario, P. (2002). Design and development of an underactuated prosthetic hand. *IEEE Int. Conf. Rob. Automat*. 4, 3374–3379. doi: 10.1109/ROBOT.2002.1014232

Matsuoka, Y., and Afshar, P. (2004). Neuromuscular strategies for dynamic finger movements: a robotic approach. *Int. Conf. of IEEE Eng. Med. Biol. Soc*. 2, 4649–4652. doi: 10.1109/IEMBS.2004.1404288

McFarland, L., Hubbard Winkler, S., Heinemann, A., Jones, M., and Esquenazi, A. (2010). Unilateral upper-limb loss: satisfaction and prosthetic-device use in veterans and servicemembers from vietnam and OIF/OEF conflicts. *J. Rehabil. Res. Dev*. 47, 299–316. doi: 10.1682/JRRD.2009.03.0027

Mengilli, U., Caliskan, U., Orhan, Z. O., and Patoglu, V. (2020). *Two-Port Analysis of Stability and Transparency in Series Damped Elastic Actuation*. CoRR.

Merlet, J. (2006). *Parallel Robots, 2nd Edn*. Springer.

Migliore, S. A., Brown, E. A., and DeWeerth, S. P. (2007). Novel nonlinear elastic actuators for passively controlling robotic joint compliance. *J. Mech. Design* 129, 406–412. doi: 10.1115/1.2429699

Plagenhoef, S., Evans, F., and Abdelnour, T. (1983). Anatomical data for analyzing human motion. *Q. Exerc. Sport* 54, 169–178. doi: 10.1080/02701367.1983.10605290

Prattichizzo, D., Malvezzi, M., Gabiccini, M., and Bicchi, A. (2012). On the manipulability ellipsoids of underactuated robotic hands with compliance. *Rob. Auton. Syst*. 60, 337–346. doi: 10.1016/j.robot.2011.07.014

Shadow Robot Company Ltd. (2022). [Online]. Available online at: https://www.shadowrobot.com/products/dexterous-hand/

Shimoga, K., and Goldenberg, A. (1992). Soft materials for robotic fingers. *IEEE Int. Conf. Rob. Automat*. 2, 1300–1305. doi: 10.1109/ROBOT.1992.220069

Takaki, T., and Omata, T. (2011). High-performance anthropomorphic robot hand with grasping-force-magnification mechanism. *IEEE/ASME Trans. Mech*. 16, 583–591. doi: 10.1109/TMECH.2010.2047866

Tosun, F. E., and Patoglu, V. (2020). Necessary and sufficient conditions for the passivity of impedance rendering with velocity-sourced series elastic actuation. *IEEE Trans. Rob*. 36, 757–772. doi: 10.1109/TRO.2019.2962332

Touch Bionics Inc. (2022). [Online]. Available online at: http://www.touchbionics.com/products/active-prostheses/i-limb-ultra/

Touvet, F., Daoud, N., Gazeau, J., Zeghloul, S., Maier, M. A., and Eskiizmirliler, S. (2012). A biomimetic reach and grasp approach for mechanical hands. *Robot. Auton. Syst*. 60, 473–486. doi: 10.1016/j.robot.2011.07.017

Wolf, S., Eiberger, O., and Hirzinger, G. (2011). "The DLR FSJ: energy based design of a variable stiffness joint," in *IEEE International Conference on Robotics and Automation* (Shanghai: IEEE), 5082–5089.

Xu, K., Liu, H., Liu, Z., Du, Y., and Zhu, X. (2015). "A single-actuator prosthetic hand using a continuum differential mechanism," in *IEEE International Conference on Robotics and Automation* (Seattle, WA: IEEE), 6457–6462.

ya Nagase, J., Wakimoto, S., Satoh, T., Saga, N., and Suzumori, K. (2011). Design of a variable-stiffness robotic hand using pneumatic soft rubber actuators. *Smart Mater. Struct*. 20, 105015. doi: 10.1088/0964-1726/20/10/105015

Conflict of Interest: The authors declare that the research was conducted in the absence of any commercial or financial relationships that could be construed as a potential conflict of interest.

Publisher's Note: All claims expressed in this article are solely those of the authors and do not necessarily represent those of their affiliated organizations, or those of the publisher, the editors and the reviewers. Any product that may be evaluated in this article, or claim that may be made by its manufacturer, is not guaranteed or endorsed by the publisher.

frontiers in Neurorobotics

ORIGINAL RESEARCH
published: 11 March 2022
doi: 10.3389/fnbot.2022.789341

sEMG-Based Natural Control Interface for a Variable Stiffness Transradial Hand Prosthesis

Elif Hocaoglu[1,2]* *and Volkan Patoglu*[1]

[1] Faculty of Engineering and Natural Sciences, Sabancı University, Istanbul, Turkey, [2] School of Engineering and Natural Sciences, Istanbul Medipol University, Istanbul, Turkey

We propose, implement, and evaluate a natural human-machine control interface for a variable stiffness transradial hand prosthesis that achieves tele-impedance control through surface electromyography (sEMG) signals. This interface, together with variable stiffness actuation (VSA), enables an amputee to modulate the impedance of the prosthetic limb to properly match the requirements of a task while performing activities of daily living (ADL). Both the desired position and stiffness references are estimated through sEMG signals and used to control the VSA hand prosthesis. In particular, regulation of hand impedance is managed through the impedance measurements of the intact upper arm; this control takes place naturally and automatically as the amputee interacts with the environment, while the position of the hand prosthesis is regulated intentionally by the amputee through the estimated position of the shoulder. The proposed approach is advantageous since the impedance regulation takes place naturally without requiring amputees' attention and diminishing their functional capability. Consequently, the proposed interface is easy to use, does not require long training periods or interferes with the control of intact body segments. This control approach is evaluated through human subject experiments conducted over able volunteers where adequate estimation of references and independent control of position and stiffness are demonstrated.

Keywords: tele-impedance control, sEMG-based control interface, variable stiffness actuation, transradial hand prosthesis, impedance modulation

OPEN ACCESS

Edited by:
Chad Gregory Rose,
Auburn University, United States

Reviewed by:
Udaya B. Rongala,
Lund University, Sweden
Alperen Acemoglu,
Italian Institute of Technology (IIT), Italy
Hsien-Yung Huang,
Imperial College London,
United Kingdom

***Correspondence:**
Elif Hocaoglu
ehocaoglu@medipol.edu.tr

Received: *04 November 2021*
Accepted: *28 January 2022*
Published: *11 March 2022*

Citation:
Hocaoglu E and Patoglu V (2022) sEMG-Based Natural Control Interface for a Variable Stiffness Transradial Hand Prosthesis. Front. Neurorobot. 16:789341. doi: 10.3389/fnbot.2022.789341

1. INTRODUCTION

According to the WHO, there are about 40 million amputees living in developing countries (Marino et al., 2015), and this number is expected to rise in the future (Ziegler-Graham et al., 2007). Many prosthetic devices have been proposed to raise the living standards of amputees by helping them restore their functional abilities, enabling them to perform daily chores, and return back to their work (Millstein et al., 1985).

Despite many potential benefits, a substantial percentage of people with upper-limb amputation prefer not to wear prostheses. In the literature, the mean rejection rates for the use of electric and body-powered prostheses are reported for the pediatric population as 35 and 45%, and for the adult population as 23 and 26%, respectively (Biddiss and Chau, 2007). Some of the reasons behind the low acceptance rate of body-powered hands are reported as slow movement, heavy-weight, inadequate grip force, limited functionality, inconvenience of harnessing, unnatural use, and discomfort (Biddiss and Chau, 2007).

Many research groups have investigated means to close the acceptance gap by orienting their studies to increase the dexterity and functionality of prosthetic hand devices. In both academic studies (Riillo et al., 2014; Naik et al., 2016; Wang et al., 2017) and commercial applications (Bebionic, 2022; Motion Control Inc., 2022; Ossur Inc., 2022; Ottobock, 2022), the most common means to control dexterous hand prosthesis is based on classifying surface electromyography (sEMG) signals recorded from different muscle groups and assigning a grip pattern to each class. Recently, some studies have also integrated different sources of data, such as mechanomiographic (MMG) biosignals (Kurzynski et al., 2016), near-infrared spectroscopy (NIRS) (Guo et al., 2017), and inertial measurement unit (IMU) (Kyranou et al., 2016), to improve the classification performance of multi-functional hand prostheses. Although such studies are aimed to make the amputees' life easier by enabling hand prostheses to have more functions, these devices demand long-training periods (Herle, 2016) stemming from their non-intuitive control interface and have not been shown to provide a viable solution for the high abandonment rate of prosthetic devices (Atkins et al., 1996).

To enable natural dexterity and an intuitive control interface for prosthetic hand devices, one of the prominent features of human neuromuscular system specialized to be competent at realizing various physical activities may provide a solution. In particular, most of the daily activities that require physical interactions with human hands are successfully performed because of the unrivaled capability of human adaptation. Such ability originates from predicting the type of the interaction and regulating the impedance of the limb based on the activity (Franklin and Milner, 2003; Franklin et al., 2003a,b, 2004; Popescu et al., 2003; Perreault et al., 2004). The impedance regulation of limbs is realized through the modulation of the contraction levels of antagonistic muscle pairs and reflexive reactions that contribute to neuromotor control to assist the stability of human-object interaction. All these abilities enable humans to actively and naturally perform activities of daily living (ADL). For instance, during tasks that require high precision (such as writing), humans raise the stiffness of their arm to guarantee the precise positioning against perturbations, while during interactions with soft/fragile objects, humans regulate their limbs to become more compliant in order to prevent damage to the object (Hogan, 2002).

The impedance modulation ability of humans has become inspiring in robotics. Along these lines, several studies on prosthetic devices have been conducted to imitate the stiffness regulation feature of humans, while physically interacting with their environment (Abul-Haj and Hogan, 1990a,b; Rao et al., 2010). Moreover, systematic human subject experiments have provided evidence that task-dependent impedance regulation improves human performance while using a virtual arm prosthesis (Blank et al., 2011, 2012, 2013). Recently, authors have proposed a variable stiffness transradial hand prosthesis (Hocaoglu and Patoglu, 2012, 2019b). Variable stiffness actuation (VSA) of this prosthesis is based on antagonistically arranged tendons coupled to nonlinear springs driven through a Bowden cable based power transmission. Unlike in the control based impedance modulation, VSA based prosthesis possesses high energy efficiency, since its actuators are not in use at all times to maintain the desired stiffness level. Furthermore, since the resulting stiffness of VSA is an inherent physical property of the device, it is valid over the whole frequency spectrum, including the frequencies over the controllable bandwidth of the actuators.

In this study, we propose, implement, and evaluate a natural human-machine interface for a variable stiffness transradial hand prosthesis to achieve tele-impedance control through sEMG signals. The mechatronic design of the transradial hand prosthesis, presented in Hocaoglu and Patoglu (2019a), employs a VSA based on the antagonistic actuation principle with quadratic springs and enables amputees to regulate the stiffness and position of the hand prosthesis independently. For the tele-impedance control of the variable stiffness transradial hand prosthesis, we benefit from sEMG signals generated during the muscular activity captured by biopotential electrodes, by means of which amputees can naturally be a part of the control architecture.

Our human machine interface is based on using four channels of sEMG signals responsible for controlling the position and impedance of the variable stiffness transradial hand prosthesis. In particular, as commonly done in the literature (Dalley et al., 2009; Bennett et al., 2016; Lenzi et al., 2016; Kim et al., 2019), the motion control of the hand prosthesis is regulated through intentional muscular activities generated at chest and shoulder mapped to the opening/closing of the fingers. However, in contrast to other interfaces, the stiffness of the prosthesis is regulated automatically based on the estimated stiffness of the *intact* muscle groups of the upper arm. As a result, while the proposed human machine interface requires the amputee to intentionally control the position of the VSA prosthesis, the stiffness regulation takes place automatically based on the instantaneous stiffness of the intact portion of the limb. Such an approach is advantageous since the impedance regulation takes place effortlessly from task to task or during the execution of a single task without requiring amputees' attention and diminishing their functional capability. Consequently, such an interface is easy to use, does not require long training periods, and does not interfere with the control of intact body segments. Furthermore, it has been pointed out in the literature that energetic interactions with the environment influence the determination of the impedance by the intact neuromuscular system (Franklin et al., 2004). Hence, regulating the prosthesis to mimic the impedance of an intact portion of the limb promises to be a more plausible control strategy than requiring the amputee to determine and control the proper impedance using dysfunctional muscles that lack such physical feedback, since these muscles are not physically coupled to the environment.

A preliminary study regarding tele-impedance control of variable stiffness transradial hand prosthesis has been presented in Hocaoglu and Patoglu (2012). This study significantly

extends (Hocaoglu and Patoglu, 2012). To the best of the authors' knowledge, this study, along with Hocaoglu and Patoglu (2012), presents one of the first human-machine control interfaces for a VSA hand prosthesis. Furthermore, the human subject experiments presented in this study complement the ones in the literature (Blank et al., 2011, 2012, 2013; Hocaoglu and Patoglu, 2012), as physical interactions with the environment are enabled.

The contributions are summarized as follows: (i) A natural human-machine interface compatible with a variable stiffness transradial hand prosthesis is proposed. (ii) A muscle fatigue compensator responsible for the reference signal generation is designed and embedded into the proposed control architecture. (iii) The independent and simultaneous stiffness and position controls of variable stiffness hand prosthesis have been experimentally verified. (iv) Evidence is provided through human-subject experiments conducted over able volunteers on various tasks that the upper and lower arm impedance modulation display similar characteristics and impedances of both parts of the arm are modulated simultaneously for many tasks. (v) Experimental verification of the effectiveness of stiffness modulation and the need for short training periods have been demonstrated.

The rest of the article is organized as follows: Section 2 introduces sEMG-based tele-impedance control of the variable stiffness transradial hand prosthesis, details the construction of control references through sEMG based stiffness and position estimations, explains the independent control of the position and stiffness for the antagonist VSA, presents the compensation strategy used against muscle fatigue, and provides a set of experiments to verify the hypothesis that the stiffness modulation of the upper arm and the forearm are correlated. Section 3 experimentally verifies the independent control of the position and stiffness through the sEMG-based tele-impedance control of a VSA transradial hand prosthesis and provides evidence that the natural human-machine interface is an effective strategy in control. Section 4 concludes the article and discusses the limitations of the study.

2. MATERIALS AND METHODS

This section conveys the technical details of our approach and presents the experimental verification of the effectiveness of each module in the approach. Accordingly, the tele-impedance control paradigm of a variable stiffness hand prosthesis is introduced in section 2.1, the modules constituting the paradigm are detailed, and experimental evaluations of each function in the modules are elaborated in sections 2.1.1 and 2.1.2. The compensation technique proposed for muscle fatigue due to co-contraction of the muscle pairs is circumstantiated through human-subject experiments in section 2.1.3. Moreover, the experimental validations of the methodologies to estimate the stiffness and position parameters through sEMG signals to be employed for the control of hand prosthesis are detailed in section 2.1.4. Section 2 is concluded with the experimental verification of the correlated stiffness adaptation of antagonistic muscle pairs.

2.1. sEMG Based Tele-Impedance Control of a Variable Stiffness Transradial Hand Prosthesis

Surface electromyography based tele-impedance controller is developed to control a VSA transradial hand prosthesis (Hocaoglu and Patoglu, 2019a). The transradial hand prosthesis features tendon driven underactuated compliant fingers that naturally adapt the hand shape to wrap around a wide variety of object geometries. Abiding by the definition of underactuation, two movable pulleys on the palm actuated by a VSA mechanism are assigned for the extension and flexion of the 12 DoF tendon-driven hand mechanism. Antagonistically arranged tendons of the prosthesis enable the modulation of the stiffness of the fingers and control of their position. Adaptation of the mechanical impedance of prosthesis based on changing physical conditions enables the amputee to perform various tasks with high dexterity.

Figure 1 presents an overview of the tele-impedance control architecture. The proposed control architecture consists of two modules. The first module handles the measurement of sEMG signals, their conditioning, and the estimation of reference values for the hand position and stiffness control. In the second module, the closed-loop motion controller [Proportional integral derivative (PID) controller] ensures the position and stiffness regulation of the VSA prosthetic hand based on the reference values estimated in the first module. In order to translate the meaning of normalized sEMG signals as physical references, namely position and stiffness references for the closed loop control system, one-to-one correspondence is assigned between the upper and lower limits of the normalized sEMG signals and angular position and stiffness limits of the fingers. Throughout the control, visual feedback and physical coupling provide information for the amputees to adapt their sEMG signals to match the task requirements.

Given that transradial upper extremity amputees lack the muscle groups responsible for hand and forearm motions, sEMG signals for the position control of the hand prosthesis are measured from the chest and the shoulder, while sEMG signals measured from the intact muscle pairs on the upper arm are used for the impedance control. Estimation of the hand position and stiffness from the sEMG signal involves modeling of hand motion/stiffness based on sEMG signals, empirical determination of model parameters for use in real-time control, and incorporation of fatigue compensation.

2.1.1. Stiffness Estimation Through sEMG Signals

Muscle groups play a crucial role in the human body in terms of both the torque and impedance (stiffness and damping) modulation of a joint to properly interact with different environmental conditions. Particularly, impedance matching to the varying environment dynamics is carried out by means of the prominent features of muscles, such as regulation of co-contraction levels and reflex gains. The mechanical impedance of joints is an important parameter in the control of limbs under both static and dynamic conditions.

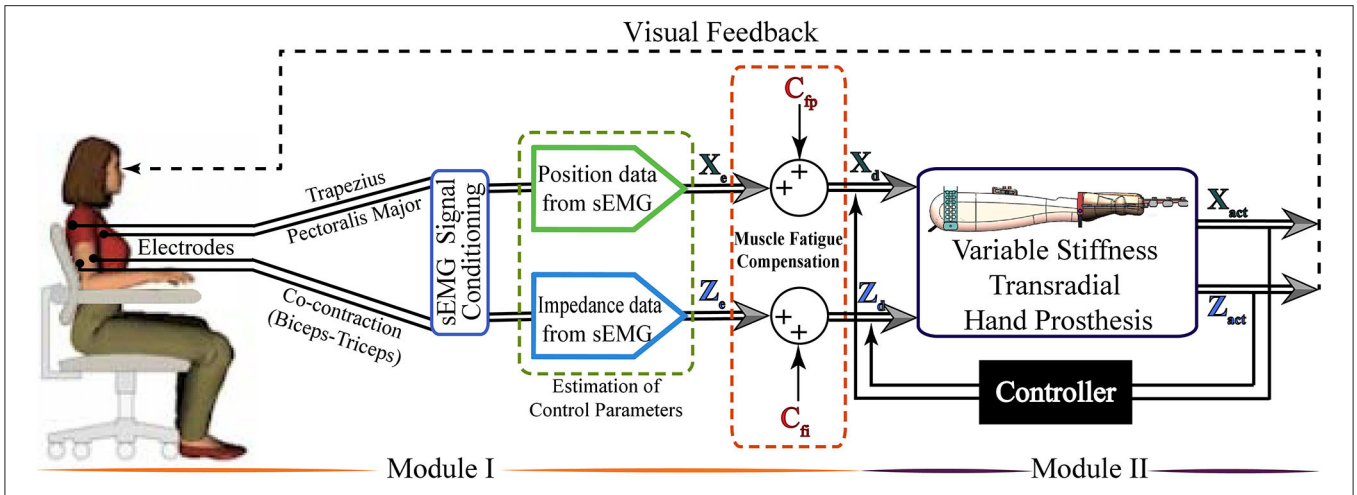

FIGURE 1 | The control interface of the variable stiffness transradial hand prosthesis: In the first module, raw surface electromyography (sEMG) signals are measured from the upper arm and muscle groups placed under the chest and shoulder, sEMG signals are conditioned by a series of filters, and the position and stiffness references are estimated. The second module implements the position and stiffness control of the variable stiffness transradial hand prosthesis to follow the references estimated in the first module. Figure reproduced from Hocaoglu and Patoglu (2022).

In the literature, many researchers have addressed the characterization of joint stiffness by focusing on multi-joint arm movements (Gomi and Kawato, 1996; Burdet et al., 2000, 2001). These studies are mainly focused on point-to-point reaching movements of subjects under perturbations and disturbance forces. The stiffness of the arm is estimated based on the relation between the deviations of the trajectories with respect to the undisturbed trajectories and the applied perturbation forces. Such methods are not viable for real-time applications, such as use with prosthetic limbs, as they require coupling users to a computer controlled manipulator. Index of muscle co-contraction around the joint (IMCJ) (Osu et al., 2002) approach is based on sEMG signals and provides a stiffness estimation technique that is feasible for real-time use. In this approach, the stiffness estimation is realized through the estimation of the co-contraction levels of antagonistic muscle groups. In the literature, the IMCJ method has been employed to reveal the mechanical characteristics of the musculoskeletal system (Hunter and Kearney, 1982; Basmajian and De Luca, 1985; Gomi and Osu, 1998).

Index of muscle co-contraction around the joint describes the working principle of antagonistic muscle groups around a joint through rectified sEMG signals and utilizes Equations (1)–(2) for stiffness estimation of the joint (Osu et al., 2002).

$$\tau = \sum_{i=1}^{k} \left[\kappa_i . agon(sEMG_i) - \lambda_i . anta(sEMG_i) \right] \quad (1)$$

$$S = \sum_{i=1}^{k} \left[|\kappa_i| . agon(sEMG_i) + |\lambda_i| . anta(sEMG_i) \right] \quad (2)$$

Here, i is the index that labels each muscle group, τ symbolizes the joint torque of the limb, while $agon(sEMG)$ and $anta(sEMG)$ denote the normalized muscular activity of the agonist and antagonist muscles, respectively. Symbols κ and λ capture the moment arms in charge of converting muscle activity to muscle tension responsible for generating muscle torque. The relation between the muscle torque and the muscle impedance (Murray et al., 1995; Kuechle et al., 1997; Gomi and Osu, 1998) is mapped to the correlation between the joint torque and the joint impedance (Hunter and Kearney, 1982; Gomi and Osu, 1998), leading to the joint stiffness estimates S *via* Equation (2), where κ and λ are estimated according to Equation (1).

In this study, Equations (1)–(2) were used to estimate the joint stiffness through a series of experiments as follows. Eight healthy volunteers (2 women, 6 men), who were students of Sabancı University participated in the experiments. Participants had no prior experience with the experimental setup. The participants did not report any sensory or motor impairment. All participants in all experimental studies presented in this article signed informed consent forms approved by the IRB of Sabancı University.

The experimental task was to grasp a dumbbell while positioning the elbow at 90°, as shown in **Figure 2**. In particular, the forearm was configured horizontally, while the upper arm was kept perpendicular to the forearm with the palm was facing down. To maintain this configuration, the antagonistic muscle groups placed on the upper arm were isometrically contracted not to change the palm configuration and to exert appropriate forces to keep the joint angle at the desired value.

Participants started by lifting their forearm when their hand was free, and then the load was gradually increased using dumbbells of 0.5 kg, 1 kg, 1.28 kg, 2.26 kg, 2.76 kg, and 3.76 kg, respectively. Each condition was tested for 20 trials, where each trial lasted 20 s, on average.

The net torque applied at the elbow joint is calculated using the weight of the load W_{load} and the weight of the forearm $W_{forearm}$ together with the moment arm corresponding to the load L_{ld} and the center of gravity of the forearm L_f with respect to the elbow joint.

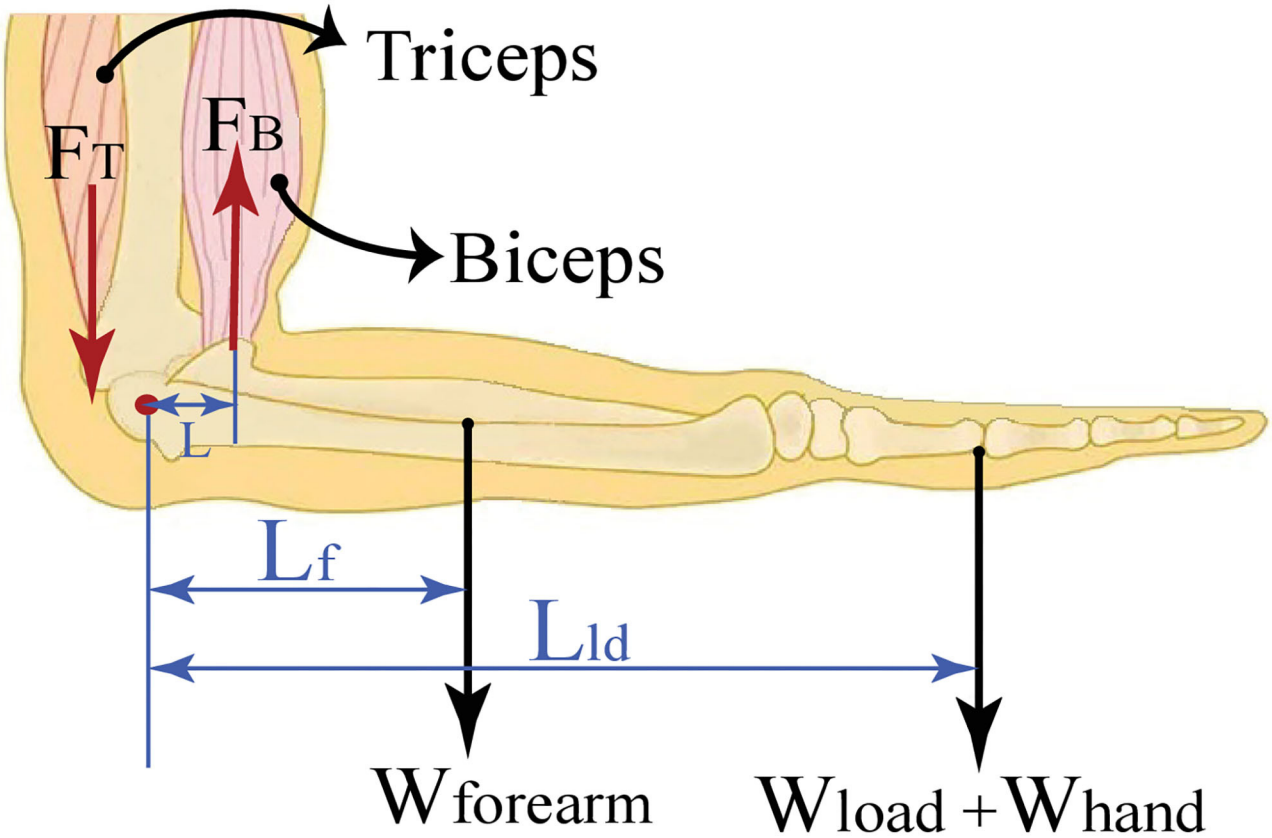

FIGURE 2 | The biomechanical model with the pivot at the elbow joint and the elbow positioned at 90°.

The antagonistic muscle pairs, biceps and triceps, responsible for generating the sEMG signals for the stiffness estimation are shown in **Figure 3a**. sEMG signals were measured by means of surface electrodes of an sEMG signal acquisition device with a sampling rate of 1 kHz. Raw sEMG signals were collected during the trials and conditioned by means of a full-wave rectifier, a 200 sample moving average filter, and an envelope detector. During the analysis, the first 500 samples of each trial were omitted from the experimental data to exclude signal outliers owing to initialization and motion artifacts.

The sequential processes of signal conditioning and reference estimation are illustrated in **Figure 3c**, while a sample signal extracted from a real-time experiment is presented in **Figure 3d**. After measuring the raw sEMG signals from two antagonistic muscle pairs responsible for stiffness and position controls of the hand prosthesis, they were filtered against inherent and environmental noises and motion artifacts utilizing a Butterworth band-pass filter with a frequency range of 20–500 Hz. After improving the signal-to-noise ratio of the sEMG signal, as illustrated in the purple dashed frame, the signal was full-wave rectified to correlate the behavior of muscles' contractions with physical variables, of position and stiffness references. As presented in **Figure 3d**, a moving window over a period of 0.5 s was employed to reveal the muscle's response against the task at hand. In addition, an envelope detector was utilized to filter out the ripples of the averaged signal. Such conditioning methods a play crucial role in revealing the relation between the joint torque and sEMG signals. Finally, the normalization of sEMG signals was carried out using the maximum voluntary contraction (MVC) of the participants, since these signals show different characteristics for each participant and vary their features at different time intervals. As depicted with the green dashed frame in **Figure 3c**, the signals were prepared for the estimation of the control parameters to correlate the finger and VSA kinematics with the normalized position and stiffness signals, respectively.

The parameters in Equation (1) were estimated using multiple linear regression by means of recorded data streams of $agon(sEMG)$, $anta(sEMG)$, and τ. For this linear model, the regression coefficients were obtained with 95% confidence bounds. The estimations for a subject are presented in **Table 1**. The quality of the estimation for all subjects was evaluated to be high, with $R^2 > 0.99$ and $RMSE < 0.03$. Please note that this estimation procedure is repeated for each subject, before each use of the prosthetic hand.

2.1.2. Position Estimation Through sEMG Signals

In order to achieve independent and simultaneous position and stiffness control, the overlap of sEMG signals corresponding to

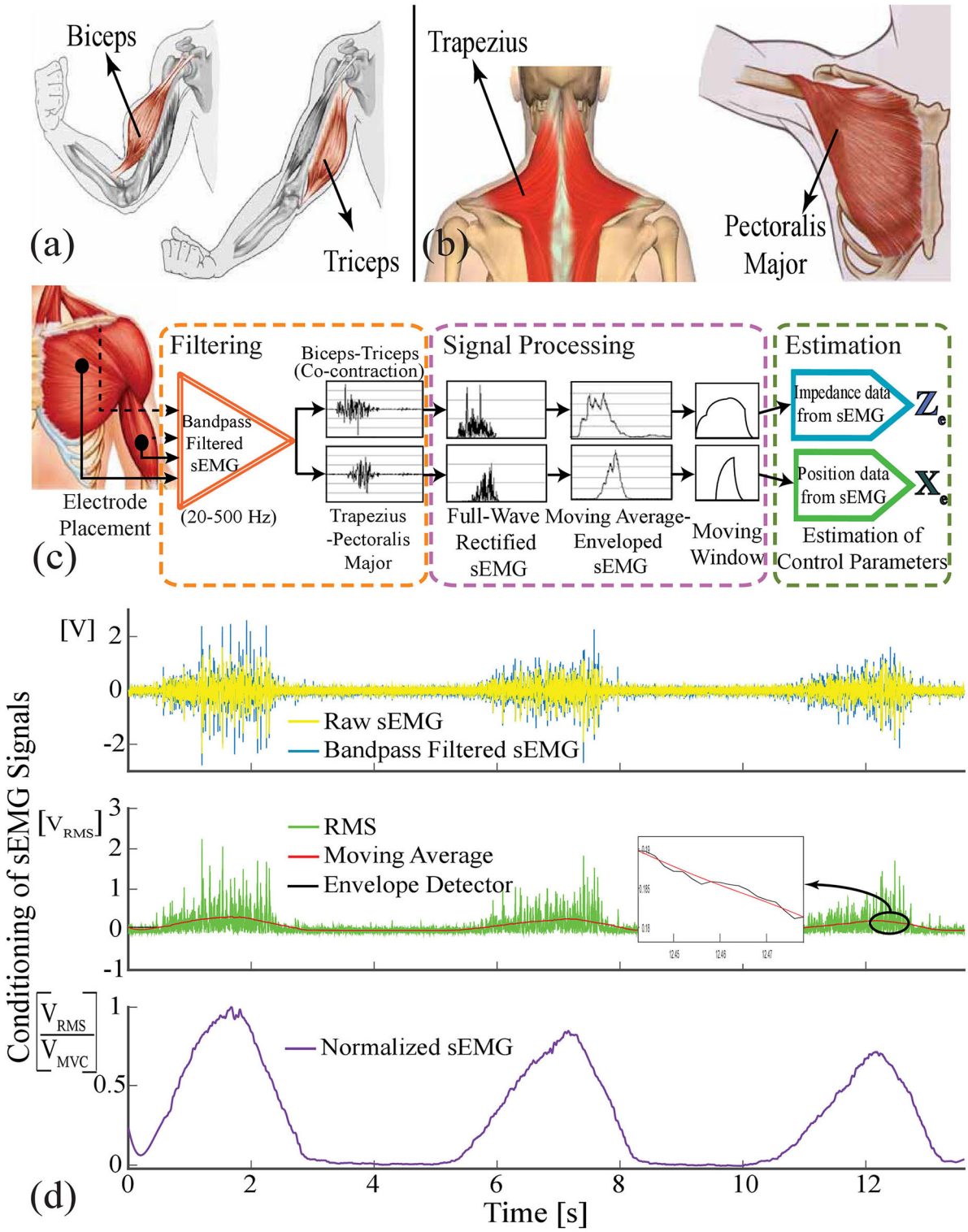

FIGURE 3 | (a) Biceps and triceps muscles are responsible for the stiffness modulation. **(b)** Trapezius and pectoralis major muscles are employed for position regulation. **(c)** sEMG signal flow: Raw sEMG signals (yellow) are bandpass filtered (blue) and full wave rectified. Then, these signals are averaged using 0.5 second moving window and undesired ripples are omitted by means of envelope detection. **(d)** On the top graph, the raw sEMG data filtered against the inherent and environmental noises, and artifacts are represented with the blue signal. The second graph depicts the rectified (green), moving averaged (red), enveloped (black) sEMG signal. The bottom figure shows the normalized sEMG signal.

TABLE 1 | Estimated parameters of the stiffness model.

κ	λ	R^2	RMSE
1.8612	1	0.9938	0.02941

the stiffness reference with sEMG signals corresponding to the position reference has to be avoided. All muscle groups on the arm take part in the isometric contraction. Since sEMG signals measured from the upper arm are used to estimate stiffness reference, to avoid any overlap, pectoralis major and trapezius muscles placed in the chest and shoulder, shown in **Figure 3b**, are preferred for the position control of hand prosthesis. This selection ensures the independent location of muscle pairs responsible for stiffness modulation and position control, such that their activities do not directly affect each other.

The position of the underactuated variable stiffness hand prosthesis is controlled intentionally under visual feedback. The hand prosthesis in this study is a highly underactuated mechanism, as all fingers are connected to two main joints responsible for flexion and extension. VSA mechanism is actuated by two DC motors and controls the position and stiffness of the fingers. For the position control of the fingers, the required position reference signal is provided by the sEMG signals of the amputee. The exact positions of the fingers depend on the interaction between the prosthesis and the environment, as well as the position controller tracking the reference signal generated by the amputee. In this application, the precise estimation of position reference is not of critical importance, since the amputee can adjust the position of the prosthetic hand based on visual feedback. The position of the transradial prosthetic hand is controlled through a direct proportional relation between the intensity of sEMG signals with the desired joint angle of the fingers. Along these lines, the normalized sEMG signal responsible for position reference is expressed as ten discrete values, and each value is matched between the angular positions of the fingers in the rest and the fist states. In other words, different contraction levels of the responsible muscle groups indicate different ranges of normalized sEMG signals, and these values are mapped to different closure states of the fingers. For example, while the volunteer's normalized sEMG signals increase from 0 to 1 by contracting his/her muscles intentionally, the fingers start to rotate from their rest positions to reach a fist state. Since the required angular positions of the fingers to grasp the different geometric shapes of objects are different, volunteers adjust the contraction level of their muscles responsible for position control to different ranges based on visual feedback.

Another design parameter while constructing the position control references is the MVC percentage that is used for normalization. Instead of mapping 100% MVC to fully close/open the hand, a lower MVC can be set to decrease muscle fatigue to a great extent. In our study, the MVC level is selected as 70%, such that the position reference for the actuation of VSAs is calculated using the following normalized sEMG signal

$$sEMG_{normpos} = \frac{sEMG_{position} - sEMG_{bias}}{sEMG_{\%70MVC}} \quad (3)$$

where $sEMG_{normpos}$ denotes the normalized sEMG signals corresponding to position reference, $sEMG_{position}$ represents the conditioned sEMG signals measured from pectoralis major and trapezius muscles, $sEMG_{\%70MVC}$ is 70% MVC of the responsible muscles, and $sEMG_{bias}$ is the bias on the signal.

Another undesirable condition is the contamination of sEMG signals generated by pectoralis major responsible for the opening of the hand by electrocardiography (ECG) signals. ECG crosstalk effect is prevented from sEMG signals by avoiding the electrode placement in the contamination zone and by adding extra bias term to the sEMG signals until the ECG signal effect is suppressed.

2.1.3. Compensation Against Muscle Fatigue

Muscle fatigue can be defined as a decline in the muscle strength to generate force, that is, a decrease in the sEMG amplitude as a result of the reduction in active muscle fibers during ceaseless muscle activity (Al-Mulla et al., 2011). The reason for muscle fatigue encompasses the metabolic, structural, and energetic alternations in muscles owing to insufficient oxygen level, inadequate blood circulation responsible for supplying nutritive substances, and also decrease in the efficiency of the nervous system (Merletti et al., 2005).

Myoelectric signals collected on the surface of the skin can be used for real-time monitoring of muscle fatigue (De Luca, 1984). This method is commonly preferred since it can provide uninterrupted data recordings related to muscle fatigue with a non-invasive technique, even though this method has certain disadvantages, such as the difficulties associated with exact positioning of surface electrodes on desired muscles and undesired cross-talk of the myoelectric signals with the neighboring muscles. A large number of studies have been performed to establish signal-based quantitative criteria to characterize muscle fatigue under static and dynamic tasks. Along these lines, numerous classical and modern signal processing methods have been established for sEMG-based muscle fatigue evaluation (Cifrek et al., 2009).

In this study, we rely on a time-domain root-mean-square (RMS) feature of sEMG signals to compensate for the fatigue effect (Bilodeau et al., 2003). In particular, during the use of the prosthetic device, the muscle performance decreases as a function of use time; as muscle fatigue increases, the sEMG-based stiffness reference estimates deteriorate. RMS feature based fatigue compensation estimates the decrease in sEMG signal power as a function of use time and introduces a compensation factor to counteract this fatigue.

Muscle fatigue compensation is activated in the control loop when a threshold is exceeded. A moving average window of 2,000 samples runs to check the presence of the consecutive contractions, by comparing the average level of enveloped sEMG signal under the moving window with the threshold. The threshold commissioned for activation of the fatigue compensation is empirically determined as about 20% MVC and varies slightly among volunteers. **Figure 4** illustrates muscle fatigue captured by sEMG signals when a volunteer repeatedly co-contracts her muscles within 5 s. In the figure, the green line

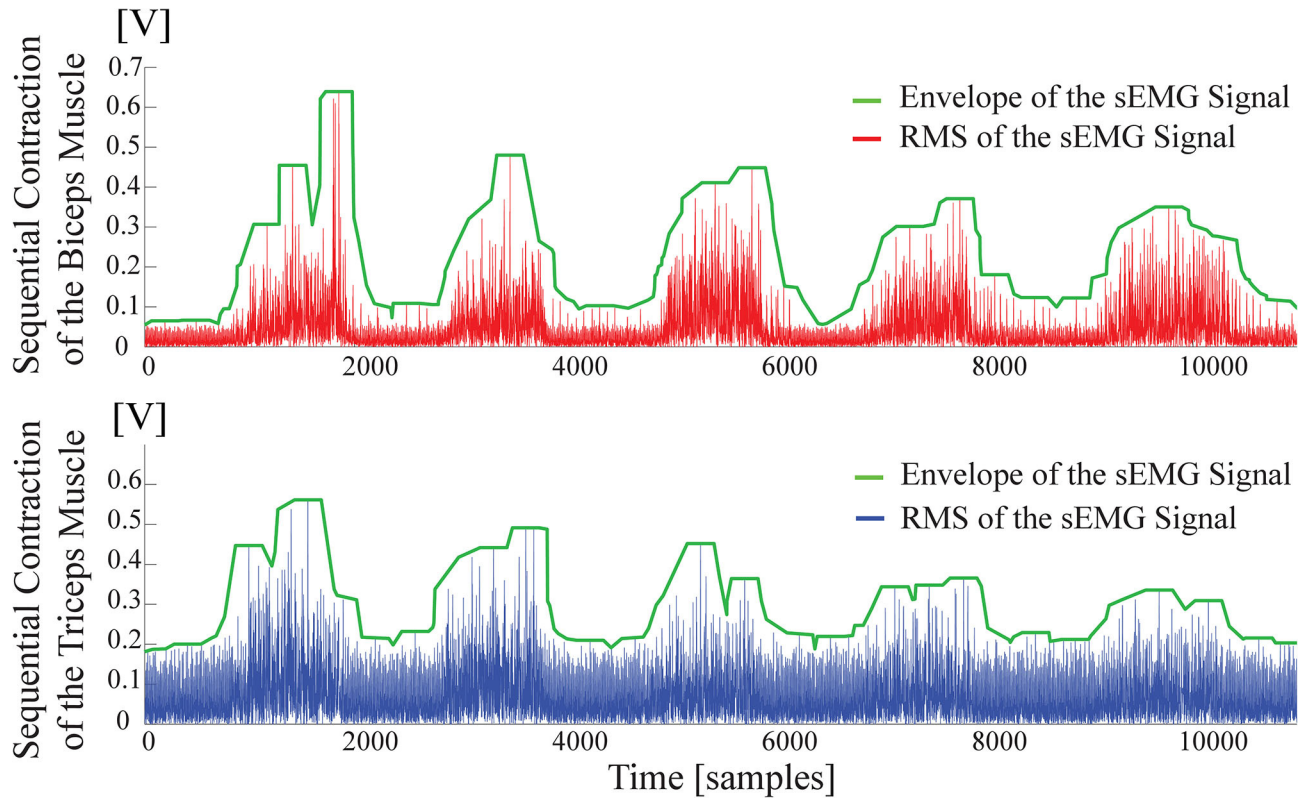

FIGURE 4 | Surface electromyography signal features capturing the average fatigue characteristics of biceps and triceps muscles.

presents the envelope of RMS of sEMG signals and the decrease of signal power can be observed.

To estimate the fatigue characteristics from sEMG signals, an experiment is conducted where a volunteer is requested to realize sustained isometric contractions periodically. In each session, the volunteers are instructed to perform isometric contractions five times. The experiment includes 10 sessions with each session including 5 trials lasting for 30 s.

The fatigue behavior of the individual is extracted from the sEMG data through three sequential signal conditioning stages. First, the raw sEMG signals are band-pass filtered with a frequency band between 20-500 Hz to remove undesired signals due to electronic noise, motion artifacts, ECG cross-talk, and power-line interference. Second, the filtered sEMG signal is normalized with the MVC of the volunteer. Finally, the RMS of the sEMG signal is calculated.

Figure 5 presents sample results characterizing the fatigue observed on the biceps and triceps muscles as a function of the time. The muscle fatigue behavior during a session, i.e., the RMS of each contraction (trial) in a session is represented by the same geometric symbol in **Figure 5**. Each session has its own respective symbols to help with the identification of muscle fatigue. In particular, the star symbol represents a consecutive contraction, namely the trial, of the subject in a session. The average of 10 sessions is represented by a dark blue star icon in the graph. Linear fits, as presented in **Figure 5**, are sufficient to capture the time dependent fatigue characteristics embedded in this data set, as evidenced by the good quality of curve fits ($R^2 > 0.8$). Once these linear estimates are at hand, they can be incorporated in the stiffness reference estimation as a feed-forward compensation term denoted by C_{fi} in **Figure 1**. Unlike the impedance modulation, position control typically does not require sequential contractions; hence, the muscle fatigue is neglected during position regulation, that is, no feed-forward compensation is performed for the position control by setting C_{fp}=0 in **Figure 1**.

2.1.4. Position and Stiffness Regulation With Antagonist VSA

Given the sEMG based position and stiffness reference estimation and fatigue compensation processes, the second module of the interface is a controller that ensures tracking of these references by the VSA prosthetic hand. In particular, the position and stiffness of the VSA are controlled through position control of Bowden cables driven by two geared DC motors. **Figure 6** presents a schematic representation of the VSA, where α and β denote the angular position of DC motors, while S and θ represent the joint stiffness and angle, respectively.

Under quasi-static conditions (English and Russell, 1999; Migliore et al., 2007), the angular position of DC motors α and β for a given reference position θ_r and stiffness S_r can be calculated

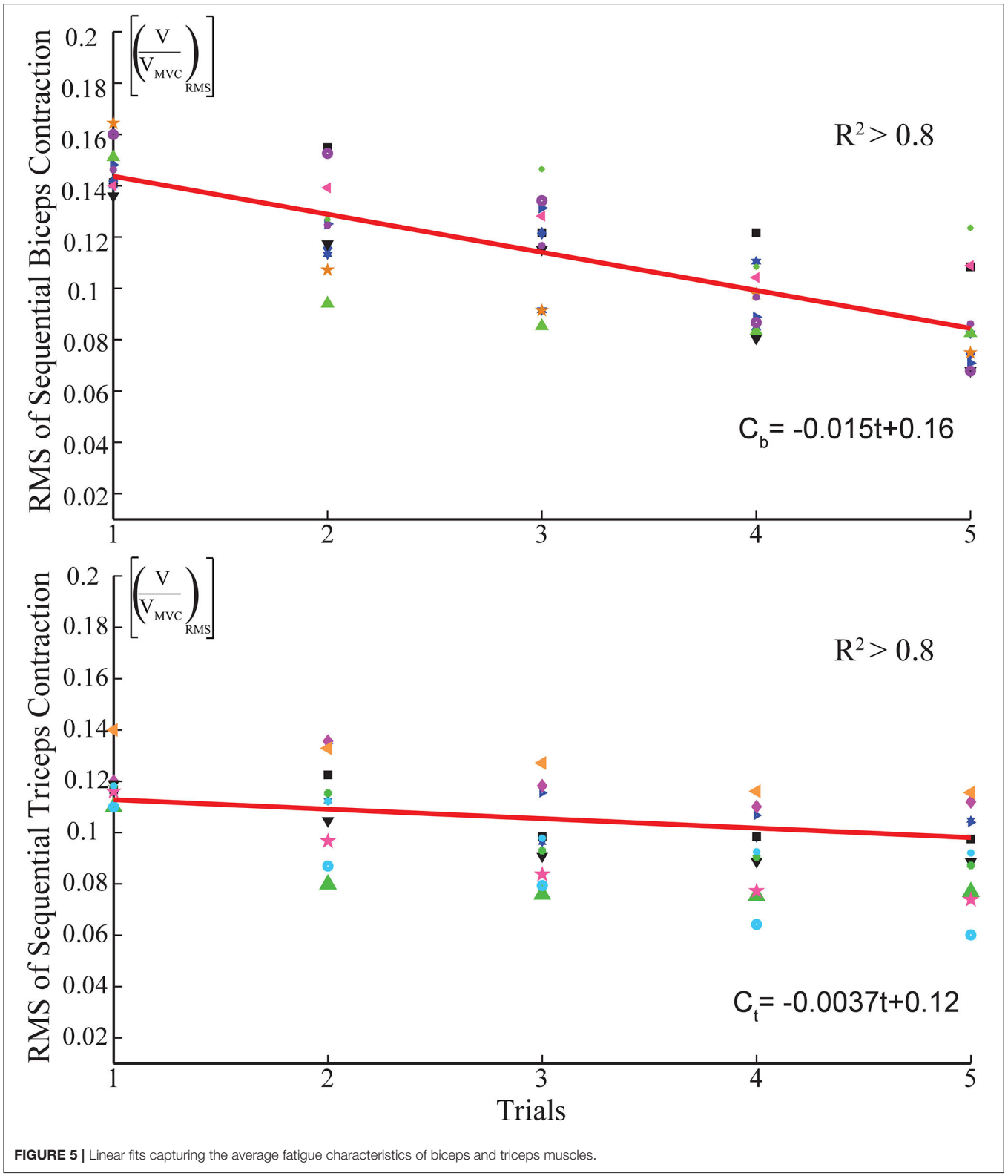

FIGURE 5 | Linear fits capturing the average fatigue characteristics of biceps and triceps muscles.

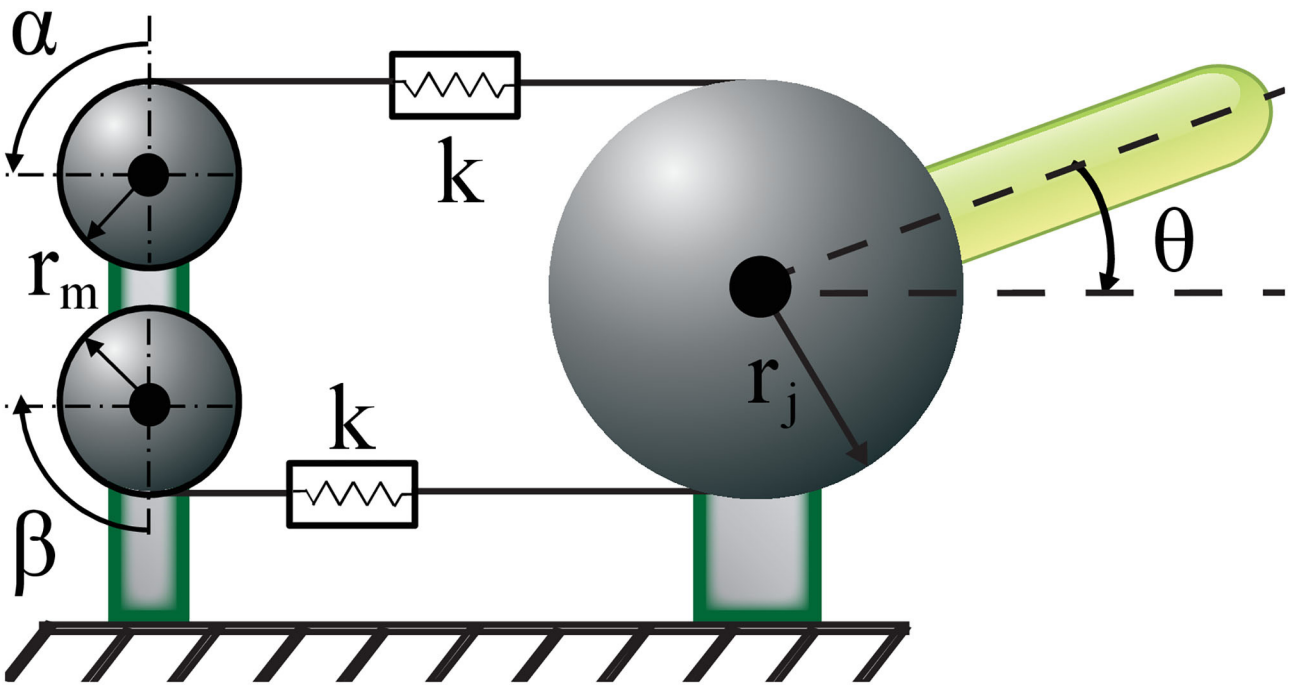

FIGURE 6 | Schematic model of an antagonistically driven VSA, where *k* represents the nonlinear springs.

as

$$\alpha = (S_r - 2br_j^2)/4ar_m r_j^2 + (r_j/r_m)((\tau_{load}/S_r) - \theta_r) \quad (4)$$

$$\beta = (S_r - 2br_j^2)/4ar_m r_j^2 - (r_j/r_m)((\tau_{load}/S_r) - \theta_r) \quad (5)$$

where r_m represents the radius of the pulleys attached to the geared DC motors, r_j is the radius of the drive pulley, a and b are the parameters that characterize the expanding contour cam as detailed in Hocaoglu and Patoglu (2019a), while the external torque applied to VSA is denoted by τ_{load}. When control references belonging to joint position and stiffness are estimated through sEMG signals, desired motor positions are computed according to Equations (4)–(5) with $\tau_{load} = 0$ and motors are motion controlled to these values under real-time control.

2.2. Verification of Correlated Stiffness Adaptation of Antagonistic Muscle Pairs

The stiffness of the prosthesis is regulated automatically based on the estimated stiffness of the *intact* muscle groups of the upper arm. This control strategy, in which the prosthesis mimics the impedance of an intact portion of the limb, relies on the assumption that the impedance of the upper and lower arm change similarly, during energetic interactions with the environment.

We have conducted a series of experiments to test the validity of this assumption. During these experiments, the stiffness of both the forearm and upper arm of participants is estimated through the sEMG signals collected from the relevant antagonistic muscle pairs, using the technique detailed in section 2.1.1. Hence, during these experiments, the stiffness estimations of the upper and lower arm are performed based on sEMG signals and the load applied. Eight healthy volunteers took place in the experiments. The experiments were conducted for two tasks: i) a load bearing task and ii) interaction with the various objects with different impedance characteristics.

The first task aims to observe resistance of the hand, forearm, and upper arm against displacement stemmed from the weight of an object with respect to the arm's normal posture. During the first task, participants were asked to keep their arms straight and forward as depicted in **Figure 7**. The stiffness of the upper arm and forearm were estimated as the load at the hand was increased incrementally. In particular, the load was gradually increased from no load to 0.5, 1, 1.5, 2, and 3 kg. Each task was repeated 5 times and each trial lasted about 8 s. Sufficient rest time was provided between consecutive trials to prevent muscle fatigue.

Stiffness estimation was performed as detailed in section 2.1.1. sEMG signals were collected from the antagonistic muscle groups of flexor digitorum profundis and extensor digitorum at the forearm, and biceps and triceps at the upper arm. Since the stiffness of both the upper arm and forearm was estimated, two separate biomechanical models were derived around the elbow and wrist joints, respectively. The net torque applied on the joints was calculated considering the weight of the grasped load W_{load}, the hand W_{hand}, the forearm $W_{forearm}$, and the upper arm $W_{upperarm}$ together with their respective moment arms.

Figure 8 depicts the estimated stiffness levels at the forearm and the upper arm, under various loading conditions. As expected, as the load is increased, the stiffness of both the upper arm and the forearm increases. As presented in **Figure 8**, the change in stiffness levels is statistically significant between almost

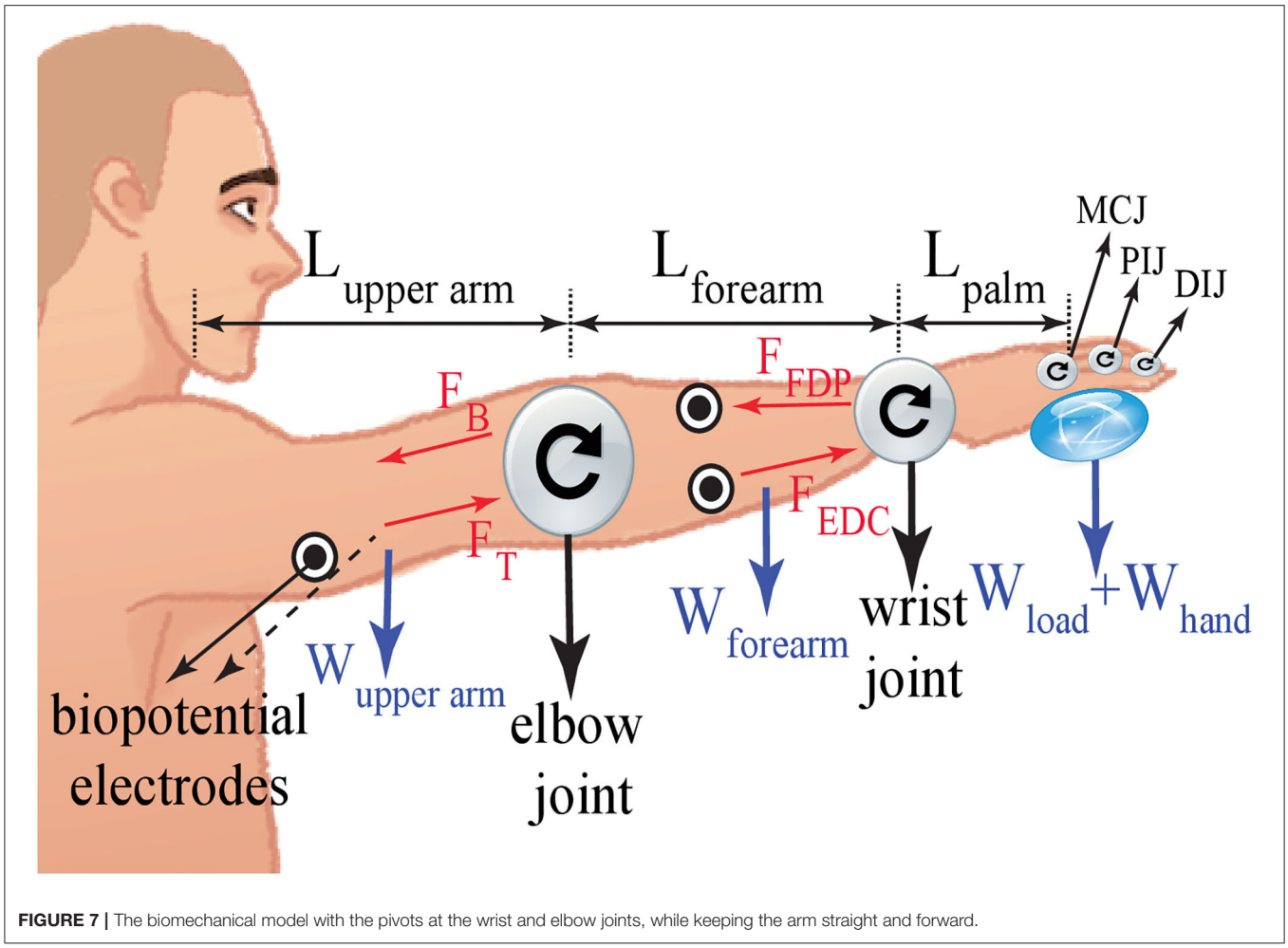

FIGURE 7 | The biomechanical model with the pivots at the wrist and elbow joints, while keeping the arm straight and forward.

all pairs of loading conditions (with $p < 0.05$). More importantly, one can observe from these plots that the stiffness increase in the forearm and the upper arm are strongly correlated, and there exists no statistically significant difference between the forearm and the upper arm stiffness levels for each loading condition, for the load bearing task.

The second task tested the adaptation of the upper arm and the forearm impedance levels while interacting with several objects, to mimic common interactions taking place during ADL. In particular, participants started at a rest position, lifted their arm, reached toward the object, grasped it, held it for a while, released it on the table, and returned to their initial configuration. Three different object types were included in the experiment: A sponge, an empty glass, and a water-filled glass were employed for different impedance requirements. Each object was grasped five times and each trial took about 7 s. Sufficient rest time was provided to volunteers between sequential trials to prevent muscle fatigue.

The objects were selected such that their manipulation emphasized different control strategies, ranging from precise motion control to robust force control. Due to the complexity of the task that involved multiple sub-movements, participants' stiffness levels went over continual changes throughout the trials. To quantitatively characterize the correlation between the stiffness of the upper arm and the forearm for each subject, a moving average filter is used to extract average stiffness variations from the instantaneous estimates. **Table 2** presents the Pearson's correlation coefficient for these time series comparisons for each subject. In this table, the concordance correlation coefficients have large values of about 0.8, providing strong evidence that the impedance adaptation behavior of the upper arm and the forearm were in good agreement with each other throughout the complex manipulation task.

3. EXPERIMENTAL EVALUATION OF THE NATURAL CONTROL INTERFACE

In this section, we present the evaluation of the integrated system, where stiffness and position estimation modules and sEMG based control are utilized simultaneously. We verify the feasibility and effectiveness of the proposed sEMG based human-machine interface that automatically modulates the impedance of VSA prosthetic hand while users intentionally control the

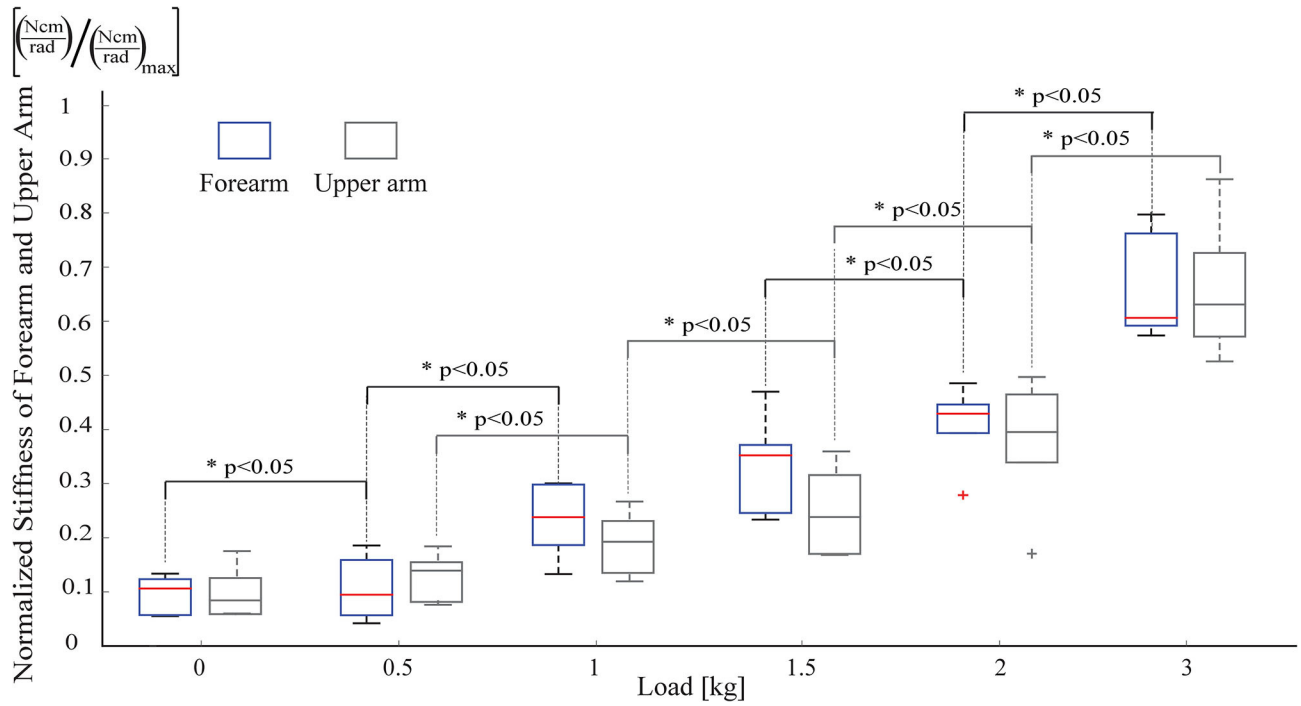

FIGURE 8 | Stiffness estimates from the forearm and the upper arm of participants, while resisting against increasing loads.

TABLE 2 | Pearson's correlation coefficient between the stiffness modulation of the upper arm and the forearm muscles.

Subject	Sponge	Glass	Water filled glass
Subject 1	0.9246	0.9914	0.9447
Subject 2	0.9771	0.9180	0.9000
Subject 3	0.9863	0.9134	0.9222
Subject 4	0.9000	0.9234	0.9216
Subject 5	0.9000	0.9260	0.9715
Subject 6	0.9685	0.9158	0.9363
Subject 7	0.9062	0.9892	0.9148
Subject 8	0.9611	0.9425	0.9775

hand position. For this purpose, we present two experiments where the independent control of hand position and stiffness were demonstrated. Section 3.1 details the experimental set-up and procedure used to verify the effectiveness and utility of the proposed sEMG-based control architecture to control VSA prosthesis. Section 3.2 presents the position and stiffness control tasks and experimental procedures used in the experiments. Section 3.3 details the results of the experiment, while Section 3.4 provides illustrative experiments where volunteers perform various grasps for different stiffness and geometric shape of objects.

3.1. Experimental Setup

Human-subject experiments on able volunteers were conducted using the VSA transradial hand prosthesis detailed in Hocaoglu and Patoglu (2019a). In the current design, the prosthesis does not feature a thumb but relies on passive elastic support that can counteract finger forces. This decision is intentional and helps to keep the system and the controller simple. Our experiences with the volunteers indicate that the passive support is adequate for implementing a wide variety of functional grasps.

Throughout the experiments, sEMG signals were collected from biceps and triceps muscles for stiffness modulation and from trapezius and pectoralis major muscles for position control using a data acquisition system with active electrodes. Stiffness and position references were estimated as discussed in section 2.1 and fed to the tracking controller that controlled two geared Direct Current (DC) motors under Proportional Derivative (PD) control in real-time at 500 Hz through a PC based Data Acquisition (DAQ) card. The robust position controller of each DC motor enables the system to achieve the desired joint position and joint stiffness settings as computed according to Equations (4)–(5) by properly actuating the angular positions (α and β) of the motors. A direct drive linear actuator combined with a precision position encoder was placed under the fingers of the hand prosthesis, as shown in **Figure 9** to render forces and measure finger deflections. During the experiments, the gravitational force acting on the linear actuator was compensated with a counter mass, while the linear actuator was force controlled.

3.2. Experimental Procedure

Experiments were conducted to test the independent control of the position and the stiffness of the prosthetic hand under sEMG based tele-impedance control interface.

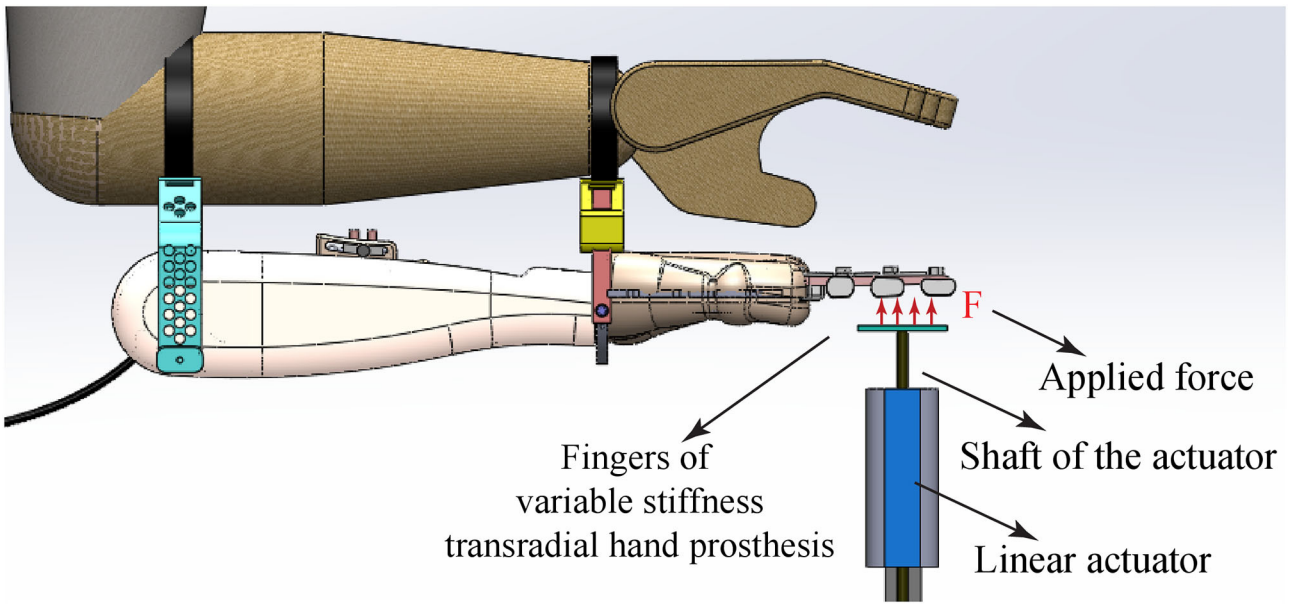

FIGURE 9 | Schematic representation of the experimental setup: The linear actuator is used to apply controlled forces to the fingers and to measure their deflection under position and stiffness modulation tasks. Figure reproduced from Hocaoglu and Patoglu (2022).

Throughout the experiments, the transradial hand prosthesis was worn by the volunteers, such that interaction forces with the environment provided direct power coupling with the volunteer. Note that such feedback is a crucial part of any prosthesis; however, has been neglected in Virtual Reality (VR) based studies (Blank et al., 2011, 2012, 2013).

Five healthy volunteers took place in the experiments. The prosthesis was worn parallel to the volunteers' lower arm, such that consistent placement of the prosthesis was ensured for proper hand-eye coordination.

The experiments were composed of two tasks with 10 repetitions for each condition of each task. During the first task, the position of the VSA hand prosthesis was kept constant at 0° while the stiffness of VSA was adjusted by the volunteers to five distinct stiffness values that correspond to a low, three intermediate, and a high stiffness level for the fingers. The stiffness of the fingers was experimentally determined by applying a linearly increasing force to flex the fingers and recording their deflection.

During the second task, the stiffness of the VSA hand prosthesis was kept constant at its intermediate level by the volunteers, while the position of the VSA was adjusted by the volunteers to three distinct position values that correspond to low, intermediate, and high flexion of the fingers. The position of the fingers was determined by recording the position of the linear actuator under zero force control, while the stiffness of the fingers was determined by applying a constant force to resist the flexion of the fingers at their equilibrium position and recording the resulting deflection.

3.3. Experimental Results

Figure 10a presents the experimental results for the case when the volunteers adjusted the VSA stiffness to five distinct values that correspond to a low, three intermediate, and a high stiffness level for the fingers, while the finger positions were kept constant. In particular, shaded regions represent all the linear fits recorded for 10 trials, while the dark line represents their mean. The slopes of these lines indicate that the high, three intermediate, and the low stiffness for the fingers were $k_h = 1.7$ N/mm, $k_i^1 = 0.3$ N/mm, $k_i^2 = 0.16$ N/mm, $k_i^3 = 0.12$ N/mm, and $k_l = 0.091$ N/mm, respectively. The R^2 values for these linear fits are higher than 0.97.

Figure 10b presents the experimental results for the case when the volunteers kept the VSA stiffness at an intermediate level, while the finger positions of the fingers were regulated by the volunteers to 0°, 30°, and 60°, respectively. Once again, the shaded regions represent all the linear fits recorded for 10 trials, while the dark line represents their mean. The slopes of these lines indicate that the stiffness levels of the fingers were $k_{0^\circ} = 0.16$ N/mm, $k_{30^\circ} = 0.17$ N/mm, and $k_{60^\circ} = 0.17$ N/mm, respectively. The R^2 values for these linear fits are higher than 0.98.

The fingers' response shown in **Figure 10** closely matches the characteristics of human fingers, as presented in Howe et al. (1985). The characterization results are also compatible with the results presented in Matsuoka and Afshar (2004), as flexion/extension movements performed by an anatomically human-like robotic index finger necessitate a similar amount of muscle forces.

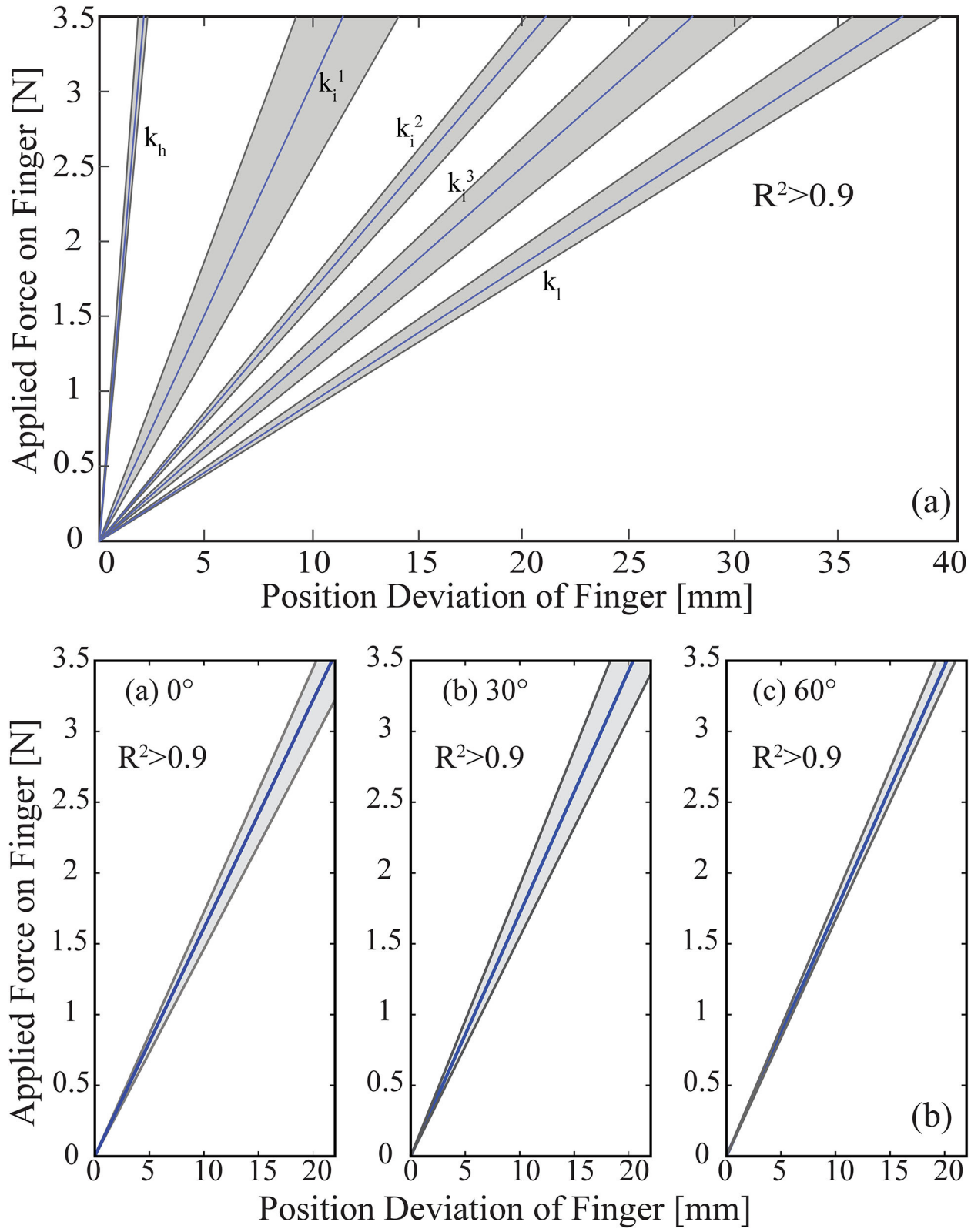

FIGURE 10 | (a) Stiffness modulation of hand prosthesis through sEMG based tele-impedance control. **(b)** Position control of hand prosthesis through sEMG based tele-impedance control. In the figures, gray zones present the results of each trial, and the blue lines represent the average value of ten trials. Figure reproduced from Hocaoglu and Patoglu (2022).

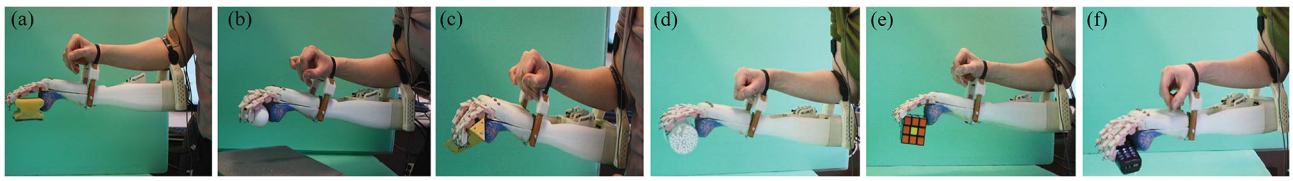

FIGURE 11 | Demonstration of variable stiffness transradial hand prosthesis performing various grasps with the sEMG based tele-impedance control interface, while interacting with **(a)** a deformable object, **(b)** a fragile object, **(c)** a triangular rigid object, **(d)** a cylindrical rigid object, **(e)** a square rigid object, and **(f)** a rectangular rigid object.

Experimental results indicate that the sEMG based impedance controlled VSA hand prosthesis possesses very similar performance to the case with an external reference generator, as presented in Hocaoglu and Patoglu (2019a). In particular, volunteers were able to modulate their stiffness levels to the minimum and maximum stiffness limits of the prosthetic hand, as well as to various intermediate ranges, by means of the sEMG based tele-impedance control. These results provide evidence that the stiffness and position of the transradial hand prosthesis can be controlled independently by users, with high repeatability.

3.4. Illustrative Experiments and Evaluations

Given that only the position and the stiffness of the drive tendon can be directly regulated by the volunteers, in general, the resulting position and the stiffness of the fingers depending on the interaction. To test the usefulness of the sEMG based tele-impedance control interface of the variable stiffness transradial hand prosthesis, the device was attached to six volunteers, as shown in **Figure 9**, and the volunteers were given control of the position and stiffness of the prosthesis through the sEMG based tele-impedance controller. In particular, sEMG signals measured from the surface of the upper arm were used to automatically adjust the stiffness level of the prosthesis to that of the upper arm, while the position regulation was intentionally controlled by the volunteers by moving their shoulder muscles.

The volunteers were instructed to grasp 16 objects with a broad array of geometries (e.g., cylindrical, square, oval, or unstructured) and elasticities (e.g., stiff, soft), as shown in **Figure 11**. In **Figure 11a**, a deformable sponge, in **Figure 11b**, a fragile raw egg were grasped by the volunteers with this natural control interface, without damaging the objects. In **Figures 11c–f**, rigid objects with various shapes were grasped by the volunteers using different stiffness levels. Videos demonstrating several illustrative grasps by a volunteer are available at https://youtu.be/fGFIKSSmtDg. The average time required to grasp and release the objects in the video is calculated as 1.218 ± 0.564 s and 0.819 ± 0.48 s, respectively. The time elapsed to make a fist is about 2 s. The commercial prosthetic hand devices (Ossur Inc., 2022) present quite the same grasping performance as the proposed variable stiffness hand prosthesis.

The proposed tele-impedance controller interface emphasizes simplicity, ease of use, and adaptability; hence, implements automatic modulation of prosthetic hand stiffness to match that of the upper arm, while intentional control of the position of the underactuated prosthetic hand is left to the user. Under the observation that humans tend to modulate the impedance of their limb as a whole while executing different tasks (as shown in section 3), the tele-impedance controller implemented for the prosthesis automatically modulates the stiffness of the hand to match that of the intact part of the arm. Automatic stiffness modulation increases the dexterity of the prosthetic hand, without introducing complexity to the human control interface.

Successful interactions with the prosthesis depend on the amputee making proper decisions on how to interact with the object under visual feedback and physical coupling. Our extensive experiments with six healthy volunteers indicate that humans are very skillful at learning how to interact with the environment with such a device under the proposed sEMG based natural control interface. All volunteers were able to adapt to the device on average in 3.2 ± 1.3 min and successfully complete the required manipulation tasks without any prior training. Furthermore, it has been observed that the stiffness modulation property is effective in increasing the performance of the transradial prosthesis.

Volunteers suffer from the high complexity of the controller when intentional control of both the stiffness and the position of the device is left to the user. During our tests, volunteers indicated a strong preference for the automatic impedance adjustment property. Furthermore, it has been observed that volunteers are more successful at interactions when the impedance of the prosthesis is automatically adjusted.

4. DISCUSSION

Tele-impedance control of a VSA prosthetic hand is implemented through stiffness and position estimates decoded from sEMG signals of muscle groups embedded in the upper arm, chest, and shoulder. In particular, the IMCJ method is used to estimate the stiffness of the intact upper arm through agonist/antagonist muscle pairs, while shoulder/chest muscles are employed to estimate position references. Then, these stiffness and position estimates are used to control a VSA prosthetic hand.

The feasibility of tele-impedance control through the proposed human machine interface is demonstrated with two human subject experiments, where the position and the stiffness of the VSA prosthetic hand were successfully modulated. The

results demonstrate that both position and stiffness estimations from sEMG signals are adequate for the control of a VSA transradial hand prosthesis.

Variable stiffness actuation hand prosthesis together with the proposed control interface necessitates less effort and concentration to control and is easier for the amputee to learn to use. Impedance modulation takes place naturally from task to task or while performing a task, i.e., ADL, without requiring amputees' attention, and this feature improves the performance of the prosthesis while interacting with unstructured environments.

The human subject experiments presented in this study have been performed on able volunteers. Our future studies include validation of the results on amputees. While special attention has been given to the selection of muscle groups used for sEMG based control, such that the same muscle groups can be recruited for transradial amputees, possible complications may arise in amputees due to muscle weakness stemming from infrequent use of the remnant limbs in ADL. Along these lines, the lack of verifications with amputees is a limitation of this study.

Second, the position and impedance regulation experiments have been performed on carefully controlled environments, as tight control of the experimental conditions was necessary to ensure that the results are statistically reliable with no confounding factors. Furthermore, sEMG based position and stiffness models can only provide rough estimations of human behavior. This study aims to provide easy control of a variable stiffness prosthetic hand instead of actually copying human behavior. While the same level of accuracy with the human arm may not be achieved in real-life use, our experiments with healthy volunteers presented in section 3.4 provide evidence that the level of control that can be achieved during grasping different objects is adequate to provide the required level of performance.

As part of future study, different control modes may be introduced to the system, for instance, to avoid the need for voluntary contraction once an object is successfully grasped. Additional feedback pathways, such as vibrotactile feedback, may be added to the system to decrease the need for visual feedback during grasping. Furthermore, sEMG related coefficients can be identified online to avoid the need for calibration of device.

DATA AVAILABILITY STATEMENT

The raw data supporting the conclusions of this article will be made available by the authors, without undue reservation.

ETHICS STATEMENT

The studies involving human participants were reviewed and approved by the University Research Ethics Council of Sabancı University. The patients/participants provided their written informed consent to participate in this study.

AUTHOR CONTRIBUTIONS

EH was responsible for the design and experimental evaluation of the natural control interface of the variable stiffness hand prosthesis. VP conceived and supervised the study. Both authors contributed to the editing and scientific presentation of the article.

FUNDING

This work has been partially supported by Tubitak Grants 219M586, 111M186, 115M698 and Marie Curie IRG Rehab-DUET.

REFERENCES

Abul-Haj, C., and Hogan, N. (1990a). Functional assessment of control systems for cybernetic elbow prostheses. i. description of the technique. *IEEE Trans. Biomed. Eng.* 37, 1025–1036. doi: 10.1109/TBME.1990.1438510

Abul-Haj, C., and Hogan, N. (1990b). Functional assessment of control systems for cybernetic elbow prostheses. ii. application of the technique. *IEEE Trans. Biomed. Eng.* 37, 1037–1047. doi: 10.1109/10.61028

Al-Mulla, M., Sepulveda, F., and Colley, M. (2011). A review of non-invasive techniques to detect and predict localised muscle fatigue. *Sensors* 11, 3545–3594. doi: 10.3390/s110403545

Atkins, D., Heard, D., and Donovan, W. (1996). Epidemiologic overview of individuals with upper limb loss and their reported research priorities. *J. Prosthet. Orthot.* 8, 2–11. doi: 10.1097/00008526-199600810-00003

Basmajian, J. V., and De Luca, C. J. (1985). *Muscles Alive*. Baltimore, MD: Williams and Wilkins.

Bebionic (2022). Available online at: https://www.ottobockus.com/prosthetics/upper-limb-prosthetics/solution-overview/bebionic-hand/

Bennett, D. A., Mitchell, J. E., Truex, D., and Goldfarb, M. (2016). Design of a myoelectric transhumeral prosthesis. *IEEE/ASME Trans. Mech.* 21, 1868–1879. doi: 10.1109/TMECH.2016.2552999

Biddiss, E., and Chau, T. (2007). Upper limb prosthesis use and abandonment: a survey of the last 25 years. *Prosthet. Orthot. Int.* 31, 236–257. doi: 10.1080/03093640600994581

Bilodeau, M., Schindler-Ivens, S., Williams, D., Chandran, R., and Sharma, S. (2003). EMG frequency content changes with increasing force and during fatigue in the quadriceps femoris muscle of men and women. *J. Electromyogr. Kinesiol.* 13, 83–92. doi: 10.1016/S1050-6411(02)00050-0

Blank, A., Okamura, A., and Whitcomb, L. (2011). "Task-dependent impedance improves user performance with a virtual prosthetic arm," in *IEEE International Conference on Robotics and Automation (ICRA)* (Shanghai: IEEE), 2235–2242.

Blank, A., Okamura, A., and Whitcomb, L. (2012). "User comprehension of task performance with varying impedance in a virtual prosthetic arm: a pilot study," in *4th IEEE RAS EMBS International Conference on Biomedical Robotics and Biomechatronics* (Rome: IEEE), 500–507.

Blank, A., Okamura, A., and Whitcomb, L. (2013). Task-dependent impedance and implications for upper-limb prosthesis control. *Int. J. Rob. Res.* 3, 827–846. doi: 10.1177/0278364913517728

Burdet, E., Osu, R., Franklin, D. W., Milner, T. E., and Kawato, M. (2001). The central nervous system stabilizes unstable dynamics by learning optimal impedance. *Nature* 414, 446–449. doi: 10.1038/35106566

Burdet, E., Osu, R., Franklin, D. W., Yoshioka, T., Milner, T. E., and Kawato, M. (2000). A method for measuring endpoint stiffness during multi-joint arm movements. *J. Biomech.* 33, 1705–1709. doi: 10.1016/S0021-9290(00)00142-1

Cifrek, M., Medved, V., Tonkovic, S., and Ostojic, S. (2009). Surface EMG based muscle fatigue evaluation in biomechanics. *Clin. Biomech.* 24, 327–340. doi: 10.1016/j.clinbiomech.2009.01.010

Dalley, S. A., Wiste, T. E., Withrow, T. J., and Goldfarb, M. (2009). Design of a multifunctional anthropomorphic prosthetic hand with extrinsic actuation. *IEEE/ASME Trans. Mech.* 14, 699–706. doi: 10.1109/TMECH.2009.2033113

De Luca, C. (1984). Myoelectrical manifestations of localized muscular fatigue in humans. *Crit Rev. Biomed. Eng.* 11, 251–279.

English, C., and Russell, D. (1999). Mechanics and stiffness limitations of a variable stiffness actuator for use in prosthetic limbs. *Mech. Mach. Theory* 34, 7–25. doi: 10.1016/S0094-114X(98)00026-3

Franklin, D., Burdet, E., Osu, R., Kawato, M., and Milner, T. (2003a). Functional significance of stiffness in adaptation of multijoint arm movements to stable and unstable dynamics. *Exp. Brain Res*. 151, 145–157. doi: 10.1007/s00221-003-1443-3

Franklin, D., Kawato, M., So, U., and Milner, T. (2003b). "Interacting with our environment: Impedance control balances stability and metabolic cost," in *IEEE Engineering in Medicine and Biology Society, Vol. 2* (Cancun: IEEE), 1440–1443.

Franklin, D., and Milner, T. (2003). Adaptive control of stiffness to stabilize hand position with large loads. *Exp. Brain Res*. 152, 211–220. doi: 10.1007/s00221-003-1540-3

Franklin, D., So, U., Kawato, M., and Milner, T. (2004). Impedance control balances stability with metabolically costly muscle activation. *J. Neurophysiol*. 92, 3097–3105. doi: 10.1152/jn.00364.2004

Gomi, H., and Kawato, M. (1996). Equilibrium-point control hypothesis examined by measured arm stiffness during multijoint movement. *Science* 272, 117–120. doi: 10.1126/science.272.5258.117

Gomi, H., and Osu, R. (1998). Task-dependent viscoelasticity of human multijoint arm and its spatial characteristics for interaction with environments. *J. Neurosci*. 18, 8965–8978. doi: 10.1523/JNEUROSCI.18-21-08965.1998

Guo, W., Sheng, X., Liu, H., and Zhu, X. (2017). Toward an enhanced human-machine interface for upper limb prosthesis control with combined EMG and NIRS signals. *IEEE Trans. Hum. Mach. Syst*. 47, 564–575. doi: 10.1109/THMS.2016.2641389

Herle, S. (2016). "Design of a reference signal generator for an upper limb prosthesis myoelectric controller," in *IEEE International Conference on Automation, Quality and Testing, Robotics (AQTR)* (Cluj-Napoca: IEEE), 1–6.

Hocaoglu, E., and Patoglu, V. (2012). "Tele-impedance control of a variable stiffness prosthetic hand," in *IEEE International Conference on Robotics and Biomimetics (ROBIO)* (Guangzhou: IEEE), 1576–1582.

Hocaoglu, E., and Patoglu, V. (2019a). Design, implementation and evaluation of a variable stiffness transradial hand prosthesis. *arXiv [Preprint]*. arXiv: 1910.12569. Available online at: https://arxiv.org/pdf/1910.12569.pdf (accessed October 29, 2019).

Hocaoglu, E. and Patoglu, V. (2019b). sEMG-based natural control interface for a variable stiffness transradial hand prosthesis. *arXiv [Preprint]*. arXiv: 1910.11946. Available online at: https://arxiv.org/pdf/1910.11946.pdf (accessed October 25, 2019).

Hocaoglu, E., and Patoglu, V. (2022). Design, implementation, and evaluation of a variable stiffness transradial hand prosthesis. *Front. Neurorobot*. 16:789210. doi: 10.3389/fnbot.2022.789210

Hogan, N. (2002). Skeletal muscle impedance in the control of motor actions. *J. Mech. Med. Biol*. 02, 359–373. doi: 10.1142/S0219519402000460

Howe, A., Thompson, D., and Wright, V. (1985). Reference values for metacarpophalangeal joint stiffness in normals. *Ann. Rheum. Dis*. 44, 469–476. doi: 10.1136/ard.44.7.469

Hunter, I. W., and Kearney, R. E. (1982). Dynamics of human ankle stiffness: variation with mean ankle torque. *J. Biomech*. 15, 747–752. doi: 10.1016/0021-9290(82)90089-6

Kim, N., Yun, S., and Shin, D. (2019). A bio-inspired lightweight wrist for high-dof robotic prosthetic arms. *IEEE/ASME Trans. Mech*. 24, 2674–2683. doi: 10.1109/TMECH.2019.2941279

Kuechle, D., Newman, S. R., Itoi, E., Morrey, B., and An, K. N. (1997). Shoulder muscle moment arms during horizontal flexion and elevation. *J. Shoulder Elbow Surg*. 6, 429–439. doi: 10.1016/S1058-2746(97)70049-1

Kurzynski, M., Krysmann, M., Trajdos, P., and Wolczowski, A. (2016). Multiclassifier system with hybrid learning applied to the control of bioprosthetic hand. *Comput. Biol. Med*. 69, 286–297. doi: 10.1016/j.compbiomed.2015.04.023

Kyranou, I., Krasoulis, A., Erden, M. S., Nazarpour, K., and Vijayakumar, S. (2016). "Real-time classification of multi-modal sensory data for prosthetic hand control," in *IEEE International Conference on Biomedical Robotics and Biomechatronics* (Singapore: IEEE), 536–541.

Lenzi, T., Lipsey, J., and Sensinger, J. W. (2016). The RIC arm-a small anthropomorphic transhumeral prosthesis. *IEEE/ASME Trans. Mech*. 21, 2660–2671. doi: 10.1109/TMECH.2016.2596104

Marino, M., Pattni, S., Greenberg, M., Miller, A., Hocker, E., Ritter, S., et al. (2015). "Access to prosthetic devices in developing countries: pathways and challenges," in *IEEE Global Humanitarian Technology Conference (GHTC)* (Seattle, WA: IEEE), 45–51.

Matsuoka, Y., and Afshar, P. (2004). Neuromuscular strategies for dynamic finger movements: a robotic approach. *Int. Conf. IEEE Eng. Med. Biol. Soc*. 2, 4649–4652. doi: 10.1109/IEMBS.2004.1404288

Merletti, R., Rainoldi, A., and Farina, D. (2005). *Myoelectric Manifestations of Muscle Fatigue*. Hoboken, NJ: John Wiley & Sons, Inc.

Migliore, S. A., Brown, E. A., and DeWeerth, S. P. (2007). Novel nonlinear elastic actuators for passively controlling robotic joint compliance. *J. Mech. Design* 129, 406–412. doi: 10.1115/1.2429699

Millstein, S., Bain, D., and Hunter, G. (1985). A review of employment patterns of industrial amputees-Factors influencing rehabilitation. *Prosthet. Orthot. Int*. 9, 69–78. doi: 10.3109/03093648509164708

Motion Control Inc. (2022). Available online at: https://www.utaharm.com/motion-control-electric-hand-terminal-device.php

Murray, W., Delp, S., and Buchanan, T. (1995). Variation of muscle moment arms with elbow and forearm position. *J. Biomech*. 28, 513–525. doi: 10.1016/0021-9290(94)00114-J

Naik, G. R., Al-Timemy, A. H., and Nguyen, H. T. (2016). Transradial amputee gesture classification using an optimal number of semg sensors: an approach using ica clustering. *IEEE Trans. Neural Syst. Rehabil. Eng*. 24, 837–846. doi: 10.1109/TNSRE.2015.2478138

Ossur Inc. (2022). Available online at: https://www.ossur.com/prosthetic-solutions/products/touch-solutions/i-limb-ultra

Osu, R., Franklin, D. W., Kato, H., Gomi, H., Domen, K., Yoshioka, T., et al. (2002). Short- and long-term changes in joint co-contraction associated with motor learning as revealed from surface EMG. *J. Neurophysiol*. 88, 991–1004. doi: 10.1152/jn.2002.88.2.991

Ottobock Inc. (2022). Available online at: http://www.ottobock.com/cps/rde/xchg/ob_com_en/hs.xsl/384.html

Perreault, E. J., Kirsch, R., and Crago, P. (2004). Multijoint dynamics and postural stability of the human arm. *Exp. Brain Res*. 157, 507–517. doi: 10.1007/s00221-004-1864-7

Popescu, F., Hidler, J., and Rymer, W. (2003). Elbow impedance during goal-directed movements. *Exp. Brain Res*. 152, 17–28. doi: 10.1007/s00221-003-1507-4

Rao, S., Carloni, R., and Stramigioli, S. (2010). "Stiffness and position control of a prosthetic wrist by means of an EMG interface," in *2010 Annual International Conference of the IEEE Engineering in Medicine and Biology* (Buenos Aire: IEEE), 495–498.

Riillo, F., Quitadamo, L., Cavrini, F., Gruppioni, E., Pinto, C., Pasto, N. C., et al. (2014). Optimization of emg-based hand gesture recognition: Supervised vs. unsupervised data preprocessing on healthy subjects and transradial amputees. *Biomed. Signal Process. Control* 14, 117–125. doi: 10.1016/j.bspc.2014.07.007

Wang, N., Lao, K., and Zhang, X. (2017). Design and myoelectric control of an anthropomorphic prosthetic hand. *J. Bionic Eng*. 14, 47–59. doi: 10.1016/S1672-6529(16)60377-3

Ziegler-Graham, K., MacKenzie, E., Ephraim, P., Travison, T., and Brookmeyer, R. (2007). Estimating the prevalence of limb loss in the united states: 2005 to 2050. *Arch. Phys. Med. Rehabil*. 89, 422–429. doi: 10.1016/j.apmr.2007.11.005

Conflict of Interest: The authors declare that the research was conducted in the absence of any commercial or financial relationships that could be construed as a potential conflict of interest.

frontiers in Neurorobotics

ORIGINAL RESEARCH
published: 16 March 2022
doi: 10.3389/fnbot.2022.809380

Biomechanical Impacts of Toe Joint With Transfemoral Amputee Using a Powered Knee-Ankle Prosthesis

Shawanee' Patrick[1]*, *Namita Anil Kumar*[1], *Woolim Hong*[1] and *Pilwon Hur*[2]*

[1] Human Rehabilitation Group, Texas A&M University, Mechanical Engineering, College Station, TX, United States, [2] Gwangju Institute of Science and Technology, Department of Mechanical Engineering, Gwangju, South Korea

Transfemoral amputees are currently forced to utilize energetically passive prostheses that provide little to no propulsive work. Among the several joints and muscles required for healthy walking, the ones most vital for push-off assistance include the knee, ankle, and metatarsophalangeal (MTP) joints. There are only a handful of powered knee-ankle prostheses (also called powered transfemoral prostheses) in literature and few of them comprise a toe-joint. However, no one has researched the impact of toe-joint stiffness on walking with a power transfemoral prosthesis. This study is aimed at filling this gap in knowledge. We conducted a study with an amputee and a powered transfemoral prosthesis consisting of a spring loaded toe-joint. The prosthesis's toe-joint stiffness was varied between three values: 0.83 Nm/deg, 1.25 Nm/deg, and infinite (rigid). This study found that 0.83 Nm/deg stiffness reduced push-off assistance and resulted in compensatory movements that could lead to issues over time. While the joint angles and moments did not considerably vary across 1.25 Nm/deg and rigid stiffness, the latter led to greater power generation on the prosthesis side. However, the 1.25 Nm/deg joint stiffness resulted in the least power production from the intact side. We, thus, concluded that the use of a stiff toe-joint with a powered transfemoral prosthesis can reduce the cost of transport of the intact limb.

Keywords: prosthesis, flexible foot, kinetics, kinematics, powered prosthesis, symmetry, transfemoral, biomechanics

OPEN ACCESS

Edited by:
Chad Gregory Rose,
Auburn University, United States

Reviewed by:
Kevin Fite,
Clarkson University, United States
Giovanna Catavitello,
Catholic University of Louvain, Belgium

***Correspondence:**
Shawanee' Patrick
spatrick2012@gmail.com
Pilwon Hur
pilwonhur@gist.ac.kr

Received: *04 November 2021*
Accepted: *09 February 2022*
Published: *16 March 2022*

Citation:
Patrick S, Anil Kumar N, Hong W and Hur P (2022) Biomechanical Impacts of Toe Joint With Transfemoral Amputee Using a Powered Knee-Ankle Prosthesis. Front. Neurorobot. 16:809380. doi: 10.3389/fnbot.2022.809380

1. INTRODUCTION

There are over 1.3 million lower limb amputees in the United States alone (Ziegler-Graham et al., 2008). Over the next 50 years, this number is predicted to increase to 3.6 million (Ziegler-Graham et al., 2008). Out of this number, more than half are transfemoral (25.8 %) or transtibial (27.6 %) amputations (Dillingham et al., 2002). Transtibial (i.e., below knee) amputees do not have ankle and metatarsophalangeal (MTP) joints. Transfemoral (i.e., above knee) amputees lack a knee joint in addition to the prior listed joints. The performance with prosthesis relies on the nature of feet, the extent of actuation, comfortable fit, etc. Studies have shown that current prostheses do not account for all customer needs. Long-term use of current prosthetic feet can cause many issues such as osteoarthritis, osteopenia, and scoliosis (Gailey et al., 2008). This is due to walking asymmetries, and the missing joints and muscles required to propel the body forward during walking (Kaufman et al., 2012; Jayaraman et al., 2018). In particular, the ankle and MTP joints are vital to helping in gait progression (Stokes et al., 1979; Weerakkody et al., 2017; Honert et al., 2018, 2020). In walking the primary role of the MTP joints are to aid in stability (Fujita, 1985; Zhang et al., 2014).

MTP joints were also found to be necessary to help aid in energy storage and propulsion for able bodied individuals (Goldmann and Brüggemann, 2012; Jeong et al., 2014). Although there are many prosthetic feet currently on the market, none can replicate the complex dynamics of MTP joints.

1.1. Evaluation of Prosthetic Feet

The most common type of prosthetic feet on the market are conventional feet (CF), and Energy Storage and Return (ESR) feet (Cherelle et al., 2014). ESR feet are claimed to be more beneficial for amputees due to a flexible keel that possibly aids with push-off during walking (Versluys et al., 2008). However, the improvements seen in energy storing and cost of transport were found to be very small (Gardiner et al., 2016). Furthermore, the push-off assistance offered by CF and ESR feet is far lesser than that of able-bodied feet. This has led researchers to attempt increasing push-off assistance by attempting to replace the action of the MTP joints by adding a toe-joint. A study by McDonald et al. (2021) added a toe-joint to a passive ankle-foot prosthesis and found no significant differences in kinetics and kinematics. However, a passive foot with a flexible toe-joint by Honert et al. (2020) showed there was a difference using a custom foot with a wider base, longer arch, and a toe-joint. So, there is no consistency in the benefits of passive feet with flexible toes. While these studies only looked at the impact of a toe-joint on transtibial amputees, the impact on transfemoral amputees is yet to be explored.

1.2. Powered Prosthetic Ankles

Lower limb prostheses are either powered or passive, with the latter being more popular. There is currently only one powered prosthetic ankle on the market, the BiOM. This powered ankle has significantly improved ankle power and cost of transport for transtibial amputees (Ferris et al., 2012; Herr and Grabowski, 2012). Several other powered prostheses have been explored in the research community (Sup et al., 2008; Grabowski et al., 2010; Zhu et al., 2014; Lenzi et al., 2017; Quintero et al., 2018). There has been some work on combining powered ankles with toe-joints (Zhu et al., 2014). This study's foot design has an active toe-joint and active ankle, which produced more symmetric walking than passive feet in terms of joint angles and GRF. However, none have investigated the impact of toe-joints on the performance of powered knee-ankle prosthesis. Due to the positive impact of the MTP joint and powered ankles for transtibial amputees, we must study whether transfemoral amputees also stand to benefit from such joints. Given that transfemoral amputees makeup almost 26% of the ever growing lower limb amputee community, it is of paramount importance that we address this gap in knowledge (Dillingham et al., 2002). When researching powered prostheses, we cannot limit our observations to the impact of the toe-joint alone. We must also consider the nature of the prosthesis control, which affects how the user interacts with the device as well as kinetic and kinematic outcomes.

This study analyzed the use of an actuated knee-ankle prosthesis with a toe-joint for transfemoral amputees. We explore how three different toe-joint stiffnesses impact spatiotemporal measures, kinetics, and kinematics. Our hypothesis is that the lower stiffness spring will provide less push-off power during walking compared to a stiffer and rigid stiffness foot. The article is organized as follows. Section 2 presents the equipment overview, experiment setup, protocol, and data processing methods. The results are presented in Section 3 followed by the discussion in Section 4. The final section consists of our concluding remarks.

2. METHODS

2.1. Equipment Overview

This study utilized AMPRO II, a powered knee and ankle prosthesis (**Figure 1**), which is operated by a microprocessor (element14, BeagleBone Black) that controls actuated ankle and knee joints. The prosthesis is equipped with a 3D printed foot with an MTP joint (**Figure 2**). The toe-joint was equipped with an leaf spring utilizing spring steel sheets. The stiffness of the joint was varied by varying the number of spring steel sheets. The lowest stiffness (0.83 Nm/deg) was found to be within 0.01 Nm/deg of the average estimated stiffness of the MTP joint during able bodied walking (Mager et al., 2018). Furthermore, a force sensor (Tekscan, FlexiForce A502) placed under the heel helps detect heel-strike, while an Inertial Measurement Unit (SparkFun Electronics, MPU 9150) affixed to the user's thigh measures the thigh angle. This thigh angle is used to estimate the user's walking progress and thereby the user's intent (Hong et al., 2021). This powered prosthesis is controlled using impedance control during the stance phase and trajectory tracking control during the swing phase. The stance phase is divided into 3 states: (i) heel-strike to flat-foot, (ii) flat-foot to heel-off, and (iii) heel-off to toe-off. The torque generated by the impedance control strategy is given by

$$\tau = K(\theta - \theta_{ref}) + D\dot{\theta} \tag{1}$$

where K and D are the joint stiffness and damping parameters. The term θ_{ref} is the joint's reference or equilibrium angle. θ and $\dot{\theta}$ are the joint's instantaneous position and velocity, making the impedance control scheme very responsive to the user's kinematics. The user can increase the amount of generated torque by deviating more from θ_{ref}. Thus, the user has some control over the generated torque or push-off assistance (Lawson et al., 2014). Both K and D varied as polynomials of the user's walking progression, while θ_{ref} was constant during each state. These parameters were found through a data-driven approach wherein a least squares optimization minimized the difference between Equation (1) and healthy human walking joint torque. The optimized parameters vary such that each joint can dampen, support, and propel the user in accordance with the walking progress. For example, the ankle's stiffness increases as the user progress from heel-strike to heel-off, with the peak occurring at max push-off torque. More details on the optimization and the control strategy can be found in Anil Kumar et al. (2022).

All experiments were conducted in a motion capture lab that utilizes 44 motion capture cameras (Vantage, Vicon Motion Systems Ltd., Oxford, UK) and a force-sensing tandem instrumented treadmill (AMTI, Watertown, MA, USA). The

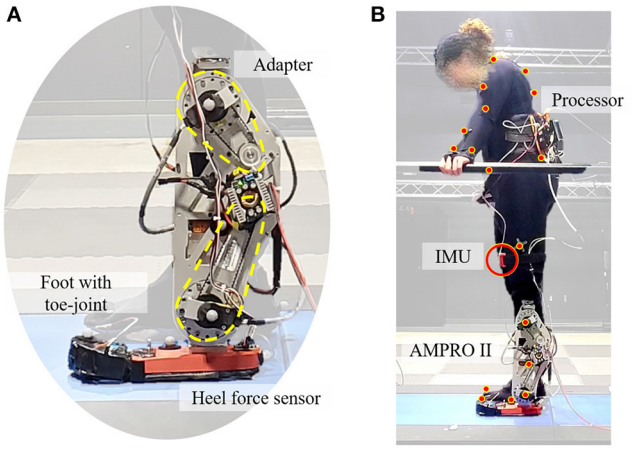

FIGURE 1 | Experimental setup: **(A)** is the powered transfemoral prosthesis, AMPRO II, **(B)** shows the amputee walking with AMPRO II in a motion capture environment.

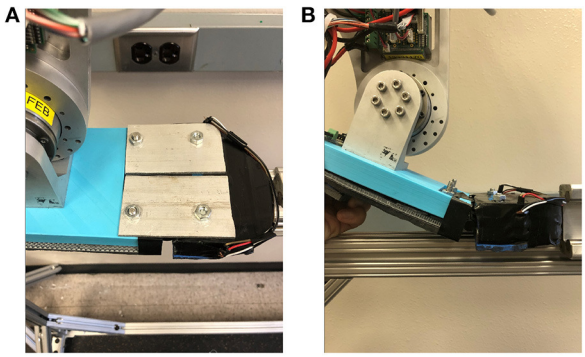

FIGURE 2 | (A) AMPRO II with locked rigid Foot, **(B)** AMPRO II with Flexed foot.

motion capture camera was collected at 100 Hz and the treadmill force plate data were collected at 1,000 Hz.

2.2. Experiment Overview

This study had one participant who is a unilateral transfemoral amputee (female, 164 cm, 66 kg w/o prosthesis). She currently utilizes an X3 microprocessor Knee (Ottobock, Duderstadt, Germany) with a Freedom Runaway Foot (Ottobock, Duderstadt, Germany). In order to collect motion capture data, the full-body plug-in gait marker set from Vicon Nexus was used (Vicon Motion Systems Ltd., Oxford, UK).

2.2.1. Protocol

The participant underwent eight practice sessions to get accustomed to the powered prosthesis and different feet. The participant was most comfortable walking at a speed of 0.67 m/s. The participant walked with three joint stiffness conditions: 0.83 Nm/deg, 1.25 Nm/deg, and Infinite (Rigid). Motion capture and force plate data were collected for each foot variation. Each walking trial lasted 90 s with 10 min breaks between foot changes. The participant was allowed to take a longer rest if requested.

2.3. Data Processing

All post-processing was done in Vicon Nexus and Visual3D (C-Motion, Germantown, MD, USA). The marker trajectories and the force data were filtered in Vicon Nexus with a low-pass third-order butter worth filter at 10 and 20 HZ, respectively. The hip, knee, and ankle joint angle, moment, and power were calculated in the sagittal plane using the Visual3D software.

The following spatiotemporal metrics were collected using marker data and force data: total step length, step time, swing time, and stance time. These were collected for both the intact and prosthetic limbs. Step length was calculated to be the total distance from heel-strike of one foot to heel-strike of the opposite foot. Step time is the time from heel-strike of one foot to heel-strike of the opposite foot. Swing time is measured to be the time from toe-off to heel-strike. Stance time is measured to be the time from heel-strike to toe-off.

To see how much the stiffness impacts symmetry between the intact and prosthesis side, the symmetry index (SI) was calculated for each of the measured spatiotemporal metrics. Ideally, the step time, swing time, and step length should be relatively close between both limbs. The higher the deviations are, the less symmetric the walking (Robinson et al., 1987). We will use Equation (2) where X_P is the spatiotemporal metric on the prosthesis side and X_I is the metric on the intact leg. If this value is negative, the dominant leg for the corresponding metric is the intact leg. The desire is for this value to be as close to zero as possible. The values fall between −100 and 100.

$$SI = \frac{(X_P - X_I)}{0.5(X_P + X_I)} * 100 \tag{2}$$

For all spatiotemporal metrics, one-way repeated-measures ANOVA was done using python's statsmodel library with $\alpha = 0.05$. If this showed significant impact of toe-joint stiffness, two-tailed paired t-tests were conducted for all combinations of toe-joint stiffness using python's scipy library with $\alpha = 0.05$.

3. RESULTS

3.1. Spatiotemporal Data

On the prosthesis side, there was a significant impact of toe-joint stiffness on step time ($p < 0.001$), stance time ($p = 0.001$), swing time ($p = 0.001$), and step length ($p = 0.02$). Mean step time with the 0.83 Nm/deg joint stiffness, was shown to be significantly greater than with the 1.25 Nm/deg and rigid joint stiffness ($p <= 0.003$ for both comparisons). This is also true for step length ($p < 0.03$), stance time ($p <= 0.001$), and swing time ($p < 0.02$) metrics.

On the intact side, there was a significant impact of toe-joint stiffness on step time ($p < 0.001$), stance time ($p < 0.001$), swing time ($p < 0.001$), and step length ($p < 0.001$). Per pairwise t-tests, step time ($p < 0.001$), swing time ($p < 0.001$), and stance time ($p < 0.003$) were significantly greater with 0.83 Nm/deg joint stiffness than those with the 1.25 Nm/deg and rigid

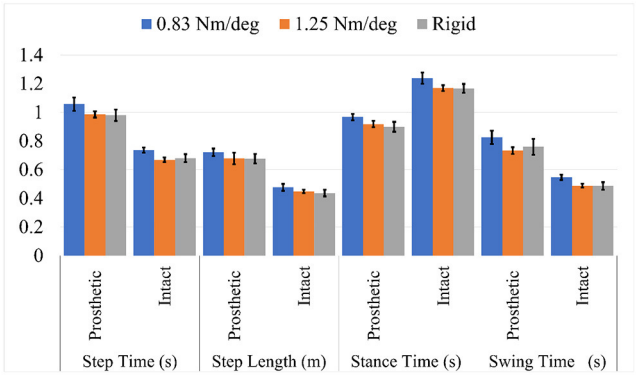

FIGURE 3 | Spatiotemporal metrics for intact and prosthesis legs.

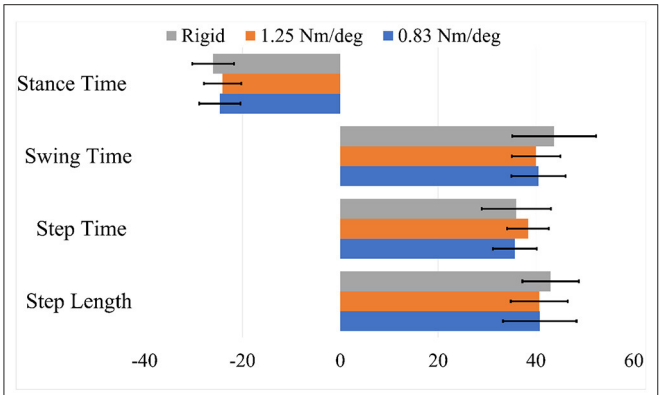

FIGURE 4 | Symmetry index (SI) for spatiotemporal metrics.

joint stiffness. The aforementioned *p* values are for both pairwise comparisons: 0.83 vs. 1.25 Nm/deg and 0.83 Nm/deg vs. rigid. This can be seen in **Figure 3**.

Although the step lengths and step times were significantly greater while using the 0.83 Nm/deg joint stiffness, the SI index for all spatiotemporal values was found not to vary significantly with toe-joint stiffness ($p > 0.34$). The 1.25 Nm/deg joint stiffness was found to be slightly more symmetric for stance and swing time, but these differences were not found to be significant (**Figure 4**).

3.2. Kinetics and Kinematics

With the 0.83 Nm/deg joint stiffness, the hip flexion at the end of the swing was 10 degrees greater than the rigid joint stiffness and 12 degrees greater than the 1.25 Nm/deg joint stiffness (**Figure 5A1**). The maximum hip torque increased with stiffness (**Figure 5A2**). Hip angles and hip moments on the intact side (**Figure 5B1,5B2**) had similar trends between stiffnesses.

There were very few changes in knee range of motion for different toe stiffness. On the prosthesis side, there was greater flexion torque in early stance when using the 0.83 Nm/deg joint stiffness compared to the 1.25 Nm/deg joint stiffness (+0.13 Nm/kg) and rigid stiffness (+0.20 Nm/kg) (**Figure 6A2**). When using the 0.83 Nm/deg joint stiffness less extension torque early before push off compared to the 1.25 Nm/deg joint stiffness (−0.15 Nm/kg) and rigid stiffness (+0.22 Nm/kg) (**Figure 6A2**). There were also higher peak knee flexion moments for the 0.83 Nm/deg joint stiffness (**Figure 6B2**) on the intact side. Range of motion of the knee for both the intact side (±2 degrees) (**Figure 6B1**) and prosthesis side (±3 degrees) (**Figure 6B2**) differed very little between foot stiffnesses. On the prosthesis side, the ankle range of motion was very similar (± 2 degrees) (**Figure 7A1**). The ankle moment on the prosthesis side decreased with stiffness at the beginning of stance and decreased with stiffness before push off (**Figure 7A2**). The intact ankle resulted in more dorsiflexion at the end of stance for the 1.25 Nm/deg (+ 5 degrees for 0.83 Nm/deg joint stiffness, +1.75 degrees for Rigid joint stiffness) (**Figure 7B1**). However, both the rigid and the 0.83 Nm/deg joint stiffness had approximately 5.4 degrees more plantar flexion than the 1.25 Nm/deg foot (**Figure 7B1**). The plantar flexion ankle moment before push-off with the 0.83 Nm/deg joint stiffness was less than the 1.25 Nm/deg and rigid joint stiffness by 0.5 and 0.4 Nm/Kg, respectively (**Figure 7B2**).

As seen in (**Figures 8A1, 8B1**, and **9**), peak power did increase with stiffness on the prosthesis side. On the prosthesis side, 0.83 Nm/deg joint was found to produce significantly lower peak power than the 1.25 Nm/deg joint and the rigid joint ($p = 0.0001$). The rigid toe joint was found to have a significantly higher peak power than the 0.83 and 1.25 Nm/deg joint ($p < 0.0009$). On the intact side, the power decreased in the order 0.83 Nm/deg, rigid, and 1.25 Nm/deg. The rigid joint resulted in significantly higher peak power($p = 0.023$).

4. DISCUSSION

While steps with the 0.83 Nm/deg joint stiffness were longer, they did not produce a more symmetric gait. Longer stance time on the prosthesis is only beneficial if it is more symmetric. Amputees on average spend less time on the side of their prosthesis resulting in overloading of the intact leg (Nolan and Lees, 2000; Nolan et al., 2003; Cutti et al., 2018; Brandt et al., 2019). Increased time on the prosthesis side compared to other feet can seemingly be a positive thing, however, this increased time must be measured against time on the intact leg to notice if it is beneficial. Due to there being no significant differences in SI for all spatiotemporal metrics this longer stance does not provide a benefit to the user.

In the case of 0.83 Nm/deg, there were some compensatory motions that resulted. On the prosthesis side, an increased hip flexion at the end of the stance was observed. On the intact side, an increased peak knee moment, increased knee flexion and ankle dorsiflexion during heel-strike, and an increased plantarflexion before toe-off were observed. As stated in Section 2.1, deviating from the reference angle increases the generated joint torque. With the lower toe-joint stiffness, it is possible the participant is attempting to get more push-off support by elongating the step. Despite these efforts, the resulting ankle push-off torque and power were lower compared to those of 1.25 Nm/deg and rigid joint stiffnesses (**Figure 9**). This shows the toe-joint stiffness of 0.83 Nm/deg counters the positive impact of the powered knee-ankle prosthesis in terms of push-off assistance. In order

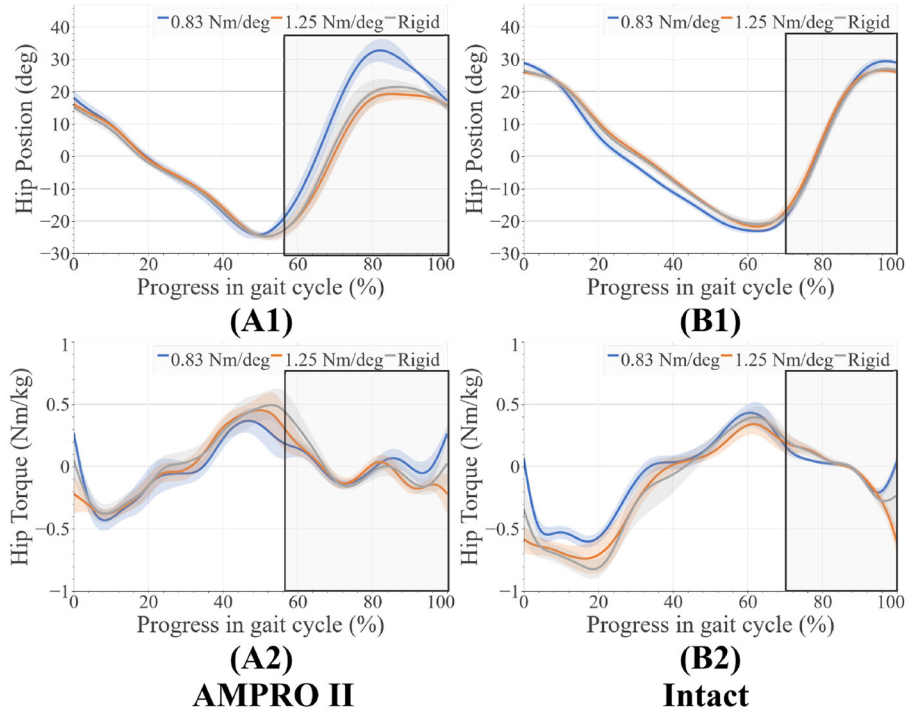

FIGURE 5 | (A1) Hip angles on prosthesis side, **(A2)** hip moments on prosthesis side, **(B1)** hip angles on intact side, **(B2)** hip moments on intact side, average swing phase for each case is boxed in the gray.

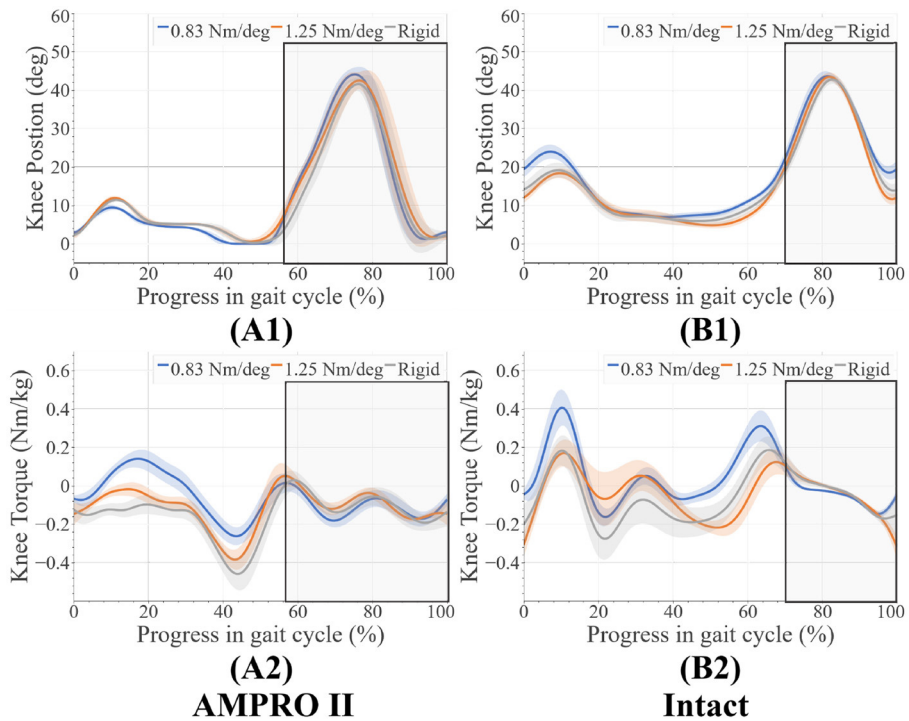

FIGURE 6 | (A1) Knee angles on prosthesis side, **(A2)** knee moments on prosthesis side, **(B1)** knee angles on intact side, **(B2)** knee moments on intact side, average swing phase for each case is boxed in the gray.

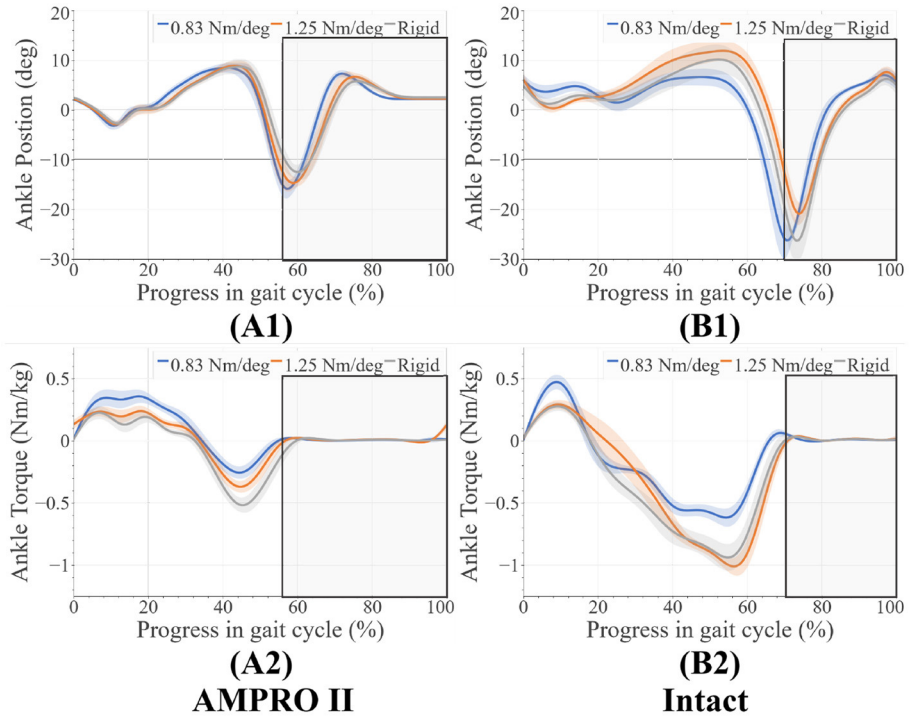

FIGURE 7 | (A1) Ankle angles on prosthesis side, **(A2)** ankle moments on prosthesis side, **(B1)** ankle angles on intact side, **(B2)** ankle moments on intact side, average swing phase for each case is boxed in the gray.

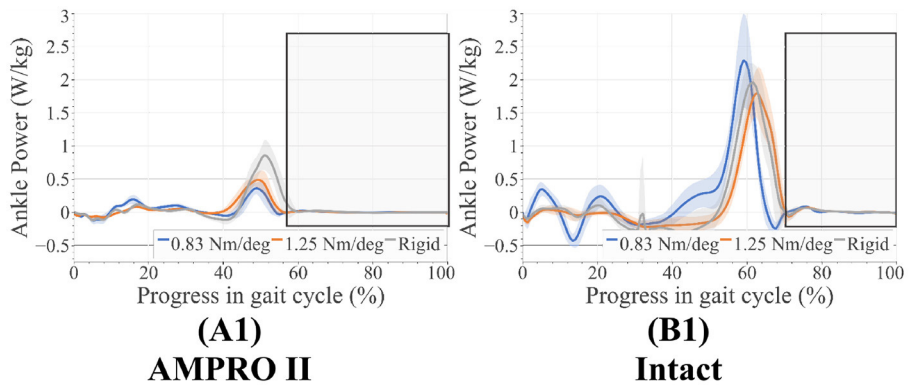

FIGURE 8 | (A1) Ankle power on prosthesis side, **(B1)** ankle power on intact side, average swing phase for each case is boxed in the gray.

to achieve these longer steps, the participant had to increase hip flexion during swing. The peak hip moments on the prosthesis side increased with foot stiffness. This value for the rigid stiffness was similar to the intact leg's hip moment values. This indicates more similar loading trends between the intact leg and the prosthesis as stiffness increases.

The increased knee flexion moments on the intact limb in the 0.83 Nm/deg case (**Figure 6B2**) indicate that there could be less stability during walking. Increased knee flexion has been correlated to knee instability during walking (Morgenroth et al., 2012). These higher moments over time have been associated with osteoarthritis (Chen et al., 2016). Using this stiffness with a powered prosthesis could counter the benefits reported in previous studies (Sup et al., 2008; Zhu et al., 2014; Lenzi et al., 2017; Quintero et al., 2018). Higher loading of the intact leg can be seen in the higher intact ankle peak power values (**Figures 8**, **9**). The use of this foot also led to the increase of dorsiflexion moment at the beginning of stance on the intact leg, indicating an increased need for more stability at push-off. The participant was seen compensating more with their intact leg in order to walk forward with this toe-joint stiffness.

The difference in moments and power production between the prosthesis and intact leg, as well as the compensatory motion mentioned above, are some of the reasons for high incidences of

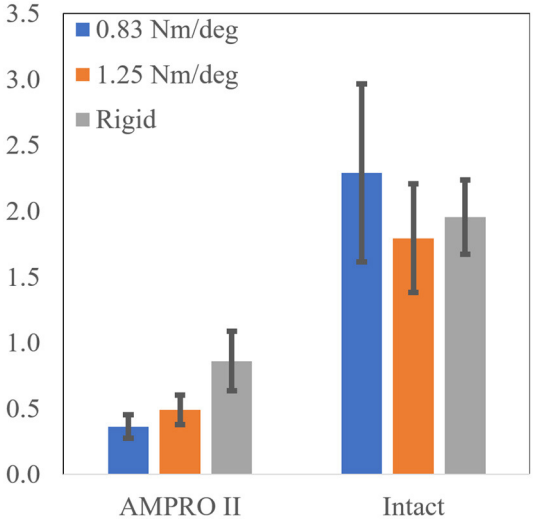

FIGURE 9 | Pushoff ankle power.

arthritis in amputees (Morgenroth et al., 2011). One of the main reasons for device abandonment is discomfort (Klute et al., 2001). If users have to make these compensatory motions with a heavier powered device, they may not wish to use it. It is possible with the 0.83 Nm/deg toe-joint the participant could feel less stable during heel-strike and push-off resulting in the compensatory movements mentioned above.

These compensatory responses were not observed in the cases pertaining to 1.25 Nm/deg and the rigid foot. The latter performed best in terms of power production on the prosthesis side. This could mean that the stability provided by a locked toe-joint through stance could prove to be beneficial with some transfemoral amputees and powered devices. The rigid and 1.25 Nm/deg toe-joint scored relatively close in terms of other metrics. Although the rigid foot produced the most power on the prosthesis side, that did not result in the least power production on the intact side. The 1.25 Nm/deg case resulted in the least power production on the intact side. This shows that increased power production on the prosthesis side does not always result in lesser demand for power from the intact side. In other words, this increased power does not always minimize overloading. Given that the results with a 1.25 Nm/deg case were slightly more symmetric, this could indicate that using a toe-joint can help reduce intact limb overloading.

We postulate that the addition of a toe-joint can make a difference while walking with a powered knee-ankle prosthesis. However, a wider range of toe joint stiffness needs to be tested in order to verify if this is true. Two of the shortcomings of this study is that it involved only three stiffnesses and a single participant. Using a foot that has a stiffness greater than 1.25 Nm/deg but not fully rigid could improve the results observed in this study. Human toe joint stiffness is shown as a nonlinear trend during walking. Studies such as Um et al. (2021) have proposed using toe-joints with nonlinear stiffness. Future efforts will be directed at studying the performance of transfemoral prostheses with nonlinear stiffness toe-joints.

5. CONCLUSION

From this study, we determined the impact of using a toe-joint with a powered prosthesis for a transfemoral amputee. We tested three different stiffness. It was determined that foot stiffness is related to power production on the prosthesis leg, with higher stiffness resulting in higher push-off assistance. The lowest stiffness had the least push-off power, demanding more power production from the intact leg. Even though low stiffness (i.e., 0.83 Nm/deg) has the benefit of easy rollover during the mid-stance, it resulted in longer step time and step length and compensatory movements that could negatively impact users over time. We conclude that a toe joint with a stiffness that is too low can negatively impact the user. However, a toe joint with a suitably selected stiffness can reduce the loading on the intact leg. In addition, power production alone is not enough to indicate the effectiveness of lower limb prostheses. It is desired to look at spatiotemporal changes as well as kinetic and kinematic responses. More stiffness and toe-joint designs need to be explored with transfemoral amputees to determine if they are able to replicate the benefits of the human MTP joints.

DATA AVAILABILITY STATEMENT

The raw data supporting the conclusions of this article will be made available by the authors, without undue reservation.

ETHICS STATEMENT

The studies involving human participants were reviewed and approved by Texas A&M IRB (IRB2015-0607F). The patients/participants provided their written informed consent to participate in this study.

AUTHOR CONTRIBUTIONS

SP: primary contributor to experiment design, data collection, and processing. NAK: contributed to data collection and analysis. WH: assisted with the implementation of the control scheme. PH: served as the principal investigator. All the authors contributed to writing and reviewing this article.

ACKNOWLEDGMENTS

We would like to acknowledge Starlab at Texas A&M University for allowing the use of the motion capture space.

REFERENCES

Anil Kumar, N., Patrick, S., Hong, W., and Hur, P. (2022). Control framework for sloped walking with a powered transfemoral prosthesis. *Front. Neurorobot.* 15, 790060. doi: 10.3389/fnbot.2021.790060

Brandt, A., Riddick, W., Stallrich, J., Lewek, M., and Huang, H. H. (2019). Effects of extended powered knee prosthesis stance time via visual feedback on gait symmetry of individuals with unilateral amputation: a preliminary study. *J. NeuroEng. Rehabil.* 16, 112. doi: 10.1186/s12984-019-0583-z

Chen, B., Ma, H., Qin, L. Y., Gao, F., Chan, K. M., Law, S. W., et al. (2016). Recent developments and challenges of lower extremity exoskeletons. *J. Orthopaedic Transl.* 5, 26–37. doi: 10.1016/j.jot.2015.09.007

Cherelle, P., Mathijssen, G., Wang, Q., Vanderborght, B., and Lefeber, D. (2014). "Advances in propulsive bionic feet and their actuation principles. *Adv. Mech Eng.* 6, 1–21. doi: 10.1155/2014/984046

Cutti, A. G., Verni, G., Migliore, G. L., Amoresano, A., and Raggi, M. (2018). Reference values for gait temporal and loading symmetry of lower-limb amputees can help in refocusing rehabilitation targets. *J. NeuroEng. Rehabil.* 15, 1–12. doi: 10.1186/s12984-018-0403-x

Dillingham, T. R., Pezzin, L. E., and MacKenzie, E. J. (2002). Limb amputation and limb deficiency: epidemiology and recent trends in the United States. *Southern Med. J.* 95, 875–883. doi: 10.1097/00007611-200208000-00018

Ferris, A. E., Aldridge, J. M., Rábago, C. A., and Wilken, J. M. (2012). Evaluation of a powered ankle-foot prosthetic system during walking. *Arch. Phys. Med. Rehabil.* 93, 1911–1918. doi: 10.1016/j.apmr.2012.06.009

Fujita, M. (1985). Role of the metatarsophalangeal (MTP) joints of the foot in level walking. *J. Jpn Orthopaedic Assoc.* 59, 985–997.

Gailey, R., Allen, K., Castles, J., Kucharik, J., and Roeder, M. (2008). Review of secondary physical conditions associated with lower-limb amputation and long-term prosthesis use. *J. Rehabil. Res. Develop.* 45, 15–30. doi: 10.1682/jrrd.2006.11.0147

Gardiner, J., Bari, A. Z., Howard, D., and Kenney, L. (2016). Transtibial amputee gait efficiency: energy storage and return versus solid ankle cushioned heel prosthetic feet. *J. Rehabil. Res. Develop.* 53, 1133–1138. doi: 10.1682/JRRD.2015.04.0066

Goldmann, J. P., and Brüggemann, G. P. (2012). The potential of human toe flexor muscles to produce force. *J. Anat.* 221, 187–194. doi: 10.1111/j.1469-7580.2012.01524.x

Grabowski, A. M., Rifkin, J., and Kram, R. (2010). K3 promoter? prosthetic foot reduces the metabolic cost of walking for unilateral transtibial amputees. *J. Prosthetics Orthotics* 22(2):113–120. doi: 10.1097/JPO.0b013e3181cca79c

Herr, H. M., and Grabowski, A. M. (2012). Bionic ankle-foot prosthesis normalizes walking gait for persons with leg amputation. *Proc. R. Soc. B Biol. Sci.* 279, 457–464. doi: 10.1098/rspb.2011.1194

Honert, E. C., Bastas, G., and Zelik, K. E. (2018). Effect of toe joint stiffness and toe shape on walking biomechanics. *Bioinspir. Biomim.* 13, 066007. doi: 10.1088/1748-3190/aadf46

Honert, E. C., Bastas, G., and Zelik, K. E. (2020). Effects of toe length, foot arch length and toe joint axis on walking biomechanics. *Hum. Mov. Sci.* 70, 102594. doi: 10.1016/j.humov.2020.102594

Hong, W., Anil Kumar, N., and Hur, P. (2021). A phase-shifting based human gait phase estimation for powered transfemoral prostheses. *IEEE Robot. Autom. Lett.* 6, 113–5120. doi: 10.1109/LRA.2021.3068907

Jayaraman, C., Hoppe-Ludwig, S., Deems-Dluhy, S., McGuire, M., Mummidisetty, C., Siegal, R., Naef, A., Lawson, B. E., Goldfarb, M., Gordon, K. E., et al. (2018). Impact of powered knee-ankle prosthesis on low back muscle mechanics in transfemoral amputees: a case series. *Front. Neurosci.* 12, 134. doi: 10.3389/fnins.2018.00134

Jeong, B., Kim, S., Son, J., and Kim, Y. (2014). Kinetic analysis of the metatarsophalangeal joint in normal subjects and hallux valgus patients during walking using a four-segment foot model. *J. Foot Ankle Res.* 7, 1–2. doi: 10.1186/1757-1146-7-S1-A125

Kaufman, K. R., Frittoli, S., and Frigo, C. A. (2012). Gait asymmetry of transfemoral amputees using mechanical and microprocessor-controlled prosthetic knees. *Clin. Biomech.* 27, 460–465. doi: 10.1016/j.clinbiomech.2011.11.011

Klute, G. K., Kallfelz, C. F., and Czerniecki, J. M. (2001). Mechanical properties of prosthetic limbs: Adapting to the patient. *J. Rehabil. Res. Dev.* 38, 299–307. Available online at: https://www.rehab.research.va.gov/jour/01/38/3/pdf/Klute.pdf

Lawson, B. E., Mitchell, J., Truex, D., Shultz, A., Ledoux, E., and Goldfarb, M. (2014). A robotic leg prosthesis: design, control, and implementation. *IEEE Robot. Autom. Mag.* 21, 70–81. doi: 10.1109/MRA.2014.2360303

Lenzi, T., Cempini, M., Newkirk, J., Hargrove, L. J., and Kuiken, T. A. (2017). "A lightweight robotic ankle prosthesis with non-backdrivable cam-based transmission," in *IEEE International Conference on Rehabilitation Robotics* (London: IEEE Computer Society), 1142–1147.

Mager, F., Richards, J., Hennies, M., Dötzel, E., Chohan, A., Mbuli, A., and Capanni, F. (2018). Determination of ankle and metatarsophalangeal stiffness during walking and jogging. *J. Appl. Biomech.* 34, 448–453. doi: 10.1123/jab.2017-0265

McDonald, K. A., Teater, R. H., Cruz, J. P., Kerr, J. T., Bastas, G., and Zelik, K. E. (2021). Adding a toe joint to a prosthesis: walking biomechanics, energetics, and preference of individuals with unilateral below-knee limb loss. *Sci. Rep.* 11, 1924. doi: 10.1038/s41598-021-81565-1

Morgenroth, D. C., Gellhorn, A. C., and Suri, P. (2012). Osteoarthritis in the disabled population: A mechanical perspective. *PM & R.* 4, S20–S27. doi: 10.1016/j.pmrj.2012.01.003

Morgenroth, D. C., Segal, A. D., Zelik, K. E., Czerniecki, J. M., Klute, G. K., Adamczyk, P. G., et al. (2011). The effect of prosthetic foot push-off on mechanical loading associated with knee osteoarthritis in lower extremity amputees. *Gait Posture.* 34, 502–507. doi: 10.1016/j.gaitpost.2011.07.001

Nolan, L. and Lees, A. (2000). The functional demands on the intact limb during walking for active trans-femoral and trans-tibial amputees. *Prosthet. Orthot. Int.* 24, 117–125.doi: 10.1080/03093640008726534

Nolan, L., Wit, A., Dudziński, K., Lees, A., Lake, M., and Wychowański, M. (2003). Adjustments in gait symmetry with walking speed in trans-femoral and trans-tibial amputees. *Gait Posture.* 17, 142–151. doi: 10.1016/s0966-6362(02)00066-8

Quintero, D., Villarreal, D. J., Lambert, D. J., Kapp, S., and Gregg, R. D. (2018). Continuous-phase control of a powered knee-ankle prosthesis: amputee experiments across speeds and inclines. *IEEE Trans. Robot.* 34, 686–701. doi: 10.1109/TRO.2018.2794536

Robinson, R. O., Herzog, W., and Nigg, B. M. (1987). Use of force platform variables to quantify the effects of chiropractic manipulation on gait symmetry. *J. Manipulative Physiol. Therapeutics.* 10, 172–176.

Stokes, I. A., Hutton, W. C., and Stott, J. R. (1979). Forces acting on the metatarsals during normal walking. *J. Anat.* 129, 579.

Sup, F., Bohara, A., and Goldfarb, M. (2008). Design and control of a powered transfemoral prosthesis. *Int. J. Robot. Res.* 27, 263–273. doi: 10.1177/0278364907084588

Um, H.-J., Kim, H.-S. H.-S., Hong, W., Kim, H.-S. H.-S., and Hur, P. (2021). Design of 3D printable prosthetic foot to implement nonlinear stiffness behavior of human toe joint based on finite element analysis. *Sci. Rep.* 11, 19780. doi: 10.1038/s41598-021-98839-3

Versluys, R., Desomer, A., Lenaerts, G., Beyl, P., Van Damme, M., Vanderborght, B., et al. (2008). "From conventional prosthetic feet to bionic feet: a review study," in *Proceedings of the 2nd Biennial IEEE/RAS-EMBS International Conference on Biomedical Robotics and Biomechatronics, BioRob 2008* (Scottsdale, AZ), 49–54.

Weerakkody, T. H., Lalitharatne, T. D., and Gopura, R. A. (2017). Adaptive foot in lower-limb prostheses. *J. Robot.* 2017, 9618375. doi: 10.1155/2017/9618375

Zhang, J., Si, Y., Zhang, Y., and Liu, Y. (2014). The effects of restricting the flexion-extension motion of the first metatarsophalangeal joint on human walking gait. *Bio Med. Mater. Eng.* 24, 2577–2584. doi: 10.3233/BME-141073

Zhu, J., Wang, Q., and Wang, L. (2014). On the Design of a Powered Transtibial Prosthesis With Stiffness Adaptable Ankle and Toe Joints. *IEEE Trans. Ind. Electron.* 61, 4797. doi: 10.1109/TIE.2013.2293691

Ziegler-Graham, K., MacKenzie, E. J., Ephraim, P. L., Travison, T. G., and Brookmeyer, R. (2008). Estimating the prevalence of limb loss in the

United States: 2005 to 2050. *Arch. Phys. Med. Rehabil.* 89, 422–429. doi: 10.1016/j.apmr.2007.11.005

Conflict of Interest: The authors declare that the research was conducted in the absence of any commercial or financial relationships that could be construed as a potential conflict of interest.

Publisher's Note: All claims expressed in this article are solely those of the authors and do not necessarily represent those of their affiliated organizations, or those of the publisher, the editors and the reviewers. Any product that may be evaluated in this article, or claim that may be made by its manufacturer, is not guaranteed or endorsed by the publisher.

frontiers in Neurorobotics

ORIGINAL RESEARCH
published: 30 March 2022
doi: 10.3389/fnbot.2022.807826

Effect of Torso Kinematics on Gait Phase Estimation at Different Walking Speeds

Woolim Hong[1], *Jinwon Lee*[2] *and Pilwon Hur*[3]*

[1] J. Mike Walker '66 Department of Mechanical Engineering, Texas A&M University, College Station, TX, United States, [2] School of Mechanical Engineering, Korea University, Seoul, South Korea, [3] School of Mechanical Engineering, Gwangju Institute of Science and Technology, Gwangju, South Korea

Human gait phase estimation has been studied in the field of robotics due to its importance for controlling wearable devices (e.g., prostheses or exoskeletons) in a synchronized manner with the user. As data-driven approaches have recently risen in the field, researchers have attempted to estimate the user gait phase using a learning-based method. Thigh and torso information have been widely utilized in estimating the human gait phase for wearable devices. Torso information, however, is known to have high variability, specifically in slow walking, and its effect on gait phase estimation has not been studied. In this study, we quantified torso variability and investigated how the torso information affects the gait phase estimation result at various walking speeds. We obtained three different trained models (i.e., general, slow, and normal-fast models) using long short-term memory (LSTM). These models were compared to identify the effect of torso information at different walking speeds. In addition, the ablation study was performed to identify the isolated effect of the torso on the gait phase estimation. As a result, when the torso segment's angular velocity was used with thigh information, the accuracy of gait phase estimation was increased, while the torso segment's angular position had no apparent effect on the accuracy. This study suggests that the torso segment's angular velocity enhances human gait phase estimation when used together with the thigh information despite its known variability.

Keywords: gait phase estimation, machine learning, torso variability, exoskeletons and prostheses, biomechanics

OPEN ACCESS

Edited by:
Irfan Hussain,
Khalifa University, United Arab Emirates

Reviewed by:
Giovanna Catavitello,
Catholic University of Louvain, Belgium
Yannick Aoustin,
Université de Nantes, France
Amy R. Wu,
Queen's University, Canada

***Correspondence:**
Pilwon Hur
pilwonhur@gist.ac.kr

Received: *02 November 2021*
Accepted: *07 February 2022*
Published: *30 March 2022*

Citation:
Hong W, Lee J and Hur P (2022) Effect of Torso Kinematics on Gait Phase Estimation at Different Walking Speeds. Front. Neurorobot. 16:807826. doi: 10.3389/fnbot.2022.807826

1. INTRODUCTION

The gait cycle is a key concept in explaining human locomotion. The gait cycle commonly starts with heel-strike and ends with the next heel-strike of the ipsilateral leg (Alamdari and Krovi, 2017; Kawalec, 2017). A gait phase indicates the walking state (or progression) of the user within the gait cycle and estimating this user gait phase is crucial for controlling wearable assistive devices, such as powered prostheses (Gregg et al., 2014; Quintero et al., 2018; Hong et al., 2021; Lee et al., 2021) or exoskeletons (Kang et al., 2019; Seo et al., 2019; Sawicki et al., 2020). This is because wearable assistive devices should provide a synchronized motion with the user for stable walking, requiring an accurate user gait phase estimation (Gregg et al., 2014; Quintero et al., 2018; Kang et al., 2019; Seo et al., 2019; Sawicki et al., 2020; Hong et al., 2021; Lee et al., 2021). Conventionally, a discrete gait phase estimation (i.e., gait event detection) has been widely studied using different wearable sensor sets; several gait phase models have been proposed to separate the gait cycle into a different

number of phases (Jasiewicz et al., 2006; Kotiadis et al., 2010; Abaid et al., 2013; Mannini et al., 2013; Allseits et al., 2017). Some researchers focused on heel-strike and toe-off detection with a rule-based algorithm using different sensor combinations (Jasiewicz et al., 2006; Allseits et al., 2017). Kotiadis et al. (2010) additionally detected the heel-off phase based on shank information. The hidden Markov model was also used to detect four different gait phases: heel-strike, flat-foot, heel-off, and toe-off (Abaid et al., 2013; Mannini et al., 2013). These discrete gait phase estimators could be used in the wearable device application to provide a synchronized motion control to the user.

Continuous gait phase estimation would be more effective in the seamless control of wearable devices since humans show continuously varying joint kinematics/kinetics trends (Rouse et al., 2014; Lee et al., 2016; Shorter and Rouse, 2018; Hong et al., 2019; Anil Kumar et al., 2020). Furthermore, for even more accurate gait phase estimation in a continuous manner, data-driven estimation techniques have recently evolved, utilizing diverse kinematics/kinetics information as an input dataset (Kang et al., 2019; Seo et al., 2019; Lee et al., 2021). Kang et al. (2019) achieved a neural network-based gait phase estimation relying on multiple sensors: encoders at the hip and IMUs at the thigh and torso. Seo et al. (2019) also implemented a recurrent neural network (RNN) model to estimate user gait phase using shank-mounted IMUs and additional foot pressure information for their model training. Lee et al. (2021) focused on angular positions and velocities of thigh and torso segments to estimate the user gait phase for their powered prosthesis application. As a result, they all achieved robust and accurate estimation in a continuous manner at different walking speeds (Kang et al., 2019; Seo et al., 2019; Lee et al., 2021). Even with those successful estimation results, the error rate varied according to walking speed. To be more specific, a larger deviation of error was found during the mid-stance phase in slow-walking (Lee et al., 2021). As suggested by Kang et al. (2019) and Lee et al. (2021), the torso movement exhibits a certain pattern during locomotion (Cappozzo, 1981; Thorstensson et al., 1984; Ceccato et al., 2009), thereby being used for estimating the gait phase. For instance, the torso maintains a particular forward inclination and oscillates around this position two times per gait cycle in the sagittal plane, and its rotation occurs one time per gait cycle in the horizontal plane (Ceccato et al., 2009). The torso information (e.g, segment's position and velocity), however, is also known to have high variability as per individual, and this variability becomes even higher in slow-walking (Thorstensson et al., 1984; Kerrigan et al., 2001; Dingwell and Marin, 2006; Asgari et al., 2015). We do not know yet whether this variability affects the estimation results at various walking speeds, especially at slow speeds.

Therefore, this article focuses on how torso information (i.e., segment's angular position and velocity) affects the accuracy of learning-based gait phase estimation at various walking speeds. We hypothesize that torso movement affects human gait phase estimation results at different walking speeds due to its known variability. To the authors' knowledge, the effect of the torso on the accuracy of gait phase estimation has not been spotlighted. In section 2, our gait phase estimation model is briefly explained. Also, the ablation study is described to identify the contribution of torso information to the estimation. In section 3, training results are presented and discussed based on the torso variability shown in the correlation matrix. To validate the proposed idea, prediction results are also shown in this section. We additionally present a heel-strike detection error for further evaluation. All the results are discussed and concluded in sections 4 and 5, respectively.

2. METHODS

We previously proposed a speed-adaptive gait phase estimation model in Lee et al. (2021). Interestingly, it was found that gait phase estimation errors became larger during the mid-stance phase in slow-walking (Lee et al., 2021). In this study, we speculate on a possible remedy for this. The large estimation error may be because the torso deviates more while maintaining the balance in slow-walking (Dingwell and Marin, 2006; Asgari et al., 2015). This could be interpreted that torso kinematics may affect the estimation result. Therefore, we investigate the effect of torso kinematics on estimating the human gait phase by comparing the resulting estimations when torso information is included or excluded in model training.

2.1. Training Dataset

We utilized an open-source dataset, which can be found in Schreiber and Moissenet (2019), for our model training to guarantee a sufficient size of input data. This dataset included walkway walking data of 50 healthy subjects (26 male and 24 female) in five different speed conditions, such as C_1: 0.0–0.4 m/s, C_2: 0.4–0.8 m/s, C_3: 0.8–1.2 m/s, C_4: self-selected speeds (1.0–1.4 m/s), and C_5: self-selected fast speeds (1.4–1.8 m/s). Fifty-two whole-body reflective markers were used to provide an individual's 3D motion information (Schreiber and Moissenet, 2019). We were able to generate the torso segment vector using the markers at the anterior-superior and posterior-superior iliac spine of both sides of the leg, and at the spinous process of the 10^{th} thoracic vertebrae. The thigh segment vector was generated using the markers at the greater trochanter and the lateral femoral epicondyle. We calculated the angular positions and velocities of the thigh and torso segments in the sagittal plane and utilized them for training our model. Furthermore, heel-strike and toe-off information could be estimated using ground reaction forces from two force plates. The data was sampled at 100 and 1.5 kHz for markers and force plates, respectively. Forty-two individuals' datasets were randomly selected for model training and validation, while the others were used for prediction.

2.2. Ground Truth Labeling

Heel-strike is conventionally used as a cue of gait initiation because the human gait cycle is usually defined from heel-strike to the next heel-strike on the same leg (Taborri et al., 2016; Vu et al., 2020). Based on the heel-strike, we labeled the data using a polar coordinate encoding method in the training session (Kang et al., 2019; Lee et al., 2021). This was because the nominal linear label is vulnerable to the discontinuity at heel-strike due to gait initiation (as shown in **Figure 1**), resulting in an undesired loss (i.e., mean-squared error) during model training. In **Figure 1**, ϕ

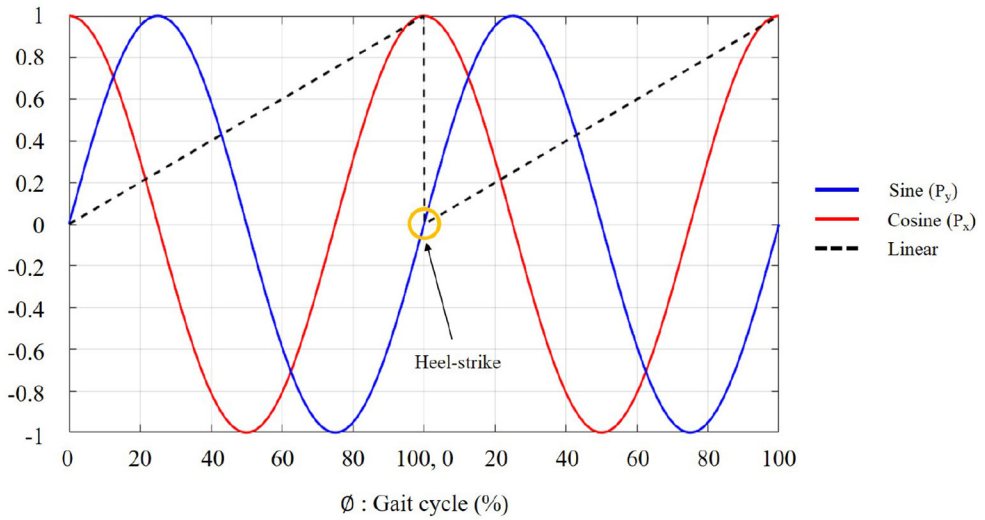

FIGURE 1 | Ground truth labeling. Sine **(Blue)** and cosine **(Red)** functions are transformed into a bounded linear function **(Black)**. Gait initiation occurs at the heel-strike.

refers to the percentage of the gait cycle, representing the user's walking progression between the heel-strikes, where $\phi \in [0, 100]$. As shown in Equation (1), this walking progression (i.e., ϕ) can be mapped into θ during the entire gait cycle for the polar coordinate transformations, where $\theta \in [0, 2\pi]$. By having two continuous sinusoidal functions as the ground truth (i.e., P_x and P_y in Equation (2), we could prevent the undesired error from the discontinuity at heel-strikes.

$$\theta = \frac{2\pi}{100} \cdot \phi \tag{1}$$

$$(P_x, P_y) = (\cos\theta, \sin\theta) \tag{2}$$

Following Equations (3) and (4), those sine and cosine functions can be transformed into a linear function $\hat{\tau}$, which is bounded in [0,1], representing the continuous gait phase. This linear gait phase estimation is usually utilized for controlling wearable devices (Kang et al., 2019; Hong et al., 2021).

$$\tau = \frac{1}{2\pi} \operatorname{atan2}(Py, Px) \tag{3}$$

$$\hat{\tau} = \begin{cases} \tau & P_y \geq 0 \\ \tau + 1 & P_y < 0 \end{cases} \tag{4}$$

2.3. Neural Network

Torso movement is known to have higher variability compared to thigh movement during walking. Even though highly variable signals may have the potential for more information, we still do not know whether the torso information enhances the gait phase estimation accuracy. In order to investigate the contribution of torso information to gait phase estimation, an ablation study was performed in this study using torso angular position and velocity. We prepared four input datasets for model training: (Set 1) angular positions and velocities of thigh and torso segments; (Set 2) angular position and velocity of the thigh segment and angular velocity of the torso segment; (Set 3) angular position and velocity of the thigh segment and angular position of the torso segment; and (Set 4) angular position and velocity of the thigh segment. As shown above, both the thigh segment's angle and velocity were always included in the four datasets, while the torso segment's angular position and velocity conditions were changed. Also, three different speed conditions (e.g., C_2, $C_2 - C_5$, and $C_3 - C_5$) were given for the model training to be generalized to diverse walking speeds. The trained model only utilizing C_2 was named the *slow model*, while the models using $C_2 - C_5$ and $C_3 - C_5$ were called the *general model* and *normal-fast model*, respectively. C_1 was excluded because it referred to extremely slow speeds. A long short-term memory (LSTM) was utilized in this study due to its powerful performance with chronological data, such as time series prediction (Hochreiter, 1997; Kang et al., 2019; Lee et al., 2021). Further, bidirectional LSTM (Bi-LSTM) was implemented to achieve both forward and backward learning during the training process (Graves, 2005). This allowed the given model to learn from past and future information. The size of the sliding windows for the model was chosen to be 100, which was deemed to be appropriate for the collected data with relatively short lengths. **Figure 2** shows the proposed network architecture. Our network consists of five layers with LSTM and Bi-LSTM. Layer 1–4 has 128, 64, 64, and 32 units, respectively. As depicted in **Figure 2**, the current input (x_0) updates the cell state (C_0) and the output (h_0). The cell state updates the information from input data and transfers the previously learned information to the next block. Layer 5 results in the output as the sine and cosine functions, as explained in section 2.2. We selected the last value in the sequence to get the gait phase at time t. The network model was trained with the Adam optimizer and mean-squared error

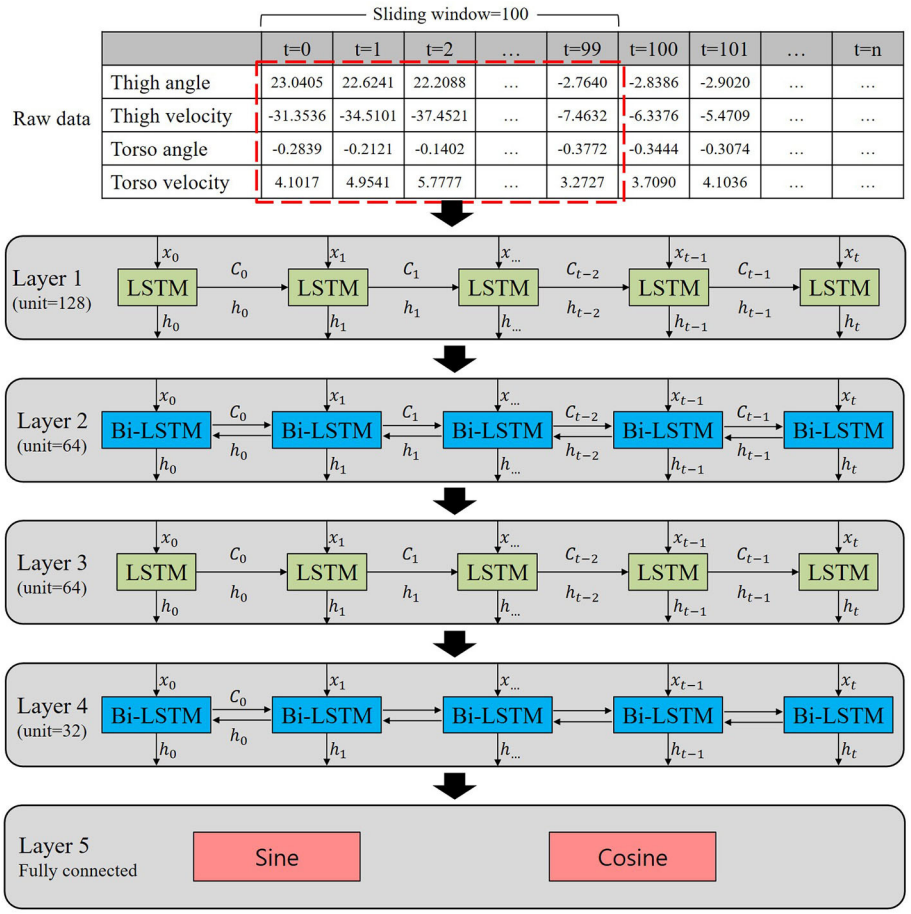

FIGURE 2 | Proposed neural network architecture for the gait phase estimation. The network consists of five layers with long short-term memory (LSTM) and bidirectional LSTM (Bi-LSTM). Layer 1–4 has 128, 64, 64, and 32 units, respectively. Layer 5 is fully connected and results in the output as sine and cosine functions.

(MSE) was used as a loss function with a batch size of 64. To prevent the over-fitting, the model was trained for a maximum of 100 epochs, stopping early if the validation loss did not continue to decrease in 10 epochs.

2.4. Statistical Analysis

Statistical analysis was performed to determine the significance of the torso information in the gait phase estimation model using RStudio statistical software (RStudio ver. 1.3.1093). For model training, we used three models (i.e., general, slow, and normal-fast models) with four input datasets (i.e., Sets 1–4). For the training results, we performed a two-way ANOVA to identify the effects of the training dataset (i.e., Sets 1–4) and three different models (i.e., general, slow, and normal-fast). For the prediction results, three two-way ANOVAs (each for a speed-dependent model) were performed to examine the effect of the trained dataset (i.e., Sets 1–4) and the speed condition (C_2 – C_5). We performed another two-way ANOVA for the heel-strike detection error to identify the effect of the dataset and the speed condition. In a multiple comparison, Bonferroni correction was used as a *post-hoc* test. A significance level of 0.05 was used in all analyses. Throughout this article, the statistical significance was symbolized as follow: * = $p \leq 0.05$, ** = $p \leq 0.01$, and *** = $p \leq 0.001$.

3. RESULTS

Throughout this section, a total of 12 conditions are given based on four different training sets (i.e., Sets 1–4) and three different speed-dependent models: general, slow, and normal-fast. We performed a training process for each condition and collected the final loss-value (i.e., MSE) for each independent model.

3.1. Training Results

The two-way ANOVA for the training results found that both training sets ($p < 0.001$) and three different models ($p < 0.001$) were significant. Training results using four different training sets (Sets 1–4) were compared to investigate the torso information effect on the estimation (see **Figure 3**). Note that Set 4 was considered as the baseline because it only contained thigh information. As shown in **Figure 3**, there was no significant difference when the torso angle was included compared to Set 4

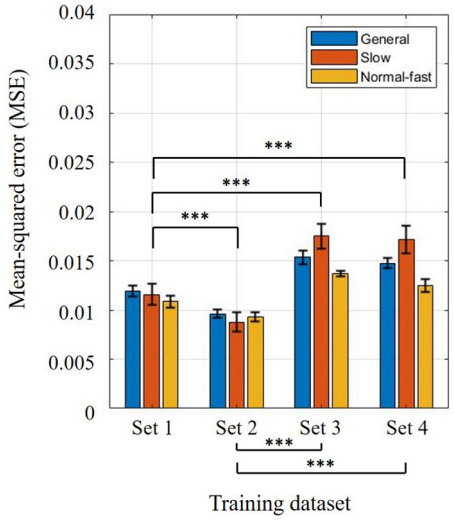

FIGURE 3 | Training results using four different training sets: **(Set 1)** angular positions and velocities of thigh and torso segments, **(Set 2)** angular position and velocity of thigh segment, and torso segment angular velocity, **(Set 3)** angular position and velocity of thigh segment, and torso segment angular position, **(Set 4)** position and velocity of thigh segment. Bar colors correspond to three different trained models: general, slow, and normal-fast walking. Bar graphs and error bars correspond to the mean and ± 1SD.

(Set 3 vs. Set 4, $p = 0.052$). The highest accuracy was found when position and velocity of the thigh segment and torso segment velocity were utilized for model training (Set 2, $p < 0.001$), while the second-highest accuracy was achieved with both angular positions and velocities of the thigh and torso segments (Set 1, $p < 0.001$). Between Sets 1 and 2, the error increased when the torso angle was included ($p < 0.001$). On the other hand, the estimation errors were reduced when the torso angular velocity was included in the training set (Sets 1 and 2 vs. Sets 3 and 4, $p < 0.001$). This implies that the contribution of torso angular position and velocity may differ. Considering the speed-dependent model conditions, it was obvious that the slow model shows the highest error in Sets 3 and 4 ($p < 0.001$). To identify a link between torso variability and gait phase estimation results, we additionally checked how much deviations the thigh and torso have per individual at different walking speeds.

As depicted in **Figure 4A**, the correlation matrix was generated using 51 variables, having 51×51 dimensions. The given variable set consists of a single mean trajectory of all subjects (A) and each subject's mean trajectory (S_i, where i refers to subject id). Each cell in the matrix shows the correlation between two variables. Our matrix starts with the mean trajectory of all subjects (A) and ends with the 50th subject's mean trajectory (S_{50}). So, we could only focus on the first row or column (red box in **Figure 4A**) to see the correlation between each individual's trajectory ($S_{1,2,...,49,50}$) and the mean trajectory of all subjects (A). The mean and SD of those correlation coefficients are presented in **Table 1**. According to **Table 1**, both the thigh and the torso show the highest variability in slow-walking (C_1), which is consistent with other studies (Dingwell and Marin, 2006; Asgari et al., 2015). The torso correlations are specifically smaller than those of the thigh. Compared to the normal and fast speed conditions, the slow walking data (i.e., C1 and C2) showed significantly higher variability for both thigh and torso. The torso data was specifically more sensitive to the walking speed according to **Table 1**. Even at the normal walking (i.e., the highest correlation result), the torso shows less correlation (e.g., position: 0.7032 ± 0.2546, velocity: 0.7996 ± 0.2011 in C_3) when the thigh correlation is close to 1 (e.g., position: 0.9925 ± 0.0057, velocity: 0.9835 ± 0.0085 in C_3). Between torso angular position and velocity, the torso velocity shows a higher correlation per individual than the torso position throughout all speed conditions. In **Figure 4**, the correlation matrix is also illustrated using a colormap. **Figures 4B,C** depict the correlation matrix of thigh and torso information at two different walking speeds: C_1 and C_3. It is obvious that thigh information shows a much higher correlation with each other than torso information in both slow and fast walking (as shown in **Figures 4B,C**). It is also apparent that faster walking speed (**Figure 4C**) shows a higher correlation than slower walking speed (**Figure 4B**) for all information.

3.2. Prediction Results

A two-way ANOVA was performed for each speed-dependent model (i.e., general, slow, and normal-fast models) to identify the significance of the trained dataset (i.e., Sets 1–4) and the speed conditions (i.e., $C_2 - C_5$). The prediction process was performed using Sets 1–4. Data from eight subjects were randomly selected to be used for the prediction. Also, individuals' walking data at four different speeds (i.e., $C_2 - C_5$) were used for evaluating the prediction results. The prediction errors are described in **Figure 5** to identify the torso kinematics effect on the gait phase estimation. **Figure 5A** shows the prediction result of the general model. In this model, both training sets ($p = 0.002$) and speed conditions ($p < 0.001$) were significant. **Figures 5B,C** show the results of the slow model and the normal-fast model, respectively. In the cases of the slow model and the normal-fast model, both models also showed the significant effects of the training sets ($p < 0.001$) and the speed conditions ($p < 0.001$) according to each two-way ANOVA. The estimation error specifically increased when the walking speed became faster in the slow model ($p < 0.001$). On the other hand, in the normal-fast model, the highest error was observed at slow walking speed ($p < 0.001$). In general, **Figure 5A** shows the best estimation result while covering all different speed conditions (i.e., $C_2 - C_5$). The relatively high errors were still shown at slow speeds due to the high variability of the dataset in slow-walking. This could be further explained by comparing the results of each dataset. In **Figure 5A**, there was no significant interaction effect between the prediction dataset and walking speed. Among the given datasets, Set 4 showed the highest error in the prediction compared to Sets 1 ($p = 0.0438$) and 2 ($p = 0.0042$). Set 3 had no significant difference from Set 4. According to the *post-hoc* test based on speed conditions, all of them showed a significant difference from each other, except C_3 and C_5.

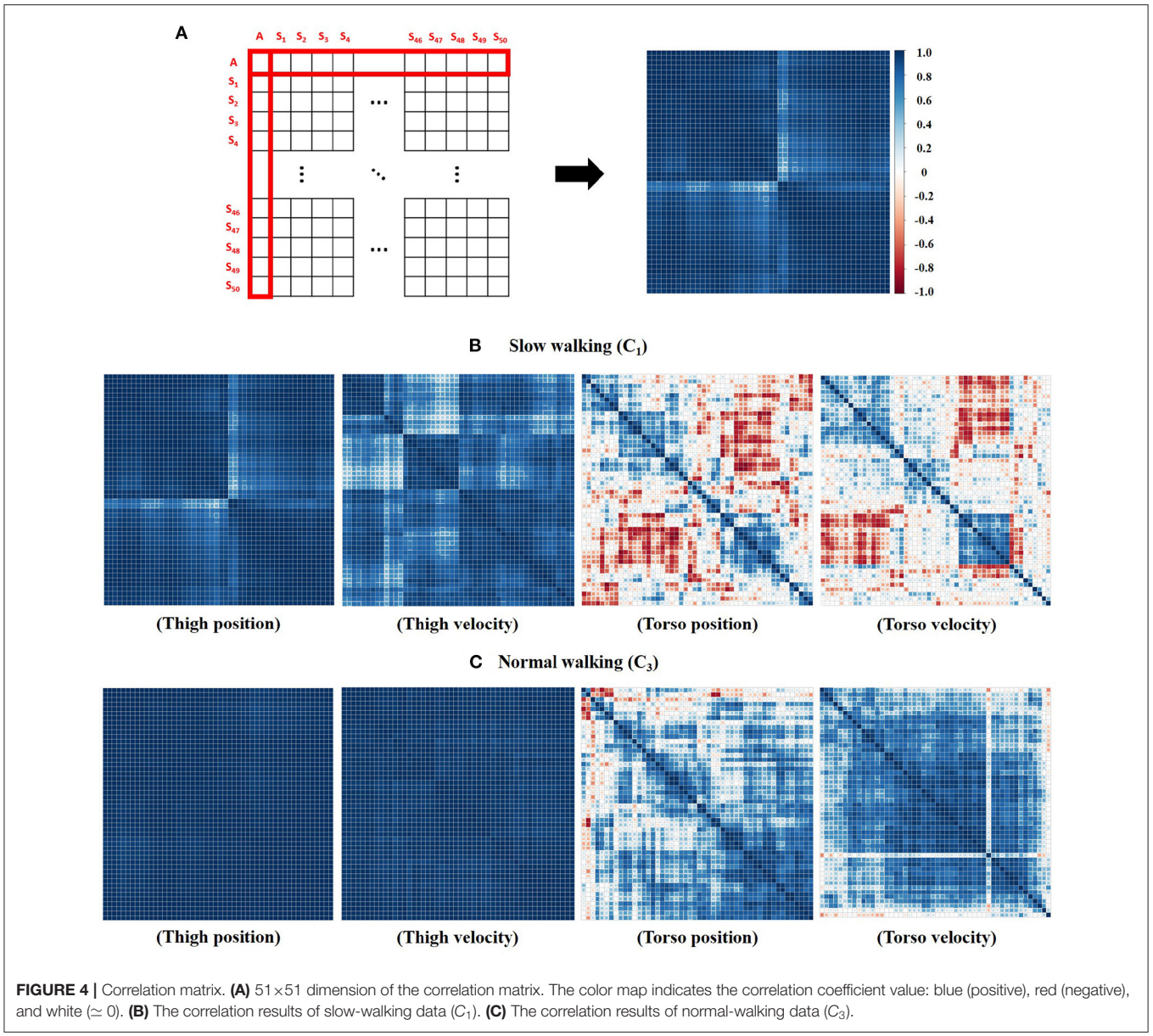

FIGURE 4 | Correlation matrix. **(A)** 51×51 dimension of the correlation matrix. The color map indicates the correlation coefficient value: blue (positive), red (negative), and white ($\simeq$ 0). **(B)** The correlation results of slow-walking data (C_1). **(C)** The correlation results of normal-walking data (C_3).

TABLE 1 | Mean and SD of correlation coefficients for each dataset in five different speed conditions.

Walking speed	Thigh position (mean ± 1SD)	Thigh velocity (mean ± 1SD)	Torso position (mean ± 1SD)	Torso velocity (mean ± 1SD)
C_1	0.9663 ± 0.0382	0.9059 ± 0.0656	0.1259 ± 0.3269	0.2222 ± 0.2817
C_2	0.9892 ± 0.0074	0.9726 ± 0.0169	0.4092 ± 0.5476	0.4936 ± 0.5278
C_3	0.9925 ± 0.0057	0.9835 ± 0.0085	0.7032 ± 0.2546	0.7996 ± 0.2011
C_4	0.9917 ± 0.0096	0.9824 ± 0.0063	0.6638 ± 0.3098	0.7630 ± 0.2857
C_5	0.9941 ± 0.0047	0.9876 ± 0.0063	0.5643 ± 0.3098	0.6999 ± 0.2857

The correlation results were calculated between each subject's trajectory (S_i) and the mean trajectory of all subjects (A).

Another two-way ANOVA was performed to identify the effects of training sets and walking speeds on the heel-strike detection errors in the general model. This error refers to the temporal difference between actual heel-strike and predicted heel-strike (as shown in **Figure 6A**). The two-way ANOVA for heel-strike prediction found that both training sets ($p = 0.046$)

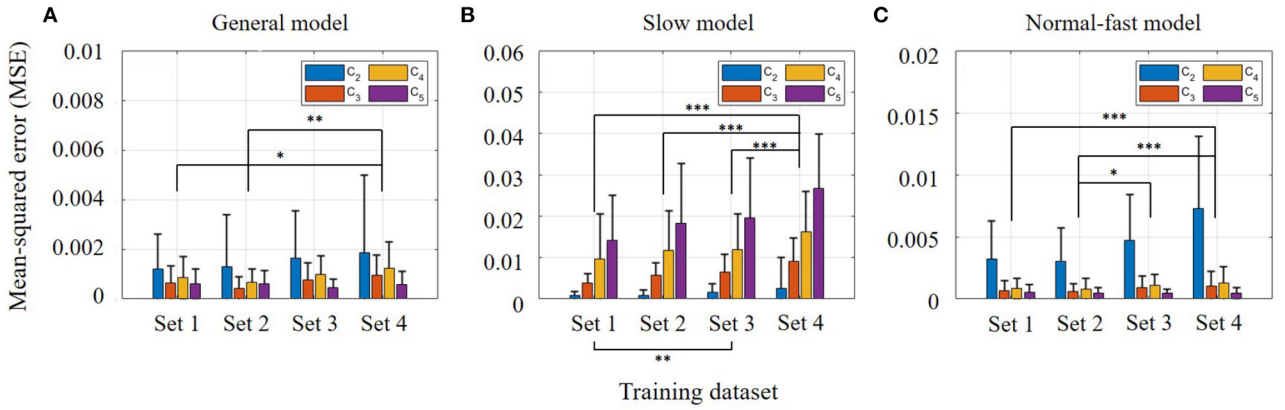

FIGURE 5 | Prediction results from three trained models: **(A)** General model using $C_2 - C_5$. **(B)** Slow model using only C_2 **(C)** Normal-fast model using $C_3 - C_5$. Bar graphs and error bars correspond to the mean and + 1SD. Bar colors correspond to walking speeds: $C_2 - C_5$.

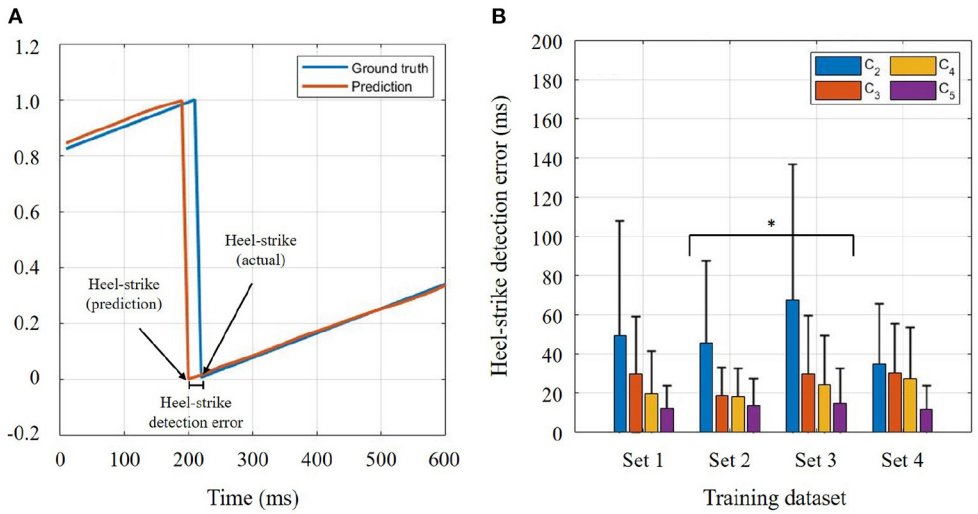

FIGURE 6 | Heel-strike detection error. **(A)** Temporal difference between actual heel-strike and predicted heel-strike. **(B)** Heel-strike detection error in four different speed conditions. The general model was chosen for the comparison. Bar graphs and error bars correspond to the mean and + 1SD. Bar colors correspond to walking speeds: C_2, C_3, C_4, and C_5.

and speed conditions ($p < 0.001$) were significant. According to the *post-hoc* comparison, only Sets 2 and 3 were significantly different ($p = 0.044$) in the training set condition. In **Figure 6B**, C_2 showed the highest error in the heel-strike detection ($p < 0.001$) compared to the other speed conditions. At the fast speed, the detection error was significantly reduced compared to C_3 ($p = 0.002$), but it was not significant compared to C_4 ($p = 0.076$). There was no significant difference between C_3 and C_4.

4. DISCUSSION

It is no doubt that thigh information is a key factor for human gait phase estimation (Quintero et al., 2018; Kang et al., 2019; Seo et al., 2019; Hong et al., 2021; Lee et al., 2021). Across all walking speeds, its robustness can also be shown in **Table 1**. On the other hand, it is obvious that the torso information has higher variability compared to the thigh information during walking. Owing to the fact that the torso segment's angular position showed even higher variability than the torso segment's angular velocity, we could assume that torso position information may hinder a successful estimation of the user's gait phase. Assuming Set 4 as a baseline, Sets 3 and 4 comparison tells the isolated effect of torso segment's angular position on gait phase estimation. To be more specific, when the torso position information was solely utilized with the thigh information, no apparent effect was found in the prediction result according to **Figure 5**. Likewise, the effect of the torso segment's angular velocity can be identified by the comparison between Sets 2 and 4. Unlike the torso position information, significant error

reductions were found in predicting the user's gait phase when torso velocity information was included in the training set. This implies that the torso segment's angular velocity is beneficial to gait phase estimation despite its relatively high variability compared to thigh information (as shown in **Table 1**). However, the heel-strike detection error result showed a different trend in the slow walking speed condition. Compared to Set 4, the heel-strike detection error became greater at slow speed (C_2) when any torso information was contained. This may imply that heel-strike detection is more sensitive to torso variability in slow-walking. Higher torso variability at slow speed (Dingwell and Marin, 2006) may hinder the accurate detection of the heel-strike. For other speeds, torso velocity information also showed a beneficial effect on gait phase estimation.

As we mentioned in section 2.3, we did not have much choice in the size of the sliding window for our model training. Since, the chosen dataset was collected on a walkway, it contained relatively short time-series data (compared to treadmill walking), including only a single gait cycle at most. We considered an alternative dataset, but the selected dataset contained an abundant number of subjects, which guaranteed to show individuals' variability. The chosen window size may affect the estimation accuracy, but we obtained sufficiently high accuracy in our estimation. To be fair with validating this claim, we implemented the same window size (i.e., 100) as our previous model (Lee et al., 2021) and compared its training results (i.e., MSE) to this study. As a result, there was no significant difference between them (Lee et al., 2021; 1.10E-02 vs. this study: 1.19E-02), thereby alleviating the concern about the window size. Furthermore, compared to Lee et al. (2021), we improved the estimation accuracy during the mid-stance phase at slow walking speed (i.e., C_2). In this work, we computed the mean-squared error during 30–50% of the gait cycle and compared it to the result of Lee et al. (2021). The prior model, Lee et al. (2021), yielded 9.88E-04 $\pm$ 8.47E-04, while the proposed model yielded 5.34E-04 $\pm$ 7.11E-04 in this study.

In future work, the authors plan to develop a user-adaptive gait phase estimator for enhancing an individual's gait trait adaptability. This is important for providing user-specific control of wearable devices based on user-specific gait estimation. This is because all individuals have their own gait traits, considering these traits is expected to give a better estimation of the individual. Also, we plan to implement a convolutional neural network (CNN) with LSTM to obtain faster estimation. The proposed method will be implemented to control a custom-built powered prosthesis. The authors have controlled the powered prosthesis using a phase variable, deriving from the user's thigh motion (Hong et al., 2021). Unlike the phase variable, a learning-based gait phase estimation utilized a plentiful dataset, so we could expect improved robustness, leading to more stable control of the prosthesis.

5. CONCLUSION

Torso information has been used for estimating the human gait phase, but its effect on the gait phase estimation has not been studied so far. We investigated the torso segment information effect by comparing the estimation results using four different datasets (i.e., Sets 1–4). As a result, the torso segment's angular velocity supported an accurate gait phase estimation for all walking speeds despite its relatively high variability compared to thigh information. On the other hand, the torso segment's angular position had no significant effect on the accurate estimation. As walking speed became slower, the torso variability increased, and lower accuracy was obtained. This study, therefore, showed the torso segment's angular velocity is more beneficial than the torso segment's angular position for gait phase estimation.

DATA AVAILABILITY STATEMENT

The datasets and the main code utilized for this study can be found in the GitHub repository for future development: https://github.com/ulim88/Frontiers-TorsoEffect.

AUTHOR CONTRIBUTIONS

WH is the primary contributor for the proposed concept, data analysis, and methodology. JL contributed for data analysis and methodology. PH served as the principal investigator. All authors contributed to writing and reviewing this article.

REFERENCES

Abaid, N., Cappa, P., Palermo, E., Petrarca, M., and Porfiri, M. (2013). Gait detection in children with and without hemiplegia using single-axis wearable gyroscopes. *PLoS ONE* 8, e73152. doi: 10.1371/journal.pone.0073152

A. Graves, J. S. (2005). Framewise phoneme classification with bidirectional lstm and other neural network architectures. *Neural Netw.* 18, 602–610. doi: 10.1016/j.neunet.2005.06.042

Alamdari, A., and Krovi, V. N. (2017). "Chapter 2 – A review of computational musculoskeletal analysis of human lower extremities," in *Human Modelling for Bio-Inspired Robotics,* eds J. Ueda and Y. Kurita (Academic Press), 37–73. doi: 10.1016/B978-0-12-803137-7.00003-3

Allseits, E., Lučarević, J., Gailey, R., Agrawal, V., Gaunaurd, I., and Bennett, C. (2017). The development and concurrent validity of a real-time algorithm for temporal gait analysis using inertial measurement units. *J. Biomech.* 55, 27–33. doi: 10.1016/j.jbiomech.2017.02.016

Anil Kumar, N., Hong, W., and Hur, P. (2020). "Impedance control of a transfemoral prosthesis using continuously varying ankle impedances and multiple equilibria," in *2020 IEEE International Conference on Robotics and Automation (ICRA)* (Paris), 1755–1761.

Asgari, M., Sanjari, M. A., Mokhtarinia, H. R., Sedeh, S. M., Khalaf, K., and Parnianpour, M. (2015). The effects of movement speed on kinematic variability and dynamic stability of the trunk in healthy individuals and low back pain patients. *Clin. Biomech.* 30, 682–688. doi: 10.1016/j.clinbiomech.2015.05.005

Cappozzo, A. (1981). Analysis of the linear displacement of the head and trunk during walking at different speeds. *J. Biomech.* 14, 411–425.

Ceccato, J.-C., De Sèze, M., Azevedo, C., and Cazalets, J. (2009). Comparison of trunk activity during gait initiation and walking in humans. *PLoS ONE* 4, e8193. doi: 10.1371/journal.pone.0008193

Dingwell, J. B., and Marin, L. C. (2006). Kinematic variability and local dynamic stability of upper body motions when walking at different speeds. *J. Biomech.* 39, 444–452. doi: 10.1016/j.jbiomech.2004.12.014

Gregg, R. D., Lenzi, T., Hargrove, L. J., and Sensinger, J. W. (2014). Virtual constraint control of a powered prosthetic leg: from simulation to experiments with transfemoral amputees. *IEEE Trans. Robot.* 30, 1455–1471. doi: 10.1109/TRO.2014.2361937

Hong, W., Anil Kumar, N., and Hur, P. (2021). A phase-shifting based human gait phase estimation for powered transfemoral prostheses. *IEEE Robot. Autom. Lett.* 6, 5113–5120. doi: 10.1109/LRA.2021.3068907

Hong, W., Paredes, V., Chao, K., Patrick, S., and Hur, P. (2019). "Consolidated control framework to control a powered transfemoral prosthesis over inclined terrain conditions," in *2019 IEEE International Conference on Robotics and Automation (ICRA)* (Montreal, QC), 2838–2844.

Jasiewicz, J. M., Allum, J. H., Middleton, J. W., Barriskill, A., Condie, P., Purcell, B., and Li, R. C. T. (2006). Gait event detection using linear accelerometers or angular velocity transducers in able-bodied and spinal-cord injured individuals. *Gait Posture* 24, 502–509. doi: 10.1016/j.gaitpost.2005.12.017

Kang, I., Kunapuli, P., and Young, A. J. (2019). Real-time neural network-based gait phase estimation using a robotic hip exoskeleton. *IEEE Trans. Med. Robot. Bionics* 2, 28–37. doi: 10.1109/TMRB.2019.2961749

Kawalec, J. S. (2017). "Chapter 12 – Mechanical testing of foot and ankle implants," in *Mechanical Testing of Orthopaedic Implants,* ed E. Friis (Woodhead Publishing), 231–253. doi: 10.1016/B978-0-08-100286-5.00012-3

Kerrigan, D. C., Riley, P. O., Lelas, J. L., and Della Croce, U. (2001). Quantification of pelvic rotation as a determinant of gait. *Arch. Phys. Med. Rehabil.* 82, 217–220. doi: 10.1053/apmr.2001.18063

Kotiadis, D., Hermens, H. J., and Veltink, P. H. (2010). Inertial gait phase detection for control of a drop foot stimulator: inertial sensing for gait phase detection. *Med. Eng. Phys.* 32, 287–297. doi: 10.1016/j.medengphy.2009.10.014

Lee, H., Rouse, E. J., and Krebs, H. I. (2016). Summary of human ankle mechanical impedance during walking. *IEEE J. Transl. Eng. Health Med.* 4, 1–7. doi: 10.1109/JTEHM.2016.2601613

Lee, J., Hong, W., and Hur, P. (2021). Continuous gait phase estimation using lstm for robotic transfemoral prosthesis across walking speeds. *IEEE Trans. Neural Syst. Rehabil. Eng.* 29, 1470–1477. doi: 10.1109/TNSRE.2021.3098689

Mannini, A., Genovese, V., and Sabatini, A. M. (2013). Online decoding of hidden markov models for gait event detection using foot-mounted gyroscopes. *IEEE J. Biomed. Health Inf.* 18, 1122–1130. doi: 10.1109/JBHI.2013.2293887

Quintero, D., Villarreal, D. J., Lambert, D. J., Kapp, S., and Gregg, R. D. (2018). Continuous-phase control of a powered knee–ankle prosthesis: amputee experiments across speeds and inclines. *IEEE Trans. Robot.* 34, 686–701. doi: 10.1109/TRO.2018.2794536

Rouse, E. J., Hargrove, L. J., Perreault, E. J., and Kuiken, T. A. (2014). Estimation of Human Ankle Impedance During the Stance Phase of Walking. *IEEE Trans. Neural Syst. Rehabil. Eng.* 22, 870–878. doi: 10.1109/TNSRE.2014.2307256

Sawicki, G. S., Beck, O. N., Kang, I., and Young, A. J. (2020). The exoskeleton expansion: improving walking and running economy. *J. NeuroEng. Rehabil.* 17, 1–9. doi: 10.1186/s12984-020-00663-9

Schreiber, C., and Moissenet, F. (2019). A multimodal dataset of human gait at different walking speeds established on injury-free adult participants. *Sci. Data* 6, 1–7. doi: 10.1038/s41597-019-0124-4

Seo, K., Park, Y. J., Lee, J., Hyung, S., Lee, M., Kim, J., et al. (2019). "Rnn-based on-line continuous gait phase estimation from shank-mounted imus to control ankle exoskeletons," in *2019 IEEE 16th International Conference on Rehabilitation Robotics (ICORR)* (Toronto, ON), 809–815.

S. Hochreiter, J. S. (1997). Long short-term memory. *Neural Comput.* 9, 1735–1780.

Shorter, A. L., and Rouse, E. J. (2018). Mechanical impedance of the ankle during the terminal stance phase of walking. *IEEE Trans. Neural Syst. Rehabil. Eng.* 26, 135–143. doi: 10.1109/TNSRE.2017.2758325

Taborri, J., Palermo, E., Rossi, S., and Cappa, P. (2016). Gait partitioning methods: a systematic review. *Sensors* 16, 66. doi: 10.3390/s16010066

Thorstensson, A., Nilsson, J., Carlson, H., and Zomlefer, M. R. (1984). Trunk movements in human locomotion. *Acta Physiologica Scandinavica* 121, 9–22. doi: 10.1111/j.1748-1716.1984.tb10452.x

Vu, H. T. T., Dong, D., Cao, H.-L., Verstraten, T., Lefeber, D., Vanderborght, B., et al. (2020). A review of gait phase detection algorithms for lower limb prostheses. *Sensors* 20, 3972. doi: 10.3390/s20143972

Conflict of Interest: The authors declare that the research was conducted in the absence of any commercial or financial relationships that could be construed as a potential conflict of interest.

frontiers | Frontiers in Neurorobotics

ORIGINAL RESEARCH
published: 30 May 2022
doi: 10.3389/fnbot.2022.790070

Evaluating Knee Mechanisms for Assistive Devices

Shawanee' Patrick[1†], *Namita Anil Kumar*[1†] *and Pilwon Hur*[1,2*]

[1] Department of Mechanical Engineering, Texas A&M University, College Station, TX, United States, [2] Department of Mechanical Engineering, Gwangju Institute of Science and Technology, Gwangju, South Korea

State-of-the-art knee braces use a polycentric mechanism with a predefined locus of the instantaneous center of rotation (centrode) and most exoskeleton devices use a knee mechanism with a single axis of rotation. However, human knees do not share a common centrode nor do they have a single axis. This leads to misalignment between the assistive device's joint axis and the user's knee axis, resulting in device migration and interaction forces, which can lead to sores, pain, and abandonment of the device over time. There has been some research into self-aligning knee mechanisms; however, there is a lack of consensus on the benefit of these mechanisms. There is no research that looked purely at the impact of the knee mechanisms, either. In this article, we compare three different knee brace mechanisms: single axis (SA), polycentric with predefined centrode (PPC), and polycentric with a self-aligning center of rotation (PSC). We designed and conducted an experiment to evaluate different joint mechanisms on device migration and interaction forces. Brace material, weight, size, cuff design, fitment location, and tightness were consistent across trials, making the knee joint mechanism the sole variable. The brace mechanisms had no significant effect on walking kinematics or kinetics. However, the PPC brace had greater interaction forces on the top brace strap than the SA and PSC. The PSC and SA had significantly lower interaction forces on the bottom strap compared to the PPC brace. The PSC had significantly less migration than both the SA and PPC braces. These results show that a PPC mechanism may not be beneficial for a wide range of users. This also shows that the PSC mechanisms may improve mechanism alignment and lessen device migration.

Keywords: knee mechanism, interaction forces, polycentric, migration, orthoses, rehabilitation, assistive devices, gait

OPEN ACCESS

Edited by:
Domenico Prattichizzo, University of Siena, Italy

Reviewed by:
Wen Qi, Politecnico di Milano, Italy
Jorge Hugo Villafañe, Fondazione Don Carlo Gnocchi Onlus (IRCCS), Italy
Maria Pozzi, University of Siena, Italy

***Correspondence:**
Pilwon Hur
pilwonhur@gist.ac.kr

[†] *These authors have contributed equally to this work and share first authorship*

Received: *06 October 2021*
Accepted: *07 April 2022*
Published: *30 May 2022*

Citation:
Patrick S, Anil Kumar N and Hur P (2022) Evaluating Knee Mechanisms for Assistive Devices. Front. Neurorobot. 16:790070. doi: 10.3389/fnbot.2022.790070

1. INTRODUCTION

The human knee is not a simple pin joint; instead, the femur rotates and slides on the tibia as it flexes or extends (Morrison, 1970). This results in a joint with a varying center of rotation. At any time, the joint's axis is termed the Instantaneous Center of Rotation (ICR) and the locus of the ICR is called the centrode. Exoskeleton joint design typically requires that the joint's axis be coincident with the user's knee axis. Designing an exoskeleton knee joint that accurately tracks the user's ICR is a mighty task, and it is further compounded by the fact that the centrode is unique to the user. Although knee assistive devices have existed since the 1960s, the aforementioned challenge persists. In this article, we will investigate different solutions to this challenge in a human subject experiment.

1.1. Solutions to Knee Joint Design

The Single Axis (SA) joint knee mechanism is the simplest design to manufacture and actuate in powered devices. However, the misalignment between the device joint axis and the user's knee axis is unavoidable, which can lead to increased interaction forces and device migration (Regalbuto et al., 1989). High interaction forces may result in skin sores, additional pain, or injuries (Chen et al., 2016; Gorgey, 2018). Studies such as Pierrat et al. (2015), Anil Kumar et al. (2019), Serrancoli et al. (2019) have shown that interaction forces are strongly related to safety, comfort, and quality of walking with lower limb orthotics/exoskeletons.

Some researchers have implemented polycentric knee mechanisms, which are of two types: (i) Polycentric mechanism with a Predefined Centrode (PPC) and (ii) Polycentric mechanism with a Self-aligning Center of rotation (PSC). PPC solutions either adopt a centrode that is believed to suit a diverse group of users (Bertomeu et al., 2007) or customize the centrode to the user (Supan, 2019). The most commonly implemented PPC mechanism has meshed spur gears with a third link connecting the centers of the gears (Lee et al., 2020) (also refer to **Figure 1C**). Other PPC joint designs employ cam mechanisms (Bertomeu et al., 2007; Kapci and Unal, 2019). Despite efforts to establish a generalized centrode for a large user base, discrepancies are to be expected. On acknowledging this, some researchers chose to customize the gear or cam mechanism (thereby the associated centrode) to the user (Supan, 2019). While the performance with customized joints is expected to be better, the process of designing and manufacturing custom joints can be highly demanding. Researchers, thus, support using PSC joints which are believed to suit a diverse group of users. Though instances of PSC joints exist in the literature (Stienen et al., 2009; Celebi et al., 2013; Cai et al., 2016; Choi et al., 2016), their public usage is very limited with the likely reason being a lack of consensus and data on the performance of PSC joints. In this article, we will strive to resolve this dilemma by comparing all three types of joint designs (i.e., SA, PPC, and PSC).

1.2. Evaluating Knee Brace Mechanisms

Studies such as Brownstein (1998) have examined how different knee brace designs impact migration. While the designs belonged to the PPC category, they all varied in size, material, nature of fit, and cuff design. Work by Regalbuto et al. (1989) evaluated different joint mechanisms by observing the interaction forces at the straps of custom brace cuffs. However, the study did not look at the self-aligning joints or device migration. To our knowledge, no study has compared different joint mechanisms on the basis of interaction forces and migration. Moreover, the studies (Regalbuto et al., 1989; Brownstein, 1998) do not account for variances in the brace fitment (i.e., tightness of the cuffs) at the beginning of each trial, which heavily influences the performance of the brace. In order to perform a controlled analysis of the joint mechanisms, we must hold constant the material, weight, size, cuff design, and tightness of fit. Current experimental protocols do not account for the impact of the previously mentioned variables and limit their performance metrics to primarily device migration. Thus, there is significant room for improvement in designing experiment protocols for joint mechanism comparison. In this article, we will fill this gap in knowledge by proposing a systematic experiment protocol that evaluates both device migration and interaction forces.

Our primary contributions include: (i) the experiment protocol for evaluating different knee mechanisms, (ii) a novel PSC design inspired by Cai et al. (2016), and (iii) evidence that will help identify the superior joint mechanism design. The article is organized as follows. Section 2 presents the experiment setup, protocol, and details on the recruited subjects. The results are presented in Section 3 followed by the discussion in Section 4. The final section consists of our concluding remarks.

2. MATERIALS AND METHODS

We designed an experiment to evaluate different joint mechanisms on device migration and interaction forces. The variables accounted for were brace material, weight, size, cuff design, fitment location, and tightness. The first four and the last two variables were considered in the experiment setup and testing protocol, respectively.

2.1. Participants

Twelve healthy subjects were recruited. The method of determining outliers has been detailed in Section 2.3. Out of the 12 subjects, one was deemed an outlier and another subject was omitted from the study due to a failure in data collection. The results presented pertain to 10 healthy participants (age 28 $\pm$ 2.5 years, mass 70.5 $\pm$ 11.2 kg, height 171.3 $\pm$ 5 cm, 7 men and 3 women). Individual participant details can be found in **Table 1**. The experimental protocol was explained beforehand, and each subject signed an informed consent approved by Institutional Review Board (IRB) at Texas A&M University (TAMU IRB2018-0837D).

2.2. Experimental Setup

Compression braces, such as VIVE (Vive, 2021), consist of a fabric sleeve with slots on both sides of the knee for a geared PPC mechanism. **Figure 1A** shows the VIVE brace and highlights the slot for the mechanism (*mechanism-slot*). Such braces have the benefit of the mechanism being removable, allowing us to swap and test different mechanisms. We procured four VIVE braces and designed different Polylactic acid (PLA) 3D printed mechanisms to fit the brace's *mechanism-slot*. **Figure 1** presents all four braces. The brace in **Figure 1A** had no constraining mechanism and served as our control case, while **Figure 1B** was the SA version. **Figure 1C** was the PPC mechanism that was included with the VIVE brace. **Figure 1D** is a novel PSC joint consisting of a single axis joint at the knee, a linear allowance at the top of the *mechanism-slot* (hashed green region), and a radial allowance at the bottom of the *mechanism-slot* (hashed green region). This design draws inspiration from the easy-to-manufacture design proposed in Cai et al. (2016). The design was optimized through kinematic analysis of different brace PSC designs using Solidworks. Said analysis involved a four-bar approximation of the human knee in the sagittal plane (refer to **Figure 2**). The length of the linkages was the average of the results reported in Pons et al. (2007). **Figure 2B** shows the final

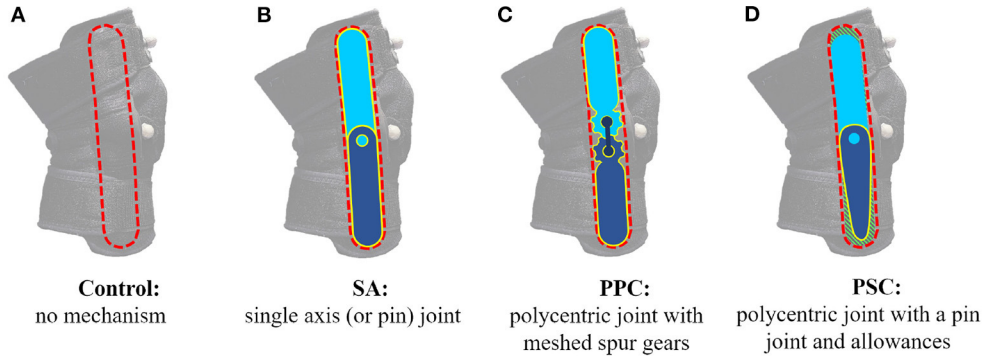

FIGURE 1 | Knee brace mechanisms: **(A)** *Control* brace with no mechanism, **(B)** single axis (SA) brace with a single axis mechanism, **(C)** polycentric mechanism with a predefined centrode (PPC) brace with a polycentric mechanism having spur gears, and **(D)** polycentric mechanism with a self-aligning center of rotation (PSC) brace with a polycentric mechanism with allowances.

TABLE 1 | Individual details for the final 10 participants.

Participant	Mass (kg)	Height (cm)	Age	BMI	Knee width (cm)	Sex
1	59.3	170.2	28.0	20.5	10.1	M
2	51.0	164.0	28.0	19.0	9.3	F
3	74.7	180.3	27.0	23.0	10.4	M
*4	85.3	177.8	26.0	27.0	10.2	M
5	65.2	172.7	28.0	21.9	9.7	M
6	69.7	169.5	27.0	24.2	11.2	F
7	71.0	170.0	32.0	24.6	11.2	M
8	79.9	172.7	30.0	26.8	11.3	F
9	63.2	166.0	23.0	22.9	9.8	M
10	85.3	170.0	30.0	29.5	12.0	M
Average	70.5	171.3	27.9	23.9	10.5	F - 3
Standard deviation	11.2	4.9	2.5	3.2	0.9	M - 7

**Not included in kinetic and kinematic analysis.*

PSC design acting in parallel with the human knee simulation. The thigh cuff was constrained to not move while the shank cuff was allowed to slide (or migrate) along the limb. The PSC design was optimized as follows: (i) vary the magnitude of allowance (ii) flex the simulated human knee to 70° and measure the device migration along the shank (iii) repeat steps (i) and (ii) until the device migration is minimal. The optimal design shown in **Figure 1D** has allowances of 5 mm. Notice that the SA, PPC, and PSC braces only vary in the joint mechanism.

All braces were fitted with two Tekscan FlexiForce A502 flexible force sensors (**Figure 3B**) which served to measure the interaction forces at the user's thigh and shank. These locations were chosen for two reasons: (i) they are along with the knee brace straps–where interaction forces are expected to be the highest; (ii) the mounted force sensors would always be in contact with the participant's limb. Unlike the sides of the brace, the front section is not always in contact with the participant's limb, making this spot not ideal for measuring interaction force. Specifically, this section of the brace separates from the limb (forming a gap) during knee flexion. The sensor readings were collected and transmitted using a wireless processing unit consisting of an Arduino Micro and XBee Pro wireless module. The unit was affixed to a vest worn around the participant's torso. The receiver unit consisted of an XBee Pro wireless module and an Arduino Uno, which transmitted the received data to a computer for storing. The experiment included walking on an instrumented treadmill (Force-sensing treadmill, AMTI, Watertown, MA AMTI, 2021) in a motion capture facility that uses 46 motion capture cameras (Vantage, Vicon Motion Systems, Oxford, UK Vicon, 2021). Reflective markers were placed on bony landmarks of the pelvis, lateral knee joint, toe, heel, and ankle. Additional markers were placed on the thigh, tibia, and front of the brace. The marker placement can be seen in **Figure 3A**.

2.3. Experiment Protocol

Each participant was instructed to wear workout leggings or tights and tennis shoes. The participants were then asked to wear the Control brace tightened to their comfort. Once worn, the brace position was marked with tape on the thigh. Each participant was then given a period of 2 min to get accustomed to the brace, during which they were asked to walk at a comfortable pace and raise their knee. After the 2-min period, device migration was measured by the distance from the top of the brace to the top of the tape (refer to **Figure 4**). If the device migration exceeded 1 cm, the brace was re-attached and the process was restarted. If participants failed the < 1 cm device migration requirement after three attempts, they were ruled as an outlier and were omitted from the study. Such participants were expected to experience even larger device migration and consequently discomfort during the rest of the trial which consisted of higher paced walking trials and several knee raises. Typically, participants with a more tapered lower limb (i.e., a larger ratio of the above knee to below knee diameter) were found to be outliers. Once a suitable fitment was determined, the position of the brace was marked using the tape. All other braces that followed were mounted at the same position, fixing the point of fitment across all trials.

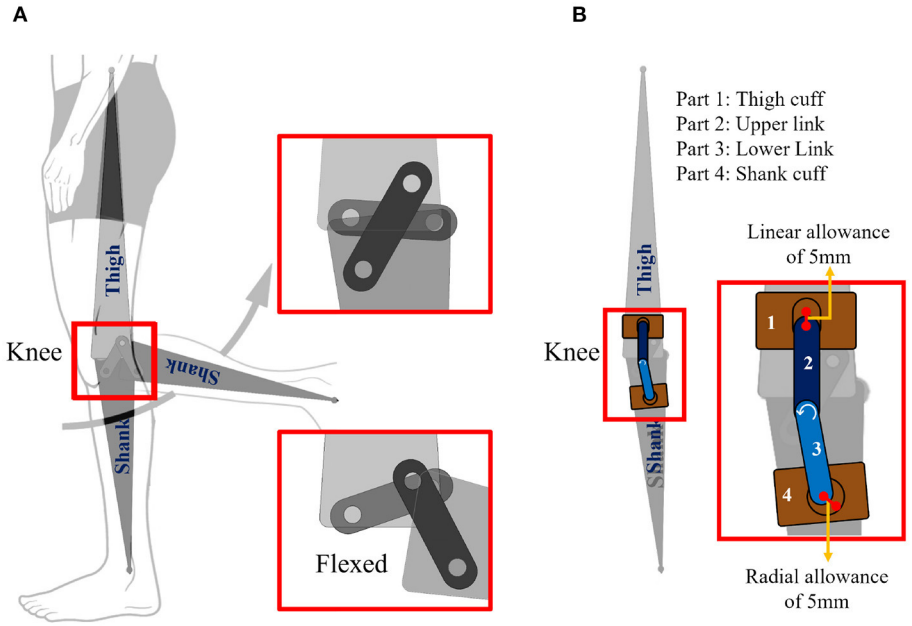

FIGURE 2 | (A) Four-bar simulation of the human knee. **(B)** Proposed PSC mechanism.

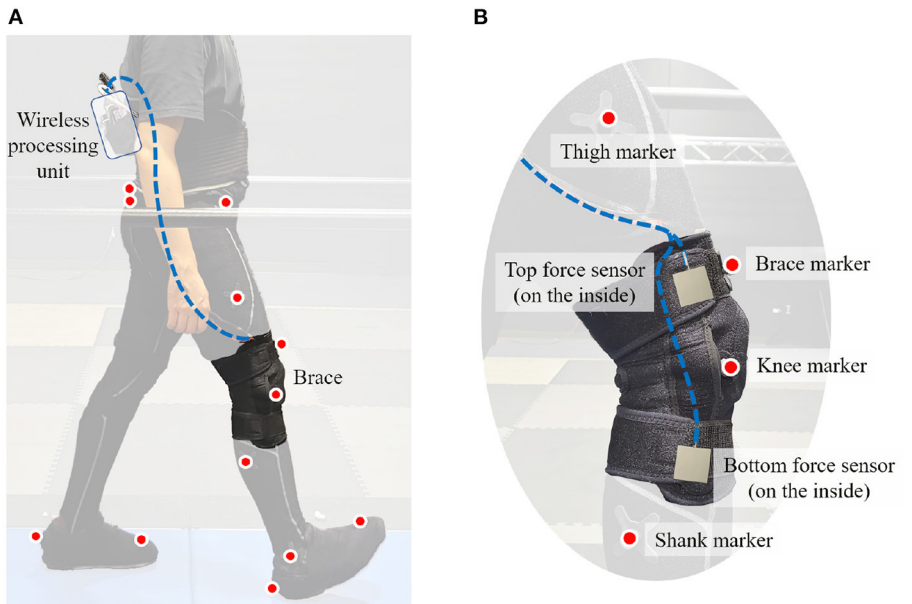

FIGURE 3 | Experiment setup: **(A)** Subject with markers and a brace, **(B)** markers and sensors mounted on the brace.

The order of the constrained braces (i.e., SA, PPC, and PSC) that followed was randomized. During the first constrained brace trial, the tightness of fit was measured using the force sensors. The force readings at the bottom and top force sensors were referred to as f^0_{bottom} and f^0_{top}. The constrained braces that followed were then fitted to within ± 1 N of said measured forces. While measuring forces, participants were asked to stand erect and still. This procedure standardized the tightness of fit across all constrained braces. Note that the forces were not measured for the Control brace because the absence of a constraining mechanism always resulted in a lower force reading.

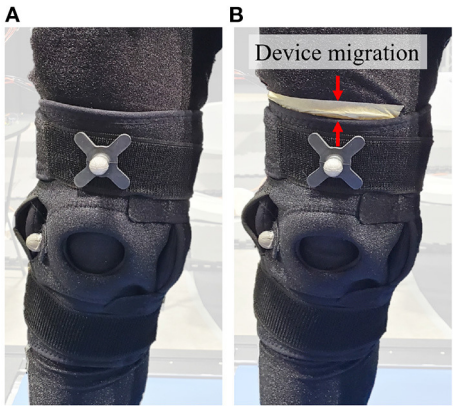

FIGURE 4 | Device Migration, **(A)** the brace at the beginning of the trial, **(B)** the brace at the end of the trial with the white tape marking the reference for measuring device migration. Red arrows show device migration as labeled on the figure.

FIGURE 5 | Each trial consisted of 20 leg raises, followed by 7 min of walking at 1.23 m/s speed, and concluded with another 20 leg raises.

Once fitted with each brace, the participants were asked to perform an exercise regime that included 20 knee raises, 7 min of fast walking at 1.23 m/s, and 20 more knee raises (refer to **Figure 5**). Motion marker data were collected before knee raises, during walking (to monitor walking quality), and after knee raises. The force sensor readings were gathered throughout the trial. Due to the data being used to assess the potential impact of walking assistive devices, the exercise routine was designed not to be labor intensive. The goal was to see the impact primarily during walking. Device migration was measured after the exercise routine for each brace device.

2.4. Metrics and Data Analysis

Three metrics were used to compare the knee braces: (i) device migration; (ii) maximum interaction force at the bottom and top force sensors; (iii) knee angles and moments during walking.

The device migration, M_i, for each constrained brace (i = SA, PPC, PSC) was defined as follows

$$M_i = \frac{m_i - m_{Control}}{m_{Control}} \tag{1}$$

where m_i is the raw (un-normalized) migration for each constrained brace (i = SA, PPC, PSC) and $m_{Control}$ is the migration with the Control brace. The normalization process helps account, to some extent, for the impact of the compression sleeve on device migration, leaving behind the impact of the mechanism alone. The set of normalized migration values for each brace, across all subjects, was checked for normality using the Shapiro-Wilk test ($\alpha = 0.05$, *scipy*'s *stats* library for Python). One-way repeated measures ANOVA was used to find the effect of the knee mechanism on device migration ($\alpha = 0.05$, the *statsmodels* library for Python). *Post-hoc* tests used Fisher's least significant difference. Note that the device migration with the constrained mechanisms was not compared against the Control brace. Device migration with the Control brace is known to be lesser than the constrained ones and the objective of this article is to compare different constraining mechanisms.

The force values were first filtered using a Butterworth low pass filter with a cut-off frequency of 10 Hz, following which the maximum value was determined. Let f^*_{bottom} and f^*_{top} be the maximum force values at the bottom and top sensor, respectively. These values were then normalized for each constrained brace as follows.

$$F^*_{bottom} = \frac{f^*_{bottom} - f^0_{bottom}}{f^0_{bottom}} \tag{2}$$

F^*_{top} was calculated in a similar manner. Similar to M_i, the set of all normalized force values was also checked for normality. A significant effect of the mechanism on force values was found *via* one-way repeated measures ANOVA, followed by the *post-hoc* tests with Fisher's least significant difference.

The joint angles and moments were derived using motion capture and forces collected with the AMTI instrumented treadmill and processed with the Vicon Nexus analysis system. The moments and angles were averaged for each participant for 30 s of the 7-min walking trial in each brace. The braced knee angle is determined to be the angle between the thigh and shank segments with the leg fully extended being 0 degrees. The range of motion for each braced knee was termed the difference between the maximum and minimum knee angle in each walking trial. These values were, averaged across all participants for each brace. The result was called the average range of motion. The braced knee moments were derived using inverse dynamics with the Vicon Nexus Plug-in Gait Model, after which the peak sagittal plane knee moments were determined. We checked if the nature of the brace mechanism impacted the peak knee moments and the knee ranges of motion using one-way repeated-measures ANOVA.

3. RESULTS

The following subsections present the results for the final 10 subjects in **Table 1**. **Figures 6**, **7** present the knee angle and knee moment results, respectively. The normalized device migration and interaction force values have been shown in **Figure 8**.

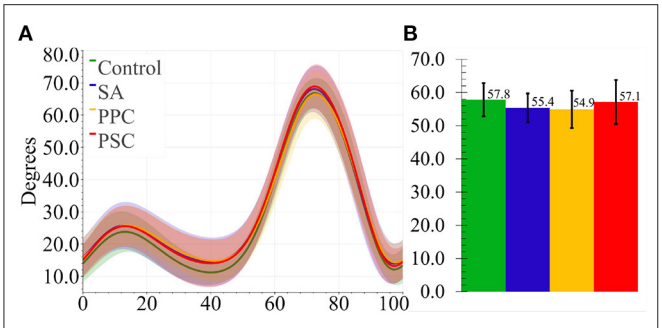

FIGURE 6 | (A) Average knee angles for all four braces. The shaded region represented 1 SD. **(B)** Average knee range of motion for all braces. The ticks represent 1 SD.

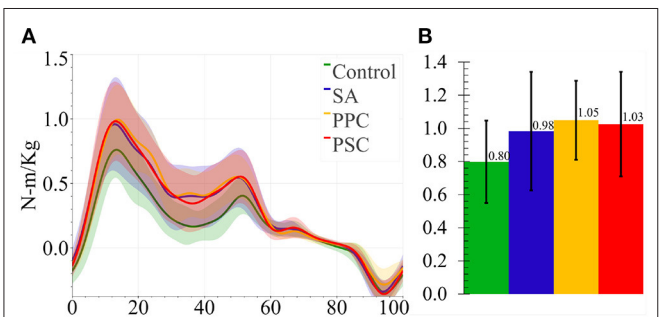

FIGURE 7 | (A) Average knee moments for all four braces. The shaded region represented 1 SD. **(B)** Average peak knee moment for all braces. The ticks represent 1 SD.

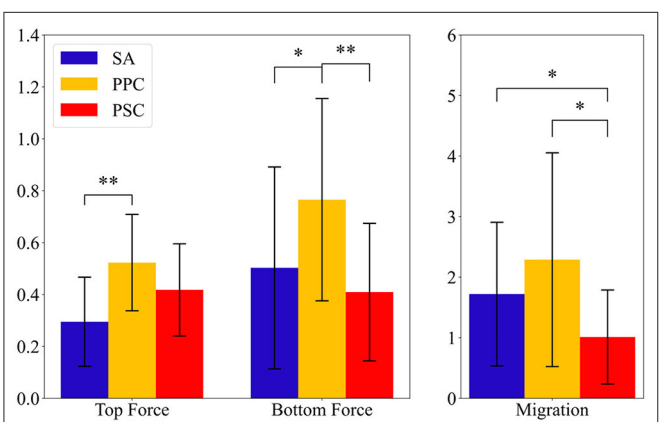

FIGURE 8 | Average interaction force at the top and bottom force sensors and average device migration results. The ticks represent 1 SD. The symbol * signifies $p < 0.05$ and ** implies $p < 0.005$.

3.1. Kinematics and Kinetics

Data from Participant 4 was not processed for biomechanical analysis due to an error in the data collection, leaving 9 participants' knee angles and moments to be analyzed. The ANOVA test revealed that the bracing mechanism did not significantly impact the knee range of motion ($p = 0.51$) (refer to **Figure 6**) nor the knee moments ($p = 0.276$) (refer to **Figure 7**).

3.2. Brace Migration and Interaction Forces

The Shapiro–Wilk test revealed the normality hypothesis cannot be dismissed for migration data ($p > 0.109$ across all braces), top force sensor readings ($p > 0.205$ across all braces), and bottom force sensor readings ($p > 0.135$ across all braces). The one-way repeated measures ANOVA revealed that the type of mechanism significantly affects device migration ($p = 0.0043$), top force sensor readings ($p = 0.007$), and bottom force sensor readings ($p = 0.0029$). The SA and PPC brace had significantly more migration than the PSC brace with $p = 0.022$ and $p = 0.007$, respectively. Although the device migration with SA was lower than that of PPC, the difference was not significant. The interaction forces on the top of the PPC brace were found to be significantly greater than the SA brace ($p = 0.004$). The interaction forces on the bottom strap for the PPC brace were found to be significantly greater than both the SA ($p = 0.016$) and PSC braces ($p = 0.005$). These results can be seen in **Figure 8**.

4. DISCUSSION

The brace type had no significant effect on the knee range of motion. This showed that none of the braces significantly altered walking gait kinematics. On the other hand, the knee moments with the Control brace were significantly lower than those with the other braces, which can be attributed to the absence of a constraining mechanism in the Control brace. In other words, the participants had to exert additional knee moments or work to overcome the constraints. Among the constrained mechanisms, no significant differences were observed. Thus, any observations made regarding device migration and interaction forces are solely due to the nature of the constraining mechanism and not the walking kinematics or kinetics.

In regards to device migration, SA performed better–but not significantly better–than PPC. The SA brace did however result in significantly lower interaction forces than PPC at both the top and bottom force sensor. We may infer that having a polycentric design alone is insufficient to perform better than SA mechanisms. However, the same polycentric design could perform better with certain types of knees over others. Going forward, we wish to investigate the relationship between knee widths and the performance (in terms of migration and interaction forces) of PPC mechanisms. If a relationship does exist, designers can use it to customize PPC designs to sections of the user population.

The PSC mechanism had significantly lower device migration than both SA and PPC, proving the benefits of self-aligning mechanisms. It also registered lower interaction forces than PPC at both the top and bottom force sensors, with the one at the bottom being significantly different. On the other hand, the interaction forces with PSC were not significantly different from those of SA. We believe that the force readings pertaining to PSC were an overestimate. The design of the PSC mechanism is such that it moves within the *mechanism-slot*, which can incur additional shearing forces. It is, thus, likely that the actual

interaction forces with PSC are lower than the ones observed in this study. Our working hypothesis is that the interaction forces and device migration are correlated and that the PSC would outperform both SA and PPC per both metrics. Future study includes designing braces wherein the mechanism is placed away from the force sensors.

We also wish to improve the force sensing mechanism. The current mechanism only measures forces at the side of the thigh and shank. Studies such as Rossi et al. (2010) have measured forces around the limb using multiple pressure sensors along the curvature of the strap. Finally, we also hope to expand the study to include participants with more tapered limbs (i.e., greater ratio of above knee diameter to below knee diameter).

5. CONCLUSION

We propose an experiment protocol and analysis that compares the impact of knee mechanisms on interaction forces, migration, knee angles, and moments. This experiment protocol standardized the weight, material, and tightness of straps across all mechanisms. We compared three mechanisms: (i) Single axis (SA), (ii) Polycentric joint with a Predefined Centrode, and (iii) Polycentric joint with a Self-aligning Center of rotation (PSC). Although initially thought to increase interaction forces and migration, the SA mechanism produced consistently fewer interaction forces than the PPC mechanism. Thus, PPC mechanisms are not guranteed to lessen the mismatch between the mechanism and the user's knee. The PSC mechanism resulted in the least migration out of all the mechanisms. The forces with PSC were, significantly less than the PPC brace on the bottom strap. The significantly lesser migration of the PSC brace shows that it can assist in reducing the joint mismatch between the mechanism and knee. This gives us evidence supporting the use of PSC mechanisms in orthotics and exoskeletons. If researchers continue to use PPC mechanisms there needs to be further research on customizing the joint to improve alignment and overall performance.

DATA AVAILABILITY STATEMENT

The raw data supporting the conclusions of this article will be made available by the authors, without undue reservation.

ETHICS STATEMENT

The studies involving human participants were reviewed and approved by Texas A&M Institutional Review Board. The patients/participants provided their written informed consent to participate in this study.

AUTHOR CONTRIBUTIONS

SP and NA contributed equally to this work. PH was the PI for this study. All authors contributed to the article and approved the submitted version.

REFERENCES

AMTI (2021). *AMTI Force-Sensing Tandem Treadmill*. Available online at: https://amti.biz/ (accessed on October 5, 2021).

Anil Kumar, N., Patrick, S., and Hur, P. (2019). "Pilot study on the needs of prospective exoskeleton users with impaired mobility," in *Proceedings of IEEE Workshop on Advanced Robotics and its Social Impacts, ARSO 2019-October* (Beijing: IEEE), 106–111.

Bertomeu, J. M. B., Lois, J. M. B., Guillem, R. B., Del, P.ozo, Á. P., Lacuesta, J., Mollà, C. G., et al. (2007). Development of a hinge compatible with the kinematics of the knee joint. *Prosthet. Orthot. Int.* 31, 371–383. doi: 10.1080/03093640601095842

Brownstein, B. (1998). *Migration and Design Characteristics of Functional Knee Braces*. Technical report.

Cai, V. A. D., Bidaud, P., Hayward, V., and Gosselin, F. (2016). Self-adjustment mechanisms and their application for orthosis design. *Meccanica* 52, 713–728. doi: 10.1007/s11012-016-0574-0

Celebi, B., Yalcin, M., and Patoglu, V. (2013). "AssistOn-knee: a self-aligning knee exoskeleton," in *IEEE International Conference on Intelligent Robots and Systems* (Tokyo: IEEE), 996–1002.

Chen, B., Ma, H., Qin, L.-Y., Gao, F., Chan, K.-M., Law, S.-W., et al. (2016). Recent developments and challenges of lower extremity exoskeletons. *J. Orthopaedic Transl.* 5, 26–37. doi: 10.1016/j.jot.2015.09.007

Choi, B., Lee, Y., Kim, J., Lee, M., Lee, J., Roh, S.-,g., et al. (2016). "A self-aligning knee joint for walking assistance devices," in *2016 38th Annual International Conference of the IEEE Engineering in Medicine and Biology Society (EMBC)* (Orlando, FL: IEEE), 2222–2227.

Gorgey, A. S. (2018). Robotic exoskeletons: the current pros and cons. *World J. Orthop.* 9, 112–119. doi: 10.5312/wjo.v9.i9.112

Kapci, M. F., and Unal, R. (2019). "Design of bio-joint shaped knee exoskeleton assisting for walking and sit-to-stance," in Wearable *Robotics: Challenges and Trends*, eds M. C. Carrozza, S. Micera, and J. L. Pons (Cham: Springer International Publishing), 495–499.

Lee, T., Lee, D., Song, B., and Baek, Y. S. (2020). Design and control of a polycentric knee exoskeleton using an electro-hydraulic actuator. *Sensors* 20, 211. doi: 10.3390/s20010211

Morrison, J. B. (1970). The mechanics of the knee joint in relation to normal walking. *J. Biomech.* 3, 51–61. doi: 10.1016/0021-9290(70)90050-3

Pierrat, B., Millot, C., Molimard, J., Navarro, L., Calmels, P., Edouard, P., et al. (2015). Characterisation of knee brace migration and associated skin deformation during flexion by full-field measurements. *Exp. Mech.* 55, 349–360. doi: 10.1007/s11340-014-9947-2

Pons, J., Moreno, J., Brunetti, F., and Rocon, E. (2007). "Lower-limb wearable exoskeleton," in *Rehabilitation Robotics, Chapter 26*, ed S. S. Kommu (Rijeka: IntechOpen).

Regalbuto, M., Rovick, J., and Walker, P. (1989). The forces in a knee brace as a function of hinge design and placement. *Am. J. Sports Med.* 17, 535–543. doi: 10.1177/036354658901700415

Rossi, S. M. M. D., Vitiello, N., Lenzi, T., Ronsse, R., Koopman, B., Persichetti, A., et al. (2010). Sensing pressure distribution on a lower-limb exoskeleton physical human-machine interface. *Sensors* 11, 207–227. doi: 10.3390/s110100207

Serrancoli, G., Falisse, A., Dembia, C., Vantilt, J., Tanghe, K., Lefeber, D., et al. (2019). Subject-exoskeleton contact model calibration leads to accurate interaction force predictions. *IEEE Trans. Neural Syst. Rehabil. Eng.* 27, 1597–1605. doi: 10.1109/TNSRE.2019.2924536

Stienen, A. H., Hekman, E. E., van der Helm, F. C., and van der Kooij, H. (2009). Self-aligning exoskeleton axes through decoupling of joint rotations

and translations. *IEEE Trans. Rob.* 25, 628–633. doi: 10.1109/TRO.2009.2019147

Supan, T. J. (2019). "Principles of fabrication," in *Atlas of Orthoses and Assistive Devices, 5th Edn*, eds J. B. Webster and D. P. Murphy (Philadelphia, PA: Elsevier), 42.e1–48.e1.

Vicon (2021). *Vicon Motion Capture System, Vantage*. Available online at: https://www.vicon.com/hardware/cameras/vantage/ (accessed on October 5, 2021).

Vive, H. (2021). *Hinged Knee Brace-Open Compression Support-Vive Health*. Available online at: https://www.vivehealth.com/products/hinged-knee-brace (accessed on October 5, 2021).

Conflict of Interest: The authors declare that the research was conducted in the absence of any commercial or financial relationships that could be construed as a potential conflict of interest.

Publisher's Note: All claims expressed in this article are solely those of the authors and do not necessarily represent those of their affiliated organizations, or those of the publisher, the editors and the reviewers. Any product that may be evaluated in this article, or claim that may be made by its manufacturer, is not guaranteed or endorsed by the publisher.

frontiers | Frontiers in Neurorobotics

ORIGINAL RESEARCH
published: 30 May 2022
doi: 10.3389/fnbot.2022.790020

Semiactive Knee Orthotic Using a MR Damper and a Smart Insole to Control the Damping Force Sensing the Plantar Pressure

David Alvarado-Rivera[1], *Paola A. Niño-Suárez*[1]* *and Leonel G. Corona-Ramírez*[2]

[1] *Instituto Politécnico Nacional, Escuela Superior de Ingeniería Mecánica y Eléctrica, México City, Mexico,* [2] *Instituto Politécnico Nacional, Unidad Profesional Interdisciplinaria en Ingeniería y Tecnologías Avanzadas, México City, Mexico*

This work presents the development of semiactive knee orthosis prototype that focus to absorb the forces and impacts in this joint during the human gait. This prototype consists of three subsystems: the first is a wireless and portable system capable of measuring the ground reaction forces in the stance phase of the gait cycle, by means of an instrumented insole with force sensing resistors strategically placed on the sole of the foot, an electronic device allows processing and transmit this information via Bluetooth to the control system. The second is a semiactive actuator, which has inside a magnetorheological fluid, highlighting its ability to modify its damping force depending on the intensity of the magnetic field that circulates through the MR fluid. It is regulated by a Proportional Derivative (PD) controller system according to the values of plantar pressure measured by the insole. The third component is a mechanical structure manufactured by 3D printing, which adapts to the morphology of the human leg. This exoskeleton is designed to support the forces on the knee controlling the action of the magnetorheological actuator by ground reaction forces. The purpose of this assistance system is to reduce the forces applied to the knee during the gait cycle, providing support and stability to this joint. The obtained experimental results indicate that the device fulfills the function by reducing 12 % of the impact forces on the user's knee.

Keywords: knee orthotic, MR damper, smart insole, PD control, GRF

OPEN ACCESS

Edited by:
Irfan Hussain,
Khalifa University,
United Arab Emirates

Reviewed by:
Felix Weber,
Maurer, Germany
Solomon Seid,
Ethiopian Defence University, Ethiopia
Xiaomin Dong,
Chongqing University, China
Hemantha Kumar,
National Institute of Technology,
Karnataka, India

***Correspondence:**
Paola A. Niño-Suárez
pninos@ipn.mx

Received: *05 October 2021*
Accepted: *14 March 2022*
Published: *30 May 2022*

Citation:
Alvarado-Rivera D, Niño-Suárez PA and Corona-Ramírez LG (2022) Semiactive Knee Orthotic Using a MR Damper and a Smart Insole to Control the Damping Force Sensing the Plantar Pressure. Front. Neurorobot. 16:790020. doi: 10.3389/fnbot.2022.790020

INTRODUCTION

Knee injuries are one of the most common problems in the population, mainly injuries in soft tissues such as ligaments, these can suffer partial or total ruptures. Then, it is necessary to use systems that can offer support and stabilization in this joint during rehabilitation process, the most common are orthoses.

A knee orthosis is an orthopedic device exerting a therapeutic or preventive effect on this joint, reducing, or rehabilitating injuries to the ligaments, mainly caused by trauma that represents a disruption in the balance and mobility of the individual who suffers them (Nordin and Frankel, 2013). The development of orthotic devices has had an important growth in recent years, incorporating new elements that allow the user to recover in less time, in addition to offering a better adaptation to the movements when walking. The semiactive lower limb orthoses (SALLO) are one of the more studied options, this type of device is obtained by incorporating elements such

as a magneto-rheological (MR) actuator to control the movement of the orthotic device and provide support to the knee joint during flexion and extension movements.

Based on the principles of mechatronics, where mechanical, electrical, and computational systems are integrated to develop a semi-active lower limb orthosis (SALLO), this system was developed which considers sensorimotor function. The objective of the SALLO presented in this article is reduce the forces on the knee is subjected during the gait cycle, controlling the damping force of a MR actuator, providing support to the structure coupled to the knee. The damping force is controlled by regulating the magnetic field flowing through the MR fluid, setting a relation between the input current and the ground reaction forces (GRF) measured by the instrumented insole.

The results obtained by carrying out different experiments with a healthy user to evaluate the efficiency of the insole during the gait cycle, indicated that the data acquired can represent the ground reaction forces since these information present changes depending on the position of the foot and contact with the ground. Similarly, the function of the orthosis is giving support of the knee joint, regulating the forces that it must withstand during rehabilitation processes or as an assistive device in the lower limb when the individual suffers knee injuries, was verified by using the orthosis with healthy subjects. At this time, the medical protocol required to perform experiments on subjects suffering from specific injuries to the knee joint is being prepared.

Section Overview of Related Work from this article presents the state of the art in the development of semi-active orthotics and GRF measurement insoles; Section Materials and Methods describes the stage design of the developed orthosis; In the Results Section, the data obtained from the experiments carried out at each of the stages of the system and the integrated system are analyzed. And in the Conclusions Section the benefit of incorporating MR actuators in the design of orthotic devices and the importance of acquiring GRF signals and using them for the control of the orthosis operation, considering the sensorimotor effects in the design, implementation, control, and use of portable robotic devices is discussed.

OVERVIEW OF RELATED WORK

The development of prototype knee orthoses has been aimed at reducing the stresses to which this lower limb joint is subjected. To this end, in recent years various investigations have proposed using additional devices to conventional orthoses to limit the forces that interact in the knee, such as MR actuators, in addition to incorporating pressure sensors to measure GRF and thus controlling the damping force affecting the knee.

One of the first works reporting the development of a LLO is presented in Zite et al. (2006), where an MR damper is incorporated into the structure of the orthosis, this device was selected for its response speed, weight, and their relatively low energy consumption. According to the results, the authors indicate the benefits and ease use of an MR actuator for controllable orthosis design are remarkable. In Chen and Liao (2006), an exoskeleton is proposed using an MR actuator with a controllable torque, which acts as a brake or clutch according to the working states defined by the knee flexion angle and the ground reaction forces, using these data the actuator on the exoskeleton becomes more energy efficient. In Bulea et al. (2012), a mechanism was developed to assist people who have suffered some paralysis in the lower limb, which integrates an MR actuator that regulates the flexion movement of the knee from a variable impedance control technique, which incorporates a mechanism of four bars providing the torques required to perform leg movements, the total weight of the orthosis is high, about 3.5 kg. The MR actuator used is LORD RD-8040-1, from which the characteristic curve was obtained, determining that the increase in current flow increases the damping force of the actuator. The mechanism was tested with injured people, showing that the proposed system serves as a brake against knee flexion movements, and allows knee movements under high loads. In the work developed by Guo and Liao (2009), the design of a knee brace is presented to support the mobility of people with motor limitations, its main function is to reduce the movement of the knee during the gait cycle, by controlling the torque on the mechanism from the configuration of the actuator MR. The results mentioned by the authors indicate that the MR actuator supports the torque generated on the knee during the gait cycle.

On the other hand, instrumented insoles have been developed for the measurement of ground reaction forces or GRF. These systems collect information on the pressures generated in the sole of the foot during the gait cycle. In the work published by Ngueleu et al. (2019), FSR sensors distributed over the sole of the foot are used to accurately count the user's steps. The advantage of this type of system is the portability and the ability to generate an analysis of the gait cycle, as in the work developed by Tabrizi et al. (2018), wherein the development of an intelligent insole incorporating FSR sensors, a Bluetooth module, a battery, an accelerometer, as well as a microprocessor, to detect force peaks depending on the area of the foot that makes contact with the ground. In a similar way in Fang et al. (2017), an insole composed of eight FSR sensors distributed mainly in the forefoot, midfoot, and heel is presented, with this configuration a graph relating the force with which the sole of the foot contacts the ground is obtained.

According to the state of the art, developing a semiactive orthotic system to reduce the forces on the knee is a viable option to bring support in this joint during walking and other daily activities. However, few studies consider the sensorimotor effects of the joint and the musculoskeletal system associated with the lower limb in the design, implementation, control, and use of these automated orthotic devices.

In this proposal, by integrating a magneto-rheological actuator to the orthosis to regulate the damping force, avoiding that the knee suffers an overstrain when it is not able to support the weight of the user, and incorporating a system to measure the GFR during the gait cycle to evaluate the data necessary to control the response of the MR damper, a SALLO was obtained that self-regulates its damping according to the phase of the user's gait cycle and their physical-motor conditions.

MATERIALS AND METHODS

One of the main daily activities in humans is walking, due to its complexity, specific characteristics of the activity carried out by the extremities of the body have been identified during the gait cycle. The gait cycle is mainly divided into two phases, the stance phase, and the swing phase. During the stance phase, the contact of the foot with the ground is contemplated, while this action is carried out the leg and in particular the knee is subjected to high forces, according to (Meireles et al., 2017) these forces reach a value three times greater than the weight of a person. In the swing phase GRF is not recorded.

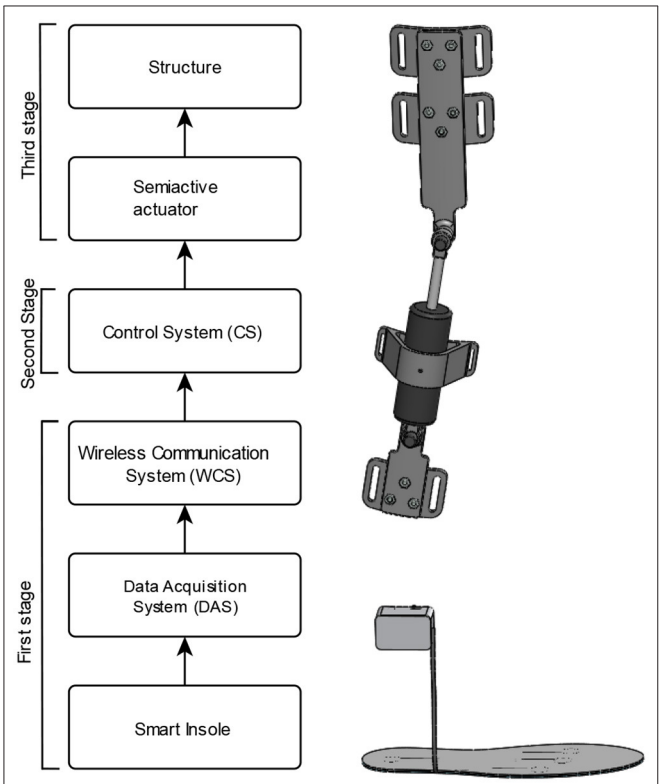

FIGURE 1 | Composition of the orthosis using a semi-active actuator.

The knee is the most complex joint that exists in the human body, it is a biarticular structure composed of the tibiofemoral joint and the patellofemoral joint. In addition, it is one of the joints performing the most work during the locomotor activities, such as walking, sitting, or getting up. Injuries to the knee ligaments cause joint pain and instability, causing the loading forces on the knee increase, causing decompensation during the gait cycle. These injuries are related to sudden movements during some physical activity, such as running, changing direction quickly, in the fall after a jump or a collision directly on the knee. Depending on the degree of the injury is the time taken for recovery, the recovery time from an injury to these tissues can range from 2 weeks and extend to 66 months. To recover from this injury, the support of therapeutic systems such as orthoses is necessary.

The orthosis system presented in this work aims to reduce the forces to which the knee is subjected during the gait cycle. For its design, the methodology "V Model," presented in Forsberg and Mooz (1992) was used. As a result of the proposed methodology, in **Figure 1**, the stages that make up the developed orthosis are observed, the first stage is the instrumented insole with its data acquisition system that is responsible for obtaining, sending and processing the GRF generated in the sole of the foot of the user during the gait cycle; the second is the MR actuator control system and finally the structure that is operated by the MR actuator is observed and supports the knee joint, engaging the user's leg. The GRF obtained vary with respect to the gait cycle, this due to the movements of the lower limb, the control

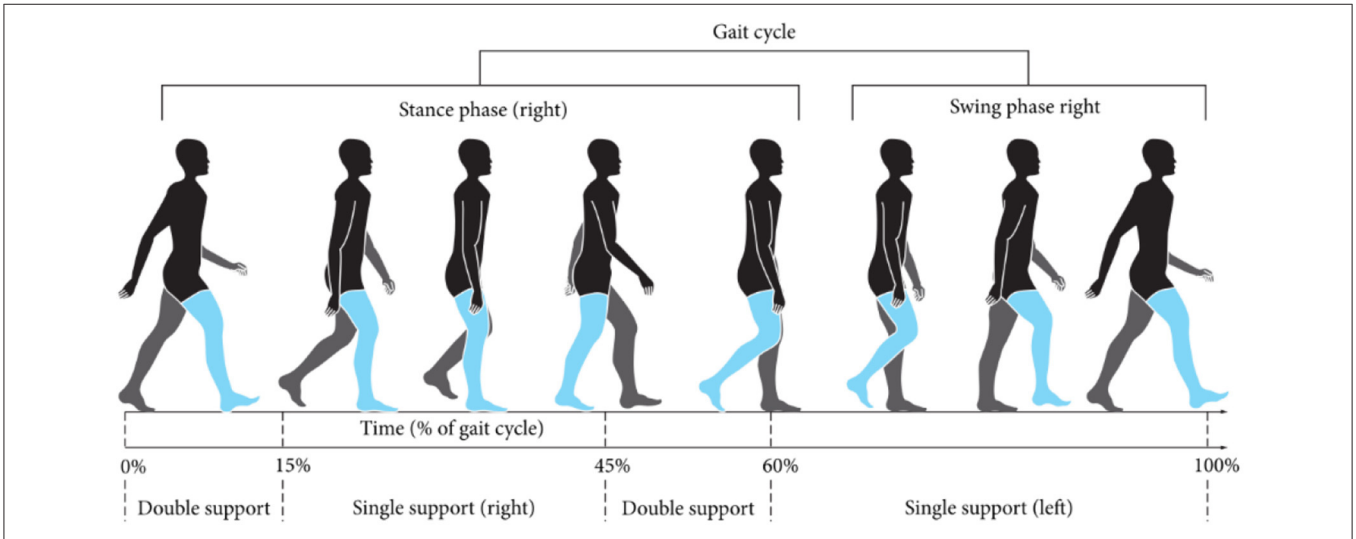

FIGURE 2 | Human gait cycle (Cheze et al., 2019).

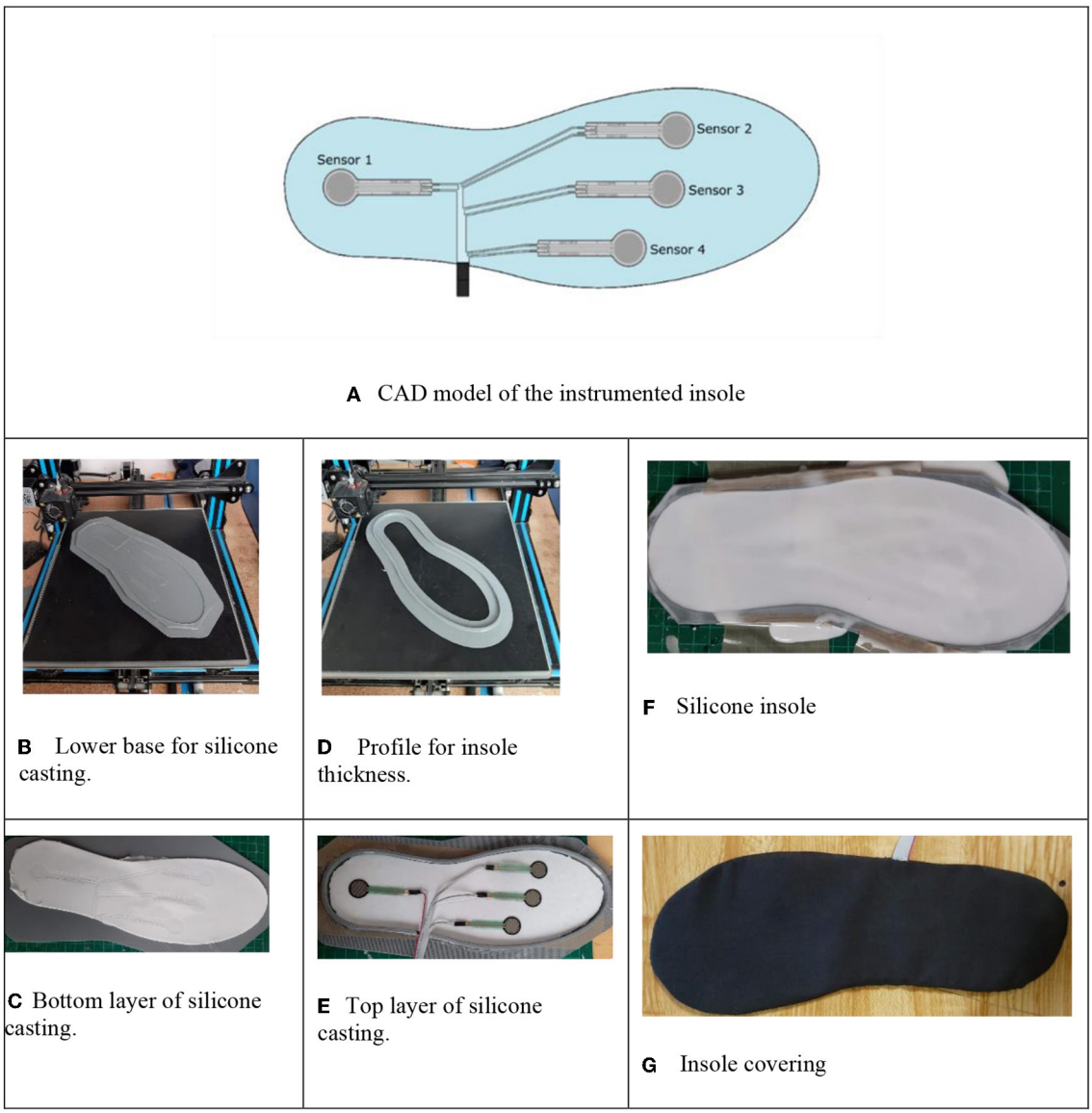

FIGURE 3 | Instrumented insole, CAD design, and manufacturing. **(A)** CAD model of the instrumented insole. **(B)** Lower base for silicone casting. **(C)** Bottom layer of silicone casting. **(D)** Profile for insole thickness. **(E)** Top layer of silicone casting. **(F)** Silicone insole. **(G)** Insole covering.

system uses these characteristics to vary the input current that reaches the MR actuator. In this way, when the GRF increases, the damping force of the actuator also increases, that means, the damping values of the system adapt according to the user's cadence, allowing control of the forces to which the knee is subjected, during different motor activities.

In the next sections will be described each stage of the SALLO developed as shown in **Figure 1**.

Insole for GFR Measurement

When analyzing the human gait cycle, it is observed that the stance phase lasts for ∼60% of the total cycle, while the remaining 40% corresponds to the take-off phase (Perry, 2010). Each phase in turn is subdivided into shorter periods, according to the movements made by each leg when taking a step. In **Figure 2,** the contact points of the foot change during the gait cycle, as does the value of the pressure exerted by each part of the foot on the ground, is observed (Muñoz-Organero et al., 2017). To measure these GFRs during the gait cycle, a flexible and lightweight instrumented insole was developed, made of silicone, which is placed inside the user's footwear. Inside the insole, four resistive force sensors, FSR, were located to measure the variation of force that exists in different areas of the foot during the gait cycle.

The sensor distribution on the insole were defined from the foot areas wherein the larger part of the GFR during the gait cycle are concentrated according to Muñoz-Organero et al. (2017), as observed in **Figure 3A**. The first contact is made on the heel, depending on the cadence when walking, the rest of the foot

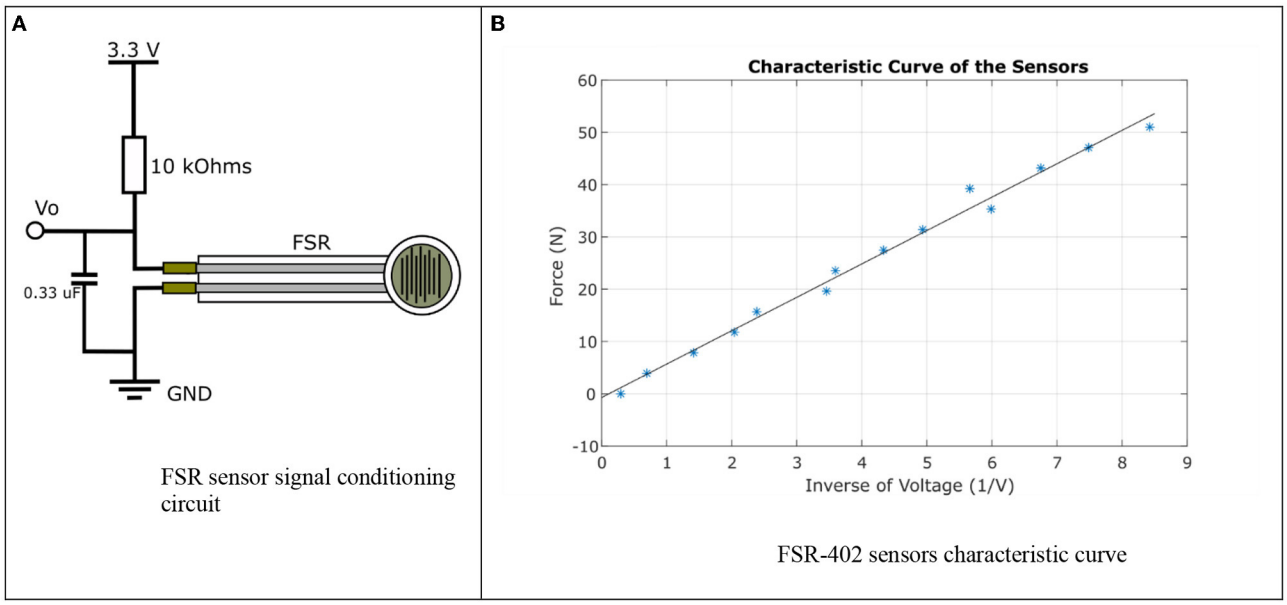

FIGURE 4 | FSR sensors characterization. **(A)** FSR sensor signal conditioning circuit. **(B)** FSR-402 sensors characteristic curve.

is gradually placed on the ground. Before starting the swing phase, it is on the tip of the foot where most of the GFRs are concentrated. From this analysis, the distribution of FSR sensors in the insole was made, as seen in the CAD model made in SolidWorks® 2016, presented in **Figure 3A**. FSR sensors vary their resistive value because a pressure on their contact area (Duarte, 2018) which is why these were selected for the development of the insole.

The fabrication of the insole follows the next process; first the deposition of the bottom layer, a base was printed by additive manufacturing that allowed to identify the position of the sensors, showed in **Figure 3B**. The first layer of silicone was poured, in a ratio of 60 g of silicone to 3 g of coagulant in **Figure 3C** is observed how the position of the sensors were marked on the silicone. A profile with a thickness of 5 mm was printed by additive manufacturing to contain the cast of the remaining silicone in **Figure 3D**, over the first layer of the insole and the sensor array are placed on the profile (**Figure 3E**). The sensors are covered with a second layer of 60 g of silicone, reaching the desired thickness (**Figure 3F**). The casting is carried out gradually to avoid the formation of air bubbles, which would cause errors in the reading of the sensors. Finally, a layer of cotton cloth is placed over the silicone, to give the appearance of a common insole, greater comfort, and ergonomics to the user (**Figure 3G**).

Sensors for GFR Measurement

Force sensitive resistor FSR 402 were selected for their size, operating range, and ease of implementation. According to its technical specifications, the sensor exhibits an approximately linear behavior when referring to its conductance. To characterize the sensor, an experiment was designed, where an FSR sensor was covered with silicone, a load was collocated on the circular area, this weight varied from 0.4 to 5.4 Kg, with 0.4 Kg increments. For each mass, 30 sensor readings were obtained through the output voltage of the conditioning stage observed in **Figure 4A**. The voltage divider implemented as a signal conditioning system allowed the sensor to reach a sensitivity of 0.8 mV/N. Additionally, an analog low pass filter was incorporated to eliminate white noise caused by the electrical system.

The statistical analysis of the data obtained was performed and the average behavior of the sensor was plotted in **Figure 4B**, where the horizontal axis corresponds to the inverse of the voltage and the vertical axis to the applied force.

From the graph in **Figure 4B**, an approximately linear mathematical model of the sensor was obtained, a first order polynomial presented in (1), where F is the resultant force to apply a load on the sensor and V_o is the inverse of the voltage measured.

$$F = 6.3841\,V_o - 0.7007 \tag{1}$$

Data Acquisition System

A data acquisition system (DAS) was designed to send the information acquired by the sensors to the MR actuator control stage, its block diagram is presented in **Figure 5A**. In **Figures 5B,C**, the hardware architecture of the DAS and the PCB card that designed to integrate surface mount device SMD, to obtain a reduced-size DAS module, is presented.

The data obtained by the DAS is sent via Bluetooth to any digital device storing it in a text document and can be graphed using a mobile application.

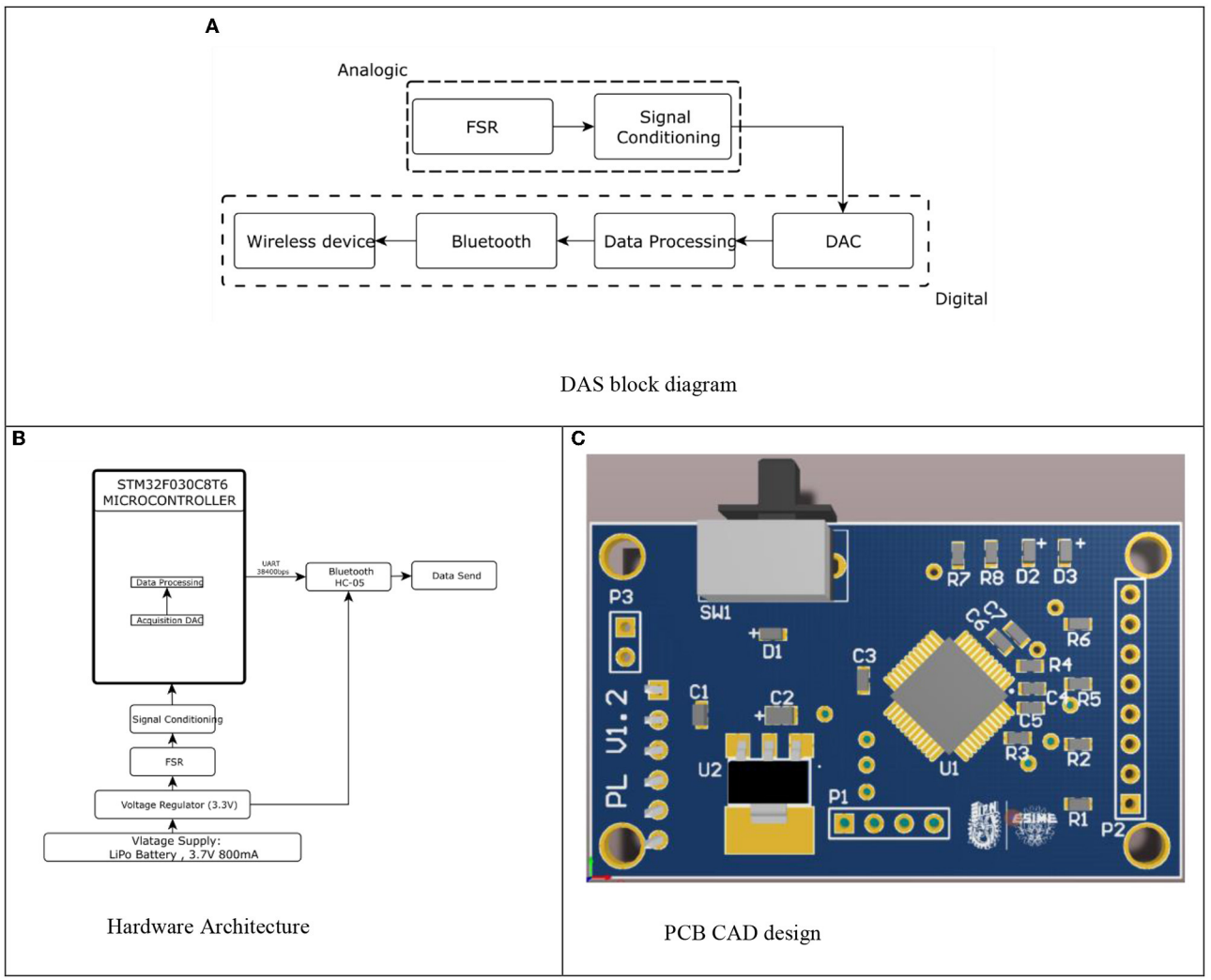

FIGURE 5 | Data acquisition system. **(A)** DAS block diagram. **(B)** Hardware Architecture. **(C)** PCB CAD design.

Instrumented Insole Validation

Experiments were carried out to verify and validate the operation of the insole with a healthy user 1.8 m tall and 80 kg weight, in a closed room with a temperature of 25°C. The test subject walks 2.5 m, which according to his height and cadence represents a complete cycle of the gait. For the experiment, 20 tests were carried out with the same individual, the data obtained during the experiment was plotted using MATLAB® 2018 software. In **Figure 6A**, graphs plotted in the software are observed with the data of the voltage variation obtained in each sensor during a gait cycle, without digitally processing them. The normalization equation given in (1) was applied to the data obtained, the results from the experiment were averaged for each of the sensors, on the horizontal axis the time is indicated in seconds, while the force value in Newtons is indicated on the vertical axis, a horizontal axis was added referring to the percentage of the gait cycle.

From the **Figure 6A**, the contact time of each part of the foot was determined, considering that the forces are only present during the stance phase of the gait cycle, because at this period there is a contact between the ground and the foot. In the graph corresponding to sensor 1, the stage called **first support** is being carried out, where the heel contacts to the ground supporting most of the body's weight for an instant, it can be seen how the force grows suddenly and then descends gradually to start the next stages when the foot contacts the ground. In the subsequent graphs corresponding to the sensors located in the anterior part of the foot (2, 3, 4), the part of the phase called **plantar support** is carried out, this is observed when the force in the three remaining sensors changes gradually, until reaching its maximum point (**terminal support**) when the heel is completely separated from the ground, finally, it is observed how instantly the force decreases, until it reaches a minimum value (**take-off** phase), ensuring that the foot has not contact with the ground starting the swing phase of the gait cycle.

The average of the GRF was obtained in (2), using the insole and the mathematical model for the sensor

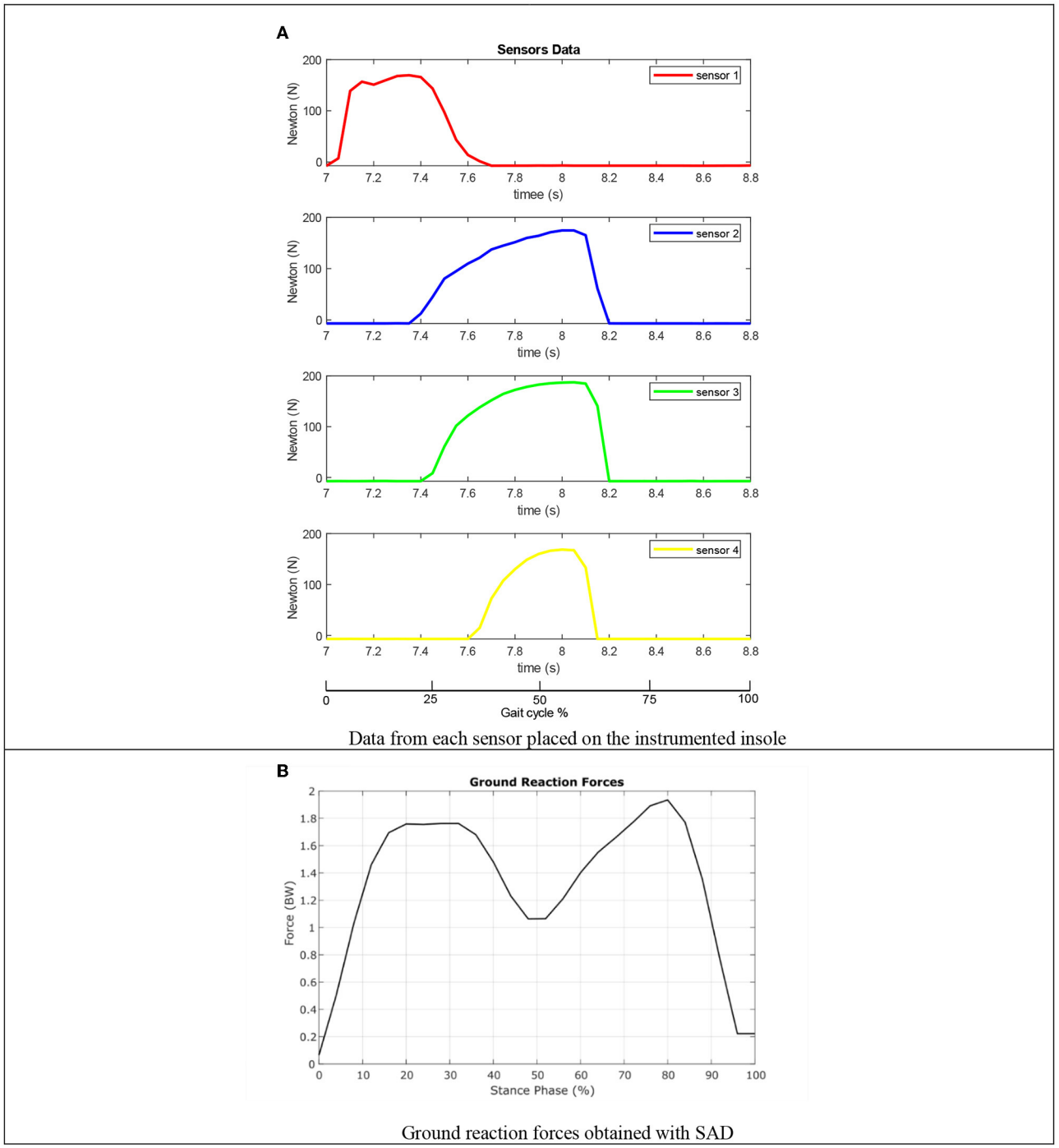

FIGURE 6 | Data processed using the DAS. **(A)** Data from each sensor placed on the instrumented insole. **(B)** Ground reaction forces obtained with SAD.

given in (1),

$$GRF_v = \frac{1}{p} \sum_{i=1}^{p} F_i(t) \quad (2)$$

Where GRF_v are average of the vertical ground reaction forces, p is the number of samples measured by the DAS, and F_i are the force value of each FSR sensor. Using (2) the graph in **Figure 6B** was obtained, where the variation of the forces depending on the percentage of the stance phase of the gait cycle. By comparing the shape and data obtained from the graph with the data reported in

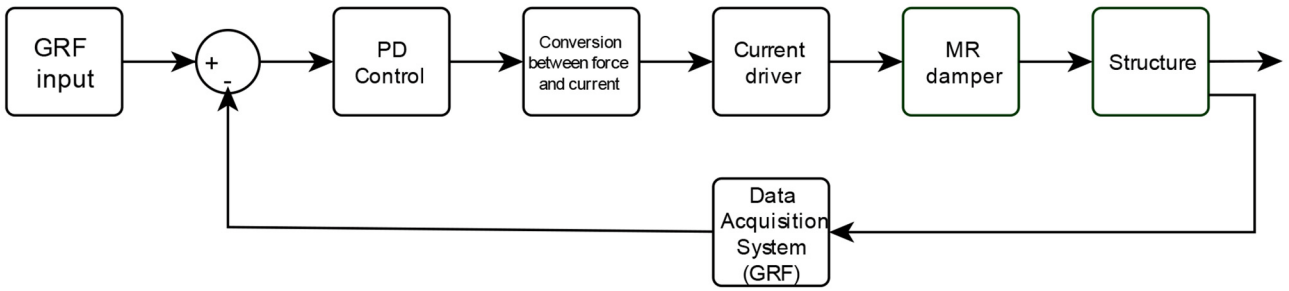

FIGURE 7 | Block diagram of the designed control system.

the literature (Nordin and Frankel, 2013) the correct functioning of the instrumented insole was verified.

The instrumented insole presents great usability and portability, it can communicate with different digital devices via Bluetooth, allowing it to be an independent system that can be used as a diagnostic tool for walking pathologies for the analysis of gait cycle measuring the GFR obtained. An additional application is described in the development of the semiactive knee orthosis presented in this article, sending GRF data to the control system to regulate the behavior of the MR damper and therefore of the orthosis.

In this way, it was verified that the information sent by the DAS are required by the control system to regulate the damping of the orthosis based on controlling the supply current of the MR actuator.

MR Actuator Control System

For the design of the control system is necessary to obtain a model that describes the function of each component of the orthosis, explaining the interconnection between the DAS, the controller designed and the change of damping force on the MR actuator (Weber, 2015). The control problem is to regulate the damping force of the semiactive damper from GRF measured by the DAS to protect the knee from forces to which it is subjected during walking. The plantar pressures regulate the current flow that reaches the MR damper, consequently, depending on this variation, the damping force of the actuator is increased or decreased, so we can say that the value of the damping force is directly related to the value of ground reaction forces and therefore depends on the characteristics of the gait cycle of each user, in **Figure 7** the block diagram of the designed control system is presented.

SALLO Model

This knee orthosis prototype incorporating an MR damper can be modeled according to Ahmadkhanlou (2008) as a Single Degree of Freedom (SDOF) system, considering the hysteresis behavior of the MR damper adding a spring mass system in **Figure 8A**, the model reacts to an input signal, which in this case corresponds to the movements generated in the knee during the gait cycle, or when performing daily activities.

The system presented in **Figure 12**, is modeled through the analysis of forces that interact in each component, in such a way that Equation (**3**) is obtained.

$$F_r = -F_{k_p} - F_{MR} \tag{3}$$

Where F_r is the resultant force of the system, and F_{kp} is the force performed by the leg muscles and F_{MR} is the damping force of the MR actuator (4), the dynamic model given in (5) is obtained,

$$m\ddot{x}_m = -k_p\,(x_m - x_b) - F_{MR} \tag{4}$$

$$\ddot{x}_m(t) = -\frac{k_p}{m}\left(x_m(t) - x_b(t)\right) - \frac{F_{MR}(t)}{m} \tag{5}$$

Where $\ddot{x}_m$ is the acceleration of the system, x_m and x_b are the positions of the system before the input signal, and F_{MR} is considered as the force due to the behavior of the damper.

MR Damper Model

Inside the SDOF model a MR actuator with a rheological fluid is included. A fluid with this property can modify its mechanical properties according to the magnetic field applied to it, which oppose a movement causing the activation of the piston when exceeds certain threshold. Specifically, magnetorheological fluids contain microscopic particles with some ferromagnetic material, when these particles are exposed to a magnetic field, this fluid changes its resistance, converting the behavior of the fluid to a semi-solid material and in the absence of the magnetic field (Russo and Terzo, 2011), it returns to being a liquid. These ferromagnetic particles orient themselves when there is interaction with an electromagnetic field. The control of these actuators is complex due to their behavior with hysteresis.

In the design of this orthosis, the MR RD-8040-1 actuator from LORD Corporation® was selected, various mathematical models have been reported in the literature to identify the behavior of this device, including the model developed in Wen (1976), where the behavior of the damper as a classic spring and damper system is considered adding the hysteresis action (**Figure 8B**).

The parametric Bouc-Wen model is used because its present low computation cost, and simplest implementation on embedded systems (Sapinski and Filús, 2003). According to the diagram in **Figure 8**, the damping force of the MR damper is described in (6)

$$F_{MR} = F_{k0} + F_{c0} + h(z) \tag{6}$$

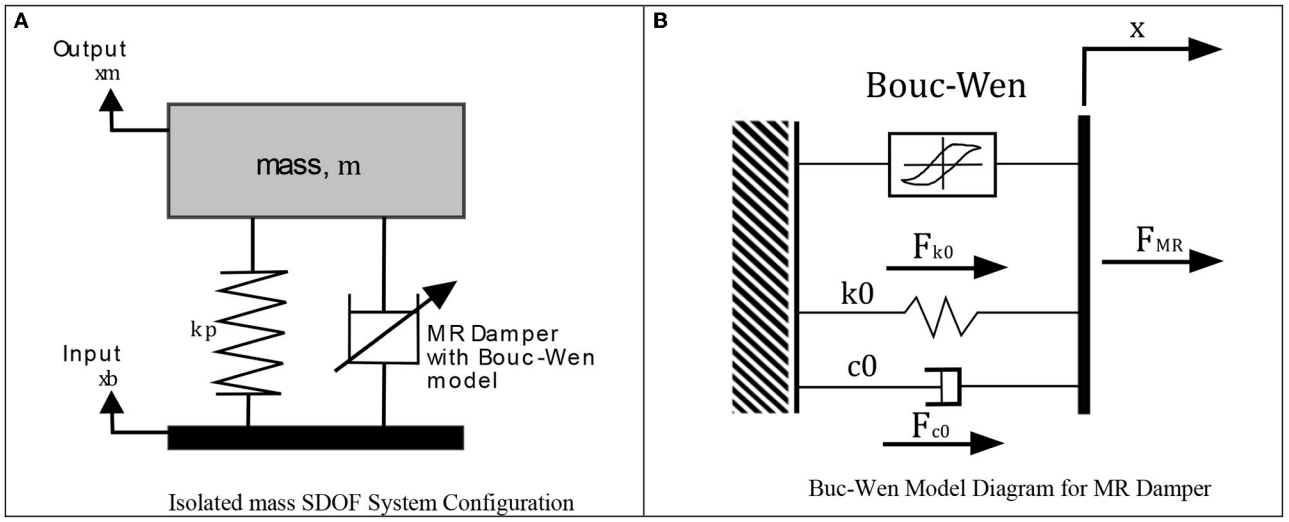

FIGURE 8 | Diagrams for the configuration of semiactive orthosis. **(A)** Isolated mass SDOF system configuration. **(B)** Buc-Wen model diagram for MR damper.

Where the term F_{MR} presents the summatory forces, due de the spring force F_{k0}, and the damping force F_{c0} generated by the displacement of the actuator piston, whereas $h(z)$ is a function that depends on the displacement of x, where z is an evolutionary variable that contains the characteristics of the behavior with hysteresis of the system, the dynamic equations of the MR actuator are presented in (7) and (8),

$$F_{MR} = c_0\dot{x} + k_0(x - x_0) + \alpha z \tag{7}$$

$$\dot{z} = -\gamma |x| z |z|^{n-1} - \beta\dot{x} |z|^n + A\dot{x} \tag{8}$$

Where c_0 represents the viscous damping coefficient; k_0 the stiffness coefficient due the accumulator; x_0 is the initial displacement; α presents the ratio of the yield value; z is the variable displacement with hysteresis; the parameters γ, β, and A control the discharge linearity; the parameter n is the coefficient of smoothness of the curve.

To define the parameters of the previous equations in Priya and Gopalakrishnan (2016), an experiment was developed specifically for the RD-8040-1 damper, using the Bouc-Wen model and the equations representing the variation of the intensity of current that flows toward the coil of this device, the variables α (9), c_0 (10), and k_0 (11) were modified.

$$\alpha(u) = \alpha_a + \alpha_b u \tag{9}$$

$$c_0(u) = c_{0a} + c_{0b} u \tag{10}$$

$$k_0(u) = k_{0a} + k_{0b} u \tag{11}$$

Where u is obtained from the input current I (12).

$$\dot{u} = -\eta(u - I) \tag{12}$$

Where η is a variable related to the response of the actuator depending of current.

Figure 9A is observed the block diagram where is implemented the simulation of the MR actuator behavior, using MATLAB® R2018 and its SIMULINK® toolbox, to identify the damping force of the semiactive damper as a function of the variation of current.

To simulate the piston displacement of the damper, a sinusoidal signal with an amplitude of 0.015 m at a frequency of 3 Hz (like walk at 1.5 ms^{-1}), and a current value of 1 A, was used as the desired piston displacement. The simulation time is 2 s, resulting in two cycles of the input signal. In **Figure 9B**, the simulation results are presented, in the upper graph the force against time is observed, the force reaches a peak value of ±1,149 N. In the lower right graph, the relation between the force and the piston displacement of the damper is observed and finally in the lower left figure the relation between the damping force and the response speed of the actuator is observed. The velocity was obtained from the numerical derivative of the displacement function, in this simulation is not considered the accumulator force of the MR damper.

With the results of the simulation, it is verified that the Bouc-Wen model adequately represents the behavior of the RD-8040-1 damper (Arias-Montiel et al., 2015), considering its response with hysteresis, as indicated by the manufacturer. The high response speed was observed before the change of the force value, it was also identified that with a current of 1 A damping forces >1,000 N are obtained, therefore its adequate performance is confirmed using a power supply of low amperage, which is one of the characteristics remarkable in this device and which is a requirement for the design of the proposed orthosis.

Using the MR damper model and Equation (7), a block diagram is generated in the SIMULINK® toolbox of the MATLAB® 2018b software to simulate the behavior of the SDOF, including the Bouc-Wen model. $m = 80$ kg and $kv = 22Nm^{-1}$ representing the mass and stiffness of the leg muscles identified

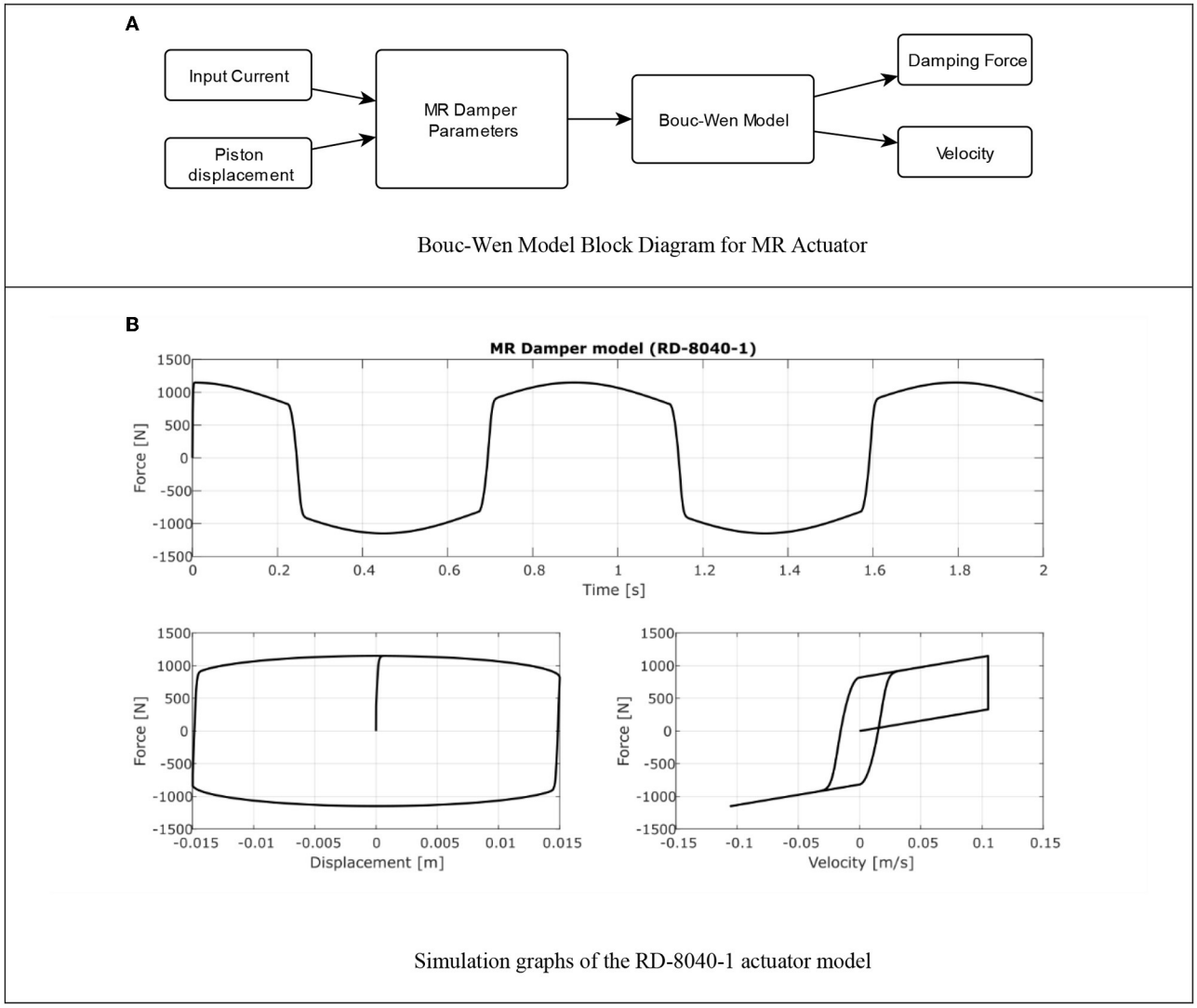

FIGURE 9 | MR Damper simulation. **(A)** Bouc-Wen model block diagram for MR actuator. **(B)** Simulation graphs of the RD-8040-1 actuator model.

in Kuitunen et al. (2011), were used as values in this experiment, this diagram is shown in **Figure 10A**.

In **Figure 10B**, three signals are presented from the simulation of the SDOF model and integrating the Bouc-Wen model for MR actuator without damping control. The signal in black x represents the input signal of the desired displacement of the piston, in this case a sinusoidal wave with a frequency of 3 Hz (like walk at 1.5 ms^{-1}) and an amplitude of 0.015 m is used, simulating small variation on the stem. The signal in blue color shows x_m which is the response of the system's displacement according to the input signal, when observing the signal, it is verified that at no time the system is stabilized. In red color the error generated between x and x_m is observed.

In such a way that, if it is desired to regulate the damping of the system, it is necessary to establish a control strategy to achieve that the error tends to zero.

Proportional Derivative Controller

The proposed objective for the control is to regulate the current required by the MR actuator to modify its damping force, for which a proportional derivative PD controller was used. The controller structure is presented in Equation (13), it is composed of two tuning variables K_p and K_v. Where K_p is the proportional gain of the control system, its main characteristic is based in that the position error is directly proportional, $\tilde{q}$; while K_v is the derivative gain which has a damping effect on joint velocity $\dot{q}$. The position error, $\tilde{q}$ is the difference between the desired position value and the obtained value $\tilde{q}(t) = q_d(t) - q(t)$. In **Figure 11A**, the block diagram is observed applying this type of controller to the system.

$$F_{PD} = K_p\tilde{q}(t) - K_v\dot{q}(t) \tag{13}$$

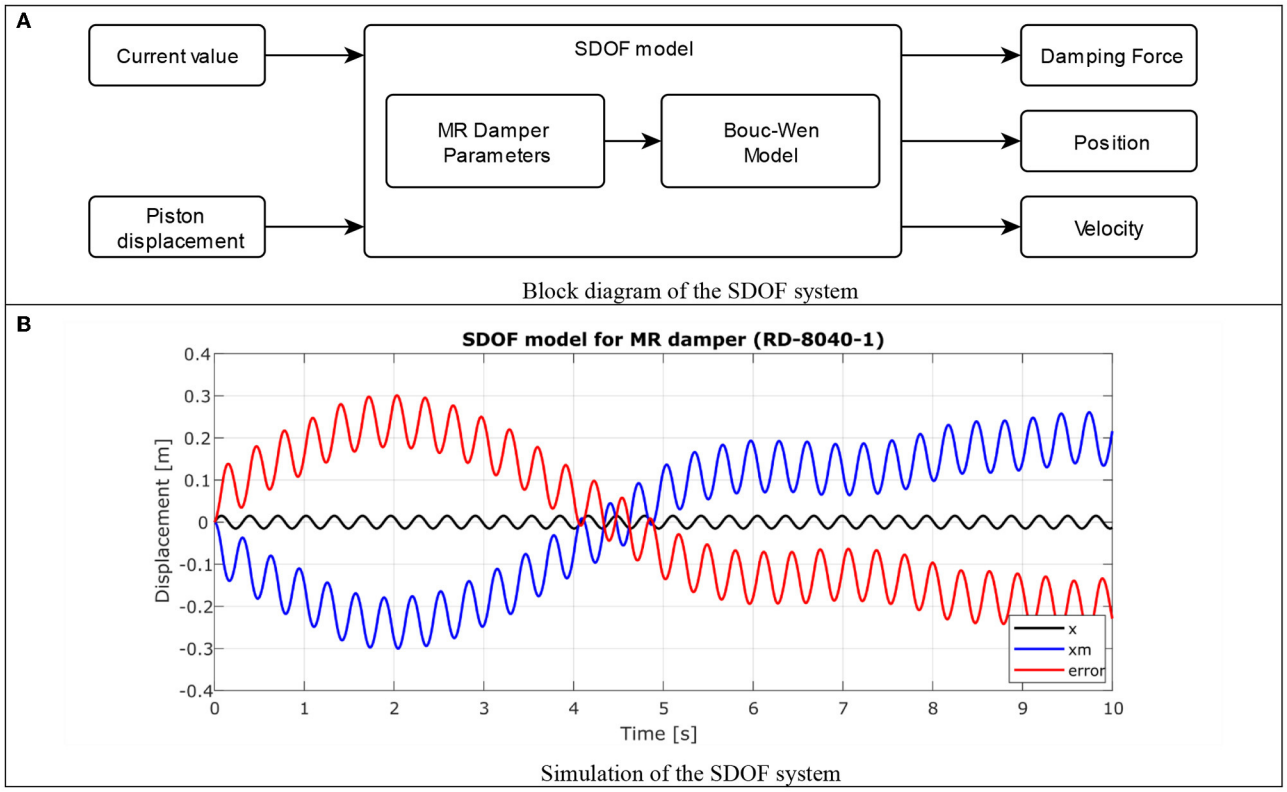

FIGURE 10 | Simulation of single degree of freedom system. **(A)** Block diagram of the SDOF system. **(B)** Simulation of the SDOF system.

Considering Equation (13), this controller is added to the simulation of the behavior of integrated system carried out in the SIMULINK® toolbox of the MATLAB® 2018b software (**Figure 11A**).

To verify the behavior of the PD controller, the input signal was initially modified by a step function, with the same amplitude of 0.015 m in **Figure 11B**, the response of the system with the controller is observed. The response obtained by the controller is the desired one, reaching the 15 mm of displacement by the stem in a time of ∼0.5 s, with an error that tends to cero, so the controller meets its objective.

For the second simulation, the signal described in the first simulation without control was used, a sinusoidal wave with a frequency of 3 Hz (like walk at 1.5 ms^{-1}) and an amplitude of 0.015 m in **Figure 11C**, the results are observed. The signal displacement x in black is followed by the current displacement x_m in blue with a signal delay due to the behavior of the damper, and the absolute error in red is around 5%. By applying the control strategy, the system response is stable according to the input signal with a minimum absolute error, in this way it is verified that the simulation control system does regulate the damping force of the semiactive actuator of the orthosis.

The designed controller adapts to the needs of the proposed system, considering the behavior of the MR actuator and the complexity of the integrated system, improving the damper's response according to the simulation executed. The simple structure of this controller allows its implementation on an embedded system where the computing capacity is relatively low.

Structure of the Prototype Knee Orthosis

For the design of the orthosis structure, different factors were taken into consideration, user requirements, easy manufacturing, accessible cost, etc. Additionally, the following specifications were considered:

1. The structure must support the MR actuator, whose mass is 800 g.
2. It should be ergonomically adapted to the contours of the leg, for a proper fit. The anthropometric measurements of the human body from the study presented in Ávila Chaurand et al. (2007) were considered, where the length of the lower limb for a man within a range of 20–40 years is 0.54 m for the thigh and 0.45 m for the leg.

The structure of the knee orthosis that incorporates a semiactive actuator was designed in the SolidWorks® 2016 CAD software, show in **Figure 12A**.

Three horizontal curved supports were designed which adapt to the morphology of the leg, in **Figure 12B** the upper support that is placed on the thigh is observed, the middle support observed (**Figure 12C**) is placed on the cylinder of the MR

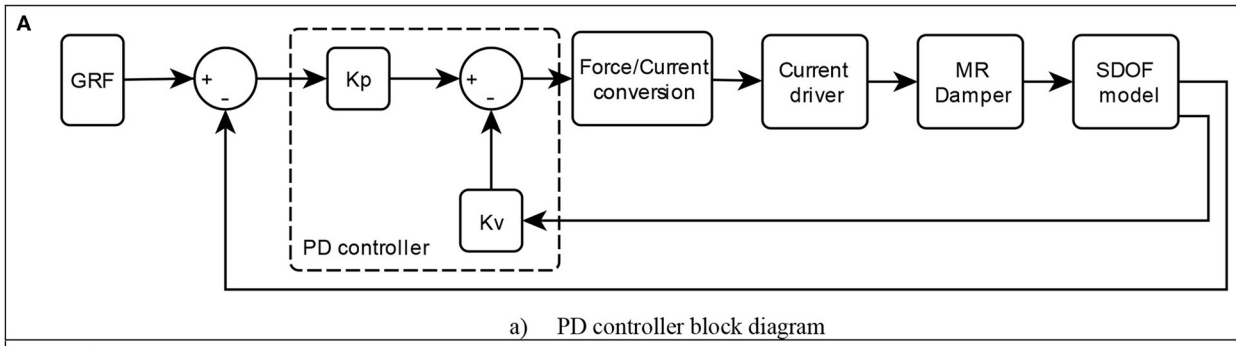

a) PD controller block diagram

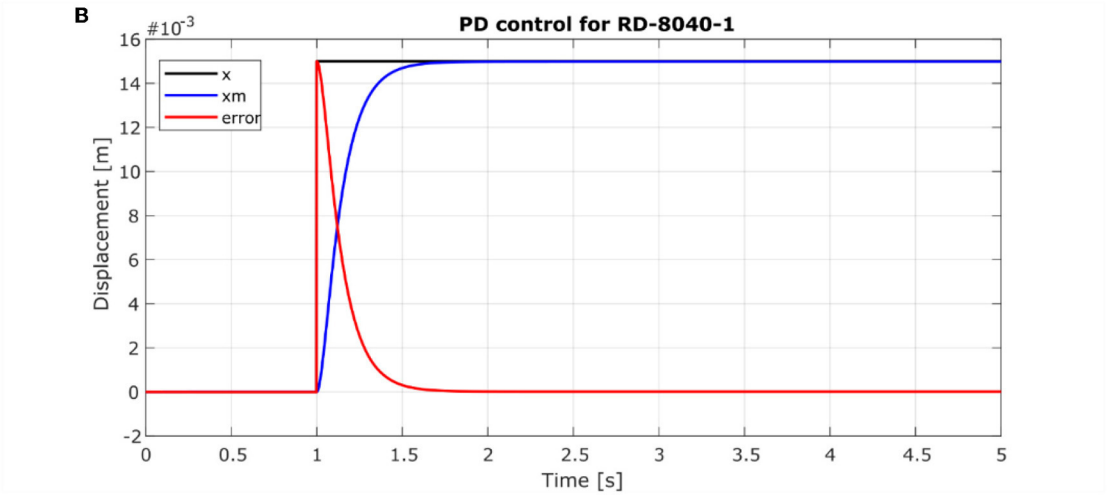

b) Response of the system with PD controller to the step function

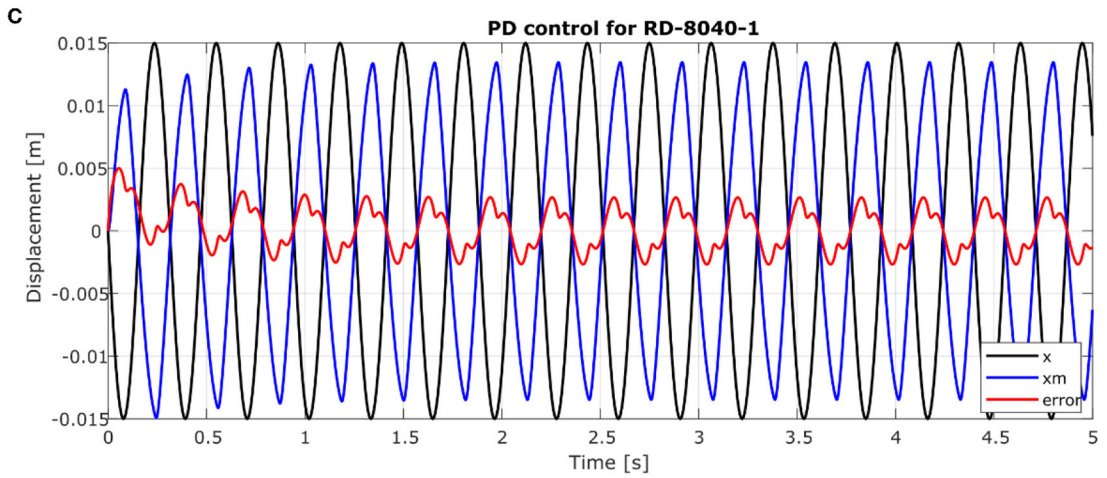

c) Simulation of the PD controller using a sinusoidal signal

FIGURE 11 | Proportional-derivative controller. **(A)** PD controller block diagram. **(B)** Response of the system with PD controller to the step function. **(C)** Simulation of the PD controller using a sinusoidal signal.

damper to give stability and location, and the third support, lower support (**Figure 12D**) is placed on the leg.

Two vertical support bars were designed, which aim to link up the two extremes of the MR actuator. The longest support (**Figure 12E**), links the upper part of the system, this bar is placed on the thigh and the extreme of the piston. The lower bar (**Figure 12F**), links the base of the actuator and positions it on the leg to secure the location of the device.

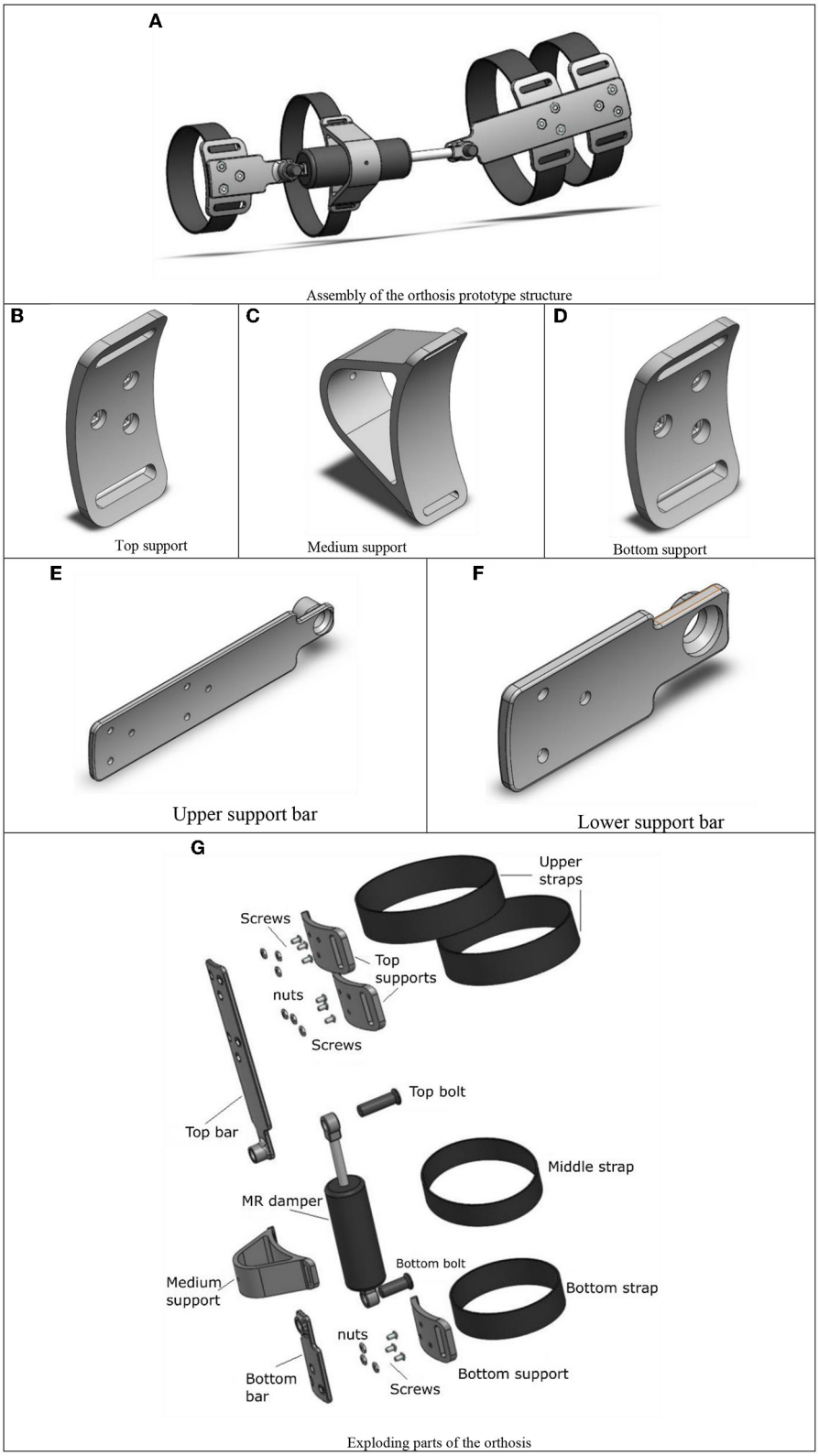

FIGURE 12 | CAD model of the semiactive orthosis. **(A)** Assembly of the orthosis prototype structure. **(B)** Top support. **(C)** Medium support. **(D)** Bottom support. **(E)** Upper support bar. **(F)** Lower support bar. **(G)** Exploding parts of the orthosis.

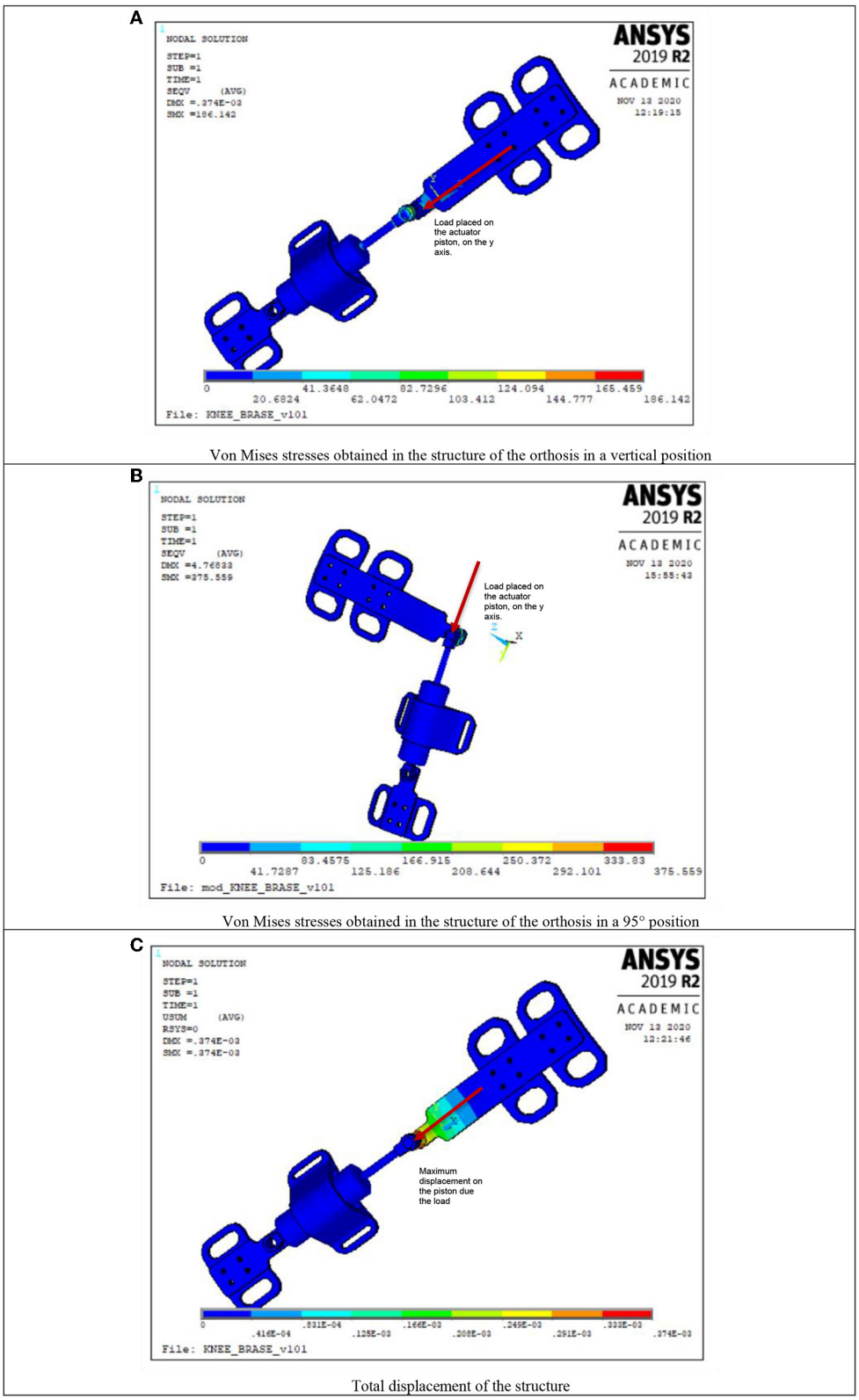

FIGURE 13 | Stress analysis on ANSYS®. **(A)** Von Mises stresses obtained in the structure of the orthosis in a vertical position. **(B)** Von Mises stresses obtained in the structure of the orthosis in a 95° position. **(C)** Total displacement of the structure.

In **Figure 12G**, each of the components of the orthosis structure is observed from an exploded, including four Velcro bands whose function is to adjust the orthosis to the user's leg.

To guarantee the safety of the user, several simulation experiments were carried out with the finite element method applied to each piece of the structure and its assembly, to determine if its structural components support the loads to which they are going to be bring under. These simulations allow to determine by the maximum displacements and von Mises stresses identify if the structure fails under a certain load.

The ANSYS® software in its 2019R version was used to simulate the conditions and considering the mechanical properties of the plastic material in which the structure was manufactured, this is a polymer named Polylactic Acid or PLA, which yields high mechanical properties in terms of traction, it also has biodegradable properties, while the MR actuator material is stainless steels 304. Importing the CAD model of the mechanism, into the ANSYS interface, adding the properties of the materials already mentioned and using 3D structural elements SOLID186, the meshing selected for each element applying a load of 800 N on the piston of the damper was performed, simulating the weight of a person of 80 kg, this point was selected because of the greatest stress supported, in addition, movement restrictions are placed in the locations where the screws were placed.

Several analyzes of the structure were carried out in different positions, especially the critical cases where the assembly supports the greatest stress. In **Figure 13A,** the results of the von Mises stresses generated during the simulation with the assembly at a 180° angle (simulating when the leg is fully extended) were presented. Similarly, in **Figure 13B**, the results of von Mises stresses with assembly of 95° (representing the knee flexion movement) were shown.

According to the results observed in **Figures 13A,B**, the von Mises stresses for the 180° angle are 186 N in the vertical position, while for the 95° assembly this value is 375 N, these values are under the yield stress of PLA which is 2.9 and 193 GPa for the stainless steel, ensuring that the operation of the structural components will not be compromised by this load. In **Figure 13C**, a maximum displacement of the structure is observed with a load of 800 N, which is only 0.37 mm.

The simulation results showed that the layout of the elements can support the efforts generated by an 80 Kg individual, considering that the manufacturing material is PLA. Once the design was validated, 3D printing was used to manufacture the components of the structure. Additive manufacturing is one of the processes that has revolutionized the visualization of prototypes, whose main peculiarity is to superimpose layers of material, and then take the desired shape, minimizing the time of processing. With the CAD models presented in **Figure 12G** each component was manufactured, using a CREALITY brand machine in its ENDER 3 model. The characteristics with which the pieces of the orthosis structure were printed, selecting a material density of 20% it is not a solid piece, since there are spaces between the layers of material, making the pieces lighter, but with high tensile strength. The measurements correspond to a scale 1 to 1, achieving a tolerance of 0.1 mm, considering the thermal expansion of the material. The printing was made following a tetrahedron pattern in a vertical direction, this due to the forces that interact in the system, avoiding a possible fracture within the components. In **Figure 14**, the printed parts and the assembly of the structure are observed from the generated model. The bands that adjust the location on the lower limb were manufactured with cotton cloth to avoid irritation on the skin, adding Velcro strips to adjust to the size of the user's leg, to link up the components standard screws was used.

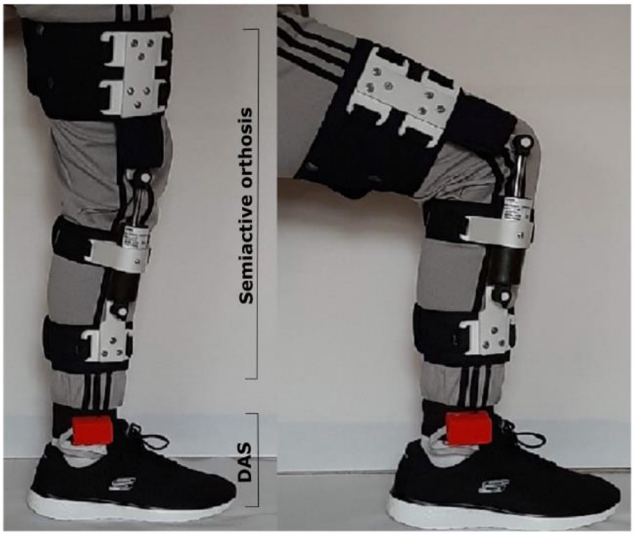

FIGURE 14 | 3D printed orthosis structure placed on the leg.

RESULTS

To validate the operation of the orthosis, it was carried out experiments with healthy users using the smart insole to measure the GRF and this data is sent to the control system to regulate the damping force to the MR actuator. Subsequently, an experiment was designed and executed to verify the behavior of the SALLO system in a healthy user, for this the GRF was measured in two cases; the first when the orthosis is utilized and the second the orthosis is not being utilized.

Experimental Validation of the Insole

To verify the behavior of the DAS integrated to the orthosis, an experiment was performed to determine the efficiency of this subsystem, the first part of this experiment contemplate a static analysis where the user stands for 4.5 s, consider that the user is 1.8 m tall and weighs 80 Kg. In **Figure 15A**, the graphs obtained using the MATLAB® 2018b software are observed after completing a series of samples, the data is plotted by averaging the values of all measurements, in black showing the ground reaction forces when standing, where the vertical axis corresponds to the forces in Newtons and the horizontal axis to time, the observed variations depend directly on the position of the user, the data indicates that the system in static mode tends to a value between

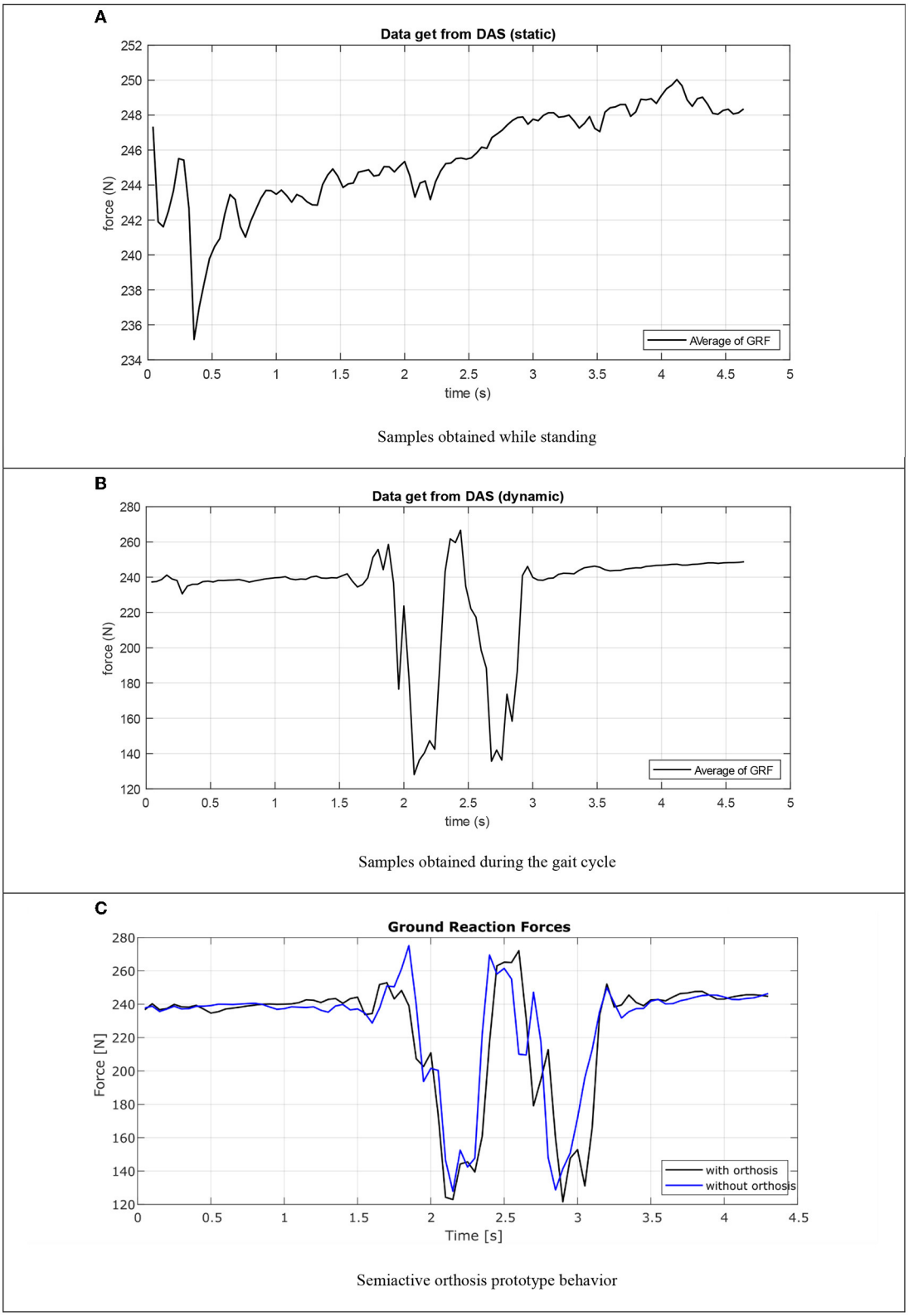

FIGURE 15 | Semi-active orthosis evaluation. **(A)** Samples obtained while standing. **(B)** Samples obtained during the gait cycle. **(C)** Semiactive orthosis prototype behavior.

TABLE 1 | Relation between GRF, current, and damping force.

GRF (*N*)	Current (A)	Damping force (*N*)
177.1405	0.16	255
185.9098	0.20	297
194.6792	0.24	340
203.4478	0.28	382
212.2178	0.32	425
220.9871	0.35	467
229.7565	0.39	510
238.5258	0.42	553
247.2951	0.46	595
256.0644	0.51	638
264.8338	0.54	680
273.6031	0.57	723
282.3724	0.61	765
291.1417	0.65	808
299.9111	0.69	851
308.6804	0.74	893
309.4520	0.78	936
318.2129	0.83	978
327.6972	0.88	1,021
336.4512	0.92	1,063
345.3688	0.96	1,106
354.7845	1	1,149

242 and 255 N after the user stabilization. **Table 1** showed the relationship between the three values of interest, the GRF measured by the data acquisition system, the value of the driving current, and the damping force on the semiactive actuator. These values are strongly related if the ground reaction forces increase the other two values also increase, in summary, the damping force value changes when the GRF changes depending completely on the characteristics of the human gait cycle.

The second experiment was carried out with the same test subject, but now the experiment consists of standing for 2 s and then taking a step and finally standing again for 2 s, the force values on this time gets averaged and plotted in black as seen in **Figure 15B** with the same axes. As in the static mode, once the user has stopped his movement, the measured forces are close to the mean value of 250 N. Considering the maximum and minimum values that the data acquisition system obtain from the measurement of ground reaction forces, a range of force values generated during the gait cycle ranging from 170 to 350 N was determined, in accordance with the information reported in the literature. It is observed that the response curve in both cases is also like the curves obtained in different works reported in the literature, where the systems use a greater number of sensors in the insole and longer processing time than that achieved with the DAS proposed in this work.

Validation of the SALLO Operation

The validation of the orthosis operation was carried out by setting up an experiment with a healthy individual weighing 80 kg and 1.8 m tall, in a closed room at room temperature. Where the individual walk distance of 2 m, which represents a complete gait cycle. The experiment begins by holding the standing position for a couple of seconds, then a full step is taken and finally it is returned to the initial standing position. The experiment was first performed on the user without wearing the orthosis and then the experiment was repeated using the orthosis.

In **Figure 15C**, GRF measurement in the individual's foot obtained with DAS is observed, the blue line represents the obtaining of data when the orthosis prototype is not used, while in the black line the GRF is plotted when the individual is wearing the semiactive orthosis prototype, the vertical axis represents the force evaluated in Newtons, while the horizontal axis measures the time in seconds.

The data from the DAS show that there is a decrease in the ground reaction forces when the SALLO prototype is used, compared to the data obtained when it is not used, the decrease is around 12%. This is because the orthosis is absorbing the forces when the individual uses the design prototype despite not suffering any injuries. It can be verified that the orthotic device fulfills the function of controlling the damping force on the semiactive actuator when the forces act on the knee during the gait cycle, as is showed in **Figure 15C**. It can be observed on the peaks where the force presents high values, for example, when the heel and forefoot contacts with the ground are made, in the graph without orthosis these peaks are higher and in the graph that represents the results when the orthosis the peaks are less pronounced, and the signal is softer. This implies that the MR actuator damping control does offer support to the knee, preventing it from being overstressed when performing daily activities such as walking.

Similarly, taking measurements on the controller signal, it was determined that the time delay that takes to modify current value for the MR actuator is <100 ms, considering that the measurements made during the gait cycle, where a step lasts between 1.5 and 2 s at a speed of 1.5 ms^{-1}, so there are 15–20 changes in the value of the current which are reflected in the damping force generated by the RD-8040-1 actuator.

CONCLUSIONS

According to the results obtained by experimentation, it was possible to design a functional prototype of a semiactive knee orthosis, which combines a structure that supports and adapts to the morphology of the leg with an MR actuator whose main function is to mitigate the forces supported by the knee increasing or decreasing its damping force by modifying the magnetic field inside the actuator, regulating the current flow according to a portable system for measuring the GRF of the user's foot embedded in an instrumented insole that goes inside the user's shoe. The system presents competitive advantages when comparing its operation with the prototypes presented in the literature, since sensorimotor effects are considered in the design from GRF data sent to the system allowing the regulation of the feed current to the MR actuator and consequently modifying its damping force depending on the period of the support phase of the gait cycle that is being executed. As a result, a decrease

in the reaction forces on the knee is observed, especially during the highest-pressure peaks, expressly during the landing on the ground of the heel and forefoot. The advantages are centered on the reduced size of the system, its autonomy of up to 3 h, a better resolution in the data acquisition when using a 12-bit ADC and the possibility of implementing the PD control in a reduced system. The software architecture developed allows modifications to improve the processing of the signal obtained from the sensors, such as adding digital filters without modifying the hardware. Additionally, a 12% reduction on the GRF, when the prototype is used, is showed, we can infer that the results can be replicating on a test subject with an abnormal gait, increasing their performance when walking.

DATA AVAILABILITY STATEMENT

The original contributions presented in the study are included in the article/supplementary material, further inquiries can be directed to the corresponding author/s.

AUTHOR CONTRIBUTIONS

DA-R, PN-S, and LC-R conceived, designed, performed the experiments, analyzed the data, and wrote the paper. All authors contributed to the article and approved the submitted version.

FUNDING

The present research has been partially financed by SIP project: 20221843, and by Consejo Nacional de Ciencia y Tecnología, CONACYT.

ACKNOWLEDGMENTS

The authors would like to thank Instituto Politécnico Nacional, CONACYT and SIP for the support provided. The authors would also like to thank to the reviewers for their constructive comments, which have greatly improved the quality of the manuscript.

REFERENCES

Ahmadkhanlou, F. (2008). *Design, Modelign and Control of Magnetorhelogical Fluid-Based Force Feedback Dampers for Telerobotic Systems*. Columbus, "OH: The Ohio State University".

Arias-Montiel, M., Florean, H., and Fransisco-Agustín, E. (2015). "Experimental characterization of magnetorheological damper by a polynomial model," in *International Conference on Mechatronics, Electronics and Automotive Engineering* (Oaxaca), 128–133.

Ávila Chaurand, R., Prado León, R., and González Muñoz, E. L. (2007). *Dimensiones Antropométricas de Población Latinoamericana: México, Cuba, Colombia, Chile*. Guadalajara: Universidad de Guadalajara, Centro Universitario de Arte, Arquitectura y Diseño, División de Tecnología y Procesos, Departamento de Producción y Desarrollo, Centro de Investigaciones en Ergonomía.

Bulea, T. C., Kobetic, R., Curtis To, S., Musa Audu, L., John Schnellenberger, R., and Triolo, R. J. (2012). A variable impedance knee mechanism for controlled stance flexion during pathological gait. *IEEE/ASME Trans. Mechatron.* 17, 822–832. doi: 10.1109/TMECH.2011.2131148

Chen, J., and Liao, W. H. (2006). "A leg exoskeleton utilizing a magnetorheological actuator," in *Proceedings of the 2006 IEEE International Conference on Robotics and Biomimetics* (Kunming), 824–829.

Cheze, L., Abid, M., Mezghani, N., and Mitiche, A. (2019). Knee joint biomechanical gait data classification for knee pathology assessment: a literature review. *Appl. Bionics Biomech.* 2019:7472039. doi: 10.1155/2019/7472039

Duarte, J. (2018). Methodology of calibration of FSR sensor for seat occupancy detection in vehicles. *Indian J. Sci. Technol.* 11, 1–7. doi: 10.17485/ijst/2018/v11i23/126554

Fang, Y., Cheng, X., Li, F., Sha, L., Zhao, W., and Kuang, S. (2017). "Development of a smart insole device for lower limb postoperative rehabilitation training," in *IEEE International Conference on Robotics and Biomimetics (ROBIO)* (Macao), 2699–2703.

Forsberg, K., and Mooz, H. (1992). The relationship of systems engineering to the project cycle. *Eng. Manage. J.* 4, 36–43.

Guo, H. T., and Liao, W. H. (2009). "Magnetorheological fluids based multifunctional actuator for assistive knee braces," in *Proceedings of the 2009 IEEE International Conference on Robotics and Biomimetics* (Guilin), 1883–1888.

Kuitunen, S., Ogiso, K., and Komi, P. (2011). Leg and joint stiffness in human hopping. *Scan. J. Med. Sci. Sports* 21, e159–e167. doi: 10.1111/j.1600-0838.2010.01202.x

Meireles, S., Wesseling, M., Smith, C., Thelen, D., Verschueren, S., and Jonkers, I. (2017). Medial knee loading is altered in subjects with early osteoarthritis during gait but not during step-up-and-over task. *PLoS ONE* 12:e0187583. doi: 10.1371/journal.pone.0187583

Muñoz-Organero, M., Parker, J., Powell, L., Davies, R., and Mawson, S. (2017). Sensor optimization in smart insoles for post-stroke gait asymmetries using total variation and L1 distances. *IEEE Sensors J.* 17, 3142–3152. doi: 10.1109/JSEN.2017.2686641

Ngueleu, A. M., Blanchette, A. K., Bouyer, L., Maltais, D., McFadyen, B. J., Moffet, H., et al. (2019). Design and accuracy of an instrumented insole using pressure sensors for step count. *Sensors* 19:984. doi: 10.3390/s19050984

Nordin, M., and Frankel, V. H. (2013). *Bases Biomechanical Musculoskeletal System*. España: Wolters Kluwer España.

Perry, J. (2010). *Gait Analysis: Normal and Pathological Function*. New Jersey, NJ: SLACK.

Priya, B. C., and Gopalakrishnan, N. (2016). Parameter Identification of long stroke and short stroke MR damper for its use in semi-active vibration control. *J. Instit. Eng.* 97, 405–414. doi: 10.1007/s40030-016-0182-y

Russo, R., and Terzo, M. (2011). "Modelling, parameter identification, and control of a shear mode magnetorheological device," in *Proceedings of the Institution of Mechanical Engineers, Part I: Journal of Systems and Control Engineering* (Naples: Department of Mechanics and Energetics; University of Naples Federico II), 549–562.

Sapinski, B., and Filús, J. (2003). Analisys of parametric models of MR linear damper. *J. Theor. Appl. Mech.* 41, 215–210.

Tabrizi, M. M., Mirzanejad, H., Fathian, A., Sharifnezhad, A., and Agheli, M. (2018). "Development of a totally embedded smart insole," in *International Design Engineering Technical Conferences and Computers and Information in Engineering Conference* (Quebec, QC: ASME), 1–5.

Weber, F. (2015). Robust force tracking control scheme for MR dampers. *Struct. Control Helath Monit.* 22, 1373–1395. doi: 10.1002/stc.1750

Wen, Y.-K. (1976). Method for random vibration of hysteretic systems. *J. Eng. Mech. Div.* 102, 249–263. doi: 10.1061/JMCEA3.0002106

Zite, J. L., Ahmadkhanlou, F., Neelakantan, V. A., and Washington, G. N. (2006). "A magnetorheological fluid based orthopedic active knee brace," in *SPIE Smart*

Structures and Materials + Nondestructive Evaluation and Health Monitoring (San Diego, CA).

Conflict of Interest: The authors declare that the research was conducted in the absence of any commercial or financial relationships that could be construed as a potential conflict of interest.

Publisher's Note: All claims expressed in this article are solely those of the authors and do not necessarily represent those of their affiliated organizations, or those of the publisher, the editors and the reviewers. Any product that may be evaluated in this article, or claim that may be made by its manufacturer, is not guaranteed or endorsed by the publisher.

Advantages of publishing in Frontiers

OPEN ACCESS
Articles are free to read for greatest visibility and readership

FAST PUBLICATION
Around 90 days from submission to decision

HIGH QUALITY PEER-REVIEW
Rigorous, collaborative, and constructive peer-review

TRANSPARENT PEER-REVIEW
Editors and reviewers acknowledged by name on published articles

Frontiers
Avenue du Tribunal-Fédéral 34
1005 Lausanne | Switzerland

Visit us: www.frontiersin.org
Contact us: frontiersin.org/about/contact

REPRODUCIBILITY OF RESEARCH
Support open data and methods to enhance research reproducibility

DIGITAL PUBLISHING
Articles designed for optimal readership across devices

FOLLOW US
@frontiersin

IMPACT METRICS
Advanced article metrics track visibility across digital media

EXTENSIVE PROMOTION
Marketing and promotion of impactful research

LOOP RESEARCH NETWORK
Our network increases your article's readership